

nature

ATOMIC WHIRLS IN MOTION

The dynamics of polar vortices in ferroelectric superlattices

Coronavirus

Can drug companies build a stockpile ready for the next pandemic?

Domino danger

Cascades of extreme events pose threat to sustainability goals

Follicular challenge

Stress hormones suppress hair growth in mice

Nature.2021.04.17

[Sat, 17 Apr 2021]

- [This Week](#)
- [News in Focus](#)
- [Books & Arts](#)
- [Opinion](#)
- [Work](#)
- [Research](#)

| [Next section](#) | [Main menu](#) |

Donation

| [Next section](#) | [Main menu](#) |

This Week

- **[The United States can help the IMF to rethink how it lends](#)** [13 April 2021]
Editorial • The funding powerhouse should encourage the International Monetary Fund to prioritize research into sustainable development.
- **[Funders, now is the time to invest big in COVID drugs](#)** [14 April 2021]
Editorial • Vaccine development has been a resounding success. But the medicine cabinet should have been better stocked.
- **[My most memorable mentors? Plants](#)** [13 April 2021]
World View • To nurture a thriving scientific community, look to the natural world for ideas.
- **[Melting glacier threatens to shove a mighty river off course](#)** [02 April 2021]
Research Highlight • Climate change could send Alaska's Alsek River into a new channel, with potentially far-reaching impacts for humans.
- **[A hurricane wrecks 'Monkey Island' — and leads to new monkey friendships](#)** [08 April 2021]
Research Highlight • Amid the devastation wrought by Hurricane Maria, rhesus macaques sought support from each other to endure hard times.
- **[Baby stars make it in a tough part of the Galaxy](#)** [06 April 2021]
Research Highlight • Star formation might be more resilient than astronomers had thought.
- **[Smoke from Australian fires turned up the heat in the southern sky](#)** [06 April 2021]
Research Highlight • The catastrophic wildfires of late 2019 and early 2020 triggered a lingering temperature rise in a section of Earth's lower atmosphere.
- **[What manta rays remember: the best spots to get spruced up](#)** [08 April 2021]
Research Highlight • Giant fish preserve a mental map of where cleaning fish provide the highest-quality pest removal.
- **[One screen, three images — some invisible in ordinary light](#)** [05 April 2021]

Research Highlight • A graphene-based device can display several images simultaneously using a range of wavelengths.

- **Want fresh results? Analysis of thousands of papers suggests trying new teammates** [09 April 2021]

Research Highlight • A deep dive into the physical-science literature links the most original research with the most recently formed teams of co-authors.

EDITORIAL

13 April 2021

The United States can help the IMF to rethink how it lends

The funding powerhouse should encourage the International Monetary Fund to prioritize research into sustainable development.



US Treasury secretary Janet Yellen (left) and IMF managing director Kristalina Georgieva must work to align their approaches to funding science. Credit: Action Press/Shutterstock, Chesnot/Getty

Last week, the world's economics and finance communities ended their annual meetings — held online this year — on a salutary note. The International Monetary Fund (IMF) proposed a US\$650-billion boost to the

foreign-currency reserves of countries with financial difficulties, following the deepest global recession in more than a century.

The allocation, known as Special Drawing Rights, enables countries that are low on US dollar reserves to access this and other global currencies to buy essential pandemic supplies, notably vaccines. But its size pales next to the Biden administration's planned \$2.3-trillion economic stimulus to reboot the US economy, which has been stalled by COVID-19. As part of this, the administration intends to ask Congress to authorize sizeable increases to the budgets of public agencies. A particular focus will be on strengthening funding and regulatory agencies working in climate change and environmental protection, public health, racial justice and scientific and health research.

In doing so, the government is upending the practice not only of its predecessor, but also of US governments going back some four decades. Most of those governments have tended to restrain public spending, especially that on the infrastructure of the state. The Biden administration has recognized that the lack of such public spending has greatly harmed some of the country's most vulnerable populations. It must now take this message to large global lending agencies such as the World Bank and the IMF. As the largest shareholder, it can and should work with the IMF to help it prioritize lending to research and universities.

Course correction

If the pandemic has taught us one thing, it is that the environment, health care, regulation and research are precisely the sectors that need to be supported if countries are to emerge stronger both during and after the pandemic. They are also [essential to meeting the United Nations flagship Sustainable Development Goals](#) (SDGs), aimed at alleviating poverty and achieving environmental sustainability. The IMF and its members are all committed to the SDGs, which is another reason why the agency must be helped to adjust its lending criteria to support the know-how needed to achieve the targets.



[More floods, fires and cyclones — plan for domino effects on sustainability goals](#)

The pandemic risks putting back most of the SDGs by a decade, according to a UN report published to coincide with the IMF meetings. Take the target to achieve universal primary education by 2030, one of the closest to being met before the pandemic. Schools educating more than 150 million children around the world have been closed for a year, according to data from Johns Hopkins University in Baltimore, Maryland, and UNICEF, the UN funding agency for protecting children's rights. As the pandemic enters its third wave in many places, it is not clear when these children will be able to return to school.

Progress towards affordable access to further and higher education has also been set back. Although many institutions are providing online learning, students from the lowest-income communities tend to lack access to broadband, personal laptops and smartphones, so are often unable to participate in classes. The paradox is that this is happening just as the UN has been recruiting universities to help countries meet their SDG obligations. Several of the world's major university networks, including the Association of African Universities and the Association of Commonwealth Universities, have been encouraging their members to implement SDGs more actively.

Many researchers have been deeply involved in the SDGs since the goals were launched in 2015. Researchers have also been [monitoring progress towards the goals](#), and have been helping countries to meet their individual targets ([Z. Xu et al. *Nature* 577, 74–78; 2020](#)). It is good that universities are being asked to do more. But this is coming at a time when most are facing financial hardship, and when international lenders such as the United Kingdom's Foreign, Commonwealth & Development Office are [making sudden and damaging cuts](#) to their support for research partnerships with low- and middle-income countries.

Basic needs

When the IMF provides loans, some countries balance the books by cutting public-sector spending, such as on energy subsidies or funding for higher education. When this approach was applied to financially distressed countries in the 1980s, development economists warned that it would damage countries' subsequent economic recovery. They also argued that funding for people's basic needs should be met by the state — as is the case in many high-income countries. Countries in Africa and Latin America suffered greatly under what were called adjustment or stabilization policies — conditions on spending to which countries had to adhere to receive IMF loans.



Reset Sustainable Development Goals for a pandemic world

Richard Jolly, an economist at the University of Sussex near Brighton, UK, and a former deputy head of UNICEF, describes how the organization had become so concerned that it commissioned a two-volume study, *Adjustment with a Human Face*, highlighting how international lending policies were harming the welfare of children and young people. But, at the time, such concerns were up against a different way of thinking: that prosperity can be achieved through lower government spending.

Now, as the pendulum looks to be swinging the other way, the IMF's shareholders, led by the United States, must allow the agency to assist countries in meeting the SDGs by lending money to strengthen universities, along with research and policy in regulation and health care.

International policy priorities in finance and economics are entering a new phase, partly as a result of the pandemic. The US government has signalled that it intends to borrow eye-watering sums of money; and that it needs to do so because of its own previous neglect of those parts of the public sector that are essential to achieving sustainable development, racial equity and social justice.

The Biden administration is rightly reconsidering the nation's previous convictions. It must now also work constructively with the IMF and other institutions over which it has influence to help them do the same.

Nature **592**, 325-326 (2021)

doi: <https://doi.org/10.1038/d41586-021-00959-3>

Jobs from Nature Careers

- - - [All jobs](#)
 -
 - [Research Associate / PhD Student](#)

Technische Universität Dresden (TU Dresden)

Dresden, Germany

JOB POST

- **PostDoc (f/m/d) in Physical chemistry or Material Chemistry - Design and synthesis of plasmonic nanostructures**

Helmholtz-Zentrum Berlin for Materials and Energy (HZB)

Berlin, Germany

JOB POST

- **Betriebspraktikum in der 9. Klasse**

Helmholtz Centre Potsdam - German Research Centre for Geosciences (GFZ)

Potsdam, Germany

JOB POST

- **55832: Physicist, engineer or similar (f/m/x) - Development, application and scientific evaluation of greenhouse gas lidar systems**

German Aerospace Center (DLR)

Oberpfaffenhofen, Germany

JOB POST

| [Section menu](#) | [Main menu](#) |

EDITORIAL

14 April 2021

Funders, now is the time to invest big in COVID drugs

Vaccine development has been a resounding success. But the medicine cabinet should have been better stocked.



Remdesivir should not have been the only ‘shovel-ready’ antiviral drug for potential COVID-19 treatment. Credit: Mohamed Hossam/EPA-EFE/Shutterstock

The global disruption caused by COVID-19 has been a shock, but not a surprise. For years, researchers have warned that a deadly viral pandemic could bring nations to their knees. They urged governments and pharmaceutical companies to work together on broad-spectrum antiviral

drugs — capable of beating a variety of viruses — and to ensure that those drugs were ready for testing in humans when disaster struck.

Influenza viruses, coronaviruses and relatives of Ebola were all considered potential threats. But when the COVID-19 pandemic hit, the medicine cabinet was all but empty. Remdesivir was one of just a few ‘shovel ready’ antiviral drugs that researchers could quickly put into human testing. In early tests, it showed some success in reducing the time that people with COVID-19 spent in hospital. But other studies have not shown the drug to be beneficial.

Coronavirus vaccines are rightly being celebrated, but antiviral drugs could — and would — have had a crucial, life-saving role. The public sector should have rallied quickly to develop them, as it did for vaccines, but this has not yet happened. Although scientists and companies are starting to make concerted efforts, most governments are not treating this issue with the same urgency as they have vaccines. Unless that changes, the world might remain just as poorly prepared for the next viral pandemic.



The race for antiviral drugs to beat COVID — and the next pandemic

The warnings — in the past 20 years alone — have been loud and clear. An outbreak of severe acute respiratory syndrome (SARS) in 2003 prompted calls for more antiviral drug development. But there was little action by

funders, partly because the threat subsided. Another warning came a decade later, after an outbreak of Middle East respiratory syndrome (MERS). Again, governments and industry paid little heed. Some drug programmes trundled on, but without proper investment towards a clear goal — the production of drugs that have been safety-tested in people and that could be made ready for fast and decisive clinical trials.

This pandemic could change that. As reported in [a News Feature this week](#), a number of initiatives are under way to right this wrong. The COVID R&D Alliance, a consortium of more than 20 life-science companies and venture-capital firms from around the world, is aiming to create an organization that will accelerate the development of drugs against coronaviruses. The consortium, which was set up last year, plans to prepare 25 candidate medicines for trials in humans, so that at least some can be ready for larger trials when the next pandemic-causing virus strikes.

The COVID R&D Alliance, and another global project called the Rapidly Emerging Antiviral Drug Development Initiative, are in the process of raising funds from industry and governments. The US National Institutes of Health (NIH) is planning to invest heavily in creating drugs to fight SARS-CoV-2. It is essential that the agency is given the funding to make strategic bets in creating drugs for the next pandemic.



The antibiotic paradox: why companies can't afford to create life-saving drugs

In contrast to these efforts, vaccine development happened at lightning speed when the richest countries agreed to provide funding while vaccines were being developed. Some countries agreed to purchase the resulting vaccines, even if they failed. A similar funding vehicle — one based on both the public and private sectors being willing to take risks — must be considered for antiviral drugs.

There are models for success here. Remdesivir was almost ready to be tested, thanks to the work of researchers backed by an NIH project called the Antiviral Drug Discovery and Development Center. This was launched in 2014 to screen drug libraries for candidates that could inhibit viruses, including influenza and coronaviruses. Remdesivir's effectiveness in animal models was established in 2017. It was tested in people and shown to be safe during an Ebola outbreak in the Democratic Republic of the Congo, Liberia and Guinea. That meant the drug was ready for more widespread human testing should the need arise.

At least twice before, world leaders were warned to build up a medicine chest of ready antiviral drugs. But momentum fizzled out as previous outbreaks ended, and because of a perennial argument between governments and industry over who should contribute what share of the bill.

The pandemic has shown that this was wrong-headed. Public health requires investments in drugs to counter any pathogen with epidemic or pandemic potential; that includes many airborne and mosquito-borne diseases, and, of course, the threat of antibiotic resistance remains. Governments collectively provided around US\$90 billion in funding for vaccines in 2020, and some of the work this has funded will help in future pandemics. They must do the same for antiviral drugs, which need to be distributed equitably. The world cannot afford to be caught with an empty cabinet again.

Nature **592**, 326 (2021)

doi: <https://doi.org/10.1038/d41586-021-00960-w>

Jobs from Nature Careers

- - - [All jobs](#)
 - - [Research Associate / PhD Student](#)
 - [Technische Universität Dresden \(TU Dresden\)](#)
[Dresden, Germany](#)
[JOB POST](#)
 - [PostDoc \(f/m/d\) in Physical chemistry or Material Chemistry - Design and synthesis of plasmonic nanostructures](#)
[Helmholtz-Zentrum Berlin for Materials and Energy \(HZB\)](#)
[Berlin, Germany](#)
[JOB POST](#)
 - [Betriebspraktikum in der 9. Klasse](#)
[Helmholtz Centre Potsdam - German Research Centre for Geosciences \(GFZ\)](#)
[Potsdam, Germany](#)
[JOB POST](#)
 - [55832: Physicist, engineer or similar \(f/m/x\) - Development, application and scientific evaluation](#)

of greenhouse gas lidar systems

German Aerospace Center (DLR)

Oberpfaffenhofen, Germany

JOB POST

This article was downloaded by **calibre** from <https://www.nature.com/articles/d41586-021-00960-w>

| [Section menu](#) | [Main menu](#) |

WORLD VIEW

13 April 2021

My most memorable mentors? Plants



To nurture a thriving scientific community, look to the natural world for ideas.

- [Beronda L. Montgomery](#) 0

1. [Beronda L. Montgomery](#)

1. Beronda L. Montgomery is a professor in the Department of Energy — Plant Research Laboratory at Michigan State University in East Lansing.

[View author publications](#)

You can also search for this author in [PubMed](#) [Google Scholar](#)

I study how plants and bacteria stay in tune with the fast-changing environment to better survive and reproduce. As the seasons change from winter to spring, light cues signal lengthening days, prompting buds and new leaves to emerge. Shadows hint at the growth of neighbouring plants and can lead branches to extend or bend in a quest for full sunlight and maximal photosynthesis.

As a Black woman professor, I am in the vast minority in my professional spaces. Even while publishing a stream of scientific papers, I have spent a lot of career time reflecting on how the conventional, transactional paths to scientific success can be at odds with nurturing a diverse community in my laboratory and discipline. Some of my most powerful personal lessons in how to thrive and help others to do so have come from the cress and cyanobacteria in my lab, and the corn and soya in university field plots.

That plants with equal ‘aptitude’ grow and survive differently, depending on their environment, helps me think about how to help colleagues thrive. For instance, going from an observation, such as spotting yellow leaves on a tobacco plant, to listing its potential causes (overwatering, underwatering, nitrogen deficiency) might prompt ideas about, say, how to support graduate students. Are their presentation slides poorly prepared because of boredom, confusion, anxiety or overwork, or is the reason family or financial stress?

Many scientists hesitate to apply the ideas that inspire their research and fuel their publications to their working lives and interactions. We’ve been trained not to. Instead, we’re socialized to construct artificial barriers between scientific and personal insights. The use of the first person is discouraged. So is seeing plants or bacteria as instructive for human beings and society, as I explain in my book *Lessons from Plants* (2021).



Collection: How to grow a healthy lab

Consider the fascination that microbiologists feel for bacteria that do not grow under standard laboratory conditions. They don't blame the bacteria; instead, they try to find and supply the correct nutrients, temperature, light or other conditions that the microbes require to thrive. This is the sort of curiosity needed to learn what contributes to the success and growth of individuals, such as those from backgrounds that are under-represented in research ([B. L. Montgomery *mSphere* 5, e01046-20; 2020](#)). Guided by this approach, in my lab, we avoid dictating strict guidelines, and focus instead on sharing general principles of success — for example, the importance of writing regularly rather than trying to pull together a manuscript in a rush, or putting it off so it never gets done. We then try to help each individual to discover the necessary framework (daily, weekly, monthly or perhaps quarterly writing) that works well for them personally to achieve a particular objective.

Now consider the clear contradictions that exist between the reality of how science is conducted by teams, and how scientists celebrate individuals. We romanticize competition and put discovering something first above supporting and recognizing a community. Beyond individuals, arbitrary divides and silos exist between units or organizations, to the benefit of those in prized positions or with insider knowledge.

So I reflect on why Indigenous peoples in the Americas have planted beans alongside corn and squash for thousands of years. The beans enrich the soil with nitrogen; the corn stalks support the twining beans and protect them from the pests and stress that the beans would be subject to if they grew along the ground; the squash suppresses weeds. Together, these crops are more productive, more resilient. The same applies to environments from wetlands to wild-flower meadows — strength lies in interactions.



The artist who co-authored a paper and expanded my professional network

Such biological metaphors have made me unafraid to pursue collective success rather than focusing solely on rankings and prestige. So, in my lab, we regularly discuss the specific ways in which teamwork has advanced our research. Did one person's sharing of their experimental expertise lead to a breakthrough for another team member? To facilitate this culture, when I'm hiring, I deliberately look for individuals with demonstrated interest in collaborative effort.

Increasingly, others are sharing their biologically inspired insights with me. One colleague compared surviving the stress of the COVID-19 pandemic to sporulation — the process by which bacteria or other organisms form a multilayered, dormant cellular structure in response to unfavourable or extreme environmental conditions, and wait until conditions are more favourable before they re-emerge. Another described the extra care and

attention needed to mentor students and postdocs during the transition to working remotely as being akin to the transitional care needed when transplanting plants from one environment, such as pots in a greenhouse, to another, such as an open field.

Some people tell me that I'm oversimplifying in thinking that plants can supply useful analogies for humans. They say such knowledge is simply not transferable. Others might counter that nature is about the survival of the fittest; that it, too, is a fierce contest for scarce resources, in which the most competitive wins. I say, let's apply all the cognitive tools we have to solving important challenges.

Even though prevailing scientific norms demand that we remain personally distant from our subjects of study, I've been deeply inspired by mine and the metaphors they offer.

Nature **592**, 327 (2021)

doi: <https://doi.org/10.1038/d41586-021-00961-9>

Jobs from Nature Careers

- - - [All jobs](#)
 - - [Research Associate / PhD Student](#)
 - [Technische Universität Dresden \(TU Dresden\)](#)
 - [Dresden, Germany](#)
 - [JOB POST](#)
 - [PostDoc \(f/m/d\) in Physical chemistry or Material Chemistry - Design and synthesis of plasmonic](#)

nanostructures

Helmholtz-Zentrum Berlin for Materials and Energy (HZB)
Berlin, Germany

JOB POST

- **Betriebspraktikum in der 9. Klasse**

Helmholtz Centre Potsdam - German Research Centre for Geosciences (GFZ)

Potsdam, Germany

JOB POST

- **55832: Physicist, engineer or similar (f/m/x) - Development, application and scientific evaluation of greenhouse gas lidar systems**

German Aerospace Center (DLR)

Oberpfaffenhofen, Germany

JOB POST

This article was downloaded by **calibre** from <https://www.nature.com/articles/d41586-021-00961-9>



Rafting and fishing on Alaska's Alsek River face an uncertain future if climate change causes the path the river follows to the sea to move. Credit: Whit Richardson/Alamy

Geology

02 April 2021

Melting glacier threatens to shove a mighty river off course

Climate change could send Alaska's Alsek River into a new channel, with potentially far-reaching impacts for humans.

The retreat of a dwindling Alaskan glacier is likely to cause a local river to change course drastically within a few decades — with profound

consequences for people in the region.

From Canada, the mighty Alsek River flows south into Alsek Lake near the Pacific Ocean, before draining into the sea. An extension of the Grand Plateau Glacier separates the lake and river from another lake and its outlet.

Michael Loso at the Wrangell–St. Elias National Park and Preserve in Copper Center, Alaska, and his colleagues surveyed the topography of the glacier bed and the surrounding terrain. They predict that the rapidly thinning glacier's retreat will soon connect the lakes. As a result, the Alsek River will probably abandon its current course in favour of a steeper outlet channel 28 kilometres to the southeast.

An alteration in the river's course could pose challenges to people who fish, hunt and raft in the current Alsek River outlet, the scientists say.

[Geomorphology \(2021\)](#)

- [Geology](#).

This article was downloaded by **calibre** from <https://www.nature.com/articles/d41586-021-00771-z>



On the island of Cayo Santiago, female macaques and their infants sit close to one another in a landscape stripped bare by Hurricane Maria. Credit: Lauren Brent

Animal behaviour

08 April 2021

A hurricane wrecks ‘Monkey Island’ — and leads to new monkey friendships

Amid the devastation wrought by Hurricane Maria, rhesus macaques sought support from each other to endure hard times.

A catastrophic hurricane brought more than 100 monkeys living on a Caribbean island closer together, helping them to survive the storm's aftermath.

For decades, scientists have tracked the alliances, power struggles and social relations of the feral rhesus macaques (*Macaca mulatta*) on Cayo Santiago, a small island near Puerto Rico. After Hurricane Maria devastated the island in 2017, Camille Testard at the University of Pennsylvania in Philadelphia and her colleagues sought to understand how the disaster affected the monkeys' social interactions.

The scientists calculated that relatively few adult macaques died in the six months after the storm. But Maria stripped away nearly two-thirds of the island's vegetation, potentially increasing competition for shade and food.

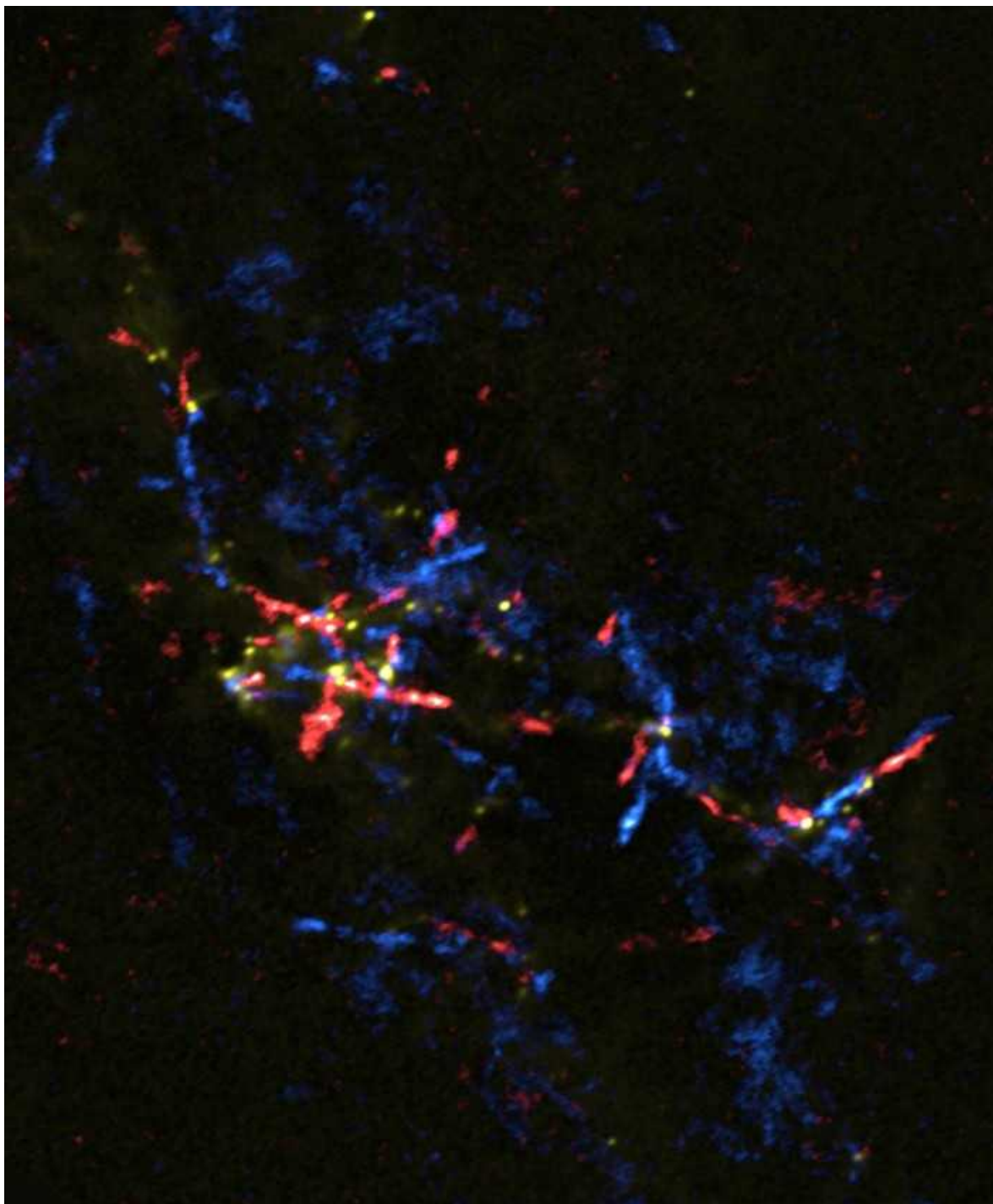
The authors compared observations of the animals' behaviour from before and after the storm and found that monkeys became more social after the hurricane: they more frequently sat close together and groomed each other. Timid, isolated monkeys sought these connections more than did outgoing monkeys, becoming friends with the friends of their friends.

Researchers think these connections might have provided social support and valuable opportunities to rest in the newly scarce shade.

[Curr. Biol. \(2021\)](#)

- [Animal behaviour](#)

This article was downloaded by **calibre** from <https://www.nature.com/articles/d41586-021-00905-3>



In the Milky Way, gas (red and blue; artificially coloured) flows outwards from ‘stellar eggs’ that could hatch into baby stars. Credit: ALMA (ESO/NAOJ/NRAO), Lu *et al.*/*Astrophys. J.*

Astronomy and astrophysics

06 April 2021

Baby stars make it in a tough part of the Galaxy

Star formation might be more resilient than astronomers had thought.

Despite its harsh conditions, the centre of the Milky Way is a birthplace for stars.

Galactic centres are full of hazards, such as powerful magnetic fields and exploding stars, that can prevent baby stars from coalescing out of clouds of gas and dust. Previous work has suggested that stars form less frequently in the innermost 500 parsecs of the Milky Way than in more distant regions.

Xing Lu at the National Astronomical Observatory of Japan in Tokyo and his colleagues used the Atacama Large Millimeter/submillimeter Array in Chile to study gassy regions near the Galactic Centre. The scientists spotted more than 800 dense pockets of gas and dust, which are probably ‘stellar eggs’ from which newborn stars might ‘hatch’.

Of these, 43 had outflows of gas — a probable sign that stars were being formed.

[*Astrophys. J. \(2021\)*](#)

- [Astronomy and astrophysics](#)

This article was downloaded by **calibre** from <https://www.nature.com/articles/d41586-021-00907-1>



Vast bush fires that swept across Australia at the end of 2019 and the start of 2020 filled the skies with enough smoke to warm a portion of the atmosphere. Credit: Saeed Khan/AFP/Getty

Atmospheric science

06 April 2021

Smoke from Australian fires turned up the heat in the southern sky

The catastrophic wildfires of late 2019 and early 2020 triggered a lingering temperature rise in a section of Earth's lower atmosphere.

Particle pollution from the devastating Australian wildfires of December 2019 and January 2020 warmed part of the atmosphere by 1 °C for roughly

six months.

Wildfire smoke contains small amounts of a type of particulate matter called black carbon. When black carbon particles are injected into the atmosphere, their dark colour causes them to absorb sunlight and warm the surrounding air.

Pengfei Yu at Jinan University in Guangzhou, China, and his colleagues used a climate model to determine the effect of the Australian wildfires on stratospheric temperatures in 2020. The stratosphere is the portion of the atmosphere that extends from roughly 10 to 50 kilometres above Earth's surface and contains the ozone layer.

When the team incorporated smoke from the wildfires into the model, parts of the Southern Hemisphere's stratosphere warmed by 1–2 °C. This warming effect persisted for approximately six months after the fires.

The model also showed that stratospheric smoke particles increased the destruction of ozone molecules in the Southern Hemisphere's skies. The wildfires probably contributed to the fact the ozone hole was larger than usual in 2020, the authors say.

[Geophys. Res. Lett. \(2021\)](#)

- [Atmospheric science](#)

This article was downloaded by **calibre** from <https://www.nature.com/articles/d41586-021-00906-2>



A reef manta ray visits a cleaning station at Lady Elliot Island, Australia.
Credit: A. O. Armstrong *et al.*/*Ecol. Evol.* ([CC BY 4.0](#))

Ecology

08 April 2021

What manta rays remember: the best spots to get spruced up

Giant fish preserve a mental map of where cleaning fish provide the highest-quality pest removal.

Even sea creatures need pampering. Manta rays make regular visits to ‘cleaning stations’, where small fish rid the rays of skin parasites at the

coral-reef equivalent of a day spa. Now it seems that rays can identify and remember spots where they have received quality cleaning.

Cleaning stations are often centred on corals inhabited by cleaner shrimp or fish. To understand how these stations influence rays' movements, Asia Armstrong at the University of Queensland in St Lucia, Australia, and her colleagues tracked 34 reef manta rays (*Mobula alfredi*) off the coast of eastern Australia for about 1.5 years.

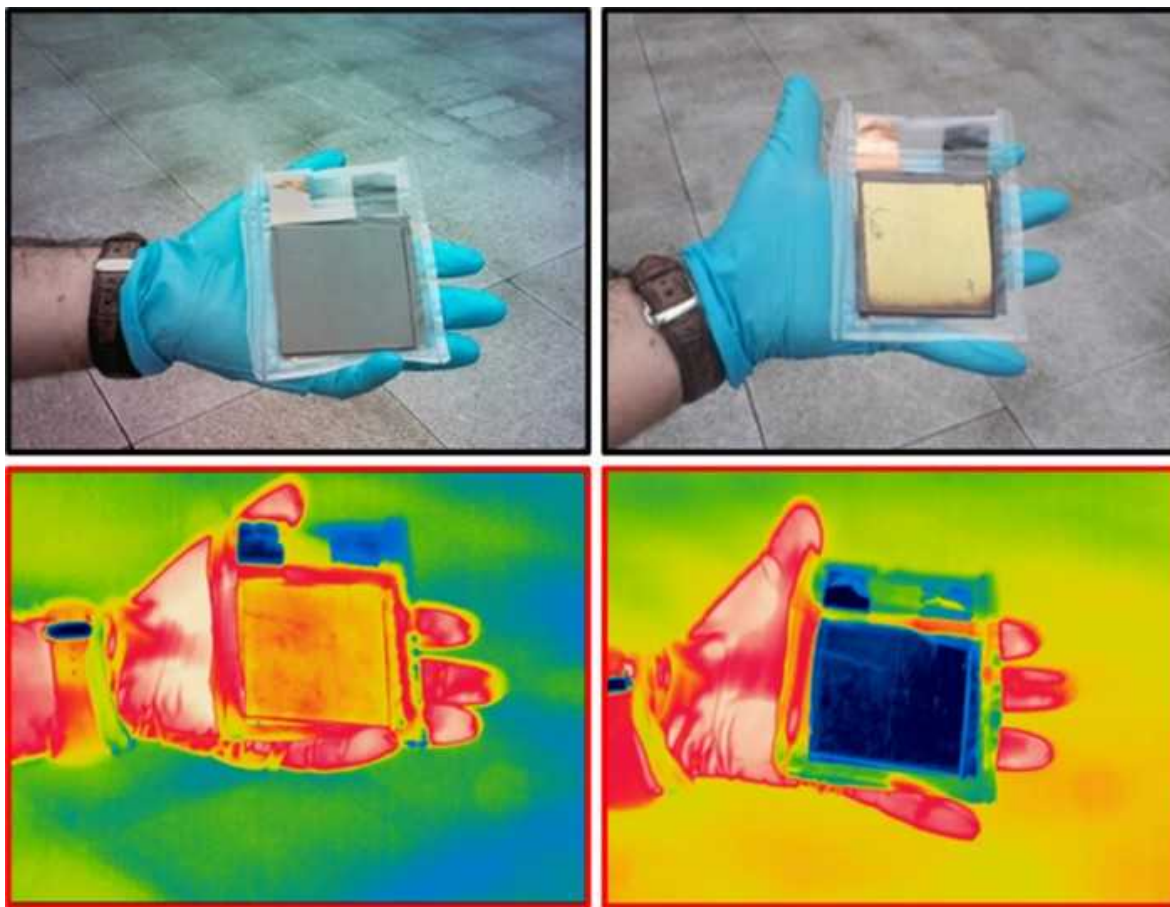
The highest density of rays was found at places where cleaning fish called blue-streak cleaner wrasses (*Labroides dimidiatus*) were most abundant. Rays typically visited cleaning stations during the day, when cleaner wrasses are most active, and favoured stations close to foraging regions.

Rays are thought to prefer stations that provide superior cleaning — where the cleaners don't bite them, for example. The rays' behaviour suggests that they have a mental map of spots that offer both high-quality cleaning and proximity to foraging grounds.

[Ecol. Evol. \(2021\)](#)

- [Ecology](#)
-

This article was downloaded by **calibre** from <https://www.nature.com/articles/d41586-021-00903-5>



A display screen in its uncharged (top left) and charged (top right) state in visible light. The screen reflects one range of infrared wavelengths when uncharged (bottom left) and another range when charged (bottom right).
Credit: M. S. Ergoktas *et al.*/*Nature Photon.*

Optics and photonics

05 April 2021

One screen, three images — some invisible in ordinary light

A graphene-based device can display several images simultaneously using a range of wavelengths.

Although your mobile phone might have a high-quality colour screen, it can't display pictures in both the visible spectrum and other wavelengths of light at the same time. Now, researchers have engineered a device that can show images in wavelengths ranging from visible to microwave simultaneously.

A team led by Coskun Kocabas at the University of Manchester, UK, made a display by layering sheets of graphene — a conductive, carbon-based film — over a foil sheet that acts a source of lithium ions. When electricity flows through the material, lithium ions trickle from the foil into the graphene. As the graphene incorporates more lithium, the display reflects a broader range of wavelengths.

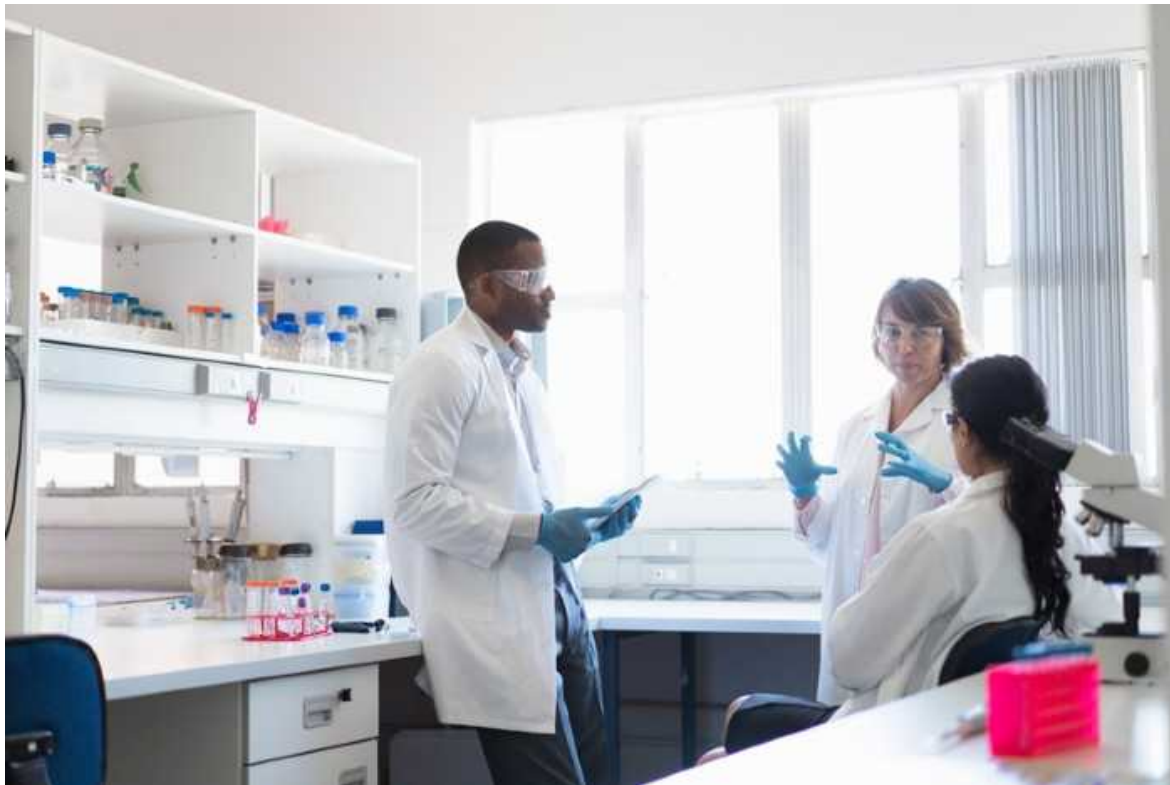
The researchers can target the flow of electricity to individual units in the display. This allows the device to generate three images at the same time, although only one can be seen with the naked eye. When the device is observed with infrared light, a second image appears alongside the first; a third image can be seen only by observing the display with wavelengths that lie between far infrared and microwave.

The authors suggest that after further development, the device could be used for message encryption and camouflage coating.

Nature Photon. (2021)

- [Optics and photonics](#)

This article was downloaded by **calibre** from <https://www.nature.com/articles/d41586-021-00904-4>



Fresh scientific collaborations lead to exciting results. Credit: Getty

Human behaviour

09 April 2021

Want fresh results? Analysis of thousands of papers suggests trying new teammates

A deep dive into the physical-science literature links the most original research with the most recently formed teams of co-authors.

The most original research papers come from the freshest teams, according to an analysis of hundreds of thousands of physical-science articles.

Teamwork has become increasingly important in science, but little is known about how the effectiveness of newly created teams compares with that of more established ones. To get a better understanding, Shlomo Havlin at Bar-Ilan University in Ramat-Gan, Israel, and his colleagues assessed the ‘freshness’ of teams of article co-authors by examining whether any of the researchers had previously written papers together, taking into account team members’ career stages and productivity. The study authors also analysed the originality of the teams’ papers and the impact of the work in different fields.

They found that the teams that had worked together previously the least produced the smallest number of research papers — but their work had the greatest originality. Their papers also had significantly more impact in several research areas than did papers from teams whose members had worked together before.

Large and fresh teams had the most original and impactful work, say the authors, who stress it is not clear whether this is a cause and effect relationship.

[Nature Hum. Behav. \(2021\)](#)

- [Human behaviour](#)

This article was downloaded by **calibre** from <https://www.nature.com/articles/d41586-021-00902-6>

News in Focus

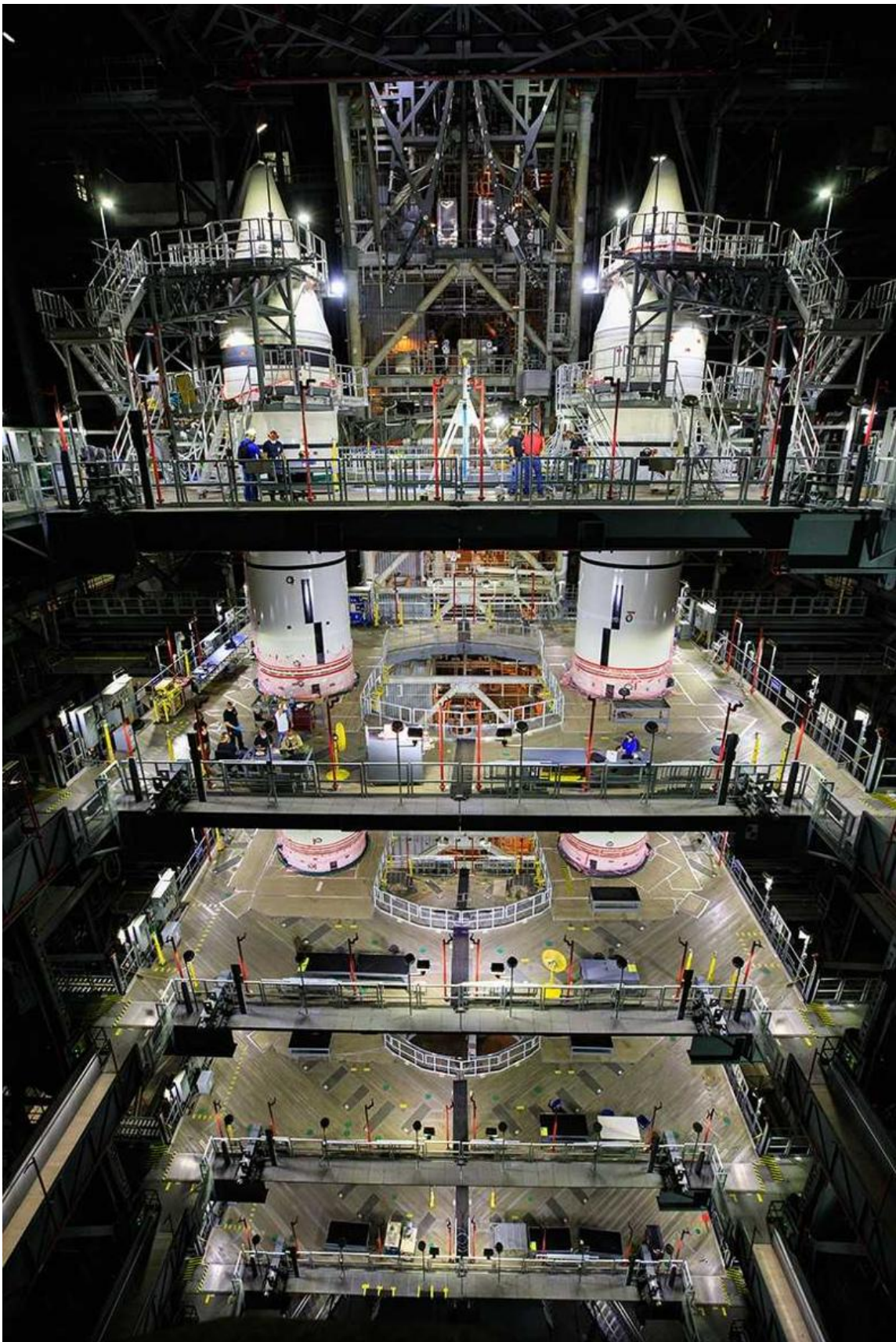
- **[Sputnik V, a host of coronavirus mutations and a rocket stack](#)** [14 April 2021]
News Round-Up • The latest science news, in brief.
- **[Is the standard model broken? Physicists cheer major muon result](#)** [07 April 2021]
News • The muon's magnetic moment is larger than expected — a hint that new elementary particles are waiting to be discovered.
- **[How could a COVID vaccine cause blood clots? Scientists race to investigate](#)** [09 April 2021]
News • Researchers are searching for possible links between unusual clotting and the Oxford–AstraZeneca coronavirus vaccine.
- **[Why US coronavirus tracking can't keep up with concerning variants](#)** [07 April 2021]
News • The country has an enormous virus-sequencing capacity, but funding and coordination roadblocks are holding it back.
- **[After the WHO report: what's next in the search for COVID's origins](#)** [01 April 2021]
News Explainer • A World Health Organization report makes a reasonable start, scientists say, but there are many questions yet to be answered.
- **[Oldest DNA from a Homo sapiens reveals surprisingly recent Neanderthal ancestry](#)** [07 April 2021]
News • Ancient human lineages interbred commonly in Europe, as well as the Middle East.
- **[The race for antiviral drugs to beat COVID — and the next pandemic](#)** [14 April 2021]
News Feature • Despite dire warnings, a stockpile of ready compounds to fight viral pandemics was sorely lacking. Can drugmakers finally do the right thing?

NEWS ROUND-UP

14 April 2021

Sputnik V, a host of coronavirus mutations and a rocket stack

The latest science news, in brief.



The SLS boosters are stacked at the Kennedy Space Center in Florida. Credit: NASA

NASA assembles powerful deep-space rocket

Engineers have assembled the twin booster rockets for NASA's massive Space Launch System (SLS) — the first deep-space rocket since Saturn V, which sent astronauts to the Moon. Since November, workers have been using a huge crane to vertically stack segments of the boosters at the Kennedy Space Center in Florida.

The boosters will eventually be attached to the rocket's 65-metre-long core stage, which is undergoing tests at Stennis Space Center near Bay St Louis in Mississippi. NASA is developing the SLS as part of its Artemis programme, which aims to land the first woman, and the next man, on the Moon by 2024.



The Sputnik V vaccine uses adenoviruses, which are a cause of the common cold, to shuttle SARS-CoV-2 genetic material into the cells of vaccinated

people.Credit: Yelena Afonina/TASS/Getty

Sputnik V vaccine is no match for a fast-spreading variant

A variant of the virus SARS-CoV-2 detected in South Africa can evade antibodies elicited by the Sputnik V vaccine against COVID-19.

Many vaccines — including Sputnik V, developed in Russia — trigger the production of antibodies targeting the SARS-CoV-2 protein called spike, which the virus uses to infect host cells. Scientists worry that the vaccines might be ineffective against SARS-CoV-2 variants with mutations in the spike-encoding gene.

Benhur Lee at the Icahn School of Medicine at Mount Sinai in New York City and his colleagues obtained samples of antibody-laden blood serum from 12 people vaccinated with Sputnik V ([S. Ikegami et al. Preprint at medRxiv https://doi.org/f5h9; 2021](https://doi.org/f5h9)). The authors tested the serum against benign viruses engineered to make the versions of spike found in certain SARS-CoV-2 variants. Eight of the 12 samples did not inhibit viruses equipped with spike from B.1.351, the variant identified in South Africa. But the samples effectively overcame viruses with spike from the B.1.1.7 variant, which was detected in Britain.

The emergence of variants might require a new generation of vaccines, the authors say. The findings have not yet been peer reviewed.



Healthcare workers screen people in Luanda for antibodies to SARS-CoV-2. Credit: Ampe Rogerio/EPA-EFE/Shutterstock

Air traveller yields a new variant bristling with mutations

A coronavirus variant identified in Angola carries more mutations than any strain previously identified.

A team led by Tului de Oliveira, at the University of KwaZulu-Natal in Durban, South Africa, and Silvia Lutucuta, at the Angola Ministry of Health in Luanda, identified the variant after sequencing samples from three people who flew to Angola from Tanzania in February 2021 ([T. de Oliveira et al. Preprint at medRxiv https://doi.org/f48g; 2021](#)). The variant, named A.VOI.V2, carries 34 mutations, including 14 in the spike protein, which the virus uses to infect cells.

The variant deserves further study, the authors say, because it carries mutations that might help it to escape some people's immune responses. The finding has not yet been peer reviewed.

Nature **592**, 331 (2021)

doi: <https://doi.org/10.1038/d41586-021-00962-8>

Jobs from Nature Careers

•

◦

- [All jobs](#)

◦

- [**Research Associate / PhD Student**](#)

[Technische Universität Dresden \(TU Dresden\)](#)

[Dresden, Germany](#)

[JOB POST](#)

- [**PostDoc \(f/m/d\) in Physical chemistry or Material Chemistry - Design and synthesis of plasmonic nanostructures**](#)

[Helmholtz-Zentrum Berlin for Materials and Energy \(HZB\)](#)

[Berlin, Germany](#)

[JOB POST](#)

- [**Betriebspraktikum in der 9. Klasse**](#)

[Helmholtz Centre Potsdam - German Research Centre for Geosciences \(GFZ\)](#)

[Potsdam, Germany](#)

[JOB POST](#)

- **55832: Physicist, engineer or similar (f/m/x) - Development, application and scientific evaluation of greenhouse gas lidar systems**

German Aerospace Center (DLR)

Oberpfaffenhofen, Germany

JOB POST

This article was downloaded by **calibre** from <https://www.nature.com/articles/d41586-021-00962-8>

| [Section menu](#) | [Main menu](#) |

NEWS

07 April 2021

Is the standard model broken? Physicists cheer major muon result

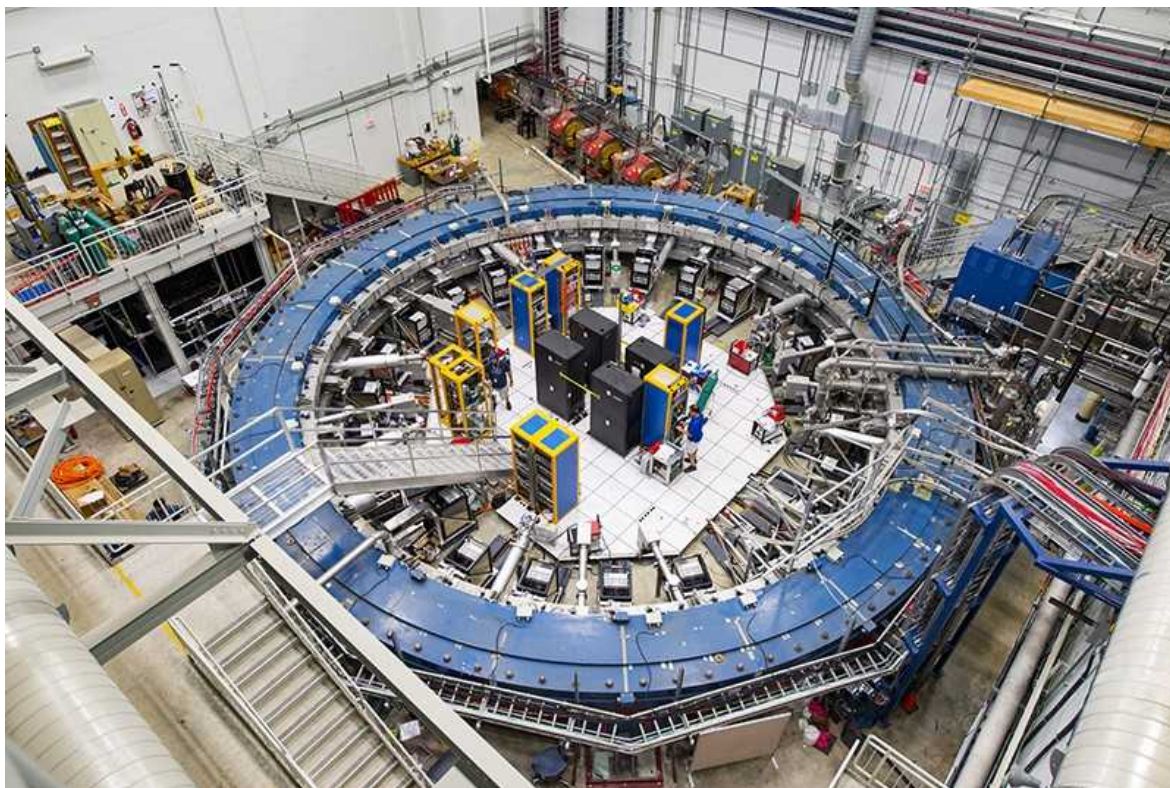
The muon's magnetic moment is larger than expected — a hint that new elementary particles are waiting to be discovered.

- [Davide Castelvecchi](#)

1. Davide Castelvecchi

[View author publications](#)

You can also search for this author in [PubMed](#) [Google Scholar](#)



The storage-ring magnet used for the $g - 2$ experiment at Fermilab. Credit: Reidar Hahn/Fermilab

Muons keep on misbehaving. An experiment in the United States has confirmed an earlier finding that the particles — massive, unstable cousins of the electron — are more magnetic than researchers originally expected. If the results hold up, they could ultimately force major changes in theoretical physics and reveal the existence of completely new fundamental particles.

The Muon $g - 2$ collaboration at the Fermi National Accelerator Laboratory (Fermilab) outside Chicago, Illinois, reported the latest measurements in a webcast on 7 April, and published them in *Physical Review Letters*¹. The results are “extremely encouraging” for those hoping to discover other particles, says Susan Gardner, a physicist at the University of Kentucky in Lexington.

Long-awaited muon physics experiment nears moment of truth

Muon $g - 2$ (pronounced ‘ g minus 2’) first hinted² that something was amiss with the muon in 2001, when the experiment was running at the Brookhaven National Laboratory in Upton, New York. Physicists measured the strength of the particle’s magnetic moment, a property that makes it act like a tiny bar magnet. The standard model of particle physics says that, in the appropriate units, the muon’s magnetic moment should be a number very close, but not equal, to 2. The Brookhaven experiment measured that tiny difference, known as $g - 2$, but found it to be slightly bigger than theorists had predicted.

The magnetic moment of elementary particles is influenced by ‘virtual’ versions of known elementary particles that continually pop out of the vacuum only to disappear a fraction of a second later. Physicists perform detailed and lengthy calculations of the contributions from all known particles, so if the experimental results differ significantly from the predicted value of $g - 2$, they reason that previously unknown types of particle must be lurking in the vacuum. The original Muon $g - 2$ experiment gave many physicists hope that new particles would soon be discovered.

Secret frequency

To verify the Brookhaven results, researchers rebuilt the experiment — which keeps muons running in circles around a superconducting ring magnet 15 metres in diameter — at Fermilab. They began collecting data in 2018, and have now presented the results from the first year of operations.

To avoid biasing its data analysis, the collaboration had blinded itself to a crucial parameter that is needed to calculate the $g - 2$ constant — the exact frequency of a digital clock in their instrumentation. Two Fermilab physicists who are not collaboration members were entrusted with the missing bit of information. As a result, the team was able to conduct a lengthy study, but could initially plot its findings only on a graph in which the axes had slightly uncertain scales.



[Step aside CERN: There's a cheaper way to break open physics](#)

Then at a 25 February teleconference that included most of the 200-plus team members, two leading members of the experiment opened an envelope that contained the secret clock frequency. When they plugged the number into their computers, it revealed the true value of their $g - 2$ measurement. It was immediately obvious to the team that the result was consistent with the one recorded at Brookhaven more than 20 years ago.

“The agreement is excellent,” says Lee Roberts at Boston University in Massachusetts, one of the original Muon $g - 2$ team members. “People were clapping and jumping up and down — as much as you can do that on Zoom.” The joyful reactions were obvious, even though “a lot of us were muted”, adds Brynn MacCoy, a physicist at the University of Washington in Seattle. The result vindicates the claim of the original experiment, Roberts says.

Other physicists agree. The latest announcement gives “a nice, clear answer” to the riddle posed by the earlier results, says theoretical physicist Gino Isidori at the University of Zurich in Switzerland. “The experiment was correct.”

But although the gap between the theoretical and experimental results has grown in statistical significance, it is still not an unambiguous proof of the existence of new particles. “Those who were sceptical will probably stay sceptical,” Isidori says. “At this point, the ball is in the theorists’ court,” he adds.

Quark calculations

The most widely accepted prediction for the muon’s magnetic moment is a number that the theoretical community published last year in a ‘consensus’ paper³. But another study published on 7 April, this time in *Nature*⁴, suggests that the gap between theory and experiment might not be as large as thought.

The hardest part to calculate is the contribution of quarks, the basic constituents of protons and neutrons, which is why physicists have conventionally supplemented their calculations with data from collider experiments.



Rare particle decays offer hope of new physics

In the *Nature* study, Zoltan Fodor at Pennsylvania State University in University Park and his collaborators recalculated the quark contributions from scratch with a simulation technique called lattice quantum chromodynamics (lattice QCD). The technique had not previously been used in $g - 2$ predictions because it was not mature enough to give high-precision results. Fodor and his team managed to improve the precision, and found $g - 2$ to be both larger than the consensus value and much closer to the experimental measurement. Other lattice QCD teams are working to match that precision so that the technique can be used in calculations for the consensus value, says Aida El-Khadra, a theoretical physicist at the University of Illinois at Urbana–Champaign. “The other collaborations are also working on reducing their errors, which requires significant computational resources,” she says.

Updating the physics

The Muon $g - 2$ team is now busy analysing some of the more recent data, as well as collecting more. The researchers ultimately expect the precision of their measurement to improve fourfold. If the discrepancy does turn out to be real, then the standard model will have to be updated to include new particles. One problem is that since 2001, many possible candidate particles

that could have inflated the muon's magnetic moment have been ruled out in other experiments, mostly by the Large Hadron Collider outside Geneva, Switzerland.

Many theories that could explain the Muon $g - 2$ results remain, but researchers see them as contrived. "To me there is not a single explanation which stands out as being far more elegant or compelling than any other one," says Dominik Stöckinger, a theoretical physicist at the Dresden University of Technology in Germany who is a member of Muon $g - 2$.

Since it was first put together in the 1970s, the standard model has passed all tests and has survived almost unchanged. But physicists are convinced that it must be incomplete, and some hope that muons will reveal its first failure. "If we confirm a difference with the standard model, that's what people have been searching for for 50 years," says Roberts.

Nature **592**, 333-334 (2021)

doi: <https://doi.org/10.1038/d41586-021-00898-z>

References

1. 1.

Abi, B. *et al. Phys. Rev. Lett.* **126**, 141801 (2021).

2. 2.

Bennett, G. W. *et al. Phys. Rev. D* **73**, 072003 (2006).

3. 3.

Aoyama, T. *et al. Phys. Rep.* **887**, 1–166 (2020).

4. 4.

Borsanyi, Sz *et al. Nature* <https://doi.org/10.1038/s41586-021-03418-1> (2021).

Jobs from Nature Careers

- - - [All jobs](#)
 - - [Research Associate / PhD Student](#)
 - [Technische Universität Dresden \(TU Dresden\)](#)
[Dresden, Germany](#)
[JOB POST](#)
 - [PostDoc \(f/m/d\) in Physical chemistry or Material Chemistry - Design and synthesis of plasmonic nanostructures](#)
[Helmholtz-Zentrum Berlin for Materials and Energy \(HZB\)](#)
[Berlin, Germany](#)
[JOB POST](#)
 - [Betriebspraktikum in der 9. Klasse](#)
[Helmholtz Centre Potsdam - German Research Centre for Geosciences \(GFZ\)](#)
[Potsdam, Germany](#)
[JOB POST](#)
 - [55832: Physicist, engineer or similar \(f/m/x\) - Development, application and scientific evaluation](#)

of greenhouse gas lidar systems

German Aerospace Center (DLR)

Oberpfaffenhofen, Germany

JOB POST

This article was downloaded by **calibre** from <https://www.nature.com/articles/d41586-021-00898-z>

| [Section menu](#) | [Main menu](#) |

NEWS
09 April 2021

How could a COVID vaccine cause blood clots? Scientists race to investigate

Researchers are searching for possible links between unusual clotting and the Oxford–AstraZeneca coronavirus vaccine.

- [Heidi Ledford](#)
 1. Heidi Ledford
[View author publications](#)

You can also search for this author in [PubMed](#) [Google Scholar](#)



A nurse immunizes a teacher in Granada, Spain, with the Oxford–AstraZeneca vaccine. Credit: Carlos Gil Andreu/Getty

The very rare occurrence of a mysterious blood-clotting disorder among some recipients of the Oxford–AstraZeneca COVID-19 vaccine has got researchers scrambling to uncover whether, and if so, how the inoculation could trigger such an unusual reaction.

After weeks of investigation, the European Medicines Agency (EMA) announced on 7 April that it is possible there is a link between the clots and the vaccine. Even so, the clotting disorder — described today in two reports in *The New England Journal of Medicine*^{1,2} — is so uncommon that the benefits of the vaccine still outweigh its risks, EMA executive director Emer Cooke told reporters. “These are very rare side effects,” she said. “The risk of mortality from COVID is much greater than the risk of mortality from these side effects.”

But the finding leaves researchers wrestling with a medical mystery: why would a vaccine trigger such an unusual condition? “Of course, there are hypotheses: maybe it’s something with the vector, maybe it’s an additive in

the vaccine, maybe it's something in the production process ... I don't know," says Sabine Eichinger, a haematologist at the Medical University of Vienna. "It could be any of these things."

Unusual locations

Eichinger was among the first to notice the clotting disorder, a strange combination of blood clots — which can be dangerous, and potentially fatal, if they block blood flow to the brain or lungs — and a counter-intuitive deficiency of cell fragments called platelets that promote clotting. The clots also appeared in unusual parts of the body, such as the brain and abdomen, rather than in the legs, where most deep-vein blood clots form.



Why is it so hard to investigate the rare side effects of COVID vaccines?

This rang alarm bells for Eichinger, who had previously encountered a similar phenomenon in a few people who had been treated with the blood-thinning drug heparin. Heparin is normally used to prevent clotting, but in very rare cases can trigger a syndrome called heparin-induced thrombocytopenia (HIT), which causes blood clots and low platelet levels.

By 22 March, the EMA had assembled 86 reports of people who had experienced blood clots in the brain or abdomen within two weeks of receiving a dose of the Oxford–AstraZeneca vaccine, developed in Britain by AstraZeneca in Cambridge and the University of Oxford. Some of these

cases have been confirmed to bear the hallmarks of HIT, even though these people had not received heparin.

Risk factors

The EMA is asking AstraZeneca to conduct a number of investigations, including laboratory studies to determine the effect of the vaccine on blood clotting, and evaluations of data from clinical trials, to try to glean any further information about risk factors. Although there are reports that the syndrome is seen more often in women than in men, particularly in women aged under 60, the EMA was unable to conclude that women are at higher risk. Many countries prioritized health-care workers to receive the inoculations, and women comprise a larger segment of this workforce.

The EMA is also supporting studies by two academic consortia centred in the Netherlands, one led by Erasmus University Medical Center in Rotterdam and the other by investigators at Utrecht University and the University Medical Center Utrecht.

Their project list is ambitious. One of the consortia, co-chaired by virologist Eric C. M. van Gorp at Erasmus, consists of 22 hospitals that have been working together to study the effects of coronavirus on blood coagulation. The team will look for potential cases of HIT among people who developed blood clots following vaccination with the Oxford–AstraZeneca vaccine or other COVID-19 vaccines. It will also conduct lab studies to look for signs that the already-small risk could be cut further by reducing the amount of vaccine administered in each dose.



What scientists do and don't know about the Oxford–AstraZeneca COVID vaccine

The EMA expects to obtain some results from the projects within the next two months, said Peter Arlett, head of the agency's Data Analytics and Methods task force. The team will also try to tease apart whether this problem is restricted to certain populations. "What we find in Western Europe will not automatically be true in South America or other populations," says van Gorp. "This is a worldwide problem; everyone is concerned."

And, crucially, van Gorp and his colleagues will try to further evaluate whether the "probable" association between the vaccine and the syndrome is real. It is notoriously difficult to confirm whether a suspected rare effect of a vaccine is truly linked to the vaccine — particularly when it is one that has been used in tens of millions of people. "Somebody who gets the vaccine could have a stroke or a heart attack a week later because they were already going to have a stroke or a heart attack," says cardiologist Behnood Bikdeli at Brigham and Women's Hospital in Boston, Massachusetts. "It's good to be vigilant about these things as we move forward and collect the data, but the absolute number of events and the event rate are so remarkably low."

Underlying causes

Bikdeli would also like to see researchers collect — and share — more data about the incidence of this clotting condition in unvaccinated populations. Heightened awareness of the possible link between vaccination and the syndrome could lead to increased reporting rates among those who have been vaccinated compared with those who have not, which could falsely inflate the perceived rate at which the syndrome occurs, he says. And such concerns could spread to other coronavirus vaccines.

Other researchers are keen to pick apart what triggers the syndrome. HIT is thought to be the result of an immune reaction to complexes formed when negatively charged heparin molecules bind to a positively charged protein called platelet factor 4, which is important for clotting. This activates platelets, kicking off a chain reaction. “Once you get the platelets activated, it’s like putting a match to tinder,” says John Kelton, a haematologist at McMaster University in Hamilton, Canada, who has been studying HIT for 40 years. “They recruit more and more platelets, and when they are activated, they explode and produce coagulant material. HIT is like a forest fire; it just self-perpetuates.”



What it will take to vaccinate the world against COVID-19

Although exceedingly rare, cases of ‘spontaneous’ HIT in the absence of heparin treatment have been reported before, with suspected triggers including infection, knee surgery and treatment with drugs that — like

heparin — are negatively charged. Kelton recalls a case he worked on years ago of a woman in her forties experiencing catastrophic strokes who had not been treated with heparin. “We tested her blood and found reactions exactly the same as reported for the AstraZeneca reactions,” he says.

Kelton’s lab is now working full time to try to determine what might be causing HIT-like symptoms in vaccine recipients, and he’s confident that other labs will be doing the same. It is a tricky phenomenon to study: its rarity makes patient samples difficult to come by, and there are no good animal models, Kelton says.

One result of all of this activity will be increased attention to the relationship between the immune system and blood coagulation, says van Gorp, and the results could inform further vaccine development. “We are going to get new coronavirus variants and are going to develop new vaccines,” he says. “We need answers for the future.”

Nature **592**, 334-335 (2021)

doi: <https://doi.org/10.1038/d41586-021-00940-0>

References

1. 1.

Greinacher, A. *et al.* *N. Engl. J. Med.*
<https://doi.org/10.1056/NEJMoa2104840> (2021).

2. 2.

Schultz, N. H. *et al.* *N. Engl. J. Med.*
<https://doi.org/10.1056/NEJMoa2104882> (2021).

Jobs from Nature Careers

•

◦

- [All jobs](#)
 -
- [**Research Associate / PhD Student**](#)

[Technische Universität Dresden \(TU Dresden\)](#)
[Dresden, Germany](#)

[JOB POST](#)
- [**PostDoc \(f/m/d\) in Physical chemistry or Material Chemistry - Design and synthesis of plasmonic nanostructures**](#)

[Helmholtz-Zentrum Berlin for Materials and Energy \(HZB\)](#)
[Berlin, Germany](#)

[JOB POST](#)
- [**Betriebspraktikum in der 9. Klasse**](#)

[Helmholtz Centre Potsdam - German Research Centre for Geosciences \(GFZ\)](#)

[Potsdam, Germany](#)

[JOB POST](#)
- [**55832: Physicist, engineer or similar \(f/m/x\) - Development, application and scientific evaluation of greenhouse gas lidar systems**](#)

[German Aerospace Center \(DLR\)](#)
[Oberpfaffenhofen, Germany](#)

JOB POST

This article was downloaded by **calibre** from <https://www.nature.com/articles/d41586-021-00940-0>

| [Section menu](#) | [Main menu](#) |

NEWS

07 April 2021

Why US coronavirus tracking can't keep up with concerning variants

The country has an enormous virus-sequencing capacity, but funding and coordination roadblocks are holding it back.

- [Amy Maxmen](#)

1. Amy Maxmen

[View author publications](#)

You can also search for this author in [PubMed](#) [Google Scholar](#)



Researchers unpack SARS-CoV-2 samples for genomic sequencing at Duke University in Durham, North Carolina. Credit: Pete Kiehart/New York Times/Redux/eyevine

As COVID-19 cases surge again in the United States, coronavirus variants are on the rise. But researchers fear that the country is ramping up surveillance of the coronavirus SARS-CoV-2 too slowly, allowing these variants — which evidence shows^{1,2} could make vaccines less effective — to spread undetected in one of the countries hit hardest by the disease.

Laboratories supported by the US government have doubled the rate at which they are sequencing SARS-CoV-2 genomes over the past two months. Still, the number of genomes that the country shared in the [online genome repository GISAID](#) in March represented only 1.6% of its positive COVID-19 cases that month. And the United States [lags behind](#) at least 30 countries in terms of the sequencing it has done throughout the pandemic, according to GISAID data.

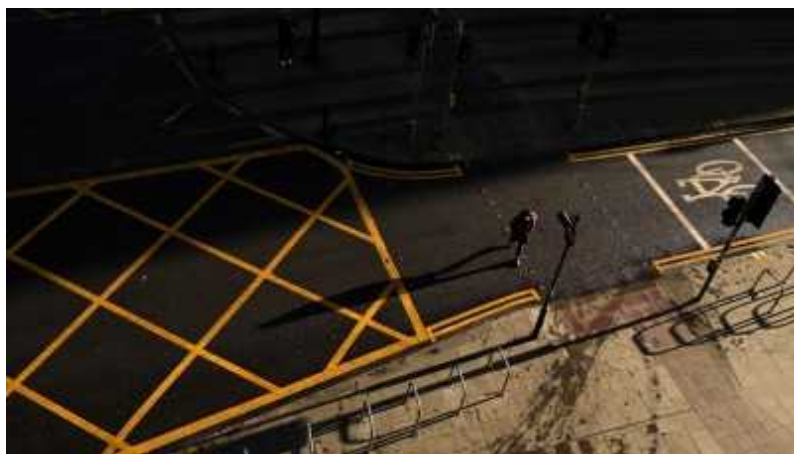


Multitude of coronavirus variants found in the US — but the threat is unclear

This frustrates researchers because the United States possesses the equipment and expertise to be doing far more. “We have enough sequencers to sequence SARS-CoV-2 from every case, 100 times over,” says Kristian

Andersen, an immunologist at the Scripps Research Institute in La Jolla, California.

A dozen academic researchers at some of the leading virus-sequencing labs in the United States tell *Nature* that a series of problems is holding the country back. Last year, university labs were doing the majority of coronavirus sequencing in the country. They are still responsible for approximately 40% of the sequences on GISAID, with companies and government labs now adding to the effort.



Alarming COVID variants show vital role of genomic surveillance

US President Joe Biden [listed variant surveillance](#) as a priority for his administration immediately after taking office in January, and it was specified as a response measure that will receive some of the US\$19 billion in COVID-19 relief funds [announced that month](#). But researchers say federal money isn't flowing fast enough and systemic problems in sharing samples and data are preventing them from ramping up.

It's not for lack of trying. The US Centers for Disease Control and Prevention (CDC) is additionally investing \$200 million to expand surveillance at university, government and company labs, and it has launched initiatives to connect researchers at these labs and track data. The agency is continuing to fund several universities as part of its long-standing Emerging Infections Program, in which academic labs partner with state health departments. But genomic surveillance at this scale has never happened anywhere before — and the fragmented US health system makes

coordination a gargantuan task, researchers agree. Hospitals, diagnostic testing labs, local health departments and sequencing centres have rarely worked in unison with one another.

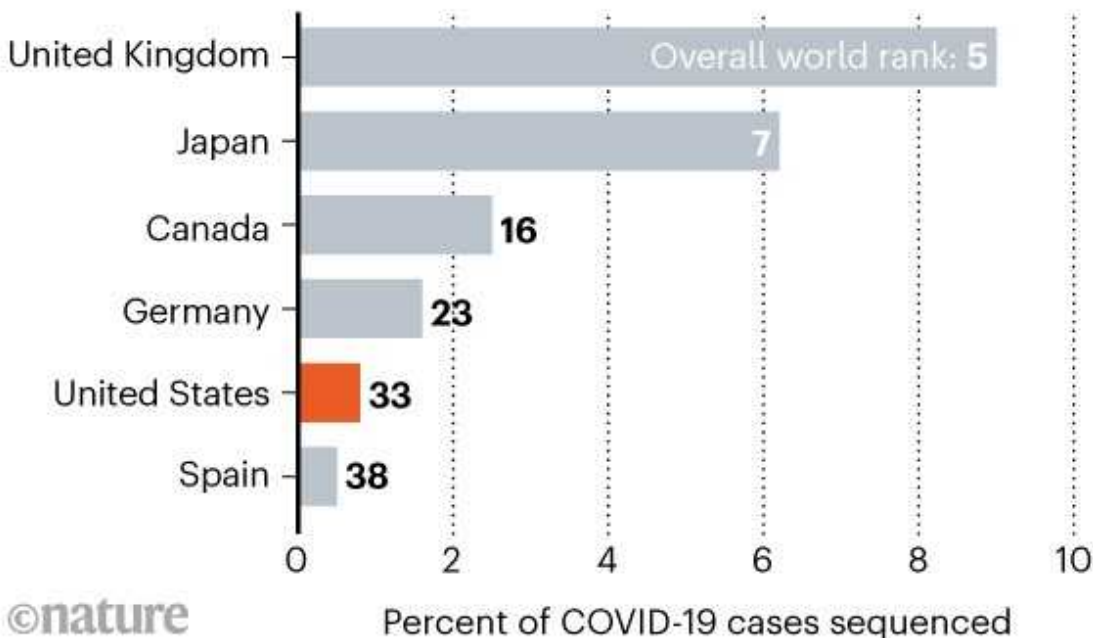
“The biggest challenge is that we don’t have a single health system,” says Art Reingold, an epidemiologist at the University of California, Berkeley. “It’s a nightmare.”

Spotty surveillance

To test for SARS-CoV-2, researchers extract RNA from a specimen and search for genetic fragments indicative of the virus. Some university labs that became testing centres during the pandemic sequenced the entire genomes of viruses when time and money allowed, putting them at the forefront of surveillance efforts last year. “Our sequencers have been humming since the start of the pandemic,” says Pavitra Roychoudhury, a computational biologist at the clinical virology department at the University of Washington (UW) in Seattle. But a lack of money for supplies and for paying researchers has frequently prevented Roychoudhury’s lab from sequencing its total capacity of about 1,000 genomes per week.

LAGGING BEHIND

The United States has sequenced the SARS-CoV-2 genomes of fewer of its COVID-19 cases than several other high-income countries hit hard by the pandemic.



Sources: GISAID, COVID-19 Genomics UK Consortium, and Covid-19 CG

Despite financial limitations, her lab and others have demonstrated the importance of sequencing. For example, at Scripps, Andersen's team identified the first coronavirus variant to appear in California in early January — the B.1.1.7 variant, which emerged in the United Kingdom. “San Diego is now at 50% B.1.1.7, and very soon everything we have will be B.1.1.7,” he says, adding that this variant has been shown³ to correlate with a higher risk of death from COVID-19.

The CDC tried to help with surveillance last spring by launching a programme, called Sequencing for Public Health Emergency Response, Epidemiology and Surveillance (SPHERES), to connect researchers at universities, companies and government labs. Although it was successful at creating a flow of information between these entities, SPHERES didn't dole out funding and therefore didn't significantly increase sequencing rates.



Pandemic whistle-blower: we need a non-political way to track viruses

With the CDC now awarding funds to university, health-department and company labs, the country's sequencing will soon accelerate, says Duncan MacCannell, the chief science officer at the CDC's Office of Advanced Molecular Detection. In March, nearly 29,000 coronavirus sequences from the United States were uploaded onto GISAID, which has the most SARS-CoV-2 sequences in the world, even though it doesn't contain all of the genomes sequenced. But at the current pace of COVID-19 infections in the United States, the country must reach about 23,000 sequences per week to sequence 5% of all cases, a benchmark considered sufficient to detect emerging variants. (This figure comes from a modelling study⁴ published on the medRxiv preprint server without peer review and funded by the biotechnology company Illumina, based in San Diego, California.)

Saving samples

But researchers at several labs say a lack of samples is as big of a problem as a lack of funding. "We could easily run 1,500 samples each week, but we're running about 380," says Lea Starita, a genomicist at the UW Northwest Genomics Center in Seattle. "Someone needs to be willing to fork samples over."

The problem is that most COVID-19 tests are conducted in diagnostic labs at companies that don't regularly do genomic sequencing. These labs

frequently discard samples after testing, because saving them requires extra labour and storage.



Why the United States is having a coronavirus data crisis

But if a health department wants a deeper investigation into an individual case, officials might ask researchers at a nearby university to sequence the sample. “So we have to scramble to go back to the [testing] lab, and say, do you still have the specimen for Mr. Jones? Save it! Save it! And that’s a huge challenge,” explains William Schaffner, an infectious-disease specialist at Vanderbilt University in Nashville, Tennessee, who works with the Tennessee Department of Health as part of the CDC’s Emerging Infections Program. Some testing sites won’t have saved the sample. Others won’t share it for privacy or proprietary reasons, explains Reingold.

The CDC is all too aware of the issues. “We have a very distributed testing system, and private testing labs that aren’t incentivized to hang onto samples,” says MacCannell. He and his colleagues are helping diagnostic labs either ramp up their own sequencing or connect with labs that can. The agency has also [provided guidance](#) on how public-health labs can partner with academic institutions for coronavirus surveillance. “One of our long-standing goals,” MacCannell says, “is to figure out better ways to engage with academics throughout the public-health system.”

Data flow

Certain university labs, such as the Broad Institute of MIT and Harvard in Cambridge, Massachusetts, don't have a problem getting samples, because they've served as major testing centres throughout the pandemic. Health departments and hospitals in their states were already shipping specimens to these labs. But every researcher interviewed by *Nature* — including MacCannell at the CDC — complained about a lack of information connected to samples.



[Massive Google-funded COVID database will track variants and immunity](#)

Such data are needed to uncover where variants are spreading, if variants make the coronavirus more contagious and whether variants help the coronavirus to evade vaccines or natural immunity from a prior infection. This information is scattered like crumbs along the path that a sample travels, but hospitals, health departments and labs are often reluctant to release data because of privacy or proprietary reasons. Stacia Wyman, a computational genomicist at the Innovative Genomics Institute at the University of California, Berkeley, says, “It’s tough to know what’s allowed, and public-health departments don’t have a huge bandwidth for this.”

MacCannell says siloed data have been a problem for the CDC for many years. “Historically, disease surveillance has been very difficult because many states are uncomfortable with details being provided in public databases.” But he’s heartened that the need to keep tabs on coronavirus variants has raised the profile of this issue, and hopes that it will help researchers at disconnected institutions to find ways to share information that could save lives.

In that vein, a platform to share de-identified data on individual COVID-19 cases [launched last month](#). And a philanthropic organization funding the platform, the Rockefeller Foundation, [has announced plans](#) to build an even larger version, with the goal of including data from genomic sequencing and analyses presented in ways to help inform policies.

However, MacCannell and other researchers argue that a government agency, such as the CDC, is best positioned to cut through the red tape that prevents samples from moving to sequencing labs or data from flowing. “I’m convinced that we can do this, and that we can be nimble,” says MacCannell. “But, you know, it is challenging in a pandemic.”

Nature **592**, 336-337 (2021)

doi: <https://doi.org/10.1038/d41586-021-00908-0>

References

1. 1.

McCallum, M. *et al.* Preprint at bioRxiv
<https://doi.org/10.1101/2021.03.31.437925> (2021).

2. 2.

Garcia-Beltran, W. F. *et al.* *Cell*
<https://doi.org/10.1016/j.cell.2021.03.013> (2021).

3. 3.

Davies, N. G. *et al.* *Nature* <https://doi.org/10.1038/s41586-021-03426-1> (2021).

4. 4.

Vavrek, D. *et al.* Preprint at medRxiv
<https://doi.org/10.1101/2021.01.12.21249613> (2021).

Jobs from Nature Careers

- - - [All jobs](#)
 - - [Research Associate / PhD Student](#)
 - [Technische Universität Dresden \(TU Dresden\)](#)
[Dresden, Germany](#)
[JOB POST](#)
 - [PostDoc \(f/m/d\) in Physical chemistry or Material Chemistry - Design and synthesis of plasmonic nanostructures](#)
[Helmholtz-Zentrum Berlin for Materials and Energy \(HZB\)](#)
[Berlin, Germany](#)
[JOB POST](#)
 - [Betriebspraktikum in der 9. Klasse](#)
 - [Helmholtz Centre Potsdam - German Research Centre for Geosciences \(GFZ\)](#)

Potsdam, Germany

JOB POST

- **55832: Physicist, engineer or similar (f/m/x) - Development, application and scientific evaluation of greenhouse gas lidar systems**

German Aerospace Center (DLR)

Oberpfaffenhofen, Germany

JOB POST

This article was downloaded by **calibre** from <https://www.nature.com/articles/d41586-021-00908-0>

| [Section menu](#) | [Main menu](#) |

NEWS EXPLAINER

01 April 2021

After the WHO report: what's next in the search for COVID's origins

A World Health Organization report makes a reasonable start, scientists say, but there are many questions yet to be answered.

- [Smriti Mallapaty](#)

1. Smriti Mallapaty

[View author publications](#)

You can also search for this author in [PubMed](#) [Google Scholar](#)



Food and surfaces are sampled for traces of the virus at a wet market in China.Credit: Wei Liang/China News Service via Getty

Researchers say that a World Health Organization (WHO) report on the pandemic's origins offers an in-depth summary of available data, including unseen granular details. But much remains to be done to establish the provenance of the virus — knowledge that will help to prevent future pandemics.

The report was the result of a joint investigation between Chinese and international researchers that included a four-week trip earlier this year to Wuhan, China, where COVID-19 was first detected.

The details in the report were helpful, but didn't include much new information, says David Robertson, a virologist at the University of Glasgow, UK. "The extensive data presented confirmed a lot of what was already known, particularly on the timing of events and early cases in Wuhan."

Challenges remaining include finding the animal that probably carried the virus from bats to humans, and determining how that spillover into people occurred.

"This is just a very first step on an expectedly long trip to find the origin," said WHO team member Thea Fisher, a public-health virologist at the North Zealand Hospital in Copenhagen, at a press briefing on 30 March.

Nature spoke to scientists about what needs to come next.

What's new in the report?

The report [describes the results of many lines of investigation](#), including when SARS-CoV-2 was first detected in people and which animals might have harboured it. It places the start of the outbreak in the months before mid-December, when the virus could have been spreading undetected. It was perhaps introduced to the community through an unknown animal that acted as an intermediary between bats, which carried an ancestral virus, and people.



[WHO report into COVID pandemic origins zeroes in on animal markets, not labs](#)

The team didn't find that species, even though researchers in China tested tens of thousands of wildlife and livestock samples, but team members point to wild-animal markets for future leads. They also conclude that it is "extremely unlikely" that the virus leaked from a laboratory.

The report reveals much about the first known people to contract COVID-19 — and about their links to the Huanan market, where many early cases were identified — says Virginie Courtier, an evolutionary geneticist at the Jacques Monod Institute in Paris. It is the most comprehensive molecular epidemiological study on the Wuhan outbreak, she adds.

What do scientists still want to know?

Many key questions remain, including about the intermediate animal carrier and where and when that spillover occurred. The report includes [recommendations for further studies](#), including following the trail of farmers and suppliers trading in animals and animal products at markets across Wuhan.

The priority should be to “follow the animals”, starting at the Huanan market, says Eddie Holmes, a virologist at the University of Sydney in

Australia. Given the [large number of animal species that SARS-CoV-2 can infect](#), that sampling should be as expansive as possible, say researchers.

And it should definitely include bats. The closest known relative of SARS-CoV-2 is a bat coronavirus called RaTG13, isolated from a bat in a mine in Mojiang, southern China. But it shares only 96% of its genome with SARS-CoV-2, meaning that it is only distantly related. Courtier says that more bats should be sampled from that mine, and that researchers should share the sequences of other coronaviruses isolated there.

But Linfa Wang, a virologist at Duke–National University of Singapore Medical School, doubts whether closer relatives will be found, given the exhaustive sampling done in the cave by researchers over the past decade. “If you gave me a billion dollars, I would not sample in Mojiang cave. I would sample in southeast Asia,” adds Wang, who says that sampling should extend to [lesser-sampled regions such as Thailand and Cambodia](#), where other relatives of SARS-CoV-2 have recently been isolated.

To pin down when the virus first occurred in people, the “obvious low-hanging fruit” is to test archived blood samples for antibodies at the Wuhan Blood Center, says Wang. The centre receives 200,000 donations a year and stores them for two years. The report recommends testing samples in blood banks across China and globally, focusing on the six months before the first known cases.

Other researchers say that more details about the first known cases are needed, including full genome sequences to reveal their diversity and what the early virus looked like.

What will happen next in the origins search?

With many unanswered questions, a lot still needs to be done. The visit to Wuhan was the first phase in a WHO process that started in May 2020; it will be followed by longer-term studies, according to an agreement between China and the WHO.

Dominic Dwyer, a virologist at New South Wales Health Pathology in Sydney, and a WHO team member, says that some of the work has already

started, including a re-analysis of surveillance data on influenza-like illnesses in China before January 2020. But other work, including testing donated blood, will take longer to get under way. Other projects are identifying wildlife farms supplying markets in Wuhan and assessing how long the virus can [persist in frozen foods](#) that might also have been a source of transmission.

Tedros Adhanom Ghebreyesus, the WHO's director-general, said in a statement that the organization was committed to continuing the search. "It is clear that we need more research across a range of areas, which will entail further field visits."

The focus of research into COVID-19's origins should now be to mitigate future spillovers from animals to people of SARS-CoV-2 and other viruses with pandemic potential, says David Heymann, an infectious-disease epidemiologist at the London School of Hygiene & Tropical Medicine. "We need to change the paradigm from rapid detection and response, to prevention at the source," he adds.

Robertson agrees that assessing the risk of such events should be a priority. "If, as the data suggests, SARS-CoV-2 didn't have to change much, or at all, to be so transmissible in humans, there's very little barrier to future emergence," he says.

Groups not involved with the WHO study have already ramped up sampling and sequencing of archived samples from bats and possible intermediate animals, in China and across southeast Asia, to look for potential ancestral viruses. In the past month, researchers in Yunnan, a province in the southwest of China, have identified several new bat coronaviruses that are closely related to SARS-CoV-2.



Crocodile meat is prepared for sale at a seafood market in Guangzhou. Credit: Alex Lee/Reuters

What's next for the lab-leak theory?

The report concludes that the chances of COVID-19 having originated in a lab accident are slim. But there is growing pressure, including some from researchers, for a more comprehensive inquiry into this possible route.

WHO team members did not have the required background to investigate a biosafety breach, says Filippa Lentzos, a biosecurity researcher at King's College London.

Tedros agreed that further investigation was needed, and was willing to send additional missions involving relevant experts. He said that the team's assessment, based on lab visits and interviews with researchers, was not extensive enough, adding that "as far as WHO is concerned, all hypotheses remain on the table".

A key argument against the lab-leak hypothesis is that SARS-CoV-2 was an unknown virus before the pandemic, with no trail in public databases and research articles. But some researchers say that it is not possible to know exactly which viruses had been sampled around the world.

Wang says it's highly unlikely that a lab would keep such information secret, but he adds that there's a small chance that someone doing research on bats inadvertently got infected by an unknown virus while collecting bat samples in a cave, and that this infection seeded the pandemic.

Nikolai Petrovsky, an immunologist at Flinders University in Adelaide, Australia, says that given the lack of evidence, the team "would have been best to have been silent on the question because, scientifically, we simply don't know".

What do scientists think about the WHO's handling of the joint mission?

The question of the pandemic's origins has been politically fraught from the start. Many researchers say that the team did an excellent job of synthesizing the available evidence under difficult circumstances.



[Can COVID spread from frozen wildlife? Scientists probe pandemic origins](#)

Given the constraints the investigators were under, the report is a “useful and thorough appraisal of what we know and what we need to do”, says Holmes. These constraints included the brief, four-week time frame, restrictions on access to material and the narrow scope of the work, he says.

But others are disappointed with how politics seems to have overshadowed the search for answers. The “WHO have handled this as a diplomatic mission and not as an independent scientific investigation into all possible sources”, says Petrovsky.

Following the report’s release, the United States and more than a dozen other countries issued a statement raising concerns about delays and the team’s limited access to raw data. This called for “a renewed commitment by WHO and all member states to access, transparency, and timeliness”.

However, others point out that for China to open up and allow the team in to conduct such an investigation was in itself unusual. “If you consider other highly industrialized countries, I am not sure they would,” says Heymann.

Will scientists ever find the origin of the virus?

Given the politics and the many unanswered questions, some scientists have wondered whether the origins of the pandemic might forever remain elusive. But those familiar with tracing origins say that it takes time, and a bit of luck.

The sources of many human viruses took years to understand, says Robertson. “Viruses are tricky, as rare events can have massive implications.” However, with sufficient sampling of animals, researchers should be able to identify where, and in which animals, the ancestors of SARS-CoV-2 were circulating, he says.

Courtier is optimistic that studies of molecular evolution will help to confirm whether the outbreak was the result of a laboratory accident or a natural spillover, because they will show whether viruses have been stored or manipulated.

But Lentzos argues that the origins might forever be shrouded in uncertainty. “I seriously doubt we’ll find a smoking gun,” she says. “There won’t be an undisputable origins answer. All we’ll have are likelihoods and probabilities.”

Nature **592**, 337-338 (2021)

doi: <https://doi.org/10.1038/d41586-021-00877-4>

Jobs from Nature Careers

- - - [All jobs](#)
 - - [Research Associate / PhD Student](#)
 - [Technische Universität Dresden \(TU Dresden\)](#)
 - [Dresden, Germany](#)
 - [JOB POST](#)
 - [PostDoc \(f/m/d\) in Physical chemistry or Material Chemistry - Design and synthesis of plasmonic nanostructures](#)
 - [Helmholtz-Zentrum Berlin for Materials and Energy \(HZB\)](#)
 - [Berlin, Germany](#)
 - [JOB POST](#)
 - [Betriebspraktikum in der 9. Klasse](#)

Helmholtz Centre Potsdam - German Research Centre for Geosciences (GFZ)

Potsdam, Germany

JOB POST

- **55832: Physicist, engineer or similar (f/m/x) - Development, application and scientific evaluation of greenhouse gas lidar systems**

German Aerospace Center (DLR)

Oberpfaffenhofen, Germany

JOB POST

This article was downloaded by **calibre** from <https://www.nature.com/articles/d41586-021-00877-4>

| [Section menu](#) | [Main menu](#) |

NEWS

07 April 2021

Oldest DNA from a *Homo sapiens* reveals surprisingly recent Neanderthal ancestry

Ancient human lineages interbred commonly in Europe, as well as the Middle East.

- [Ewen Callaway](#)
 1. Ewen Callaway
[View author publications](#)

You can also search for this author in [PubMed](#) [Google Scholar](#)



The skull of a modern human female individual from Zlatý kůň. Credit: Marek Jantač

Scientists have sequenced the oldest *Homo sapiens* DNA on record, showing that many of Europe's first humans had Neanderthals in their family trees. Yet these individuals are not related to later Europeans, according to two genome studies of remains dating back more than 45,000 years from caves in Bulgaria and the Czech Republic^{1,2}.

The research adds to growing evidence that modern humans mixed regularly with Neanderthals and other extinct relatives, says Viviane Slon, a palaeogeneticist at the University of Tel Aviv in Israel. "It's different times, different places, and it happens again and again."

The genetic history of the earliest humans in Europe and Asia has been blurred. Although researchers have sequenced DNA from Neanderthals and other extinct human relatives dating as far back as 430,000 years, there is a scarcity of genetic information from the period between around 47,000 and

40,000 years ago, known as the Initial Upper Palaeolithic, and no *Homo sapiens* DNA at all from before this period. Genomes belonging to humans from Siberia and Romania showed no connection to later waves of Europeans, but a 40,000-year-old individual from China is a partial ancestor of modern East Asian people.

Like all present-day people whose ancestry isn't solely African, these early Eurasians carried Neanderthal DNA. Researchers thought that probably originated from mixing between the groups in the Middle East 50,000–60,000 years ago. But a 2015 study³ of the genome of the 40,000-year-old Romanian individual, from a site called [Peștera cu Oase](#), held a surprise: a Neanderthal ancestor in the past four to six generations, suggesting that humans interbred with Neanderthals in Europe, too.

It was not clear from the [Oase man](#)'s genome whether interbreeding was common in Europe. He lived around the time when Neanderthal populations, already sparse, were beginning to vanish from the region.

Genetic mixture

The latest genome studies, both published on 7 April, clarify the relationships between Europe's first modern humans, later *Homo sapiens* and Neanderthals, but also throw up some new questions. One study, in *Nature*¹, is based on a tooth and fragmentary remains from Bacho Kiro Cave in Bulgaria; the other, in *Nature Ecology and Evolution*², looks at a nearly complete skull from a cave known as Zlatý kůň in the Czech Republic.

The three oldest Bacho Kiro individuals, dated to between 45,900 and 42,600 years old, all had recent Neanderthal forebears, reports a team led by molecular biologist Mateja Hajdinjak and evolutionary geneticist Svante Pääbo, both at the Max Planck Institute for Evolutionary Anthropology (MPI-EVA) in Leipzig, Germany. The genomes of modern non-Africans usually harbour about 2% Neanderthal ancestry, but the Bacho Kiro individuals had slightly more at 3.4–3.8%, and the chromosome segments — which shorten in successive generations — were considerably longer.

By measuring these segments, the researchers estimated that the Bacho Kiro individuals had Neanderthal ancestors as recently as the past six or seven generations — and probably in Europe, not the Middle East. “We saw these huge chunks. It was completely amazing,” says Hajdinjak, who is now at the Francis Crick Institute in London and was part of the team that identified the same patterns in the Oase man’s genome. “What are the chances of finding them again?”

The Zlatý kůň woman’s Neanderthal ancestry goes back considerably longer: 70–80 generations, or perhaps 2,000–3,000 years, says Johannes Krause, a palaeogeneticist at the MPI-EVA who co-led the study. His team could not date the skull accurately because of contamination. But on the basis of its Neanderthal ancestry, Krause suspects it is well over 45,000 years old, and in the same ballpark as the oldest remains from Bacho Kiro. “We do have, now, some of the oldest human genomes out there,” adds Hajdinjak.

Tracing the lineage

The oldest individuals from Bacho Kiro and the Zlatý kůň female are not related to later Europeans, ancient or modern, meaning that their lineages must have disappeared from the region. But, to their surprise, Hajdinjak and her colleagues found that the Bacho Kiro people shared a connection with contemporary East Asians and Native Americans. Hajdinjak suggests that the Bacho Kiro remains represent a population that once lived across Eurasia, but vanished from Europe and lived on in Asia.

The fact that several humans from Bacho Kiro had very recent Neanderthal relatives suggests that the groups mixed routinely in Europe, says Marie Soressi, an archaeologist at the University of Leiden in the Netherlands who plans to examine European archaeology through this lens.

Stone tools and other artefacts common to the Initial Upper Palaeolithic — and distinct from typical Neanderthal and later human toolkits — could be a product of cultural exchanges or even mixed populations, she says. “We really want to better understand what happened, what was the historical process and how peaceful were those encounters.”

Nature **592**, 339 (2021)

doi: <https://doi.org/10.1038/d41586-021-00916-0>

References

1. 1.

Hajdinjak, M. *et al.* *Nature* <https://doi.org/10.1038/s41586-021-03335-3> (2021).

2. 2.

Prüfer, K. *et al.* *Nature Ecol. Evol.* <https://doi.org/10.1038/s41559-021-01443-x> (2021).

3. 3.

Fu, Q. *et al.* *Nature* **524**, 216–219 (2015).

Jobs from Nature Careers

- - - [All jobs](#)
 - - [Research Associate / PhD Student](#)
 - [Technische Universität Dresden \(TU Dresden\)](#)
 - [Dresden, Germany](#)
 - [JOB POST](#)
 - [PostDoc \(f/m/d\) in Physical chemistry or Material Chemistry - Design and synthesis of plasmonic](#)

nanostructures

Helmholtz-Zentrum Berlin for Materials and Energy (HZB),
Berlin, Germany

JOB POST

- **Betriebspraktikum in der 9. Klasse**

Helmholtz Centre Potsdam - German Research Centre for
Geosciences (GFZ)

Potsdam, Germany

JOB POST

- **55832: Physicist, engineer or similar (f/m/x) -
Development, application and scientific evaluation
of greenhouse gas lidar systems**

German Aerospace Center (DLR)

Oberpfaffenhofen, Germany

JOB POST

This article was downloaded by **calibre** from <https://www.nature.com/articles/d41586-021-00916-0>

NEWS FEATURE

14 April 2021

The race for antiviral drugs to beat COVID — and the next pandemic

Despite dire warnings, a stockpile of ready compounds to fight viral pandemics was sorely lacking. Can drugmakers finally do the right thing?

- [Elie Dolgin](#) ⁰

1. Elie Dolgin

1. Elie Dolgin is a science journalist in Somerville, Massachusetts.

[View author publications](#)

You can also search for this author in [PubMed](#) [Google Scholar](#)

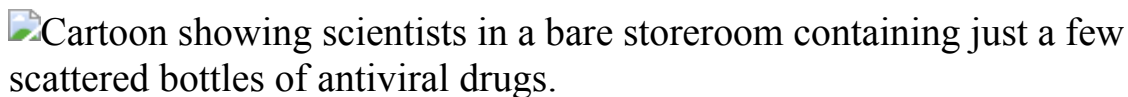


Illustration by David Parkins

The year 2003 was an ominous one for emerging infectious diseases. A pair of deadly influenza strains had leapt from birds to humans in Hong Kong and the Netherlands. And a new coronavirus was spreading around the world causing a mysterious illness that became known as severe acute respiratory syndrome, or SARS. Many experts feared they were watching the start of a global pandemic.

Fortunately, the worst-case scenario never materialized. But it was a close-enough call for Robert Webster, a leading authority on avian influenza, to start urging scientists and policymakers to prepare for the next outbreak.

One of his top recommendations: develop and stockpile drugs that target a wide range of viral pathogens¹.

Drug researchers did not heed his call. After the SARS threat subsided, interest evaporated — and the world paid the price. “The scientific community really should have developed universal antivirals against SARS,” says Webster, now an emeritus member of St Jude Children’s Research Hospital in Memphis, Tennessee. “Then we would have had something in the stockpile for the emergence of COVID,” which is a caused by SARS-CoV-2, a close relative of the virus responsible for SARS.

Another warning shot came in 2012, when Middle East respiratory syndrome (MERS) — caused by another relative of SARS-CoV-2 — started spreading through a handful of countries. Still, the drug shelves remained largely bare — a fact that Jay Bradner, president of the Novartis Institutes for BioMedical Research in Cambridge, Massachusetts, regards as “regrettable”.

“Shame on us,” he says of the pharmaceutical industry. “We can be better prepared.”

Aside from one qualified success in remdesivir, a therapy originally developed to treat hepatitis C and Ebola, there were practically no strong antiviral drug candidates to quickly test and deploy against SARS-CoV-2. Researchers bemoan that there weren’t more options. “We need an arsenal,” says Kara Carter, head of discovery biology at the biotech company Dewpoint Therapeutics in Boston, Massachusetts, and president of the International Society for Antiviral Research.



How COVID unlocked the power of RNA vaccines

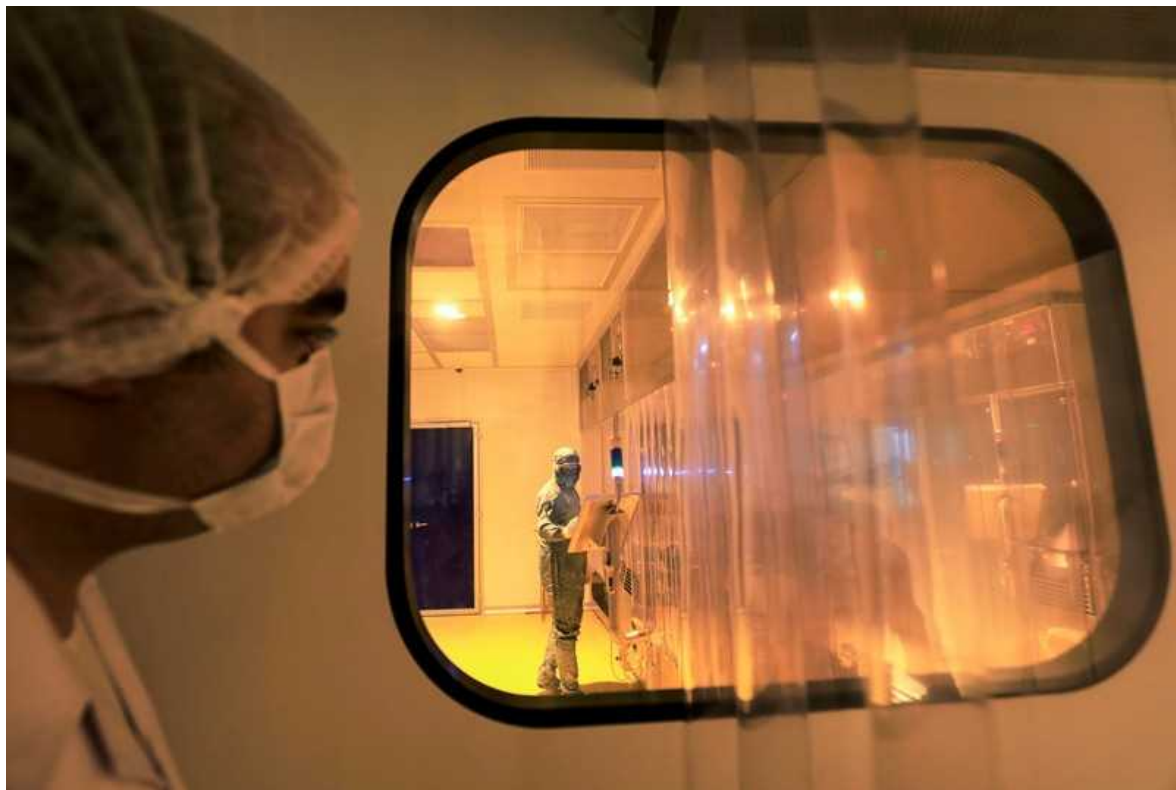
New initiatives to create that arsenal are on the horizon. The US National Institutes of Health (NIH), for one, is planning a major programme to develop therapeutics against SARS-CoV-2 variants and other viruses with pandemic potential. A new industry-backed coalition is taking aim at influenza viruses and coronaviruses. And a few groups hope to create antivirals for more distantly related pathogens that pose a pandemic risk.

These projects won't be starting from scratch. The past year has seen a bevy of SARS-CoV-2-centred drug-discovery efforts. But with the pharmaceutical industry historically focused on just a few particular viruses — HIV and hepatitis C, mostly — finding agents to fight known and imagined threats remains a tall order.

"There's a lot of work that needs to be done," says Nat Moorman, a virologist at the University of North Carolina (UNC) at Chapel Hill. But what choice does the scientific community have? "We don't want to have another year like 2020," Moorman says, "and we don't have to, if we do the work in advance."

Ready for duty

Remdesivir came about thanks to the prudent forethought of researchers involved in the Antiviral Drug Discovery and Development Center (AD3C), an NIH-backed project launched seven years ago. Its objective is to screen existing drug libraries for inhibitors of influenza, coronaviruses, alphaviruses (such as those responsible for chikungunya), and flaviviruses (the pathogens behind dengue and Zika among others). In 2017, AD3C members demonstrated the anti-coronavirus potential of remdesivir in animal models². Around the same time, trials that ran during two Ebola outbreaks in Africa showed that the drug was safe in people.



Laboratory technicians work on remdesivir at the Eva Pharma Facility in Cairo. Credit: Amr Abdallah Dalsh/Reuters

So, when COVID-19 hit, remdesivir was effectively ready to go. It could quickly go into human testing for the new coronavirus. In a large, placebo-controlled trial run over three months in early 2020, clinicians demonstrated that the drug accelerated recovery among people hospitalized with COVID-19³. But remdesivir's usefulness only goes so far. Some clinical studies have failed to confirm that it offers patients any benefit⁴. And the drug is

expensive, difficult to manufacture and must be given intravenously in a hospital — all undesirable attributes in the middle of a pandemic.

Another antiviral drug now nearing approval could address some of those issues. Molnupiravir is an easier-to-synthesize, oral drug option that has been found to shorten the duration of infectiousness among people with symptomatic COVID-19. Late-stage clinical testing is under way.



Funders, now is the time to invest big in COVID drugs

That drug, too, was first studied⁵ — pre-pandemic — by AD3C scientists, who have also identified promising leads against alphaviruses and flaviviruses. According to AD3C leader Richard Whitley, a paediatric infectious-disease specialist at the University of Alabama at Birmingham, all these drug candidates function as fake genetic building blocks that gum up the ability of viruses to copy their genomes faithfully. Instead of inserting the correct RNA bases during replication, a viral enzyme called polymerase is tricked into incorporating derivatives of the drugs. Human polymerases are unfooled, however, so only viruses are affected. (Similar drugs are used to treat hepatitis B, HIV and several other viruses.)

Because viruses in general are poor at catching genetic mistakes, these types of therapy — called nucleoside analogues — often work across viral families. Antiviral drugs that bind enzymes directly and block their function

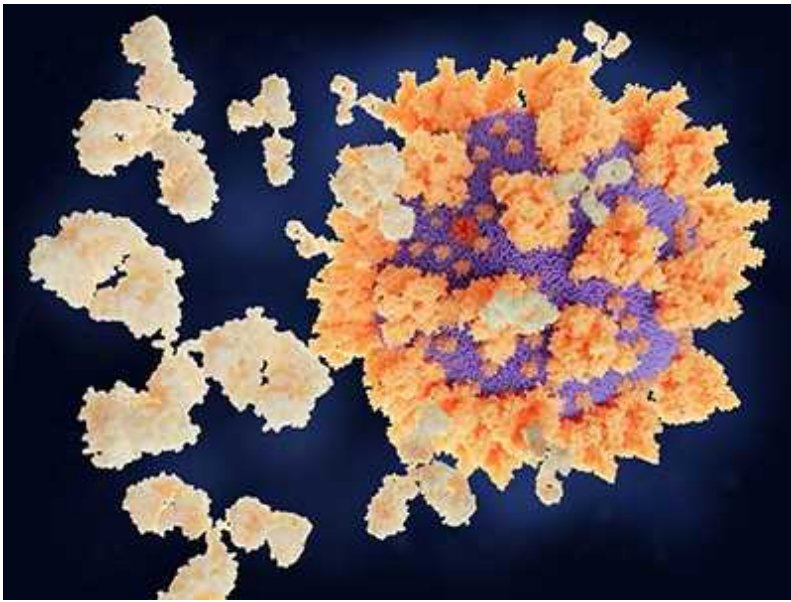
— which is to say, the vast majority of antivirals — do not typically have such broad activity. In principle, scientists could design drugs that work in many viruses by going after the most highly conserved regions of target proteins, says Jasper Fuk-Woo Chan, an emerging infectious-disease researcher at the University of Hong Kong. But, he adds, “traditionally, it’s always been a ‘one bug, one drug’ approach”.

That philosophy has served the industry well when it comes to making new medicines for HIV or hepatitis C. “But it’s proven inefficient in terms of rapidly addressing epidemics or pandemics,” Chan says.

Tricky targets

In many ways, the narrow activity of existing antivirals boils down to the nature of viruses themselves. Other types of pathogen — bacteria, fungi, parasites — are more easily contained because their cellular properties offer an abundance of targets for drug activity. Think about penicillin, which blocks cell-wall synthesis. Or azole antifungals, which disrupt the cell membrane.

Viruses, with their compact genomes and lack of cellular anatomy, offer many fewer druggable targets. Add in a high rate of replication — a typical SARS-CoV-2 infection, for instance, is thought to produce more than one million virions per person per day⁶ — coupled with an inherent genetic mutability, and it’s no wonder that most existing antivirals proved useless for COVID-19.



[COVID antibody treatments show promise for preventing severe disease](#)

The plasticity of viruses means that a drug with activity against, say, herpes is unlikely to make a dent against a coronavirus. Alejandro Chavez, a bioengineer and antiviral drug researcher at Columbia University Irving Medical Center in New York City, thus doubts that anyone will find a “godly inhibitor that’s basically going to block everything”.

“What we will hopefully find”, he says, “are inhibitors that work on, if you’re really lucky, an entire family.” That would make the best-case scenario a pan-coronavirus inhibitor. But a more reasonable goal might be developing a drug for a subset of coronaviruses, such as alphacoronaviruses, which currently cause non-lethal infections in humans, and having a different drug for betacoronaviruses, the group responsible for SARS, MERS, and COVID-19.

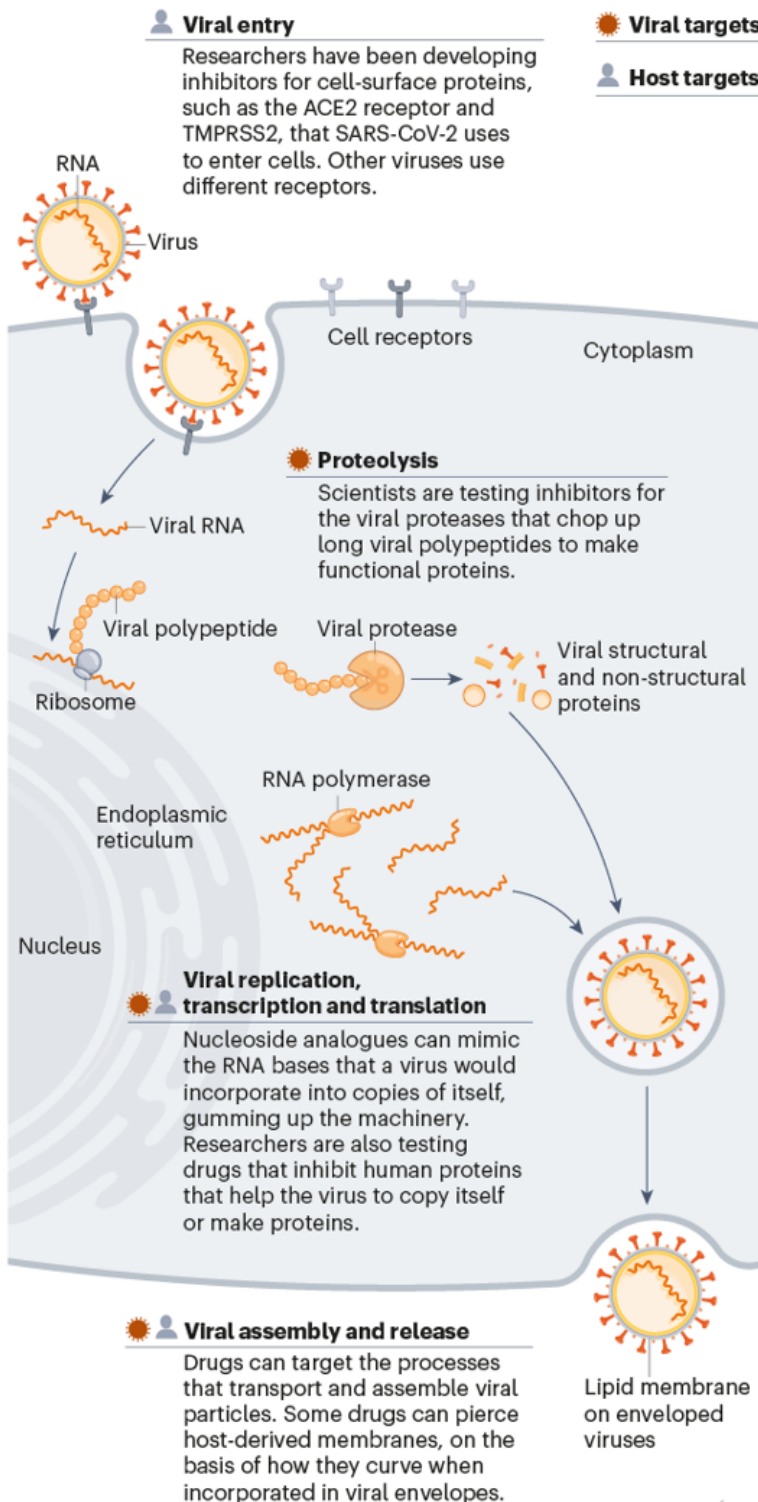
Once the viral lineage is identified, “the same principles of drug discovery apply”, says Marnix Van Loock, head of emerging pathogens at Johnson & Johnson’s global public-health unit in Beerse, Belgium. As he explains, researchers need to find ‘druggable pockets’ on the surface of essential enzymes that are conserved between related viruses and can be used to design active molecules.

At least, that is, if the drug is directed at the virus itself. Some drug researchers instead aim to interfere with human pathways that a broad array of viruses commandeer for their own purposes. Jeffrey Glenn, for one, is developing a drug that blocks a fat-regulating enzyme used by many viruses to promote cellular entry and replication. By inhibiting this enzyme, “you deprive the virus access to a host function upon which it depends”, says Glenn, a gastroenterologist and molecular virologist at Stanford University School of Medicine in California.

Another host-directed antiviral strategy comes from two of Glenn’s former trainees — Nam-Joon Cho, a materials scientist at Nanyang Technological University in Singapore, and Joshua Jackman, a chemical engineer at Sungkyunkwan University in Seoul. They have developed small peptide drugs that poke holes in the lipid wrappings found around enveloped viruses⁷. These lipids come from the membrane surface of human cells. But the peptides penetrate only lipids that encase viruses, not cells, because of differences in the size of the membrane structure and how much it bends (see ‘The many ways to thwart viruses’).

THE MANY WAYS TO THWART VIRUSES

To fight a broad array of viruses, antiviral drugs can target highly conserved features of the viruses themselves — or they can interfere with biological processes in the host that viruses exploit to infect cells and spread. Here are some of the strategies that researchers are looking into.



Credit: Nik Spencer/*Nature*

Cho describes the lipid coating as the “common denominator” of all enveloped viruses — a group that includes flaviviruses, alphaviruses, coronaviruses, filoviruses, retroviruses and more. No other shared feature exists broadly across all those diverse viruses, which is why he thinks host-targeted antivirals might have greater potential as pandemic-preparedness tools.

Human biology also offers many more potentially druggable targets than do viruses. Plus, viruses are less able to develop resistance against host-targeted antivirals. A viral protein might need just a mutation or two to thwart drug binding, for example, whereas a host-targeted therapy could force the virus to exploit entirely different cellular processes.

Some scientists fear that tampering with human molecular pathways could cause unwanted side effects — but Shirit Einav, a virologist and infectious-disease specialist at Stanford University, thinks those toxicity concerns are overblown. “We treat every other disease by targeting a host function,” she says, and drug companies manage to find molecules and dosing regimens that people can tolerate. So, why should antivirals be any different? What’s more, she adds, “treating acute infections requires only several days of therapy” — not months or years, as for chronic illnesses — “which also helps reduce toxicity”.

Prep work

A combination of host-targeted and direct-acting drugs might offer the best insurance against future viral threats. But whatever strategy scientists pursue, experts agree that any drug intended for pandemic preparedness must, at a minimum, be fully tested in animal models and go through some trials in healthy human volunteers. “Then, when there’s a pandemic, we can rapidly deploy them at the best dose range in people,” says chemist Kelly Chibale, head of the Drug Discovery and Development Centre at the University of Cape Town, South Africa.

The goal would be to approve and distribute such a drug in the crucial window when other types of rapid-response medicine — such as vaccines or antibody treatments — are not yet available.

Drug developers took on some of that advance work in the wake of SARS. At drug company Pfizer's La Jolla laboratories in California, for example, scientists responded to the 2003 outbreak by designing a molecule⁸ that inhibits a protein integral to coronavirus replication, an enzyme known as the main protease (M^{pro}), which chops up long chains of viral proteins into their functional parts.



What scientists do and don't know about the Oxford–AstraZeneca COVID vaccine

For about six months, “it was a very intense effort”, says chemist Rob Kania, who led Pfizer’s SARS project. But infections soon petered out. And after the last cases of SARS were reported in 2004, Pfizer and other companies working on SARS drugs shelved their programmes. There just wasn’t a future market for the therapy. As UNC virologist Timothy Sheahan, who previously worked in pharmaceuticals, points out: “It’s hard to convince a company to make a drug against something that doesn’t exist.”

Kania’s team never had a chance to fully optimize its lead candidate for clinical use, let alone to test the therapy in mice or in people. So, when

SARS-CoV-2 came along and genomic analyses revealed that the virus's M^{pro} protein was almost identical to that from the original SARS pathogen, there was still a lot of chemical fine-tuning to do. By the time the drug, in a slightly different form, was ready for human testing⁹, the first wave of the pandemic had already subsided and almost one million people had died from the infection worldwide.

That drug, called PF-07304814, entered trials last September as an intravenously administered agent. Although the research could have been further advanced, at least Pfizer was not starting from scratch, says Charlotte Allerton, head of medicine design for the company. Although others are working to block the same target, Pfizer is the only drug maker with an experimental M^{pro} inhibitor in human testing today — two of them, in fact. Aside from its reformulated SARS drug, Pfizer started trials of a different oral candidate, PF-07321332, last month.

“Am I glad that we were in a position to move fast and that we'd done the pre-work? Yes,” says Allerton. “Do I wish we'd been even further down the line and been able to bring treatment options sooner? Absolutely.”

A wake-up call

Companies that hadn't done the same kind of legwork are now pledging not to be caught empty-handed again. The pandemic has been “a wake-up call”, says John Young, global head of infectious diseases at pharmaceutical company Roche in Basel, Switzerland. “It's just a matter of time before the next one,” he says, “and we need to prepare ourselves as an industry.”

To that end, leaders of the COVID R&D Alliance, a coalition of more than 20 life-sciences companies and venture-capital firms that came together last year to tackle SARS-CoV-2 collaboratively, are now launching a side project geared at broad-spectrum antivirals for coronaviruses and influenza viruses. According to Elliott Levy, the head of research and development strategy and operations at Amgen in Thousand Oaks, California, who is spearheading the effort, the group plans to advance around 25 candidate antivirals into initial human studies and build the clinical-trial infrastructure necessary for parallel testing when the next deadly virus strikes.



[Latin America's embrace of an unproven COVID treatment is hindering drug trials](#)

The US government has similar ambitions. Antivirals for coronaviruses are “task number one”, says NIH director Francis Collins. But, he told *Nature*, the initiative “certainly was intended to stretch to other viral families, if the funds are available”.

Complementary efforts come from the Corona Accelerated R&D in Europe project — a €75.8-million (US\$90.1-million), five-year enterprise. It is geared at finding medicines both for the current COVID-19 pandemic and for future coronavirus outbreaks. Moorman and other UNC researchers, through their Rapidly Emerging Antiviral Drug Development Initiative, also hope to raise \$500 million from governments, industry sponsors and foundations to develop broad-spectrum, direct-acting antivirals.

Meanwhile, some big pharmaceutical companies are ramping up their internal efforts. Novartis, for example, is now optimizing a pan-coronavirus inhibitor of the M^{pro} enzyme. According to John Tallarico, head of chemical biology and therapeutics at Novartis, the company is still at least a year away from human clinical testing, at which point COVID-19 might be well under control. Nonetheless, he says, Novartis is committed to moving this programme forward.

But, says Levy, “the level of investment from the industry today is not proportional to the threat” — which is why he hopes to raise around \$1 billion from drug companies alone for the COVID R&D Alliance’s pandemic-preparedness spin-off venture. Extra funds could also come from non-profit organizations and other stakeholders, he says.

Andy Plump, president of research and development at Takeda Pharmaceutical in Cambridge, Massachusetts, and one of the leaders of the alliance, is optimistic about the programme’s chances of success. “Right now, you have a lot of energy behind this because there is the immediacy of SARS-CoV-2,” Plump says. But he doesn’t want apathy to set in again, like it did after SARS and MERS. “We need to lock in right now.”

Nature **592**, 340-343 (2021)

doi: <https://doi.org/10.1038/d41586-021-00958-4>

References

1. 1.

Knobler, S. *et al.* (eds) *Learning from SARS: Preparing for the Next Disease Outbreak: Workshop Summary* (National Academies Press, 2004).

2. 2.

Sheahan, T. P. *et al.* *Sci. Transl. Med.* **9**, eaal3653 (2017).

3. 3.

Beigel, J. H. *et al.* *N. Engl. J. Med.* **383**, 1813–1826 (2020).

4. 4.

WHO Solidarity Trial Consortium *N. Engl. J. Med.* **384**, 497–511 (2021).

5. 5.

Sheahan, T. P. *et al. Sci. Transl. Med.* **12**, eabb5883 (2020).

6. 6.

Sender, R. *et al.* Preprint at medRxiv
<https://doi.org/10.1101/2020.11.16.20232009> (2020).

7. 7.

Jackman, J. A. *et al. Nature Mater.* **17**, 971–977 (2018).

8. 8.

Hoffman, R. L. *et al. J. Med. Chem.* **63**, 12725–12747 (2020).

9. 9.

Boras, B. *et al.* Preprint at bioRxiv
<https://doi.org/10.1101/2020.09.12.293498> (2021).

Jobs from Nature Careers

- - - [All jobs](#)
 -

- [Research Associate / PhD Student](#)

[Technische Universität Dresden \(TU Dresden\)](#)

[Dresden, Germany](#)

[JOB POST](#)

PostDoc (f/m/d) in Physical chemistry or Material Chemistry - Design and synthesis of plasmonic nanostructures

Helmholtz-Zentrum Berlin for Materials and Energy (HZB)

Berlin, Germany

JOB POST

▪ **Betriebspraktikum in der 9. Klasse**

Helmholtz Centre Potsdam - German Research Centre for Geosciences (GFZ)

Potsdam, Germany

JOB POST

▪ **55832: Physicist, engineer or similar (f/m/x) - Development, application and scientific evaluation of greenhouse gas lidar systems**

German Aerospace Center (DLR)

Oberpfaffenhofen, Germany

JOB POST

This article was downloaded by **calibre** from <https://www.nature.com/articles/d41586-021-00958-4>

Books & Arts

- **[Toilets – what will it take to fix them?](#)** [12 April 2021]
Book Review • The global dearth of safe sewage systems needs innovation and advocacy.
- **[A physicist takes on academic racism; green economic growth; and Stephen Hawking's self-promotion: Books in brief](#)** [06 April 2021]
Book Review • Andrew Robinson reviews five of the week's best science picks.

BOOK REVIEW

12 April 2021

Toilets – what will it take to fix them?

The global dearth of safe sewage systems needs innovation and advocacy.

- [Josie Glausiusz](#) 0

1. Josie Glausiusz

1. Josie Glausiusz is a science journalist in Israel. Twitter: [@josiegz](#)

[View author publications](#)

You can also search for this author in [PubMed](#) [Google Scholar](#)



A bus in Pune, India, that has been turned into a mobile toilet where women can feel safe.Credit: Indranil Mukherjee/AFP/Getty

Pipe Dreams: The Urgent Global Quest to Transform the Toilet *Chelsea Wald* Avid Reader/Simon & Schuster (2021)

Waste: One Woman's Fight Against America's Dirty Secret *Catherine Coleman Flowers* The New Press (2020)

Since the sixth century bc, when the Romans began building their Cloaca Maxima (“Greatest Sewer”), a safe sewage system has epitomized civilization. More than two millennia later, one Victorian novelist called a good sewer “nobler” and “holier” than the most admired Madonna ever painted. For sound reasons: the construction of a massive London sewer network in the 1860s ended waterborne epidemics of cholera that had killed tens of thousands of people. In 2007, more than 11,300 readers of *The BMJ* chose the sanitary revolution — the introduction of clean water and sewage disposal — as the most important medical milestone since 1840.

The need for innovative toilets is enormous. In 2017, two billion people lacked a minimally adequate toilet, and 673 million people still had to defecate in the open. Poor sanitation is linked to the transmission of diseases including cholera, typhoid, polio, hepatitis A and trachoma. Access to clean water and sanitation for all by 2030 is one of the United Nations' Sustainable Development Goals (SDGs), but the cost of achieving this is tens of billions of dollars per year, as two new books explore: *Pipe Dreams*, by Chelsea Wald; and *Waste*, by Catherine Coleman Flowers.

Today, “toilets no longer look quite so miraculous as they once did”, writes Wald in her deeply researched, entertaining and impassioned exploration of sanitation ancient and innovative. As cities grow, their aged sewage infrastructures become overwhelmed, especially during storms. Once-noble conduits are now frequently clogged by fatbergs, vast accretions of grease and wet wipes with the consistency of concrete and the weight of several elephants.

“Modern sanitation infrastructure has created the illusion that our excreta just disappear like magic,” Wald writes. “But poop doesn’t just drive down the highway into the sunset.” Often, it remains untreated, poisoning people and ecosystems. A new generation of toilets is needed, she argues: one that squanders less water, nutrients and energy. And so Wald travels from Alaska to Indonesia and many places in-between, interviewing scientists, public-health officials and toilet entrepreneurs.



A makeshift toilet by a sewage stream in Nairobi, Kenya.Credit: Daniel Irungu/EPA-EFE/Shutterstock

Many countries are edging their way towards the SDGs by implementing inventive sanitation projects at minimal expense. In the town of Sneek in the Netherlands, Wald visits a company called DeSaH, which has put vacuum toilets into more than 200 apartments, whooshing away waste and treating it in a small local facility. Each toilet uses 1 litre of water per flush, compared with the usual eight. Vacuum systems are in use at sites in wealthy nations including the Netherlands and Sweden, and at Bloomberg's European headquarters in London. But scaling up this water-saving technology on a global scale is challenging, Wald notes, given financial and other hurdles.



Ecodesign: The bottom line

In Kenya, a social enterprise named Sanivation collects human faeces, treats it and presses it into “poop briquettes” for fuel, Wald writes. The company has sold 1,500 tonnes of the small spheres so far, saving 88 trees for every tonne. In Indonesia, where there are few sewers, Wald shadows “sanitation entrepreneur” Koen Irianto Uripan, who put thousands of fibreglass septic tanks in the yards of homes in the city of Surabaya. With jokes and a papier-mâché poop prop, Uripan markets a cheap, easily installed indoor toilet connected to one of these tanks, in which bacteria break down waste. The work is part of a much larger, countrywide campaign to reduce the number of people who have to defecate in the open.

Our universal disgust over excretion inspires both humour and anxiety. The ancient Babylonians recognized a privy demon called Šulak that could trigger bad luck, injury or illness. In the Jewish tradition, rabbis composed blessings for angels who accompanied a person to the “house of the chair” and waited outside, and a blessing is recited on exiting the lavatory.

But fear is all too real for those without secure and hygienic toilets. Women who must share with strangers, or go outdoors, are at greatly increased risk of being raped, studies in South Africa and India have shown^{1,2}. Toilets with doors that lock from the inside, and have shelves for clean menstrual products, can help women and girls — cisgender and transgender — to feel

safe and dignified; and those still at school will be less likely to skip classes. In Durban, South Africa, among other places, city planners have refitted shipping containers for the purpose.



Catherine Coleman Flowers advocates for the more than 2 million US citizens who live without running water and basic indoor plumbing. Credit: John D. and Catherine T. MacArthur Foundation ([CC BY 4.0](#))

Inadequate sanitation extends to the United States, where more than two million people live without running water and basic indoor plumbing. Enter environmental-health advocate Catherine Coleman Flowers.

In *Waste*, Flowers details her decades-long campaign to raise awareness of inadequate sanitation in rural US communities. She focuses on Lowndes County, Alabama, an area inhabited largely by poor Black people who, like her, are descendants of enslaved people. An estimated 90% of Lowndes households have failing or inadequate waste-water systems. A study published in 2017³ found that more than one-third of those tested in the county were infected by hookworm (*Necator americanus*), which is transmitted through faeces.

To fix this failing infrastructure, Flowers argues, a “virtual hurricane” is needed — a public-health crisis comparable to the revelations of lead-contaminated drinking water in Flint, Michigan. As we’ve seen with COVID-19, politicians can quickly summon huge amounts of money. But it’s difficult to conceive of a whirlwind that could bring decent sewage systems to, say, the majority-Black community of Centreville, Illinois, where untreated waste flows alongside homes, even though residents pay for the municipal waste-water service.

Perhaps what’s really needed is a collective human hurricane, typified by Flowers and the partnerships that she builds between her neighbours, lawmakers and global organizations to deliver effective sanitation to those without. As Flowers has said: “All of us have a human right to water and sanitation.”

Nature **592**, 345–346 (2021)

doi: <https://doi.org/10.1038/d41586-021-00953-9>

References

1. 1.

Jadhav, A., Weitzman, A. & Smith-Greenaway, E. *BMC Public Health* **16**, 1139 (2016).

2. 2.

Gibbs, A., Reddy, T., Khanyile, D. & Cawood, C. *Glob. Public Health* **16**, 590–596 (2021).

3. 3.

McKenna, M. L. *et al. Am. J. Trop. Med. Hyg.* **97**, 1623–1628 (2017).

Jobs from Nature Careers

- - - [All jobs](#)
 - - [**Research Associate / PhD Student**](#)
[Technische Universität Dresden \(TU Dresden\)](#),
[Dresden, Germany](#)
[JOB POST](#)
 - [**PostDoc \(f/m/d\) in Physical chemistry or Material Chemistry - Design and synthesis of plasmonic nanostructures**](#)
[Helmholtz-Zentrum Berlin for Materials and Energy \(HZB\)](#),
[Berlin, Germany](#)
[JOB POST](#)
 - [**Betriebspraktikum in der 9. Klasse**](#)
[Helmholtz Centre Potsdam - German Research Centre for Geosciences \(GFZ\)](#),
[Potsdam, Germany](#)
[JOB POST](#)
 - [**55832: Physicist, engineer or similar \(f/m/x\) – Development, application and scientific evaluation of greenhouse gas lidar systems**](#)
[German Aerospace Center \(DLR\)](#)

Oberpfaffenhofen, Germany

JOB POST

This article was downloaded by **calibre** from <https://www.nature.com/articles/d41586-021-00953-9>

| [Section menu](#) | [Main menu](#) |

BOOK REVIEW

06 April 2021

A physicist takes on academic racism; green economic growth; and Stephen Hawking's self-promotion: Books in brief

Andrew Robinson reviews five of the week's best science picks.

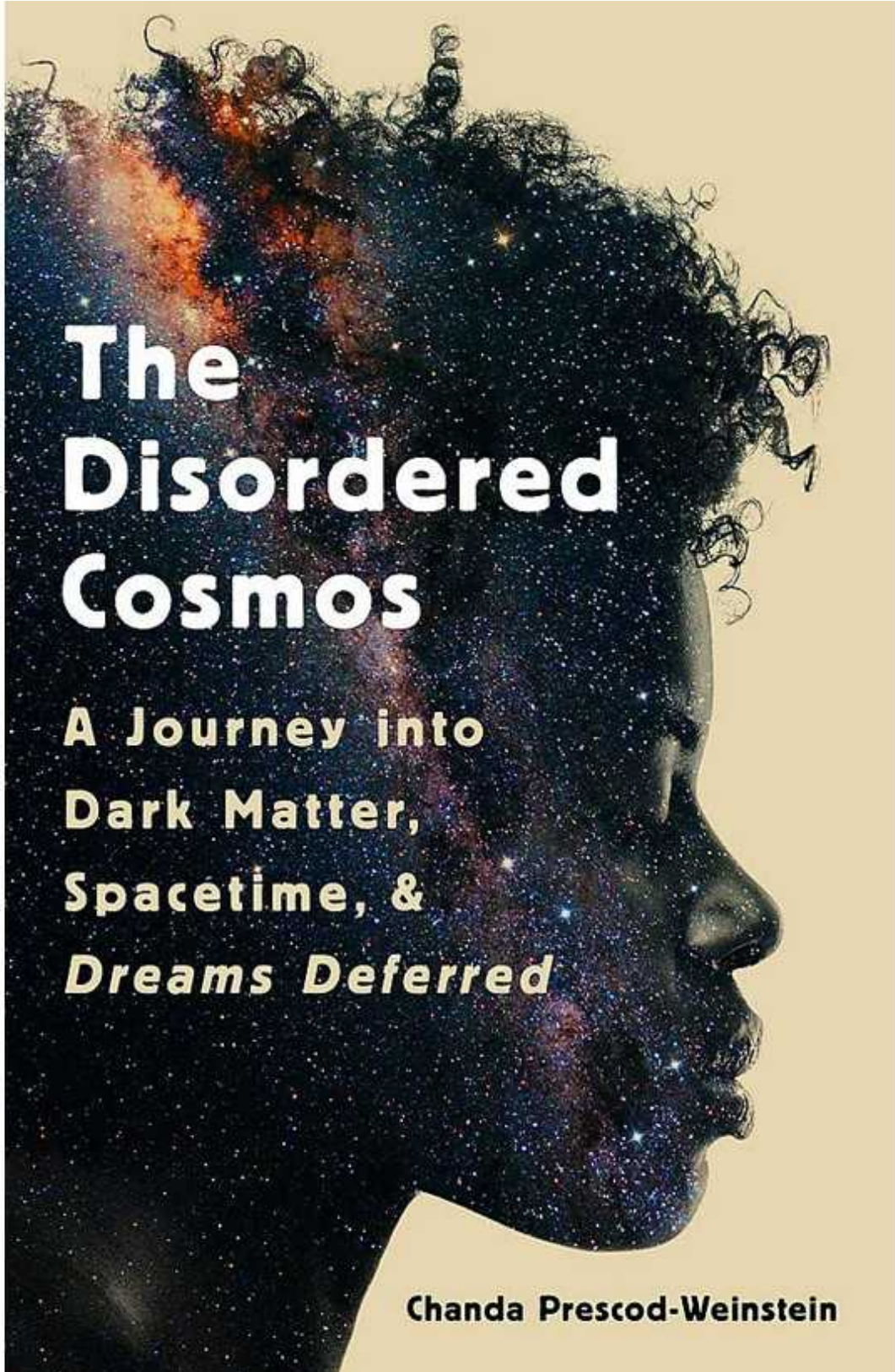
- [Andrew Robinson](#) 0

1. [Andrew Robinson](#)

1. Andrew Robinson's many books include *Lost Languages: The Enigma of the World's Undeciphered Scripts* and *Einstein on the Run: How Britain Saved the World's Greatest Scientist*. He is based in London.

[View author publications](#)

You can also search for this author in [PubMed](#) [Google Scholar](#)



The Disordered Cosmos

A Journey into
Dark Matter,
Spacetime, &
Dreams Deferred

Chanda Prescod-Weinstein

The Disordered Cosmos

Chanda Prescod-Weinstein *Bold Type* (2021)

Aged ten, writes theoretical physicist Chanda Prescod-Weinstein, “I thought that I could keep my curiosity about the mathematics of the universe and the existence and function of racism separate.” In fact, she became a leading Black activist in US academia, [co-organizing last year’s Strike for Black Lives](#). Speaking out against “those who are good at physics, but who are not good to people”, she makes a courageous call for action that mingles cosmology, politics and memoir to share a fresh vision of dark matter and the stars.

Per Espen Stoknes

foreword by Paul Hawken

Tomorrow's Economy

A Guide
to Creating
Healthy
Green Growth



Tomorrow's Economy

Per Espen Stoknes *MIT Press* (2021)

Not many green activists are employed by a business school; few economists have been successful therapists. Per Espen Stoknes — psychologist, economist, climate-strategy researcher and green-tech entrepreneur — is thus unusually well informed, balanced and rewarding as he grapples with future economic expansion. What, he asks, will lure minds towards green growth? He is optimistic. Healthy growth provably benefits the “four main factors for modern corporate valuation”: brand, performance, risk and talent.

THE SELLING OF A SCIENTIFIC CELEBRITY

HAWKING

HAWKING

CHARLES SEIFE

Hawking Hawking

Charles Seife *Basic* (2021)

Stephen Hawking was born precisely 300 years after the death of Galileo Galilei, and died on Albert Einstein's birthday — facts “that he would have found hilarious”, suggests science writer Charles Seife in his penetrating dissection of the physicist's celebrity. He is probably correct: Hawking insisted he was not comparable with these giants, while hawking such comparisons when proffered by the press. In his posthumously published 2018 book *Brief Answers to the Big Questions*, he analyses Einstein's “genius”, but gives no hint he saw himself as one.

HOW TO MAKE A VACCINE



AN ESSENTIAL GUIDE FOR COVID-19 & BEYOND

JOHN RHODES

How to Make a Vaccine

John Rhodes *Univ. Chicago Press* (2021)

When immunologist John Rhodes started his PhD decades ago, he caught a heart-threatening disease from lab guinea pigs. Recovery brought “an enduring zest for life” and “a lifelong interest in zoonotic viruses”. His keen guide to viral disease and vaccination, inevitably focused on COVID-19, mixes science and scientists, for example the fact that June Almeida, one of the originators of the term coronavirus ([in *Nature* in 1968](#)), was the daughter of a Glasgow bus driver. Skilfully pitched at non-specialists, it regrettably lacks illustrations.

#1 NEW YORK TIMES BESTSELLING AUTHOR

MICHIO KAKU



GOD THE EQUATION

THE QUEST FOR A THEORY OF
EVERYTHING

The God Equation

Michio Kaku *Doubleday* (2021)

A ‘theory of everything’ would encompass all physics, from the expanding Universe to dancing subatomic particles. Might it exist? “This is not just an academic question,” writes physicist Michio Kaku. If found, it should lead to astonishing technologies, as did the theories of gravitation, electromagnetism, relativity and quanta. Kaku describes the history of these ideas, and the untestable string theory — his pursuit since 1968. Authoritative and accessible, the book oddly omits pioneer Thomas Young when discussing interference of light.

Nature **592**, 346 (2021)

doi: <https://doi.org/10.1038/d41586-021-00915-1>

Jobs from Nature Careers

- - - [All jobs](#)
 - - [Research Associate / PhD Student](#)
 - [Technische Universität Dresden \(TU Dresden\)](#)
[Dresden, Germany](#)
[JOB POST](#)
 - [PostDoc \(f/m/d\) in Physical chemistry or Material Chemistry - Design and synthesis of plasmonic nanostructures](#)
 - [Helmholtz-Zentrum Berlin for Materials and Energy \(HZB\)](#)
[Berlin, Germany](#)

JOB POST

- **Betriebspraktikum in der 9. Klasse**

Helmholtz Centre Potsdam - German Research Centre for Geosciences (GFZ)

Potsdam, Germany

JOB POST

- **55832: Physicist, engineer or similar (f/m/x) - Development, application and scientific evaluation of greenhouse gas lidar systems**

German Aerospace Center (DLR)

Oberpfaffenhofen, Germany

JOB POST

This article was downloaded by **calibre** from <https://www.nature.com/articles/d41586-021-00915-1>

Opinion

- **[More floods, fires and cyclones — plan for domino effects on sustainability goals](#)** [13 April 2021]
Comment • Without new models, better metrics and more investment, cascades of extreme events could derail the United Nations Sustainable Development Goals.
- **[Quantum computing's reproducibility crisis: Majorana fermions](#)** [12 April 2021]
Comment • The controversy over Majorana particles is eroding confidence in the field. More accountability and openness are needed — from authors, reviewers and journal editors.
- **[Thousands protest against funding cuts to SDG work](#)** [12 April 2021]
Correspondence •
- **[Social and political justice hit by UK aid cuts](#)** [12 April 2021]
Correspondence •
- **[Add Himalaya's Grand Canyon to China's first national parks](#)** [13 April 2021]
Correspondence •

COMMENT

13 April 2021

More floods, fires and cyclones — plan for domino effects on sustainability goals

Without new models, better metrics and more investment, cascades of extreme events could derail the United Nations Sustainable Development Goals.

- [Markus Reichstein](#) ⁰,
- [Felix Riede](#) ¹ &
- [Dorothea Frank](#) ²

1. [Markus Reichstein](#)

1. Markus Reichstein is director of the Biogeochemical Integration Department at the Max Planck Institute for Biogeochemistry, Jena, Germany.

[View author publications](#)

You can also search for this author in [PubMed](#) [Google Scholar](#)

2. Felix Riede

1. Felix Riede is professor of climate change archaeology at the School of Culture and Society, Aarhus University, Denmark.

[View author publications](#)

You can also search for this author in [PubMed](#) [Google Scholar](#)

3. Dorothea Frank

1. Dorothea Frank is scientific coordinator in the Biogeochemical Integration Department at the Max Planck Institute for Biogeochemistry, Jena, Germany.

[View author publications](#)

You can also search for this author in [PubMed](#) [Google Scholar](#)



A flooded school in Mozambique after Cyclone Eloise in January. Disrupted education can harm lives, livelihoods and economies for decades. Credit: Alfredo Zuniga/AFP via Getty

Climate change is provoking ever-more-extreme events, from storms and droughts to floods and cyclones. The risk of such hazards increases as the planet warms, and these risks interact across many environmental and social systems. A heatwave can spark forest fires, which lead to air pollution, thus damaging public health. Drought-wrecked harvests can result in food-price volatility, which can increase social unrest or migration.

Yet these domino effects are barely considered in most countries' strategies for achieving the United Nations Sustainable Development Goals (SDGs) by 2030.

Set in 2015, the 17 SDGs range from 'zero hunger' (SDG2) to 'affordable and clean energy' (SDG7) and 'sustainable cities and communities' (SDG11). Many countries that are working hard to attain these goals insufficiently consider the impact of extreme weather. Take Germany, a leader on climate action in many ways. Its 2018 strategy on sustainable development runs to 60 pages¹, yet the word 'disaster' appears only once. There is no analysis of the ramifications of an increase in such events.

Although many people are now aware that climate change is making fires, floods, heatwaves and storms more frequent, more severe or both, this knowledge isn't changing policy or research enough². Part of the problem is perception. Future catastrophes feel unreal to decision-makers, as we've experienced with so many governments' lack of pandemic preparedness, despite years of warning that something similar to COVID-19 was a case of when, not if³. Other obstacles are inadequate national and international governance, and communication challenges. The research community has not yet provided the interdisciplinary modelling required to quantify these complex cascades.



[Reset Sustainable Development Goals for a pandemic world](#)

As a consequence, many efforts to attain the SDGs will, like a house of cards, fall at the first tremor. Witness the way in which the pandemic has set back progress on global poverty, hunger, childhood immunizations, educational inequalities, advancements for women and girls, and more⁴. Our global efforts need to be much more robust to the changing and interconnected nature of risk in a warming world.

Good preparation is not just a matter of money and engineering, but of knowledge and foresight. Unfortunately, the ways in which different risks from climate extremes are interlinked and dependent on each other are among the greatest potential causes of future catastrophes^{5,6}. They are also some of the most under-studied. This cuts across all aspects of social and physical sciences.

What now? Researchers must create models that are more understandable and useful to policymakers. When possible, SDG targets and indicators should be redesigned to capture vulnerability to heatwaves, fires, droughts, floods, hurricanes, mudslides and more. And politicians need to be convinced to invest in precautionary measures and adaptation.

Recognizing risk

The fact that climate extremes imperil development was recognized by the UN Conference on Environment and Development in 1992. It is also noted in the 2015–30 Sendai Framework, the global agreement to “reduce and prevent disaster risks across the globe”. Yet there has been little progress on these ideas.



The United States can help the IMF to rethink how it lends

There are examples of preparedness. Flood barriers in the Netherlands and in Venice, Italy, are designed to protect against future sea-level rise. But the idea of flooding from rising sea levels is easier to grasp than are the effects of complex and compounding events, which are sometimes counter-intuitive and connected over long distances in both space and time (see Supplementary information).

For instance, in 2018, heavy rains that fell one month after wildfires on steep slopes in southern California caused fatal mudflows. Another example is a wet winter in which there is a lot of plant growth — this can be a big fire risk if a hot and dry summer follows, because of the build-up of forest fuel⁷. Protections against river floods need to consider droughts as well as high water flows, because dry material in dykes can shrink, crack and become unstable⁸.



A 2018 wildfire caused power lines in Oklahoma to explode. Such infrastructure collapse has far-reaching ripple effects. Credit: Nick Oxford/Reuters

Extreme weather can fuel a vicious cycle of vulnerability — physical, social and economic. In Mozambique, for example, droughts and floods in the mid-2000s that destroyed infrastructure and crops had a domino effect on housing, jobs, education and social ties. To recover, families had to sell their homes or land, or needed to put their children to work. This came at the cost of longer-term income and well-being. National food consumption fell by more than one-quarter, ill health in children increased fourfold in flooded areas, school participation fell drastically and poverty levels increased by up to 17.5 percentage points⁹.

These cascades across different systems have received concentrated academic attention only in the past few years, and the social aspects, in particular, are still not well understood¹⁰.

Modified models

Most current models cannot forecast these complexities. They might not allow for interactions between farming, ecosystems, households, companies, financial institutions, social cohesion and governance. All of this should be explicitly modelled, and the indirect long-term effects quantified.

This is hugely challenging. Agent-based modelling can help. In this approach, the interactions of autonomous agents (individuals, organizations or groups) are modelled as they react to changing conditions. Critics have long argued that such models are too complex and uncertain to yield reliable results. In our view, the technique is now coming of age, thanks to huge amounts of data, improved artificial intelligence (AI) and greater computational power.



Time to revise the Sustainable Development Goals

Such models have been shown to work retrospectively on the somewhat simpler systems of past societies. One example is how the Cahokia people responded to repeated droughts¹¹ in midwestern North America between ad 900 and 1200. These models have also shown potential in estimating the emerging risks of major floods in Austria. Researchers mapped out the impacts of flooding on building and infrastructure value, credit provision and government finances — factors that would impede reconstruction after a disaster¹².

Whatever the tools, more researchers must map complex social systems using economic and census data. Such an approach needs harmonized data at high resolution (county or state level), but this information is often inadequate. Importantly, big-data efforts need to be combined with qualitative work by social scientists — including anthropologists, economists, historians and archaeologists — that is culturally sensitive and place-specific.

Data science and AI are playing an increasingly important part in disaster preparedness, response and recovery. For instance, analysing satellite images and other Earth-observation data can help to pinpoint where to deliver humanitarian aid most efficiently, and AI supports early-warning systems and risk assessment. An example of the interplay of good data, models and governance was the early warning, preparedness and evacuation of around three million people in India and Bangladesh before Cyclone Amphan struck in May 2020. There is plenty of scope for developing and using AI to anticipate long-term vulnerabilities.

Improved indicators

Alongside modelling efforts, researchers should help to rework SDG indicators so that they are better at tracking progress towards resilient sustainable development.

Good indicators account for variability and vulnerability. For example, one of the metrics for success in achieving SDG2 (zero hunger) is the domestic food price volatility index. This reports the standard deviation around the mean of the price index of cereals, vegetable oil, dairy, meat and sugar. Thus, it takes into account the certainty and stability of food availability from year to year and within each year, which is affected by climate extremes. This variability is important for capturing the effects of temporary food scarcity, which disproportionately affects poor people because they spend a large share of their income on food. Yet this indicator is regularly reported only nationally — not regionally or locally, where variability needs to be captured.



A farmer restores his rice field in South Korea after torrential rains and flooding during the prolonged monsoon season of 2020.

Most other SDG targets and indicators ignore risk and variability entirely. Metrics such as the “proportion of water bodies with good water quality” and “annual mean levels of fine particulate matter” are measured only as yearly averages. Adding variability measures would be an important first step towards revealing vulnerability in those systems and tracking how that changes as the world warms.

In the past few years, researchers have tried to map out the ‘sustainome’ — the web of interactions between SDGs (see Fig. 1 of ref. 13, for example). Important work such as this helps to capture synergies and trade-offs between various SDGs in different nations. Along these lines, SDG indicators — and Sendai indicators for disaster risks — should be woven together into compound indicators of systemic risk. More work is needed to understand how to achieve this and explore which models and data might help.

Targeted investment

Creating models of interacting risks that are realistic, tracking vulnerability and putting figures on such risks are all crucial in helping policymakers and investors to decide where to channel money and attention.

Many researchers are focused on breeding more-nutritious crops to help achieve zero hunger, for example. They need to know whether future droughts will lead to the failure of those varieties, or which crops, combinations or practices will adversely affect biodiversity, ecosystem resilience or the roughly 500 million smallholder farmers in ways that influence other SDGs. System models fed with observational data will help to identify which factors should be modified to increase resilience.



Heed blame for extreme weather

Large investments in resilience measures can be difficult for politicians to justify to electorates because there are often no immediate returns, and the timing and magnitude of future extreme events are unknown. But avoiding such spending is much more costly in the long run, as shown by the current pandemic¹⁴.

A 2019 report on low- and middle-income countries found that investing 3% more than business-as-usual levels in the infrastructures of three sectors — power, water and sanitation, and transport — would make those infrastructures more resilient to extreme events. The report found that this would pay off in the long run by an average of US\$4 for every \$1 invested — and would have greater pay-offs as climate extremes worsen¹⁵. Such improvements to infrastructure protect against direct damage and against subsequent disruptions to economic activities. In Hamburg, Germany, for example, an investment of 2.2 billion (US\$2.6 billion) in flood protection after a 1962 storm surge is estimated to have avoided losses of more than 20 billion since then (see go.nature.com/3sx8ren).

Luckily, risk assessment does not need to be reinvented. It is mature in the insurance industry, such as in the context of earthquake hazards. The challenge now is to model, quantify and accommodate the changing risks and far-reaching impacts of the extreme weather events that are inevitable in a warming world — and the sooner the better.

Nature **592**, 347-349 (2021)

doi: <https://doi.org/10.1038/d41586-021-00927-x>

References

1. 1.

The Federal Government. *German Sustainable Development Strategy* (Federal Government, 2018).

2. 2.

Michel-Kerjan, E. *Nature* **491**, 497 (2012).

3. 3.

World Economic Forum. *Outbreak Readiness and Business Impact: Protecting Lives and Livelihoods Across the Global Economy* (WEF, 2019).

4. 4.

United Nations Development Programme. *COVID-19 and Human Development: Assessing the Crisis, Envisioning the Recovery* (UNDP, 2020).

5. 5.

World Economic Forum. *Global Risks Report 2020* (WEF, 2020).

6. 6.

Renn, O., Lucas, K., Haas, A. & Jaeger, C. *J. Risk Res.* **22**, 401–415 (2017).

7. 7.

Reichstein, M., Frank, D., Sillmann, J. & Sippel, S. in *Climate Extremes and Their Implications for Impact and Risk Assessment* (eds Sillmann, J., Sippel, S. & Russo, S.) 341–353 (Elsevier, 2020).

8. 8.

Li, Z., Ye, W., Marence, M. & Bricker, J. D. *Geosciences* **9**, 17 (2019).

9. 9.

Baez, J. E., Caruso, G. & Niu, C. *Econ. Disasters Clim. Change* **4**, 103–127 (2019).

10. 10.

Zscheischler, J. *et al. Nature Rev. Earth Environ.* **1**, 333–347 (2020).

11. 11.

d'Alpoim Guedes, J. A., Crabtree, S. A., Bocinsky, R. K. & Kohler, T. A. *Proc. Natl Acad. Sci. USA* **113**, 14483–14491 (2016).

12. 12.

Poledna, S. *et al.* Preprint at <https://arxiv.org/abs/1801.09740> (2018).

13. 13.

Lusseau, D. & Mancini, F. *Nature Sustain.* **2**, 242–247 (2019).

14. 14.

Sridhar, D. *Nature Med.* **26**, 1812–1812 (2020).

15. 15.

Hallegatte, S., Rentschler, J. & Rozenberg, J. *Lifelines: The Resilient Infrastructure Opportunity. Sustainable Infrastructure Series* (World Bank, 2019).

Supplementary Information

1. [Systemic effects of climate extremes](#)

[Jobs from Nature Careers](#)

- - - [All jobs](#)
 - - [Research Associate / PhD Student](#)
 - [Technische Universität Dresden \(TU Dresden\)](#)
 - [Dresden, Germany](#)
 - [JOB POST](#)
 - [PostDoc \(f/m/d\) in Physical chemistry or Material Chemistry - Design and synthesis of plasmonic](#)

nanostructures

Helmholtz-Zentrum Berlin for Materials and Energy (HZB),
Berlin, Germany

JOB POST

- **Betriebspraktikum in der 9. Klasse**

Helmholtz Centre Potsdam - German Research Centre for
Geosciences (GFZ)

Potsdam, Germany

JOB POST

- **55832: Physicist, engineer or similar (f/m/x) -
Development, application and scientific evaluation
of greenhouse gas lidar systems**

German Aerospace Center (DLR)

Oberpfaffenhofen, Germany

JOB POST

This article was downloaded by **calibre** from <https://www.nature.com/articles/d41586-021-00927-x>

COMMENT

12 April 2021

Quantum computing's reproducibility crisis: Majorana fermions

The controversy over Majorana particles is eroding confidence in the field. More accountability and openness are needed — from authors, reviewers and journal editors.

- [Sergey Frolov](#) 0

1. [Sergey Frolov](#)

1. Sergey Frolov is associate professor of physics at the University of Pittsburgh, Pennsylvania, USA.

[View author publications](#)

You can also search for this author in [PubMed](#) [Google Scholar](#)



Experiments to find Majorana signals are performed by loading a nanowire into a dilution refrigerator capable of cooling it down to close to absolute zero. Credit: HGA Architects and Engineers

A shadow has fallen over the race to detect a new type of quantum particle, the Majorana fermion, that could power quantum computers. As someone who works in this area, I've become concerned that, after a series of false starts, a significant fraction of the Majorana field is fooling itself. Several key experiments claiming to have detected Majorana particles, initially considered as breakthroughs, have not been confirmed. One recent case ended in a high-profile retraction from *Nature* (see [*Nature* 591, 354–355; 2021](#)), which I initiated with my colleague Vincent Mourik, a physicist at the University of New South Wales in Sydney, Australia. We raised concerns after obtaining additional data from the original experiments that were not included with the published paper.

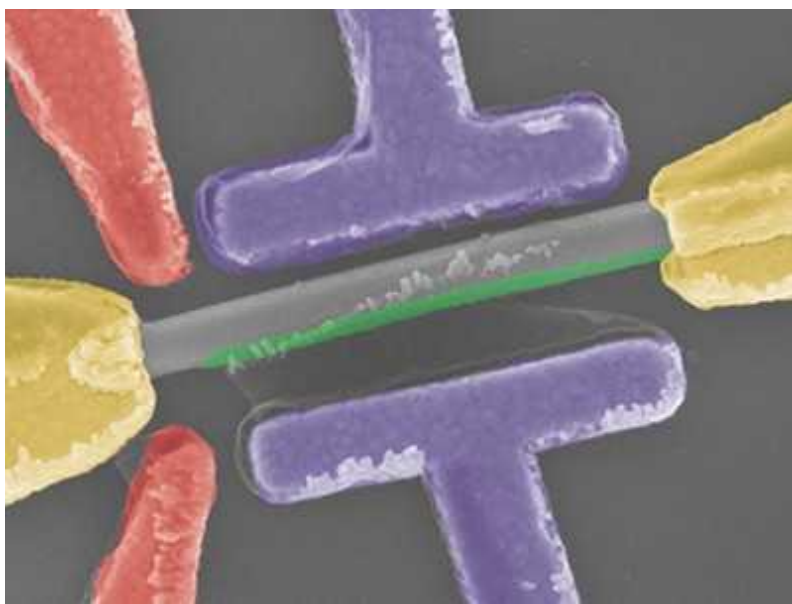
Much is at stake. Majorana particles are in theory their own antiparticles, and were predicted in 1937 by Italian physicist Ettore Majorana. Computer

giant Microsoft hopes to use Majorana particles to build a reliable quantum computer: the particles should make for exceptionally stable quantum bits. The scientific excitement around them is on a par with gravitational waves and the Higgs boson.

Experimentally, researchers are at loggerheads over whether Majoranas have been detected at all, let alone whether they're an asset for quantum computing. As scepticism of the claims creeps beyond the cognoscenti, the field is at risk of getting a bad reputation, despite its untapped promise.

Challenging science

Producing Majoranas in the laboratory is very hard. Experiments combine cutting-edge fields such as nanotechnology, superconductivity, device engineering and materials science. In the most developed approach, researchers must first grow a nanowire crystal — a feat in itself — to produce a column of atoms 100 nanometres (one-thousandth the width of a human hair) across. Then they must connect the wire to a circuit sensitive enough to measure single electrons travelling through it. The whole experiment must be done at about one-hundredth of a degree above absolute zero, in a magnetic field 10,000 times that of Earth's.



[Evidence of elusive Majorana particle dies — but computing hope lives on](#)

Under those extremes, when all the electrons in the wire are magnetized, Majorana particles should emerge from the two wire ends. In theory.

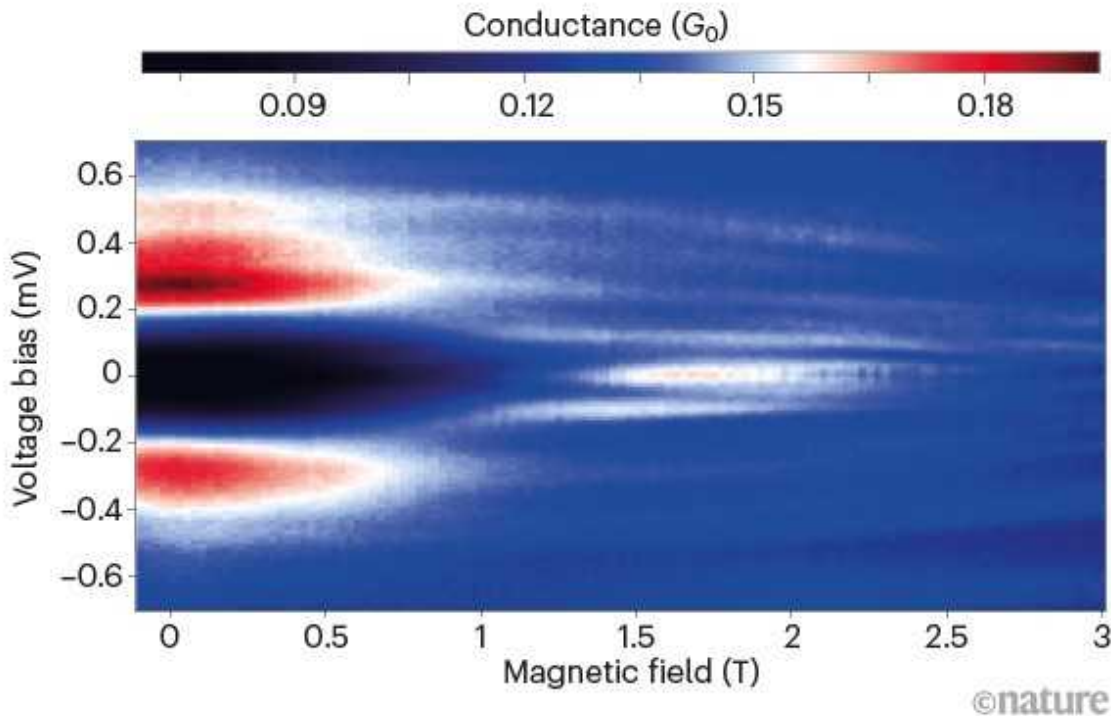
More than 100 groups have tried this. Two dozen have reported Majorana manifestations. These usually appear in the form of a characteristic electronic signal: a narrow peak in current as voltage is varied across the nanowire. I was a member of one of the first teams to observe this, in 2012¹. More papers soon appeared. Detections of a quantized value of the current, first predicted in theory and then reported in experiments published in *Science*² in 2017 and *Nature*³ in 2018, were interpreted by many to be the ultimate evidence of Majoranas.

In 2020, these observations came under scrutiny after replication experiments were conducted. *Science* published an experiment led by researchers at Pennsylvania State University in University Park contradicting the 2017 report⁴. My group reproduced patterns from the 2018 *Nature* study, but demonstrated that they need not originate from Majorana⁵. We did a cross-check on both ends of the same nanowire, but found a current peak on only one end. This violated the basic expectation from the theory that Majoranas always come in pairs. The rate of rebuttal is speeding up: researchers have not been able to confirm the findings^{6,7} of two separate papers claiming to have found Majorana regimes in nanowires^{8,9}. And reports of current peaks in a new iron-based superconductor, Fe(Te,Se), that were attributed to Majoranas^{10–12} in *Science* and *Nature Communications* will need to become more nuanced after a *Physical Review Letters* publication this year¹³.

The lesson: Majorana particles aren't necessary to produce the current peak signals. At least since 2014, we have known of more-mundane explanations, such as other quantum states that are not Majoranas¹⁴, accidental signals caused by imperfections in the nanowire, or fascinating but previously explored cooperative behaviour of numerous electrons (see 'Mixed signals'). Yet, affirmative papers kept coming out without even mentioning alternative explanations, creating the impression that a debate is raging between Majorana optimists and pessimists.

MIXED SIGNALS

The bright streak that runs through the middle, between 1.5 and 2 tesla, is expected of Majorana particles, but could also be explained by other quantum states or imperfections in the nanowire.



Source: Peng Yu/Frolov lab

Reflection needed

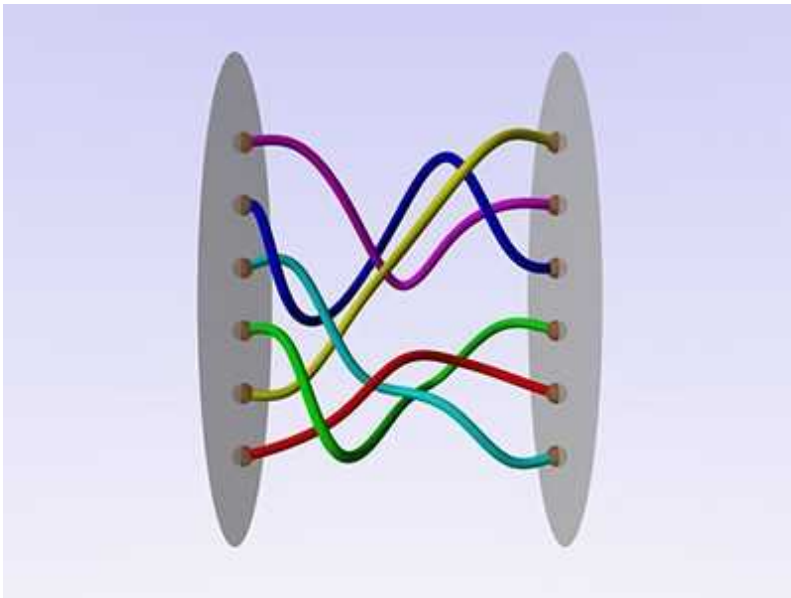
As someone who has published and reviewed positive and negative Majorana claims, I sense a wider problem. The controversy has already begun to erode confidence in the basic experimental method of passing current through quantum objects, even though this powerful technique has been used in many great discoveries, including Nobel-prizewinning observations in superconductivity, the quantum Hall effect and tunnelling.

It has already begun to affect me. Prospective graduate students ask whether I'm stopping Majorana research. Grant reviewers assume it is the methodology, not selective data reporting, that causes confusion in the field.

In my view, nothing is wrong with the basic method often dubbed ‘quantum transport’. I feel that selective data presentation is the main problem. If all papers included full or at least appropriately selected sets of data, quantum physicists could assign correct explanations, Majorana or not.

But I think that researchers are cherry-picking — focusing on data that agree with the Majorana theory and sidelining those that don’t. A case in point: a 2020 *Science* paper on Fe(Te,Se) reported quantized behaviour of current, which the authors saw in a single vortex, out of 60 assessed¹⁰. I contend that data-selecting researchers can be enabled by some journals and reviewers who might be insufficiently stringent. (When asked about the 2020 paper, a spokesperson for *Science* said that results and conclusions, including alternative mechanisms to explain the observed quantization, were presented carefully.) Time and time again, I and other reviewers argued for journals not to publish papers based on selective data presentation, only to see them appear in other (or sometimes the same) journals. Sometimes there really is no need to present all of your data, if a single graph tells the whole story. But for Majorana particles, simply searching through the data to identify peaks of the right height is not enough to stake a detection claim, especially when alternative theories exist.

It is all too easy for selection bias to take over in hypothesis-driven experimental research. The ‘best’ data are often considered to be those that fit the theory. So deviations are too readily dismissed as experimental or human error that can thus be discarded.



[Inside Microsoft's quest for a topological quantum computer](#)

Another problem is the breadth of peer review needed to check Majorana claims. Scrutiny is hard in any multidisciplinary field. Referees tend to be expert in one subject and struggle to judge others, and that leaves gaps. For example, a theoretical physicist might be comfortable assessing the calculations but not the experimental process, and a materials scientist, who understands how to grow nanowires, might skip the theory part. But a holistic view of the whole study is needed to properly assess it.

It is an all too familiar story. In a *Nature* survey of the ‘reproducibility crisis’ across chemistry, biology, physics, engineering and medical sciences (see [Nature 533, 452–454; 2016](#)), selective reporting of results was a top culprit. We’ve seen this for decades. Physicist Robert Millikan’s oil-drop experiments of more than a century ago famously omitted some data points. He did get close to the actual value of the electron charge — but science cannot depend on these sorts of fluke. Some Majorana papers are turning out to be unreliable because of how data are selected.

Ways forward

The behavioural norms across the condensed-matter physics community need updating. There is only one solution, and it is more accountability

across the board. The following steps will help both Majorana research and fields far beyond.

Open data. Scientists should disclose all data in a repository and comply with sharing standards, such as FAIR (findability, accessibility, interoperability and reusability)¹⁵. Some curation is unavoidable. The volume of data collected in a modern physics laboratory is high: computer scripts control the equipment, which might run 24 hours a day. A remedy is to clearly explain the protocol that is used to perform any data selection — so others might reuse or scrutinize it. Remember, data selection is a form of data processing.



Reform retractions to make them more transparent

Journals, funders (including corporations), research labs and universities should demand such open data practices, as they do in clinical trials, genomics, Earth sciences and a handful of other disciplines. Sharing data improves reliability, fosters collaborations and speeds up progress. The high-energy physics community, for example, could teach others how to share study protocols so that each paper is repeatable or reproducible¹⁶.

Although it is not widely known, access to further data is already required by many publication policies and government codes of research conduct. Notably, the United States does not have a national code, in contrast with

other countries investing heavily in research. Further efforts are needed to make such sharing automatic and not ‘upon request’. As the case of the Majorana paper recently retracted from *Nature* showed, seeing full data can be crucial for evaluating an experiment.

Critics will counter that simply sharing data does not capture all that goes on in the lab, that experience and insight — craft — have value that cannot be described in a protocol. I argue that robust, useful science is built on reliable processes that can be revisited, verified and re-examined as many times as necessary.

Open process. Reviewers need to be more questioning of extraordinary claims. Are the results too good to be true? Have enough data been presented? Have other explanations been considered? Cross-checks should be conducted, making it harder to stake an unreliable claim. For Majorana physics, this is as basic as comparing the magnetic- and electric-field dependence of current peaks with what would be expected theoretically. If done consistently, this would thwart many false claims.

But even the most rigorous reviews can be ignored. If the paper is rejected, the authors are free to disregard all input they were given and send their manuscript to another journal. I have seen Majorana papers that have received multiple negative reviews and rejections on scientific grounds published with only minor changes in another high-profile journal. Opening up the notoriously opaque publication process is key to cutting down on the proliferation of bad research.



Reproducibility: A tragedy of errors

Editors should take responsibility: it is they who decide, even if they lack in-depth expertise for that particular paper's topic. Each accepted paper should have its editor's name published alongside it. For each retraction, the editors should provide their view on what happened. All journals, especially high-impact ones, need to have community oversight. Editorial retraction should be applied widely, because waiting on authors to retract papers on their own can take an eternity. At the moment, most journals do not even have the capacity to run their own investigations into claims of mistakes in their papers. They should build this capacity, with the help of the research community.

Journals deserve praise for publishing negative results and for normalizing verification studies in physics. Researchers willing to share their results should receive well-deserved attention. For example, the American Physical Society ran an invited session on negative Majorana results at its virtual 2021 March meeting.

What of Majorana research? It remains viable and important. But, in my view, the key discoveries have yet to be made. A concentrated effort is now needed to improve our nanowire materials, experimental techniques and data analysis, as well as to tease out alternative explanations. Reliable proof is

needed that the particles are indeed their own antiparticles — with our eyes on the full data.

Only then will we be ready to develop Majorana quantum computers.

Nature **592**, 350-352 (2021)

doi: <https://doi.org/10.1038/d41586-021-00954-8>

References

1. 1.

Mourik, V. *et al.* *Science* **336**, 1003–1007 (2012).

2. 2.

He, Q. L. *et al.* *Science* **357**, 294–299 (2017).

3. 3.

Zhang, H. *et al.* *Nature* **556**, 74–79 (2018).

4. 4.

Kayyalha, M. *et al.* *Science* **367**, 64–67 (2020).

5. 5.

Yu, P. *et al.* *Nature Phys.* <https://doi.org/10.1038/s41567-020-01107-w> (2021).

6. 6.

Valentini, M. *et al.* Preprint at <https://arxiv.org/abs/2008.02348> (2020).

7. 7.

Saldaña, J. C. E. *et al.* Preprint at <https://arxiv.org/abs/2101.10794> (2021).

8. 8.

Albrecht, S. M. *et al.* *Nature* **531**, 206–209 (2016).

9. 9.

Vaitiekėnas, S. *et al.* *Science* **367**, eaav3392 (2020).

10. 10.

Zhu, S. *et al.* *Science* **367**, 189–192 (2020).

11. 11.

Wang, D. *et al.* *Science* **362**, 333–335 (2018).

12. 12.

Fan, P. *et al.* *Nature Commun.* **12**, 1348 (2021).

13. 13.

Wang, D., Wiebe, J., Zhong, R., Gu, G. & Wiesendanger, R. *Phys. Rev. Lett.* **126**, 076802 (2021).

14. 14.

Lee, E. J. H. *et al.* *Nature Nanotechnol.* **9**, 79–84 (2014).

15. 15.

Wilkinson, M. D. *et al.* *Sci. Data* **3**, 160018 (2016).

16. 16.

Chen, X. *et al.* *Nature Phys.* **15**, 113–119 (2019).

Jobs from Nature Careers

- - - [All jobs](#)
 - - [Research Associate / PhD Student](#)
 - [Technische Universität Dresden \(TU Dresden\)](#)
[Dresden, Germany](#)
[JOB POST](#)
 - [PostDoc \(f/m/d\) in Physical chemistry or Material Chemistry - Design and synthesis of plasmonic nanostructures](#)
[Helmholtz-Zentrum Berlin for Materials and Energy \(HZB\)](#)
[Berlin, Germany](#)
[JOB POST](#)
 - [Betriebspraktikum in der 9. Klasse](#)
[Helmholtz Centre Potsdam - German Research Centre for Geosciences \(GFZ\)](#)
[Potsdam, Germany](#)
[JOB POST](#)
 - [55832: Physicist, engineer or similar \(f/m/x\) - Development, application and scientific evaluation](#)

of greenhouse gas lidar systems

German Aerospace Center (DLR)

Oberpfaffenhofen, Germany

JOB POST

This article was downloaded by **calibre** from <https://www.nature.com/articles/d41586-021-00954-8>

| [Section menu](#) | [Main menu](#) |

CORRESPONDENCE

12 April 2021

Thousands protest against funding cuts to SDG work

- [Jenni Barclay](#)⁰,
- [Kent Buse](#)¹,
- [Claire J. Horwell](#)² &
- [Sarah Hawkes](#)³

1. [Jenni Barclay](#)

1. University of East Anglia, Norwich, UK.

[View author publications](#)

You can also search for this author in [PubMed](#) [Google Scholar](#)

2. Kent Buse

1. George Institute for Global Health, London, UK.

[View author publications](#)

You can also search for this author in [PubMed](#) [Google Scholar](#)

3. Claire J. Horwell

1. Durham University, UK.

[View author publications](#)

You can also search for this author in [PubMed](#) [Google Scholar](#)

4. Sarah Hawkes

1. University College London, UK.

[View author publications](#)

You can also search for this author in [PubMed](#) [Google Scholar](#)

We spearheaded the writing of two open letters demanding the reversal of a 70% cut to UK Research and Innovation's Official Development Assistance funding, from £422 million (US\$580 million) in 2020–21 to £125 million for 2021–22 (see go.nature.com/3fssqrg). Grants from the fund support work on urgent challenges linked to the United Nations' Sustainable Development Goals (SDGs). More than 800 projects worldwide could be truncated or terminated, taking with them trust in the United Kingdom as a partner. The timing could not be worse.

One letter has been signed by more than 5,000 people (see go.nature.com/3ckpwpw); the second, on global health (see go.nature.com/2pt87kt), has been signed by 4,000. Signatories come from 160 UK universities, 71 UK organizations and some 270 international organizations. They include scientific leaders, such as academy presidents and members of the UK government's Scientific Advisory Group for Emergencies. Also significant are the early-career scientists, in the United Kingdom and elsewhere, who face abrupt termination of their contracts and an uncertain future.

Both documents reflect the groundswell of rage and concern for the damaged and abandoned projects, and the partnerships they represent. These cuts will not just affect researchers like us: they will hurt the marginalized communities with which we work.

Nature **592**, 353 (2021)

doi: <https://doi.org/10.1038/d41586-021-00941-z>

[**Jobs from Nature Careers**](#)

- - - [All jobs](#)
 - - [**Research Associate / PhD Student**](#)

[Technische Universität Dresden \(TU Dresden\)](#)
[Dresden, Germany](#)

[JOB POST](#)

 - [**55832: Physicist, engineer or similar \(f/m/x\) - Development, application and scientific evaluation of greenhouse gas lidar systems**](#)

[German Aerospace Center \(DLR\)](#)
[Oberpfaffenhofen, Germany](#)

[JOB POST](#)
 - [**PhD Position – Characterization of advanced alkaline water electrolyzers**](#)

[Jülich Research Centre \(FZJ\)](#)
[Jülich, Germany](#)

[JOB POST](#)
 - [**PhD Position - Conception, Design and Development of Neuromorphic Learning Systems with Supercomputer Support**](#)

Jülich Research Centre (FZJ)

Jülich, Germany

JOB POST

This article was downloaded by **calibre** from <https://www.nature.com/articles/d41586-021-00941-z>

| [Section menu](#) | [Main menu](#) |

CORRESPONDENCE
12 April 2021

Social and political justice hit by UK aid cuts

- [Rana Dajani](#) ⁰,
- [Heather D. Flowe](#) ¹ &
- [Ben Warwick](#) ²

1. [Rana Dajani](#)

1. Hashemite University, Zarqa, Jordan.

[View author publications](#)

You can also search for this author in [PubMed](#) [Google Scholar](#)

2. Heather D. Flowe

1. University of Birmingham, UK.

[View author publications](#)

You can also search for this author in [PubMed](#) [Google Scholar](#)

3. Ben Warwick

1. University of Birmingham, UK.

[View author publications](#)

You can also search for this author in [PubMed](#) [Google Scholar](#)

Funding cuts at the United Kingdom's Global Challenges Research Fund imperil the [Rights for Time Network](#). This supports studies of humanitarian protection in developing nations and in Britain. It informs decision-makers about 'what works' in conflict resolution, for social and political justice, and in mitigating forced displacement. It also builds capacity for in-country research that aligns with global challenges and engenders good practice in safeguarding and equity.

The network catalyses South–South knowledge transfer. It helps researchers like us to learn from each other, rather than reinventing the wheel. Scholars in Jordan and Palestine are studying initiatives that protect refugees, children and families from the intergenerational impacts of forced displacement and conflict. In Kenya, led by survivors of sexual violence, researchers are investigating the cumulative harms suffered as people struggle to access crucial medical care and security services, and to seek justice. In Rwanda and Lebanon, researchers are studying the histories of violence and discrimination.

Cutting aid to the network and its partners — possibly by up to 85% — will undermine the United Kingdom's leadership in forging equitable partnerships with researchers in developing countries to solve global challenges. This will damage trust, destroy relationships and leave vulnerable people more so.

Nature **592**, 353 (2021)

doi: <https://doi.org/10.1038/d41586-021-00955-7>

Jobs from Nature Careers

- - - [All jobs](#)
 - - [Research Associate / PhD Student](#)

Technische Universität Dresden (TU Dresden)

Dresden, Germany

JOB POST

- **PostDoc (f/m/d) in Physical chemistry or Material Chemistry - Design and synthesis of plasmonic nanostructures**

Helmholtz-Zentrum Berlin for Materials and Energy (HZB)

Berlin, Germany

JOB POST

- **Betriebspraktikum in der 9. Klasse**

Helmholtz Centre Potsdam - German Research Centre for Geosciences (GFZ)

Potsdam, Germany

JOB POST

- **55832: Physicist, engineer or similar (f/m/x) - Development, application and scientific evaluation of greenhouse gas lidar systems**

German Aerospace Center (DLR)

Oberpfaffenhofen, Germany

JOB POST

| [Section menu](#) | [Main menu](#) |

CORRESPONDENCE

13 April 2021

Add Himalaya's Grand Canyon to China's first national parks

- [Fang Wang](#)⁰,
- [Zhixiang Zhang](#)¹,
- [Cheng Li](#)²,
- [Ge Sun](#)³,
- [Xiang Zhao](#)⁴ &
- [Zhi Lu](#) ORCID: <http://orcid.org/0000-0001-7428-2846>⁵

1. Fang Wang

1. Fudan University, Shanghai, China.

[View author publications](#)

You can also search for this author in [PubMed](#) [Google Scholar](#)

2. Zhixiang Zhang

1. Beijing Forestry University, Beijing, China.

[View author publications](#)

You can also search for this author in [PubMed](#) [Google Scholar](#)

3. Cheng Li

1. Xizijiang Conservation Center, Shenzhen, China.

[View author publications](#)

You can also search for this author in [PubMed](#) [Google Scholar](#)

4. Ge Sun

1. Research Institute of Forest Ecology, Environment and Protection, Beijing, China.

[View author publications](#)

You can also search for this author in [PubMed](#) [Google Scholar](#)

5. Xiang Zhao

1. Shanshui Conservation Center, Beijing, China.

[View author publications](#)

You can also search for this author in [PubMed](#) [Google Scholar](#)

6. [Zhi Lu](#)

1. Peking University; Beijing, China.

[View author publications](#)

You can also search for this author in [PubMed](#) [Google Scholar](#)



The Yarlung Tsangpo Grand Canyon in the eastern Himalayas is the deepest canyon in the world, and one of the longest.Credit: Dong Lei/NaturePL

As China sets about designating its first national parks, we propose that the Yarlung Tsangpo Grand Canyon in the eastern Himalayas on the Brahmaputra River, close to the Indian border, should be included. The canyon's unique biodiversity is currently under threat from tourism, climate change and construction projects that could include several hydroelectric dams.

The canyon is the deepest and one of the longest in the world. It runs through sacred Tibetan land and is a biodiversity hotspot ([L. Deng et al. Sci. Silvae Sin. 47, 1–6; 2011](#)), accounting for 65% of the vascular plants and 50% of the mammals found on the Tibetan Plateau. Species include the white-cheeked macaque (*Macaca leucogenys*), which was first described scientifically as recently as 2015 ([C. Li et al. Am. J. Primatol. 77, 753–766; 2015](#)).

We consider that the region would benefit from an evaluation of the environmental costs of further development, from a land-management plan

and from stronger cross-border collaboration. Protecting the site by making it a national park would demonstrate China's commitment to conservation targets, which will be discussed at the next United Nations' biodiversity conference, to be held in Kunming, China, in October. In our view, the park should encompass an area of about 40,000 square kilometres to take in the region's main watersheds.

Nature **592**, 353 (2021)

doi: <https://doi.org/10.1038/d41586-021-00942-y>

Jobs from Nature Careers

- - - [All jobs](#)
 - - [Research Associate / PhD Student](#)
 - [Technische Universität Dresden \(TU Dresden\)](#)
 - [Dresden, Germany](#)
 - [JOB POST](#)
 - [PostDoc \(f/m/d\) in Physical chemistry or Material Chemistry - Design and synthesis of plasmonic nanostructures](#)
 - [Helmholtz-Zentrum Berlin for Materials and Energy \(HZB\)](#)
 - [Berlin, Germany](#)
 - [JOB POST](#)
 - [Betriebspraktikum in der 9. Klasse](#)

Helmholtz Centre Potsdam - German Research Centre for Geosciences (GFZ)

Potsdam, Germany

JOB POST

- **55832: Physicist, engineer or similar (f/m/x) - Development, application and scientific evaluation of greenhouse gas lidar systems**

German Aerospace Center (DLR)

Oberpfaffenhofen, Germany

JOB POST

This article was downloaded by **calibre** from <https://www.nature.com/articles/d41586-021-00942-y>.

| [Section menu](#) | [Main menu](#) |

Work

- **How junior scientists can land a seat at the leadership table**

[13 April 2021]

Career Feature • Early-career researchers bring energy, talent and diverse voices to leadership and advisory roles.

- **A ‘no-brainer’ decision to become a COVID-19 vaccine-centre volunteer** [12 April 2021]

Where I Work • Hannah Franklin is one of 300 staff members at the Francis Crick Institute in London, helping to bring the pandemic to an end.

CAREER FEATURE

13 April 2021

How junior scientists can land a seat at the leadership table

Early-career researchers bring energy, talent and diverse voices to leadership and advisory roles.

- [Kendall Powell](#) ⁰

1. Kendall Powell

1. Kendall Powell is a freelance writer in Boulder, Colorado.

[View author publications](#)

You can also search for this author in [PubMed](#) [Google Scholar](#)

[Find a new job](#)



Thomas Mboa inspects an incubator he built with his team. Credit: Mboalab

Alfredo Giron-Nava didn't spot many peers at the inaugural meeting of the United Nations Decade of Ocean Sciences for Sustainable Development.

The postdoctoral researcher was one of only six junior scientists at the event, held in Copenhagen in May 2019. Four of them began discussions on how to boost the representation of junior scientists in the initiative, which sets global research priorities for ocean sciences.

After they persuaded organizers to give them a concluding talk slot, Giron-Nava, now a fisheries researcher at Stanford University in California, told the meeting, "It's important to have early-career researchers who, at the end of the decade, will feel ownership and leadership of the objectives we are deciding here." The room erupted into applause.

Anecdotally, steps by junior researchers to claim seats at science's decision-making tables are becoming more common. Doctoral students, postdocs and

people who have had their PhD for less than ten years are joining advisory boards, oversight councils and conference-organizing committees. Others have started their own advocacy and research initiatives by founding non-profit organizations and companies, bringing fresh perspectives and up-to-date expertise to boardrooms and advisory committees. And they gain organizational, management and leadership experience.

Junior researchers who are interested in leadership roles should seize opportunities sooner rather than later, says Juan Pablo Alperin, who studies scholarly communications at Simon Fraser University in Vancouver, Canada. Alperin served as the first early-career researcher on the advisory board of the Scholarly Publishing and Academic Resources Coalition (SPARC), a global open-access advocacy organization. “Stay in touch with shaping the profession you are going to be living in — leadership positions do that in a direct way,” he advises.

Opening doors

Open science and open-access-publishing movements have created early-career leadership opportunities, specialists say. Mark Patterson, former executive director of eLife, which runs the open-access journal *eLife* in Cambridge, UK, says he detects a strong appetite among junior researchers for systemic change in how science is shared and published.

Members of a group eLife set up in 2014 to represent the needs and aspirations of early-stage researchers convinced Patterson, who is now retired, and his colleagues to involve more junior scientists in the running of the journal. In response, the non-profit organization added a dedicated early-career-researcher seat to its board of directors, and created a pool of junior peer reviewers for articles. The board position is currently held by cell biologist Prachee Avasthi at Geisel School of Medicine at Dartmouth College in Hanover, New Hampshire. Other publishers have added early-career advisers either on their boards (PLOS) or in their advisory groups (*Journal of Cell Biology*). *Nature* and the Nature-branded journals, which are published by Springer Nature, do not have a formal advisory board or panel. The company is recruiting junior researchers for a soon-to-be launched Springer Nature US Research Advisory Council.

In March, eLife announced a partnership with PREreview, a preprint review platform, to engage more early-career researchers and those from under-represented groups in peer review.

Brianne Kent, a neuroscientist at Simon Fraser University in Burnaby, Canada, says more junior researchers are in positions of influence because so many are active in movements around open science, open access and reproducibility. Those include non-profit advocacy groups such as ASAPBio in San Francisco, California, and the Future of Research in Boston, Massachusetts. “Early-career researchers are really driving these initiatives to change scientific culture,” says Kent, who is the first, and currently the only, junior scientist to sit on the Canadian Institutes of Health Research’s 16-member governing council.

The council oversees how federal funding for health research in Canada is spent. Kent, who joined in 2019 when she was a postdoc, says her position is not a dedicated junior seat, but grew out of a general call for applications to diversify the council. She was one of four members to draw up the council’s strategic plan for 2021–31, directing which health priorities the council will fund in the coming decade. Both Kent and Avasthi say that senior board colleagues have welcomed them and encouraged them to participate fully. “I love being on the eLife board so much because everyone on it is so dissatisfied with the status quo in publishing,” says Avasthi. She’s been a vocal proponent of new policies for peer reviewing preprints. Her seat is 100% an equal seat, she says, with her feedback sought and taken seriously.



Brianne Kent is the first junior scientist to sit on one Canadian institute's governing council. Credit: eLife

Nick Shockley, SPARC's director of programmes and engagement in Washington DC, says that junior researchers are the very audience that journals, professional societies and conferences need to reach most. "Not to have the diversity of their perspective on boards is a real handicap," he adds.

The inclusion of early-career researchers in advisory roles, even in small numbers to start with, will, by the very nature of their demographic, automatically bring diversity to boards and governing bodies. "Early-career researchers today look very different from people who reached their research positions 30 years ago," says Alperin. An early-career adviser brings with them not only a beginner's viewpoint, but also fresh perspectives. They might have different cultural, ethnic or socio-economic backgrounds — they could be first-generation immigrants, Indigenous researchers or people from sexual and gender minorities, for example.

Senior researchers say that their junior colleagues often have the most up-to-date expertise on technology and methodologies in their research fields. They still get their hands dirty at the bench or in the field, and dive deeply into the literature daily.

Many early-career leaders also boast the digital skills that drive today's globalized research. They tend to be digital natives, often know basic software coding and are comfortable working with big data on cloud-based platforms. Many also deftly connect with other researchers and communities through social media.

Ecologist Monica Granados, policy adviser at Environment and Climate Change Canada, the national agency in Gatineau that coordinates environmental policy, compares graduate students and postdocs to those who work hands-on in an assembly line. For example, she says, they have been early adopters of digital lab notebooks that share data immediately on the Internet. "They see where mistakes and inefficiencies are and the ways that the science could be improved," she says.

Value added

Early-career researchers not only bring new skills and diverse perspectives, they also pick up valuable skills managing teams and projects, organizing and planning events and honing their verbal and written communication. Sometimes, it's possible to publish advisory work, as Giron-Nava did with his commentary on the early-career initiatives of the UN decade project ([A. Giron-Nava *Mar. Technol. Soc. J.* 53, 7–11; 2019](#)). These publications, often cited or shared widely on social media, showcase junior researchers' service and can raise their profiles.



Five ‘power skills’ for becoming a team leader

Granados used her knowledge about the latest open-science technologies and initiatives when working on a report that summarizes how many peer-reviewed publications and how much data the government of Canada has made openly accessible ([SBDAs Open Science Metrics Working Group. Preprint at Zenodo https://doi.org/f5jr; 2019](#)).

Many early-career leaders are motivated to give back to their communities or research fields, and, for those living abroad, to improve the opportunities for their own fledgling careers at home. After studying in France and the United States, molecular biologist Khadidiatou Sall had always planned to return to Senegal to put her technical skills to use. “The African continent missed the second industrial revolution, and it did not go well for us,” says Sall. “We cannot miss the digital revolution.”

In 2017, she founded a non-profit organization called Science Education Exchange for Sustainable Development (SeeSD), as well as an innovation lab start-up in Dakar named Ubbil. “In the Senegalese context, you realize that you can’t put things off, because that has a consequence for everyone, including you,” she says.

Ubbil uses open-source software to build low-cost digital tools for Senegalese businesses to manage their inventories, accounting and customer

relations. The lab's biotechnology component trains scientists in genomics, gene sequencing and bioinformatics. It also manufactures face shields for health-care workers at 60 hospitals in Senegal for use during the COVID-19 pandemic.

SeeSD promotes science, technology, engineering, mathematics (STEM) and arts education in schoolchildren in Senegal, using culturally relevant methods, in local languages and by including examples of Indigenous and traditional knowledge.

Sall relied on a wide community of family, friends, school directors and others working in the education sector to get SeeSD up and running while she was still a doctoral student in the United States.

Collection: Research leadership

Thomas Mboa was also a doctoral student, in science communication, when he founded Mboalab in Yaoundé, Cameroon. The innovation lab provides space for Internet-based study, a wet biology lab and ‘do-it-yourself’ science environment where people can “find local solutions to fix local problems”, he says. (The lab is named after the word *mboa*, which means ‘new’, ‘unique’ or ‘village’ in local languages.)

For example, the Kossamtor project at Mboalab built an incubator to help local people safely ferment a type of yogurt called kossam. Mboa, now a postdoc at the Open African Innovation Research Partnership at the University of Ottawa in Canada, also leads a project producing dried diagnostic and research enzymes. These do not need to be stored in refrigerators, which can be difficult to access in parts of Africa. “Decision-makers here are not always at the same level of understanding about how technology is evolving,” says Mboa, who splits his time between Canada and Cameroon. “It is better for young Africans to take action.”

Both Sall and Mboa felt that conventional academic careers would limit their freedom to pursue their entrepreneurial ideas. However, that means they are both doing multiple jobs. “Sometimes I feel like a principal investigator because I’m doing a lot of training and answering questions,”

adds Sall, who also teaches genomics and bioinformatics at University Cheikh Anta Diop in Dakar.

Side benefits

The professional development Sall gains from running these initiatives is at least equal to what she would achieve as an assistant professor, she says. Others say that the professional benefits from their advisory, advocacy and leadership roles far outweigh the time taken away from their research. The biggest boon might be the researchers' greatly expanded professional networks and amplified profile.

“Professionally, having access to this network — and the future prospects of jobs it represents — is amazing,” says Giron-Nava, who is also at the World Economic Forum’s Centre for the Fourth Industrial Revolution in San Francisco, California. Through the UN decade initiative, he has direct access to global scientific and policy directors, as well as to top scientists at leading research centres around the world.

These connections lead to speaking engagements, collaborations and research projects, as well as other advisory roles.



[How lab heads can learn to lead](#)

As a postdoc, Kelly Ramirez co-founded the advocacy organization 500 Women Scientists to promote the voices and stories of women in STEM. She says her advocacy and policy work helped her to “sell herself” during the two years of interviews before she landed a job as an assistant professor at the University of Texas at El Paso.

“For job talks, I already had the practice of telling things in a succinct, storytelling way,” she says. And her work running an organization meant she understood budgets, fundraising and managing a diverse team. That showed her future faculty colleagues that she had the skills to be a successful group leader.

Early-career leaders who participate in peer review and on tenure-review committees get to pull the curtain back on evaluation processes that they will also go through. “A lot of the mystery is gone when you are using that experience in your own process,” says Avasthi. From her work at eLife, she says, she has learnt to take reviews of her own work less personally and to embrace transparency in evaluations.

These junior scientists are also picking up soft skills rarely gained in the lab or field. After 18 months of co-leading the Early Career Ocean Professionals programme for the UN decade project, Giron-Nava has polished his diplomacy skills, learning how to negotiate and argue scientific points in a way that respects cultural differences and international viewpoints. “We have faced many situations in which our usual Western approach to collaboration does not resonate with colleagues in eastern Africa or southeast Asia. We have had to navigate this challenge to develop a truly inclusive programme,” he says.

On SPARC’s board, Alperin got the insider’s view of national political lobbying when the Fair Access to Science and Technology Research law — to make taxpayer-funded research publications available to the public after 12 months — was being stewarded through the US Congress. “It was fascinating to hear the strategizing of meetings with lawmakers and to see how things move into policy and law,” he says.

And Granados and Sall have turned their networking and leadership skills into the ultimate benefit — a full-time job doing something they are

passionate about.



Step up to leadership for mid-career growth

“What I can do through my own research pales in comparison to bringing the open-science tools and ethos to other researchers,” says Julia Stewart Lowndes, who runs Openscapes, a programme she developed at the National Center for Ecological Analysis and Synthesis in Santa Barbara, California, to increase the efficiency of scientific collaboration.

Through this programme, she has advised dozens of US academic and government research teams on how to engage in open-data science. She says that more such ‘horizontal leadership’ positions — which support, train or aid research colleagues at various career stages and levels — should be created and funded for early-career researchers.

Participation on boards or in leading initiatives can come at a cost: time taken from an individual’s projects, publications or grants. But many early-career leaders have developed strategies for time management and work–life balance to mitigate the downsides of their intense involvement.

Time investment

Some positions require significant amounts of time for in-person or virtual meetings, or frequent phone or video-conference calls. Hard deadlines for conferences or reports mean that research papers can slide to the back burner.

Giron-Nava sets firm work boundaries — by dedicating at least 80% of his work time to fisheries research and other fellowship work. Pre-pandemic, he scheduled travel so that he had at least 7–10 consecutive days at home in California, and restricted his UN reading and work to long international flights when possible. During the pandemic, he blocks off at least one day per week to be free of video-conference meetings.

Mboa says that overstretched junior scientists need to say ‘no’ sometimes. He has learnt to turn down invitations to speak on panels — especially when he feels that he is being asked because organizers want to simply tick a box to say they have “someone coming from Black Africa”.

Sall, who teaches, leads a non-profit organization and runs a company, sets weekly and monthly goals for each initiative. But despite delegating tasks to others, she still works six days per week, often late into the night, which can be mentally exhausting. She takes Sundays off and relaxes by listening to podcasts and audiobooks, watching television and films, and spending time with her family.

Ramirez wonders how her work on 500 Women Scientists will be valued in her tenure review. Many early-career advisers and advocates face pressure from their research supervisors and peers to spend more time on their own research. “Science continues to value science first,” she says.

Navigating that criticism can be tricky, but many early-career researchers say the advantages of their leadership work are worth it. Their passion projects keep them energized and pushing forward in their research and other roles.

As a group, Shockley says, junior scientists are less entrenched in specific scientific methodologies or processes, have fewer work commitments beyond their own research, and bring high levels of energy and creativity to endeavours. “That energy is absolutely a real thing,” he says.

But, he adds, that energy can easily be dismissed by organizations as not being as valuable as decades of experience. To his mind, that's a mistake. "Excitement coupled with ideas", he says, "is what drives things forward."

Nature **592**, 475-477 (2021)

doi: <https://doi.org/10.1038/d41586-021-00956-6>

Jobs from Nature Careers

- - - [All jobs](#)
 - - [Research Associate / PhD Student](#)
 - [Technische Universität Dresden \(TU Dresden\)](#)
[Dresden, Germany](#)
[JOB POST](#)
 - [PostDoc \(f/m/d\) in Physical chemistry or Material Chemistry - Design and synthesis of plasmonic nanostructures](#)
[Helmholtz-Zentrum Berlin for Materials and Energy \(HZB\)](#)
[Berlin, Germany](#)
[JOB POST](#)
 - [Betriebspraktikum in der 9. Klasse](#)
[Helmholtz Centre Potsdam - German Research Centre for Geosciences \(GFZ\)](#)

Potsdam, Germany

JOB POST

- **55832: Physicist, engineer or similar (f/m/x) - Development, application and scientific evaluation of greenhouse gas lidar systems**

German Aerospace Center (DLR)

Oberpfaffenhofen, Germany

JOB POST

This article was downloaded by **calibre** from <https://www.nature.com/articles/d41586-021-00956-6>

| [Section menu](#) | [Main menu](#) |

WHERE I WORK

12 April 2021

A ‘no-brainer’ decision to become a COVID-19 vaccine-centre volunteer

Hannah Franklin is one of 300 staff members at the Francis Crick Institute in London, helping to bring the pandemic to an end.

- [David Payne](#)

1. David Payne

[View author publications](#)

You can also search for this author in [PubMed](#) [Google Scholar](#)

Phd student Hannah Franklin photographed at the Francis Crick Institute, London.

Hannah Franklin is a PhD student in neuroscience at University College London, and is based at the Francis Crick Institute. Credit: Leonora Saunders for *Nature*

A ground-floor gallery space at the Francis Crick Institute in London, where I’m 18 months into my PhD, opened as a COVID-19 vaccination centre in January. It operates from 8 a.m. to 8 p.m., 7 days a week. I signed up immediately as a part-time staff volunteer; we number more than 300.

Our training was 10 hours of online modules plus one in-person day, when we learnt vaccination techniques using a dummy arm, and how to don and doff personal protective equipment. We also learnt basic life-support skills and how to recognize signs of an anaphylactic reaction to the vaccine.

By early April, I'd given almost 300 vaccine doses. If I'm not vaccinating, I'm checking people in or marshalling them.

Some people haven't been out of the house in a year. One woman in her 80s brought us flowers from her garden. On another day, I saw my dad, who had come for his vaccination. That was nice, because lockdown restrictions mean I haven't been able to see my family much.

This picture was taken on a very cold day, when I spent most of the shift outside, checking people in. One of them said how kind and helpful the volunteers were — that warmed me up a little! The Crick is a beautiful modern building; it's not like a hospital environment, which I think helps to allay people's vaccine anxieties.

I'm doing my PhD in Rickie Patani's laboratory, which uses human stem cells to investigate neurodegenerative diseases such as motor neuron disease (amyotrophic lateral sclerosis).

Knowing how viruses mutate can make you feel less positive about tackling the COVID-19 situation, but the Crick is doing a fantastic job with its coronavirus research, and now with its vaccination centre. This whole time has been so shocking, but volunteering was a no-brainer: a perfect opportunity to do something useful.

Nature **592**, 480 (2021)

doi: <https://doi.org/10.1038/d41586-021-00957-5>

Jobs from Nature Careers

- - - [All jobs](#)
 - - [Research Associate / PhD Student](#)

Technische Universität Dresden (TU Dresden)

Dresden, Germany

JOB POST

- **PostDoc (f/m/d) in Physical chemistry or Material Chemistry - Design and synthesis of plasmonic nanostructures**

Helmholtz-Zentrum Berlin for Materials and Energy (HZB)

Berlin, Germany

JOB POST

- **Betriebspraktikum in der 9. Klasse**

Helmholtz Centre Potsdam - German Research Centre for Geosciences (GFZ)

Potsdam, Germany

JOB POST

- **55832: Physicist, engineer or similar (f/m/x) - Development, application and scientific evaluation of greenhouse gas lidar systems**

German Aerospace Center (DLR)

Oberpfaffenhofen, Germany

JOB POST

| [Section menu](#) | [Main menu](#) |

Research

- **[An exceptional view of phase transitions in non-equilibrium systems](#)** [14 April 2021]

News & Views • Phase transitions in certain non-equilibrium systems cannot be described using the classical laws of statistical mechanics. A mathematical approach involving features called exceptional points now solves this far-reaching problem.

- **[Relax to grow more hair](#)** [31 March 2021]

News & Views • A stress hormone has been found to signal through skin cells to repress the activation of hair-follicle stem cells in mice. When this signalling is blocked, hair growth is stimulated. Stressed humans, watch out.

- **[Dynamics of polarization vortices revealed in a ferroelectric material](#)** [14 April 2021]

News & Views • Vortices of electrical polarization have been observed to vibrate at extremely high frequencies in a material called a ferroelectric. Such motion could be directly controlled by electric fields for ultrafast data processing.

- **[A critical period that shapes neuronal motor circuits](#)** [07 April 2021]

News & Views • A mechanism has been found in fruit flies that enables cells called astrocytes to signal to neurons, closing a developmental window during which locomotor behaviour is shaped.

- **[Non-reciprocal phase transitions](#)** [14 April 2021]

Article • A theoretical study of non-reciprocity in collective phenomena reveals the emergence of time-dependent phases heralded by exceptional points in contexts ranging from synchronization and flocking to pattern formation.

- **[A quantum magnetic analogue to the critical point of water](#)** [14 April 2021]

Article • The pressure dependence and magnetic field dependence of the specific heat of a quantum magnet, SrCu₂(BO₃)₂, demonstrate that its phase diagram contains a line of first-order transitions terminating at a critical point, in analogy with water.

- **[Subterahertz collective dynamics of polar vortices](#)** [14 April 2021]

Article • A dynamical study shows that vortices of electrical polarization have higher frequencies and smaller size than their magnetic counterparts, properties that are promising for electric-field-driven data processing.

- **Pseudo-halide anion engineering for α -FAPbI₃ perovskite solar cells** [05 April 2021]
Article • Incorporation of the pseudo-halide anion formate during the fabrication of α -FAPbI₃ perovskite films eliminates deleterious iodide vacancies, yielding solar cell devices with a certified power conversion efficiency of 25.21 per cent and long-term operational stability.
- **Liquid-induced topological transformations of cellular microstructures** [14 April 2021]
Article • A two-tiered dynamic design strategy achieves topological transformations of two-dimensional polymeric cellular microstructures in a reversible and temporally controllable manner through exposure to different liquids.
- **Dynamics of large effusive eruptions driven by caldera collapse** [14 April 2021]
Article • A model for eruptions resulting in caldera collapse reconciles observations of quasi-periodic stick-slip events along annular faults and the large erupted volumes characteristic of such events, highlighting the role of topography-generated pressures.
- **Protecting the global ocean for biodiversity, food and climate** [17 March 2021]
Article • Using a globally coordinated strategic conservation framework to plan an increase in ocean protection through marine protected areas can yield benefits for biodiversity, food provisioning and carbon storage.
- **Measuring human capital using global learning data** [10 March 2021]
Article • Analyses of a global database reveal that in many developing countries progress in learning remains limited despite increasing enrolment in primary and secondary education, and uncover links between human capital and economic development.
- **Inter-mosaic coordination of retinal receptive fields** [10 March 2021]
Article • Complementary types of retinal ganglion cell form mosaics with receptive fields that are farther apart than would be expected by chance, supporting the efficient coding of natural scenes.
- **Astrocytes close a motor circuit critical period** [07 April 2021]
Article • The duration of a critical period of plasticity in the developing Drosophila motor circuit, during which motor neurons display activity-dependent refinement of neurite structure and connectivity, is dependent on astrocyte to motor neuron Neuroligin–Neurexin signalling.
- **Primate cell fusion disentangles gene regulatory divergence in neurodevelopment** [17 March 2021]

Article • Cortical organoids derived from tetraploid human–chimpanzee fused induced pluripotent stem cells provide a platform for untangling unique molecular features of human brain development.

- **Corticosterone inhibits GAS6 to govern hair follicle stem-cell quiescence** [31 March 2021]

Article • Stress inhibits hair growth in mice through the release of the stress hormone corticosterone from the adrenal glands, which inhibits the activation of hair follicle stem cells by suppressing the expression of a secreted factor, GAS6, from the dermal niche.

- **Fertilized egg cells secrete endopeptidases to avoid polytubey** [31 March 2021]

Article • Fertilized *Arabidopsis* egg cells secrete endopeptidases into the extracellular space that cleave the pollen tube attractor LURE1, preventing polytubey.

- **Detection of a SARS-CoV-2 variant of concern in South Africa** [09 March 2021]

Article • The 501Y.V2 variant of SARS-CoV-2 in South Africa became dominant over other variants within weeks of its emergence, suggesting that this variant is linked to increased transmissibility or immune escape.

- **Auto-aggressive CXCR6+ CD8 T cells cause liver immune pathology in NASH** [24 March 2021]

Article • Liver resident CD8 T cells have an essential role in immunopathology in a mouse model of nonalcoholic steatohepatitis, by becoming auto-aggressive following sequential transcriptional and metabolic activation steps .

- **NASH limits anti-tumour surveillance in immunotherapy-treated HCC** [24 March 2021]

Article • In hepatocellular carcinoma driven by non-alcoholic steatohepatitis, aberrant T cell activation and impaired immune surveillance seem to make hepatocellular carcinoma less responsive to anti-PD1 or anti-PDL1 immunotherapy.

- **Expansile residence decentralizes immune homeostasis** [17 March 2021]

Article • Investigations in mice using parabiosis and cohousing experiments reveal that nonlymphoid organs serve as reservoirs of tissue-autonomous cellular immunity, leading to the decentralization of organism-level immune homeostasis.

- **A vaccine targeting mutant IDH1 in newly diagnosed glioma** [24 March 2021]

Article • A phase 1 clinical trial provides evidence that a vaccine against mutant IDH1 is safe and produces a T helper immune response in patients with glioma.

- **Structural insights into the lipid and ligand regulation of serotonin receptors** [24 March 2021]

Article • Cryo-electron microscopy structures of three different serotonin receptors in complex with serotonin and other agonists provide insights into the role of lipids in regulating these receptors and the structural basis of ligand recognition.

| [Main menu](#) | [Previous section](#) |

NEWS AND VIEWS

14 April 2021

An exceptional view of phase transitions in non-equilibrium systems

Phase transitions in certain non-equilibrium systems cannot be described using the classical laws of statistical mechanics. A mathematical approach involving features called exceptional points now solves this far-reaching problem.

- [Cynthia J. O. Reichhardt](#) ⁰ &
 - [Charles Reichhardt](#) ¹
1. [Cynthia J. O. Reichhardt](#)

1. Cynthia J. O. Reichhardt is in the Theoretical Division, Los Alamos National Laboratory, Los Alamos, New Mexico 87544, USA.

[View author publications](#)

You can also search for this author in [PubMed](#) [Google Scholar](#)

2. Charles Reichhardt

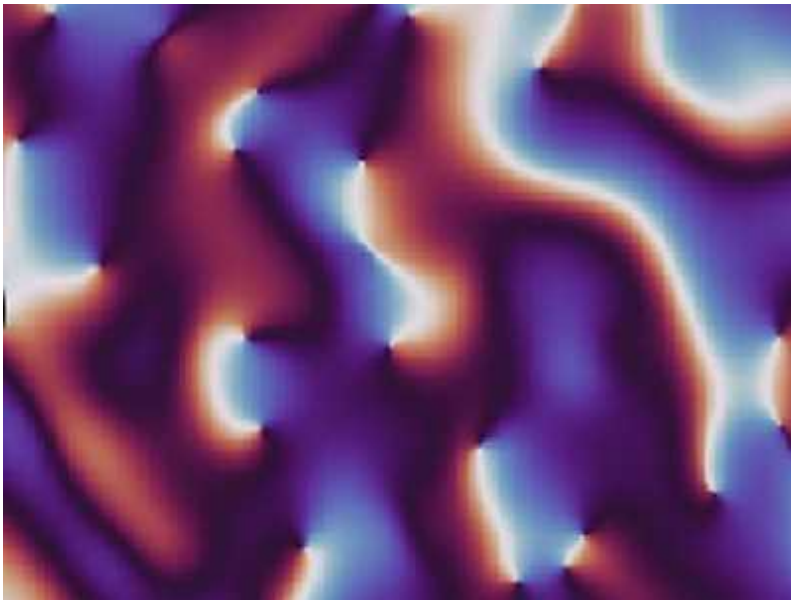
1. Charles Reichhardt is in the Theoretical Division, Los Alamos National Laboratory, Los Alamos, New Mexico 87544, USA.

[View author publications](#)

You can also search for this author in [PubMed](#) [Google Scholar](#)

Newton's third law, which states that every action has an equal and opposite reaction, is such a foundational element of classical mechanics that it is often taken for granted. But an increasing number of studies involve non-equilibrium systems in which the equality of action and reaction is broken, leading to non-reciprocal interactions between the constituent elements of the system¹. The standard machinery of classical statistical mechanics is incapable of describing the phase transitions that occur in such systems.

[Writing in *Nature*](#), Fruchart *et al.*² report that a mathematical model involving exceptional points — locations in the parameter space of a system at which two or more modes of the system coalesce into a single mode — successfully captures the behaviour of non-reciprocal phase transitions. The findings pave the way for the future analysis and eventual harnessing of these phase transitions in a variety of applications.



[Read the paper: Non-reciprocal phase transitions](#)

What is a non-reciprocal interaction, and how can it arise? In its simplest form, a non-reciprocal interaction between elements A and B is one in which A does not have the same effect on B as B has on A. Such interactions are impossible if all forces in the system are conservative — that is, if the total work done by the forces is independent of the path taken, a condition that guarantees the overall conservation of energy. Non-reciprocal interactions are therefore associated with either a gain or a loss of energy.

Strongly non-reciprocal interactions and non-conservative forces can arise in social interactions, such as those that occur when pedestrians avoid each other, or when birds fly together as a flock³. These systems are examples of ‘active matter’, in which each element (a person or bird, in our examples) contains an internal energy source that injects energy into the system by enabling each element to move under its own propulsion⁴. By contrast, ordinary non-active matter is purely passive, such as a leaf drifting on a river in response to the underlying currents.

Let’s consider the example of non-reciprocal interactions between flocking birds (Fig. 1a). To maintain a flocking arrangement, each bird adjusts its flight on the basis of the movement of the other birds in its immediate vicinity. Bird eyes, however, did not evolve to provide vision in all directions simultaneously. Instead, each bird responds only to other birds within its forward cone of vision⁵. If bird A is in the vision cone of bird B, then B responds to the motion of A; but if B is outside the vision cone of A, then A does not respond to the motion of B. In other words, the equivalence of action and reaction is lost.

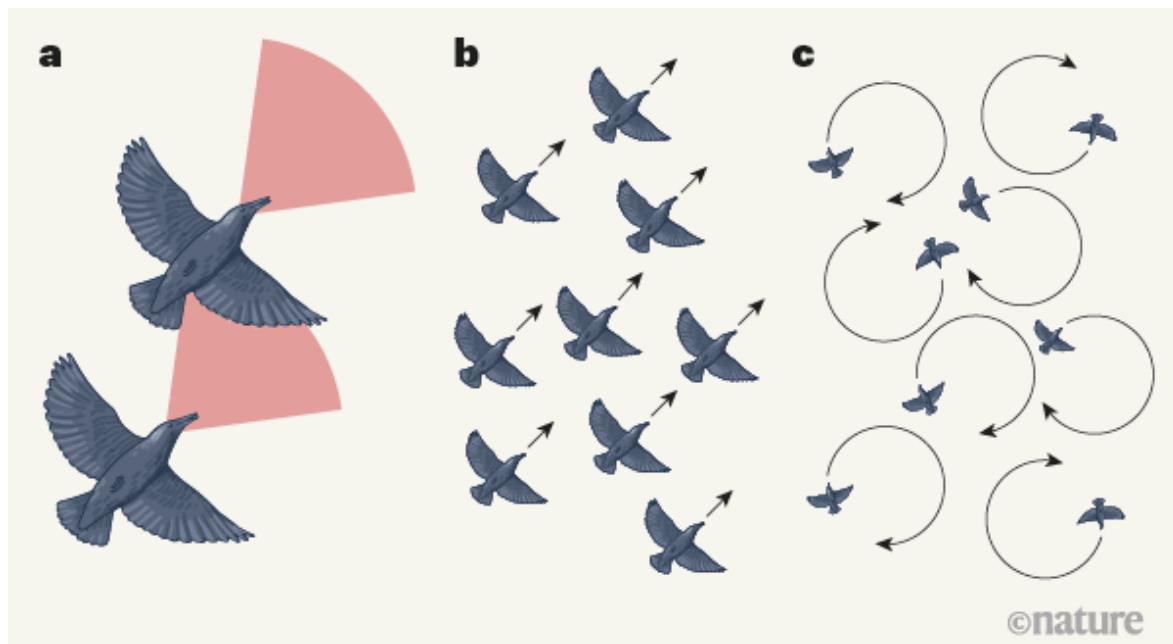
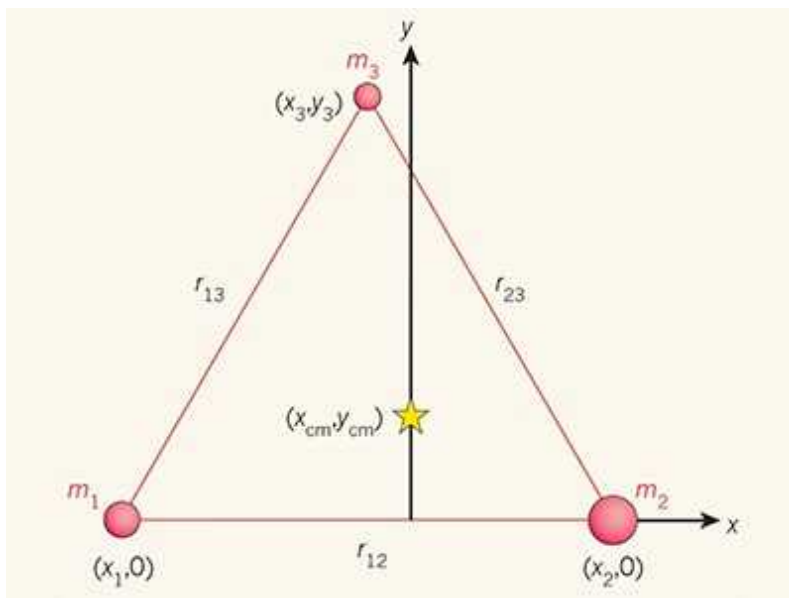


Figure 1 | Non-reciprocal interactions in bird flocking. **a**, Birds adjust their flight in response to other birds’ movements to maintain flocking, but each individual responds only to the birds in its cone of vision (pink). Here, the lower bird responds to the bird above it, but not vice versa. Such

interactions are said to be non-reciprocal. **b**, **c**, Non-reciprocal systems can undergo phase transitions in which a spontaneously broken symmetry is regained. For example, flocks spontaneously break continuous spatial symmetry if all the birds fly in one direction (**b**), but this symmetry can be restored if the birds enter a chiral state in which they all fly clockwise or anticlockwise in circles (**c**). Fruchart *et al.*² report a mathematical approach that describes how chiral states can emerge through the transition of the system through an exceptional point — a position in a numerical plot of a system's parameters at which several modes of the system coalesce into a single mode.

In materials, non-reciprocal interactions are generally associated with the loss of a property called detailed balance, which arises when the reversal of a process occurs at the same rate as the process itself. When detailed balance is violated, the propagation of a signal in one direction differs from that in the opposite direction, either as a result of energy losses or because energy is injected by some type of pumping device. Imagine, for example, a system in which an elastic beam connects two devices that are sensitive to the compression or extension of the beam⁶. When the length of the beam is varied, the devices consume power and exert a torsional force on the beam. By contrast, a torque exerted on the beam by an outside force does not produce a response from the devices. Non-reciprocal interactions therefore arise from the asymmetry between torque and compression of the beam.

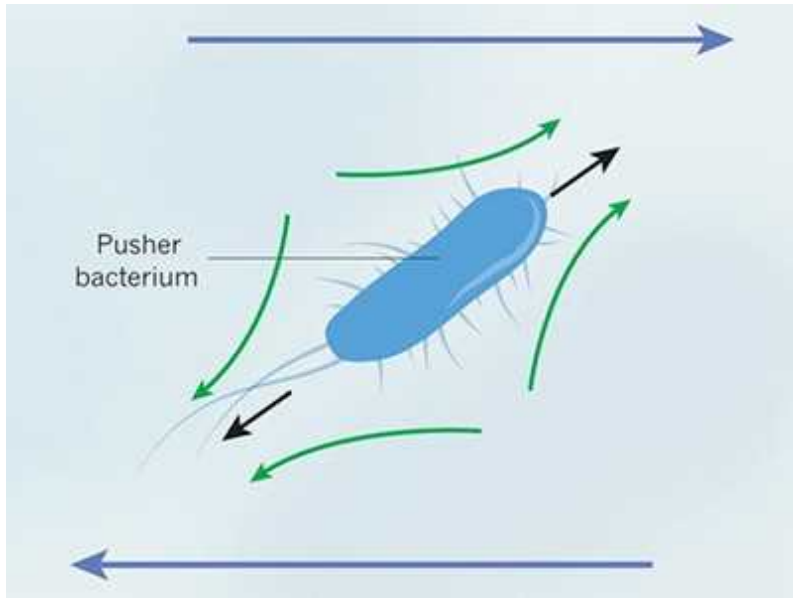


Fresh solutions to the four-body problem

Non-reciprocal systems can undergo phase transitions in which a spontaneously broken symmetry is regained dynamically. For example, in the Vicsek model of flocking birds³, a steady-state flock flies in a particular direction, thereby breaking spatial symmetry (Fig. 1b). When the interactions between birds are non-reciprocal, a state can emerge in which the birds fly in circles (Fig. 1c). The spatial symmetry in this state is restored because the birds fly in all directions. Importantly, this state has a chirality — the birds either all fly clockwise or all fly anticlockwise — that is stabilized by the many interactions between the birds. This stabilization prevents the system from flipping back and forth between the two chiralities, which would produce an average chirality of zero.

Fruchart *et al.* now show that the emergence of the chiral state occurs at a transition between symmetry and broken symmetry that is controlled by an exceptional point. By contrast, transitions in systems at equilibrium occur at mathematically distinct ‘critical points’ that are associated with the closing of an energy gap, which causes two distinct states of the system to have the same energy. The energy of a dynamic system can be described numerically by a mathematical function called a Hamiltonian, and fundamental modes of the system are characterized by vectors known as eigenvectors. The Hamiltonian of a system that has non-reciprocal interactions is non-Hermitian¹, which means that the eigenvectors are not fully independent. When the directions of these eigenvectors are varied by changing a control parameter of the system, two of the eigenvectors can coalesce at an exceptional point.

The authors show that in a many-body system, one of the two overlapping modes is known as a long-wavelength Goldstone mode, and is associated with the breaking of rotational invariance. In the case of a flock of birds, the Goldstone mode corresponds to a uniform movement of all birds along the flocking direction, whereas other modes control the relative motion of birds within the flock with respect to each other.



Frictionless fluids from bacterial teamwork

At the exceptional point, the complete overlap of the Goldstone mode with one of the other modes allows the system to freely switch between all possible ground states, instead of remaining trapped in one state. For the birds, this corresponds to the emergence of chiral rotation across the entire system. In other words, Fruchart *et al.* report how symmetry that was spontaneously broken on one side of the exceptional point can be dynamically restored.

Although exceptional points have received considerable attention in photonics⁷, where they have been shown to describe properties such as the one-way transmission of light through a material, Fruchart and colleagues expand their use to many-body systems that are out of equilibrium. Indeed, the authors' findings apply to any system containing two key ingredients: non-reciprocal interactions and a spontaneously broken continuous symmetry. This opens up the possibility of engineering devices whose function depends on the behaviour of a non-reciprocal system that is close to its exceptional-point transition — by analogy to existing devices that exploit behaviour near ordinary phase transitions (such as a refrigerator, which repeatedly vaporizes and condenses its coolant).

For example, materials could be developed that exhibit one-way elasticity — that is, in which mechanical waves propagate undisturbed in one direction,

but are totally reflected in the opposite direction. Devices could be engineered to produce coherent phonons, the mechanical equivalent of a laser beam. And it might be possible to develop mechanical strain cloaking, in which a portion of a material is fully isolated from vibrations or shocks.

Nature **592**, 355-356 (2021)

doi: <https://doi.org/10.1038/d41586-021-00886-3>

References

1. 1.

Ivlev, A. V. *et al. Phys. Rev. X* **5**, 011035 (2015).

2. 2.

Fruchart, M., Hanai, R., Littlewood, P. B. & Vitelli, V. *Nature* **592**, 363–369 (2021).

3. 3.

Vicsek, T., Czirók, A., Ben-Jacob, E., Cohen, I. & Shochet, O. *Phys. Rev. Lett.* **75**, 1226–1229 (1995).

4. 4.

Bechinger, C. *et al. Rev. Mod. Phys.* **88**, 045006 (2016).

5. 5.

Lavergne, F. A., Wendehenne, H., Bauerle, T. & Bechinger, C. *Science* **364**, 70–74 (2019).

6. 6.

Chen, Y., Li, X., Scheibner, C., Vitelli, V. & Huang, G. Preprint at <https://arxiv.org/abs/2009.07329> (2020).

7. 7.

Miri, M.-A. & Alu, A. *Science* **363**, eaar7709 (2019).

Jobs from Nature Careers

- - - [All jobs](#)
 -
 - [Research Associate / PhD Student](#)

[Technische Universität Dresden \(TU Dresden\)](#)

[Dresden, Germany](#)

[JOB POST](#)

- [PostDoc \(f/m/d\) in Physical chemistry or Material Chemistry - Design and synthesis of plasmonic nanostructures](#)

[Helmholtz-Zentrum Berlin for Materials and Energy \(HZB\)](#)

[Berlin, Germany](#)

[JOB POST](#)

- [Betriebspraktikum in der 9. Klasse](#)

[Helmholtz Centre Potsdam - German Research Centre for Geosciences \(GFZ\)](#)

[Potsdam, Germany](#)

[JOB POST](#)

- **55832: Physicist, engineer or similar (f/m/x) - Development, application and scientific evaluation of greenhouse gas lidar systems**

German Aerospace Center (DLR)

Oberpfaffenhofen, Germany

JOB POST

This article was downloaded by **calibre** from <https://www.nature.com/articles/d41586-021-00886-3>

| [Section menu](#) | [Main menu](#) |

NEWS AND VIEWS

31 March 2021

Relax to grow more hair

A stress hormone has been found to signal through skin cells to repress the activation of hair-follicle stem cells in mice. When this signalling is blocked, hair growth is stimulated. Stressed humans, watch out.

- [Rui Yi](#) 0

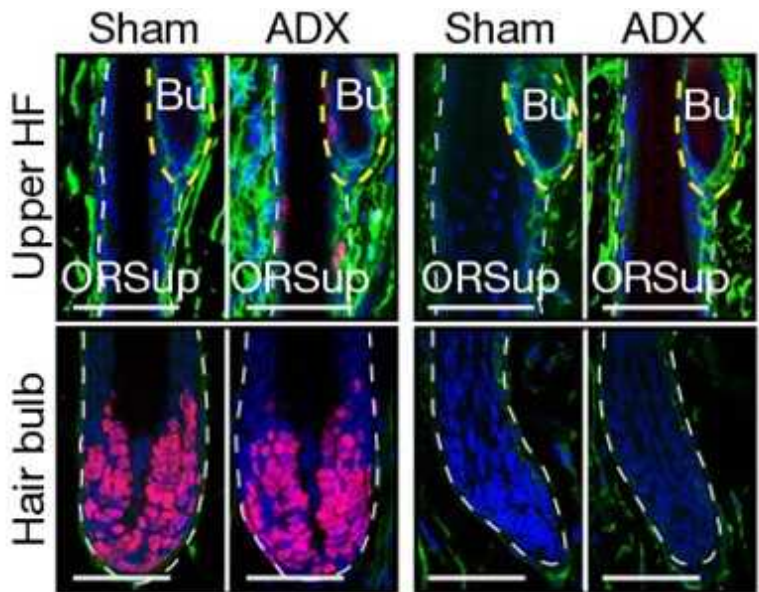
1. [Rui Yi](#)

1. Rui Yi is in the Department of Pathology and the Department of Dermatology, Northwestern University Feinberg School of Medicine, Chicago, Illinois 60611, USA.

[View author publications](#)

You can also search for this author in [PubMed](#) [Google Scholar](#)

When American football quarterback Aaron Rodgers told his fans to relax after his team's poor start one season, little did he know that he was also giving a hair-care tip. His advice is particularly helpful now, after a long pandemic year. About one-quarter of people who contract COVID-19 experience hair loss six months after the onset of symptoms¹, probably because of the systemic shock caused by the ordeal of infection and recovery. Chronic stress has long been associated with hair loss, but the underlying mechanism that links stress to the dysfunction of hair-follicle stem cells has been elusive. [Writing in Nature](#), Choi *et al.*² uncover the connection in mice.



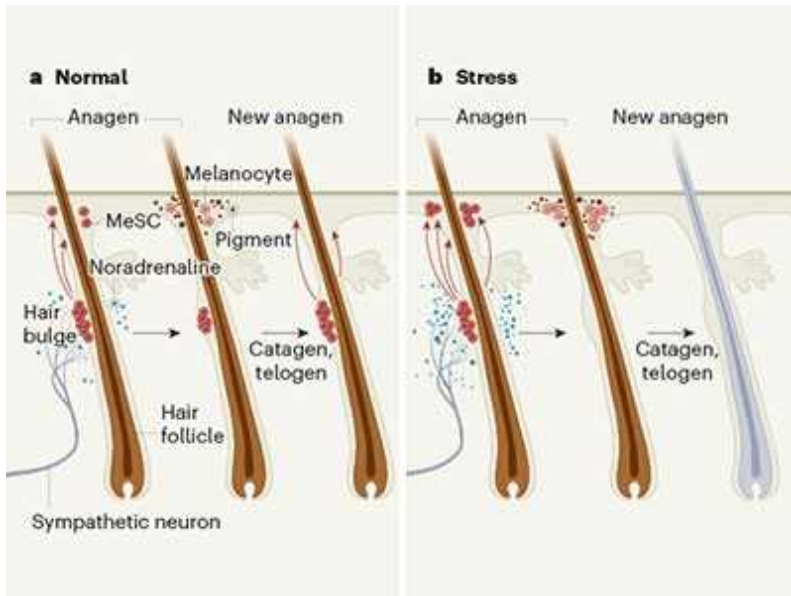
[Read the paper: Corticosterone inhibits GAS6 to govern hair follicle stem cell quiescence](#)

Throughout a person's lifespan, hair growth cycles through three stages: growth (anagen), degeneration (catagen) and rest (telogen). During anagen, a hair follicle continuously pushes out a growing hair shaft. During catagen, hair growth stops and the lower portion of the hair follicle shrinks, but the hair (now known as a club hair) remains in place. During telogen, the club hair remains dormant for some time, eventually falling out. Under severe stress, many hair follicles enter telogen prematurely and the hair quickly falls out.

Hair-follicle stem cells (HFSCs) are located in a region of the hair follicle called the bulge. These cells have a crucial role in governing hair growth by interpreting both internal and external signals. For example, during telogen, HFSCs are kept in a quiescent state and so do not divide^{3,4}. When hair growth is initiated in the next anagen phase, HFSCs are instructed to divide and produce progenitor cells. These progenitors then begin a journey of differentiation, generating several layers of hair follicles and, ultimately, the hair shaft.

Since HFSCs were identified in the bulge region more than 30 years ago^{5–7}, many regulatory molecules — such as gene-transcription factors and signalling proteins — have been shown to control the cells' quiescence and

activation^{3,4}. Nearly all of these regulators are produced by either HFSCs or their neighbouring cells, including dermal papilla cells, which usually function as a supportive ‘niche’ for HFSCs^{8,9}. But how systemic conditions such as chronic stress affect the activity of HFSCs is incompletely understood.



How the stress of fight or flight turns hair white

To answer this question, Choi and colleagues first tested the role of adrenal glands — which produce stress hormones and constitute a key endocrine organ — in the regulation of hair growth, by surgically removing them from mice. Telogen phases were much shorter in the hair follicles of these animals (which the team dubbed ADX mice) than in control mice (less than 20 days compared with 60–100 days), and the follicles engaged in hair growth roughly three times as often. The authors were able to suppress this frequent hair growth and restore the normal hair cycle by feeding the ADX mice corticosterone (a stress hormone normally produced by the animals’ adrenal glands). Interestingly, when they unpredictably applied various mild stressors to normal mice for nine weeks, they observed elevated corticosterone levels accompanied by reduced hair growth, supporting the idea that corticosterone produced by the adrenal glands during chronic stress inhibits the initiation of hair growth.

How do HFSCs sense corticosterone? Because corticosterone signals through a protein known as the glucocorticoid receptor, selective deletion of this receptor in different cell types in the skin should reveal which cells are required to receive the signal. Choi *et al.* found that selective deletion in the dermal papillae blocked the inhibitory effects of corticosterone on hair growth, whereas deletion in HFSCs themselves had no effect. This suggests that HFSCs do not sense the stress hormone directly — and that, instead, the dermal papillae have a crucial role in signal transmission.

To understand how dermal papillae relay the stress signal onwards to HFSCs, the authors profiled the messenger RNAs (which serve as the template for protein production) that are expressed in dermal papillae. This pointed to a secreted protein called growth arrest-specific 6 (GAS6) as a candidate molecular messenger. Indeed, delivering GAS6 into the skin using an adenovirus vector (a common tool in gene therapy) not only stimulated hair growth in normal mice, but also restored hair growth during chronic stress or corticosterone feeding.

Next, Choi and colleagues found that the protein AXL — a receptor for GAS6 that is expressed by HFSCs — passes the signal on to HFSCs to stimulate cell division. These and other data generated by the authors show that corticosterone signalling, triggered by chronic stress, leads to inhibition of GAS6 production in dermal papillae, and that forced expression of GAS6 in the dermis can bypass the inhibitory effect of chronic stress on hair growth (Fig. 1).

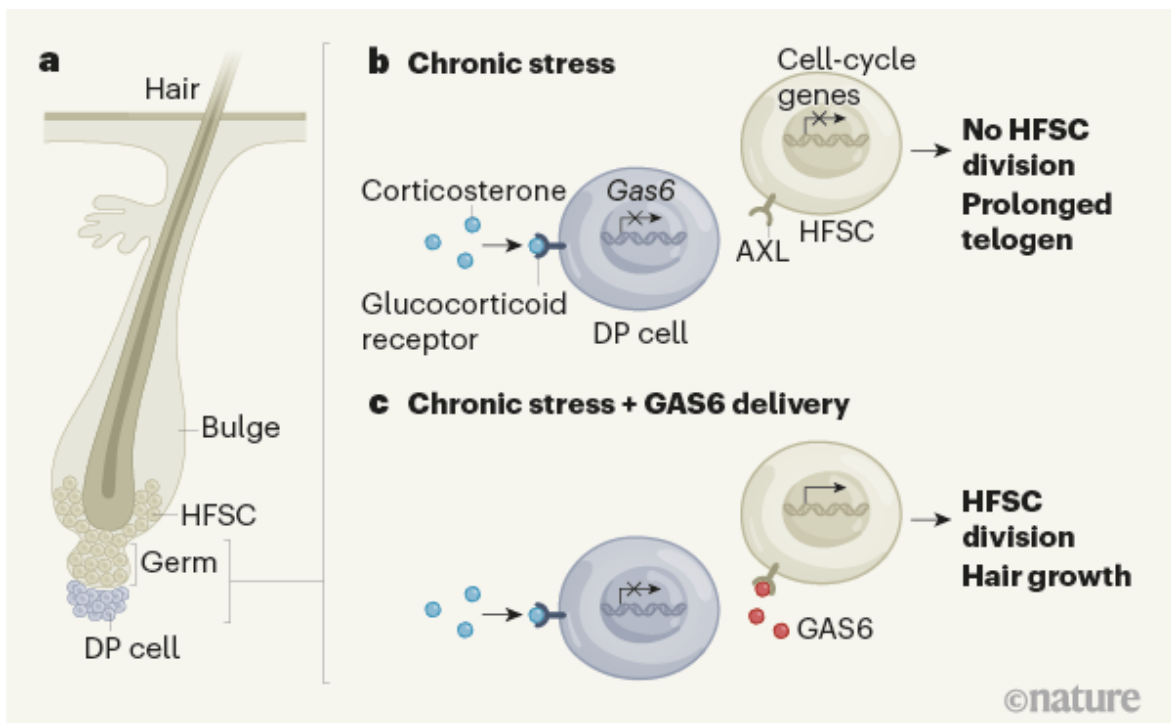
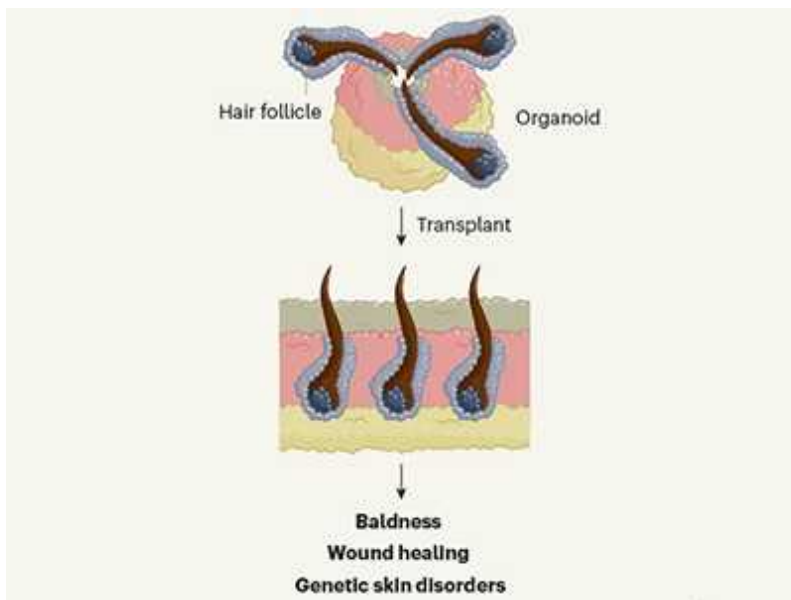


Figure 1 | Stress and hair growth in mice. **a**, Hair is generated from hair-follicle stem cells (HFSCs), which are thought to reside in the bulge and germ region of hair follicles during a ‘resting’ phase of hair growth called telogen. HFSCs are supported by neighbouring dermal papilla (DP) cells. Choi *et al.*² have discovered a pathway in mice that modulates hair growth in response to stress. **b**, Chronic stress causes mice to produce the hormone corticosterone. The authors show that corticosterone binds to the glucocorticoid receptor protein on DP cells, which leads to a block in expression of the *Gas6* gene. GAS6 protein would normally activate the AXL receptor protein on HFSCs. Its absence means that no activation signal is passed to the HFSCs, and no genes associated with the cell cycle are activated. The telogen phase is prolonged, and so the hair does not grow. **c**, When GAS6 is delivered into the skin using a viral vector (vector not shown), it can bind to AXL on HFSCs, triggering expression of genes involved in cell division. The HFSCs multiply, and hair growth follows.

These exciting findings establish a foundation for exploring treatments for hair loss caused by chronic stress. Before this knowledge can be applied to humans, however, several issues should be carefully examined. First, although corticosterone is considered to be the rodent equivalent of human cortisol, we do not yet know whether cortisol signals in a similar fashion in

humans. Characterization of GAS6 expression in human dermal papillae during the hair-growth cycle, and under stressed conditions, will be one of the first steps to take.

Second, the duration of hair-cycle phases is different in mice and humans. In adult mice, most hair follicles are in the telogen phase at any given time, compared with only around 10% of human hair follicles¹⁰. This point is particularly important because, in inhibiting GAS6 production, Choi *et al.* showed that corticosterone had a role in prolonging telogen. They did not comprehensively evaluate the anagen phase, which accounts for the status of roughly 90% of follicles in the human scalp. It will be interesting to see whether chronic stress, and perhaps cortisol, can ‘push’ anagen hair follicles into telogen in humans, or whether these factors serve only to prolong telogen, as in mice.



Regenerative medicine could pave the way to treating baldness

Third, although hair shedding in response to severe stress usually occurs during telogen, it is not well understood how a prolonged telogen contributes to the reduced anchorage of hair follicles, eventually leading to hair loss. In both mice and humans, the loss of telogen hair follicles through hair plucking usually stimulates a new round of hair growth. So perhaps hair loss that is induced by chronic stress is promoted by mechanisms that both reduce the anchorage of follicles and inhibit entry to the anagen phase.

Finally, Choi *et al.* have shown that GAS6 promotes the expression of several genes involved in cell division in HFSCs, without interfering with known transcription factors and signalling pathways. So, the authors might have uncovered a previously unknown mechanism that stimulates HFSC activation directly by promoting cell division. In ageing skin, most progenitor cells harbour DNA mutations — including harmful ones that are often found in skin cancers — without forming tumours¹¹. It will be crucial to see whether forced GAS6 expression could inadvertently unleash the growth potential of these quiescent but potentially mutation-containing HFSCs.

Although further studies are needed, Choi *et al.* have beautifully uncovered a cellular and molecular mechanism that links stress hormones produced by adrenal glands to the activation of HFSCs through the control of GAS6 expression in dermal papillae. Moreover, they have shown that injecting GAS6 into the skin can reinitiate hair growth in mice even when the animals are experiencing chronic stress. Modern life for humans is inevitably stressful. But perhaps, one day, it will prove possible to combat the negative impact of chronic stress on our hair, at least — by adding some GAS6.

Nature **592**, 356–357 (2021)

doi: <https://doi.org/10.1038/d41586-021-00656-1>

References

1. 1.

Huang, C. *et al.* Lancet **397**, 220–232 (2021).

2. 2.

Choi, S. *et al.* Nature **592**, 428–432 (2021).

3. 3.

Blanpain, C. & Fuchs, E. Science **344**, 1242281 (2014).

4. 4.

Yi, R. *Stem Cells* **35**, 2323–2330 (2017).

5. 5.

Cotsarelis, G., Sun, T.-T. & Lavker, R. M. *Cell* **61**, 1329–1337 (1990).

6. 6.

Tumbar, T. *et al.* *Science* **303**, 359–363 (2004).

7. 7.

Morris, R. J. *et al.* *Nature Biotechnol.* **22**, 411–417 (2004).

8. 8.

Driskell, R. R., Clavel, C., Rendl, M. & Watt, F. M. *J. Cell Sci.* **124**, 1179–1182 (2011).

9. 9.

Hsu, Y.-C., Li, L. & Fuchs, E. *Nature Med.* **20**, 847–856 (2014).

10. 10.

Oh, J. W. *et al.* *J. Invest. Dermatol.* **136**, 34–44 (2016).

11. 11.

Murai, K. *et al.* *Cell Stem Cell* **23**, 687–699 (2018).

Jobs from Nature Careers

- - - [All jobs](#)
 -

- **Research Associate / PhD Student**

Technische Universität Dresden (TU Dresden),

Dresden, Germany

JOB POST

- **PostDoc (f/m/d) in Physical chemistry or Material Chemistry - Design and synthesis of plasmonic nanostructures**

Helmholtz-Zentrum Berlin for Materials and Energy (HZB),

Berlin, Germany

JOB POST

- **Betriebspraktikum in der 9. Klasse**

Helmholtz Centre Potsdam - German Research Centre for Geosciences (GFZ),

Potsdam, Germany

JOB POST

- **55832: Physicist, engineer or similar (f/m/x) - Development, application and scientific evaluation of greenhouse gas lidar systems**

German Aerospace Center (DLR),

Oberpfaffenhofen, Germany

JOB POST

This article was downloaded by **calibre** from <https://www.nature.com/articles/d41586-021-00656-1>

| [Section menu](#) | [Main menu](#) |

NEWS AND VIEWS

14 April 2021

Dynamics of polarization vortices revealed in a ferroelectric material

Vortices of electrical polarization have been observed to vibrate at extremely high frequencies in a material called a ferroelectric. Such motion could be directly controlled by electric fields for ultrafast data processing.

- [Igor Luk'yanchuk](#) ⁰ &
- [Valerii M. Vinokur](#) ¹

1. [Igor Luk'yanchuk](#)

1. Igor Luk'yanchuk is at the Laboratory of Condensed Matter Physics, University of Picardie, Amiens 80039, France, and in the Faculty of Physics, Southern Federal University, Rostov-on-Don, Russia.

[View author publications](#)

You can also search for this author in [PubMed](#) [Google Scholar](#)

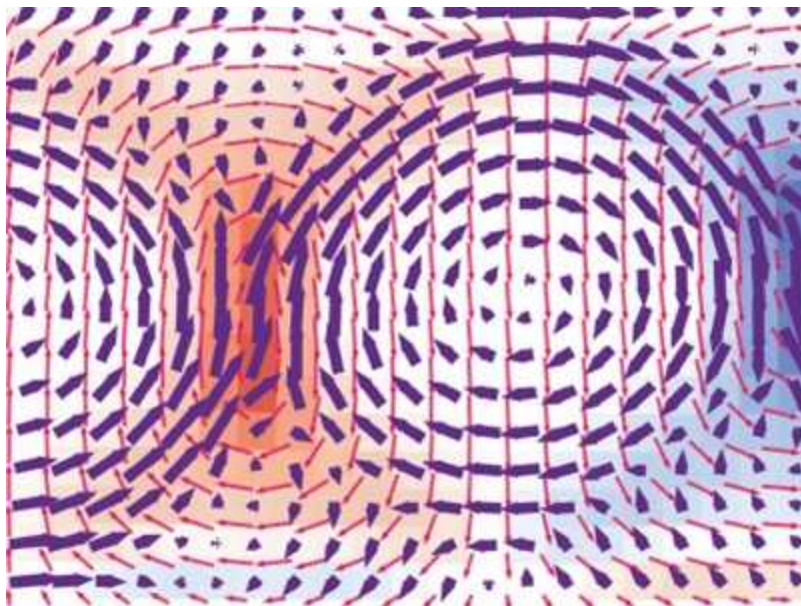
2. [Valerii M. Vinokur](#)

1. Valerii M. Vinokur is at Terra Quantum AG, Rorschach 9400, Switzerland.

[View author publications](#)

You can also search for this author in [PubMed](#) [Google Scholar](#)

The ancient Greek philosopher Democritus viewed swirling vortices of matter, along with atoms, as fundamental components of the Universe. Nowadays, vortices are seen at all scales — from spiral galaxies and whirlpools to microscopic examples in superconductors and quantum fluids. Moreover, vortices have been found to greatly affect the properties of many materials, including superconductors, ferromagnets (materials exhibiting the familiar form of magnetism found in iron) and ferroelectrics (the electrical counterparts of ferromagnets). In [a paper in *Nature*](#), Li *et al.*¹ report that vortices of electrical polarization in ferroelectrics can vibrate at terahertz-level frequencies (1 THz is 10^{12} Hz). The collective dynamics of such vortices potentially offer a platform for ultrafast data processing driven by electric fields.



[Read the paper: Subterahertz collective dynamics of polar vortices](#)

Ferroelectrics have an intrinsic electrical polarization that is caused by a slight relative shift of positively and negatively charged ions in opposite directions. In nanometre-scale ferroelectrics, these ions not only interact with an applied electric field, but also produce a substantial internal electric field owing to charges arising at the material surfaces. The resulting self-interaction of the ions through this internal field generates a plethora of polarization patterns — such as vortices and intricate structures called

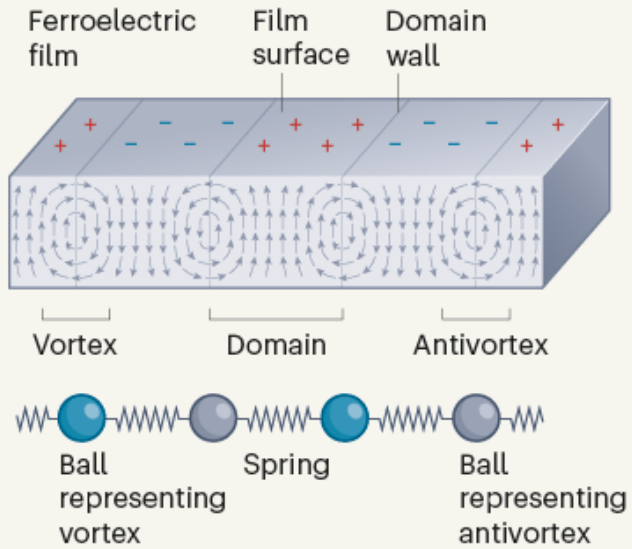
skyrmions and hopfions. Until now, the dynamics of these polarization patterns had been conjectured^{2–5}, but not demonstrated experimentally.

To address this lack, Li and colleagues used a structure called a ferroelectric superlattice, which consists of stacked alternating films of a ferroelectric and an electrical insulator. Since the dawn of solid-state physics^{6,7}, it has been known that magnetic films harbour periodic domains of alternating oppositely oriented magnetization. But it was recognized only in the past few decades that similar polarization domains arise in ferroelectrics. The polarization pattern is more elaborate in ferroelectric superlattices than in isolated ferroelectrics, and gradually changes between domains⁸. Moreover, this pattern has been shown experimentally to evolve into a periodic system of vortices and antivortices (whirls that rotate in the opposite direction to vortices)⁹.

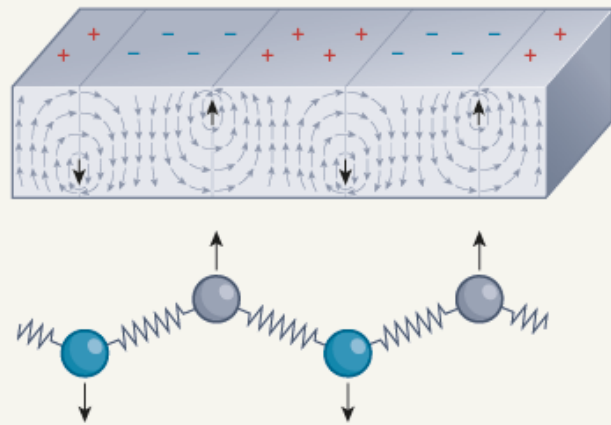
The authors used ultrashort pulses of terahertz radiation to generate vortex motion in the ferroelectric films of the superlattice. They then used a technique known as ultrafast X-ray diffraction to probe the dynamics of the periodic vortex–antivortex structure. These state-of-the-art experimental methods allowed Li *et al.* to induce and analyse the collective movement of the polarization vortices directly on picosecond timescales (1 ps is 10^{-12} s). The authors detected a single mode of vibration at 0.08 THz and a set of such modes at 0.3–0.4 THz.

In terms of dynamics, the vortex–antivortex system (Fig. 1a) resembles a linear chain of balls connected by elastic springs. The role of elastic forces is taken by electrostatic interactions between the ions that maintain vortex periodicity. The system can host two types of collective vibration, an up-and-down (transverse) motion (Fig. 1b) and a side-to-side (longitudinal) motion (Fig. 1c).

a Vortex–antivortex system



b Transverse vibrations



c Longitudinal vibrations

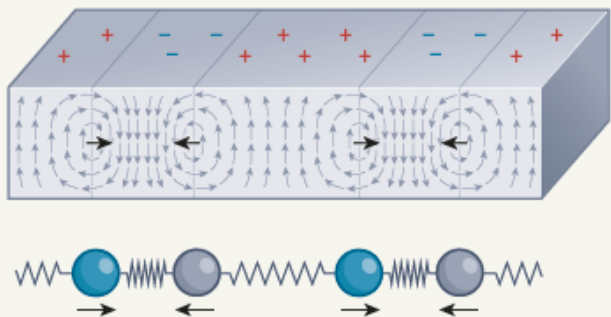
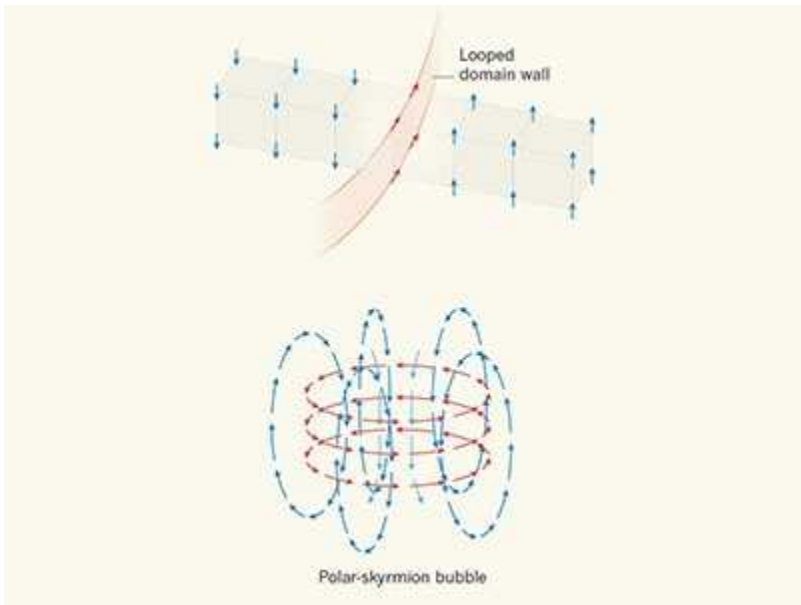


Figure 1 | Polarization vortices in a ferroelectric film. **a**, A film of a material known as a ferroelectric contains domains separated by boundaries called domain walls. Adjacent domains carry opposite charges (indicated by plus and minus symbols) on the film surface. In the equilibrium state, these positive and negative charges have equal magnitude. The pattern of electrical polarization (shown by arrows) is a periodic system of vortices and antivortices (whirls that rotate in the opposite direction to vortices). The dynamics of this system have been investigated by Li *et al.*¹ and can be modelled by a chain of balls connected by springs. **b**, The vortex–antivortex system can undergo transverse vibrations (indicated by black arrows). The domain walls do not move, and the magnitudes of the surface charges remain balanced. **c**, The system can also undergo longitudinal vibrations (indicated by black arrows). The associated displacements of domain walls cause the positive and negative surface charges to differ in magnitude.

Li *et al.* attributed their detected 0.08-THz mode to transverse vibrations. This previously unseen vortex motion indicates that an instability accompanies a structural transition to a state in which the vortex centres form a zigzag chain. Compared with the 0.08-THz mode, those at 0.3–0.4 THz are associated with more-intricate vortex dynamics and can be less easily attributed to a particular type of vibration.

To unravel the full picture of vortex dynamics, future work needs to distinguish between inter-vortex motion, intra-vortex motion and vortex bending. Moreover, the longitudinal mode of vibration must be identified. This mode is associated with a sequence of alternating displacements of domain walls (the boundaries between domains) and has remarkable properties that arise from the associated dynamics of surface charges.



Electrifying skyrmion bubbles

In metals, surface charges oscillate at frequencies corresponding to ultraviolet light (about 10^{15} Hz), and the collective oscillations are known as plasmons. Similarly, in a ferroelectric film, the longitudinal mode causes surface charges to oscillate at terahertz frequencies, and the collective oscillations can be thought of as polarization plasmons. In such a film, as in metals, a quantity called the dielectric constant is negative when the frequency of an applied electric field is lower than the plasmon oscillation frequency. Surprisingly, the dielectric constant in the ferroelectric film remains negative as the frequency of the applied field tends to zero, resulting in a negative-capacitance effect⁵ — a phenomenon that promises to reduce the power consumption of next-generation nanoscale electronic devices.

The past decade has seen remarkable progress in developing terahertz semiconductor devices, working in the frequency range between radio waves and infrared light. The potential applications of these devices span wireless transmission of vast amounts of data, detection of distant security threats, 6G wireless technology and opportunities for non-invasive medical imaging. Li and colleagues' discovery that polarization vortices in nanoscale ferroelectric films can vibrate at terahertz-level frequencies could help to scale down terahertz devices to the nanoscale and achieve high-

speed, high-density data processing driven by electric fields. Such advances might enable the development of terahertz optoelectronics and plasmonics (plasmon-based photonics), ultrafast data exchange and intra-chip communications in emerging computer circuits.

Nature **592**, 359-360 (2021)

doi: <https://doi.org/10.1038/d41586-021-00887-2>

References

1. 1.

Li, Q. *et al.* Nature **592**, 376–380 (2021).

2. 2.

Zhang, Q., Herchig, R. & Ponomareva, I. *Phys. Rev. Lett.* **107**, 177601 (2011).

3. 3.

Gui, Z. & Bellaiche, L. *Phys. Rev. B* **89**, 064303 (2014).

4. 4.

Hlinka, J., Paściak, M., Körbel, S. & Marton, P. *Phys. Rev. Lett.* **119**, 057604 (2017).

5. 5.

Luk'yanchuk, I., Sené, A. & Vinokur, V. M. *Phys. Rev. B* **98**, 024107 (2018).

6. 6.

Landau, L. D. & Lifshitz, E. M. *Phys. Z. Sowjet.* **8**, 153–169 (1935).

7. 7.

Kittel, C. *Phys. Rev.* **70**, 965–971 (1946).

8. 8.

De Guerville, F., Luk'yanchuk, I., Lahoche, L. & El Marssi, M. *Mater. Sci. Eng. B* **120**, 16–20 (2005).

9. 9.

Yadav, A. K. *et al. Nature* **530**, 198–201 (2016).

Jobs from Nature Careers

- - - [All jobs](#)
 - - [Research Associate / PhD Student](#)
 - [Technische Universität Dresden \(TU Dresden\)](#)
[Dresden, Germany](#)
[JOB POST](#)
 - [PostDoc \(f/m/d\) in Physical chemistry or Material Chemistry - Design and synthesis of plasmonic nanostructures](#)
 - [Helmholtz-Zentrum Berlin for Materials and Energy \(HZB\)](#)
[Berlin, Germany](#)
[JOB POST](#)

▪ **Betriebspraktikum in der 9. Klasse**

Helmholtz Centre Potsdam - German Research Centre for Geosciences (GFZ)

Potsdam, Germany

JOB POST

▪ **55832: Physicist, engineer or similar (f/m/x) - Development, application and scientific evaluation of greenhouse gas lidar systems**

German Aerospace Center (DLR)

Oberpfaffenhofen, Germany

JOB POST

This article was downloaded by **calibre** from <https://www.nature.com/articles/d41586-021-00887-2>

| [Section menu](#) | [Main menu](#) |

NEWS AND VIEWS

07 April 2021

A critical period that shapes neuronal motor circuits

A mechanism has been found in fruit flies that enables cells called astrocytes to signal to neurons, closing a developmental window during which locomotor behaviour is shaped.

- [Laura Sancho](#) ⁰ &
- [Nicola J. Allen](#) ¹

1. [Laura Sancho](#)

1. Laura Sancho is in the Molecular Neurobiology Laboratory, Salk Institute for Biological Studies, La Jolla, California 92037, USA.

[View author publications](#)

You can also search for this author in [PubMed](#) [Google Scholar](#)

2. [Nicola J. Allen](#)

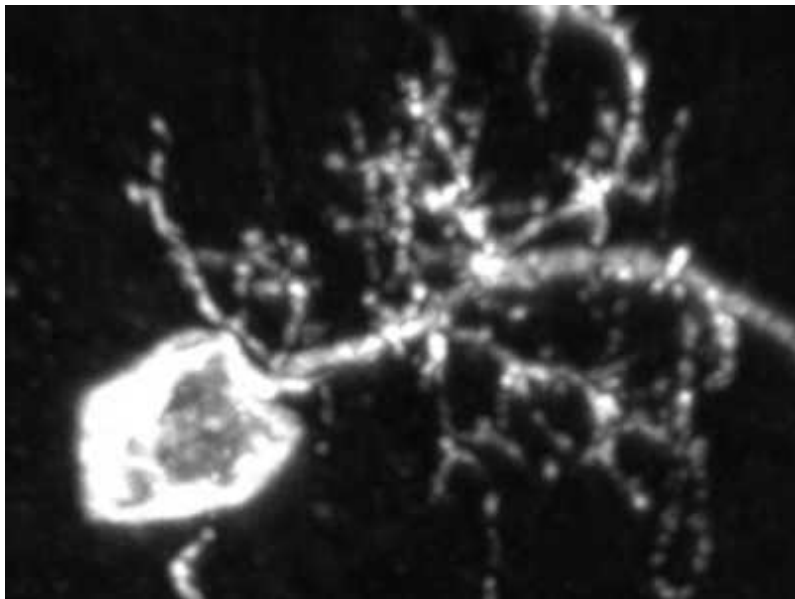
1. Nicola J. Allen is in the Molecular Neurobiology Laboratory, Salk Institute for Biological Studies, La Jolla, California 92037, USA.

[View author publications](#)

You can also search for this author in [PubMed](#) [Google Scholar](#)

There are times in an organism's development when parts of the forming nervous system are particularly sensitive to changing inputs. Disrupting these critical periods can have lifelong effects on neuronal connectivity and brain function¹. For example, there is a critical period during childhood for

language acquisition². And altered critical periods have been suggested to play a part in neurodevelopmental disorders, including autism spectrum disorder³ and schizophrenia⁴. Critical periods have been extensively described in the visual system¹, but, until now, there has been less focus on non-sensory systems. [Writing in Nature](#), Ackerman *et al.*⁵ close this gap. The authors identify a critical period for motor-circuit development in the fruit fly *Drosophila melanogaster*, and establish the cellular and molecular underpinnings of critical-period closure in this system.



[Read the paper: Astrocytes close a motor circuit critical period](#)

During a critical period, neuronal connections can be reshaped in several ways. Ackerman *et al.* mainly address homeostatic plasticity, in which changes occur across an entire neuron — including in the size of structures called dendrites, which receive synaptic connections from other neurons, in synapse numbers and in the strength of electrical impulses transmitted by synapses⁶.

First, the authors used a technique called optogenetics to activate or inhibit neuronal activity in two classes of neuron called aCC and RP2 motor neurons. When they silenced the neurons, both the length and volume of the cells' dendrites increased. By contrast, optogenetic activation led to dendritic retraction. These changes occurred only when neuronal activity

was manipulated in the 8 hours after larval hatching, and just 15 minutes of manipulation was necessary to see effects.

Next, Ackerman and colleagues asked if the changes in dendrite shape translated into changes in the numbers of excitatory and inhibitory synaptic connections on the aCC and RP2 motor neurons (these synapses activate and inhibit neuronal activity, respectively). Optogenetic silencing of the neurons resulted in a reduction in inhibitory-synapse numbers and an increase in excitatory synapses. Together, the expansion of dendrites and the shift in synapse composition allowed the neurons to rebalance neuronal activity, counteracting the effect of optogenetic silencing. Optogenetic activation of aCC and RP2 neurons led to a decrease in the number of excitatory synapses, but not to an increase in inhibitory synapses, perhaps owing to the limited amount of cell membrane available for the formation of connections after dendrite retraction. Together, this first batch of findings indicates that there is a critical period for homeostatic changes to dendritic structure and synapse number in the developing motor system of *D. melanogaster* (Fig. 1a, b).

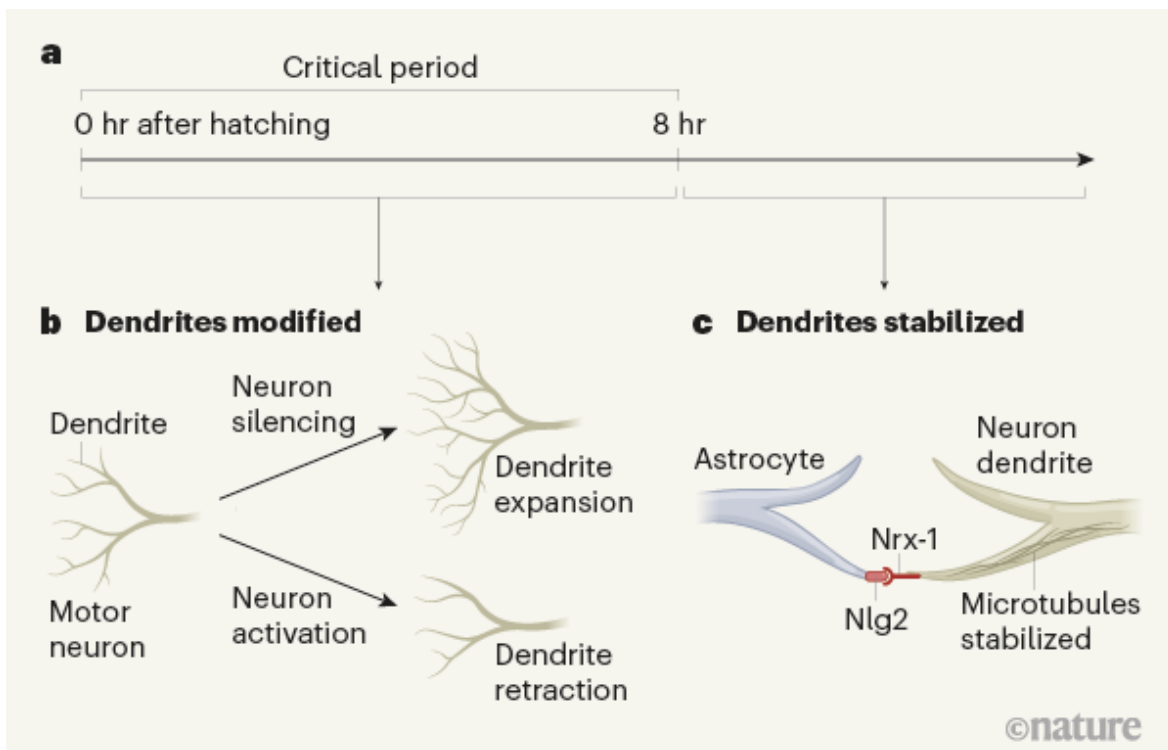
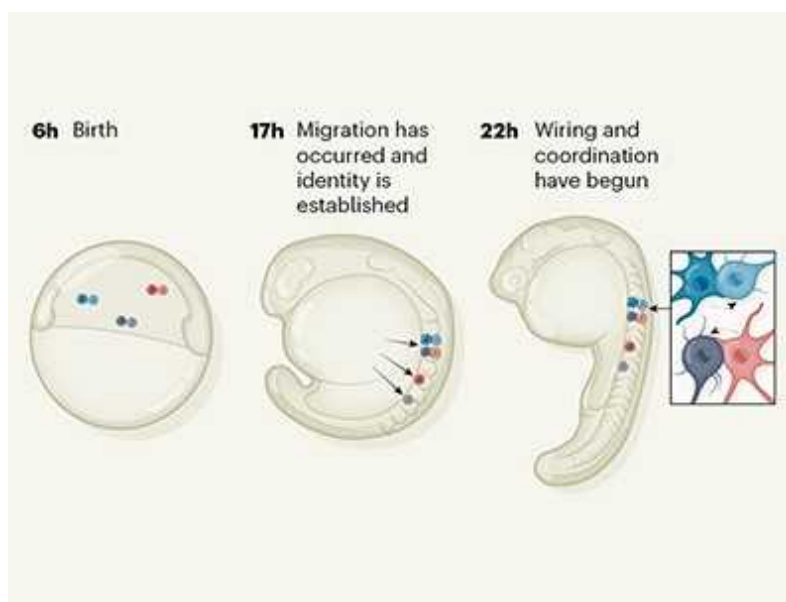


Figure 1 | Shaping a motor circuit. **a**, Ackerman *et al.*⁵ have identified a critical period during which motor circuits involving motor neurons called aCC and RP2 are shaped in the fruit fly *Drosophila melanogaster*. In the eight hours after larval hatching, structures called dendrites, which receive synaptic inputs from other neurons, can be modified, but these dendrites stabilize after the critical period has closed. **b**, Silencing the activity of the neurons during the critical period leads to the expansion of dendrites. By contrast, neuronal activation leads to dendrite retraction. **c**, The critical period closes as neighbouring cells called astrocytes mature. The maturing cells produce the protein Nlg2, which interacts with Nrx-1 protein on the neuronal dendrite. This interaction leads to the stabilization of structures called microtubules, which, in turn, prevents further dendritic remodelling.

What induces these changes? Neurons are often in close contact with cells called astrocytes, which help to regulate synaptic development and maintain brain function⁷. Ackerman *et al.* therefore used genetic engineering to eliminate all astrocytes in their fruit flies. Dendritic remodelling continued beyond eight hours after larval hatching in the mutant flies, but there was no increase in the amount of remodelling that occurred before the eight-hour period had elapsed. These findings indicate that astrocytes regulate the timing of critical-period closure for the aCC/RP2 system, but not the potential for plasticity during this time. This is a key distinction, because it suggests that different mechanisms underlie the two phenomena.

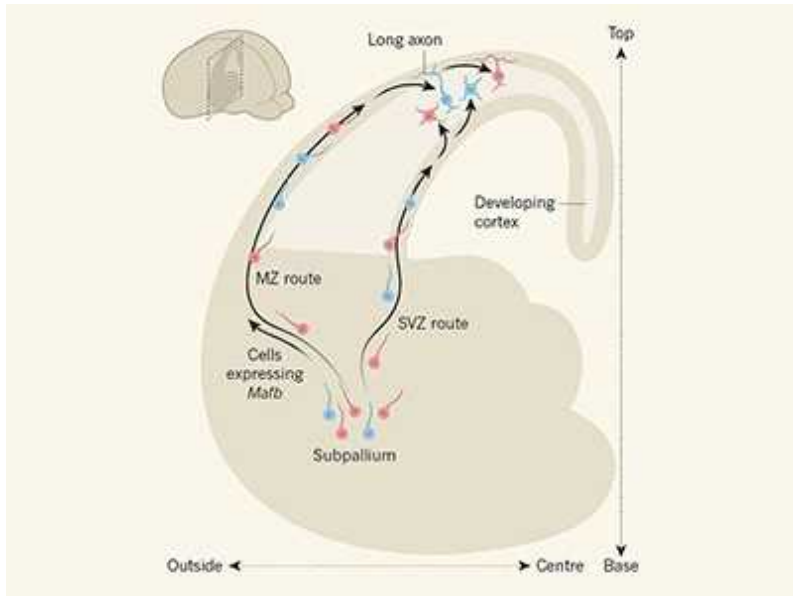


Cell-tracking pipeline reveals how motor circuits are built

Consequently, Ackerman and colleagues sought to identify the mechanisms involved in the closure of the critical period. They used a technique called an RNA interference screen to inhibit the translation of different messenger RNA molecules into protein in the astrocytes of larvae, and then analysed the time at which the critical period closed in each of the resulting flies. This allowed them to identify genes that might regulate closure of the critical period. There were several genes for which RNA interference led to an extension of the critical period, but in many cases their inhibition also had a profound impact on astrocyte shape, making it hard to dissociate a role in astrocyte development from a specific role in regulating the critical period. The authors chose to focus on the gene *nlg2*, inhibition of which extended the critical period without altering astrocyte shape.

The equivalent gene family in mice, neuroligins, has been linked to astrocyte maturation during the critical period in the visual cortex of the brain, and astrocyte maturation coincides closely with the closure of this critical period⁸. In *D. melanogaster*, Nlg2 protein interacts with the protein neurexin-1 (Nrx-1), which Ackerman and colleagues found to be located in motor neuron dendrites. The authors showed that inhibition of *nrx-1* in aCC and RP2 neurons using RNA interference extended the critical period — thus, Nrx-1 is probably the neuronal receptor for astrocytic Nlg2 in regulation of critical-period closure (Fig. 1c). In line with this idea, overexpressing either *nlg2* in astrocytes or *nrx-1* in aCC/RP2 dendrites closed the critical period prematurely, shortening it to four hours after larval hatching.

Disrupting critical periods can have lasting consequences for neural-circuit function and behaviour. Indeed, Ackerman and co-workers found that extending the critical period (through manipulation of either *nrx-1* or *nlg2*) resulted in abnormal locomotor behaviour, with the larvae moving in abnormal spiralling patterns 1.5 days after the manipulation — a good time period to analyse because, at this stage, the larvae are actively feeding and moving through the culture medium. These alterations in behaviour highlight the importance of proper timing for critical periods.



Developing neurons are innately inclined to learn on the job

Ackerman and colleagues' work raises questions for future experiments. For example, how does the interaction between Nlg2 and Nrx-1 regulate the critical period? The current work identified a role for the interaction in stabilizing structural polymers called microtubules, and so in stabilizing the structure of dendrites themselves. However, the mechanism leading to microtubule stability remains to be explored. Furthermore, the dynamics of Nlg2 and Nrx-1 production are still to be determined. Can these proteins be regulated by dendritic retraction or expansion? Would dendritic retraction result from a decrease in *nlg2* expression in astrocytes?

The authors provide compelling evidence for the prominent role of astrocytes in regulating closure of a critical period. Astrocytes regulate aspects of critical-period plasticity in the mammalian visual system⁹, including through the actions of the secreted proteins chordin-like 1¹⁰ and hevin¹¹. The present work demonstrates that astrocytes can regulate critical periods not just in sensory systems, but also in motor systems. Identifying the mechanisms that govern critical-period closure is of particular interest because alterations in closure can disrupt proper neurodevelopment — the findings could therefore lead to insight into mechanisms involved in neurodevelopmental disorders such as schizophrenia³. Furthermore, identifying mechanisms of critical-period closure can enable researchers to

understand how the brain becomes less plastic in adulthood, providing new avenues for therapeutics aimed at increasing neural plasticity after brain injury or disease.

The work also shows that the role of astrocytes in regulating critical periods extends to invertebrates, thus highlighting the centrality of these cells to nervous system development and maturation. It is becoming apparent that astrocytes and related cell types (collectively called glia) are master regulators of neuronal plasticity, particularly in the context of homeostatic and circuit changes. Moving forwards, research into critical periods must take into account the contribution of glia.

Nature **592**, 360-361 (2021)

doi: <https://doi.org/10.1038/d41586-021-00680-1>

References

1. 1.
Espinosa, J. S. & Stryker, M. P. *Neuron* **75**, 230–249 (2012).
2. 2.
Friedmann, N. & Rusou, D. *Curr. Opin. Neurobiol.* **35**, 27–34 (2015).
3. 3.
LeBlanc, J. J. & Fagiolini, M. *Neural Plastic.* **2011**, 921680 (2011).
4. 4.
Insel, T. R. *Nature* **478**, 187–193 (2010).
5. 5.
Ackerman, S. D., Perez-Catalan, N. A., Freeman, M. R. & Doe, C. Q. *Nature* **592**, 414–420 (2021).

6. 6.

Turrigiano, G. G. & Nelson, S. B. *Nature Rev. Neurosci.* **5**, 97–107 (2004).

7. 7.

Allen, N. J. *Annu. Rev. Cell Dev. Biol.* **30**, 439–463 (2014).

8. 8.

Stogsdill, J. A. *et al.* *Nature* **551**, 192–197 (2017).

9. 9.

Sancho, L., Contreras, M. & Allen, N. J. *Neurosci. Res.* <https://doi.org/10.1016/j.neures.2020.11.005> (2021).

10. 10.

Blanco-Suarez, E., Liu, T.-F., Kopelevich, A. & Allen, N. J. *Neuron* **100**, 1116–1132 (2018).

11. 11.

Singh, S. K. *et al.* *Cell* **164**, 183–196 (2016).

Jobs from Nature Careers

- - - [All jobs](#)
 -
 - [Research Associate / PhD Student](#)

[Technische Universität Dresden \(TU Dresden\)](#)

Dresden, Germany

JOB POST

- **PostDoc (f/m/d) in Physical chemistry or Material Chemistry - Design and synthesis of plasmonic nanostructures**

Helmholtz-Zentrum Berlin for Materials and Energy (HZB)

Berlin, Germany

JOB POST

- **Betriebspraktikum in der 9. Klasse**

Helmholtz Centre Potsdam - German Research Centre for Geosciences (GFZ)

Potsdam, Germany

JOB POST

- **55832: Physicist, engineer or similar (f/m/x) - Development, application and scientific evaluation of greenhouse gas lidar systems**

German Aerospace Center (DLR)

Oberpfaffenhofen, Germany

JOB POST

- Article
- [Published: 14 April 2021](#)

Non-reciprocal phase transitions

- [Michel Fruchart¹](#) [na1](#),
- [Ryo Hanai^{1,2,3}](#) [na1](#),
- [Peter B. Littlewood¹](#) &
- [Vincenzo Vitelli](#) [ORCID: orcid.org/0000-0001-6328-8783^{1,4}](#)

[Nature](#) volume **592**, pages363–369(2021) [Cite this article](#)

- 2963 Accesses
- 1 Citations
- 16 Altmetric
- [Metrics details](#)

Subjects

- [Applied mathematics](#)
- [Statistical physics, thermodynamics and nonlinear dynamics](#)

Abstract

Out of equilibrium, a lack of reciprocity is the rule rather than the exception. Non-reciprocity occurs, for instance, in active matter^{1,2,3,4,5,6}, non-equilibrium systems^{7,8,9}, networks of neurons^{10,11}, social groups with conformist and contrarian members¹², directional interface growth phenomena^{13,14,15} and metamaterials^{16,17,18,19,20}. Although wave propagation in non-reciprocal media has recently been closely

studied^{1,16,17,18,19,20}, less is known about the consequences of non-reciprocity on the collective behaviour of many-body systems. Here we show that non-reciprocity leads to time-dependent phases in which spontaneously broken continuous symmetries are dynamically restored. We illustrate this mechanism with simple robotic demonstrations. The resulting phase transitions are controlled by spectral singularities called exceptional points²¹. We describe the emergence of these phases using insights from bifurcation theory^{22,23} and non-Hermitian quantum mechanics^{24,25}. Our approach captures non-reciprocal generalizations of three archetypal classes of self-organization out of equilibrium: synchronization, flocking and pattern formation. Collective phenomena in these systems range from active time-(quasi)crystals to exceptional-point-enforced pattern formation and hysteresis. Our work lays the foundation for a general theory of critical phenomena in systems whose dynamics is not governed by an optimization principle.

[Access through your institution](#)

[Change institution](#)

[Buy or subscribe](#)

Access options

Subscribe to Journal

Get full journal access for 1 year

\$199.00

only \$3.90 per issue

[Subscribe](#)

All prices are NET prices.

VAT will be added later in the checkout.

Tax calculation will be finalised during checkout.

Rent or Buy article

Get time limited or full article access on ReadCube.

from \$8.99

[Rent or Buy](#)

All prices are NET prices.

Additional access options:

- [Log in](#)
- [Access through your institution](#)
- [Learn about institutional subscriptions](#)

Fig. 1: Exceptional transitions: examples and mechanism.

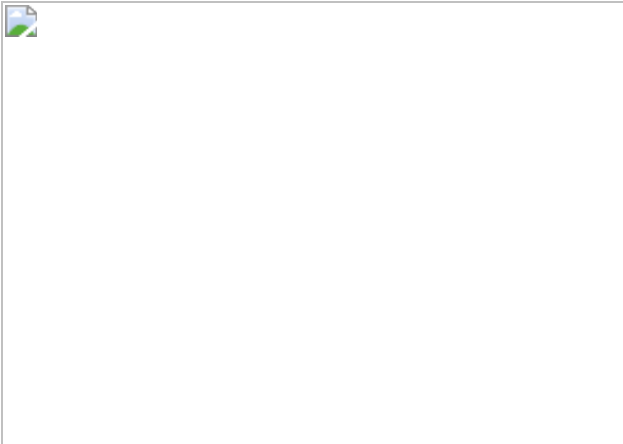


Fig. 2: Phase diagrams and active time (quasi)crystals.

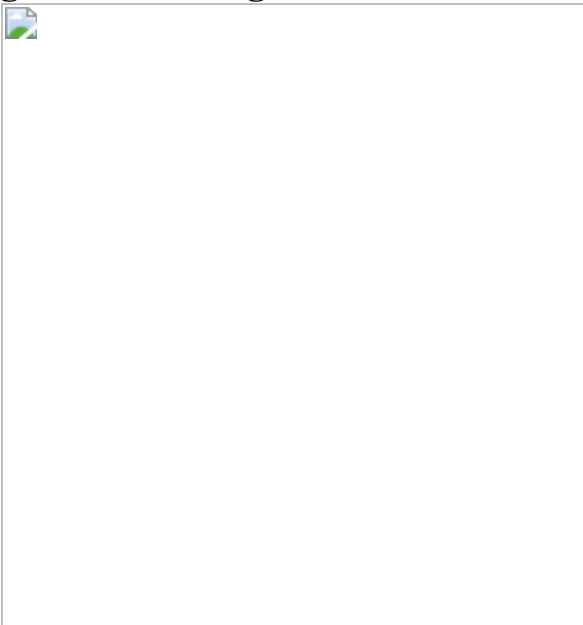


Fig. 3: Exceptional-point-enforced pattern formation and topological defects.

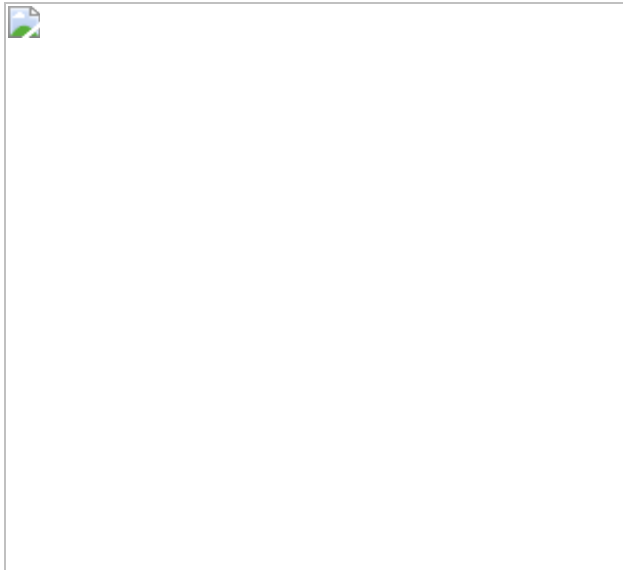
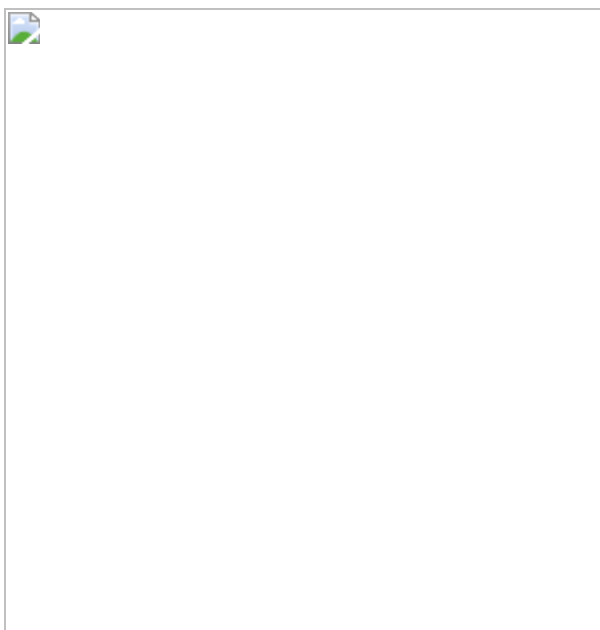


Fig. 4: A visual procedure to identify and analyse exceptional transitions.



Data availability

No data were generated during the course of this study.

Code availability

The computer code used in this study is available on Zenodo at
<https://doi.org/10.5281/zenodo.4605984> under the 2-clause BSD licence.

References

1. 1.

Shankar, S., Souslov, A., Bowick, M. J., Marchetti, M. C. & Vitelli, V. Topological active matter. Preprint at <https://arxiv.org/abs/2010.00364> (2020).

2. 2.

Uchida, N. & Golestanian, R. Synchronization and collective dynamics in a carpet of microfluidic rotors. *Phys. Rev. Lett.* **104**, 178103 (2010).

[ADS](#) [PubMed](#) [Google Scholar](#)

3. 3.

Saha, S., Ramaswamy, S. & Golestanian, R. Pairing, waltzing and scattering of chemotactic active colloids. *New J. Phys.* **21**, 063006 (2019).

[ADS](#) [MathSciNet](#) [CAS](#) [Google Scholar](#)

4. 4.

Nagy, M., Ákos, Z., Biro, D. & Vicsek, T. Hierarchical group dynamics in pigeon flocks. *Nature* **464**, 890–893 (2010).

[ADS](#) [CAS](#) [PubMed](#) [Google Scholar](#)

5. 5.

Yllanes, D., Leoni, M. & Marchetti, M. C. How many dissenters does it take to disorder a flock? *New J. Phys.* **19**, 103026 (2017).

[ADS](#) [Google Scholar](#)

6. 6.

Lavergne, F. A., Wendehenne, H., Bäuerle, T. & Bechinger, C. Group formation and cohesion of active particles with visual perception–dependent motility. *Science* **364**, 70–74 (2019).

[ADS](#) [CAS](#) [Google Scholar](#)

7. 7.

van Zuiden, B. C., Paulose, J., Irvine, W. T. M., Bartolo, D. & Vitelli, V. Spatiotemporal order and emergent edge currents in active spinner materials. *Proc. Natl Acad. Sci. USA* **113**, 12919 (2016).

[ADS](#) [PubMed](#) [Google Scholar](#)

8. 8.

Ivlev, A. V. et al. Statistical mechanics where Newton’s third law is broken. *Phys. Rev. X* **5**, 011035 (2015).

[Google Scholar](#)

9. 9.

Lahiri, R. & Ramaswamy, S. Are steadily moving crystals unstable? *Phys. Rev. Lett.* **79**, 1150–1153 (1997).

[ADS](#) [CAS](#) [Google Scholar](#)

10. 10.

Montbrió, E. & Pazó, D. Kuramoto model for excitation-inhibition-based oscillations. *Phys. Rev. Lett.* **120**, 244101 (2018).

[ADS](#) [PubMed](#) [Google Scholar](#)

11. 11.

Sompolinsky, H. & Kanter, I. Temporal association in asymmetric neural networks. *Phys. Rev. Lett.* **57**, 2861–2864 (1986).

[ADS](#) [CAS](#) [PubMed](#) [Google Scholar](#)

12. 12.

Hong, H. & Strogatz, S. H. Kuramoto model of coupled oscillators with positive and negative coupling parameters: an example of conformist and contrarian oscillators. *Phys. Rev. Lett.* **106**, 054102 (2011).

[ADS](#) [PubMed](#) [Google Scholar](#)

13. 13.

Malomed, B. & Tribelsky, M. Bifurcations in distributed kinetic systems with aperiodic instability. *Physica D* **14**, 67–87 (1984).

[ADS](#) [MathSciNet](#) [MATH](#) [Google Scholar](#)

14. 14.

Coullet, P., Goldstein, R. E. & Gunaratne, G. H. Parity-breaking transitions of modulated patterns in hydrodynamic systems. *Phys. Rev. Lett.* **63**, 1954–1957 (1989).

[ADS](#) [CAS](#) [PubMed](#) [Google Scholar](#)

15. 15.

Pan, L. & de Bruyn, J. R. Spatially uniform traveling cellular patterns at a driven interface. *Phys. Rev. E* **49**, 483–493 (1994).

[ADS](#) [CAS](#) [Google Scholar](#)

16. 16.

Fleury, R., Sounas, D. L., Sieck, C. F., Haberman, M. R. & Alù, A. Sound isolation and giant linear nonreciprocity in a compact acoustic circulator. *Science* **343**, 516–519 (2014).

[ADS](#) [CAS](#) [PubMed](#) [Google Scholar](#)

17. 17.

Brandenbourger, M., Locsin, X., Lerner, E. & Coulais, C. Non-reciprocal robotic metamaterials. *Nat. Commun.* **10**, 4608 (2019).

[ADS](#) [PubMed](#) [PubMed Central](#) [Google Scholar](#)

18. 18.

Miri, M.-A. & Alù, A. Exceptional points in optics and photonics. *Science* **363**, eaar7709 (2019).

[MathSciNet](#) [CAS](#) [MATH](#) [Google Scholar](#)

19. 19.

Scheibner, C. et al. Odd elasticity. *Nat. Phys.* **16**, 475–480 (2020).

[CAS](#) [Google Scholar](#)

20. 20.

Helbig, T. et al. Generalized bulk–boundary correspondence in non-Hermitian topoelectrical circuits. *Nat. Phys.* **16**, 747–750 (2020).

[CAS](#) [Google Scholar](#)

21. 21.

Kato, T. *Perturbation Theory for Linear Operators* 2nd edn (Springer, 1984).

22. 22.

Golubitsky, M. & Stewart, I. *The Symmetry Perspective* (Birkhäuser, 2002).

23. 23.

Kuznetsov, Y. A. *Elements of Applied Bifurcation Theory* (Springer, 2004).

24. 24.

Hatano, N. & Nelson, D. R. Localization transitions in non-Hermitian quantum mechanics. *Phys. Rev. Lett.* **77**, 570–573 (1996).

[ADS](#) [CAS](#) [PubMed](#) [Google Scholar](#)

25. 25.

Bender, C. M. & Boettcher, S. Real spectra in non-Hermitian Hamiltonians having PT symmetry. *Phys. Rev. Lett.* **80**, 5243–5246 (1998).

[ADS](#) [MathSciNet](#) [CAS](#) [MATH](#) [Google Scholar](#)

26. 26.

Bricard, A., Caussin, J.-B., Desreumaux, N., Dauchot, O. & Bartolo, D. Emergence of macroscopic directed motion in populations of motile colloids. *Nature* **503**, 95–98 (2013).

[ADS](#) [CAS](#) [PubMed](#) [Google Scholar](#)

27. 27.

Palacci, J., Sacanna, S., Steinberg, A. P., Pine, D. J. & Chaikin, P. M. Living crystals of light-activated colloidal surfers. *Science* **339**, 936–940 (2013).

[ADS](#) [CAS](#) [PubMed](#) [Google Scholar](#)

28. 28.

Sieberer, L. M., Huber, S. D., Altman, E. & Diehl, S. Dynamical critical phenomena in driven-dissipative systems. *Phys. Rev. Lett.* **110**, 195301 (2013).

[ADS](#) [CAS](#) [PubMed](#) [Google Scholar](#)

29. 29.

Metelmann, A. & Clerk, A. A. Nonreciprocal photon transmission and amplification via reservoir engineering. *Phys. Rev. X* **5**, 021025 (2015).

[Google Scholar](#)

30. 30.

Hanai, R., Edelman, A., Ohashi, Y. & Littlewood, P. B. Non-Hermitian phase transition from a polariton Bose–Einstein condensate to a photon laser. *Phys. Rev. Lett.* **122**, 185301 (2019).

[ADS](#) [CAS](#) [PubMed](#) [Google Scholar](#)

31. 31.

Hanai, R. & Littlewood, P. B. Critical fluctuations at a many-body exceptional point. *Phys. Rev. Res.* **2**, 033018 (2020).

[CAS](#) [Google Scholar](#)

32. 32.

Hohenberg, P. C. & Halperin, B. I. Theory of dynamic critical phenomena. *Rev. Mod. Phys.* **49**, 435–479 (1977).

[ADS](#) [CAS](#) [Google Scholar](#)

33. 33.

Acebrón, J. A., Bonilla, L. L., Vicente, C. J. P., Ritort, F. & Spigler, R. The Kuramoto model: a simple paradigm for synchronization phenomena. *Rev. Mod. Phys.* **77**, 137–185 (2005).

[ADS](#) [Google Scholar](#)

34. 34.

Vicsek, T., Czirók, A., Ben-Jacob, E., Cohen, I. & Shochet, O. Novel type of phase transition in a system of self-driven particles. *Phys. Rev. Lett.* **75**, 1226–1229 (1995).

[ADS](#) [MathSciNet](#) [CAS](#) [Google Scholar](#)

35. 35.

Toner, J. & Tu, Y. Long-range order in a two-dimensional dynamical XY model: how birds fly together. *Phys. Rev. Lett.* **75**, 4326–4329 (1995).

[ADS](#) [CAS](#) [PubMed](#) [Google Scholar](#)

36. 36.

Sakaguchi, H. & Kuramoto, Y. A soluble active rotater model showing phase transitions via mutual entertainment. *Prog. Theor. Phys.* **76**, 576–581 (1986).

[ADS](#) [Google Scholar](#)

37. 37.

Daido, H. Quasientainment and slow relaxation in a population of oscillators with random and frustrated interactions. *Phys. Rev. Lett.* **68**, 1073–1076 (1992).

[ADS](#) [CAS](#) [PubMed](#) [Google Scholar](#)

38. 38.

Das, J., Rao, M. & Ramaswamy, S. Driven Heisenberg magnets: nonequilibrium criticality, spatiotemporal chaos and control. *Europhys. Lett.* **60**, 418–424 (2002).

[ADS](#) [CAS](#) [Google Scholar](#)

39. 39.

Bonilla, L. L. & Trenado, C. Contrarian compulsions produce exotic time-dependent flocking of active particles. *Phys. Rev. E* **99**, 012612 (2019).

[ADS](#) [CAS](#) [PubMed](#) [Google Scholar](#)

40. 40.

Cross, M. C. & Hohenberg, P. C. Pattern formation outside of equilibrium. *Rev. Mod. Phys.* **65**, 851–1112 (1993).

[ADS](#) [CAS](#) [MATH](#) [Google Scholar](#)

41. 41.

Rabaud, M., Michalland, S. & Couder, Y. Dynamical regimes of directional viscous fingering: spatiotemporal chaos and wave propagation. *Phys. Rev. Lett.* **64**, 184–187 (1990).

[ADS](#) [CAS](#) [PubMed](#) [Google Scholar](#)

42. 42.

Oswald, P., Bechhoefer, J. & Libchaber, A. Instabilities of a moving nematic–isotropic interface. *Phys. Rev. Lett.* **58**, 2318–2321 (1987).

[ADS](#) [CAS](#) [Google Scholar](#)

43. 43.

Faivre, G., de Cheveigne, S., Guthmann, C. & Kurowski, P. Solitary tilt waves in thin lamellar eutectics. *Europhys. Lett.* **9**, 779–784 (1989).

[ADS](#) [Google Scholar](#)

44. 44.

Brunet, P., Flesselles, J.-M. & Limat, L. Parity breaking in a one-dimensional pattern: a quantitative study with controlled wavelength. *Europhys. Lett.* **56**, 221–227 (2001).

[ADS](#) [CAS](#) [Google Scholar](#)

45. 45.

Hassan, A. U., Hodaei, H., Miri, M.-A., Khajavikhan, M. & Christodoulides, D. N. Nonlinear reversal of the PT-symmetric phase transition in a system of coupled semiconductor microring resonators. *Phys. Rev. A* **92**, 063807 (2015).

[ADS](#) [Google Scholar](#)

46. 46.

Nixon, M., Ronen, E., Friesem, A. A. & Davidson, N. Observing geometric frustration with thousands of coupled lasers. *Phys. Rev. Lett.* **110**, 184102 (2013).

[ADS](#) [PubMed](#) [Google Scholar](#)

47. 47.

Parto, M., Hayenga, W., Marandi, A., Christodoulides, D. N. & Khajavikhan, M. Realizing spin Hamiltonians in nanoscale active photonic lattices. *Nat. Mater.* **19**, 725–731 (2020).

[ADS](#) [CAS](#) [PubMed](#) [Google Scholar](#)

48. 48.

Ramos, A., Fernández-Alcázar, L., Kottos, T. & Shapiro, B. Optical phase transitions in photonic networks: a spin-system formulation. *Phys. Rev. X* **10**, 031024 (2020).

[CAS](#) [Google Scholar](#)

49. 49.

Ashida, Y., Furukawa, S. & Ueda, M. Parity-time-symmetric quantum critical phenomena. *Nat. Commun.* **8**, 15791 (2017).

[ADS](#) [CAS](#) [PubMed](#) [PubMed Central](#) [Google Scholar](#)

50. 50.

Strack, P. & Vitelli, V. Soft quantum vibrations of a PT-symmetric nonlinear ion chain. *Phys. Rev. A* **88**, 053408 (2013).

[ADS](#) [Google Scholar](#)

51. 51.

Biancalani, T., Jafarpour, F. & Goldenfeld, N. Giant amplification of noise in fluctuation-induced pattern formation. *Phys. Rev. Lett.* **118**, 018101 (2017).

[ADS](#) [PubMed](#) [Google Scholar](#)

52. 52.

Trefethen, L. N., Trefethen, A. E., Reddy, S. C. & Driscoll, T. A. Hydrodynamic stability without eigenvalues. *Science* **261**, 578–584 (1993).

[ADS](#) [MathSciNet](#) [CAS](#) [PubMed](#) [MATH](#) [Google Scholar](#)

53. 53.

Winfree, A. T. *The Geometry of Biological Time* (Springer, 2001).

54. 54.

Khemani, V., Moessner, R. & Sondhi, S. L. A brief history of time crystals. Preprint at <https://arxiv.org/abs/1910.10745> (2019).

55. 55.

You, Z., Baskaran, A. & Marchetti, M. C. Nonreciprocity as a generic route to traveling states. Preprint at <https://arxiv.org/abs/2005.07684> (2020).

56. 56.

Saha, S., Agudo-Canalejo, J. & Golestanian, R. Scalar active mixtures: the nonreciprocal Cahn–Hilliard model. Preprint at <https://arxiv.org/abs/2005.07101> (2020).

57. 57.

Landau, L. & Khalatnikov, I. On the anomalous absorption of sound near a second-order phase transition point. *Dokl. Akad. Nauk SSSR* **96**, 469–472 (1954).

[Google Scholar](#)

58. 58.

Cugliandolo, L. F. & Kurchan, J. Weak ergodicity breaking in mean-field spin-glass models. *Philos. Mag. B* **71**, 501–514 (1995).

[ADS](#) [CAS](#) [Google Scholar](#)

59. 59.

Keim, N. C., Paulsen, J. D., Zeravcic, Z., Sastry, S. & Nagel, S. R. Memory formation in matter. *Rev. Mod. Phys.* **91**, 035002 (2019).

[ADS](#) [MathSciNet](#) [CAS](#) [Google Scholar](#)

60. 60.

Van Hove, L. Time-dependent correlations between spins and neutron scattering in ferromagnetic crystals. *Phys. Rev.* **95**, 1374–1384 (1954).

[ADS](#) [MATH](#) [Google Scholar](#)

61. 61.

Hohenberg, P. & Krehov, A. An introduction to the Ginzburg–Landau theory of phase transitions and nonequilibrium patterns. *Phys. Rep.* **572**, 1–42 (2015).

[ADS](#) [MathSciNet](#) [MATH](#) [Google Scholar](#)

62. 62.

Wilson, K. The renormalization group and the epsilon expansion. *Phys. Rep.* **12**, 75–199 (1974).

[ADS](#) [Google Scholar](#)

63. 63.

Laguës, M. & Lesne, A. *Invariances d'Échelle: des Changements d'États à la Turbulence* (Belin, 2003).

64. 64.

Muñoz, M. A. Criticality and dynamical scaling in living systems. *Rev. Mod. Phys.* **90**, 031001 (2018).

[ADS](#) [MathSciNet](#) [Google Scholar](#)

65. 65.

Sornette, D. *Critical Phenomena in Natural Sciences* (Springer, 2000).

66. 66.

van Saarloos, W. The complex Ginzburg–Landau equation for beginners. *Spatio-temporal Patterns in Nonequilibrium Complex Systems* Vol. XXI (eds Cladis, P. E. & Palffy-Muhoray, P.) (Addison-Wesley, 1994).

67. 67.

Aranson, I. S. & Kramer, L. The world of the complex Ginzburg–Landau equation. *Rev. Mod. Phys.* **74**, 99–143 (2002).

[ADS](#) [MathSciNet](#) [MATH](#) [Google Scholar](#)

68. 68.

Golubitsky, M. & Schaeffer, D. G. *Singularities and Groups in Bifurcation Theory* Vol. I (Springer, 1985).

69. 69.

Golubitsky, M., Stewart, I. & Schaeffer, D. G. *Singularities and Groups in Bifurcation Theory* Vol. II (Springer, 1988).

70. 70.

Crawford, J. D. & Knobloch, E. Symmetry and symmetry-breaking bifurcations in fluid dynamics. *Annu. Rev. Fluid Mech.* **23**, 341–387 (1991).

[ADS](#) [MathSciNet](#) [MATH](#) [Google Scholar](#)

71. 71.

Chossat, P. & Lauterbach, R. *Methods in Equivariant Bifurcations and Dynamical Systems* (World Scientific, 2000).

72. 72.

Haken, H. (ed.) *Synergetics* (Springer, 1977).

73. 73.

Henkel, M., Hinrichsen, H. & Lübeck, S. *Non-equilibrium Phase Transitions* Vol. 1 (Springer, 2008).

74. 74.

Henkel, M. & Pleimling, M. *Non-equilibrium Phase Transitions* Vol. 2 (Springer, 2010).

75. 75.

Livi, R. & Politi, P. *Nonequilibrium Statistical Physics: A Modern Perspective* (Cambridge Univ. Press, 2017).

76. 76.

Aron, C. & Chamon, C. Landau theory for non-equilibrium steady states, *SciPost Phys.* **8**, 074 (2020).

[ADS](#) [MathSciNet](#) [Google Scholar](#)

77. 77.

Marchetti, M. C. et al. Hydrodynamics of soft active matter. *Rev. Mod. Phys.* **85**, 1143 (2013).

[ADS](#) [CAS](#) [Google Scholar](#)

78. 78.

Trefethen, L. N. & Embree, M. *Spectra and Pseudospectra* (Princeton Univ. Press, 2005).

79. 79.

Böberg, L. & Brosa, U. Onset of turbulence in a pipe. *Z. Naturforsch. A* **43**, 697–726 (1988).

[ADS](#) [Google Scholar](#)

80. 80.

Farrell, B. F. & Ioannou, P. J. Variance maintained by stochastic forcing of non-normal dynamical systems associated with linearly stable shear flows. *Phys. Rev. Lett.* **72**, 1188–1191 (1994).

[ADS](#) [CAS](#) [PubMed](#) [Google Scholar](#)

81. 81.

Dauchot, O. & Manneville, P. Local versus global concepts in hydrodynamic stability theory. *J. Phys. II* **7**, 371–389 (1997).

[CAS](#) [Google Scholar](#)

82. 82.

Grossmann, S. The onset of shear flow turbulence. *Rev. Mod. Phys.* **72**, 603–618 (2000).

[ADS](#) [Google Scholar](#)

83. 83.

1. Chomaz, J.-M. Global instabilities in spatially developing flows: non-normality and nonlinearity. *Annu. Rev. Fluid Mech.* **37**, 357–392 (2005).

[ADS](#) [MathSciNet](#) [MATH](#) [Google Scholar](#)

2. 84.

Wu, J.-Z., Ma, H.-Y. & Zhou, M.-D. *Vorticity And Vortex Dynamics* (Springer, 2006).

3. 85.

Schmid, P. J. Nonmodal stability theory. *Annu. Rev. Fluid Mech.* **39**, 129–162 (2007).

[ADS](#) [MathSciNet](#) [MATH](#) [Google Scholar](#)

4. 86.

Kerswell, R. Nonlinear nonmodal stability theory. *Annu. Rev. Fluid Mech.* **50**, 319–345 (2018).

[ADS](#) [MathSciNet](#) [MATH](#) [Google Scholar](#)

5. 87.

Chajwa, R., Menon, N., Ramaswamy, S. & Govindarajan, R. Waves, algebraic growth, and clumping in sedimenting disk arrays. *Phys. Rev. X* **10**, 041016 (2020).

[CAS](#) [Google Scholar](#)

6. 88.

Murphy, B. K. & Miller, K. D. Balanced amplification: a new mechanism of selective amplification of neural activity patterns. *Neuron* **61**, 635–648 (2009); correction **89**, 235 (2016).

[CAS](#) [PubMed](#) [PubMed Central](#) [Google Scholar](#)

7. 89.

Hennequin, G., Vogels, T. P. & Gerstner, W. Non-normal amplification in random balanced neuronal networks. *Phys. Rev. E* **86**, 011909 (2012).

[ADS](#) [Google Scholar](#)

8. 90.

Amir, A., Hatano, N. & Nelson, D. R. Non-Hermitian localization in biological networks. *Phys. Rev. E* **93**, 042310 (2016).

[ADS](#) [MathSciNet](#) [PubMed](#) [Google Scholar](#)

9. 91.

Asllani, M. & Carletti, T. Topological resilience in non-normal networked systems. *Phys. Rev. E* **97**, 042302 (2018).

[ADS](#) [CAS](#) [PubMed](#) [Google Scholar](#)

10. 92.

Asllani, M., Lambiotte, R. & Carletti, T. Structure and dynamical behavior of non-normal networks. *Sci. Adv.* **4**, eaau9403 (2018).

[ADS](#) [PubMed](#) [PubMed Central](#) [Google Scholar](#)

11. 93.

Baggio, G., Rutten, V., Hennequin, G. & Zampieri, S. Efficient communication over complex dynamical networks: the role of matrix non-normality. *Sci. Adv.* **6**, eaba2282 (2020).

[ADS](#) [PubMed](#) [PubMed Central](#) [Google Scholar](#)

12. 94.

Nicolaou, Z. G., Nishikawa, T., Nicholson, S. B., Green, J. R. & Motter, A. E. Non-normality and non-monotonic dynamics in complex reaction networks. *Phys. Rev. Res.* **2**, 043059 (2020).

[CAS](#) [Google Scholar](#)

13. 95.

Neubert, M. G. & Caswell, H. Alternatives to resilience for measuring the responses of ecological systems to perturbations. *Ecology* **78**, 653–665 (1997).

[Google Scholar](#)

14. 96.

Nelson, D. R. & Shnerb, N. M. Non-Hermitian localization and population biology. *Phys. Rev. E* **58**, 1383 (1998).

[ADS](#) [MathSciNet](#) [CAS](#) [Google Scholar](#)

15. 97.

Neubert, M. G., Klanjscek, T. & Caswell, H. Reactivity and transient dynamics of predator–prey and food web models. *Ecol. Modell.* **179**, 29 (2004).

[Google Scholar](#)

16. 98.

Townley, S., Carslake, D., Kellie-smith, O., McCarthy, D. & Hodgson, D. Predicting transient amplification in perturbed ecological systems. *J. Appl. Ecol.* **44**, 1243 (2007).

[Google Scholar](#)

17. 99.

Ridolfi, L., Camporeale, C., D’Odorico, P. & Laio, F. Transient growth induces unexpected deterministic spatial patterns in the Turing process. *Europhys. Lett.* **95**, 18003 (2011).

[ADS](#) [Google Scholar](#)

18. 100.

Feng, L., El-Ganainy, R. & Ge, L. Non-Hermitian photonics based on parity–time symmetry. *Nat. Photon.* **11**, 752 (2017).

[ADS](#) [CAS](#) [Google Scholar](#)

19. 101.

Makris, K., Ge, L. & Türeci, H. Anomalous transient amplification of waves in non-normal photonic media. *Phys. Rev. X* **4**, 041044 (2014).

[Google Scholar](#)

20. 102.

Ashida, Y., Gong, Z. & Ueda, M. Non-Hermitian physics. Preprint at <https://arxiv.org/abs/2006.01837> (2020).

21. 103.

Tripathi, V., Galda, A., Barman, H. & Vinokur, V. M. Parity–time symmetry-breaking mechanism of dynamic Mott transitions in dissipative systems. *Phys. Rev. B* **94**, 041104 (2016).

[ADS](#) [Google Scholar](#)

22. 104.

Bernier, N. R., Torre, E. G. D. & Demler, E. Unstable avoided crossing in coupled spinor condensates. *Phys. Rev. Lett.* **113**, 065303 (2014).

[ADS](#) [PubMed](#) [Google Scholar](#)

23. 105.

Aharonyan, M. & Torre, E. G. D. Many-body exceptional points in colliding condensates. *Mol. Phys.* **117**, 1971 (2019).

[ADS](#) [CAS](#) [Google Scholar](#)

24. 106.

Mostafazadeh, A. Pseudo-Hermiticity versus PT symmetry: the necessary condition for the reality of the spectrum of a non-Hermitian Hamiltonian. *J. Math. Phys.* **43**, 205 (2002).

[ADS](#) [MathSciNet](#) [MATH](#) [Google Scholar](#)

25. 107.

Mostafazadeh, A. Pseudo-Hermiticity versus PT-symmetry. II: A complete characterization of non-Hermitian Hamiltonians with a real spectrum. *J. Math. Phys.* **43**, 2814 (2002).

[ADS](#) [MathSciNet](#) [MATH](#) [Google Scholar](#)

26. 108.

Mostafazadeh, A. Pseudo-Hermiticity versus PT-symmetry. III: Equivalence of pseudo-Hermiticity and the presence of antilinear symmetries. *J. Math. Phys.* **43**, 3944 (2002).

[ADS](#) [MathSciNet](#) [MATH](#) [Google Scholar](#)

27. 109.

Bender, C. M., Berry, M. V. & Mandilara, A. Generalized PT symmetry and real spectra. *J. Phys. Math. Gen.* **35**, L467 (2002).

[ADS](#) [MathSciNet](#) [MATH](#) [Google Scholar](#)

28. 110.

Bender, C. M. & Mannheim, P. D. PT symmetry and necessary and sufficient conditions for the reality of energy eigenvalues. *Phys. Lett. A* **374**, 1616–1620 (2010).

[ADS](#) [MathSciNet](#) [CAS](#) [MATH](#) [Google Scholar](#)

29. 111.

Mostafazadeh, A. Physics of spectral singularities. In *Trends in Mathematics* (eds Kielanowski, P. et al.) 145–165 (Springer, 2015).

30. 112.

Bender, C. M. Making sense of non-Hermitian Hamiltonians. *Rep. Prog. Phys.* **70**, 947 (2007).

[ADS](#) [MathSciNet](#) [Google Scholar](#)

31. 113.

Weigert, S. PT-symmetry and its spontaneous breakdown explained by anti-linearity. *J. Opt. B* **5**, S416 (2003).

[ADS](#) [Google Scholar](#)

32. 114.

Wigner, E. P. Normal form of antiunitary operators. *J. Math. Phys.* **1**, 409 (1960).

[ADS](#) [MathSciNet](#) [MATH](#) [Google Scholar](#)

33. 115.

Konotop, V. V., Yang, J. & Zezyulin, D. A. Nonlinear waves in PT-symmetric systems. *Rev. Mod. Phys.* **88**, 035002 (2016).

[ADS](#) [Google Scholar](#)

34. 116.

van Kampen, N. G. *Stochastic Processes in Physics and Chemistry* Vol. 1 (Elsevier, 2007).

35. 117.

Risken, H. *The Fokker–Planck Equation* (Springer, 1989).

36. 118.

Gardiner, C. W. *Handbook of Stochastic Methods* (Springer, 2004).

37. 119.

Lan, G., Sartori, P., Neumann, S., Sourjik, V. & Tu, Y. The energy–speed–accuracy trade-off in sensory adaptation. *Nat. Phys.* **8**, 422 (2012).

[CAS](#) [PubMed](#) [PubMed Central](#) [Google Scholar](#)

38. 120.

Weiss, J. B. Coordinate invariance in stochastic dynamical systems. *Tellus A* **55**, 208–218 (2003).

[ADS](#) [Google Scholar](#)

39. 121.

Newton, I. *Philosophiae Naturalis Principia Mathematica* (1687).

40. 122.

Ermak, D. L. & McCammon, J. A. Brownian dynamics with hydrodynamic interactions. *J. Chem. Phys.* **69**, 1352 (1978).

[ADS](#) [CAS](#) [Google Scholar](#)

41. 123.

Di Leonardo, R. et al. Hydrodynamic interactions in two dimensions. *Phys. Rev. E* **78**, 031406 (2008).

[ADS](#) [Google Scholar](#)

42. 124.

Lahiri, R., Barma, M. & Ramaswamy, S. Strong phase separation in a model of sedimenting lattices. *Phys. Rev. E* **61**, 1648 (2000).

[ADS](#) [CAS](#) [Google Scholar](#)

43. 125.

Kryuchkov, N. P., Ivlev, A. V. & Yurchenko, S. O. Dissipative phase transitions in systems with nonreciprocal effective interactions. *Soft Matter* **14**, 9720 (2018).

[ADS](#) [CAS](#) [PubMed](#) [Google Scholar](#)

44. 126.

Soto, R. & Golestanian, R. Self-assembly of catalytically active colloidal molecules: tailoring activity through surface chemistry. *Phys. Rev. Lett.* **112**, 068301 (2014).

[ADS](#) [PubMed](#) [Google Scholar](#)

45. 127.

Agudo-Canalejo, J. & Golestanian, R. Active phase separation in mixtures of chemically interacting particles. *Phys. Rev. Lett.* **123**, 018101 (2019).

[ADS](#) [CAS](#) [PubMed](#) [Google Scholar](#)

46. 128.

Dholakia, K. & Zemánek, P. Gripped by light: optical binding. *Rev. Mod. Phys.* **82**, 1767–1791 (2010).

[ADS](#) [Google Scholar](#)

47. 129.

Yifat, Y. D. et al. Reactive optical matter: light-induced motility in electrodynamically asymmetric nanoscale scatterers. *Light Sci. Appl.* **7**, 105 (2018).

[ADS](#) [CAS](#) [PubMed](#) [PubMed Central](#) [Google Scholar](#)

48. 130.

Peterson, C. W., Parker, J., Rice, S. A. & Scherer, N. F. Controlling the dynamics and optical binding of nanoparticle homodimers with transverse phase gradients. *Nano Lett.* **19**, 897–903 (2019).

[ADS](#) [PubMed](#) [Google Scholar](#)

49. 131.

Krakauer, J. W., Ghazanfar, A. A., Gomez-Marin, A., MacIver, M. A. & Poeppel, D. Neuroscience needs behavior: correcting a reductionist bias. *Neuron* **93**, 480 (2017).

[CAS](#) [Google Scholar](#)

50. 132.

Parisi, G. Asymmetric neural networks and the process of learning. *J. Phys. Math. Gen.* **19**, L675 (1986).

[ADS](#) [MathSciNet](#) [Google Scholar](#)

51. 133.

Derrida, B., Gardner, E. & Zippelius, A. An exactly solvable asymmetric neural network model. *Europhys. Lett.* **4**, 167 (1987).

[ADS](#) [Google Scholar](#)

52. 134.

Dayan, P. & Abbott, L. *Theoretical Neuroscience: Computational and Mathematical Modelling of Neural Systems* (MIT Press, 2001).

53. 135.

Hong, H. & Strogatz, S. H. Conformists and contrarians in a Kuramoto model with identical natural frequencies. *Phys. Rev. E* **84**, 046202 (2011).

[ADS](#) [Google Scholar](#)

54. 136.

Pluchino, A., Latora, V. & Rapisarda, A. Changing opinions in a changing world: a new perspective in sociophysics. *Int. J. Mod. Phys. C* **16**, 515 (2005).

[ADS](#) [MATH](#) [Google Scholar](#)

55. 137.

Morin, A., Caussin, J.-B., Eloy, C. & Bartolo, D. Collective motion with anticipation: flocking, spinning, and swarming. *Phys. Rev. E* **91**, 012134 (2015).

[ADS](#) [MathSciNet](#) [Google Scholar](#)

56. 138.

Ginelli, F. et al. Intermittent collective dynamics emerge from conflicting imperatives in sheep herds. *Proc. Natl Acad. Sci. USA* **112**, 12729 (2015).

[ADS](#) [CAS](#) [PubMed](#) [Google Scholar](#)

57. 139.

Dadhichi, L. P., Kethapelli, J., Chajwa, R., Ramaswamy, S. & Maitra, A. Nonmutual torques and the unimportance of motility for long-range order in two-dimensional flocks. *Phys. Rev. E* **101**, 052601 (2020).

[ADS](#) [CAS](#) [PubMed](#) [Google Scholar](#)

58. 140.

Barberis, L. & Peruani, F. Large-scale patterns in a minimal cognitive flocking model: incidental leaders, nematic patterns, and aggregates. *Phys. Rev. Lett.* **117**, 248001 (2016).

[ADS](#) [PubMed](#) [Google Scholar](#)

59. 141.

Gupta, R. K., Kant, R., Soni, H., Sood, A. K. & Ramaswamy, S. Active nonreciprocal attraction between motile particles in an elastic medium. Preprint at <https://arxiv.org/abs/2007.04860> (2020).

60. 142.

Maitra, A., Lenz, M. & Voituriez, R. Chiral active hexatics: giant number fluctuations, waves and destruction of order. *Phys. Rev. Lett.* **125**, 238005 (2020).

[ADS](#) [CAS](#) [PubMed](#) [Google Scholar](#)

61. 143.

Durve, M., Saha, A. & Sayeed, A. Active particle condensation by non-reciprocal and time-delayed interactions. *Eur. Phys. J. E* **41**, 49 (2018).

[PubMed](#) [Google Scholar](#)

62. 144.

Costanzo, A. Milling-induction and milling-destruction in a Vicsek-like binary-mixture model. *Europhys. Lett.* **125**, 20008 (2019).

[ADS](#) [Google Scholar](#)

63. 145.

Lin, Z. et al. Unidirectional invisibility induced by PT-symmetric periodic structures. *Phys. Rev. Lett.* **106**, 213901 (2011).

[ADS](#) [PubMed](#) [Google Scholar](#)

64. 146.

Coulais, C., Sounas, D. & Alù, A. Static non-reciprocity in mechanical metamaterials. *Nature* **542**, 461 (2017).

[ADS](#) [CAS](#) [PubMed](#) [Google Scholar](#)

65. 147.

Ghatak, A., Brandenbourger, M., van Wezel, J. & Coulais, C. Observation of non-Hermitian topology and its bulk–edge correspondence in an active mechanical metamaterial. *Proc. Natl Acad. Sci. USA* **117**, 29561 (2020).

[ADS](#) [CAS](#) [PubMed](#) [Google Scholar](#)

66. 148.

Rosa, M. I. N. & Ruzzene, M. Dynamics and topology of non-Hermitian elastic lattices with non-local feedback control interactions. *New J. Phys.* **22**, 053004 (2020).

[ADS](#) [MathSciNet](#) [Google Scholar](#)

67. 149.

Chen, Y., Li, X., Scheibner, C., Vitelli, V. & Huang, G. Self-sensing metamaterials with odd micropolarity. Preprint at <https://arxiv.org/abs/2009.07329> (2020).

68. 150.

Das, J., Rao, M. & Ramaswamy, S. Nonequilibrium steady states of the isotropic classical magnet. Preprint at <https://arxiv.org/abs/cond-mat/0404071> (2004).

69. 151.

Tasaki, H. Hohenberg–Mermin–Wagner-type theorems for equilibrium models of flocking. *Phys. Rev. Lett.* **125**, 220601 (2020).

[ADS](#) [MathSciNet](#) [CAS](#) [PubMed](#) [Google Scholar](#)

70. 152.

Fodor, É. et al. How far from equilibrium is active matter? *Phys. Rev. Lett.* **117**, 038103 (2016).

[ADS](#) [MathSciNet](#) [PubMed](#) [Google Scholar](#)

71. 153.

Loos, S. A. M. & Klapp, S. H. L. Thermodynamic implications of non-reciprocity. Preprint at <https://arxiv.org/abs/2008.00894> (2020).

72. 154.

Loos, S. A. M., Hermann, S. M. & Klapp, S. H. L. Non-reciprocal hidden degrees of freedom: a unifying perspective on memory, feedback, and activity. Preprint at <https://arxiv.org/abs/1910.08372> (2019).

73. 155.

Malzard, S., Poli, C. & Schomerus, H. Topologically protected defect states in open photonic systems with non-Hermitian charge conjugation and parity–time symmetry. *Phys. Rev. Lett.* **115**, 200402 (2015).

[ADS](#) [PubMed](#) [Google Scholar](#)

74. 156.

Lee, C. H. & Thomale, R. Anatomy of skin modes and topology in non-Hermitian systems. *Phys. Rev. B* **99**, 201103 (2019).

[ADS](#) [CAS](#) [Google Scholar](#)

75. 157.

Lee, C. H., Li, L., Thomale, R. & Gong, J. Unraveling non-Hermitian pumping: emergent spectral singularities and anomalous responses. *Phys. Rev. B* **102**, 085151 (2020).

[ADS](#) [CAS](#) [Google Scholar](#)

76. 158.

Okuma, N., Kawabata, K., Shiozaki, K. & Sato, M. Topological origin of non-Hermitian skin effects. *Phys. Rev. Lett.* **124**, 086801 (2020).

[ADS](#) [MathSciNet](#) [CAS](#) [PubMed](#) [Google Scholar](#)

77. 159.

Hofmann, T., Helbig, T., Lee, C. H., Greiter, M. & Thomale, R. Chiral voltage propagation and calibration in a topoelectrical Chern circuit. *Phys. Rev. Lett.* **122**, 247702 (2019).

[ADS](#) [CAS](#) [PubMed](#) [Google Scholar](#)

78. 160.

Lee, C. H., Li, L. & Gong, J. Hybrid higher-order skin-topological modes in nonreciprocal systems. *Phys. Rev. Lett.* **123**, 016805 (2019).

[ADS](#) [CAS](#) [PubMed](#) [Google Scholar](#)

79. 161.

Zhang, K., Yang, Z. & Fang, C. Correspondence between winding numbers and skin modes in non-Hermitian systems. *Phys. Rev. Lett.* **125**, 126402 (2020).

[ADS](#) [MathSciNet](#) [CAS](#) [PubMed](#) [Google Scholar](#)

80. 162.

Achenbach, J. D. *Reciprocity in Elastodynamics* (Cambridge Univ. Press, 2004).

81. 163.

1. Nassar, H. et al. Nonreciprocity in acoustic and elastic materials. *Nat. Rev. Mater.* (2020).

2. 164.

Potton, R. J. Reciprocity in optics. *Rep. Prog. Phys.* **67**, 717 (2004).

[ADS](#) [Google Scholar](#)

3. 165.

Estep, N. A., Sounas, D. L., Soric, J. & Alù, A. Magnetic-free non-reciprocity and isolation based on parametrically modulated coupled-resonator loops. *Nat. Phys.* **10**, 923 (2014).

[CAS](#) [Google Scholar](#)

4. 166.

Caloz, C. et al. Electromagnetic nonreciprocity. *Phys. Rev. Appl.* **10**, 047001 (2018).

[ADS](#) [CAS](#) [Google Scholar](#)

5. 167.

Masoud, H. & Stone, H. A. The reciprocal theorem in fluid dynamics and transport phenomena. *J. Fluid Mech.* **879**, P1 (2019).

[ADS](#) [MathSciNet](#) [MATH](#) [Google Scholar](#)

6. 168.

Scheibner, C., Irvine, W. T. M. & Vitelli, V. Non-Hermitian band topology and skin modes in active elastic media. *Phys. Rev. Lett.* **125**, 118001 (2020).

[ADS](#) [MathSciNet](#) [CAS](#) [PubMed](#) [Google Scholar](#)

7. 169.

Zhou, D. & Zhang, J. Non-Hermitian topological metamaterials with odd elasticity. *Phys. Rev. Res.* **2**, 023173 (2020).

[CAS](#) [Google Scholar](#)

8. 170.

Groot, S. R. D. & Mazur, P. *Non-Equilibrium Thermodynamics* (Dover Publications, 1962).

9. 171.

Maltman, K. & Laidlaw, W. G. Onsager symmetry and the diagonalizability of the hydrodynamic matrix. *J. Math. Phys.* **16**, 1561 (1975).

[ADS](#) [MathSciNet](#) [Google Scholar](#)

10. 172.

Avron, J. E. Odd viscosity. *J. Stat. Phys.* **92**, 543–557 (1998).

[MathSciNet](#) [MATH](#) [Google Scholar](#)

11. 173.

Banerjee, D., Souslov, A., Abanov, A. G. & Vitelli, V. Odd viscosity in chiral active fluids. *Nat. Commun.* **8**, 1573 (2017).

[ADS](#) [PubMed](#) [PubMed Central](#) [Google Scholar](#)

12. 174.

Souslov, A., Dasbiswas, K., Fruchart, M., Vaikuntanathan, S. & Vitelli, V. Topological waves in fluids with odd viscosity. *Phys. Rev. Lett.* **122**, 128001 (2019).

13. 175.

Soni, V. et al. The odd free surface flows of a colloidal chiral fluid. *Nat. Phys.* **15**, 1188–1194 (2019).

[CAS](#) [Google Scholar](#)

14. 176.

Han, M. et al. Statistical mechanics of a chiral active fluid. Preprint at <https://arxiv.org/abs/2002.07679> (2020).

15. 177.

Arnold, V. I. *Geometrical Methods in the Theory of Ordinary Differential Equations* (Springer, 1988).

16. 178.

Bogdanov, R. I. Bifurcations of a limit cycle for a family of vector fields on the plane. *Selecta Math. Sov.* **1**, 373 (1981); translated from *Trudy Sem. Petrovsk.* **2**, 23–35 (1976).

17. 179.

Bogdanov, R. I. Versal deformations of a singularity of a vector field on the plane in the case of zero eigenvalues. *Selecta Math. Sov.* **1**, 389 (1981); translated from *Trudy Sem. Petrovsk.* **2**, 37–65 (1976).

18. 180.

Takens, F. in *Global Analysis of Dynamical Systems* (eds Broer, H. W. et al.) 1–63 (IOP, 2001); reprinted from *Commun. Math. Inst. Rijksuniv. Utrecht* **2**, 1–111 (1974).

19. 181.

Nambu, Y. Quasi-particles and gauge invariance in the theory of superconductivity. *Phys. Rev.* **117**, 648 (1960).

[ADS](#) [MathSciNet](#) [Google Scholar](#)

20. 182.

Goldstone, J. Field theories with superconductor solutions. *Nuovo Cim.* **19**, 154–164 (1961).

[ADS](#) [MathSciNet](#) [MATH](#) [Google Scholar](#)

21. 183.

Goldstone, J., Salam, A. & Weinberg, S. Broken symmetries. *Phys. Rev.* **127**, 965 (1962).

[ADS](#) [MathSciNet](#) [MATH](#) [Google Scholar](#)

22. 184.

Hidaka, Y. Counting rule for Nambu–Goldstone modes in nonrelativistic Systems. *Phys. Rev. Lett.* **110**, 091601 (2013).

[ADS](#) [PubMed](#) [Google Scholar](#)

23. 185.

Watanabe, H. Counting rules of Nambu–Goldstone modes. *Annu. Rev. Condens. Matter Phys.* **11**, 169 (2020).

[CAS](#) [Google Scholar](#)

24. 186.

Watanabe, H. & Murayama, H. Unified description of Nambu–Goldstone bosons without Lorentz invariance. *Phys. Rev. Lett.* **108**, 251602 (2012).

[ADS](#) [PubMed](#) [Google Scholar](#)

25. 187.

Nielsen, H. & Chadha, S. On how to count Goldstone bosons. *Nucl. Phys. B* **105**, 445 (1976).

[ADS](#) [Google Scholar](#)

26. 188.

Leroy, L. On spontaneous symmetry breakdown in dynamical systems. *J. Phys. Math. Gen.* **25**, L987 (1992).

[ADS](#) [MATH](#) [Google Scholar](#)

27. 189.

Minami, Y. & Hidaka, Y. Spontaneous symmetry breaking and Nambu–Goldstone modes in dissipative systems. *Phys. Rev. E* **97**, 012130 (2018).

[ADS](#) [Google Scholar](#)

28. 190.

Hongo, M., Kim, S., Noumi, T. & Ota, A. Effective Lagrangian for Nambu–Goldstone modes in nonequilibrium open systems. Preprint at <https://arxiv.org/abs/1907.08609> (2019).

29. 191.

Von Neumann, J. & Wigner, E. P. Über das Verhalten von Eigenwerten bei adiabatischen Prozessen *Physik. Zeit.* **30**, 467 (1929); translated in *Symmetry in the Solid State* (eds Knox, R. S. & Gold, A.) (Benjamin, New York, 1964).

30. 192.

Arnold, V. I. Modes and quasimodes. *Funct. Anal. Appl.* **6**, 94 (1972); translated from *Funktional. Anal. i Prilozhen.* **6**, 12–20 (1972).

31. 193.

Arnold, V. I. Remarks on eigenvalues and eigenvectors of Hermitian matrices, Berry phase, adiabatic connections and quantum Hall effect. *Selecta Mathematica* **1**, 1–19 (1995).

[ADS](#) [MathSciNet](#) [MATH](#) [Google Scholar](#)

32. 194.

Seyranian, A. P., Kirillov, O. N. & Mailybaev, A. A. Coupling of eigenvalues of complex matrices at diabolic and exceptional points. *J. Phys. Math. Gen.* **38**, 1723 (2005).

[ADS](#) [MathSciNet](#) [MATH](#) [Google Scholar](#)

33. 195.

Julien, K. A. Strong spatial interactions with 1:1 resonance: a three-layer convection problem. *Nonlinearity* **7**, 1655 (1994).

[ADS](#) [MathSciNet](#) [MATH](#) [Google Scholar](#)

34. 196.

Renardy, Y. Y., Renardy, M. & Fujimura, K. Takens–Bogdanov bifurcation on the hexagonal lattice for double-layer convection. *Physica D* **129**, 171 (1999).

[ADS](#) [MathSciNet](#) [MATH](#) [Google Scholar](#)

35. 197.

Guckenheimer, J. A codimension two bifurcation with circular symmetry. In *Multiparameter Bifurcation Theory* (eds Golubitsky, M. & Guckenheimer, J. M.) 175–184 (AMS, 1986).

36. 198.

Dangelmayr, G. & Knobloch, E. The Takens–Bogdanov bifurcation with $O(2)$ symmetry. *Phil. Trans. R. Soc. Lond. A* **322**, 243–279 (1987).

[ADS](#) [MathSciNet](#) [MATH](#) [Google Scholar](#)

37. 199.

Krupa, M. Bifurcations of relative equilibria. *SIAM J. Math. Anal.* **21**, 1453 (1990).

[MathSciNet](#) [MATH](#) [Google Scholar](#)

38. 200.

Field, M. J. Equivariant dynamical systems. *Trans. Am. Math. Soc.* **259**, 185 (1980).

[MathSciNet](#) [MATH](#) [Google Scholar](#)

39. 201.

Toner, J. & Tu, Y. Flocks, herds, and schools: a quantitative theory of flocking. *Phys. Rev. E* **58**, 4828 (1998).

[ADS](#) [MathSciNet](#) [CAS](#) [Google Scholar](#)

40. 202.

Geyer, D., Morin, A. & Bartolo, D. Sounds and hydrodynamics of polar active fluids. *Nat. Mater.* **17**, 789 (2018).

[ADS](#) [CAS](#) [PubMed](#) [Google Scholar](#)

41. 203.

Bain, N. & Bartolo, D. Dynamic response and hydrodynamics of polarized crowds. *Science* **363**, 46 (2019).

[ADS](#) [MathSciNet](#) [CAS](#) [PubMed](#) [MATH](#) [Google Scholar](#)

42. 204.

Dean, D. S. Langevin equation for the density of a system of interacting Langevin processes. *J. Phys. Math. Gen.* **29**, L613 (1996).

[ADS](#) [MathSciNet](#) [CAS](#) [Google Scholar](#)

43. 205.

Bertin, E., Droz, M. & Grégoire, G. Boltzmann and hydrodynamic description for self-propelled particles. *Phys. Rev. E* **74**, 022101 (2006).

[ADS](#) [Google Scholar](#)

44. 206.

Bertin, E., Droz, M. & Grégoire, G. Hydrodynamic equations for self-propelled particles: microscopic derivation and stability analysis. *J. Phys. A Math. Theor.* **42**, 445001 (2009).

[MATH](#) [Google Scholar](#)

45. 207.

Farrell, F. D. C., Marchetti, M. C., Marenduzzo, D. & Tailleur, J. Pattern formation in self-propelled particles with density-dependent motility. *Phys. Rev. Lett.* **108**, 248101 (2012).

[ADS](#) [CAS](#) [PubMed](#) [Google Scholar](#)

46. 208.

Chaté, H. & Mahault, B. Dry, aligning, dilute, active matter: a synthetic and self-contained overview. Preprint at <https://arxiv.org/abs/1906.05542> (2019).

47. 209.

Peshkov, A., Bertin, E., Ginelli, F. & Chaté, H. Boltzmann–Ginzburg–Landau approach for continuous descriptions of generic Vicsek-like models. *Eur. Phys. J. Spec. Top.* **223**, 1315 (2014).

[Google Scholar](#)

48. 210.

Ihle, T. Kinetic theory of flocking: derivation of hydrodynamic equations. *Phys. Rev. E* **83**, 030901 (2011).

[ADS](#) [Google Scholar](#)

49. 211.

Mahault, B., Ginelli, F. & Chaté, H. Quantitative assessment of the Toner and Tu theory of polar flocks. *Phys. Rev. Lett.* **123**, 218001 (2019).

[ADS](#) [CAS](#) [PubMed](#) [Google Scholar](#)

50. 212.

Oza, A. U. & Dunkel, J. Antipolar ordering of topological defects in active liquid crystals. *New J. Phys.* **18**, 093006 (2016).

[ADS](#) [Google Scholar](#)

51. 213.

Suzuki, R., Weber, C. A., Frey, E. & Bausch, A. R. Polar pattern formation in driven filament systems requires non-binary particle collisions. *Nat. Phys.* **11**, 839 (2015).

[CAS](#) [PubMed](#) [PubMed Central](#) [Google Scholar](#)

52. 214.

Nishiguchi, D., Nagai, K. H., Chaté, H. & Sano, M. Long-range nematic order and anomalous fluctuations in suspensions of swimming filamentous bacteria. *Phys. Rev. E* **95**, 020601 (2017).

[ADS](#) [PubMed](#) [Google Scholar](#)

53. 215.

Tsai, J.-C., Ye, F., Rodriguez, J., Gollub, J. P. & Lubensky, T. C. A chiral granular gas. *Phys. Rev. Lett.* **94**, 214301 (2005).

[ADS](#) [PubMed](#) [Google Scholar](#)

54. 216.

Liebchen, B. & Levis, D. Collective behavior of chiral active matter: pattern formation and enhanced flocking. *Phys. Rev. Lett.* **119**, 058002 (2017).

[ADS](#) [PubMed](#) [Google Scholar](#)

55. 217.

O’Keeffe, K. P., Hong, H. & Strogatz, S. H. Oscillators that sync and swarm. *Nat. Commun.* **8**, 1504 (2017).

[ADS](#) [PubMed](#) [PubMed Central](#) [Google Scholar](#)

56. 218.

Levis, D., Pagonabarraga, I. & Liebchen, B. Activity induced synchronization: mutual flocking and chiral self-sorting. *Phys. Rev. Res.* **1**, 023026 (2019).

[CAS](#) [Google Scholar](#)

57. 219.

Burns, K. J., Vasil, G. M., Oishi, J. S., Lecoanet, D. & Brown, B. P. Dedalus: a flexible framework for numerical simulations with spectral methods. *Phys. Rev. Res.* **2**, 023068 (2020).

[CAS](#) [Google Scholar](#)

58. 220.

Caussin, J.-B. et al. Emergent spatial structures in flocking models: a dynamical system insight. *Phys. Rev. Lett.* **112**, 148102 (2014).

[ADS](#) [PubMed](#) [Google Scholar](#)

59. 221.

Mishra, S., Baskaran, A. & Marchetti, M. C. Fluctuations and pattern formation in self-propelled particles. *Phys. Rev. E* **81**, 061916 (2010).

[ADS](#) [Google Scholar](#)

60. 222.

Grégoire, G. & Chaté, H. Onset of collective and cohesive motion. *Phys. Rev. Lett.* **92**, 025702 (2004).

[ADS](#) [PubMed](#) [Google Scholar](#)

61. 223.

Aditi Simha, R. & Ramaswamy, S. Hydrodynamic fluctuations and instabilities in ordered suspensions of self-propelled particles. *Phys. Rev. Lett.* **89**, 058101 (2002).

[ADS](#) [CAS](#) [PubMed](#) [MATH](#) [Google Scholar](#)

62. 224.

Kuramoto, Y. *Chemical Oscillations, Waves, and Turbulence* (Springer, 1984).

63. 225.

Daido, H. Population dynamics of randomly interacting self-oscillators. I: Tractable models without frustration. *Prog. Theor. Phys.* **77**, 622 (1987).

[ADS](#) [MathSciNet](#) [Google Scholar](#)

64. 226.

Omata, S., Yamaguchi, Y. & Shimizu, H. Entrainment among coupled limit cycle oscillators with frustration. *Physica D* **31**, 397 (1988).

[ADS](#) [MathSciNet](#) [MATH](#) [Google Scholar](#)

65. 227.

Martens, E. A. et al. Exact results for the Kuramoto model with a bimodal frequency distribution. *Phys. Rev. E* **79**, 026204 (2009).

[ADS](#) [MathSciNet](#) [CAS](#) [Google Scholar](#)

66. 228.

Bonilla, L., Vicente, C. P. & Spigler, R. Time-periodic phases in populations of nonlinearly coupled oscillators with bimodal frequency distributions. *Physica D* **113**, 79 (1998).

[ADS](#) [MathSciNet](#) [MATH](#) [Google Scholar](#)

67. 229.

Hong, H. & Strogatz, S. H. Mean-field behavior in coupled oscillators with attractive and repulsive interactions. *Phys. Rev. E* **85**, 056210 (2012).

[ADS](#) [Google Scholar](#)

68. 230.

Ott, E. & Antonsen, T. M. Low dimensional behavior of large systems of globally coupled oscillators. *Chaos* **18**, 037113 (2008).

[ADS](#) [MathSciNet](#) [PubMed](#) [MATH](#) [Google Scholar](#)

69. 231.

Abrams, D. M., Mirollo, R., Strogatz, S. H. & Wiley, D. A. Solvable model for chimera states of coupled oscillators. *Phys. Rev. Lett.* **101**, 084103 (2008).

[ADS](#) [PubMed](#) [Google Scholar](#)

70. 232.

Pikovsky, A. & Rosenblum, M. Partially integrable dynamics of hierarchical populations of coupled oscillators. *Phys. Rev. Lett.* **101**, 264103 (2008).

[ADS](#) [PubMed](#) [Google Scholar](#)

71. 233.

Martens, E. A., Bick, C. & Panaggio, M. J. Chimera states in two populations with heterogeneous phase-lag. *Chaos* **26**, 094819 (2016).

[ADS](#) [MathSciNet](#) [PubMed](#) [MATH](#) [Google Scholar](#)

72. 234.

Choe, C.-U., Ri, J.-S. & Kim, R.-S. Incoherent chimera and glassy states in coupled oscillators with frustrated interactions. *Phys. Rev. E* **94**, 032205 (2016).

[ADS](#) [PubMed](#) [Google Scholar](#)

73. 235.

Gallego, R., Montbrió, E. & Pazó, D. Synchronization scenarios in the Winfree model of coupled oscillators. *Phys. Rev. E* **96**, 042208 (2017).

[ADS](#) [PubMed](#) [Google Scholar](#)

74. 236.

Ott, E. & Antonsen, T. M. Long time evolution of phase oscillator systems. *Chaos* **19**, 023117 (2009).

[ADS](#) [MathSciNet](#) [PubMed](#) [MATH](#) [Google Scholar](#)

75. 237.

Watanabe, S. & Strogatz, S. H. Integrability of a globally coupled oscillator array. *Phys. Rev. Lett.* **70**, 2391 (1993).

[ADS](#) [MathSciNet](#) [CAS](#) [PubMed](#) [MATH](#) [Google Scholar](#)

76. 238.

Watanabe, S. & Strogatz, S. H. Constants of motion for superconducting Josephson arrays. *Physica D* **74**, 197 (1994).

[ADS](#) [MATH](#) [Google Scholar](#)

77. 239.

Marvel, S. A., Mirollo, R. E. & Strogatz, S. H. Identical phase oscillators with global sinusoidal coupling evolve by Möbius group action. *Chaos* **19**, 043104 (2009).

[ADS](#) [MathSciNet](#) [PubMed](#) [MATH](#) [Google Scholar](#)

78. 240.

Pikovsky, A. & Rosenblum, M. Dynamics of heterogeneous oscillator ensembles in terms of collective variables. *Physica D* **240**, 872 (2011).

[ADS](#) [MathSciNet](#) [CAS](#) [MATH](#) [Google Scholar](#)

79. 241.

Tyulkina, I. V., Goldobin, D. S., Klimenko, L. S. & Pikovsky, A. Dynamics of noisy oscillator populations beyond the Ott–Antonsen ansatz. *Phys. Rev. Lett.* **120**, 264101 (2018).

[ADS](#) [CAS](#) [PubMed](#) [Google Scholar](#)

80. 242.

Montbrió, E., Pazó, D. & Roxin, A. Macroscopic description for networks of spiking neurons. *Phys. Rev. X* **5**, 021028 (2015).

1. [Google Scholar](#)

2. 243.

Bick, C., Goodfellow, M., Laing, C. R. & Martens, E. A. Understanding the dynamics of biological and neural oscillator networks through exact mean-field reductions: a review. *J. Math. Neurosci.* **10**, 9 (2020).

[MathSciNet](#) [PubMed](#) [PubMed Central](#) [MATH](#) [Google Scholar](#)

3. 244.

Pazó, D. & Montbrió, E. Existence of hysteresis in the Kuramoto model with bimodal frequency distributions. *Phys. Rev. E* **80**, 046215 (2009).

[ADS](#) [Google Scholar](#)

4. 245.

Pietras, B., Deschle, N. & Daffertshofer, A. First-order phase transitions in the Kuramoto model with compact bimodal frequency distributions. *Phys. Rev. E* **98**, 062219 (2018).

[ADS](#) [MathSciNet](#) [Google Scholar](#)

5. 246.

Doppler, J. et al. Dynamically encircling an exceptional point for asymmetric mode switching. *Nature* **537**, 76 (2016).

[ADS](#) [CAS](#) [PubMed](#) [Google Scholar](#)

6. 247.

Dembowski, C. et al. Encircling an exceptional point. *Phys. Rev. E* **69**, 056216 (2004).

[ADS](#) [CAS](#) [Google Scholar](#)

7. 248.

Milburn, T. J. et al. General description of quasiadiabatic dynamical phenomena near exceptional points. *Phys. Rev. A* **92**, 052124 (2015).

[ADS](#) [Google Scholar](#)

8. 249.

Maillybaev, A. A., Kirillov, O. N. & Seyranian, A. P. Geometric phase around exceptional points. *Phys. Rev. A* **72**, 014104 (2005).

[ADS](#) [Google Scholar](#)

9. 250.

Galda A. & Vinokur, V. M. Parity–time symmetry breaking in magnetic systems. *Phys. Rev. B* **94**, 020408(R) (2016); erratum **100**, 209902 (2019).

[ADS](#) [Google Scholar](#)

10. 251.

Galda, A. & Vinokur, V. M. Exceptional points in classical spin dynamics. *Sci. Rep.* **9**, 17484 (2019).

[ADS](#) [PubMed](#) [PubMed Central](#) [Google Scholar](#)

11. 252.

Kepesidis, K. V. et al. PT-symmetry breaking in the steady state of microscopic gain–loss systems. *New J. Phys.* **18**, 095003 (2016).

[ADS](#) [Google Scholar](#)

12. 253.

Graefe, E.-M., Korsch, H. J. & Niederle, A. E. Quantum–classical correspondence for a non-Hermitian Bose–Hubbard dimer. *Phys. Rev. A* **82**, 013629 (2010).

[ADS](#) [Google Scholar](#)

13. 254.

Cartarius, H., Main, J. & Wunner, G. Discovery of exceptional points in the Bose–Einstein condensation of gases with attractive $1/r$ interaction. *Phys. Rev. A* **77**, 013618 (2008).

[ADS](#) [Google Scholar](#)

14. 255.

Gutöhrlein, R., Main, J., Cartarius, H. & Wunner, G. Bifurcations and exceptional points in dipolar Bose–Einstein condensates. *J. Phys. A* **46**, 305001 (2013).

[MathSciNet](#) [MATH](#) [Google Scholar](#)

15. 256.

Hoyle, R. *Pattern Formation* (Cambridge Univ. Press, 2006).

16. 257.

Cross, M. & Greenside, H. *Pattern Formation and Dynamics in Nonequilibrium Systems* (Cambridge Univ. Press, 2009).

17. 258.

Meron, E. *Nonlinear Physics of Ecosystems* (CRC Press, 2015).

18. 259.

Swift, J. & Hohenberg, P. C. Hydrodynamic fluctuations at the convective instability. *Phys. Rev. A* **15**, 319 (1977).

[ADS](#) [Google Scholar](#)

19. 260.

Coullet, P. & Fauve, S. Propagative phase dynamics for systems with galilean invariance. *Phys. Rev. Lett.* **55**, 2857 (1985).

[ADS](#) [CAS](#) [PubMed](#) [Google Scholar](#)

20. 261.

Brachet, M. E., Coullet, P. & Fauve, S. Propagative phase dynamics in temporally intermittent systems. *Europhys. Lett.* **4**, 1017 (1987).

[ADS](#) [CAS](#) [Google Scholar](#)

21. 262.

Douady, S., Fauve, S. & Thual, O. Oscillatory phase modulation of parametrically forced surface waves. *Europhys. Lett.* **10**, 309 (1989).

[ADS](#) [Google Scholar](#)

22. 263.

Coullet, P. & Iooss, G. Instabilities of one-dimensional cellular patterns. *Phys. Rev. Lett.* **64**, 866 (1990).

[ADS](#) [MathSciNet](#) [CAS](#) [PubMed](#) [MATH](#) [Google Scholar](#)

23. 264.

Fauve, S., Douady, S. & Thual, O. Drift instabilities of cellular patterns. *J. Phys. II* **1**, 311 (1991).

[Google Scholar](#)

24. 265.

Knobloch, E., Hettel, J. & Dangelmayr, G. Parity-breaking bifurcation in inhomogeneous systems. *Phys. Rev. Lett.* **74**, 4839 (1995).

[ADS](#) [CAS](#) [PubMed](#) [MATH](#) [Google Scholar](#)

25. 266.

Armbruster, D., Guckenheimer, J. & Holmes, P. Heteroclinic cycles and modulated travelling waves in systems with O(2) symmetry. *Physica D* **29**, 257 (1988).

[ADS](#) [MathSciNet](#) [MATH](#) [Google Scholar](#)

26. 267.

Proctor, M. R. E. & Jones, C. A. The interaction of two spatially resonant patterns in thermal convection. Part 1. Exact 1:2 resonance. *J. Fluid Mech.* **188**, 301 (1988).

[ADS](#) [MathSciNet](#) [MATH](#) [Google Scholar](#)

27. 268.

Dangelmayr, G., Hettel, J. & Knobloch, E. Parity-breaking bifurcation in inhomogeneous systems. *Nonlinearity* **10**, 1093 (1997).

[ADS](#) [MathSciNet](#) [MATH](#) [Google Scholar](#)

28. 269.

Simon, A. J., Bechhoefer, J. & Libchaber, A. Solitary modes and the Eckhaus instability in directional solidification. *Phys. Rev. Lett.* **61**, 2574 (1988).

[ADS](#) [CAS](#) [PubMed](#) [Google Scholar](#)

29. 270.

Flesselles, J.-M., Simon, A. & Libchaber, A. Dynamics of one-dimensional interfaces: an experimentalist's view. *Adv. Phys.* **40**, 1 (1991).

[ADS](#) [CAS](#) [Google Scholar](#)

30. 271.

Melo, F. & Oswald, P. Destabilization of a faceted smectic-A–smectic-B interface. *Phys. Rev. Lett.* **64**, 1381 (1990).

[ADS](#) [CAS](#) [PubMed](#) [Google Scholar](#)

31. 272.

Faivre, G. & Mergy, J. Dynamical wavelength selection by tilt domains in thin-film lamellar eutectic growth. *Phys. Rev. A* **46**, 963 (1992).

[ADS](#) [CAS](#) [PubMed](#) [Google Scholar](#)

32. 273.

Kassner, K. & Misbah, C. Parity breaking in eutectic growth. *Phys. Rev. Lett.* **65**, 1458–1461 (1990).

[ADS](#) [CAS](#) [PubMed](#) [Google Scholar](#)

33. 274.

Ginibre, M., Akamatsu, S. & Faivre, G. Experimental determination of the stability diagram of a lamellar eutectic growth front. *Phys. Rev. E* **56**, 780–796 (1997).

[ADS](#) [CAS](#) [Google Scholar](#)

34. 275.

Cummins, H. Z., Fourtune, L. & Rabaud, M. Successive bifurcations in directional viscous fingering. *Phys. Rev. E* **47**, 1727–1738 (1993).

[ADS](#) [CAS](#) [Google Scholar](#)

35. 276.

Bellon, L., Fourtune, L., Minassian, V. T. & Rabaud, M. Wave-number selection and parity-breaking bifurcation in directional viscous fingering. *Phys. Rev. E* **58**, 565–574 (1998).

[ADS](#) [CAS](#) [Google Scholar](#)

36. 277.

Counillon, C. et al. Global drift of a circular array of liquid columns. *Europhys. Lett.* **40**, 37 (1997).

[ADS](#) [CAS](#) [Google Scholar](#)

37. 278.

Knobloch, E. & Proctor, M. R. E. Nonlinear periodic convection in double-diffusive systems. *J. Fluid Mech.* **108**, 291–316 (1981).

[ADS](#) [MathSciNet](#) [MATH](#) [Google Scholar](#)

38. 279.

Cross, M. C. & Kim, K. Linear instability and the codimension-2 region in binary fluid convection between rigid impermeable boundaries. *Phys. Rev. A* **37**, 3909–3920 (1988).

[ADS](#) [MathSciNet](#) [CAS](#) [Google Scholar](#)

39. 280.

Cross, M. C. Traveling and standing waves in binary-fluid convection in finite geometries. *Phys. Rev. Lett.* **57**, 2935–2938 (1986).

[ADS](#) [CAS](#) [PubMed](#) [Google Scholar](#)

40. 281.

Coullet, P. H. & Spiegel, E. A. Amplitude equations for systems with competing instabilities. *SIAM J. Appl. Math.* **43**, 776–821 (1983).

[MathSciNet](#) [MATH](#) [Google Scholar](#)

41. 282.

Cross, M. C. Structure of nonlinear traveling-wave states in finite geometries. *Phys. Rev. A* **38**, 3593–3600 (1988).

[ADS](#) [CAS](#) [Google Scholar](#)

42. 283.

Brand, H. R., Hohenberg, P. C. & Steinberg, V. Amplitude equation near a polycritical point for the convective instability of a binary fluid mixture in a porous medium. *Phys. Rev. A* **27**, 591–593 (1983).

[ADS](#) [CAS](#) [Google Scholar](#)

43. 284.

Brand, H. R., Hohenberg, P. C. & Steinberg, V. Codimension-2 bifurcations for convection in binary fluid mixtures. *Phys. Rev. A* **30**, 2548–2561 (1984).

[ADS](#) [CAS](#) [Google Scholar](#)

44. 285.

Guckenheimer, J. Multiple bifurcation problems of codimension two. *SIAM J. Math. Anal.* **15**, 1–49 (1984).

[ADS](#) [MathSciNet](#) [MATH](#) [Google Scholar](#)

45. 286.

Moses, E. & Steinberg, V. Flow patterns and nonlinear behavior of traveling waves in a convective binary fluid. *Phys. Rev. A* **34**, 693–696 (1986); erratum **35**, 1444–1445 (1987).

[ADS](#) [CAS](#) [Google Scholar](#)

46. 287.

Walden, R. W., Kolodner, P., Passner, A. & Surko, C. M. Traveling waves and chaos in convection in binary fluid mixtures. *Phys. Rev. Lett.* **55**, 496–499 (1985).

[ADS](#) [CAS](#) [PubMed](#) [Google Scholar](#)

47. 288.

Coullet, P., Fauve, S. & Tirapegui, E. Large scale instability of nonlinear standing waves. *J. Physique Lett.* **46**, 787–791 (1985).

[Google Scholar](#)

48. 289.

Bensimon, D., Pumir, A. & Shraiman, B. Nonlinear theory of traveling wave convection in binary mixtures. *J. Phys. France* **50**, 3089–3108 (1989).

[Google Scholar](#)

49. 290.

Knobloch, E. & Moore, D. R. Minimal model of binary fluid convection. *Phys. Rev. A* **42**, 4693–4709 (1990).

[ADS](#) [CAS](#) [PubMed](#) [Google Scholar](#)

50. 291.

Schöpf, W. & Zimmermann, W. Convection in binary fluids: amplitude equations, codimension-2 bifurcation, and thermal fluctuations. *Phys. Rev. E* **47**, 1739–1764 (1993).

[ADS](#) [MathSciNet](#) [Google Scholar](#)

51. 292.

Bressloff, P. C., Cowan, J. D., Golubitsky, M., Thomas, P. J. & Wiener, M. C. Geometric visual hallucinations, Euclidean symmetry and the functional architecture of striate cortex. *Phil. Trans. R. Soc. Lond. B* **356**, 299–330 (2001).

[CAS](#) [Google Scholar](#)

52. 293.

Bressloff, P. C., Cowan, J. D., Golubitsky, M., Thomas, P. J. & Wiener, M. C. What geometric visual hallucinations tell us about the visual cortex. *Neural Comput.* **14**, 473–491 (2002).

[PubMed](#) [MATH](#) [Google Scholar](#)

53. 294.

Cho, M. W. & Kim, S. Understanding visual map formation through vortex dynamics of spin Hamiltonian models. *Phys. Rev. Lett.* **92**, 018101 (2004).

[ADS](#) [PubMed](#) [Google Scholar](#)

54. 295.

Schnabel, M., Kaschube, M. & Wolf, F. Pinwheel stability, pattern selection and the geometry of visual space. Preprint at <https://arxiv.org/abs/0801.3832> (2008).

55. 296.

Butler, T. C. et al. Evolutionary constraints on visual cortex architecture from the dynamics of hallucinations. *Proc. Natl Acad. Sci. USA* **109**, 606–609 (2012).

[ADS](#) [CAS](#) [PubMed](#) [Google Scholar](#)

56. 297.

Curtu, R. & Ermentrout, B. Pattern formation in a network of excitatory and inhibitory cells with adaptation. *SIAM J. Appl. Dyn. Syst.* **3**, 191–231 (2004).

[ADS](#) [MathSciNet](#) [MATH](#) [Google Scholar](#)

57. 298.

Adini, Y., Sagi, D. & Tsodyks, M. Excitatory–inhibitory network in the visual cortex: psychophysical evidence. *Proc. Natl Acad. Sci. USA* **94**, 10426–10431 (1997).

[ADS](#) [CAS](#) [PubMed](#) [Google Scholar](#)

58. 299.

Hensch, T. K. & Fagiolini, M. in *Progress in Brain Research* (eds van Pelt, J. et al.) 115–124 (Elsevier, 2005).

59. 300.

Chossat, P. & Iooss, G. *The Couette–Taylor Problem* (Springer, 1994).

60. 301.

Riecke, H. & Paap, H.-G. Parity-breaking and Hopf bifurcations in axisymmetric Taylor vortex flow. *Phys. Rev. A* **45**, 8605–8610 (1992).

[ADS](#) [CAS](#) [PubMed](#) [Google Scholar](#)

61. 302.

Tennakoon, S. G. K., Andereck, C. D., Hegseth, J. J. & Riecke, H. Temporal modulation of traveling waves in the flow between rotating cylinders with broken azimuthal symmetry. *Phys. Rev. E* **54**, 5053–5065 (1996).

[ADS](#) [CAS](#) [Google Scholar](#)

62. 303.

Mutabazi, I. & Andereck, C. D. Mode resonance and wavelength-halving instability in the Taylor–Dean system. *Phys. Rev. E* **51**, 4380–4390 (1995).

[ADS](#) [CAS](#) [Google Scholar](#)

63. 304.

Bot, P., Cadot, O. & Mutabazi, I. Secondary instability mode of a roll pattern and transition to spatiotemporal chaos in the Taylor–Dean system. *Phys. Rev. E* **58**, 3089–3097 (1998).

[ADS](#) [CAS](#) [Google Scholar](#)

64. 305.

Wiener, R. J. & McAlister, D. F. Parity breaking and solitary waves in axisymmetric Taylor vortex flow. *Phys. Rev. Lett.* **69**, 2915–2918 (1992).

[ADS](#) [CAS](#) [PubMed](#) [Google Scholar](#)

65. 306.

Andereck, C. D., Liu, S. S. & Swinney, H. L. Flow regimes in a circular Couette system with independently rotating cylinders. *J. Fluid Mech.* **164**, 155–183 (1986).

[ADS](#) [Google Scholar](#)

66. 307.

Altmeyer, S. & Hoffmann, C. Secondary bifurcation of mixed-cross-spirals connecting travelling wave solutions. *New J. Phys.* **12**, 113035 (2010).

[ADS](#) [Google Scholar](#)

67. 308.

Pinter, A., Lücke, M. & Hoffmann, C. Competition between traveling fluid waves of left and right spiral vortices and their different amplitude combinations. *Phys. Rev. Lett.* **96**, 044506 (2006).

[ADS](#) [CAS](#) [PubMed](#) [Google Scholar](#)

68. 309.

Hong, H. Periodic synchronization and chimera in conformist and contrarian oscillators. *Phys. Rev. E* **89**, 062924 (2014).

[ADS](#) [Google Scholar](#)

69. 310.

Kemeth, F. P., Haugland, S. W., Schmidt, L., Kevrekidis, I. G. & Krischer, K. A classification scheme for chimera states. *Chaos* **26**, 094815 (2016).

[ADS](#) [PubMed](#) [Google Scholar](#)

70. 311.

Golubitsky, M. & Stewart, I. Hopf bifurcation in the presence of symmetry. *Arch. Ration. Mech. Anal.* **87**, 107–165 (1985).

[MathSciNet](#) [MATH](#) [Google Scholar](#)

71. 312.

Shapere, A. & Wilczek, F. Classical time crystals. *Phys. Rev. Lett.* **109**, 160402 (2012).

[ADS](#) [PubMed](#) [Google Scholar](#)

72. 313.

Wilczek, F. Quantum time crystals. *Phys. Rev. Lett.* **109**, 160401 (2012).

[ADS](#) [PubMed](#) [Google Scholar](#)

73. 314.

Yao, N. Y. & Nayak, C. Time crystals in periodically driven systems. *Phys. Today* **71**, 40 (2018).

[Google Scholar](#)

74. 315.

Prigogine, I. & Lefever, R. Symmetry-breaking instabilities in dissipative systems. *II. J. Chem. Phys.* **48**, 1695–1700 (1968).

[ADS](#) [Google Scholar](#)

75. 316.

Giergiel, K., Miroszewski, A. & Sacha, K. Time crystal platform: from quasicrystal structures in time to systems with exotic interactions. *Phys. Rev. Lett.* **120**, 140401 (2018).

[ADS](#) [MathSciNet](#) [CAS](#) [PubMed](#) [Google Scholar](#)

76. 317.

Autti, S., Eltsov, V. & Volovik, G. Observation of a time quasicrystal and its transition to a superfluid time crystal. *Phys. Rev. Lett.* **120**, 215301 (2018).

[ADS](#) [CAS](#) [PubMed](#) [Google Scholar](#)

[Download references](#)

Acknowledgements

We thank A. Alù, D. Bartolo, D. Christodoulides, A. Clerk, A. Edelman, A. Galda, M. Han, K. Husain, T. Kottos, Z. Lu, M. C. Marchetti, M.-A. Miri, B. Roussel, C. Scheibner, D. Schuster, J. Simon and B. van Zuiden. M.F. acknowledges support from a MRSEC-funded Kadanoff–Rice fellowship (DMR-2011854) and the Simons Foundation. R.H. was supported by a Grand-in-Aid for JSPS fellows (grant number 17J01238). V.V. was supported by the Complex Dynamics and Systems Program of the Army Research Office under grant number W911NF-19-1-0268 and the Simons Foundation. This work was partially supported by the University of Chicago Materials Research Science and Engineering Center, which is funded by National Science Foundation under award number DMR-2011854. This work was completed in part with resources provided by the University of Chicago’s Research Computing Center. Some of us benefited from participation in the KITP programme on Symmetry, Thermodynamics and Topology in Active Matter supported by grant number NSF PHY-1748958.

Author information

Author notes

1. These authors contributed equally: Michel Fruchart, Ryo Hanai

Affiliations

1. James Franck Institute and Department of Physics, University of Chicago, Chicago, IL, USA

Michel Fruchart, Ryo Hanai, Peter B. Littlewood & Vincenzo Vitelli

2. Department of Physics, Osaka University, Toyonaka, Japan

Ryo Hanai

3. Pritzker School of Molecular Engineering, University of Chicago, Chicago, IL, USA

Ryo Hanai

4. Kadanoff Center for Theoretical Physics, University of Chicago, Chicago, IL, USA

Vincenzo Vitelli

Authors

1. Michel Fruchart

[View author publications](#)

You can also search for this author in [PubMed](#) [Google Scholar](#)

2. Ryo Hanai

[View author publications](#)

You can also search for this author in [PubMed](#) [Google Scholar](#)

3. Peter B. Littlewood

[View author publications](#)

You can also search for this author in [PubMed](#) [Google Scholar](#)

4. Vincenzo Vitelli

[View author publications](#)

You can also search for this author in [PubMed](#) [Google Scholar](#)

Contributions

M.F., R.H., P.B.L. and V.V. designed the research, performed the research, and wrote the paper.

Corresponding author

Correspondence to [Vincenzo Vitelli](#).

Ethics declarations

Competing interests

The authors declare no competing interests.

Additional information

Peer review information *Nature* thanks the anonymous reviewers for their contribution to the peer review of this work.

Publisher's note Springer Nature remains neutral with regard to jurisdictional claims in published maps and institutional affiliations.

Extended data figures and tables

Extended Data Fig. 1 Codimensions of eigenvalue degeneracies.

This graph gives the codimension (codim) of twofold degeneracies of eigenvalues in different matrix spaces; see ref. [194](#). These degeneracies can be exceptional points (EP) or diabolic points (DP, also known as Dirac points). An identical graph can be drawn by replacing ‘real symmetric’ with ‘purely imaginary symmetric’, ‘Hermitian’ with ‘anti-Hermitian’ and ‘real’ with ‘imaginary’.

Extended Data Fig. 2 Many-body suppression of noise-activated chirality inversions.

a, A change in the sign of the angle $\Delta\phi$ between the order parameters v_A and v_B (in blue and red) flips the chirality (clockwise or anticlockwise) of the chiral phase. Qualitatively, the two steady-state values $\pm\Delta\phi_c$ towards which the system relaxes correspond to the minima of an effective potential $U(\Delta\phi)$, with a barrier ΔU separating these minima. The lifetime of the chiral phase is the average time τ separating two flips of chirality (represented in green), namely the Kramers escape time required to jump from one minimum to the other under the effect of noise. **b**, The standard deviations quantifying the fluctuations of the order parameters v_a in the chiral phase decrease approximately as \sqrt{N} with the number of agents N . The grey lines are equally spaced \sqrt{N} curves and are meant as a guide to the eye (not a fit). The data are obtained from simulations of the Kuramoto model equation (2) with $J_{AA} = J_{BB} = 1$, $J_{AB} = 1$, $J_{BA} = -1.1$, $\eta = 8 \times 10^{-2}$ and all-to-all couplings. The total duration is $T_{\text{sim}}/\delta t = 4,000$ with $\delta t = 0.5$, over which the standard deviation is computed.

Extended Data Fig. 3 Effect of non-conservative forces.

In this simplified pictorial representation, the order parameter (represented by a ball) evolves in a potential-energy landscape shaped like a sombrero. In a conservative system, the order parameter would relax straight to the bottom of the potential (dashed blue line). Here, transverse non-conservative forces push the order parameter in the direction defined by the bottom of the potential, leading to a curved trajectory (red continuous line) starting from the same initial condition. In the systems we considered, the non-conservative forces arise from the non-reciprocal coupling between two order parameters. This aspect is not captured by this simplified picture.

Extended Data Fig. 4 Phase diagram of the PT-symmetric non-reciprocal Kuramoto model and exceptional point in the spectrum of the Jacobian.

a, Phase diagram computed numerically from equation (15). The states are defined in Extended Data Table 1. **b**, The two most unstable eigenvalues $\lambda_i = \sigma_i + i\omega_i$ of L coalesce at $j_c \approx 0.007$. This value coincides with the transition from travelling waves (TW) to coherent states, marked by a red dashed line. Note that this coalescence occurs at $\lambda = 0$ (not at finite frequency nor at finite growth rate). The corresponding eigenvectors become collinear (this can be verified, for instance, by computing the determinant of the matrix of eigenvectors, that vanishes at the exceptional point). The imaginary parts ω_i (not shown) are all zero. We have set $j_{AA} = j_{BB} = 1$, $\Delta_A = \Delta_B = 0.25$ and $\omega_A = \omega_B = 0$. In **b**, $j = 0.1$ (a similar behaviour is observed for neighbouring values of j).

Extended Data Fig. 5 Hysteresis in the chiral Kuramoto model.

When chirality is explicitly broken, exceptional points have codimension two, that is, they are typically points in a two-dimensional parameter space. **a**, We plot the frequency Ω of the steady state of the Kuramoto model with explicitly broken PT symmetry as a function of the difference $\Delta\omega =$

$\omega_A - \omega_B$ between the two communities (also called detuning) and the deviation $\langle \{ \rm{delta} \} \{ j \} \{ - \} = \{ j \} \{ - \} - \{ j \} \{ - \}^* \{ \{ \rm{E} \} \{ \{ \rm{P} \} \} \} \rangle$ of the non-reciprocal part j_- of the coupling between the communities from its value $\langle \{ j \} \{ - \}^* \{ \{ \rm{EP} \} \} \rangle$ at the exceptional point. The system exhibits a region where two possible steady states with different properties coexist (the two steady states are the continuation of the clockwise and anticlockwise chiral phases present in the PT-symmetric case $\Delta\omega = 0$). This region (red triangle) starts at the exceptional point (red point) and its size increases with the amount of non-reciprocity (here $\langle \{ j \} \{ - \}^* \{ \{ \rm{EP} \} \} \rangle \approx 0.2915 > 0$). The system exhibits hysteresis in the coexistence region (red points). **b–e**, Slices from **a** at fixed δj_- (marked by green dotted lines in **a**). After the exceptional point, there is hysteresis/first-order (discontinuous) behaviour. In **d**, the hysteresis curve bends outwards near the transition. This is due to the oscillation of the norm of the order parameter (which we refer to as swap or periodic synchronization elsewhere) for large enough δj_- . This additional complication does not occur for moderate values of δj_- , such as in **c**. The solution of the dynamical system equation (15) were computed along lines at fixed δj_- , starting at large $|\delta\omega|$ (in a region without phase coexistence) from a random initial condition. The solution (after convergence) was used as an initial value for the next point in the line with fixed δj_- . This procedure was carried out two times, starting from positive and negative large $|\delta\omega|$. We have set $j_+ = 0.08$, $j_{AA} = j_{BB} = 1$, $\Delta_A = \Delta_B = 0.25$, $\omega_A = \omega_B = \Delta\omega/2$.

Extended Data Fig. 6 Non-reciprocal pattern formation.

We show a space-time density plot of the field $u_1(x, t)$ in different phases, as well as snapshots of the fields $u_1(x, t)$ and $u_2(x, t)$ at time $t = 200$. **a**, We observe a disordered phase where both field vanish. **b**, An aligned phase where both patterns are static and in phase (superimposed). **c**, An antialigned phase where the patterns are static and completely out of phase. **d**, A chiral phase where the patterns move at constant velocity, either to the left or to the right (spontaneously breaking parity), and in which the fields have a finite phase difference, usually neither zero nor π . **e**, A swap phase

where the patterns essentially jump by a phase π every period. **f**, A mix of the chiral and swap behaviours (as in the chiral phase (**d**), there is a spontaneously broken symmetry between left and right movers). The fields are obtained by direct numerical simulation of the coupled Swift–Hohenberg equations on a one-dimensional domain of size $2L$ with periodic boundary conditions, starting from random initial conditions. The simulations are performed using the open-source pseudospectral solver Dedalus²¹⁹. We have used $g = 0.25$ in all cases. In **a**, $r_{11} = r_{22} = -0.5$ and $r_+ = r_- = 0.00$. In the other cases, we have set $r_{11} = r_{22} = 0.5$ (**b–f**) and $r_+ = 0.50$, $r_- = 0.00$ (**b**); $r_+ = -0.50$, $r_- = 0.00$ (**c**); $r_+ = 0.00$, $r_- = 0.25$ (**d**); $r_+ = 0.87$, $r_- = 1.00$ (**e**); $r_+ = 0.85$, $r_- = 1.00$ (**f**).

[Extended Data Fig. 7 Exceptional point in directional interface growth.](#)

The spectrum of the Jacobian L corresponding to equation (20) exhibits an exceptional point at the transition between static patterns and travelling patterns with spontaneous parity breaking (that is, the patterns travel with equal probability to the left or to the right). The two most unstable eigenvalues $\lambda_i = \sigma_i + i\omega_i$ of L coalesce at $\mu_1 \approx 0.064$ (red circle). This value coincides with the transition from a constant solution to travelling waves, marked by a red dashed line. The coalescence occurs at $\lambda = 0$ (not at finite frequency nor at finite growth rate), and the corresponding eigenvectors become collinear. Note that another exceptional point occurs near $\mu_1 \approx 0.014$ (green circle), but with a strictly negative growth rate: this does not correspond to a bifurcation. We also show the dephasing $\Delta\phi = 2\phi_1 - \phi_2$ between the amplitudes, which undergoes a pitchfork bifurcation; the direction of motion of the pattern is set by $\Delta\phi$. We have set $\alpha = \beta = \gamma = \delta = 1$, $\varepsilon = +1$ and $\mu_2 = -0.1$.

Extended Data Table 1 An O(2) ‘Rosetta stone’ [Full size table](#)

Supplementary information

Supplementary Information

This file contains derivations of the results presented in the main text and additional discussions.

Supplementary Video 1

Demonstration with programmable robots. See Sec. XIV of the Supplementary Notes.

Supplementary Video 2

Evolution of the order parameters v_A (blue) and v_B (red) in the time-dependent phases (chiral, swap, chiral+swap) computed from the dynamical system Eq. (S84).

Supplementary Video 3

Molecular dynamics simulation of the microscopic non-reciprocal flocking model. See Sec. V B of the Supplementary Notes. In the bottom part, we show the instantaneous order parameter obtained by averaging the individual directions of the self-propelled particles.

Supplementary Video 4

Numerical simulation of the hydrodynamic field theory showing pattern formation at fixed density when the incompressibility constraint is not enforced. See Sec. XV of the Supplementary Notes.

Supplementary Video 5

Numerical simulation of the hydrodynamic field theory showing pattern formation with the incompressibility constraint enforced. See Sec. XV B of the Supplementary Notes.

Rights and permissions

[Reprints and Permissions](#)

About this article



Check for
updates

Cite this article

Fruchart, M., Hanai, R., Littlewood, P.B. *et al.* Non-reciprocal phase transitions. *Nature* **592**, 363–369 (2021). <https://doi.org/10.1038/s41586-021-03375-9>

[Download citation](#)

- Received: 09 April 2020
- Accepted: 19 February 2021
- Published: 14 April 2021
- Issue Date: 15 April 2021
- DOI: <https://doi.org/10.1038/s41586-021-03375-9>

Further reading

- [An exceptional view of phase transitions in non-equilibrium systems](#)
 - Cynthia J. O. Reichhardt
 - & Charles Reichhardt

Nature (2021)

Comments

By submitting a comment you agree to abide by our [Terms](#) and [Community Guidelines](#). If you find something abusive or that does not comply with our terms or guidelines please flag it as inappropriate.

[Access through your institution](#)

[Change institution](#)

[Buy or subscribe](#)

Associated Content

Nature | News & Views

[An exceptional view of phase transitions in non-equilibrium systems](#)

- Cynthia J. O. Reichhardt
- & Charles Reichhardt

This article was downloaded by **calibre** from <https://www.nature.com/articles/s41586-021-03375-9>

| [Section menu](#) | [Main menu](#) |

- Article
- [Published: 14 April 2021](#)

A quantum magnetic analogue to the critical point of water

- [J. Larrea Jiménez^{1,2},](#)
- [S. P. G. Crone^{3,4},](#)
- [E. Fogh ORCID: orcid.org/0000-0001-8305-4466²](#),
- [M. E. Zayed⁵,](#)
- [R. Lortz⁶,](#)
- [E. Pomjakushina ORCID: orcid.org/0000-0002-2446-3830⁷](#),
- [K. Conder⁷,](#)
- [A. M. Läuchli ORCID: orcid.org/0000-0002-2272-2691⁸](#),
- [L. Weber⁹,](#)
- [S. Wessel ORCID: orcid.org/0000-0002-6353-5083⁹](#),
- [A. Honecker¹⁰,](#)
- [B. Normand^{2,11},](#)
- [Ch. Rüegg^{2,11,12,13},](#)
- [P. Corboz^{3,4},](#)
- [H. M. Rønnow ORCID: orcid.org/0000-0002-8832-8865²](#) &
- [F. Mila²](#)

[Nature](#) volume **592**, pages 370–375(2021) [Cite this article](#)

- 1496 Accesses
- 69 Altmetric
- [Metrics details](#)

Subjects

- [Characterization and analytical techniques](#)
- [Computational science](#)
- [Magnetic properties and materials](#)
- [Phase transitions and critical phenomena](#)

Abstract

At the liquid–gas phase transition in water, the density has a discontinuity at atmospheric pressure; however, the line of these first-order transitions defined by increasing the applied pressure terminates at the critical point¹, a concept ubiquitous in statistical thermodynamics². In correlated quantum materials, it was predicted³ and then confirmed experimentally^{4,5} that a critical point terminates the line of Mott metal–insulator transitions, which are also first-order with a discontinuous charge carrier density. In quantum spin systems, continuous quantum phase transitions⁶ have been controlled by pressure^{7,8}, applied magnetic field^{9,10} and disorder¹¹, but discontinuous quantum phase transitions have received less attention. The geometrically frustrated quantum antiferromagnet $\text{SrCu}_2(\text{BO}_3)_2$ constitutes a near-exact realization of the paradigmatic Shastry–Sutherland model^{12,13,14} and displays exotic phenomena including magnetization plateaus¹⁵, low-lying bound-state excitations¹⁶, anomalous thermodynamics¹⁷ and discontinuous quantum phase transitions^{18,19}. Here we control both the pressure and the magnetic field applied to $\text{SrCu}_2(\text{BO}_3)_2$ to provide evidence of critical-point physics in a pure spin system. We use high-precision specific-heat measurements to demonstrate that, as in water, the pressure–temperature phase diagram has a first-order transition line that separates phases with different local magnetic energy densities, and that terminates at an Ising critical point. We provide a quantitative explanation of our data using recently developed finite-temperature tensor-network methods^{17,20,21,22}. These results further our understanding of first-order quantum phase transitions in quantum magnetism, with potential applications in materials where anisotropic spin interactions produce the topological properties^{23,24} that are useful for spintronic applications.

[Access through your institution](#)

[Change institution](#)

[Buy or subscribe](#)

Access options

Subscribe to Journal

Get full journal access for 1 year

\$199.00

only \$3.90 per issue

[Subscribe](#)

All prices are NET prices.

VAT will be added later in the checkout.

Tax calculation will be finalised during checkout.

Rent or Buy article

Get time limited or full article access on ReadCube.

from \$8.99

[Rent or Buy](#)

All prices are NET prices.

Additional access options:

- [Log in](#)
- [Access through your institution](#)
- [Learn about institutional subscriptions](#)

Fig. 1: Specific heat of water and of SrCu₂(BO₃)₂, shown together with calculated critical properties of the Shastry–Sutherland model.

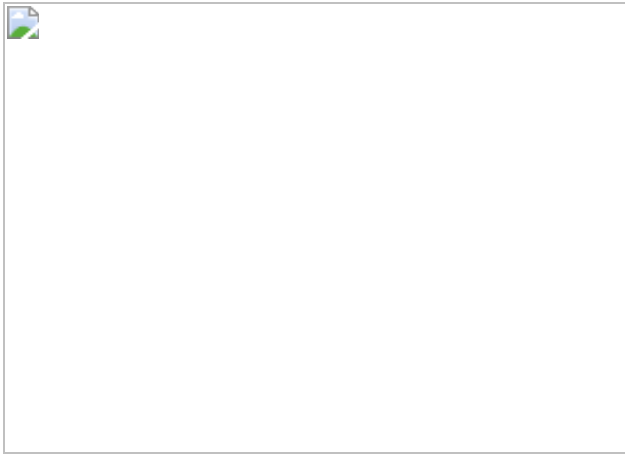


Fig. 2: Specific heat and critical scaling at zero magnetic field.

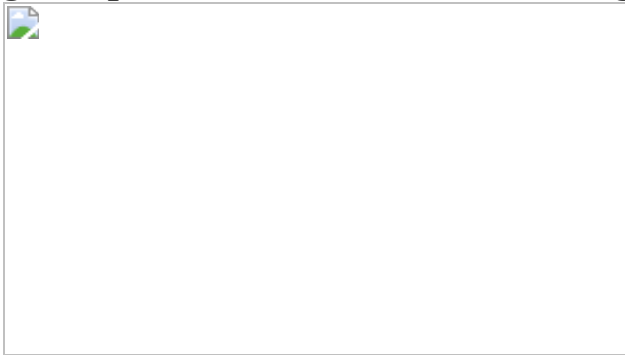


Fig. 3: Evolution of the specific heat with magnetic field around the QPT.

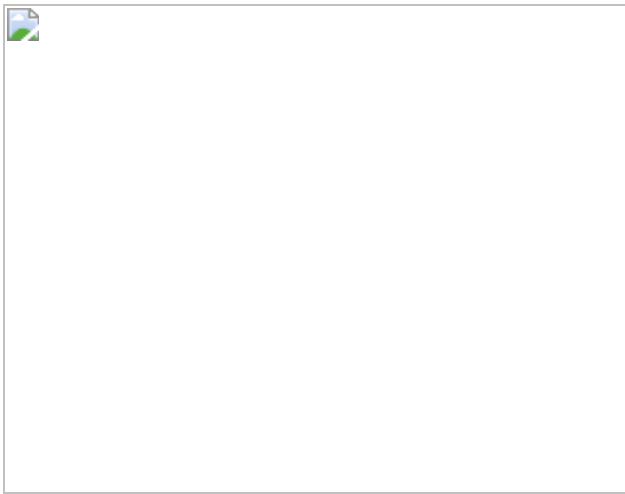
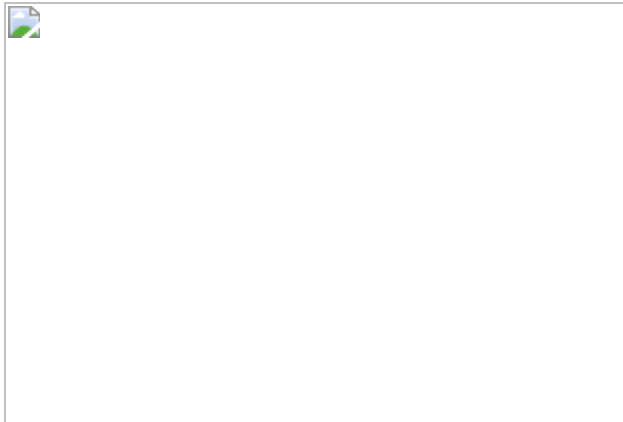


Fig. 4: Phase diagram of SrCu₂(BO₃)₂ in pressure, field and temperature.



Data availability

The data that support the findings of this study are available at <https://doi.org/10.5281/zenodo.4455613> and from the corresponding author upon reasonable request.

Code availability

The code that supports the findings of this study is available from the corresponding author upon reasonable request.

References

1. 1.

Cagniard de la Tour, C. Exposé de quelques résultats obtenus par l'action combinée de la chaleur et de la compression sur certains liquides, tels que l'eau, l'alcool, l'éther sulfurique et l'essence de pétrole rectifié. *Ann. Chim Phys.* **21**, 127–132 (1822).

[Google Scholar](#)

2. 2.

Chaikin, P. M. & Lubensky, T. C. *Principles of Condensed Matter Physics* (Cambridge Univ. Press, 1995).

3. 3.

Georges, A., Kotliar, G., Krauth, W. & Rozenberg, M. J. Dynamical mean-field theory of strongly correlated fermion systems and the limit of infinite dimensions. *Rev. Mod. Phys.* **68**, 13–125 (1996).

[ADS](#) [MathSciNet](#) [CAS](#) [Google Scholar](#)

4. 4.

Limelette, P. et al. Universality and critical behavior at the Mott transition. *Science* **302**, 89–92 (2003).

[ADS](#) [CAS](#) [Google Scholar](#)

5. 5.

Kagawa, F., Miyagawa, K. & Kanoda, K. Unconventional critical behaviour in a quasi-two-dimensional organic conductor. *Nature* **436**, 534–537 (2005).

[ADS](#) [CAS](#) [Google Scholar](#)

6. 6.

Sachdev, S. *Quantum Phase Transitions* (Cambridge Univ. Press, 2011).

7. 7.

Rüegg, C. et al. Quantum magnets under pressure: controlling elementary excitations in $TlCuCl_3$. *Phys. Rev. Lett.* **100**, 205701 (2008).

[ADS](#) [Google Scholar](#)

8. 8.

Merchant, P. et al. Quantum and classical criticality in a dimerized quantum antiferromagnet. *Nat. Phys.* **10**, 373–379 (2014).

[CAS](#) [Google Scholar](#)

9. 9.

Giamarchi, T., Rüegg, C. & Tchernyshyov, O. Bose–Einstein condensation in magnetic insulators. *Nat. Phys.* **4**, 198–204 (2008).

[CAS](#) [Google Scholar](#)

10. 10.

Thielemann, B. et al. Direct observation of magnon fractionalization in a quantum spin ladder. *Phys. Rev. Lett.* **102**, 107204 (2009).

[ADS](#) [CAS](#) [Google Scholar](#)

11. 11.

Yu, R. et al. Bose glass and Mott glass of quasiparticles in a doped quantum magnet. *Nature* **489**, 379–384 (2012).

[ADS](#) [CAS](#) [Google Scholar](#)

12. 12.

Shastry, B. S. & Sutherland, B. Exact ground state of a quantum mechanical antiferromagnet. *Physica B+C* **108**, 1069–1070 (1981).

[ADS](#) [CAS](#) [Google Scholar](#)

13. 13.

Miyahara, S. & Ueda, K. Theory of the orthogonal dimer Heisenberg spin model for $\text{SrCu}_2(\text{BO}_3)_2$. *J. Phys. Condens. Matter* **15**, 327–366 (2003).

[ADS](#) [Google Scholar](#)

14. 14.

Corboz, P. & Mila, F. Tensor network study of the Shastry–Sutherland model in zero magnetic field. *Phys. Rev. B* **87**, 115144 (2013).

[ADS](#) [Google Scholar](#)

15. 15.

Matsuda, Y. H. et al. Magnetization of $\text{SrCu}_2(\text{BO}_3)_2$ in ultrahigh magnetic fields up to 118 T. *Phys. Rev. Lett.* **111**, 137204 (2013).

[ADS](#) [CAS](#) [Google Scholar](#)

16. 16.

Knetter, C., Bühler, A., Müller-Hartmann, E. & Uhrig, G. S. Dispersion and symmetry of bound states in the Shastry–Sutherland model. *Phys. Rev. Lett.* **85**, 3958–3961 (2000).

[ADS](#) [CAS](#) [Google Scholar](#)

17. 17.

Wietek, A. et al. Thermodynamic properties of the Shastry–Sutherland model throughout the dimer-product phase. *Phys. Rev. Res.* **1**, 033038 (2019).

[CAS](#) [Google Scholar](#)

18. 18.

Zayed, M. E. et al. 4-spin plaquette singlet state in the Shastry–Sutherland compound $\text{SrCu}_2(\text{BO}_3)_2$. *Nat. Phys.* **13**, 962–966 (2017).

[CAS](#) [Google Scholar](#)

19. 19.

Guo, J. et al. Quantum phases of $\text{SrCu}_2(\text{BO}_3)_2$ from high-pressure thermodynamics. *Phys. Rev. Lett.* **124**, 206602 (2020).

[ADS](#) [CAS](#) [Google Scholar](#)

20. 20.

Verstraete, F. & Cirac, J. I. Renormalization algorithms for quantum-many body systems in two and higher dimensions. Preprint at <https://arxiv.org/abs/cond-mat/0407066> (2004).

21. 21.

Jordan, J., Orús, R., Vidal, G., Verstraete, F. & Cirac, J. I. Classical simulation of infinite-size quantum lattice systems in two spatial dimensions. *Phys. Rev. Lett.* **101**, 250602 (2008).

[ADS](#) [CAS](#) [Google Scholar](#)

22. 22.

Czarnik, P., Dziarmaga, J. & Corboz, P. Time evolution of an infinite projected entangled pair state: an efficient algorithm. *Phys. Rev. B* **99**, 035115 (2019).

[ADS](#) [CAS](#) [Google Scholar](#)

23. 23.

Witczak-Krempa, W., Chen, G., Kim, Y.-B. & Balents, L. Correlated quantum phenomena in the strong spin–orbit regime. *Annu. Rev. Condens. Matter Phys.* **5**, 57–82 (2014).

[ADS](#) [CAS](#) [Google Scholar](#)

24. 24.

Chacon, A. et al. Observation of two independent skyrmion phases in a chiral magnetic material. *Nat. Phys.* **14**, 936–941 (2018).

[CAS](#) [Google Scholar](#)

25. 25.

Wagner, W. et al. The IAPWS Industrial Formulation 1997 for the Thermodynamic Properties of Water and Steam. *J. Eng. Gas Turbine. Power* **122**, 150–184 (2000).

[CAS](#) [Google Scholar](#)

26. 26.

Orlov, K. A., Alexandrov, A. A., Ochkov, A. V. & Ochkov, V. F. WaterSteamPro documentation www.wsp.ru (2021).

27. 27.

Stapmanns, J. et al. Thermal critical points and quantum critical end point in the frustrated bilayer Heisenberg antiferromagnet. *Phys. Rev. Lett.* **121**, 127201 (2018).

[ADS](#) [CAS](#) [Google Scholar](#)

28. 28.

Kageyama, H. et al. Exact dimer ground state and quantized magnetization plateaus in the two-dimensional spin system SrCu₂(BO₃)₂. *Phys. Rev. Lett.* **82**, 3168–3171 (1999).

[ADS](#) [CAS](#) [Google Scholar](#)

29. 29.

Larrea J, J., Martelli, V. & Rønnow, H. M. High-pressure specific heat technique to uncover novel states of quantum matter. *J. Phys. Conf. Ser.* **1609**, 012008 (2020).

[Google Scholar](#)

30. 30.

Boos, C. et al. Competition between intermediate plaquette phases in $\text{SrCu}_2(\text{BO}_3)_2$. *Phys. Rev. B* **100**, 140413 (2019).

[ADS](#) [CAS](#) [Google Scholar](#)

31. 31.

Nojiri, H., Kageyama, H., Onizuka, K., Ueda, Y. & Motokawa, M. Direct observation of the multiple spin gap excitations in two-dimensional dimer system $\text{SrCu}_2(\text{BO}_3)_2$. *J. Phys. Soc. Jpn.* **68**, 2906–2909 (1999).

[ADS](#) [CAS](#) [Google Scholar](#)

32. 32.

Fisher, M. E. & Upton, P. J. Universality and interfaces at critical end points. *Phys. Rev. Lett.* **65**, 2402 (1990).

[ADS](#) [MathSciNet](#) [CAS](#) [MATH](#) [Google Scholar](#)

33. 33.

Fisher, M. E. & Barbosa, M. C. Phase boundaries near critical end points. I. Thermodynamics and universality. *Phys. Rev. B* **43**, 11177–11184 (1991).

[ADS](#) [CAS](#) [Google Scholar](#)

34. 34.

Bettler, S., Stoppel, L., Yan, Z., Gvasaliya, S. & Zhedulev, Z. Competition between intermediate plaquette phases in $\text{SrCu}_2(\text{BO}_3)_2$. *Phys. Rev. Res.* **2**, 012010 (2020).

[CAS](#) [Google Scholar](#)

35. 35.

Lee, J. Y., You, Y.-Z., Sachdev, S. & Vishwanath, A. Signatures of a deconfined phase transition on the Shastry–Sutherland lattice: applications to quantum critical $\text{SrCu}_2(\text{BO}_3)_2$. *Phys. Rev. X* **9**, 041037 (2019).

[CAS](#) [Google Scholar](#)

36. 36.

Waki, T. et al. A novel ordered phase in $\text{SrCu}_2(\text{BO}_3)_2$ under high pressure. *J. Phys. Soc. Jpn.* **76**, 073710 (2007).

[ADS](#) [Google Scholar](#)

37. 37.

Maxim, F. et al. Visualization of supercritical water pseudo-boiling at Widom line crossover. *Nat. Commun.* **10**, 4114 (2019).

[ADS](#) [PubMed](#) [PubMed Central](#) [Google Scholar](#)

38. 38.

Sordi, G., Haule, K. & Tremblay, A.-M. S. Finite doping signatures of the Mott transition in the two-dimensional Hubbard model. *Phys. Rev. Lett.* **104**, 226402 (2010).

[ADS](#) [CAS](#) [Google Scholar](#)

39. 39.

Terletska, H., Vučičević, J., Tanasković, D. & Dobrosavljević, V. Quantum critical transport near the Mott transition. *Phys. Rev. Lett.* **107**, 026401 (2011).

[ADS](#) [CAS](#) [Google Scholar](#)

40. 40.

Eisenlohr, H., Lee, S.-S. B. & Vojta, M. Mott quantum criticality in the one-band Hubbard model: dynamical mean-field theory, power-law spectra, and scaling. *Phys. Rev. B* **100**, 155152 (2019).

[ADS](#) [CAS](#) [Google Scholar](#)

41. 41.

Furukawa, T., Miyagawa, K., Taniguchi, H., Kato, R. & Kanoda, K. Quantum criticality of Mott transition in organic materials. *Nat. Phys.* **11**, 221–224 (2015).

[CAS](#) [Google Scholar](#)

42. 42.

Kageyama, H., Onizuka, K., Yamauchi, T. & Ueda, Y. Crystal growth of the two-dimensional spin gap system $\text{SrCu}_3(\text{BO}_2)_2$. *J. Cryst. Growth* **206**, 65–67 (1999).

[ADS](#) [CAS](#) [Google Scholar](#)

43. 43.

Jorge, G. A. et al. High magnetic field magnetization and specific heat of the 2D spin-dimer system $\text{SrCu}_2(\text{BO}_3)_2$. *J. Alloys Compd.* **369**, 90–92 (2004).

[CAS](#) [Google Scholar](#)

44. 44.

Gmelin, E. Classical temperature-modulated calorimetry: a review. *Thermochim. Acta* **304–305**, 1–26 (1997).

[Google Scholar](#)

45. 45.

Wessel, S. et al. Thermodynamic properties of the Shastry–Sutherland model from quantum Monte Carlo simulations. *Phys. Rev. B* **98**, 174432 (2018).

[ADS](#) [Google Scholar](#)

46. 46.

Nishio, Y., Maeshima, N., Gendiar, A. & Nishino, T. Tensor product variational formulation for quantum systems. Preprint at <https://arxiv.org/abs/cond-mat/0401115> (2004).

47. 47.

Li, W. et al. Linearized tensor renormalization group algorithm for the calculation of thermodynamic properties of quantum lattice models. *Phys. Rev. Lett.* **106**, 127202 (2011).

[ADS](#) [Google Scholar](#)

48. 48.

Czarnik, P., Cincio, L. & Dziarmaga, J. Projected entangled pair states at finite temperature: imaginary time evolution with ancillas. *Phys. Rev. B* **86**, 245101 (2012).

[ADS](#) [Google Scholar](#)

49. 49.

Czarnik, P. & Dziarmaga, J. Projected entangled pair states at finite temperature: iterative self-consistent bond renormalization for exact imaginary time evolution. *Phys. Rev. B* **92**, 035120 (2015).

[ADS](#) [Google Scholar](#)

50. 50.

Kshetrimayum, A., Rizzi, M., Eisert, J. & Orús, R. Tensor network annealing algorithm for two-dimensional thermal states. *Phys. Rev. Lett.* **122**, 070502 (2019).

[ADS](#) [CAS](#) [Google Scholar](#)

51. 51.

Jiang, H. C., Weng, Z. Y. & Xiang, T. Accurate determination of tensor network state of quantum lattice models in two dimensions. *Phys. Rev. Lett.* **101**, 090603 (2008).

[ADS](#) [CAS](#) [Google Scholar](#)

52. 52.

Singh, S., Pfeifer, R. N. C. & Vidal, G. Tensor network states and algorithms in the presence of a global U(1) symmetry. *Phys. Rev. B* **83**, 115125 (2011).

[ADS](#) [Google Scholar](#)

53. 53.

Bauer, B., Corboz, P., Orús, R. & Troyer, M. Implementing global Abelian symmetries in projected entangled-pair state algorithms. *Phys. Rev. B* **83**, 125106 (2011).

[ADS](#) [Google Scholar](#)

54. 54.

Corboz, P., Rice, T. M. & Troyer, M. Competing states in the $t-J$ model: uniform d -wave state versus stripe state. *Phys. Rev. Lett.* **113**, 046402 (2014).

[ADS](#) [CAS](#) [Google Scholar](#)

55. 55.

Nishino, T. & Okunishi, K. Corner transfer matrix renormalization group method. *J. Phys. Soc. Jpn.* **65**, 891–894 (1996).

[ADS](#) [CAS](#) [MATH](#) [Google Scholar](#)

56. 56.

Orús, R. & Vidal, G. Simulation of two-dimensional quantum systems on an infinite lattice revisited: corner transfer matrix for tensor contraction. *Phys. Rev. B* **80**, 094403 (2009).

[ADS](#) [Google Scholar](#)

57. 57.

Luo, J., Xu, L., Stanley, H. E. & Buldyrev, S. V. Behavior of the Widom line in critical phenomena. *Phys. Rev. Lett.* **112**, 135701 (2014).

[ADS](#) [Google Scholar](#)

[Download references](#)

Acknowledgements

We are grateful to R. Gaal, J. Piatek and M. de Vries for technical assistance. We acknowledge discussions with D. Badrtdinov, C. Boos, T. Fennell, A. Sandvik, A.-M. Tremblay, A. Turrini, A. Wietek and A. Zheludev. We thank the São Paulo Research Foundation (FAPESP) for financial support under grant no. 2018/08845-3, the Qatar Foundation for support through Carnegie Mellon University in Qatar’s Seed Research programme, the Swiss National Science Foundation (SNSF) for support under grant no. 188648 and the European Research Council (ERC) for support under the EU Horizon 2020 research and innovation programme (grant no. 677061), as well as from the ERC Synergy Grant HERO. We are grateful to the Deutsche Forschungsgemeinschaft for the support of RTG

1995 and to the IT Center at RWTH Aachen University and the JSC Jülich for access to computing time through JARA-HPC. The statements made herein are not the responsibility of the Qatar Foundation.

Author information

Affiliations

1. Laboratory for Quantum Matter under Extreme Conditions, Institute of Physics, University of São Paulo, São Paulo, Brazil

J. Larrea Jiménez

2. Institute of Physics, Ecole Polytechnique Fédérale de Lausanne (EPFL), Lausanne, Switzerland

J. Larrea Jiménez, E. Fogh, B. Normand, Ch. Rüegg, H. M. Rønnow & F. Mila

3. Institute for Theoretical Physics, University of Amsterdam, Amsterdam, The Netherlands

S. P. G. Crone & P. Corboz

4. Delta Institute for Theoretical Physics, University of Amsterdam, Amsterdam, The Netherlands

S. P. G. Crone & P. Corboz

5. Department of Physics, Carnegie Mellon University in Qatar, Doha, Qatar

M. E. Zayed

6. Department of Physics, Hong Kong University of Science and Technology, Kowloon, Hong Kong

R. Lortz

7. Laboratory for Multiscale Materials Experiments, Paul Scherrer Institute, Villigen-PSI, Switzerland

E. Pomjakushina & K. Conder
8. Institut für Theoretische Physik, Universität Innsbruck, Innsbruck, Austria

A. M. Läuchli
9. Institut für Theoretische Festkörperphysik, RWTH Aachen University, Aachen, Germany

L. Weber & S. Wessel
10. Laboratoire de Physique Théorique et Modélisation, CNRS UMR 8089, CY Cergy Paris Université, Cergy-Pontoise, France

A. Honecker
11. Paul Scherrer Institute, Villigen-PSI, Switzerland

B. Normand & Ch. Rüegg
12. Institute for Quantum Electronics, ETH Zürich, Hönggerberg, Switzerland

Ch. Rüegg
13. Department of Quantum Matter Physics, University of Geneva, Geneva, Switzerland

Ch. Rüegg

Authors

1. J. Larrea Jiménez
[View author publications](#)

You can also search for this author in [PubMed](#) [Google Scholar](#)

2. S. P. G. Crone

[View author publications](#)

You can also search for this author in [PubMed](#) [Google Scholar](#)

3. E. Fogh

[View author publications](#)

You can also search for this author in [PubMed](#) [Google Scholar](#)

4. M. E. Zayed

[View author publications](#)

You can also search for this author in [PubMed](#) [Google Scholar](#)

5. R. Lortz

[View author publications](#)

You can also search for this author in [PubMed](#) [Google Scholar](#)

6. E. Pomjakushina

[View author publications](#)

You can also search for this author in [PubMed](#) [Google Scholar](#)

7. K. Conder

[View author publications](#)

You can also search for this author in [PubMed](#) [Google Scholar](#)

8. A. M. Läuchli

[View author publications](#)

You can also search for this author in [PubMed](#) [Google Scholar](#)

9. L. Weber

[View author publications](#)

You can also search for this author in [PubMed](#) [Google Scholar](#)

10. S. Wessel

[View author publications](#)

You can also search for this author in [PubMed](#) [Google Scholar](#)

11. A. Honecker

[View author publications](#)

You can also search for this author in [PubMed](#) [Google Scholar](#)

12. B. Normand

[View author publications](#)

You can also search for this author in [PubMed](#) [Google Scholar](#)

13. Ch. Rüegg

[View author publications](#)

You can also search for this author in [PubMed](#) [Google Scholar](#)

14. P. Corboz

[View author publications](#)

You can also search for this author in [PubMed](#) [Google Scholar](#)

15. H. M. Rønnow

[View author publications](#)

You can also search for this author in [PubMed](#) [Google Scholar](#)

16. F. Mila

[View author publications](#)

You can also search for this author in [PubMed](#) [Google Scholar](#)

Contributions

The experimental project was conceived by H.M.R. and Ch.R. and the theoretical framework was put forward by F.M. The crystals were grown by E.P. and K.C. Specific-heat measurements were performed by J.L.J. with assistance from M.E.Z., R.L. and H.M.R. S.P.G.C. and P.C. performed iPEPS calculations. A.M.L. performed complementary exact diagonalization calculations. L.W. and S.W. performed quantum Monte Carlo simulations on the fully frustrated bilayer model. Data analysis and figure preparation were performed by J.L.J., E.F., S.P.G.C., L.W., S.W., P.C. and H.M.R. The detailed theoretical analysis was provided by P.C., S.P.G.C., F.M., A.H., B.N., L.W. and S.W. The manuscript was written by B.N. and F.M. with assistance from all the authors.

Corresponding author

Correspondence to [H. M. Rønnow](#).

Ethics declarations

Competing interests

The authors declare no competing interests.

Additional information

Peer review information *Nature* thanks Jong Yeon Lee and the other, anonymous, reviewer(s) for their contribution to the peer review of this work. Peer reviewer reports are available.

Publisher's note Springer Nature remains neutral with regard to jurisdictional claims in published maps and institutional affiliations.

Extended data figures and tables

[Extended Data Fig. 1 a.c. calorimetry on SrCu₂\(BO₃\)₂.](#)

a, The a.c. calorimeter was prepared by depositing two Pt thin films (the shinier surfaces) over both halves of the sample. One film was used as the heater and the other for optimal thermal contact and measurement. The heating current (I_{ex} at frequency f) was supplied through the pair of Constantan wires labelled H_{1a} and H_{1b} , and H_{2a} and H_{2b} were used to measure the electrical resistance, R_{Pt} , of the Pt film. TC_1 and TC_2 are thermocouples and K represents the thermal contact between the sample and the cryostat (through the pressure cell). **b**, Isothermal ($T = 4.5$ K) and isobaric ($P = 20$ kbar) f -dependence of the modulated pick-up voltage, V_{ac} , which is directly proportional to the temperature differential, ΔT_{ac} , measured by the thermocouples at two different positions. **c**, Isobaric ($P = 18.2$ kbar) f -dependence measurements of V_{ac} at different temperatures with $I_0 = 1.6$ mA at $T \geq 3.9$ K, $I_0 = 0.8$ mA at $T = 2$ K and $I_0 = 0.4$ mA at $T < 2$ K. **d**, Sample heat capacity normalized to the input heating power ($\langle P \rangle_0 = \langle I \rangle_0^2 R \langle \text{rm} \{ \text{Pt} \} \rangle$), comparing the fit of $V_{\text{ac}}(f)$ obtained from the steady-state equation (' f scan')²⁹ with values obtained directly from a variable-temperature measurement performed at the fixed working frequency $f_C = 1.5$ Hz (' T scan'). Solid and dashed lines in **b** and **c** represent fits using the steady-state equation^{29,44}.

Extended Data Fig. 2 Correlation length.

ξ/a for the Shastry–Sutherland model, calculated by iPEPS with $D = 8$ as a function of the coupling ratio, J/J_D , at a fixed temperature $T_c(D = 8) = 0.0522J_D/k_B$. The three panels show increasing magnification of the J/J_D axis from the equivalent of Fig. 1 (upper right) through the step sizes of Fig. 2c,d ($10^{-3}J/J_D$, centre) to $10^{-5}J/J_D$ (lower left).

Extended Data Fig. 3 Critical point in the presence of Dzyaloshinskii–Moriya interactions.

Thermodynamic data obtained from iPEPS calculations with $D = 10$ performed for the Shastry–Sutherland model in the presence of Dzyaloshinskii–Moriya interactions. These interactions, of strength D_D , are

placed on the dimer (J_D) bonds and have the magnitude known for $\text{SrCu}_2(\text{BO}_3)_2$. They create an entangled ground state in the dimer phase, which resolves the numerical instabilities observed for the pure Shastry–Sutherland model at low temperatures, although the reduced symmetry limits the maximum D to 10. **a**, Specific heat, $C(J/J_D, T)/T$, shown in the same format as for Fig. 1b. **b**, Correlation length, ξ/a , showing clearly the region of ‘pressure’ and temperature over which Ising correlations develop. **c**, Dimer spin–spin correlation function, $\langle \mathbf{S}_i \cdot \mathbf{S}_j \rangle$, emphasizing the abrupt onset with decreasing temperature of a sharp discontinuity as a function of J/J_D . It is clear that these Dzyaloshinskii–Moriya interactions have no qualitative effect whatsoever on the physics of the critical point.

Extended Data Fig. 4 Ising critical points in different lattice models.

Specific heat, C/T , for a number of 2D models, illustrating its universal behaviour around the Ising critical point. **a**, Ising model on the square lattice in a longitudinal magnetic field, h , obtained by contracting the exact $D = 2$ tensor-network representation of the partition function using the corner-transfer-matrix method with a boundary bond dimension $\chi = 24$ (ref. 55). **b**, Fully frustrated bilayer model, obtained by using the stochastic series expansion quantum Monte Carlo approach developed in refs. 27,45 to perform simulations on systems of sizes up to $2 \times 32 \times 32$ as a function of J_\perp/J_\parallel . **c**, Shastry–Sutherland model, obtained by iPEPS calculations with $D = 20$ as in Fig. 1c. The dashed lines show the positions of the local maxima of the specific heat, $C(J/J_D)$, which we label by their temperatures, T_{\max} . These two lines reach an absolute minimum, $T_{\max} = T_c$, where they meet at the Ising critical point, with T_{\max} increasing as the control parameter is changed away from the QPT. Thus the specific heat defines two characteristic lines in the phase diagram of the Ising critical point, instead of the single line given by the correlation length (Fig. 1d) and the critical isochore (Fig. 1e). This contrasting behaviour has been demonstrated in models where the critical pressure is temperature-independent⁵⁷ and the issue of characteristic lines has also been discussed in the Mott metal–insulator phase diagram^{38,40}. We stress that such

behaviour is a fundamental property of the Ising model, and hence of all models sharing its physics. For the Shastry–Sutherland model (**c**), the two lines of maxima can be taken to provide a qualitative definition of regimes dominated by ‘dimer-like’ spin correlations (lower left) and by ‘plaquette-like’ correlations (lower right, but above the plaquette-ordered phase), accompanied by a third regime (above both lines) bearing no clear hallmarks of either $T = 0$ phase. We remark that the values of T_c in units of the relevant energy scale, $T_c/J \approx 2.3$ (**a**), $T_c/J \approx 0.53$ (**b**) and $T_c/J \approx 0.04$ (**c**), vary widely among the three models. This can be traced to the change in slope of the ground-state energy at the transition, the compensation of which by entropy effects restores a derivable free energy at T_c .

Supplementary information

[Peer Review File](#)

Rights and permissions

[Reprints and Permissions](#)

About this article



Cite this article

Jiménez, J.L., Crone, S.P.G., Fogh, E. *et al.* A quantum magnetic analogue to the critical point of water. *Nature* **592**, 370–375 (2021).
<https://doi.org/10.1038/s41586-021-03411-8>

[Download citation](#)

- Received: 30 September 2020

- Accepted: 26 February 2021
- Published: 14 April 2021
- Issue Date: 15 April 2021
- DOI: <https://doi.org/10.1038/s41586-021-03411-8>

Comments

By submitting a comment you agree to abide by our [Terms](#) and [Community Guidelines](#). If you find something abusive or that does not comply with our terms or guidelines please flag it as inappropriate.

[Access through your institution](#)

[Change institution](#)

[Buy or subscribe](#)

This article was downloaded by **calibre** from <https://www.nature.com/articles/s41586-021-03411-8>

| [Section menu](#) | [Main menu](#) |

- Article
- [Published: 14 April 2021](#)

Subterahertz collective dynamics of polar vortices

- [Qian Li](#) ORCID: [orcid.org/0000-0001-7922-598X^{1,11 na1}](https://orcid.org/0000-0001-7922-598X),
- [Vladimir A. Stoica](#) ORCID: [orcid.org/0000-0002-2734-7819^{1,2 na1}](https://orcid.org/0000-0002-2734-7819),
- [Marek Paściak³](#),
- [Yi Zhu¹](#),
- [Yakun Yuan²](#),
- [Tiannan Yang](#) ORCID: [orcid.org/0000-0002-2071-4778²](https://orcid.org/0000-0002-2071-4778),
- [Margaret R. McCarter⁴](#),
- [Sujit Das](#) ORCID: [orcid.org/0000-0001-9823-0207⁴](https://orcid.org/0000-0001-9823-0207),
- [Ajay K. Yadav⁴](#),
- [Suji Park^{7 nAff12}](#),
- [Cheng Dai²](#),
- [Hyeon Jun Lee](#) ORCID: [orcid.org/0000-0001-8202-6471⁸](https://orcid.org/0000-0001-8202-6471),
- [Youngjun Ahn⁸](#),
- [Samuel D. Marks⁸](#),
- [Shukai Yu²](#),
- [Christelle Kadlec](#) ORCID: [orcid.org/0000-0003-2820-4462³](https://orcid.org/0000-0003-2820-4462),
- [Takahiro Sato⁹](#),
- [Matthias C. Hoffmann](#) ORCID: [orcid.org/0000-0002-3596-9853⁹](https://orcid.org/0000-0002-3596-9853),
- [Matthieu Chollet⁹](#),
- [Michael E. Kozina⁹](#),
- [Silke Nelson⁹](#),
- [Diling Zhu⁹](#),
- [Donald A. Walko¹](#),
- [Aaron M. Lindenberg](#) ORCID: [orcid.org/0000-0003-3233-7161^{7,10}](https://orcid.org/0000-0003-3233-7161),

- [Paul G. Evans](#) ORCID: [orcid.org/0000-0003-0421-6792⁸](https://orcid.org/0000-0003-0421-6792),
- [Long-Qing Chen](#) ORCID: [orcid.org/0000-0003-3359-3781²](https://orcid.org/0000-0003-3359-3781),
- [Ramamoorthy Ramesh](#) ORCID: [orcid.org/0000-0003-0524-1332^{4,5,6}](https://orcid.org/0000-0003-0524-1332),
- [Lane W. Martin](#) ORCID: [orcid.org/0000-0003-1889-2513^{4,6}](https://orcid.org/0000-0003-1889-2513),
- [Venkatraman Gopalan](#) ORCID: [orcid.org/0000-0001-6866-3677²](https://orcid.org/0000-0001-6866-3677),
- [John W. Freeland](#) ORCID: [orcid.org/0000-0003-4814-5308¹](https://orcid.org/0000-0003-4814-5308),
- [Jirka Hlinka](#) ORCID: [orcid.org/0000-0002-9293-4462³](https://orcid.org/0000-0002-9293-4462) &
- [Haidan Wen](#) ORCID: [orcid.org/0000-0002-5427-175X¹](https://orcid.org/0000-0002-5427-175X)

[Nature](#) volume **592**, pages376–380(2021)[Cite this article](#)

- 2062 Accesses
- 1 Citations
- 99 Altmetric
- [Metrics details](#)

Subjects

- [Ferroelectrics and multiferroics](#)
- [Topological defects](#)

Abstract

The collective dynamics of topological structures^{1,2,3,4,5,6} are of interest from both fundamental and applied perspectives. For example, studies of dynamical properties of magnetic vortices and skyrmions^{3,4} have not only deepened our understanding of many-body physics but also offered potential applications in data processing and storage⁷. Topological structures constructed from electrical polarization, rather than electron spin, have recently been realized in ferroelectric superlattices^{5,6}, and these are promising for ultrafast electric-field control of topological orders. However, little is known about the dynamics underlying the functionality of such complex extended nanostructures. Here, using terahertz-field excitation and

femtosecond X-ray diffraction measurements, we observe ultrafast collective polarization dynamics that are unique to polar vortices, with orders-of-magnitude higher frequencies and smaller lateral size than those of experimentally realized magnetic vortices³. A previously unseen tunable mode, hereafter referred to as a vortexon, emerges in the form of transient arrays of nanoscale circular patterns of atomic displacements, which reverse their vorticity on picosecond timescales. Its frequency is considerably reduced (softened) at a critical strain, indicating a condensation (freezing) of structural dynamics. We use first-principles-based atomistic calculations and phase-field modelling to reveal the microscopic atomic arrangements and corroborate the frequencies of the vortex modes. The discovery of subterahertz collective dynamics in polar vortices opens opportunities for electric-field-driven data processing in topological structures with ultrahigh speed and density.

[Access through your institution](#)

[Change institution](#)

[Buy or subscribe](#)

Access options

Subscribe to Journal

Get full journal access for 1 year

\$199.00

only \$3.90 per issue

[Subscribe](#)

All prices are NET prices.

VAT will be added later in the checkout.

Tax calculation will be finalised during checkout.

Rent or Buy article

Get time limited or full article access on ReadCube.

from \$8.99

[Rent or Buy](#)

All prices are NET prices.

Additional access options:

- [Log in](#)
- [Access through your institution](#)
- [Learn about institutional subscriptions](#)

Fig. 1: Emergence of the collective dynamics of polar vortices and its experimental detection.



Fig. 2: High-frequency collective modes.



Fig. 3: Tunable vortexon mode.



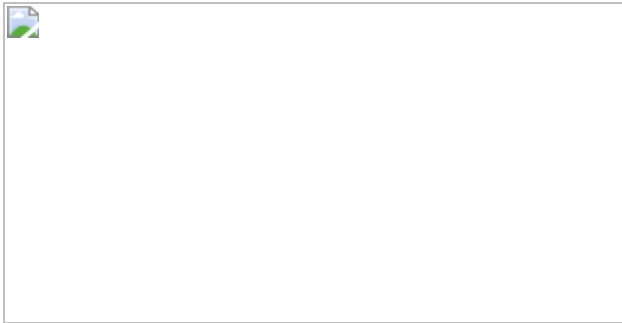
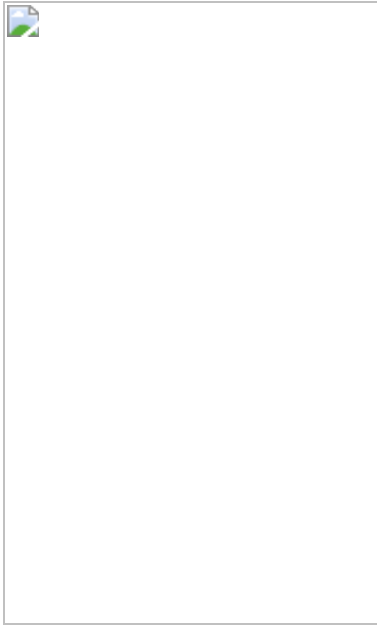


Fig. 4: Atomistic calculation and dynamical phase-field simulation.



Data availability

The data that support the findings of this study are available from the corresponding author upon request.

Code availability

The codes that support the findings of this study are available from the corresponding author upon request.

References

1. 1.

Naumov, I. I., Bellaiche, L. & Fu, H. Unusual phase transitions in ferroelectric nanodisks and nanorods. *Nature* **432**, 737–740 (2004).

[ADS](#) [CAS](#) [PubMed](#) [Google Scholar](#)

2. 2.

Huang, F.-T. & Cheong, S.-W. Aperiodic topological order in the domain configurations of functional materials. *Nat. Rev. Mater.* **2**, 17004 (2017).

[ADS](#) [Google Scholar](#)

3. 3.

Choe, S.-B. et al. Vortex core-driven magnetization dynamics. *Science* **304**, 420–422 (2004).

[ADS](#) [CAS](#) [PubMed](#) [Google Scholar](#)

4. 4.

Büttner, F. et al. Dynamics and inertia of skyrmionic spin structures. *Nat. Phys.* **11**, 225–228 (2015).

[Google Scholar](#)

5. 5.

Yadav, A. K. et al. Observation of polar vortices in oxide superlattices. *Nature* **530**, 198–201 (2016).

[ADS](#) [CAS](#) [Google Scholar](#)

6. 6.

Das, S. et al. Observation of room-temperature polar skyrmions. *Nature* **568**, 368–372 (2019).

[ADS](#) [CAS](#) [PubMed](#) [Google Scholar](#)

7. 7.

Nagaosa, N. & Tokura, Y. Topological properties and dynamics of magnetic skyrmions. *Nat. Nanotechnol.* **8**, 899–911 (2013).

[ADS](#) [CAS](#) [PubMed](#) [Google Scholar](#)

8. 8.

Yadav, A. K. et al. Spatially resolved steady-state negative capacitance. *Nature* **565**, 468–471 (2019).

[ADS](#) [CAS](#) [PubMed](#) [Google Scholar](#)

9. 9.

Íñiguez, J., Zubko, P., Luk'yanchuk, I. & Cano, A. Ferroelectric negative capacitance. *Nat. Rev. Mater.* **4**, 243–256 (2019).

[ADS](#) [Google Scholar](#)

10. 10.

Stoica, V. A. et al. Optical creation of a supercrystal with three-dimensional nanoscale periodicity. *Nat. Mater.* **18**, 377–383 (2019).

[ADS](#) [CAS](#) [PubMed](#) [Google Scholar](#)

11. 11.

Büttner, F., Lemesh, I. & Beach, G. S. D. Theory of isolated magnetic skyrmions: from fundamentals to room temperature applications. *Sci. Rep.* **8**, 4464 (2018).

[ADS](#) [PubMed](#) [PubMed Central](#) [Google Scholar](#)

12. 12.

Seidel, J. Domain walls as nanoscale functional elements. *J. Phys. Chem. Lett.* **3**, 2905–2909 (2012).

[CAS](#) [Google Scholar](#)

13. 13.

Gu, Z. et al. Resonant domain-wall-enhanced tunable microwave ferroelectrics. *Nature* **560**, 622–627 (2018).

[ADS](#) [CAS](#) [PubMed](#) [Google Scholar](#)

14. 14.

Cochard, C., Spielmann, T. & Granzow, T. Dielectric tunability of ferroelectric barium titanate at millimeter-wave frequencies. *Phys. Rev. B* **100**, 184104 (2019).

[ADS](#) [CAS](#) [Google Scholar](#)

15. 15.

Catalan, G., Seidel, J., Ramesh, R. & Scott, J. F. Domain wall nanoelectronics. *Rev. Mod. Phys.* **84**, 119–156 (2012).

[ADS](#) [CAS](#) [Google Scholar](#)

16. 16.

Wu, X. et al. Low-energy structural dynamics of ferroelectric domain walls in hexagonal rare-earth manganites. *Sci. Adv.* **3**, e1602371 (2017).

[ADS](#) [PubMed](#) [PubMed Central](#) [Google Scholar](#)

17. 17.

Luk'yanchuk, I., Sené, A. & Vinokur, V. M. Electrodynamics of ferroelectric films with negative capacitance. *Phys. Rev. B* **98**, 024107

(2018).

[ADS](#) [Google Scholar](#)

18. 18.

Hlinka, J., Paściak, M., Körbel, S. & Marton, P. Terahertz-range polar modes in domain-engineered BiFeO₃. *Phys. Rev. Lett.* **119**, 057604 (2017).

[ADS](#) [Google Scholar](#)

19. 19.

Gui, Z. & Bellaiche, L. Terahertz dynamics of ferroelectric vortices from first principles. *Phys. Rev. B* **89**, 064303 (2014).

[ADS](#) [Google Scholar](#)

20. 20.

Zhang, Q., Herchig, R. & Ponomareva, I. Nanodynamics of ferroelectric ultrathin films. *Phys. Rev. Lett.* **107**, 177601 (2011).

[ADS](#) [Google Scholar](#)

21. 21.

Ogawa, N., Seki, S. & Tokura, Y. Ultrafast optical excitation of magnetic skyrmions. *Sci. Rep.* **5**, 9552 (2015).

[ADS](#) [CAS](#) [PubMed](#) [PubMed Central](#) [Google Scholar](#)

22. 22.

Hong, Z. et al. Stability of polar vortex lattice in ferroelectric superlattices. *Nano Lett.* **17**, 2246–2252 (2017).

[ADS](#) [CAS](#) [PubMed](#) [Google Scholar](#)

23. 23.

Scott, J. F. Soft-mode spectroscopy: experimental studies of structural phase transitions. *Rev. Mod. Phys.* **46**, 83–128 (1974).

[ADS](#) [CAS](#) [Google Scholar](#)

24. 24.

Li, X. et al. Terahertz field-induced ferroelectricity in quantum paraelectric SrTiO₃. *Science* **364**, 1079–1082 (2019).

[ADS](#) [CAS](#) [PubMed](#) [Google Scholar](#)

25. 25.

Nova, T. F., Disa, A. S., Fechner, M. & Cavalleri, A. Metastable ferroelectricity in optically strained SrTiO₃. *Science* **364**, 1075–1079 (2019).

[ADS](#) [CAS](#) [PubMed](#) [Google Scholar](#)

26. 26.

Bargheer, M. et al. Coherent atomic motions in a nanostructure studied by femtosecond X-ray diffraction. *Science* **306**, 1771–1773 (2004).

[ADS](#) [CAS](#) [PubMed](#) [Google Scholar](#)

27. 27.

Zhu, H. et al. Observation of chiral phonons. *Science* **359**, 579–582 (2018).

[ADS](#) [MathSciNet](#) [CAS](#) [PubMed](#) [Google Scholar](#)

28. 28.

Qi, T., Shin, Y.-H., Yeh, K.-L., Nelson, K. & Rappe, A. Collective coherent control: synchronization of polarization in ferroelectric PbTiO_3 by shaped THz fields. *Phys. Rev. Lett.* **102**, 247603 (2009).

[ADS](#) [PubMed](#) [Google Scholar](#)

29. 29.

Chen, F. et al. Ultrafast terahertz-field-driven ionic response in ferroelectric BaTiO_3 . *Phys. Rev. B* **94**, 180104 (2016).

[ADS](#) [Google Scholar](#)

30. 30.

Kozina, M. et al. Terahertz-driven phonon upconversion in SrTiO_3 . *Nat. Phys.* **15**, 387–392 (2019).

[CAS](#) [Google Scholar](#)

31. 31.

Kubacka, T. et al. Large-amplitude spin dynamics driven by a THz pulse in resonance with an electromagnon. *Science* **343**, 1333–1336 (2014).

[ADS](#) [CAS](#) [PubMed](#) [Google Scholar](#)

32. 32.

Damodaran, A. R. et al. Phase coexistence and electric-field control of toroidal order in oxide superlattices. *Nat. Mater.* **16**, 1003–1009 (2017).

[ADS](#) [CAS](#) [PubMed](#) [Google Scholar](#)

33. 33.

Li, Q. et al. Quantification of flexoelectricity in $\text{PbTiO}_3/\text{SrTiO}_3$ superlattice polar vortices using machine learning and phase-field modeling. *Nat. Commun.* **8**, 1468 (2017).

[ADS](#) [CAS](#) [PubMed](#) [PubMed Central](#) [Google Scholar](#)

34. 34.

Yang, T., Wang, B., Hu, J.-M. & Chen, L.-Q. Domain dynamics under ultrafast electric-field pulses. *Phys. Rev. Lett.* **124**, 107601 (2020).

[ADS](#) [CAS](#) [PubMed](#) [Google Scholar](#)

35. 35.

Trigo, M. et al. Probing unfolded acoustic phonons with X rays. *Phys. Rev. Lett.* **101**, 025505 (2008).

[ADS](#) [CAS](#) [PubMed](#) [Google Scholar](#)

36. 36.

Zhang, L. & Niu, Q. Angular momentum of phonons and the Einstein–de Haas effect. *Phys. Rev. Lett.* **112**, 085503 (2014).

[ADS](#) [Google Scholar](#)

37. 37.

von Hoegen, A., Mankowsky, R., Fechner, M., Först, M. & Cavalleri, A. Probing the interatomic potential of solids with strong-field nonlinear phononics. *Nature* **555**, 79–82 (2018).

[ADS](#) [Google Scholar](#)

38. 38.

Tamura, S., Hurley, D. C. & Wolfe, J. P. Acoustic-phonon propagation in superlattices. *Phys. Rev. B* **38**, 1427–1449 (1988).

[ADS](#) [CAS](#) [Google Scholar](#)

39. 39.

Daranciang, D. et al. Ultrafast photovoltaic response in ferroelectric nanolayers. *Phys. Rev. Lett.* **108**, 087601 (2012).

[ADS](#) [PubMed](#) [Google Scholar](#)

40. 40.

Chollet, M. et al. The X-ray Pump–Probe instrument at the Linac Coherent Light Source. *J. Synchrotron Radiat.* **22**, 503–507 (2015).

[CAS](#) [PubMed](#) [PubMed Central](#) [Google Scholar](#)

41. 41.

Kozina, M. et al. Ultrafast X-ray diffraction probe of terahertz field-driven soft mode dynamics in SrTiO₃. *Struct. Dyn.* **4**, 054301 (2017).

[CAS](#) [PubMed](#) [PubMed Central](#) [Google Scholar](#)

42. 42.

Sato, T. et al. A simple instrument to find spatiotemporal overlap of optical/X-ray light at free-electron lasers. *J. Synchrotron Radiat.* **26**, 647–652 (2019).

[CAS](#) [PubMed](#) [PubMed Central](#) [Google Scholar](#)

43. 43.

Glownia, J. M. et al. Pump–probe experimental methodology at the Linac Coherent Light Source. *J. Synchrotron Radiat.* **26**, 685–691 (2019).

[CAS](#) [PubMed](#) [PubMed Central](#) [Google Scholar](#)

44. 44.

Sepliarsky, M., Asthagiri, A., Phillpot, S. R., Stachiotti, M. G. & Mignoni, R. L. Atomic-level simulation of ferroelectricity in oxide materials. *Curr. Opin. Solid State Mater. Sci.* **9**, 107–113 (2005).

[ADS](#) [CAS](#) [Google Scholar](#)

45. 45.

Sepliarsky, M. & Cohen, R. E. First-principles based atomistic modeling of phase stability in PMN–xPT. *J. Phys. Condens. Matter* **23**, 435902 (2011).

[ADS](#) [CAS](#) [PubMed](#) [Google Scholar](#)

46. 46.

Stachiotti, M. G. & Sepliarsky, M. Toroidal ferroelectricity in PbTiO₃ nanoparticles. *Phys. Rev. Lett.* **106**, 137601 (2011).

[ADS](#) [CAS](#) [PubMed](#) [Google Scholar](#)

47. 47.

Gale, J. D. & Rohl, A. L. The General Utility Lattice Program (GULP). *Mol. Simul.* **29**, 291–341 (2003).

[CAS](#) [MATH](#) [Google Scholar](#)

[Download references](#)

Acknowledgements

We acknowledge discussions with M. Trigo, D. Xiao, Z. Hong, I. Luk'yanchuk and V. M. Vinokur. This work was primarily supported by the US Department of Energy, Office of Science, Basic Energy Sciences, Materials Sciences and Engineering Division: experimental design, data

collection, data analysis, and part of simulations by Q.L. and H.W. were supported under the DOE Early Career Award; ultrafast measurements and sample synthesis by V.A.S., Y.Y., S.P., L.W.M., C.D., S.Y., A.L., L.-Q.C., V.G., J.W.F. and H.W. were supported under award no. DE-SC-0012375; ancillary ultrafast X-ray measurements by H.L., S.M., Y.A. and P.E. were supported under award no. DE-FG02-04ER46147. M.M., S.D., and R.R. acknowledge support for part of sample synthesis through the Quantum Materials programme (KC 2202) funded by the US Department of Energy, Office of Science, Basic Energy Sciences, Materials Sciences Division under contract no. DE-AC02-05-CH11231. J.H. and M.P. were supported by the Czech Science Foundation (project no. 19-28594X) and acknowledge the access to computing facilities owned by parties and projects contributing to the National Grid Infrastructure MetaCentrum, provided under programme no. Cesnet LM2015042. T.Y. and L.-Q.C. acknowledge partial support from the US Department of Energy, Office of Science, Basic Energy Sciences, under award no. DE-SC0020145 as part of the Computational Materials Sciences Program and from NSF under award DMR-1744213. Y.Z. and H.W. acknowledge support by ANL-LDRD for preliminary X-ray measurements. Q.L. acknowledges support by the Basic Science Center Project of NSFC under grant no. 51788104 for completing phase-field simulations at Tsinghua University. S.M. acknowledges support from the Office of Science Graduate Student Research (SCGSR) programme (DOE contract no. DE-SC0014664) and from the UW-Madison Materials Research Science and Engineering Center (NSF DMR-1720415). H.L. acknowledges support by the National Research Foundation of Korea under grant 2017R1A6A3A11030959. Use of the Linac Coherent Light Source is supported by the US Department of Energy, Office of Science, Office of Basic Energy Sciences under contract no. DE-AC02-76SF00515. Use of the Advanced Photon Source is supported by the US Department of Energy, Office of Science, Office of Basic Energy Sciences under contract no. DE-AC02-06CH11357.

Author information

Author notes

1. Suji Park

Present address: Center for Functional Nanomaterials, Brookhaven National Laboratory, Upton, NY, USA

2. These authors contributed equally: Qian Li, Vladimir A. Stoica

Affiliations

1. Advanced Photon Source, Argonne National Laboratory, Lemont, IL, USA

Qian Li, Vladimir A. Stoica, Yi Zhu, Donald A. Walko, John W. Freeland & Haidan Wen

2. Department of Materials Science and Engineering, The Pennsylvania State University, University Park, PA, USA

Vladimir A. Stoica, Yakun Yuan, Tiannan Yang, Cheng Dai, Shukai Yu, Long-Qing Chen & Venkatraman Gopalan

3. Institute of Physics of the Czech Academy of Sciences, Prague, Czech Republic

Marek Paściak, Christelle Kadlec & Jirka Hlinka

4. Department of Materials Science and Engineering, University of California, Berkeley, Berkeley, CA, USA

Margaret R. McCarter, Sujit Das, Ajay K. Yadav, Ramamoorthy Ramesh & Lane W. Martin

5. Department of Physics, University of California, Berkeley, Berkeley, CA, USA

Ramamoorthy Ramesh

6. Materials Sciences Division, Lawrence Berkeley National Laboratory, Berkeley, CA, USA

Ramamoorthy Ramesh & Lane W. Martin

7. SIMES, SLAC National Accelerator Laboratory, Menlo Park, CA, USA

Suji Park & Aaron M. Lindenberg

8. Department of Materials Science and Engineering, University of Wisconsin-Madison, Madison, WI, USA

Hyeon Jun Lee, Youngjun Ahn, Samuel D. Marks & Paul G. Evans

9. Linac Coherent Light Source, SLAC National Accelerator Laboratory, Menlo Park, CA, USA

Takahiro Sato, Matthias C. Hoffmann, Matthieu Chollet, Michael E. Kozina, Silke Nelson & Diling Zhu

10. Department of Materials Science and Engineering, Stanford University, Stanford, CA, USA

Aaron M. Lindenberg

11. School of Materials Science and Engineering, Tsinghua University, Beijing, China

Qian Li

Authors

1. Qian Li

[View author publications](#)

You can also search for this author in [PubMed](#) [Google Scholar](#)

2. Vladimir A. Stoica

[View author publications](#)

You can also search for this author in [PubMed](#) [Google Scholar](#)

3. Marek Paściak

[View author publications](#)

You can also search for this author in [PubMed](#) [Google Scholar](#)

4. Yi Zhu

[View author publications](#)

You can also search for this author in [PubMed](#) [Google Scholar](#)

5. Yakun Yuan

[View author publications](#)

You can also search for this author in [PubMed](#) [Google Scholar](#)

6. Tiannan Yang

[View author publications](#)

You can also search for this author in [PubMed](#) [Google Scholar](#)

7. Margaret R. McCarter

[View author publications](#)

You can also search for this author in [PubMed](#) [Google Scholar](#)

8. Sujit Das

[View author publications](#)

You can also search for this author in [PubMed](#) [Google Scholar](#)

9. Ajay K. Yadav

[View author publications](#)

You can also search for this author in [PubMed](#) [Google Scholar](#)

10. Suji Park

[View author publications](#)

You can also search for this author in [PubMed](#) [Google Scholar](#)

11. Cheng Dai

[View author publications](#)

You can also search for this author in [PubMed](#) [Google Scholar](#)

12. Hyeon Jun Lee

[View author publications](#)

You can also search for this author in [PubMed](#) [Google Scholar](#)

13. Youngjun Ahn

[View author publications](#)

You can also search for this author in [PubMed](#) [Google Scholar](#)

14. Samuel D. Marks

[View author publications](#)

You can also search for this author in [PubMed](#) [Google Scholar](#)

15. Shukai Yu

[View author publications](#)

You can also search for this author in [PubMed](#) [Google Scholar](#)

16. Christelle Kadlec

[View author publications](#)

You can also search for this author in [PubMed](#) [Google Scholar](#)

17. Takahiro Sato

[View author publications](#)

You can also search for this author in [PubMed](#) [Google Scholar](#)

18. Matthias C. Hoffmann

[View author publications](#)

You can also search for this author in [PubMed](#) [Google Scholar](#)

19. Matthieu Chollet

[View author publications](#)

You can also search for this author in [PubMed](#) [Google Scholar](#)

20. Michael E. Kozina

[View author publications](#)

You can also search for this author in [PubMed](#) [Google Scholar](#)

21. Silke Nelson

[View author publications](#)

You can also search for this author in [PubMed](#) [Google Scholar](#)

22. Diling Zhu

[View author publications](#)

You can also search for this author in [PubMed](#) [Google Scholar](#)

23. Donald A. Walko

[View author publications](#)

You can also search for this author in [PubMed](#) [Google Scholar](#)

24. Aaron M. Lindenberg

[View author publications](#)

You can also search for this author in [PubMed](#) [Google Scholar](#)

25. Paul G. Evans

[View author publications](#)

You can also search for this author in [PubMed](#) [Google Scholar](#)

26. Long-Qing Chen

[View author publications](#)

You can also search for this author in [PubMed](#) [Google Scholar](#)

27. Ramamoorthy Ramesh

[View author publications](#)

You can also search for this author in [PubMed](#) [Google Scholar](#)

28. Lane W. Martin

[View author publications](#)

You can also search for this author in [PubMed](#) [Google Scholar](#)

29. Venkatraman Gopalan

[View author publications](#)

You can also search for this author in [PubMed](#) [Google Scholar](#)

30. John W. Freeland

[View author publications](#)

You can also search for this author in [PubMed](#) [Google Scholar](#)

31. Jirka Hlinka

[View author publications](#)

You can also search for this author in [PubMed](#) [Google Scholar](#)

32. Haidan Wen

[View author publications](#)

You can also search for this author in [PubMed](#) [Google Scholar](#)

Contributions

Q.L., V.A.S., Y.Y., M.R.M., S.P., H.J.L., Y.A., S.D.M., T.S., M.C.H., M.C., M.E.K., S.N., D.Z., A.M.L., P.G.E., V.G., J.W.F. and H.W. performed the experiment at the Linac Coherent Light Source. Y.Z., V.A.S., D.A.W. and H.W. performed preliminary experiments at the Advanced Photon Source. M.P. and J.H. performed atomistic modelling. Q.L., C.D., T.Y. and L.-Q.C. performed phase-field simulation. T.Y., L.-Q.C. and J.H. developed the

analytical model. S.D., M.R.M., A.K.Y., L.W.M. and R.R. prepared the samples. S.Y. and C.K. performed THz spectroscopy measurements. Q.L. and H.W. wrote the manuscript with input from all authors. H.W. conceived and supervised the project.

Corresponding author

Correspondence to [Haidan Wen](#).

Ethics declarations

Competing interests

The authors declare no competing interests.

Additional information

Peer review information *Nature* thanks Igor Luk'yanchuk, Daniel Schick and the other, anonymous, reviewer(s) for their contribution to the peer review of this work.

Publisher's note Springer Nature remains neutral with regard to jurisdictional claims in published maps and institutional affiliations.

Extended data figures and tables

[Extended Data Fig. 1 Diffraction patterns of probed Bragg peaks and the corresponding diffraction geometry.](#)

a, Diffraction patterns of 023, 113 and 004 peaks in logarithmic scale as recorded by a two-dimensional X-ray area detector. The projected q -axis labels indicate the approximate directions in reciprocal space. **b**, Schematics of diffraction geometry for probing the 023, 113 and 004 peaks. The dashed circle represents the horizontal plane. The red and blue stripes represent

vortex structure with opposite vorticities. The THz field is polarized vertically.

Extended Data Fig. 2 The response of the FE (a_1/a_2) structure upon THz field excitation.

a, 3D schematic of diffraction peaks of the film around the 023 or 113 substrate peaks in reciprocal space. The dashed arrows indicate the reciprocal axes through the centres of the FE or vortex SL peaks that are offset along the q_y -axis owing to the lattice constant difference along the y -axis. Only two SL and their satellite peaks are shown for simplicity. **b**, Normalized change of diffraction intensity of the 113 FE satellite peak (red curve) measured at the delay of 4 ps indicated by the red arrow in **e**, and normalized change of diffraction intensity of the 004 FE SL peak (blue curve) measured at the delay of 35 ps indicated by the blue arrow in **g**, as a function of the applied THz peak field. Lines are linear and quadratic fits to the measured data, in agreement with the field-driven structure factor modulation and the THz-induced Bragg peak shift (heating), respectively. **c**, Rocking curve of 023 FE SL peak. **d**, Normalized change of diffraction intensity as a function of delay measured at various incident angles indicated by the magenta, grey and blue arrows in **c**. **e**, Normalized change of diffraction intensity of the 113 FE SL peak and its satellites as a function of delay. The curves are vertically offset for clarity. **f**, Fourier spectra of **e**. **g**, Normalized change of diffraction intensity as a function of delay measured at the lower-angle side of the 004 FE SL peaks, indicated by the green arrow in **h**. **h**, Rocking curves of 004 FE SL peak measured at the delay of 35 ps with and without THz excitation. The peak shift shows a strain of 2.5×10^{-5} , corresponding to a 2 K temperature rise as calibrated by the temperature-dependent X-ray diffraction measurements shown in Extended Data Fig. [7b](#).

Extended Data Fig. 3 The dielectric properties of vortex structures as a function of strain and frequency from atomistic calculations.

a, Frequency–strain diagram with the diagonal oscillator strength (S_{ii}) of each mode reflected in the size of the markers (the area is proportional to $\log(S_{ii} + 1 \text{ THz}^2)$), where i represents x , y or z . The dielectric strength of the m th mode ($\Delta \{\epsilon\}_{ii,m}$) is directly related to the oscillator strength via $\Delta \{\epsilon\}_{ii,m} = S_{ii,m} / \omega_m^2$, where ω_m is the mode’s frequency. The 15 lowest-frequency modes are considered; the zz signal is multiplied 5 times for better visibility. The orange area indicates the high-frequency regime. **b**, Frequency-dependent permittivity for two different strain values, $\varepsilon_x = -0.25\%$ and 0.2% . The imaginary part is presented in the main plots, while the left-hand insets show diagonal components $(\{\epsilon\}_{xx}^{\prime\prime}, \{\epsilon\}_{yy}^{\prime\prime}, \{\epsilon\}_{zz}^{\prime\prime})$ and the right-hand insets present off-diagonal spectra $(\{\epsilon\}_{xy}^{\prime\prime}, \{\epsilon\}_{xz}^{\prime\prime}, \{\epsilon\}_{yz}^{\prime\prime})$. The arrows indicate modes that are analysed in the Extended Data Fig. 4. All dielectric properties are calculated for the PTO layer only.

Extended Data Fig. 4 Decomposition of selected modes with strain $\varepsilon_x = -0.25\%$ in the atomistic model.

The modes are characterized by the highest oscillator strengths in the x -direction (below the frequency of 0.41 THz, marked by the arrows in Extended Data Fig. 3b), and the first two of them are also described in the main text. **a–d**, Each column contains microscopic configurations at $t = \tau/4$ of (a) Pb and Ti displacements; (b) O displacements of the mode’s eigenvectors; (c) change in polarization caused by these atomic displacements (overlaid on a $(\nabla \times \mathbf{P})$ map of the equilibrium structure); (d) polarization patterns and the respective $(\nabla \times \mathbf{P})$ map of a structure subjected to the mode’s perturbation. The origin **O** and vector **R** in a are related to the calculation of the angular momentum of the vortexon in the boxed region detailed in Supplementary Note 1B. The displacement vectors are scaled arbitrarily, while perturbed (**P**) configurations are calculated for maximum ionic displacements of 30 pm. We note that there are additional modes with the y -component of the

oscillator strength that contribute to the diversity of the collective dynamics in the frequency range 0.3–0.4 THz.

Extended Data Fig. 5 Polarization dependent response and analysis of the vortexon mode.

a, Normalized change of diffraction intensity of 004 vortex Bragg peak as a function of time when the THz field is applied parallel to and perpendicular to the crystalline x -axis. **b**, Baseline-subtracted normalized change of diffraction intensity of the 004 vortex superlattice peak (red curve) as a function delay. Raw data shown in grey are from Fig. 4b. The green curve shows a sinusoidal wave (see Supplementary Note 5), with its minima (green arrows) deviating from the data (red arrows) at later times. The vertical dashed line indicates the time when the THz field turns on.

Extended Data Fig. 6 Dynamical phase-field simulation results.

a, b, Fourier transform of the simulated polarization dynamics, which is represented by spatially averaged **(a)** $\langle\langle P \rangle\rangle_z^2$ and **(b)** $\langle\langle P \rangle\rangle_x^2$ in the simulation box on application of the THz-field pulse aligned along the x -, y - or z -axis. **c**, Calculated frequency spectra of $\langle\langle P \rangle\rangle_x^2$ with various values of the direct-current (DC) electric field along the x -axis. **d**, Frequency and amplitude of the vortexon mode as a function of the applied electric field (E_x). Such an in-plane electric field can be applied using a pair of coplanar electrodes, as schematically shown in the inset to **d**. **e**, Histograms of the Pb and Sr ionic displacement \mathbf{u} away from its equilibrium positions along the x - and z -axes, corresponding to the maximum diffraction intensity change of 4% of 004 SL peak at a delay of 9 ps in the simulation.

Extended Data Fig. 7 Equilibrium characterizations of $(\text{PbTiO}_3)_{16}/(\text{SrTiO}_3)_{16}$ superlattice.

a, Room-temperature RSM of the superlattice grown on DSO substrate, cutting through the substrate specular 004 peak, which shows vortex (V) and FE superlattice diffraction peaks in the q_x-q_z plane. The satellites (V

Sat) due to the in-plane vortex ordering appear along the q_x direction around the corresponding superlattice (V) peaks. **b**, The measured average lattice parameters with linear fits for the vortex and FE structures as a function of temperature. The error bars represent systematic errors of the measurement. **c**, Room-temperature RSM of the superlattice grown on $\text{Sr}_2\text{Al}_{0.3}\text{Ga}_{0.7}\text{TaO}_6$ (SAGT) substrate, cutting through the substrate specular 002 peak, which shows the vortex SL diffraction peaks and satellites. **d**, Room-temperature imaginary dielectric constant extracted from the THz time-domain absorption spectroscopy measurements of superlattices grown on DSO and SAGT substrates. The error bars represent the estimated experimental errors in the frequency ranges of the shaded and unshaded regimes.

Extended Data Fig. 8 X-ray diffraction simulations based on dynamical phase-field modelling.

a, Model geometry of the PTO/STO superlattice film and the DSO substrate. The colour scale denotes the vorticity of the polarization vectors. The boundary conditions ([Methods](#)) are marked on the right. **b**, Schematics for the method used to map the phase-field modelling output to atomistic configurations, based on which kinematic X-ray scattering intensities are calculated ([Supplementary Note 2](#)). CoM, center of mass; V and C denote the vortex and cubic phases of PbTiO_3 , respectively. **c**, Measured and simulated HOL -cut (along the q_x – q_z plane in reciprocal lattice units (r.l.u)) RSMs near the 004 reflection with the intensity shown on a logarithmic colour scale. The fringes in the simulated RSM are due to the finite lateral size of the simulation box.

Extended Data Fig. 9 Structural dynamics excited by 400-nm optical pulses.

a, Normalized changes of 004-vortex peak intensity as a function delay. **b**, Fourier spectra of **a**. L and T represent the acoustic waves that travel along the out-of-plane direction with longitudinal and transverse sound speeds, respectively. **c**, Calculated phonon dispersion curves. The vertical dashed line indicates the boundary of the folded Brillouin zones. The shaded region

corresponds to the scattering vectors probed in the experiment. The solid circles show the measured modes upon 400-nm excitation, while the stars show the measured modes upon THz excitation. The error bars show the full-width at half-maximum of the peaks in the Fourier spectra. d_{SL} , superlattice periodicity.

Supplementary information

[Supplementary Information](#)

This file contains Supplementary text, Supplementary Notes 1 to 7, Supplementary Tables 1 – 3 and Supplementary References.

[Supplementary Video 1.](#)

[Supplementary Video 2.](#)

[Supplementary Video 3.](#)

[Supplementary Video 4.](#)

Rights and permissions

[Reprints and Permissions](#)

About this article



Check for
updates

Cite this article

Li, Q., Stoica, V.A., Paściak, M. *et al.* Subterahertz collective dynamics of polar vortices. *Nature* **592**, 376–380 (2021). <https://doi.org/10.1038/s41586-021-03342-4>

[Download citation](#)

- Received: 23 June 2020
- Accepted: 08 February 2021
- Published: 14 April 2021
- Issue Date: 15 April 2021
- DOI: <https://doi.org/10.1038/s41586-021-03342-4>

Further reading

- [**Dynamics of polarization vortices revealed in a ferroelectric material**](#)
 - Igor Lukâyanchuk
 - & Valerii M. Vinokur

Nature (2021)

Comments

By submitting a comment you agree to abide by our [Terms](#) and [Community Guidelines](#). If you find something abusive or that does not comply with our terms or guidelines please flag it as inappropriate.

[Access through your institution](#)

[Change institution](#)

[Buy or subscribe](#)

Associated Content

Nature | News & Views

Dynamics of polarization vortices revealed in a ferroelectric material

- Igor Luk'yanchuk
- & Valerii M. Vinokur

This article was downloaded by **calibre** from <https://www.nature.com/articles/s41586-021-03342-4>

| [Section menu](#) | [Main menu](#) |

- Article
- [Published: 05 April 2021](#)

Pseudo-halide anion engineering for α -FAPbI₃ perovskite solar cells

- [Jaeki Jeong](#) [ORCID: orcid.org/0000-0001-9062-9934](#)^{1,2,3 na1},
- [Minjin Kim](#)^{4 na1},
- [Jongdeuk Seo](#) [ORCID: orcid.org/0000-0002-5374-7904](#)^{1 na1},
- [Haizhou Lu](#) [ORCID: orcid.org/0000-0001-9692-7860](#)^{2,3 na1},
- [Paramvir Ahlawat](#) [ORCID: orcid.org/0000-0003-2355-3663](#)⁵,
- [Aditya Mishra](#)⁶,
- [Yingguo Yang](#) [ORCID: orcid.org/0000-0002-1749-2799](#)⁷,
- [Michael A. Hope](#) [ORCID: orcid.org/0000-0002-4742-9336](#)⁶,
- [Felix T. Eickemeyer](#)²,
- [Maengsuk Kim](#)¹,
- [Yung Jin Yoon](#) [ORCID: orcid.org/0000-0002-2760-9639](#)¹,
- [In Woo Choi](#)⁴,
- [Barbara Primera Darwich](#)⁸,
- [Seung Ju Choi](#)⁴,
- [Yimhyun Jo](#)⁴,
- [Jun Hee Lee](#) [ORCID: orcid.org/0000-0001-5121-244X](#)¹,
- [Bright Walker](#) [ORCID: orcid.org/0000-0002-0613-8866](#)⁹,
- [Shaik M. Zakeeruddin](#)²,
- [Lyndon Emsley](#) [ORCID: orcid.org/0000-0003-1360-2572](#)⁶,
- [Ursula Rothlisberger](#)⁵,
- [Anders Hagfeldt](#) [ORCID: orcid.org/0000-0001-6725-8856](#)^{3 nAff10},
- [Dong Suk Kim](#) [ORCID: orcid.org/0000-0002-1230-340X](#)⁴,
- [Michael Grätzel](#) [ORCID: orcid.org/0000-0002-0068-0195](#)² &
- [Jin Young Kim](#) [ORCID: orcid.org/0000-0002-6595-4468](#)¹

[Nature](#) volume 592, pages381–385(2021)[Cite this article](#)

- 11k Accesses
- 71 Altmetric
- [Metrics details](#)

Subjects

- [Devices for energy harvesting](#)
- [Electronic devices](#)
- [Solar cells](#)

This article has been [updated](#)

Abstract

Metal halide perovskites of the general formula ABX_3 —where A is a monovalent cation such as caesium, methylammonium or formamidinium; B is divalent lead, tin or germanium; and X is a halide anion—have shown great potential as light harvesters for thin-film photovoltaics^{1,2,3,4,5}. Among a large number of compositions investigated, the cubic α -phase of formamidinium lead triiodide (FAPbI_3) has emerged as the most promising semiconductor for highly efficient and stable perovskite solar cells^{6,7,8,9}, and maximizing the performance of this material in such devices is of vital importance for the perovskite research community. Here we introduce an anion engineering concept that uses the pseudo-halide anion formate (HCOO^-) to suppress anion-vacancy defects that are present at grain boundaries and at the surface of the perovskite films and to augment the crystallinity of the films. The resulting solar cell devices attain a power conversion efficiency of 25.6 per cent (certified 25.2 per cent), have long-term operational stability (450 hours) and show intense electroluminescence with external quantum efficiencies of more than 10 per cent. Our findings provide a direct route to eliminate the most abundant and deleterious lattice

defects present in metal halide perovskites, providing a facile access to solution-processable films with improved optoelectronic performance.

[Access through your institution](#)

[Change institution](#)

[Buy or subscribe](#)

Access options

Subscribe to Journal

Get full journal access for 1 year

\$199.00

only \$3.90 per issue

[Subscribe](#)

All prices are NET prices.

VAT will be added later in the checkout.

Tax calculation will be finalised during checkout.

Rent or Buy article

Get time limited or full article access on ReadCube.

from \$8.99

[Rent or Buy](#)

All prices are NET prices.

Additional access options:

- [Log in](#)
- [Access through your institution](#)
- [Learn about institutional subscriptions](#)

Fig. 1: Characterization of the FAPbI₃ films.

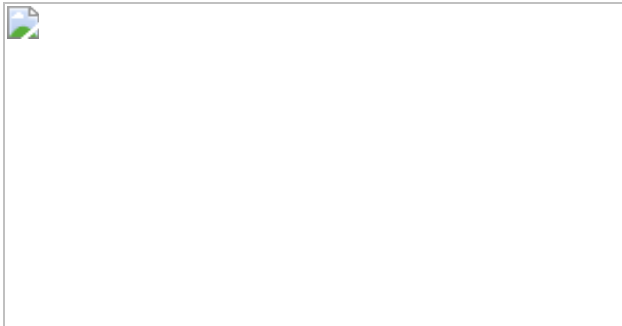


Fig. 2: Solid-state NMR spectra and molecular dynamics simulations.



Fig. 3: Characterization of the photovoltaic performance of the FAPbI₃ PSCs.

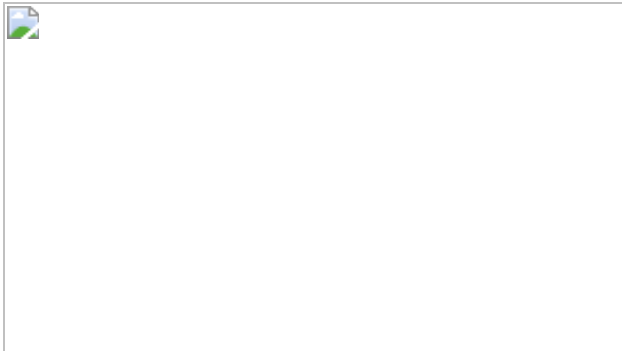
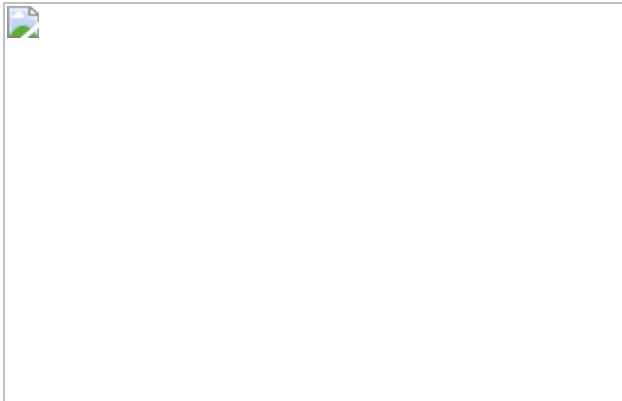


Fig. 4: Stability of the FAPbI3 PSCs.



Data availability

The data that support the findings of this study are available from the corresponding author upon reasonable request.

Code availability

The code used for this study is available from the corresponding author upon reasonable request.

Change history

- 08 April 2021

This Article was amended to correct the Peer review information.

References

1. 1.

Kojima, A., Teshima, K., Shirai, Y. & Miyasaka, T. Organometal halide perovskites as visible-light sensitizers for photovoltaic cells. *J. Am. Chem. Soc.* **131**, 6050–6051 (2009).

[Article](#) [CAS](#) [Google Scholar](#)

2. 2.

Grätzel, M. The light and shade of perovskite solar cells. *Nat. Mater.* **13**, 838–842 (2014).

[ADS](#) [Article](#) [CAS](#) [Google Scholar](#)

3. 3.

Park, N.-G. et al. Towards stable and commercially available perovskite solar cells. *Nat. Energy* **1**, 16152 (2016).

[ADS](#) [Article](#) [CAS](#) [Google Scholar](#)

4. 4.

Correa-Baena, J. P. et al. Promises and challenges of perovskite solar cells. *Science* **358**, 739–744 (2017).

[ADS](#) [Article](#) [CAS](#) [Google Scholar](#)

5. 5.

Lu, H., Krishna, A., Zakeeruddin, S. M., Grätzel, M. & Hagfeldt, A. Compositional and interface engineering of organic-inorganic lead halide perovskite solar cells. *iScience* **23**, 101359 (2020).

[ADS](#) [Article](#) [CAS](#) [Google Scholar](#)

6. 6.

Eperon, G. E. et al. Formamidinium lead trihalide: a broadly tunable perovskite for efficient planar heterojunction solar cells. *Energy Environ. Sci.* **7**, 982–988 (2014).

[Article](#) [CAS](#) [Google Scholar](#)

7. 7.

Pellet, N. et al. Mixed-organic-cation perovskite photovoltaics for enhanced solar-light harvesting. *Angew. Chem. Int. Ed.* **53**, 3151–3157 (2014).

[Article](#) [CAS](#) [Google Scholar](#)

8. 8.

Jeon, N. J. et al. Compositional engineering of perovskite materials for high-performance solar cells. *Nature* **517**, 476–480 (2015).

[ADS](#) [Article](#) [CAS](#) [Google Scholar](#)

9. 9.

Lu, H. et al. Vapor-assisted deposition of highly efficient, stable black-phase FAPbI₃ perovskite solar cells. *Science* **370**, eabb8985 (2020).

[Article](#) [CAS](#) [Google Scholar](#)

10. 10.

De Wolf, S. et al. Organometallic halide perovskites: sharp optical absorption edge and its relation to photovoltaic performance. *J. Phys. Chem. Lett.* **5**, 1035–1039 (2014).

[Article](#) [CAS](#) [Google Scholar](#)

11. 11.

Stranks, S. D. et al. Electron-hole diffusion lengths exceeding 1 micrometer in an organometal trihalide perovskite absorber. *Science* **342**, 341–344 (2013).

[ADS](#) [Article](#) [CAS](#) [Google Scholar](#)

12. 12.

Herz, L. M. et al. Charge-carrier mobilities in metal halide perovskites: fundamental mechanisms and limits. *ACS Energy Lett.* **2**, 1539–1548 (2017).

[Article](#) [CAS](#) [Google Scholar](#)

13. 13.

NREL. *Best Research-Cell Efficiency Chart*
<https://www.nrel.gov/pv/cell-efficiency.html> (accessed 17 March 2021).

14. 14.

Zheng, X. et al. Managing grains and interfaces via ligand anchoring enables 22.3%-efficiency inverted perovskite solar cells. *Nat. Energy* **5**, 131–140 (2020).

[ADS](#) [Article](#) [CAS](#) [Google Scholar](#)

15. 15.

Liu, Z. et al. A holistic approach to interface stabilization for efficient perovskite solar modules with over 2,000-hour operational stability. *Nat. Energy* **5**, 596–604 (2020).

[ADS](#) [Article](#) [CAS](#) [Google Scholar](#)

16. 16.

Saliba, M. et al. Cesium-containing triple cation perovskite solar cells: improved stability, reproducibility and high efficiency. *Energy Environ. Sci.* **9**, 1989–1997 (2016).

[Article](#) [CAS](#) [Google Scholar](#)

17. 17.

Kim, M. et al. Methylammonium chloride induces intermediate phase stabilization for efficient perovskite solar cells. *Joule* **3**, 2179–2192 (2019).

[Article](#) [CAS](#) [Google Scholar](#)

18. 18.

Min, H. et al. Efficient, stable solar cells by using inherent bandgap of α -phase formamidinium lead iodide. *Science* **366**, 749–753 (2019).

[ADS](#) [Article](#) [CAS](#) [Google Scholar](#)

19. 19.

Yang, S. et al. Thiocyanate assisted performance enhancement of formamidinium based planar perovskite solar cells through a single one-step solution process. *J. Mater. Chem. A* **4**, 9430–9436 (2016).

[Article](#) [CAS](#) [Google Scholar](#)

20. 20.

Kim, D. H. et al. Bimolecular additives improve wide-band-gap perovskites for efficient tandem solar cells with CIGS. *Joule* **3**, 1734–1745 (2019).

[Article](#) [CAS](#) [Google Scholar](#)

21. 21.

Kim, D. et al. Efficient, stable silicon tandem cells enabled by anion-engineered wide-bandgap perovskites. *Science* **368**, 155–160 (2020).

[ADS](#) [Article](#) [CAS](#) [Google Scholar](#)

22. 22.

Walker, B., Kim, G. H. & Kim, J. Y. Pseudohalides in lead-based perovskite semiconductors. *Adv. Mater.* **31**, 1807029 (2019).

[Article](#) [CAS](#) [Google Scholar](#)

23. 23.

Moore, D. T. et al. Direct crystallization route to methylammonium lead iodide perovskite from an ionic liquid. *Chem. Mater.* **27**, 3197–3199 (2015).

[ADS](#) [Article](#) [CAS](#) [Google Scholar](#)

24. 24.

Seo, J. et al. Ionic liquid control crystal growth to enhance planar perovskite solar cells efficiency. *Adv. Energy Mater.* **6**, 1600767 (2016).

[Article](#) [CAS](#) [Google Scholar](#)

25. 25.

Nayak, P. K. et al. Mechanism for rapid growth of organic–inorganic halide perovskite crystals. *Nat. Commun.* **7**, 13303 (2016).

[ADS](#) [Article](#) [CAS](#) [Google Scholar](#)

26. 26.

Meng, L. et al. Improved perovskite solar cell efficiency by tuning the colloidal size and free ion concentration in precursor solution using formic acid additive. *J. Energy Chem.* **41**, 43–51 (2020).

[Article](#) [Google Scholar](#)

27. 27.

Khan, Y. et al. Waterproof perovskites: high fluorescence quantum yield and stability from a methylammonium lead bromide/formate mixture in water. *J. Mater. Chem. C* **8**, 5873–5881 (2020).

[Article](#) [CAS](#) [Google Scholar](#)

28. 28.

Askar, A. M. et al. Composition-tunable formamidinium lead mixed halide perovskites via solvent-free mechanochemical synthesis: decoding the Pb environments using solid-state NMR spectroscopy. *J. Phys. Chem. Lett.* **9**, 2671–2677 (2018).

[Article](#) [CAS](#) [Google Scholar](#)

29. 29.

Kubicki, D. J. et al. Cation dynamics in mixed-cation $(MA)_x(FA)_{1-x}PbI_3$ hybrid perovskites from solid-state NMR. *J. Am. Chem. Soc.* **139**, 10055–10061 (2017).

[Article](#) [CAS](#) [Google Scholar](#)

30. 30.

Zhou, Z. et al. Synthesis, microwave spectra, X-ray structure, and high-level theoretical calculations for formamidinium formate. *J. Chem. Phys.* **150**, 094305 (2019).

[ADS](#) [Article](#) [CAS](#) [Google Scholar](#)

31. 31.

Ross, R. et al. Some thermodynamics of photochemical systems. *J. Chem. Phys.* **46**, 4590–4593 (1967).

[ADS](#) [Article](#) [CAS](#) [Google Scholar](#)

32. 32.

Tress, W. et al. Predicting the open-circuit voltage of $\text{CH}_3\text{NH}_3\text{PbI}_3$ perovskite solar cells using electroluminescence and photovoltaic quantum efficiency spectra: the role of radiative and non-radiative recombination. *Adv. Energy Mater.* **5**, 1400812 (2015).

[Article](#) [CAS](#) [Google Scholar](#)

33. 33.

Jiang, Q. et al. Surface passivation of perovskite film for efficient solar cells. *Nat. Photonics* **13**, 460–466 (2019).

[ADS](#) [Article](#) [CAS](#) [Google Scholar](#)

34. 34.

Yang, D. et al. Surface optimization to eliminate hysteresis for record efficiency planar perovskite solar cells. *Energy Environ. Sci.* **9**, 3071–3078 (2016).

[Article](#) [CAS](#) [Google Scholar](#)

35. 35.

Kuik, M., Koster, L. J., Wetzelaer, G. A. & Blom, P. W. Trap-assisted recombination in disordered organic semiconductors. *Phys. Rev. Lett.* **107**, 256805 (2011).

[ADS](#) [Article](#) [CAS](#) [Google Scholar](#)

36. 36.

Green, M. Accuracy of analytical expressions for solar cell fill factors. *Solar Cells* **7**, 337–340 (1982).

[ADS](#) [Article](#) [CAS](#) [Google Scholar](#)

37. 37.

Wang, Y. et al. Stabilizing heterostructures of soft perovskite semiconductors. *Science* **365**, 687–691 (2019).

[ADS Article](#) [CAS](#) [Google Scholar](#)

[Download references](#)

Acknowledgements

We thank W. R. Tress for discussions, and the staff at beamlines BL17B1, BL14B1, BL11B, BL08U and BL01B1 of the SSRF for providing the beamline, and the Swiss National Supercomputing Centre (CSCS) and EPFL computing center (SCITAS) for their support. This research was supported by the Technology Development Program to Solve Climate Changes of the National Research Foundation (NRF) funded by the Ministry of Science, ICT & Future Planning (2020M1A2A2080746). This work was also supported by ‘The Research Project Funded by U-K Brand’ (1.200030.01) of Ulsan National Institute of Science & Technology (UNIST). D.S.K. acknowledges the Development Program of the Korea Institute of Energy Research (KIER) (C0-2401 and C0-2402). L.E. acknowledges support from the Swiss National Science Foundation, grant number 200020_178860. U.R. acknowledges funding from the Swiss National Science Foundation via individual grant number 200020_185092 and the NCCR MUST. A.H. acknowledges the Swiss National Science Foundation, project ‘Fundamental studies of dye-sensitized and perovskite solar cells’, project number 200020_185041. M.G. acknowledges financial support from the European Union’s Horizon 2020 research and innovation programme under grant agreement number 881603, and the King Abdulaziz City for Science and Technology (KACST).

Author information

Author notes

1. Anders Hagfeldt

Present address: Department of Chemistry, Ångström Laboratory,
Uppsala University, Uppsala, Sweden

2. These authors contributed equally: Jaeki Jeong, Minjin Kim, Jongdeuk Seo, Haizhou Lu

Affiliations

1. Department of Energy Engineering, School of Energy and Chemical Engineering, Ulsan National Institute of Science and Technology (UNIST), Ulsan, Republic of Korea

Jaeki Jeong, Jongdeuk Seo, Maengsuk Kim, Yung Jin Yoon, Jun Hee Lee & Jin Young Kim

2. Laboratory of Photonics and Interfaces, Institute of Chemical Sciences and Engineering, École Polytechnique Fédérale de Lausanne (EPFL), Lausanne, Switzerland

Jaeki Jeong, Haizhou Lu, Felix T. Eickemeyer, Shaik M. Zakeeruddin & Michael Grätzel

3. Laboratory of Photomolecular Science, Institute of Chemical Sciences Engineering, École Polytechnique Fédérale de Lausanne (EPFL), Lausanne, Switzerland

Jaeki Jeong, Haizhou Lu & Anders Hagfeldt

4. Korea Institute of Energy Research (KIER), Ulsan, Republic of Korea

Minjin Kim, In Woo Choi, Seung Ju Choi, Yimhyun Jo & Dong Suk Kim

5. Laboratory of Computational Chemistry and Biochemistry, Institute of Chemical Sciences and Engineering, École Polytechnique Fédérale de Lausanne (EPFL), Lausanne, Switzerland

Paramvir Ahlawat & Ursula Rothlisberger

6. Laboratory of Magnetic Resonance, Institute of Chemical Sciences and Engineering, École Polytechnique Fédérale de Lausanne (EPFL), Lausanne, Switzerland

Aditya Mishra, Michael A. Hope & Lyndon Emsley

7. Shanghai Synchrotron Radiation Facility (SSRF), Zhangjiang Lab, Shanghai Advanced Research Institute, Chinese Academy of Sciences, Shanghai, P. R. China

Yingguo Yang

8. Laboratory for Molecular Engineering of Optoelectronic Nanomaterials, École Polytechnique Fédérale de Lausanne (EPFL), Lausanne, Switzerland

Barbara Primera Darwich

9. Department of Chemistry and Research Institute of Basic Sciences, Kyung Hee University, Seoul, Republic of Korea

Bright Walker

Authors

1. Jaeki Jeong

[View author publications](#)

You can also search for this author in [PubMed](#) [Google Scholar](#)

2. Minjin Kim

[View author publications](#)

You can also search for this author in [PubMed](#) [Google Scholar](#)

3. Jongdeuk Seo

[View author publications](#)

You can also search for this author in [PubMed](#) [Google Scholar](#)

4. Haizhou Lu

[View author publications](#)

You can also search for this author in [PubMed](#) [Google Scholar](#)

5. Paramvir Ahlawat

[View author publications](#)

You can also search for this author in [PubMed](#) [Google Scholar](#)

6. Aditya Mishra

[View author publications](#)

You can also search for this author in [PubMed](#) [Google Scholar](#)

7. Yingguo Yang

[View author publications](#)

You can also search for this author in [PubMed](#) [Google Scholar](#)

8. Michael A. Hope

[View author publications](#)

You can also search for this author in [PubMed](#) [Google Scholar](#)

9. Felix T. Eickemeyer

[View author publications](#)

You can also search for this author in [PubMed](#) [Google Scholar](#)

10. Maengsuk Kim

[View author publications](#)

You can also search for this author in [PubMed](#) [Google Scholar](#)

11. Yung Jin Yoon

[View author publications](#)

You can also search for this author in [PubMed](#) [Google Scholar](#)

12. In Woo Choi

[View author publications](#)

You can also search for this author in [PubMed](#) [Google Scholar](#)

13. Barbara Primera Darwich

[View author publications](#)

You can also search for this author in [PubMed](#) [Google Scholar](#)

14. Seung Ju Choi

[View author publications](#)

You can also search for this author in [PubMed](#) [Google Scholar](#)

15. Yimhyun Jo

[View author publications](#)

You can also search for this author in [PubMed](#) [Google Scholar](#)

16. Jun Hee Lee

[View author publications](#)

You can also search for this author in [PubMed](#) [Google Scholar](#)

17. Bright Walker

[View author publications](#)

You can also search for this author in [PubMed](#) [Google Scholar](#)

18. Shaik M. Zakeeruddin

[View author publications](#)

You can also search for this author in [PubMed](#) [Google Scholar](#)

19. Lyndon Emsley

[View author publications](#)

You can also search for this author in [PubMed](#) [Google Scholar](#)

20. Ursula Rothlisberger

[View author publications](#)

You can also search for this author in [PubMed](#) [Google Scholar](#)

21. Anders Hagfeldt

[View author publications](#)

You can also search for this author in [PubMed](#) [Google Scholar](#)

22. Dong Suk Kim

[View author publications](#)

You can also search for this author in [PubMed](#) [Google Scholar](#)

23. Michael Grätzel

[View author publications](#)

You can also search for this author in [PubMed](#) [Google Scholar](#)

24. Jin Young Kim

[View author publications](#)

You can also search for this author in [PubMed](#) [Google Scholar](#)

Contributions

J.J., B.W. and J.Y.K. conceived the project. J.J., Minjin Kim and H.L. prepared the samples, performed the relevant photovoltaic measurements, analysed the data and wrote the manuscript. J.S. synthesised the FAHCOO material. Minjin Kim and D.S.K. certified the efficiency of the PSCs. Y.J.Y. carried out photoluminescence and UV–vis absorption spectroscopy. S.J.C. and I.W.C. performed the time-resolved photoluminescence, SEM and XRD measurements. Y.J. and H.L. collected the light-intensity-dependent *J–V* data. P.A. and U.R. designed and performed all the DFT calculations and molecular dynamics simulations. Maengsuk Kim and J.H.L contributed to the DFT calculations. A.M., M.A.H. and L.E. conducted the solid-state NMR measurements and analysis. B.P.D. performed the atomic force

microscopy measurements. H.L. conducted the long-term operational stability measurements, EQE_{EL} measurements and analysed the data. Y.Y. performed the two-dimensional grazing-incidence XRD measurements. F.T.E contributed to the analysis of the time-resolved photoluminescence data. S.M.Z. coordinated the project. A.H. and M.G. proposed experiments and M.G. wrote the final version of the manuscript. A.H., D.S.K., M.G. and J.Y.K. directed the work. All authors analysed the data and contributed to the discussions.

Corresponding authors

Correspondence to [Anders Hagfeldt](#) or [Dong Suk Kim](#) or [Michael Grätzel](#) or [Jin Young Kim](#).

Ethics declarations

Competing interests

The authors declare no competing interests.

Additional information

Peer review information *Nature* thanks the anonymous reviewers for their contribution to the peer review of this work.

Publisher's note Springer Nature remains neutral with regard to jurisdictional claims in published maps and institutional affiliations.

Extended data figures and tables

[Extended Data Fig. 1 Characterization of the perovskite films with and without FAFo.](#)

a, The Tauc plot of the 2% Fo-FAPbI₃ perovskite film. **b**, A full photoluminescence decay of the reference, 2% Fo-FAPbI₃ and 4% Fo-

FAPbI₃ perovskite films. **c**, The distribution of the grain sizes of the reference and 2% Fo-FAPbI₃ films. The box + whisker plots show the distribution of the grain sizes for both reference and 2% Fo-FAPbI₃ perovskite films. The distribution is based on 22 data points each. **d, e**, The top-view SEM image (**d**) and the cross-sectional SEM image (**e**) of the 4% Fo-FAPbI₃ perovskite film. **f, g**, AFM images of the reference (**f**) and the 2% Fo-FAPbI₃ (**g**) perovskite films. **h**, The XRD patterns of the reference, 2% Fo-FAPbI₃ and 4% Fo-FAPbI₃ perovskite films. Peaks labelled with an asterisk are assigned to the FTO substrates, which can be seen for the 4% sample owing to the lower intensity of the perovskite reflections. **i**, Integrated one-dimensional grazing-incidence XRD pattern of the reference and 2% Fo-FAPbI₃ films.

Extended Data Fig. 2 The composition of the Fo-FAPbI₃ perovskite film.

a, b, ¹H–¹³C cross-polarization spectra of mechanosynthesized FAPbI₃ with 5% FAHCOO (**a**) and a scraped thin film of 2% Fo-FAPbI₃ (**b**), recorded at 12 kHz MAS and 100 K. In **b** the formate signal can be seen as a minor shoulder on the FAPbI₃ peak. A minor signal arising from the PTFE that is used to seal the rotor is also visible. **c, d**, TOF-SIMS measurements of the reference (**c**) and the 2% Fo-FAPbI₃ (**d**) films. **e**, Quantitative, directly detected ¹³C solid-state NMR measurement of 2% Fo-FAPbI₃ scraped thin film at 12 kHz MAS and 100 K.

Extended Data Fig. 3 Ab initio molecular dynamics simulations.

a, Molecular dynamics snapshot showing the coordination of Pb²⁺ ions with HCOO[−] anions in the perovskite precursor solution. As a guide to the eye, we highlight only Pb²⁺ and HCOO[−] ions; the remaining ions and solvent molecules are shown as transparent. **b**, The radial distribution function $g(r)$ between the oxygen atoms of HCOO[−] and Pb²⁺ over the full ab initio molecular dynamics trajectory of around 11 ps. **c**, Initial configuration of

FAPbI₃ with surface iodide replaced by HCOO⁻ anions. **d**, The top view of surface atoms on the FA⁺-terminated side. **e**, The top view of the surface atoms on the Pb²⁺-terminated side. Pb²⁺-HCOO⁻ and FA⁺-HCOO⁻ bonding and hydrogen-bonding networks are illustrated with magenta dashed lines. All ions are shown in ball-and-stick representation. Pb²⁺ ions, yellow; iodide, light pink; oxygen, red; carbon, light blue; nitrogen, dark blue; sulfur, light yellow; hydrogen, white.

Extended Data Fig. 4 DFT-relaxed slabs of FAPbI₃ with different anions adsorbed at an iodide-vacancy site on the surface.

a, Structure of a pure FAPbI₃ slab with a Pb-I terminated surface on the top and an FA-I terminated surface on the bottom side. **b–e**, Front view of the Cl⁻ (**b**), Br⁻ (**c**), BF₄⁻ (**d**) and HCOO⁻ (**e**) passivated surface. **f**, An illustration of iodide-vacancy passivation by HCOO⁻. **g, h**, DFT-relaxed FAPbI₃ slab with HCOO⁻ adsorbed at the iodide-vacancy site on the Pb-I (**g**) and the FA-I (**h**) terminated surface. All chemical species are shown in ball-and-stick representation. Pb²⁺, grey; iodide, violet; oxygen, red; carbon, dark brown; nitrogen, light blue; bromide, red-brown; chloride, light green; boron atoms, dark green; fluoride, yellow; hydrogen atoms, white.

Extended Data Fig. 5 Bonding between formamidinium and different anions on the surface of FAPbI₃.

a, Structure of a pure FAPbI₃ slab with FA-I termination on the top and Pb-I termination on the bottom side. **b, c**, The front view (**b**) and the side view (**c**) of the HCOO⁻ passivated surface. **d–f**, Cl⁻ (**d**), Br⁻ (**e**) and BF₄⁻ (**f**) passivated surface. All chemical species are shown in ball-and-stick representation. Pb²⁺, grey; iodide, violet; oxygen, red; carbon, dark brown; nitrogen, light blue; bromide, red-brown; chloride, light green; boron atoms, dark green; fluoride, yellow; hydrogen, white. **g**, Relative desorption strength of FA⁺ cations on different passivated surfaces.

Extended Data Fig. 6 Photovoltaic performance of the PSCs under different conditions.

a, $J-V$ curve of the target PSC measured without a metal mask. **b**, $J-V$ curves of the reference PSC and the PSC with 2% formamidinium acetate. **c**, $J-V$ curves of the reference and 2% Fo-FAPbI₃ PSCs without the MACl additive. **d**, $J-V$ curves of the reference and the 2% Fo-FAPbI₃ PSCs without using octylammonium iodide passivation. FF, fill factor.

Extended Data Fig. 7 $J-V$ metrics of the reference and target PSCs during the operational stability test.

a–c, The change in J_{sc} (**a**), V_{oc} (**b**) and fill factor (**c**) of the reference and target cells over the 450-h MPP tracking measurement.

Extended Data Table 1 Detailed $J-V$ parameters of the reference and target PSCs under both reverse and forward voltage scans

[Full size table](#)

Extended Data Table 2 Detailed $J-V$ parameters of the reference and target PSCs under different light intensities

[Full size table](#)

Supplementary information

Supplementary Information

This file contains Supplementary Notes 1-6, Supplementary Figs 1-3 and Supplementary References.

Video 1

The coordination of HCOO⁻ anions with Pb²⁺cations.

Video 2

MD of HCOO⁻ passivated FA-I terminated interface of FAPbI₃.

Video 3

MD of HCOO⁻ passivated Pb-I terminated interface of FAPbI₃.

Video 4

Perovskite fabrication process.

Rights and permissions

Reprints and Permissions

About this article



Check for
updates

Cite this article

Jeong, J., Kim, M., Seo, J. *et al.* Pseudo-halide anion engineering for α -FAPbI₃ perovskite solar cells. *Nature* **592**, 381–385 (2021).

<https://doi.org/10.1038/s41586-021-03406-5>

Download citation

- Received: 25 September 2020
- Accepted: 01 March 2021
- Published: 05 April 2021
- Issue Date: 15 April 2021

- DOI: <https://doi.org/10.1038/s41586-021-03406-5>

Comments

By submitting a comment you agree to abide by our [Terms](#) and [Community Guidelines](#). If you find something abusive or that does not comply with our terms or guidelines please flag it as inappropriate.

[Access through your institution](#)

[Change institution](#)

[Buy or subscribe](#)

This article was downloaded by **calibre** from <https://www.nature.com/articles/s41586-021-03406-5>

| [Section menu](#) | [Main menu](#) |

- Article
- [Published: 14 April 2021](#)

Liquid-induced topological transformations of cellular microstructures

- [Shucong Li](#) ORCID: [orcid.org/0000-0003-4407-045X^{1 na1}](https://orcid.org/0000-0003-4407-045X),
- [Bolei Deng](#) ORCID: [orcid.org/0000-0003-2589-2837^{2 na1}](https://orcid.org/0000-0003-2589-2837),
- [Alison Grinthal²](#),
- [Alyssha Schneider-Yamamura²](#),
- [Jinliang Kang](#) ORCID: [orcid.org/0000-0003-0154-1418²](https://orcid.org/0000-0003-0154-1418),
- [Reese S. Martens²](#),
- [Cathy T. Zhang²](#),
- [Jian Li](#) ORCID: [orcid.org/0000-0002-8986-2437²](https://orcid.org/0000-0002-8986-2437),
- [Siqin Yu²](#),
- [Katia Bertoldi](#) ORCID: [orcid.org/0000-0002-5787-4863²](https://orcid.org/0000-0002-5787-4863) &
- [Joanna Aizenberg](#) ORCID: [orcid.org/0000-0002-2343-8705^{1,2}](https://orcid.org/0000-0002-2343-8705)

[Nature](#) volume 592, pages386–391(2021)[Cite this article](#)

- 4556 Accesses
- 109 Altmetric
- [Metrics details](#)

Subjects

- [Mechanical engineering](#)
- [Polymers](#)

- [Self-assembly](#)
- [Structural materials](#)

Abstract

The fundamental topology of cellular structures—the location, number and connectivity of nodes and compartments—can profoundly affect their acoustic^{1,2,3,4}, electrical⁵, chemical^{6,7}, mechanical^{8,9,10} and optical¹¹ properties, as well as heat^{1,12}, fluid^{13,14} and particle transport¹⁵. Approaches that harness swelling^{16,17,18}, electromagnetic actuation^{19,20} and mechanical instabilities^{21,22,23} in cellular materials have enabled a variety of interesting wall deformations and compartment shape alterations, but the resulting structures generally preserve the defining connectivity features of the initial topology. Achieving topological transformation presents a distinct challenge for existing strategies: it requires complex reorganization, repacking, and coordinated bending, stretching and folding, particularly around each node, where elastic resistance is highest owing to connectivity. Here we introduce a two-tiered dynamic strategy that achieves systematic reversible transformations of the fundamental topology of cellular microstructures, which can be applied to a wide range of materials and geometries. Our approach requires only exposing the structure to a selected liquid that is able to first infiltrate and plasticize the material at the molecular scale, and then, upon evaporation, form a network of localized capillary forces at the architectural scale that ‘zip’ the edges of the softened lattice into a new topological structure, which subsequently restiffens and remains kinetically trapped. Reversibility is induced by applying a mixture of liquids that act separately at the molecular and architectural scales (thus offering modular temporal control over the softening–evaporation–stiffening sequence) to restore the original topology or provide access to intermediate modes. Guided by a generalized theoretical model that connects cellular geometries, material stiffness and capillary forces, we demonstrate programmed reversible topological transformations of various lattice geometries and responsive materials that undergo fast global or localized deformations. We then harness dynamic topologies to develop active surfaces with information encryption, selective particle trapping and

bubble release, as well as tunable mechanical, chemical and acoustic properties.

[Access through your institution](#)

[Change institution](#)

[Buy or subscribe](#)

Access options

Subscribe to Journal

Get full journal access for 1 year

\$199.00

only \$3.90 per issue

[Subscribe](#)

All prices are NET prices.

VAT will be added later in the checkout.

Tax calculation will be finalised during checkout.

Rent or Buy article

Get time limited or full article access on ReadCube.

from \$8.99

[Rent or Buy](#)

All prices are NET prices.

Additional access options:

- [Log in](#)
- [Access through your institution](#)
- [Learn about institutional subscriptions](#)

Fig. 1: Strategy for topological transformation of cellular structures.



Fig. 2: Experimental characterization of the assembly and disassembly of a triangular lattice.

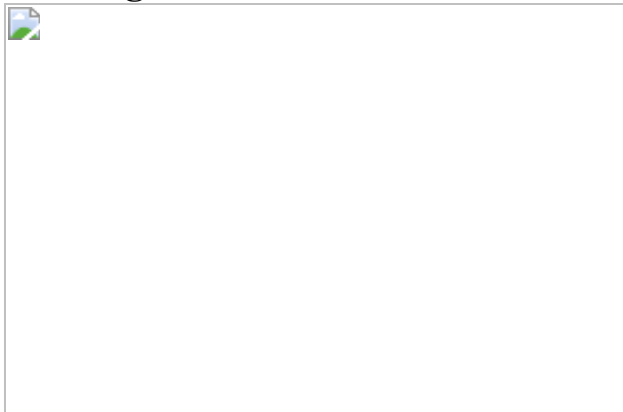


Fig. 3: Generalization of topological transformation principle.

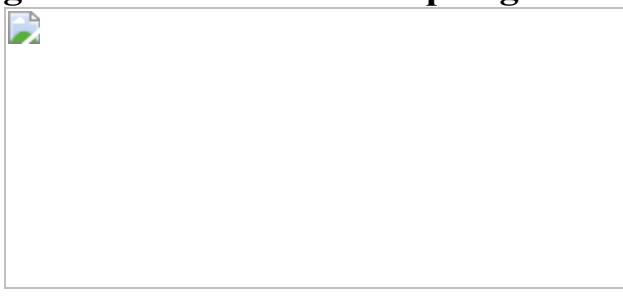
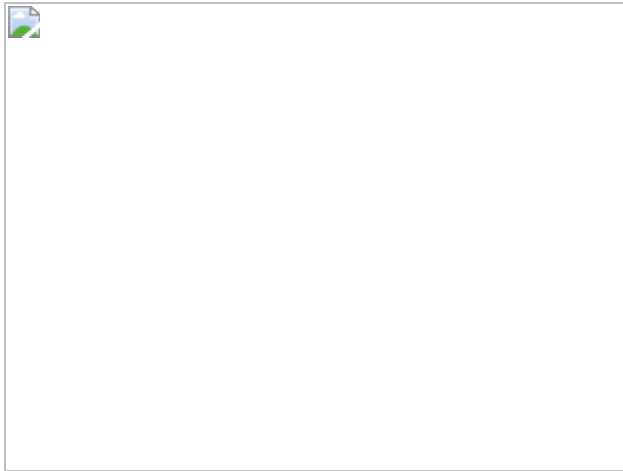


Fig. 4: Exemplary applications of lattice structures undergoing topological transformations.



Data availability

The data supporting the findings of this study are included within the paper and its Supplementary Information files and are available from the corresponding author upon reasonable request.

References

1. 1.

Gibson, L., Ashby, M. & Harley, B. *Cellular Materials in Nature and Medicine* (Cambridge Univ. Press, 2010).

2. 2.

Gibson, L. J. & Ashby, M. F. *Cellular Solids: Structure, Properties and Applications* (Cambridge Univ. Press, 1999).

3. 3.

Ruzzene, M., Scarpa, F. & Soranna, F. Wave beaming effects in two-dimensional cellular structures. *Smart Mater. Struct.* **12**, 363–372 (2003).

[ADS](#) [Google Scholar](#)

4. 4.

He, H. et al. Topological negative refraction of surface acoustic waves in a Weyl phononic crystal. *Nature* **560**, 61–64 (2018).

[ADS](#) [CAS](#) [Google Scholar](#)

5. 5.

Kang, S. et al. Stretchable lithium-ion battery based on re-entrant micro-honeycomb electrodes and cross-linked gel electrolyte. *ACS Nano* **14**, 3660–3668 (2020).

[CAS](#) [Google Scholar](#)

6. 6.

Shirman, E. et al. Modular design of advanced catalytic materials using hybrid organic–inorganic raspberry particles. *Adv. Funct. Mater.* **28**, 1704559 (2018).

[Google Scholar](#)

7. 7.

Kim, O. H. et al. Ordered macroporous platinum electrode and enhanced mass transfer in fuel cells using inverse opal structure. *Nat. Commun.* **4**, 2473 (2013).

[ADS](#) [Google Scholar](#)

8. 8.

Muth, J. T., Dixon, P. G., Woish, L., Gibson, L. J. & Lewis, J. A. Architected cellular ceramics with tailored stiffness via direct foam writing. *Proc. Natl Acad. Sci. USA* **114**, 1832–1837 (2017).

[ADS](#) [CAS](#) [Google Scholar](#)

9. 9.

Christensen, R. M. Mechanics of low density materials. *J. Mech. Phys. Solids* **34**, 563–578 (1986).

[ADS](#) [Google Scholar](#)

10. 10.

Coulais, C., Sabbadini, A., Vink, F. & van Hecke, M. Multi-step self-guided pathways for shape-changing metamaterials. *Nature* **561**, 512–515 (2018).

[ADS](#) [CAS](#) [Google Scholar](#)

11. 11.

Gan, Z., Turner, M. D. & Gu, M. Biomimetic gyroid nanostructures exceeding their natural origins. *Sci. Adv.* **2**, e1600084 (2016).

[ADS](#) [PubMed](#) [PubMed Central](#) [Google Scholar](#)

12. 12.

Maloney, K. J. et al. Multifunctional heat exchangers derived from three-dimensional micro-lattice structures. *Int. J. Heat Mass Transf.* **55**, 2486–2493 (2012).

[CAS](#) [Google Scholar](#)

13. 13.

Khan, M. I. H., Farrell, T., Nagy, S. A. & Karim, M. A. Fundamental understanding of cellular water transport process in bio-food material during drying. *Sci. Rep.* **8**, 15191 (2018).

[ADS](#) [PubMed](#) [PubMed Central](#) [Google Scholar](#)

14. 14.

Zhang, R., Hao, P., Zhang, X. & He, F. Dynamics of high Weber number drops impacting on hydrophobic surfaces with closed micro-cells. *Soft Matter* **12**, 5808–5817 (2016).

[ADS](#) [CAS](#) [Google Scholar](#)

15. 15.

Kim, J. J., Bong, K. W., Reátegui, E., Irimia, D. & Doyle, P. S. Porous microwells for geometry-selective, large-scale microparticle arrays. *Nat. Mater.* **16**, 139–146 (2017).

[ADS](#) [CAS](#) [Google Scholar](#)

16. 16.

Kang, S. H., Shan, S., Noorduin, W. L., Khan, M., Aizenberg, J. & Bertoldi, K. Buckling-induced reversible symmetry breaking and amplification of chirality using supported cellular structures. *Adv. Mater.* **25**, 3380–3385 (2013).

[CAS](#) [Google Scholar](#)

17. 17.

Boley, J. W. et al. Shape-shifting structured lattices via multimaterial 4D printing. *Proc. Natl Acad. Sci. USA* **116**, 20856–20862 (2019).

[ADS](#) [CAS](#) [Google Scholar](#)

18. 18.

Zhang, H., Guo, X., Wu, J., Fang, D. & Zhang, Y. Soft mechanical metamaterials with unusual swelling behavior and tunable stress-strain curves. *Sci. Adv.* **4**, eaar8535 (2018).

[ADS](#) [PubMed](#) [PubMed Central](#) [Google Scholar](#)

19. 19.

Kim, Y., Yuk, H., Zhao, R., Chester, S. A. & Zhao, X. Printing ferromagnetic domains for untethered fast-transforming soft materials. *Nature* **558**, 274–279 (2018).

[ADS](#) [CAS](#) [Google Scholar](#)

20. 20.

Xia, X. et al. Electrochemically reconfigurable architected materials. *Nature* **573**, 205–213 (2019).

[ADS](#) [CAS](#) [Google Scholar](#)

21. 21.

Coulais, C., Teomy, E., De Reus, K., Shokef, Y. & van Hecke, M. Combinatorial design of textured mechanical metamaterials. *Nature* **535**, 529–532 (2016).

[ADS](#) [CAS](#) [Google Scholar](#)

22. 22.

Haghpanah, B., Salari-Sharif, L., Pourrajab, P., Hopkins, J. & Valdevit, L. Multistable shape-reconfigurable architected materials. *Adv. Mater.* **28**, 7915–7920 (2016).

[CAS](#) [Google Scholar](#)

23. 23.

Fu, H. et al. Morphable 3D mesostructures and microelectronic devices by multistable buckling mechanics. *Nat. Mater.* **17**, 268–276 (2018).

[ADS](#) [CAS](#) [PubMed](#) [PubMed Central](#) [Google Scholar](#)

24. 24.

Bico, J., Roman, B., Moulin, L. & Boudaoud, A. Elastocapillary coalescence in wet hair. *Nature* **432**, 690 (2004).

[ADS](#) [CAS](#) [Google Scholar](#)

25. 25.

Pokroy, B., Kang, S. H., Mahadevan, L. & Aizenberg, J. Self-organization of a mesoscale bristle into ordered, hierarchical helical assemblies. *Science* **323**, 237–240 (2009).

[CAS](#) [Google Scholar](#)

26. 26.

Kang, S. H., Pokroy, B., Mahadevan, L. & Aizenberg, J. Control of shape and size of nanopillar assembly by adhesion-mediated elastocapillary interaction. *ACS Nano* **4**, 6323–6331 (2010).

[CAS](#) [Google Scholar](#)

27. 27.

Roman, B. & Bico, J. Elasto-capillarity: deforming an elastic structure with a liquid droplet. *J. Phys. Condens. Matter* **22**, 493101 (2010).

[CAS](#) [Google Scholar](#)

28. 28.

Cai, L. H. et al. Soft poly(dimethylsiloxane) elastomers from architecture-driven entanglement free design. *Adv. Mater.* **27**, 5132–5140 (2015).

[CAS](#) [PubMed](#) [PubMed Central](#) [Google Scholar](#)

29. 29.

Jeong, S. H., Zhang, S., Hjort, K., Hilborn, J. & Wu, Z. PDMS-based elastomer tuned soft, stretchable, and sticky for epidermal electronics. *Adv. Mater.* **28**, 5830–5836 (2016).

[CAS](#) [Google Scholar](#)

30. 30.

Matsunaga, M., Aizenberg, M. & Aizenberg, J. Controlling the stability and reversibility of micropillar assembly by surface chemistry. *J. Am. Chem. Soc.* **133**, 5545–5553 (2011).

[CAS](#) [Google Scholar](#)

31. 31.

Flory, P. J. *Principles of Polymer Chemistry* (Cornell Univ. Press, 1953).

32. 32.

Rubinstein, M. & Colby, R. H. *Polymer Physics* (Oxford Univ. Press, 2003).

33. 33.

Dimarzio, E. A. & Gibbs, J. H. Molecular interpretation of glass temperature depression by plasticizers. *J. Polym. Sci. A* **1**, 1417–1428 (1963).

[CAS](#) [Google Scholar](#)

34. 34.

Lin, H. et al. Organic molecule-driven polymeric actuators. *Macromol. Rapid Commun.* **40**, 1800896 (2019).

[Google Scholar](#)

35. 35.

Du, H. & Zhang, J. Solvent induced shape recovery of shape memory polymer based on chemically cross-linked poly(vinyl alcohol). *Soft Matter* **6**, 3370–3376 (2010).

[ADS](#) [CAS](#) [Google Scholar](#)

36. 36.

Gu, Y., Zhao, J. & Johnson, J. A. Polymer networks: from plastics and gels to porous frameworks. *Angew. Chem. Int. Ed.* **59**, 5022–5049 (2020).

[CAS](#) [Google Scholar](#)

37. 37.

Holmes, D. P., Brun, P. T., Pandey, A. & Protière, S. Rising beyond elastocapillarity. *Soft Matter* **12**, 4886–4890 (2016).

[ADS](#) [CAS](#) [Google Scholar](#)

38. 38.

Wei, Z. et al. Elastocapillary coalescence of plates and pillars. *Proc. R. Soc. A Math. Phys. Eng. Sci.* **471**, 20140593 (2015).

[ADS](#) [CAS](#) [Google Scholar](#)

39. 39.

Calvert, P. Hydrogels for soft machines. *Adv. Mater.* **21**, 743–756 (2009).

[ADS](#) [CAS](#) [Google Scholar](#)

40. 40.

Chow, T. S. Molecular interpretation of the glass transition temperature of polymer-diluent systems. *Macromolecules* **13**, 362–364 (1980).

[ADS](#) [CAS](#) [Google Scholar](#)

41. 41.

Rath, A., Geethu, P. M., Mathesan, S., Satapathy, D. K. & Ghosh, P. Solvent triggered irreversible shape morphism of biopolymer films. *Soft Matter* **14**, 1672–1680 (2018).

[ADS](#) [CAS](#) [Google Scholar](#)

42. 42.

Zhu, X., Wu, G., Dong, R., Chen, C. M. & Yang, S. Capillarity induced instability in responsive hydrogel membranes with periodic hole array. *Soft Matter* **8**, 8088–8093 (2012).

[ADS](#) [CAS](#) [Google Scholar](#)

43. 43.

Myshkin, N. & Kovalev, A. Adhesion and surface forces in polymer tribology—a review. *Friction* **6**, 143–155 (2018).

[Google Scholar](#)

44. 44.

Israelachvili, J. N. *Intermolecular and Surface Forces* (Academic Press, 2011).

45. 45.

White, T. J. & Broer, D. J. Programmable and adaptive mechanics with liquid crystal polymer networks and elastomers. *Nat. Mater.* **14**, 1087–1098 (2015).

[ADS](#) [CAS](#) [Google Scholar](#)

46. 46.

Ohm, C., Brehmer, M. & Zentel, R. Liquid crystalline elastomers as actuators and sensors. *Adv. Mater.* **22**, 3366–3387 (2010).

[CAS](#) [Google Scholar](#)

47. 47.

Yao, Y. et al. Multiresponsive polymeric microstructures with encoded predetermined and self-regulated deformability. *Proc. Natl Acad. Sci. USA* **115**, 12950–12955 (2018).

[ADS](#) [CAS](#) [Google Scholar](#)

[Download references](#)

Acknowledgements

This work was supported by the National Science Foundation (NSF) through the Designing Materials to Revolutionize and Engineer our Future (DMREF) programme under award number DMR-1922321 and the Harvard University Materials Research Science and Engineering Center (MRSEC) under award number DMR-2011754 (theory and computational studies), and by the US Department of Energy (DOE), Office of Science, Basic Energy Sciences (BES) under award number DE-SC0005247 (experiment and characterization). Microfabrication and scanning electron microscopy were performed at the Center for Nanoscale Systems (CNS) at Harvard, a member of the National Nanotechnology Coordinated Infrastructure Network (NNCI), which is supported by the NSF under NSF ECCS award number 1541959. We thank D. Y. Kim for fruitful discussions.

Author information

Author notes

1. These authors contributed equally: Shucong Li, Bolei Deng

Affiliations

1. Department of Chemistry and Chemical Biology, Harvard University, Cambridge, MA, USA

Shucong Li & Joanna Aizenberg

2. Harvard John A. Paulson School of Engineering and Applied Sciences, Harvard University, Cambridge, MA, USA

Bolei Deng, Alison Grinthal, Alyssha Schneider-Yamamura, Jinliang Kang, Reese S. Martens, Cathy T. Zhang, Jian Li, Siqin Yu, Katia Bertoldi & Joanna Aizenberg

Authors

1. Shucong Li

[View author publications](#)

You can also search for this author in [PubMed](#) [Google Scholar](#)

2. Bolei Deng

[View author publications](#)

You can also search for this author in [PubMed](#) [Google Scholar](#)

3. Alison Grinthal

[View author publications](#)

You can also search for this author in [PubMed](#) [Google Scholar](#)

4. Alyssha Schneider-Yamamura

[View author publications](#)

You can also search for this author in [PubMed](#) [Google Scholar](#)

5. Jinliang Kang

[View author publications](#)

You can also search for this author in [PubMed](#) [Google Scholar](#)

6. Reese S. Martens

[View author publications](#)

You can also search for this author in [PubMed](#) [Google Scholar](#)

7. Cathy T. Zhang

[View author publications](#)

You can also search for this author in [PubMed](#) [Google Scholar](#)

8. Jian Li

[View author publications](#)

You can also search for this author in [PubMed](#) [Google Scholar](#)

9. Siqin Yu

[View author publications](#)

You can also search for this author in [PubMed](#) [Google Scholar](#)

10. Katia Bertoldi

[View author publications](#)

You can also search for this author in [PubMed](#) [Google Scholar](#)

11. Joanna Aizenberg

[View author publications](#)

You can also search for this author in [PubMed](#) [Google Scholar](#)

Contributions

S.L., B.D., K.B. and J.A. conceived and initiated the project. S.L., A.S.-Y., J.K., R.S.M. and C.T.Z. performed the experiments. B.D. performed the theoretical modelling and image analysis. J.L. and S.Y. performed the

finite-element modelling and pattern designs. S.L., B.D. and A.G. analysed the experimental data. K.B. and J.A. supervised the project. All co-authors provided useful feedback and contributed to the manuscript.

Corresponding author

Correspondence to [Joanna Aizenberg](#).

Ethics declarations

Competing interests

The authors declare no competing interests.

Additional information

Peer review information *Nature* thanks Robin Ras, Arnaud Saint-Jalmes, Scott Waitukaitis and the other, anonymous, reviewer(s) for their contribution to the peer review of this work. Peer reviewer reports are available.

Publisher's note Springer Nature remains neutral with regard to jurisdictional claims in published maps and institutional affiliations.

Supplementary information

[Supplementary Information](#)

This file contains Supplementary Materials and Methods, Theoretical Model, Supplemental Results including Supplementary Figures 1 to 17, and legends for Supplementary Videos 1 to 7.

[Peer Review File](#)

[Supplementary Video 1](#)

Inducible relaxation of an isolated LCP microplate and a hexagonal lattice after trapping in the deformed state.

Supplementary Video 2

Elasto-capillary assembly of a triangular lattice into a hexagonal lattice.

Supplementary Video 3

Robustness of the transformed topology.

Supplementary Video 4

Disassembly of the hexagonal lattice back to the initial triangular topology.

Supplementary Video 5

Hierarchical transformation of a diamond lattice by first transforming to a hexagonal topology via acetone and then inducing a phase transition of an oriented LCP.

Supplementary Video 6

Elasto-capillary assembly over a larger area without and with phase design.

Supplementary Video 7

Demonstration of properties and applications made possible by topological transformation of the cellular structures.

Rights and permissions

[Reprints and Permissions](#)

About this article



Cite this article

Li, S., Deng, B., Grinthal, A. *et al.* Liquid-induced topological transformations of cellular microstructures. *Nature* **592**, 386–391 (2021). <https://doi.org/10.1038/s41586-021-03404-7>

[Download citation](#)

- Received: 17 August 2020
- Accepted: 01 March 2021
- Published: 14 April 2021
- Issue Date: 15 April 2021
- DOI: <https://doi.org/10.1038/s41586-021-03404-7>

Comments

By submitting a comment you agree to abide by our [Terms](#) and [Community Guidelines](#). If you find something abusive or that does not comply with our terms or guidelines please flag it as inappropriate.

[Access through your institution](#)

[Change institution](#)

[Buy or subscribe](#)

This article was downloaded by **calibre** from <https://www.nature.com/articles/s41586-021-03404-7>

- Article
- [Published: 14 April 2021](#)

Dynamics of large effusive eruptions driven by caldera collapse

- [Alberto Roman](#) ORCID: orcid.org/0000-0002-7142-8720¹ &
- [Paul Lundgren¹](#)

[Nature](#) volume 592, pages392–396(2021)[Cite this article](#)

- 576 Accesses
- 20 Altmetric
- [Metrics details](#)

Subjects

- [Geophysics](#)
- [Volcanology](#)

Abstract

The largest effusive basaltic eruptions are associated with caldera collapse and are manifest through quasi-periodic ground displacements and moderate-size earthquakes^{1,2,3}, but the mechanism that governs their dynamics remains unclear. Here we provide a physical model that explains these processes, which accounts for both the quasi-periodic stick-slip collapse of the caldera roof and the long-term eruptive behaviour of the

volcano. We show that it is the caldera collapse itself that sustains large effusive eruptions, and that triggering caldera collapse requires topography-generated pressures. The model is consistent with data from the 2018 Kīlauea eruption and allows us to estimate the properties of the plumbing system of the volcano. The results reveal that two reservoirs were active during the eruption, and place constraints on their connectivity. According to the model, the Kīlauea eruption stopped after slightly more than 60 per cent of its potential caldera collapse events, possibly owing to the presence of the second reservoir. Finally, we show that this physical framework is generally applicable to the largest instrumented caldera collapse eruptions of the past fifty years.

[Access through your institution](#)

[Change institution](#)

[Buy or subscribe](#)

Access options

Subscribe to Journal

Get full journal access for 1 year

\$199.00

only \$3.90 per issue

[Subscribe](#)

All prices are NET prices.

VAT will be added later in the checkout.

Tax calculation will be finalised during checkout.

Rent or Buy article

Get time limited or full article access on ReadCube.

from \$8.99

[Rent or Buy](#)

All prices are NET prices.

Additional access options:

- [Log in](#)
- [Access through your institution](#)
- [Learn about institutional subscriptions](#)

Fig. 1: Geodetic signature of caldera collapse.

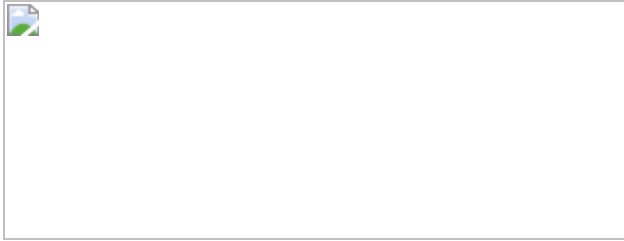


Fig. 2: Model set-up and main features of the two regimes.



Fig. 3: Comparison between data, best-fit model and posterior prediction uncertainty.

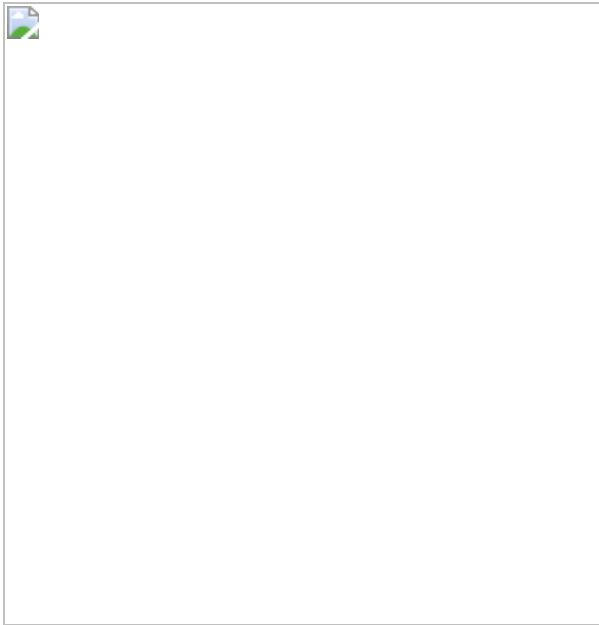
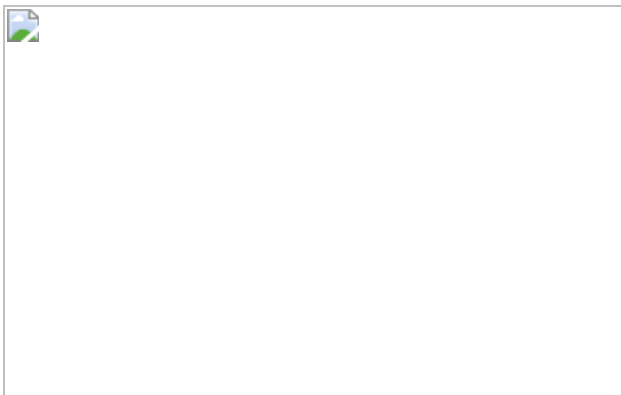


Fig. 4: Time between collapses for Piton de la Fournaise, Miyakejima, Fernandina and Kīlauea.



Data availability

Tilt data are available in ref. [5](#) and Sentinel SAR data are available at <https://sentinel.esa.int/web/sentinel/sentinel-data-access>. [Source data](#) are provided with this paper.

Code availability

The codes used in this work are available through Zenodo at https://zenodo.org/record/4500189#.YE_LI7RKiWg.

References

1. 1.

Kumagai, H. et al. Very-long-period seismic signals and caldera formation at Miyake island, Japan. *Science* **293**, 687–690 (2001).

[ADS](#) [CAS](#) [Article](#) [Google Scholar](#)

2. 2.

Michon, L., Massin, F., Famin, V., Ferrazzini, V. & Roult, G. Basaltic calderas: collapse dynamics, edifice deformation, and variations of magma withdrawal. *J. Geophys. Res. Solid Earth* **116**, B03209 (2011).

[ADS](#) [Article](#) [Google Scholar](#)

3. 3.

Neal, C. et al. The 2018 rift eruption and summit collapse of Kīlauea volcano. *Science* **363**, 367–374 (2019).

[ADS](#) [CAS](#) [Article](#) [Google Scholar](#)

4. 4.

Lipman, P. W. C. *Encyclopedia of Volcanoes* 643–662 (Academic, 2000).

5. 5.

Johanson, I. & Miklius, A. Tiltmeter data from Kīlauea Volcano, Hawai‘i, spanning the 2018 eruption and earthquake sequence. *US Geological Survey Data Release* <https://doi.org/10.5066/P9310M9N> (US Geological Survey, 2019).

6. 6.

Lundgren, P. R., Bagnardi, M. & Dietterich, H. Topographic changes during the 2018 Kīlauea eruption from single-pass airborne InSAR. *Geophys. Res. Lett.* **46**, 9554–9562 (2019).

[ADS](#) [Article](#) [Google Scholar](#)

7. 7.

Fontaine, F. R., Roult, G., Michon, L., Barruol, G. & Muro, A. D. The 2007 eruptions and caldera collapse of the Piton de la Fournaise volcano (la Réunion island) from tilt analysis at a single very broadband seismic station. *Geophys. Res. Lett.* **41**, 2803–2811 (2014).

[ADS](#) [Article](#) [Google Scholar](#)

8. 8.

Ukawa, M., Fujita, E., Yamamoto, E., Okada, Y. & Kikuchi, M. The 2000 Miyakejima eruption: crustal deformation and earthquakes observed by the NIED Miyakejima observation network. *Earth Planets Space* **52**, xix–xxvi (2000).

[Article](#) [Google Scholar](#)

9. 9.

Liu, Y.-K., Ruch, J., Vasyura-Bathke, H. & Jonsson, S. Influence of ring faulting in localizing surface deformation at subsiding calderas. *Earth Planet. Sci. Lett.* **526**, 115784 (2019).

[CAS](#) [Article](#) [Google Scholar](#)

10. 10.

Gudmundsson, M. T. et al. Gradual caldera collapse at Bárðarbunga volcano, Iceland, regulated by lateral magma outflow. *Science* **353**, aaf8988 (2016).

[Article](#) [Google Scholar](#)

11. 11.

Ripepe, M. et al. Volcano seismicity and ground deformation unveil the gravity-driven magma discharge dynamics of a volcanic eruption. *Nat. Commun.* **6**, 6998 (2015).

[ADS](#) [CAS](#) [Article](#) [Google Scholar](#)

12. 12.

Fialko, Y. A. & Rubin, A. M. What controls the along-strike slopes of volcanic rift zones? *J. Geophys. Res. Solid Earth* **104**, 20007–20020 (1999).

[Article](#) [Google Scholar](#)

13. 13.

Pinel, V. & Jaupart, C. Magma storage and horizontal dyke injection beneath a volcanic edifice. *Earth Planet. Sci. Lett.* **221**, 245–262 (2004).

[ADS](#) [CAS](#) [Article](#) [Google Scholar](#)

14. 14.

Andronov, A. A., Vitt, A. A. & Khaikin, S. E. *Theory of Oscillators: Adiwes International Series in Physics* Vol. 4 (Elsevier, 2013).

15. 15.

Anderson, K. R. et al. Magma reservoir failure and the onset of caldera collapse at Kīlauea volcano in 2018. *Science* **366**, eaaz1822 (2019).

[CAS](#) [Article](#) [Google Scholar](#)

16. 16.

Poland, M. P. et al. in *Characteristics of Hawaiian Volcanoes* Vol. 1801, 179–234 (US Geological Survey, 2014).

17. 17.

Salvatier, J., Wiecki, T. V. & Fonnesbeck, C. Probabilistic programming in Python using PyMC3. *PeerJ Comput. Sci.* **2**, e55 (2016).

[Article](#) [Google Scholar](#)

18. 18.

Patrick, M. et al. Cyclic lava effusion during the 2018 eruption of Kīlauea volcano. *Science* **366**, eaay9070 (2019).

[CAS](#) [Article](#) [Google Scholar](#)

19. 19.

Wu, S.-M., Lin, F.-C., Farrell, J., Shiro, B., Karlstrom, L., Okubo, P., and Koper, K. Spatiotemporal seismic structure variations associated with the 2018 Kīlauea eruption based on temporary dense geophone arrays. *Geophys. Res. Lett.* **47**, e2019GL086668 2019.

[ADS](#) [Google Scholar](#)

20. 20.

Costa, A., Melnik, O. & Sparks, R. Controls of conduit geometry and wallrock elasticity on lava dome eruptions. *Earth Planet. Sci. Lett.* **260**, 137–151 (2007).

[ADS](#) [CAS](#) [Article](#) [Google Scholar](#)

21. 21.

Epp, D., Decker, R. W. & Okamura, A. T. Relation of summit deformation to east rift zone eruptions on Kīlauea Volcano, Hawai‘i.

Geophys. Res. Lett. **10**, 493–496 (1983).

[ADS](#) [Article](#) [Google Scholar](#)

22. 22.

Iverson, R. M. et al. Dynamics of seismogenic volcanic extrusion at Mount St Helens in 2004–05. *Nature* **444**, 439–443 (2006).

[ADS](#) [CAS](#) [Article](#) [Google Scholar](#)

23. 23.

Roche, O. & Druitt, T. H. Onset of caldera collapse during ignimbrite eruptions. *Earth Planet. Sci. Lett.* **191**, 191–202 (2001).

[ADS](#) [CAS](#) [Article](#) [Google Scholar](#)

24. 24.

Chen, C. W. & Zebker, H. A. Network approaches to two-dimensional phase unwrapping: intractability and two new algorithms. *J. Opt. Soc. Am. A* **17**, 401–414 (2000).

[ADS](#) [CAS](#) [Article](#) [Google Scholar](#)

25. 25.

Agram, P. et al. New radar interferometric time series analysis toolbox released. *Eos* **94**, 69–70 (2013).

[ADS](#) [Article](#) [Google Scholar](#)

26. 26.

Lohman, R. B. & Simons, M. Some thoughts on the use of InSAR data to constrain models of surface deformation: noise structure and data downsampling. *Geochem. Geophys. Geosyst.* **6**, Q01007 (2005).

[ADS](#) [Article](#) [Google Scholar](#)

27. 27.

Mogi, K. Relations between the eruptions of various volcanoes and the deformations of the ground surfaces around them. *Bull. Earthq. Res. Inst.* **36**, 99–134 (1958).

[Google Scholar](#)

28. 28.

Baker, S. & Amelung, F. Top-down inflation and deflation at the summit of Kīlauea volcano, Hawai'i observed with InSAR. *J. Geophys. Res. Solid Earth* **117**, B12406 (2012).

[ADS](#) [Article](#) [Google Scholar](#)

29. 29.

Segall, P., Anderson, K. R., Pulvirenti, P., Wang, T. and Johanson I. Caldera collapse geometry revealed by near-field GPS displacements at Kīlauea Volcano in 2018. *Geophys. Res. Lett.* **47**, e2020GL088867 (2020).

[ADS](#) [Article](#) [Google Scholar](#)

30. 30.

Dietterich, H. R. et al. Lava effusion rate evolution and erupted volume during the 2018 Kīlauea lower East Rift Zone eruption. *Bull. Volcanol.* **83**, 25 (2021); <https://doi.org/10.1007/s00445-021-01443-6>.

[Download references](#)

Acknowledgements

We acknowledge I. Johanson and the Hawaiian Volcano Observatory for providing tiltmeters and GPS stations data. A.R. acknowledges support from the NASA Postdoctoral Program and the Universities Space Research Association, through a NASA-ASI (Italian Space Agency) agreement. We are grateful to M. Patrick and E. Rivalta for their constructive reviews, which helped to improve the clarity and completeness of the manuscript. Part of this research was carried out at the Jet Propulsion Laboratory, California Institute of Technology, under a contract with the National Aeronautics and Space Administration (grant 281945.02.47.05.24).

Author information

Affiliations

1. Jet Propulsion Laboratory, California Institute of Technology,
Pasadena, CA, USA

Alberto Roman & Paul Lundgren

Authors

1. Alberto Roman

[View author publications](#)

You can also search for this author in [PubMed](#) [Google Scholar](#)

2. Paul Lundgren

[View author publications](#)

You can also search for this author in [PubMed](#) [Google Scholar](#)

Contributions

A.R. developed the theory and performed the inversions. P.L. processed InSAR data and provided support with critical discussions of the results. Both authors contributed to the manuscript writing.

Corresponding author

Correspondence to [Alberto Roman](#).

Ethics declarations

Competing interests

The authors declare no competing interests.

Additional information

Peer review information *Nature* thanks Matthew Patrick and Eleonora Rivalta for their contribution to the peer review of this work. Peer reviewer reports are available.

Publisher's note Springer Nature remains neutral with regard to jurisdictional claims in published maps and institutional affiliations.

Extended data figures and tables

[Extended Data Fig. 1 Time between collapses for Piton de la Fournaise, Miyakejima, Fernandina2 and Kīlauea.](#)

The solid line corresponds to the best fit of equation (7). The time between collapses has been scaled by the value of equation (34) when $n = 0$. The collapse number has been scaled by N_{\max} . PdF, Piton de la Fournaise.

[Source data](#)

[Extended Data Fig. 2 Tilt data.](#)

a, North–south component of tilt recorded at UWD. This average signal was obtained by stacking 24-h periods of 19 collapses between 3 July and the end of the eruption. The shaded area corresponds to 2 s.d. of the stacking. The best fit of the function $A \exp(\xi_1 t) + B \exp(\xi_2 t) - C$ is shown.

The corresponding time constants ζ_1 and ζ_2 are 1.5 h and 8 d, respectively.
b, Projection of the tilt of SDH along the radial direction to HLM (blue) and to SCR (green). [Source data](#)

Extended Data Fig. 3 Sketch of the two-chamber model.

For clarity, only the additional parameters relevant to the two-chamber model are indicated. Parameters such as the geometrical properties or the position of the piston, which are the same for the one-chamber model, are not indicated (see Fig. 2). The properties of the shallow reservoir are marked with subscript s, whereas those of the deeper chamber with subscript d. For Kīlauea the shallow reservoir corresponds to the HLM source and the deep one corresponds to the SCR source. The properties of the conduit feeding the eruption are noted with subscript e, and those of the conduit connecting the two chambers with subscript c.

Extended Data Fig. 4 InSAR data.

a, b, Linear LOS velocity maps (left) and time series (right) for a point (cross on the maps) in the area of maximum subsidence (green dots, blue curve) and the radial UWD tiltmeter (triangle on the maps) time series (black line) for Sentinel-1 descending track 87 (**a**) and ascending track 124 (**b**). Grey shading represents the time interval used in the InSAR source modelling. [Source data](#)

Extended Data Fig. 5 Subsampled InSAR dataset and inversion results.

Top, data, model and residuals for Sentinel-1 ascending (right) and descending (left) geometries. Bottom, PDFs of the source locations. The horizontal origin is set at the GNSS CRIM station. [Source data](#)

Extended Data Fig. 6 Predicted volumes.

Caldera and lava volume (DRE) as a function of collapse number. The relation between the two is given by equation (9). The orange dots

correspond to the case in which only V_{HLM} is used to calculate Ψ , whereas for the yellow dots we use $V_{\text{HLM}} + V_{\text{SCR}}$. The blue dot indicates the value of the final caldera volume as measured by GLISTIN-A, which is used as an inversion constraint, and the red dot indicates the current estimate of the total erupted volume, which was not included in the inversion dataset. Error bars (2 s.d.) correspond to the uncertainty in the prediction for the $V_{\text{HLM}} + V_{\text{SCR}}$ case. Error bars for all other predictions are smaller than the marker size. [Source data](#)

Extended Data Fig. 7 PDFs of the parameters of the Kīlauea plumbing system.

V_{HLM} , the volume of the HLM reservoir, corresponds to V_{S} in Extended Data Fig. 3. V_{SCR} , the volume of the SCR reservoir, corresponds to V_{d} in Extended Data Fig. 3. For all the other parameters, see Fig. 2 and Extended Data Fig. 3. [Source data](#)

Extended Data Table 1 Parameters used in the calculations shown in Fig. 2

[Full size table](#)

Extended Data Table 2 Parameters of the model kept fixed during inversion

[Full size table](#)

Supplementary information

Supplementary Video 1

This video shows the variation of tilt measured by three stations during the collapse of the Kīlauea caldera. On the top the orange line indicates instantaneous tilt direction, whereas at the bottom the NS component of UWD and SDH station is shown. The locations of the two sources HLM and SCR inferred from InSAR are indicated by the red dots.

Supplementary Video 2

This video illustrates the characteristics of a model in which two reservoirs are connected in series. Instantaneous tilt direction and reservoirs locations are shown in map by the orange lines and the black dot respectively. The caldera is collapsing on the ‘northern’ reservoir, whereas the ‘southern’ reservoir is feeding the eruption. The color-scale indicates vertical elastic displacement, whereas the anelastic displacement due to slip of the piston block is not shown to avoid color saturation. On the bottom the temporal evolution of the tilt for the two stations is shown. The parameters used in this example are given in the Methods “Two reservoirs model” section.

[Peer Review File](#)

Source data

[Source Data Fig. 1](#)

[Source Data Fig. 2](#)

[Source Data Fig. 3](#)

[Source Data Fig. 4](#)

[Source Data Extended Data Fig. 1](#)

[Source Data Extended Data Fig. 2](#)

[Source Data Extended Data Fig. 4](#)

[Source Data Extended Data Fig. 5](#)

[Source Data Extended Data Fig. 6](#)

[Source Data Extended Data Fig. 7](#)

Rights and permissions

[Reprints and Permissions](#)

About this article



Check for
updates

Cite this article

Roman, A., Lundgren, P. Dynamics of large effusive eruptions driven by caldera collapse. *Nature* **592**, 392–396 (2021).
<https://doi.org/10.1038/s41586-021-03414-5>

[Download citation](#)

- Received: 11 June 2020
- Accepted: 02 March 2021
- Published: 14 April 2021
- Issue Date: 15 April 2021
- DOI: <https://doi.org/10.1038/s41586-021-03414-5>

Comments

By submitting a comment you agree to abide by our [Terms](#) and [Community Guidelines](#). If you find something abusive or that does not comply with our terms or guidelines please flag it as inappropriate.

[Access through your institution](#)

[Change institution](#)

Buy or subscribe

This article was downloaded by **calibre** from <https://www.nature.com/articles/s41586-021-03414-5>

| [Section menu](#) | [Main menu](#) |

- Article
- [Published: 17 March 2021](#)

Protecting the global ocean for biodiversity, food and climate

- [Enric Sala](#) [ORCID: orcid.org/0000-0003-4730-3570¹](#),
- [Juan Mayorga](#) [ORCID: orcid.org/0000-0003-1961-8313^{1,2}](#),
- [Darcy Bradley](#) [ORCID: orcid.org/0000-0003-2581-8768²](#),
- [Reniel B. Cabral](#) [ORCID: orcid.org/0000-0002-1137-381X²](#),
- [Trisha B. Atwood](#) [ORCID: orcid.org/0000-0001-7153-5190³](#),
- [Arnaud Auber](#) [ORCID: orcid.org/0000-0002-8415-1652⁴](#),
- [William Cheung](#) [ORCID: orcid.org/0000-0001-9998-0384⁵](#),
- [Christopher Costello](#) [ORCID: orcid.org/0000-0002-9646-7806²](#),
- [Francesco Ferretti⁶](#),
- [Alan M. Friedlander^{1,7}](#),
- [Steven D. Gaines](#) [ORCID: orcid.org/0000-0002-7604-3483²](#),
- [Cristina Garilao¹⁸](#),
- [Whitney Goodell^{1,7}](#),
- [Benjamin S. Halpern](#) [ORCID: orcid.org/0000-0001-8844-2302⁹](#),
- [Audra Hinson](#) [ORCID: orcid.org/0000-0002-4231-4820³](#),
- [Kristin Kaschner⁸](#),
- [Kathleen Kesner-Reyes¹⁰](#),
- [Fabien Leprieur¹¹](#),
- [Jennifer McGowan](#) [ORCID: orcid.org/0000-0001-9061-3465¹²](#),
- [Lance E. Morgan¹³](#),
- [David Mouillot](#) [ORCID: orcid.org/0000-0003-0402-2605¹¹](#),
- [Juliano Palacios-Abrantes](#) [ORCID: orcid.org/0000-0001-8969-5416⁵](#),
- [Hugh P. Possingham](#) [ORCID: orcid.org/0000-0001-7755-996X¹⁴](#),
- [Kristin D. Rechberger¹⁵](#),

- [Boris Worm¹⁶](#) &
- [Jane Lubchenco](#) ORCID: orcid.org/0000-0003-3540-5879¹⁷

Nature volume **592**, pages397–402(2021)[Cite this article](#)

- 16k Accesses
- 1 Citations
- 1652 Altmetric
- [Metrics details](#)

Subjects

- [Environmental sciences](#)
- [Ocean sciences](#)

An [Author Correction](#) to this article was published on 08 April 2021

This article has been [updated](#)

Abstract

The ocean contains unique biodiversity, provides valuable food resources and is a major sink for anthropogenic carbon. Marine protected areas (MPAs) are an effective tool for restoring ocean biodiversity and ecosystem services^{1,2}, but at present only 2.7% of the ocean is highly protected³. This low level of ocean protection is due largely to conflicts with fisheries and other extractive uses. To address this issue, here we developed a conservation planning framework to prioritize highly protected MPAs in places that would result in multiple benefits today and in the future. We find that a substantial increase in ocean protection could have triple benefits, by protecting biodiversity, boosting the yield of fisheries and securing marine

carbon stocks that are at risk from human activities. Our results show that most coastal nations contain priority areas that can contribute substantially to achieving these three objectives of biodiversity protection, food provision and carbon storage. A globally coordinated effort could be nearly twice as efficient as uncoordinated, national-level conservation planning. Our flexible prioritization framework could help to inform both national marine spatial plans⁴ and global targets for marine conservation, food security and climate action.

[Access through your institution](#)

[Change institution](#)

[Buy or subscribe](#)

Access options

Subscribe to Journal

Get full journal access for 1 year

\$199.00

only \$3.90 per issue

[Subscribe](#)

All prices are NET prices.

VAT will be added later in the checkout.

Tax calculation will be finalised during checkout.

Rent or Buy article

Get time limited or full article access on ReadCube.

from \$8.99

[Rent or Buy](#)

All prices are NET prices.

Additional access options:

- [Log in](#)
- [Access through your institution](#)
- [Learn about institutional subscriptions](#)

Fig. 1: Global conservation priorities.



Fig. 2: Co-benefits of protection.



Fig. 3: Prioritizing multiple objectives given unknown preferences.

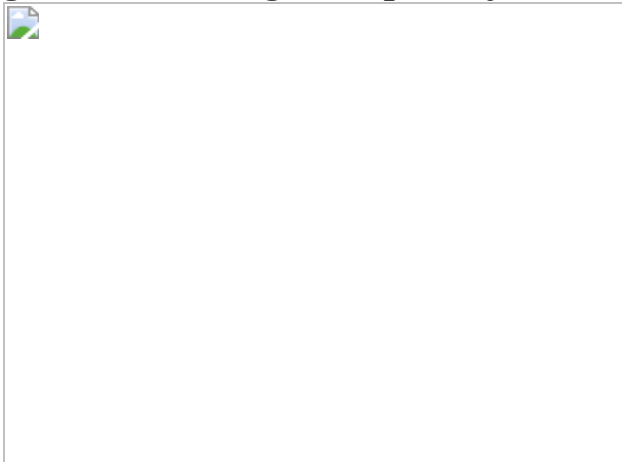
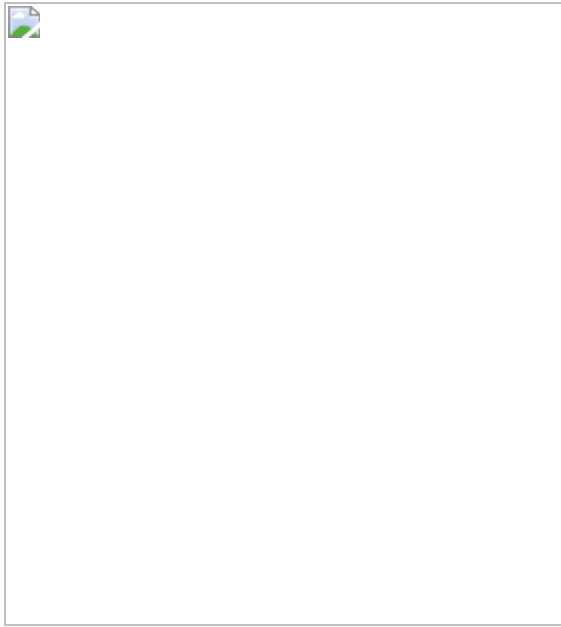


Fig. 4: National contributions to biodiversity conservation and coordinated implementation.



Data availability

The underlying data used in this study are available from the sources listed in the [Supplementary Information](#).

Code availability

The R code that supports the findings of this study is available at <https://github.com/emlab-ucsb/ocean-conservation-priorities>.

Change history

- [14 April 2021](#)

[A Correction to this paper has been published:](#)
<https://doi.org/10.1038/s41586-021-03496-1>

References

1. 1.

Sala, E. & Giakoumi, S. No-take marine reserves are the most effective protected areas in the ocean. *ICES J. Mar. Sci.* **75**, 1166–1168 (2018).

[Google Scholar](#)

2. 2.

Worm, B. et al. Impacts of biodiversity loss on ocean ecosystem services. *Science* **314**, 787–790 (2006).

[ADS](#) [PubMed](#) [CAS](#) [Google Scholar](#)

3. 3.

Marine Conservation Institute. The Marine Protection Atlas. <http://mpatlas.org> (2020).

4. 4.

Santos, C. F. et al. Integrating climate change in ocean planning. *Nat. Sustain.* **3**, 505–516 (2020).

[Google Scholar](#)

5. 5.

Costello, C. et al. The future of food from the sea. *Nature* **588**, 95–100 (2020).

[ADS](#) [PubMed](#) [Google Scholar](#)

6. 6.

Brondizio, E.S., Settele, J., Díaz, S. & Ngo, H. T. (eds) *Global Assessment Report on Biodiversity and Ecosystem Services of the Intergovernmental Science-Policy Platform on Biodiversity and Ecosystem Services* (IPBES, 2019).

7. 7.

IPCC. *Special Report on the Ocean and Cryosphere in a Changing Climate* <https://www.ipcc.ch/srocc/> (2019).

8. 8.

Horta e Costa, B. et al. A regulation-based classification system for Marine Protected Areas (MPAs). *Mar. Policy* **72**, 192–198 (2016).

[Google Scholar](#)

9. 9.

Oregon State University, IUCN World Commission on Protected Areas, Marine Conservation Institute, National Geographic Society, & UNEP World Conservation Monitoring Centre. An Introduction to The MPA Guide. <https://www.protectedplanet.net/c/mpa-guide> (2019).

10. 10.

Lester, S. et al. Biological effects within no-take marine reserves: a global synthesis. *Mar. Ecol. Prog. Ser.* **384**, 33–46 (2009).

[ADS](#) [Google Scholar](#)

11. 11.

Roberts, C. M. et al. Marine reserves can mitigate and promote adaptation to climate change. *Proc. Natl Acad. Sci. USA* **114**, 6167–6175 (2017).

[ADS](#) [PubMed](#) [CAS](#) [Google Scholar](#)

12. 12.

Roberts, C. M. et al. Marine biodiversity hotspots and conservation priorities for tropical reefs. *Science* **295**, 1280–1284 (2002).

[ADS](#) [PubMed](#) [CAS](#) [Google Scholar](#)

13. 13.

Selig, E. R. et al. Global priorities for marine biodiversity conservation. *PLoS One* **9**, e82898 (2014).

[ADS](#) [PubMed](#) [PubMed Central](#) [Google Scholar](#)

14. 14.

Kuempel, C. D., Jones, K. R., Watson, J. E. M. & Possingham, H. P. Quantifying biases in marine-protected-area placement relative to abatable threats. *Conserv. Biol.* **33**, 1350–1359 (2019).

[PubMed](#) [PubMed Central](#) [Google Scholar](#)

15. 15.

McGowan, J. et al. Prioritizing debt conversions for marine conservation. *Conserv. Biol.* **34**, 1065–1075 (2020).

[PubMed](#) [Google Scholar](#)

16. 16.

Halpern, B. S. et al. Spatial and temporal changes in cumulative human impacts on the world's ocean. *Nat. Commun.* **6**, 7615 (2015).

[ADS](#) [PubMed](#) [PubMed Central](#) [CAS](#) [Google Scholar](#)

17. 17.

Lenoir, J. et al. Species better track climate warming in the oceans than on land. *Nat. Ecol. Evol.* **4**, 1044–1059 (2020).

[PubMed](#) [Google Scholar](#)

18. 18.

Tittensor, D. P. et al. Integrating climate adaptation and biodiversity conservation in the global ocean. *Sci. Adv.* **5**, eaay9969 (2019).

[ADS](#) [PubMed](#) [PubMed Central](#) [Google Scholar](#)

19. 19.

Kaschner, K. et al. AquaMaps: predicted range maps for aquatic species. Version 08/2016c <https://www.aquamaps.org/> (2016).

20. 20.

Riahi, K. et al. RCP 8.5—a scenario of comparatively high greenhouse gas emissions. *Clim. Change* **109**, 33 (2011).

[ADS](#) [CAS](#) [Google Scholar](#)

21. 21.

Nakicenovic, N. et al. *Special Report on Emissions Scenarios (SRES): a Special Report of Working Group III of the Intergovernmental Panel on Climate Change* (Cambridge Univ. Press, 2000).

22. 22.

Goñi, R., Badalamenti, F. & Tupper, M. H. in *Marine Protected Areas: A Multidisciplinary Approach* (ed. Claudet, J.) 72–98 (Cambridge Univ. Press, 2011).

23. 23.

Halpern, B. S., Lester, S. E. & Kellner, J. B. Spillover from marine reserves and the replenishment of fished stocks. *Environ. Conserv.* **36**, 268–276 (2009).

[Google Scholar](#)

24. 24.

Lynham, J., Nikolaev, A., Raynor, J., Vilela, T. & Villaseñor-Derbez, J. C. Impact of two of the world's largest protected areas on longline fishery catch rates. *Nat. Commun.* **11**, 979 (2020).

[ADS](#) [PubMed](#) [PubMed Central](#) [CAS](#) [Google Scholar](#)

25. 25.

Gaines, S. D., Lester, S. E., Grorud-Colvert, K., Costello, C. & Pollnac, R. Evolving science of marine reserves: new developments and emerging research frontiers. *Proc. Natl Acad. Sci. USA* **107**, 18251–18255 (2010).

[ADS](#) [PubMed](#) [CAS](#) [Google Scholar](#)

26. 26.

Hastings, A. & Botsford, L. W. Equivalence in yield from marine reserves and traditional fisheries management. *Science* **284**, 1537–1538 (1999).

[ADS](#) [PubMed](#) [CAS](#) [Google Scholar](#)

27. 27.

Costello, C. et al. Global fishery prospects under contrasting management regimes. *Proc. Natl Acad. Sci. USA* **113**, 5125–5129 (2016).

[ADS](#) [PubMed](#) [CAS](#) [Google Scholar](#)

28. 28.

Cabral, R. B. et al. A global network of marine protected areas for food. *Proc. Natl Acad. Sci. USA* **117**, 28134–28139 (2020).

[PubMed](#) [CAS](#) [Google Scholar](#)

29. 29.

Atwood, T. B., Witt, A., Mayorga, J., Hammill, E. & Sala, E. Global patterns in marine sediment carbon stocks. *Front. Mar. Sci.* **7**, 165 (2020).

[Google Scholar](#)

30. 30.

Estes, E. R. et al. Persistent organic matter in oxic subseafloor sediment. *Nat. Geosci.* **12**, 126 (2019).

[ADS](#) [PubMed](#) [CAS](#) [Google Scholar](#)

31. 31.

Griscom, B. W. et al. Natural climate solutions. *Proc. Natl Acad. Sci. USA* **114**, 11645–11650 (2017).

[ADS](#) [PubMed](#) [CAS](#) [Google Scholar](#)

32. 32.

Metz, B., Davidson, O. de Coninck, H., Loos, M., & Meyer, L. (eds) *IPCC Special Report on Carbon Dioxide Capture and Storage* (Cambridge Univ. Press, 2005).

33. 33.

Gruber, N. et al. The oceanic sink for anthropogenic CO₂ from 1994 to 2007. *Science* **363**, 1193–1199 (2019).

[ADS](#) [PubMed](#) [CAS](#) [Google Scholar](#)

34. 34.

Davidson, E. A. & Ackerman, I. L. Changes in soil carbon inventories following cultivation of previously untilled soils. *Biogeochemistry* **20**, 161–193 (1993).

[CAS](#) [Google Scholar](#)

35. 35.

Legge, O. et al. Carbon on the Northwest European shelf: contemporary budget and future influences. *Front. Mar. Sci.* **7**, 143 (2020).

[Google Scholar](#)

36. 36.

Pusceddu, A. et al. Chronic and intensive bottom trawling impairs deep-sea biodiversity and ecosystem functioning. *Proc. Natl Acad. Sci. USA* **111**, 8861–8866 (2014).

[ADS](#) [PubMed](#) [CAS](#) [Google Scholar](#)

37. 37.

Beger, M. et al. Integrating regional conservation priorities for multiple objectives into national policy. *Nat. Commun.* **6**, 8208 (2015).

[ADS](#) [PubMed](#) [PubMed Central](#) [CAS](#) [Google Scholar](#)

38. 38.

Montesino Pouzols, F. et al. Global protected area expansion is compromised by projected land-use and parochialism. *Nature* **516**, 383–386 (2014).

[ADS](#) [PubMed](#) [CAS](#) [Google Scholar](#)

39. 39.

Mangel, M. Irreducible uncertainties, sustainable fisheries and marine reserves. *Evol. Ecol. Res.* **2**, 547–557 (2000).

[Google Scholar](#)

40. 40.

Rodwell, L. D. & Roberts, C. M. Fishing and the impact of marine reserves in a variable environment. *Can. J. Fish. Aquat. Sci.* **61**, 2053–2068 (2004).

[Google Scholar](#)

41. 41.

Caselle, J. E., Rassweiler, A., Hamilton, S. L. & Warner, R. R. Recovery trajectories of kelp forest animals are rapid yet spatially variable across a network of temperate marine protected areas. *Sci. Rep.* **5**, 14102 (2015).

[ADS](#) [PubMed](#) [PubMed Central](#) [CAS](#) [Google Scholar](#)

42. 42.

McCrea-Strub, A. et al. Understanding the cost of establishing marine protected areas. *Mar. Policy* **35**, 1–9 (2011).

[Google Scholar](#)

43. 43.

Ban, N. C. et al. Well-being outcomes of marine protected areas. *Nat. Sustain.* **2**, 524 (2019).

[Google Scholar](#)

44. 44.

Barbier, E. B., Burgess, J. C. & Dean, T. J. How to pay for saving biodiversity. *Science* **360**, 486–488 (2018).

[ADS](#) [PubMed](#) [CAS](#) [Google Scholar](#)

45. 45.

O'Leary, B. C. et al. Effective coverage targets for ocean protection. *Conserv. Lett.* **9**, 398–404 (2016).

[Google Scholar](#)

46. 46.

Roberts, C. M., O'Leary, B. C. & Hawkins, J. P. Climate change mitigation and nature conservation both require higher protected area targets. *Phil. Trans. R. Soc. Lond. B* **375**, 20190121 (2020).

[Google Scholar](#)

47. 47.

FAO. *The State of World Fisheries and Aquaculture 2018 – Meeting the Sustainable Development Goals* <http://www.fao.org/3/I9540EN/i9540en.pdf> (2018).

48. 48.

RAM Legacy Stock Assessment Database v.4.44 [Dataset]. <https://doi.org/10.5281/zenodo.2542919> (2018).

49. 49.

Higgs, N. & Attrill, M. Biases in biodiversity: wide-ranging species are discovered first in the deep sea. *Front. Mar. Sci.* **2**, 61 (2015).

[Google Scholar](#)

50. 50.

Clark, M. R., Watling, L., Rowden, A. A., Guinotte, J. M. & Smith, C. R. A global seamount classification to aid the scientific design of marine protected area networks. *Ocean Coast. Manage.* **54**, 19–36 (2011).

[Google Scholar](#)

51. 51.

Spalding, M. D., Agostini, V. N., Rice, J. & Grant, S. M. Pelagic provinces of the world: a biogeographic classification of the world's surface pelagic waters. *Ocean Coast. Manage.* **60**, 19–30 (2012).

[Google Scholar](#)

52. 52.

Spalding, M. D. et al. Marine ecoregions of the world: a bioregionalization of coastal and shelf areas. *Bioscience* **57**, 573–583 (2007).

[Google Scholar](#)

53. 53.

Watling, L., Guinotte, J., Clark, M. R. & Smith, C. R. A proposed biogeography of the deep ocean floor. *Prog. Oceanogr.* **111**, 91–112 (2013).

[ADS](#) [Google Scholar](#)

54. 54.

Thorson, J. T., Munch, S. B., Cope, J. M. & Gao, J. Predicting life history parameters for all fishes worldwide. *Ecol. Appl.* **27**, 2262–2276 (2017).

[PubMed](#) [Google Scholar](#)

55. 55.

Froese, R. & Pauly, D. FishBase. www.fishbase.org. (2019).

56. 56.

Palomares, M. L. D. & Pauly, D. SeaLifeBase. www.sealifebase.org (2019).

57. 57.

The Nature Conservancy. Marine Ecoregions and Pelagic Provinces of the World. <http://data.unep-wcmc.org/datasets/38> (2012).

58. 58.

Halpern, B. S. et al. Recent pace of change in human impact on the world's ocean. *Sci. Rep.* **9**, 11609 (2019).

[ADS](#) [PubMed](#) [PubMed Central](#) [Google Scholar](#)

59. 59.

IUCN. 2018 IUCN Red List of Threatened Species.
<http://www.iucnredlist.org/> (2018).

60. 60.

Lehtomäki, J. & Moilanen, A. Methods and workflow for spatial conservation prioritization using zonation. *Environ. Model. Softw.* **47**, 128–137 (2013).

[Google Scholar](#)

61. 61.

Rabosky, D. L. et al. An inverse latitudinal gradient in speciation rate for marine fishes. *Nature* **559**, 392–395 (2018).

[ADS](#) [PubMed](#) [CAS](#) [Google Scholar](#)

62. 62.

Stein, R. W. et al. Global priorities for conserving the evolutionary history of sharks, rays and chimaeras. *Nat. Ecol. Evol.* **2**, 288–298

(2018).

[PubMed](#) [Google Scholar](#)

63. 63.

Fritz, S. A., Bininda-Emonds, O. R. & Purvis, A. Geographical variation in predictors of mammalian extinction risk: big is bad, but only in the tropics. *Ecol. Lett.* **12**, 538–549 (2009).

[PubMed](#) [Google Scholar](#)

64. 64.

Jetz, W., Thomas, G. H., Joy, J. B., Hartmann, K. & Mooers, A. O. The global diversity of birds in space and time. *Nature* **491**, 444–448 (2012).

[ADS](#) [PubMed](#) [CAS](#) [Google Scholar](#)

65. 65.

Violle, C. et al. Functional rarity: the ecology of outliers. *Trends Ecol. Evol.* **32**, 356–367 (2017).

[PubMed](#) [PubMed Central](#) [Google Scholar](#)

66. 66.

May, R. M. Islands biogeography and the design of wildlife preserves. *Nature* **254**, 177–178 (1975).

[ADS](#) [Google Scholar](#)

67. 67.

Hubbell, S. P. *The Unified Neutral Theory of Biodiversity and Biogeography (MPB-32)* (Princeton Univ. Press, 2001).

68. 68.

Holt, R. D., Lawton, J. H., Polis, G. A. & Martinez, N. D. Trophic rank and the species-area relationship. *Ecology* **80**, 1495–1504 (1999).

[Google Scholar](#)

69. 69.

Tittensor, D. P. et al. Global patterns and predictors of marine biodiversity across taxa. *Nature* **466**, 1098–1101 (2010).

[ADS](#) [CAS](#) [Google Scholar](#)

70. 70.

Hopf, J. K., Jones, G. P., Williamson, D. H. & Connolly, S. R. Fishery consequences of marine reserves: short-term pain for longer-term gain. *Ecol. Appl.* **26**, 818–829 (2016).

[PubMed](#) [Google Scholar](#)

71. 71.

Walters, C. J., Hilborn, R. & Parrish, R. An equilibrium model for predicting the efficacy of marine protected areas in coastal environments. *Can. J. Fish. Aquat. Sci.* **64**, 1009–1018 (2007).

[Google Scholar](#)

72. 72.

Guénette, S. & Pitcher, T. J. An age-structured model showing the benefits of marine reserves in controlling overexploitation. *Fish. Res.* **39**, 295–303 (1999).

[Google Scholar](#)

73. 73.

Beverton, R. J. H. & Holt, S. J. *On the Dynamics of Exploited Fish Populations* (Chapman & Hall, 1957).

74. 74.

Kroodsma, D. A. et al. Tracking the global footprint of fisheries. *Science* **359**, 904–908 (2018).

[ADS](#) [PubMed](#) [CAS](#) [Google Scholar](#)

75. 75.

Eigaard, O. R. et al. Estimating seabed pressure from demersal trawls, seines, and dredges based on gear design and dimensions. *ICES J. Mar. Sci.* **73**, i27–i43 (2016).

[Google Scholar](#)

76. 76.

Hiddink, J. G. et al. Global analysis of depletion and recovery of seabed biota after bottom trawling disturbance. *Proc. Natl Acad. Sci. USA* **114**, 8301–8306 (2017).

[PubMed](#) [CAS](#) [Google Scholar](#)

77. 77.

de Madron, X. D. et al. Trawling-induced resuspension and dispersal of muddy sediments and dissolved elements in the Gulf of Lion (NW Mediterranean). *Cont. Shelf Res.* **25**, 2387–2409 (2005).

[ADS](#) [Google Scholar](#)

78. 78.

Ferré, B., De Madron, X. D., Estournel, C., Ulses, C. & Le Corre, G. Impact of natural (waves and currents) and anthropogenic (trawl) resuspension on the export of particulate matter to the open ocean:

application to the Gulf of Lion (NW Mediterranean). *Cont. Shelf Res.* **28**, 2071–2091 (2008).

[ADS](#) [Google Scholar](#)

79. 79.

Kaiser, M. J., Collie, J. S., Hall, S. J., Jennings, S. & Piner, I. R. Modification of marine habitats by trawling activities: prognosis and solutions. *Fish Fish.* **3**, 114–136 (2002).

[Google Scholar](#)

80. 80.

Oberle, F. K., Storlazzi, C. D. & Hanebuth, T. J. What a drag: quantifying the global impact of chronic bottom trawling on continental shelf sediment. *J. Mar. Syst.* **159**, 109–119 (2016).

[Google Scholar](#)

81. 81.

Palanques, A., Guillén, J. & Puig, P. Impact of bottom trawling on water turbidity and muddy sediment of an unfished continental shelf. *Limnol. Oceanogr.* **46**, 1100–1110 (2001).

[ADS](#) [Google Scholar](#)

82. 82.

Gray, J. in *Oceanography and Marine Biology Annual Review* Vol. 12 (ed. Barnes, H.) 223–261 (George Allen & Unwin, 1974).

83. 83.

McArthur, M. et al. On the use of abiotic surrogates to describe marine benthic biodiversity. *Estuar. Coast. Shelf Sci.* **88**, 21–32 (2010).

[ADS](#) [Google Scholar](#)

84. 84.

Burdige, D. J. Preservation of organic matter in marine sediments: controls, mechanisms, and an imbalance in sediment organic carbon budgets? *Chem. Rev.* **107**, 467–485 (2007).

[PubMed](#) [CAS](#) [Google Scholar](#)

85. 85.

Spinelli, G. A., Giambalvo, E. R. & Fisher, A. T. in *Hydrogeology of the Oceanic Lithosphere* (eds Davis, E. E. & Elderfield, H.) Ch. 6 (Cambridge Univ. Press, 2004).

86. 86.

Arndt, S. et al. Quantifying the degradation of organic matter in marine sediments: a review and synthesis. *Earth Sci. Rev.* **123**, 53–86 (2013).

[ADS](#) [CAS](#) [Google Scholar](#)

87. 87.

Paraska, D. W., Hipsey, M. R. & Salmon, S. U. Sediment diagenesis models: review of approaches, challenges and opportunities. *Environ. Model. Softw.* **61**, 297–325 (2014).

[Google Scholar](#)

88. 88.

Lovelock, C. E. et al. Assessing the risk of carbon dioxide emissions from blue carbon ecosystems. *Front. Ecol. Environ.* **15**, 257–265 (2017).

[Google Scholar](#)

89. 89.

Wilkinson, G. M., Besterman, A., Buelo, C., Gephart, J. & Pace, M. L. A synthesis of modern organic carbon accumulation rates in coastal and aquatic inland ecosystems. *Sci. Rep.* **8**, 15736 (2018).

[ADS](#) [PubMed](#) [PubMed Central](#) [Google Scholar](#)

90. 90.

Rodriguez, A. B., McKee, B. A., Miller, C. B., Bost, M. C. & Atencio, A. N. Coastal sedimentation across North America doubled in the 20th century despite river dams. *Nat. Commun.* **11**, 3249 (2020).

[ADS](#) [PubMed](#) [PubMed Central](#) [CAS](#) [Google Scholar](#)

91. 91.

Moilanen, A., Leathwick, J. R. & Quinn, J. M. Spatial prioritization of conservation management. *Conserv. Lett.* **4**, 383–393 (2011).

[Google Scholar](#)

92. 92.

Armsworth, P. R. Inclusion of costs in conservation planning depends on limited datasets and hopeful assumptions. *Ann. NY Acad. Sci.* **1322**, 61–76 (2014).

[ADS](#) [PubMed](#) [Google Scholar](#)

93. 93.

Carwardine, J. et al. Conservation planning when costs are uncertain. *Conserv. Biol.* **24**, 1529–1537 (2010).

[PubMed](#) [Google Scholar](#)

94. 94.

Naidoo, R. et al. Integrating economic costs into conservation planning. *Trends Ecol. Evol.* **21**, 681–687 (2006).

[PubMed](#) [Google Scholar](#)

95. 95.

Rondinini, C., Wilson, K. A., Boitani, L., Grantham, H. & Possingham, H. P. Tradeoffs of different types of species occurrence data for use in systematic conservation planning. *Ecol. Lett.* **9**, 1136–1145 (2006).

[PubMed](#) [Google Scholar](#)

96. 96.

Stock, A. & Micheli, F. Effects of model assumptions and data quality on spatial cumulative human impact assessments. *Glob. Ecol. Biogeogr.* **25**, 1321–1332 (2016).

[Google Scholar](#)

[Download references](#)

Acknowledgements

This study was funded by the National Geographic Society and the Leonardo DiCaprio Foundation. D.M. was supported by the French Foundation for Research on Biodiversity (FRB).

Author information

Affiliations

1. Pristine Seas, National Geographic Society, Washington, DC, USA

Enric Sala, Juan Mayorga, Alan M. Friedlander & Whitney Goodell

2. Environmental Market Solutions Lab, University of California Santa Barbara, Santa Barbara, CA, USA

Juan Mayorga, Darcy Bradley, Reniel B. Cabral, Christopher Costello & Steven D. Gaines

3. Department of Watershed Sciences and Ecology Center, Utah State University, Logan, UT, USA

Trisha B. Atwood & Audra Hinson

4. IFREMER, Unité Halieutique de Manche et Mer du Nord, Boulogne-sur-Mer, France

Arnaud Auber

5. Changing Ocean Research Unit, Institute for the Oceans and Fisheries, The University of British Columbia, Vancouver, British Columbia, Canada

William Cheung & Juliano Palacios-Abrantes

6. Department of Fish and Wildlife Conservation, Virginia Polytechnic Institute and State University, Blacksburg, VA, USA

Francesco Ferretti

7. Hawai‘i Institute of Marine Biology, Kāne‘ohe, HI, USA

Alan M. Friedlander & Whitney Goodell

8. Evolutionary Biology and Ecology Laboratory, Albert Ludwigs University, Freiburg, Germany

Kristin Kaschner

9. National Center for Ecological Analysis and Synthesis (NCEAS), University of California, Santa Barbara, CA, USA

Benjamin S. Halpern

10. Quantitative Aquatics, Los Baños, The Philippines

Kathleen Kesner-Reyes

11. MARBEC, Université de Montpellier, Montpellier, France

Fabien Leprieur & David Mouillot

12. The Nature Conservancy, Arlington, VA, USA

Jennifer McGowan

13. Marine Conservation Institute, Seattle, WA, USA

Lance E. Morgan

14. Centre for Biodiversity and Conservation Science (CBCS), The University of Queensland, Brisbane, Queensland, Australia

Hugh P. Possingham

15. Dynamic Planet, Washington, DC, USA

Kristin D. Rechberger

16. Ocean Frontiers Institute, Dalhousie University, Halifax, Nova Scotia, Canada

Boris Worm

17. Oregon State University, Corvallis, OR, USA

Jane Lubchenco

18. GEOMAR Helmholtz Centre for Ocean Research Kiel, Kiel, Germany

Cristina Garilao

Authors

1. Enric Sala

[View author publications](#)

You can also search for this author in [PubMed](#) [Google Scholar](#)

2. Juan Mayorga

[View author publications](#)

You can also search for this author in [PubMed](#) [Google Scholar](#)

3. Darcy Bradley

[View author publications](#)

You can also search for this author in [PubMed](#) [Google Scholar](#)

4. Reniel B. Cabral

[View author publications](#)

You can also search for this author in [PubMed](#) [Google Scholar](#)

5. Trisha B. Atwood

[View author publications](#)

You can also search for this author in [PubMed](#) [Google Scholar](#)

6. Arnaud Auber

[View author publications](#)

You can also search for this author in [PubMed](#) [Google Scholar](#)

7. William Cheung

[View author publications](#)

You can also search for this author in [PubMed](#) [Google Scholar](#)

8. Christopher Costello

[View author publications](#)

You can also search for this author in [PubMed](#) [Google Scholar](#)

9. Francesco Ferretti

[View author publications](#)

You can also search for this author in [PubMed](#) [Google Scholar](#)

10. Alan M. Friedlander

[View author publications](#)

You can also search for this author in [PubMed](#) [Google Scholar](#)

11. Steven D. Gaines

[View author publications](#)

You can also search for this author in [PubMed](#) [Google Scholar](#)

12. Cristina Garilao

[View author publications](#)

You can also search for this author in [PubMed](#) [Google Scholar](#)

13. Whitney Goodell

[View author publications](#)

You can also search for this author in [PubMed](#) [Google Scholar](#)

14. Benjamin S. Halpern

[View author publications](#)

You can also search for this author in [PubMed](#) [Google Scholar](#)

15. Audra Hinson

[View author publications](#)

You can also search for this author in [PubMed](#) [Google Scholar](#)

16. Kristin Kaschner

[View author publications](#)

You can also search for this author in [PubMed](#) [Google Scholar](#)

17. Kathleen Kesner-Reyes
[View author publications](#)

You can also search for this author in [PubMed](#) [Google Scholar](#)

18. Fabien Leprieur
[View author publications](#)

You can also search for this author in [PubMed](#) [Google Scholar](#)

19. Jennifer McGowan
[View author publications](#)

You can also search for this author in [PubMed](#) [Google Scholar](#)

20. Lance E. Morgan
[View author publications](#)

You can also search for this author in [PubMed](#) [Google Scholar](#)

21. David Mouillot
[View author publications](#)

You can also search for this author in [PubMed](#) [Google Scholar](#)

22. Juliano Palacios-Abrantes
[View author publications](#)

You can also search for this author in [PubMed](#) [Google Scholar](#)

23. Hugh P. Possingham
[View author publications](#)

You can also search for this author in [PubMed](#) [Google Scholar](#)

24. Kristin D. Rechberger
[View author publications](#)

You can also search for this author in [PubMed](#) [Google Scholar](#)

25. Boris Worm

[View author publications](#)

You can also search for this author in [PubMed](#) [Google Scholar](#)

26. Jane Lubchenco

[View author publications](#)

You can also search for this author in [PubMed](#) [Google Scholar](#)

Contributions

E.S., J. Mayorga, D.B., R.B.C., T.B.A., W.C., C.C., F.F., A.M.F., S.D.G., W.G., B.S.H., J. McGowan, D.M., H.P.P., K.D.R., B.W. and J.L. conceived the study and designed the prioritization framework; J. Mayorga, R.B.C., T.B.A., A.A., W.C., A.M.F., C.G., W.G., B.S.H., A.H., K.K., K.K.-R., F.L., L.E.M., D.M., J.P.-A. and B.W. provided data and/or conducted analyses; J. Mayorga, D.B., R.B.C. and A.H. wrote computer code; and E.S., J. Mayorga, D.B., R.B.C., T.B.A., W.C., C.C., F.F., A.M.F., S.D.G., W.G., B.S.H., J. McGowan, L.E.M., D.M., H.P.P., K.D.R., B.W. and J.L. wrote the paper.

Corresponding author

Correspondence to [Enric Sala](#).

Ethics declarations

Competing interests

The authors declare no competing interests.

Additional information

Peer review information *Nature* thanks Charles Ehler and the other, anonymous, reviewer(s) for their contribution to the peer review of this work.

Publisher's note Springer Nature remains neutral with regard to jurisdictional claims in published maps and institutional affiliations.

Supplementary information

Supplementary Information

This file contains Supplementary Figures 1-35, Supplementary Tables 1-2 and Supplementary References.

Reporting Summary

Rights and permissions

Reprints and Permissions

About this article



Check for
updates

Cite this article

Sala, E., Mayorga, J., Bradley, D. *et al.* Protecting the global ocean for biodiversity, food and climate. *Nature* **592**, 397–402 (2021).
<https://doi.org/10.1038/s41586-021-03371-z>

Download citation

- Received: 19 December 2019

- Accepted: 18 February 2021
- Published: 17 March 2021
- Issue Date: 15 April 2021
- DOI: <https://doi.org/10.1038/s41586-021-03371-z>

Further reading

- [**Variable contributions of seafloor communities to ecosystem metabolism across a gradient of habitat-forming species**](#)
 - Iván F. Rodil
 - , Karl M. Attard
 - , Camilla Gustafsson
 - & Alf Norkko

Marine Environmental Research (2021)

Comments

By submitting a comment you agree to abide by our [Terms](#) and [Community Guidelines](#). If you find something abusive or that does not comply with our terms or guidelines please flag it as inappropriate.

[Access through your institution](#)

[Change institution](#)

[Buy or subscribe](#)

This article was downloaded by **calibre** from <https://www.nature.com/articles/s41586-021-03371-z>

Measuring human capital using global learning data

[Download PDF](#)

- Article
- Open Access
- [Published: 10 March 2021](#)

Measuring human capital using global learning data

- [Noam Angrist](#) ORCID: orcid.org/0000-0003-2750-1916^{1,2},
- [Simeon Djankov](#)^{3,4},
- [Pinelopi K. Goldberg](#)^{4,5,6,7,8} &
- [Harry A. Patrinos](#)¹

Nature volume 592, pages403–408(2021)[Cite this article](#)

- 14k Accesses
- 392 Altmetric
- [Metrics details](#)

Subjects

- [Developing world](#)
- [Economics](#)
- [Education](#)

Abstract

Human capital—that is, resources associated with the knowledge and skills of individuals—is a critical component of economic development^{1,2}. Learning metrics that are comparable for countries globally are necessary to understand and track the formation of human capital. The increasing use of international achievement tests is an important step in this direction³. However, such tests are administered primarily in developed countries⁴, limiting our ability to analyse learning patterns in developing countries that may have the most to gain from the formation of human capital. Here

we bridge this gap by constructing a globally comparable database of 164 countries from 2000 to 2017. The data represent 98% of the global population and developing economies comprise two-thirds of the included countries. Using this dataset, we show that global progress in learning—a priority Sustainable Development Goal—has been limited, despite increasing enrolment in primary and secondary education. Using an accounting exercise that includes a direct measure of schooling quality, we estimate that the role of human capital in explaining income differences across countries ranges from a fifth to half; this result has an intermediate position in the wide range of estimates provided in earlier papers in the literature^{[5,6,7,8,9,10,11,12,13](#)}. Moreover, we show that average estimates mask considerable heterogeneity associated with income grouping across countries and regions. This heterogeneity highlights the importance of including countries at various stages of economic development when analysing the role of human capital in economic development. Finally, we show that our database provides a measure of human capital that is more closely associated with economic growth than current measures that are included in the Penn world tables version 9.0^{[14](#)} and the human development index of the United Nations^{[15](#)}.

[Download PDF](#)

Main

The notion of human capital was mentioned as early as in 1776^{[16](#)} and formalized two centuries later^{[17](#)}. Ever since, researchers have explored the role of human capital in economic development. For decades, studies used measures of schooling as a proxy for human capital^{[18,19,20](#)}. This applies even to the most prominent index of human capital to date, the United Nation's human development index (HDI).

However, using schooling as a proxy for human capital assumes that being in school translates to learning. Evidence suggests that this is often not the case^{[21](#)}. A recent analysis reveals that six out of ten adolescent individuals worldwide cannot meet basic proficiency levels in mathematics and reading^{[22](#)}. The gap between schooling and learning is acute in developing countries. In Kenya, Tanzania and Uganda, three-quarters of the students in grade 3 cannot read a basic sentence such as ‘the name of the dog is Puppy.’^{[1](#)}. In rural India, half of the students in grade 3 cannot solve a two-digit subtraction problem (such as $46 - 17$)^{[1](#)}.

These data from previous studies demonstrate a substantial gap in the formation of human capital: students are in school, but do not learn enough. Closing this gap is an important priority for economic development. Several studies have suggested that when human capital is measured by schooling, it does not deliver the returns predicted

by growth models. However, when measured by learning, human capital is more strongly associated with growth^{3,23,24}.

To date, much of the effort to measure learning has focused on high-income countries. This limitation is due to the absence of comparable measures of learning in low- and middle-income countries. Existing measures exclude a considerable portion of the global distribution, in particular countries with the most potential to gain from the accumulation of human capital.

In this Article we bridge this gap. We introduce a database of globally comparable learning outcomes for 164 countries covering 98% of the global population from 2000 to 2017. This is one of the largest and most-current global learning databases, one of the first to disaggregate learning results by gender and to introduce methodological improvements such as the inclusion of standard errors to quantify uncertainty around mean scores. The database, referred to as the Harmonized Learning Outcomes (HLO) database, is available for public use and updates are expected every 2 to 3 years as new learning data become available (see ‘Data availability’ in Methods). A large-scale effort to track the formation of human capital using this database is the World Bank’s new human capital index²⁵.

Of note, throughout this Article, we use the term ‘schooling’ when referring to the average years of schooling or average enrolment rates of a country at specific schooling levels. We use the term ‘learning’ when referring to the stock of basic cognitive skills, including mathematics, reading and science, as measured by standardized tests conducted in school.

HLO database

The database was produced through a large-scale effort by the World Bank to identify, collect and collate student assessment data worldwide. We include seven assessment regimes in total: three international tests, three regional standardized achievement tests and the Early Grade Reading Assessment, which adds 48 countries to the database with at least one data point in the past 10 years, including large developing economies such as Bangladesh, Nigeria and Pakistan. Each test covers between 10 and 72 countries. By combining these assessments and making them comparable, we include countries that represent 98% of the global population. A detailed description of the methodology that we use to develop harmonized learning measures as well as all data included in the database are provided in the Methods and Supplementary Information II.

The database includes mean scores as well as standard errors for each measure, in an attempt to quantify uncertainty. Scores are disaggregated by schooling level (primary

and secondary), subject (reading, mathematics and science) and gender (male and female). We include year-by-year data. We do not extend the time series before 2000 as the quality of the data is low for the period before 2000.

The coverage and detail of the database is described further in Extended Data Table 1 and the Supplementary Information. The database includes 2,023 country–year observations from 2000 to 2017 (Extended Data Table 1). Disaggregation by gender is available for 98.5% of observations. Latin America and the Caribbean and sub-Saharan Africa make up 21% of all available data. Additional descriptive statistics are provided in Supplementary Information IA.

Our methodology uses the expansion of international assessments to construct globally comparable learning outcomes. These tests are derived from assessments conducted in the USA since the 1960s, such as the Scholastic Achievement Tests (SATs) and the National Assessment of Educational Progress (NAEP). The tests are psychometrically designed, standardized assessments of cognitive skills. Since the 1990s, international assessments have been conducted by organizations such as the The Organisation for Economic Co-operation and Development (OECD). Two high-profile examples are the Programme for International Student Assessment (PISA) and the Trends in International Mathematics and Science Study (TIMSS), which covered 71 and 65 countries, respectively, in 2015. These assessments enable credible global comparisons of learning across countries and over time. However, to date most analyses of these assessments cover few developing countries^{3,26,27,28,29}.

We include 164 countries, two-thirds of which are developing countries, by linking international assessments to their regional counterparts. Regional assessments cover much of sub-Saharan Africa and Latin America but have often been excluded from international comparisons. We convert a regional test score to an international test score within subjects (mathematics, reading and science) and schooling levels (primary and secondary) and within adjacent years. By including tests across the same testing round and at the disaggregated schooling and subject level, this method minimizes the likelihood that test differences are a function of time, proficiency, schooling level or data availability. We then apply this conversion to a country that participates in a regional test but not an international test to produce a comparable score (referred to as a HLO in the database). Mean scores are also calculated for disaggregated groups—for example, scores were calculated for each gender. The detailed methodology is described in the Methods and Supplementary Information II.

By constructing a conversion method across tests between international and regional assessments, we quantify the difference between tests, adjust for this difference and place learning outcomes from regional assessments on a global scale. For a high-performance benchmark, we use the TIMSS benchmark of 625. For the low-performance benchmark, we use 300, which is the equivalent on the HLO scale of the

minimum benchmarks for regional assessments such as The Laboratorio Latinoamericano de Evaluación de la Calidad de la Educación (Latin-American Laboratory for Assessment of the Quality of Education (LLECE)) and The Programme for the Analysis of Education Systems (PASEC). This approach enables us to capture performance across the distribution of both international and regional benchmarks.

Data harmonization efforts such as the one described in this Article serve the dual purpose of compiling the best available data at a given point in time and motivating additional data collection. Thus, they set in motion a cycle that can continually improve learning data over time. For example, in the most recent release of the World Bank human capital index, 20 new countries participated in learning assessments for the first time, enabling their inclusion in subsequent versions of this database.

Schooling is not learning

We present a few descriptive trends in a first application of the database. The average learning outcomes for 164 countries from 2000 to 2017 is shown in Fig. 1. The global coverage of the database becomes immediately apparent and regions typically excluded from international tests such as PISA and TIMSS included in our database are clearly shown (Fig. 1). The database covers the vast majority of countries in sub-Saharan Africa, Latin America and the Caribbean, and South Asia—economies with considerable potential to close learning gaps.

Fig. 1: Average learning (2000–2017).

 figure1

Learning scores are calculated from our HLO database as averages for a given country across subjects and levels over the time period 2000–2017. The numbers in the legend are the lowest and highest average HLO learning scores when averaged over the time period 2000–2017. Average scores by region are as follows: East Asia and Pacific (445), Europe and Central Asia (489), Latin America and the Caribbean (402), Middle East and North Africa (399), North America (529), sub-Saharan Africa (342) and South Asia (335). A few trends emerge: sub-Saharan African regions lag behind all

regions apart from South Asia, with countries such as India (368) performing on par with lower-performing sub-Saharan African countries such as Uganda (369); within sub-Saharan Africa, a few countries such as Kenya (444) and Tanzania (416) lead, on par with many countries in Latin America such as Mexico (435); within Latin America, a few countries such as Chile (449) lead compared with some European counterparts such as Georgia (437); the Middle East performs similarly or worse than Latin America (as shown in summarized scores by region); many Asian countries outperform North American and European regions (for example, Japan (553) relative to the United States (521)).

[Full size image](#)

A few trends emerge: high-income countries far outpace developing economies. Sub-Saharan African lags behind all regions besides South Asia, with countries such as India performing similar to lower-performing sub-Saharan African countries; within sub-Saharan Africa, a few countries such as Kenya and Tanzania lead, on par with many countries in Latin America. Within Latin America, a few countries such as Chile are on par with European countries. The Middle East performs similarly or worse than Latin America and many Asian countries outperform North American and European countries.

The expected years of schooling and HLO primary learning scores for the most recent year for which data are available are shown in Extended Data Fig. 1 to contrast the quantity and quality of the education system (detailed descriptions of the variables and analyses of the trends are provided in the Methods). The graph shown in Extended Data Fig. 1 shows that although many developing countries have achieved substantial levels of schooling (a typical education system is expected to deliver 10–12 years of schooling), they have not yet realized high rates of learning (advanced proficiency in international tests is centred around a score of 625). Two examples with high schooling but low learning are Brazil and Ghana. Brazil has 11.7 years of expected schooling, yet a learning score of just 426. Ghana has 11.6 years of expected schooling, yet a learning score of only 229.

We next explore the contrast between changes in schooling and changes in learning over time. We measure schooling using adjusted enrolment ratios²⁹. We compare this measure of schooling to our measure of learning in primary school for the years 2000–2015. We use data for this period as it has the highest overlap of schooling and learning measures. We restrict our comparison to countries with data points in at least two time periods for enrolment and learning in primary school to maximize comparability over the time period. We further condition on country-fixed effects using multivariate regression for each region (see [Methods](#) for details). This accounts for potential changes in the sample composition of countries with available data for each time period.

We observe a clear trend towards increased schooling, while learning progress appears to be limited in many cases. For example, in the Middle East and North Africa enrolment rates achieved a high of 99% by 2010, increasing from 95% in 2000. By contrast, learning levels stayed low and remained the same around an initial score of 380 from 2000 to 2015 in these regions. It is possible that in regions such as sub-Saharan Africa, as enrolment gets substantially higher and new, lower-performing students participate in learning assessments, average scores decrease owing to a selection effect. However, we observe slow learning progress even in regions in which enrolment levels are relatively constant and high, such as Latin America and the Caribbean, suggesting that there is more to these trends than selection. In Extended Data Fig. 2, we explicitly condition on enrolment and find nearly identical patterns. Moreover, a regression of primary learning outcomes on primary enrolment rates using a panel of countries between 2000 and 2015 with country-fixed effects yields a negative coefficient on enrolment rates of 0.247 with a P value of 0.673, further showing that higher levels of school enrolment has no statistically significant association with better learning outcomes (see [Methods](#) for details).

The patterns in Fig. 2 and Extended Data Fig. 2 could be interpreted as indicative of a plateau effect, as at higher learning levels—for example, in North America or Europe—obtaining further gains may be difficult. However, we also see a relatively flat line in cases in which baseline learning levels are low—that is, in Latin America and the Caribbean—which suggests that learning progress is slow regardless of initial learning conditions. Data availability for each country could in principle affect the patterns that we describe, but the robustness of the patterns to the inclusion of country-fixed effects as described above suggests that they are not driven by country composition. Country-specific trends are also illustrated in Extended Data Fig. 3.

Fig. 2: Enrolment versus learning by region, conditional on country-fixed effects.

 [figure2](#)

a, b, We have 72 countries with data in primary school with at least two data points for the analysed time period (2000–2015) for enrolment (**a**) and learning (**b**). Estimates

are calculated controlling for country-fixed effects using multivariate regression by region. For each region and outcome y (primary enrolment and learning), we estimate the following specification: $\{y\}_{ct}^r = \alpha_r + \beta_r t + \delta_c + \varepsilon_{ct}$, where t represents the year and δ represents a vector of dummy variables for each country c in a given region r . On the basis of this regression, we recover regional time trends accounting for country-fixed effects. The data in this figure include primary enrolment rates. This measure captures the ratio of all individuals enrolled in a given level of schooling to the population of the age group that should be enrolled at that level according to national regulations or customs accounting for grade repetition. This measure has frequently been used in the literature^{[26,29,32](#)}. Learning estimates are taken from our database.

[Full size image](#)

Taken together, the data reveal that the rapid pace at which schooling improved across education systems, as well as the success in achieving high enrolment rates, have not been met with similarly rapid learning progress. This pattern has been referred to in the literature^{[1](#)} and by the international education community as ‘the learning crisis’^{[1,22](#)}. Using the HLO database, we demonstrate that it holds on a global scale.

Human capital and economic development

A large number of studies in the development accounting literature have explored the relative contribution of human capital to cross-country income differences. However, the results have been inconclusive, in part owing to difficulties in measuring human capital. Although direct measures of years of schooling exist, the quality of schooling has been harder to measure.

Approaches to estimate the quality of schooling across countries have relied on differences in Mincerian wage returns^{[5,6](#)}, immigrant returns^{[7](#)} and cross-country skill premia^{[8](#)}. However, these approaches face several challenges, including the need to make assumptions about the substitutability of skilled and unskilled workers^{[9](#)}. The challenges in measuring quality have contributed to substantial variation in estimates of the role of human capital in accounting for cross-country differences in income, ranging from nearly all to potentially none^{[5,6,7,8,9,10,11,12,13](#)}.

In this study, we provide a more direct and reliable measure of the quality of schooling based on our learning outcome data, which we use to construct measures of human capital stock (Methods).

Our results (Table 1) suggest that human capital accounts for between a fifth to around half of cross-country differences in income—which is an intermediate position relative to the estimates found in the literature^{5,6,7,8,9,10,11,12,13}, which range from zero to nearly all. These results are consistent with models of human capital that capture the role of educated entrepreneurs and more comprehensive measures of human capital that include schooling, learning and health^{30,31}.

Table 1 Baseline development accounting results and comparison to the literature
[Full size table](#)

The average relationship between learning and income masks significant heterogeneity across countries (Extended Data Table 2). We find that human capital explains less than two-fifths of cross-country income differences among low-income countries, but more than half among high-income countries. We find even larger differences across regions. For example, when measured by schooling, human capital accounts for 54% of cross-country income differences in advanced economies and only 4% in sub-Saharan Africa. When we include learning, this gap widens to 86% in advanced economies but only 10% in sub-Saharan Africa. This substantial heterogeneity reveals the importance of including a global distribution of countries covering multiple stages of economic development when examining the role of human capital.

Finally, we compare our measure of human capital to alternative measures that are based on prominent global databases such as the Penn world tables¹⁴, the Barro–Lee Educational Attainment dataset³² and the United Nation’s HDI¹⁵. In Table 2, we find that our measure of human capital has a stronger association with growth than alternative human capital measures. This is the case in univariate regressions that include each measure on its own (columns 1–4). We observe that a change of 1% in learning is associated with a change of 7.2% in annual growth. By contrast, a change of 1% in the other human capital measures is associated with a change of between 1.6% and 3.3% in annual growth. We further show that when we include all measures in the same multivariate regression, the association between our measure of learning and growth remains high, between 5.9% and 6.9%, and statistically significant ($P \leq 0.01$), whereas other human capital variables have a reduced and statistically nonsignificant association with growth. We find that the model fit improves only slightly when all measures are included with an R^2 value of 0.32 relative to our measure of human capital with an R^2 value of 0.30.

Table 2 Comparing measures of human capital and economic growth
[Full size table](#)

Therefore, our measure of human capital appears to have a stronger relationship with economic growth, both individually and jointly. This is probably because alternative

measures of human capital rely largely on years of schooling and omit learning. However, the use of these alternative measures remains standard practice, in part because these data have the broadest coverage. By constructing learning data across 164 countries, we fill a key gap: broad coverage over nearly two decades and a measure of human capital with strong links to economic development.

Discussion and future directions

This database comes at a moment when a series of global efforts have been launched to measure and track learning on a global scale. Although recent modelling suggests that the world is on track to achieve the goal of universal primary enrolment by 2030³³, if learning continues to stagnate, this achievement will mean little.

Accordingly, the Sustainable Development Goals include a focus on learning whereas the Millennium Development Goals focused largely on schooling. Another notable effort to measure and track learning on a global scale is the World Bank's human capital index in which the levels of human capital of countries around the world are compared². This effort aims to report measures of human capital that will encourage countries to invest in education. The human capital index includes learning outcomes from this database as one of its core components. The database in this Article will be updated regularly and made public to enable these large-scale efforts and to advance our understanding of the formation of human capital in developing economies.

Methods

Data reporting

No experiments were performed. No statistical methods were used to predetermine sample size of the harmonization of learning data or analyses done in this paper. The underlying microdata from the original learning assessments have detailed survey sampling procedures detailed in their corresponding technical reports.

Test-score-linking methodology

We include 164 countries, two-thirds of which are developing countries, by linking international assessments to their regional counterparts. Regional assessments cover much of sub-Saharan Africa and Latin America but have often been excluded from international comparisons. We convert a regional test score to an international test score within subjects and schooling levels (primary and secondary) and within adjacent years. By including tests across the same testing round and at the disaggregated schooling and subject level, this method minimizes the likelihood that test differences are a function of time, proficiency, schooling level or data availability

and maximizes the likelihood that they reflect test difficulty. We then apply this conversion to a country that participates in a regional test but not an international test to produce a comparable score (referred to as a HLO in the database).

The success of the linking approach hinges on three key assumptions. First, linked tests must capture the same underlying population. This assumption is satisfied by using sample-based assessments representative at the national level for cases in which a country participated in both a regional and an international assessment. This ensures that the underlying population tested is the same on average. Second, tests should measure similar proficiencies. To this end, we link within subjects (mathematics, reading and science) and schooling levels (primary and secondary) to ensure overlap. Third, the linking function should capture differences between tests rather than country-specific effects. This assumption is more likely to hold the larger the number of countries that participate in a given pair of tests being linked. To maximize the likelihood that this assumption holds, we construct the linking function over the entire interval. This step increases the sample size used to link tests, improving the likelihood that we capture test-specific rather than country-specific differences. In fixing the linking function, we assume that the relationship between tests stays constant across rounds. This assumption is reasonable since the mid-1990s, when assessments started to use a standardized approach and to link testing rounds with overlapping test items. A related advantage of a linking function over a fixed interval is that it guarantees that any changes in test scores over this interval are due to realized progress in learning rather than changing linking functions between tests. Of note, every update of the database increases the number of countries participating in a given pair of assessments. Thus, each update expands coverage and enhances the reliability of all estimates by enabling the construction of a more robust linking procedure.

We use multiple methods to link regional to international assessments. Our primary approach uses regression when multiple countries participate in the assessments being compared. When only one country participates, we use linear linking. Supplementary Information [IIA](#) describes both methods and the respective tests used. Both methods adjust test scores by a constant as well as by relative standard deviations across tests. These approaches build on a literature comparing scores across different tests^{[34,35](#)} as well as more recent work linking aggregate level scores across states in the USA^{[36](#)}. In Supplementary Information [IIB](#), we conduct a series of sensitivity tests, including conducting the conversion using country-fixed effects or random draws of countries and time periods. We further explore additional methods in Supplementary Information [IIB](#), such as mean linking and ratio conversions, highlighting the trade-offs of each approach and examining robustness across them. We find a 0.99 or higher correlation coefficient for scores and relative ranks across all robustness tests (Supplementary Fig. [7](#)). Limitations are described in Supplementary Information [IIC](#). Detailed descriptions of all data sources are included Supplementary Information [IID](#).

Additional methodological parameters, such as the disaggregation of the data, are described in Supplementary Information [IIE](#).

We compare our data to a smaller database using item response theory (IRT)—in which tests share common test items—and find a 0.98 correlation coefficient (Extended Data Fig. [4](#)). IRT—which is considered to be one of the most reliable methods to link tests in the psychometric literature—models the probability that a given pupil answers a given test item correctly as a function of pupil- and item-specific characteristics^{[34,37,38](#)}. This methodology is used to construct the underlying tests that we use. To use it to compare learning across assessments, we need enough overlap in the underlying test items across assessments^{[39, 40](#)}. However, such overlap does not exist for a large-enough set of tests and time periods that are needed to create a globally comparable panel dataset^{[40](#)}. For example, TIMSS 1995 and Southern and Eastern Africa Consortium for Monitoring Educational Quality (SACMEQ) 2000 included overlapping mathematics items, but had only three test questions that would enable a comparison. When this overlap is small, standard maximum likelihood estimates will reflect both true variance and measurement error, overstating the variance in the test score distribution. The various challenges of estimating IRT parameters with limited item-specific overlap have previously been discussed in more detail^{[39](#)}. Although IRT might not be a reliable approach when there is limited item-by-item overlap, we conduct comparisons in which the overlap is larger, with up to 17 common test items across tests. We compare our results to the Linking International Comparative Student Assessment (LINCS) project, which uses IRT methods and has an overlap in items for a subset of international studies focused on reading in primary schools^{[40](#)}.

We compare the average scores for the same subject (reading), schooling level (primary) and time period (2000–2010) and find a correlation coefficient of 0.984 (Extended Data Fig. [4](#)). This comparison indicates that even as we expand coverage to 164 countries in our database, we maintain high consistency with alternative measures for the subset of proficiencies, school levels and subjects for which there is overlap.

Of note, the assessments included in this database are conducted at school. Testing, and thus learning, data could be affected by enrolment patterns, and we advise users of the data to analyse learning outcomes alongside enrolment trends. For example, average test scores could be driven by lower-performing students entering the system rather than learning progress for those who were already in school. Although this is a potential concern when analysing average scores, there are several reasons why harmonized learning outcomes are still useful. First, primary enrolment rates are relatively high in all countries, reaching 90% on average. Second, learning measured with school-based tests is likely to yield a conservative upper bound of learning in a given country. As most countries at the bottom of the distribution of measured learning

are also those with relatively low enrolments, it is unlikely that new school entrants would alter conclusions related to cross-country patterns—the lowest performing countries would probably be revealed to be performing even worse.

Comparison of trends in schooling and learning

Expected years of schooling versus learning basic skills

Related to Extended Data Fig. 1. We define two key variables for analysis in this figure. First, we define our learning variable. Our measure of quality comprises the primary HLO scores, which measure the degree to which students acquire basic skills in primary school. Second, we define the schooling variable. The expected years of schooling measure is constructed by UNESCO (United Nations Educational, Scientific and Cultural Organization) and is a function of enrolment patterns and the number of years of schooling a given country formally provides. This measure is often interpreted by the international education community as a measure of a strong education system in which students attend many years of school. As the expected number of years of schooling is partially a function of enrolment, which we also use as a measure of schooling at times in this paper, these two measures are highly correlated. For countries with data available for both measures, we find an average correlation coefficient of 0.72 across them.

We find a high variance in learning conditional on years of schooling (Extended Data Figure 1). Ghana stands out as a country in which schooling is close to 12 years of schooling, yet the learning score is below the threshold of minimum proficiency of 300. Next, consider the examples of Zambia and South Africa. In Zambia, the average child is expected to have more than 9 years of schooling yet achieves a score of 301 on primary school learning. By contrast, in South Africa, with similar years of expected schooling, the average child scores 366. Given that both countries have more than 9 years of expected schooling, the primary-school learning scores are unlikely to be driven by selection. In addition, average primary enrolment rates over the 2000–2015 time period are high in both countries (98.2% in South Africa and 92.9% in Zambia). As learning outcomes are measured using tests taken in grades 4–6, primary school enrolment rates are relevant measures for schooling comparisons. Typically, large dropouts occur between schooling levels, such as the transition from primary to secondary school. However, enrolment up to the last grade within primary school is persistently high. For example, in South Africa, data from the World Bank show that 90% of students are retained until the end of primary school. This varies across contexts, but in many countries enrolment rates in primary school are relatively stable through the middle years of primary school when achievement tests are taken.

We further observe an exponential shape of the line of best fit, with a smaller correlation coefficient between schooling and learning for countries that provide 10 or fewer years of schooling on average than after this threshold (with a correlation coefficient of 0.35 relative to 0.73, respectively). The exponential curve is suggestive and should be viewed with a few caveats in mind. For example, it is conceivable that Brazil has higher learning scores than South Africa, not because the quality of education in Brazil is higher, but because of lower enrolments, which means that higher-ability students remain in the system at the time of the test. However, this is unlikely as Brazil has around 12 years of expected schooling and South Africa has around 9 years, meaning that most children progress through primary school and thus their primary-school learning scores largely reflect the quality of education rather than selection. The selection concern may be more pronounced at low levels of expected schooling. Even so, the flat part of the curve between 7 and 10 years of expected schooling is unlikely to reflect selection, given that learning is measured through tests in primary school, and primary school enrolment in countries with expected schooling of 7 or more years, is typically high. Moreover, the fact that learning levels vary substantially for a given point on the x axis reveals substantial heterogeneity in school quality even in systems in which the average student receives a similar number of years of education. These patterns suggest that schooling does not automatically translate to learning.

Regional learning and enrolment trends

The following section refers to methods used to compare trends in enrolment and learning over time. We restrict our comparison to countries with data points for at least two time periods for both enrolment and learning data in primary school to maximize comparability over the time period. The list of 72 countries included in the following analyses are: Argentina, Australia, Austria, Benin, Brazil, Bulgaria, Cameroon, Canada, Chile, Colombia, Costa Rica, Cyprus, Czech Republic, Côte d'Ivoire, Denmark, Dominican Republic, Ecuador, Finland, France, Gambia, Germany, Guatemala, Haiti, Honduras, Hong Kong, Special administrative regions of China (SAR China), Hungary, Iceland, Indonesia, Islamic Republic of Iran, Ireland, Italy, Japan, Jordan, Kenya, Korea (South), Kuwait, Lesotho, Liberia, Malawi, Malta, Mauritius, Mexico, Morocco, Mozambique, The Netherlands, New Zealand, Nicaragua, Niger, Norway, Panama, Paraguay, Peru, The Philippines, Poland, Portugal, Romania, Russian Federation, Senegal, South Africa, Spain, Eswatini (Swaziland), Sweden, Taiwan, Republic of China, Togo, Trinidad and Tobago, Tunisia, Turkey, Uganda, United States of America, Uruguay, Zambia, Zimbabwe. We average the HLO data into 5-year intervals to be analogous in structure to previously published primary enrolment data²⁹. As our learning data extends to 2015 and enrolment data extends to 2010, we make a conservative assumption that enrolment rates persist through 2015 to enable inclusion of all learning data.

Regional learning and enrolment trends conditional on county-fixed effects

In Fig. 2, estimates are calculated controlling for country-fixed effects using multivariate regression by region. For each region and outcome y (primary enrolment and learning), we estimate the following specification: $\{y\}_{ct}^r = \alpha_r + \beta_r t + \delta_c + \varepsilon_{ct}^r$, in which t represents the year and δ represents a vector of dummy variables for each country c in a given region r . On the basis of this regression, we recover regional time trends accounting for country-fixed effects.

Regional learning trends conditional on county-fixed effects and enrolment

In Extended Data Fig. 2, we further explicitly condition for enrolment effects and find nearly identical patterns to Fig. 2. For each region and outcome y we run the following specification: $\{y\}_{ct}^r = \alpha_r + \beta_r t + \delta_c + \gamma_{ct}^r + \varepsilon_{ct}^r$, in which t represents the year, δ represents a vector of dummy variables for each country c in a given region r and γ represents primary enrolment rates. We then recover regional time trends accounting for country-fixed effects and conditional on enrolment.

Enrolment and learning regression

We run the following regression: $\{y\}_{ct} = \alpha + \beta \gamma_{ct} + \delta_c + \varepsilon_{ct}$ in which c represents a country, t represents a year, γ represents primary enrolment rates and δ represents a vector of dummy variables for each country c . The coefficient of interest is β , which captures the association between learning and enrolment. As noted in the ‘Schooling is not learning’ section, we find no statistically significant relationship between schooling and learning with a negative coefficient on enrolment rates of 0.247 with a P value of 0.673, reinforcing the patterns shown in Fig. 2 and Extended Data Fig. 2. We also find an R^2 value of 0.96. We omitted four countries (Mozambique, Niger, Cameroon and Benin) that are outliers above the 95th percentile in enrolment changes, which can bias average cross-country trends. Another way to visualize the absence of an association between learning and enrolment is a scatter plot of learning and enrolment trends over time by country. This plot is provided in Supplementary Fig. 4.

Learning by country

Related to Extended Data Fig. 3. We illustrate regional patterns by focusing on a few specific examples from Latin and Central America, sub-Saharan Africa and the Middle East (Brazil, Colombia, Mexico, Uganda and Kuwait). Extended Data Figure 3 shows

that learning in all of these countries has been consistently low and improved slowly over the past two decades, ranging from 360 to 453, which translates into many students not acquiring basic skills such as being able to read a simple story, even though all of these countries have achieved high enrolment rates above 99% in all years. Moreover, in each of the country examples, as primary enrolment rates are extremely high and flat, this reinforces that slow learning trends are not a function of enrolment. Figure 2 and Extended Data Fig. 2, in which country-fixed effects are controlled for, can be thought of as the generalizations of these patterns to the regional level.

Development accounting

The contribution of human capital to cross-country income differences is analysed in studies of development accounting. We follow the literature^{5,6,41} and begin with a standard aggregate production function in its per-capita form:

$$y = Ah \left(\frac{K}{Y} \right)^{\alpha} (1-\alpha)$$

in which y represents output per worker, K denotes capital, h denotes the level of human capital per capita and A captures the residual, typically interpreted as total factor productivity. Taking the logarithm on both sides decomposes cross-country income differences into three sources: capita–output ratio, average human capital and total factor productivity. Below, we only report the share of income differences that can be explained by variation in human capital, given that human capital is the focus of this paper. In Table 1 (top), we show decompositions that have used both human capital measures that incorporate education quality and education quantity^{5,7,12}. In Table 1 (bottom), we include an additional decomposition, $\ln(h_{90}) - \ln(h_{10}) - (\ln(y_{90}) - \ln(y_{10}))$, which has been used in studies that have used human capital measures that account for education quality^{10,11,13}.

To measure human capital, we extend the standard Mincer specification that weights education by its micro-labour-market returns to include learning in addition to schooling:

$$h = rS + wL$$

in which S is the quantity of schooling, L is a measure of learning, and r and w are their respective returns. For years of schooling, we use previously published data³². For learning measures, we use the data presented in this paper. We assume rates of return on the basis of the microeconomic literature: we take the value $r = 0.10$ for the rate of return per school year, and $w = 0.20$ per standard deviation increase in learning,

based on parameter values used in the literature^{42,43}. The 0.20 value is based on US data. However, we can expect that returns to learning will be higher in developing countries in which the supply of skills is lower, as is the case with the returns to schooling literature⁴². A considerable number of studies have investigated these parameters. For the purpose of this paper, our intention is not to provide definitive results, but rather to motivate the use of the data in the development accounting literature. To this end, we take parameter values as given and conduct sensitivity analyses with values $w = 0.15$ and $w = 0.25$. We included 131 countries that have both schooling data³² and learning data.

We first compared our results to three previous studies^{5,7,12} in Table 1 (top). We find, in our estimates, that when the human capital measure only captures quantity ($w = 0$), human capital accounts for roughly 7–11% of the differences in output per worker. However, when we include measures of quality ($w > 0$), we find that this contribution increases to 14–21%. These results suggest that measuring human capital while taking into account quality substantially increases the role of human capital in explaining cross-country output per worker differences. These results are consistent with the literature showing that when quality is taken into account, the role of human capital in explaining cross-country differences in output per worker doubles⁷ relative to when only quantity is taken into account⁵.

In Table 1 (bottom), we show results focusing on $\frac{\ln(h_{90}) - \ln(h_{10})}{\ln(y_{90}) - \ln(y_{10})}$. The literature^{10,11,13} that has used this decomposition estimates that the contribution of human capital to cross-country income differences ranges from nearly 100% to close to 0%. We show that when we include our measure of quality, the share of human capital varies between 40% and 48%.

Reporting summary

Further information on research design is available in the [Nature Research Reporting Summary](#) linked to this paper.

Data availability

The data are available for public use and updated regularly on the World Bank website: <https://datacatalog.worldbank.org/dataset/harmonized-learning-outcomes-hlo-database>. The database is expected to be updated every 2–3 years as new learning data become available. The database will be updated at the same location on the World Bank website using the methodology and approach in this paper, with accompanying technical notes on additional countries and data sources added. This study used a

combination of data sources, including data that are available from online repositories and required straightforward registration and usage agreement. We also collected data from over 48 countries directly in collaboration with the World Bank and USAID.

Code availability

The code used to compile and analyse data was written in Stata v.15.1. The code to replicate analysis and tables is available from GitHub (<https://github.com/measuringhumancapital>).

References

1. 1.

World Bank. *World Development Report 2018: Learning to Realize Education's Promise* (World Bank, 2018).

2. 2.

World Bank. *World Development Report 2019: The Changing Nature of Work* (World Bank, 2019).

3. 3.

Hanushek, E. A. & Woessmann, L. Do better schools lead to more growth? Cognitive skills, economic outcomes, and causation. *J. Econ. Growth* **17**, 267–321 (2012).

[Article](#) [Google Scholar](#)

4. 4.

OECD. *PISA 2015 Technical Report*. https://www.oecd.org/pisa/data/2015-technical-report/PISA2015_TechRep_Final.pdf (OECD Publishing, 2015).

5. 5.

Hall, R. E. & Jones, C. I. Why do some countries produce so much more output per worker than others? *Q. J. Econ.* **114**, 83–116 (1999).

[Article](#) [Google Scholar](#)

6. 6.

Caselli, F. Chapter 9 Accounting for cross-country income differences. *Handb. Econ. Educ.* **1**, 679–741 (2005).

[Article](#) [Google Scholar](#)

7. 7.

Schoellman, T. Education quality and development accounting. *Rev. Econ. Stud.* **79**, 388–417 (2012).

[Article](#) [Google Scholar](#)

8. 8.

Caselli, F. & Coleman, J. The world technology frontier. *Am. Econ. Rev.* **96**, 499–522 (2006).

[Article](#) [Google Scholar](#)

9. 9.

Jones, B. F. The human capital stock: a generalized approach: reply. *Am. Econ. Rev.* **109**, 1175–1195 (2019).

[Article](#) [Google Scholar](#)

10. 10.

Jones, B. F. The human capital stock: a generalized approach. *Am. Econ. Rev.* **104**, 3752–3777 (2014).

[Article](#) [Google Scholar](#)

11. 11.

Caselli, F. & Ciccone, A. The human capital stock: a generalized approach. comment. *Am. Econ. Rev.* **109**, 1155–1174 (2019).

[Article](#) [Google Scholar](#)

12. 12.

Hendricks, L. How important is human capital for development? Evidence from immigrant earnings. *Am. Econ. Rev.* **92**, 198–219 (2002).

[Article](#) [Google Scholar](#)

13. 13.

Hendricks, L. & Schoellman, T. Human capital and development accounting: new evidence from wage gains at migration. *Q. J. Econ.* **133**, 665–700 (2018).

[Article](#) [Google Scholar](#)

14. 14.

Feenstra, R. C., Inklaar, R. & Timmer, M. P. The next generation of the Penn world table. *Am. Econ. Rev.* **105**, 3150–3182 (2015).

[Article](#) [Google Scholar](#)

15. 15.

United Nations Development Programme. *Human Development Report: Education Index*. <http://hdr.undp.org/en/content/education-index> (UNDP, accessed August 2020).

16. 16.

Smith, A. *An Inquiry into the Nature and Causes of the Wealth of Nations*, vol. 1 (W. Strahan and T. Cadell, 1776).

17. 17.

Becker, G. S. Investment in human capital: a theoretical analysis. *J. Polit. Econ.* **70**, 9–49 (1962).

[Article](#) [Google Scholar](#)

18. 18.

Mincer, J. Human capital and economic growth. *Econ. Educ. Rev.* **3**, 195–205 (1984).

[Article](#) [Google Scholar](#)

19. 19.

Mankiw, N. G., Romer, D. & Weil, D. N. A contribution to the empirics of economic growth. *Q. J. Econ.* **107**, 407–437 (1992).

[Article](#) [Google Scholar](#)

20. 20.

Lutz, W. & KC, S. Global human capital: integrating education and population. *Science* **333**, 587–592 (2011).

[ADS](#) [Article](#) [CAS](#) [Google Scholar](#)

21. 21.

Pritchett, L. *The Rebirth of Education: Schooling ain't Learning* (CGD Books, 2013).

22. 22.

UNESCO. *More Than One-half of Children and Adolescents are not Learning Worldwide*. UIS Fact Sheet No. 46
<http://uis.unesco.org/sites/default/files/documents/fs46-more-than-half-children-not-learning-en-2017.pdf> (UNESCO, 2017).

23. 23.

Krueger, A. B. & Lindahl, M. Education for growth: why and for whom? *J. Econ. Lit.* **39**, 1101–1136 (2001).

[Article](#) [Google Scholar](#)

24. 24.

Pritchett, L. Chapter 11 Does learning to add up add up? The returns to schooling in aggregate data. *Handb. Econ. Educ.* **1**, 635–695 (2006).

[Article](#) [Google Scholar](#)

25. 25.

Kraay, A. The World Bank human capital index: a guide. *World Bank Res. Obs.* **34**, 1–33 (2019).

[Article](#) [Google Scholar](#)

26. 26.

Barro, R. J. & Lee, J.-W. International data on educational attainment: updates and implications. *Oxf. Econ. Pap.* **53**, 541–563 (2001).

[Article](#) [Google Scholar](#)

27. 27.

Hanushek, E. A. & Kimko, D. D. Schooling, labor-force quality, and the growth of nations. *Am. Econ. Rev.* **90**, 1184–1208 (2000).

[Article](#) [Google Scholar](#)

28. 28.

Altinok, N., Angrist, N. & Patrinos, H. A. *Global Dataset on Education Quality 1965–2015*. World Bank Policy Research Working Paper No. 8314 (The World Bank, 2018).

29. 29.

Lee, J.-W. & Lee, H. Human capital in the long run. *J. Dev. Econ.* **122**, 147–169 (2016).

[Article](#) [Google Scholar](#)

30. 30.

Gennaioli, N., La Porta, R., Lopez-de-Silanes, F. & Shleifer, A. Human capital and regional development. *Q. J. Econ.* **128**, 105–164 (2013).

[Article](#) [Google Scholar](#)

31. 31.

Campbell, S. G. & Üngör, M. Revisiting human capital and aggregate income differences. *Econ. Model.* **91**, 43–64 (2020).

[Article](#) [Google Scholar](#)

32. 32.

Barro, R. J. & Lee, J. W. A new data set of educational attainment in the world, 1950–2010. *J. Dev. Econ.* **104**, 184–198 (2013).

[Article](#) [Google Scholar](#)

33. 33.

Friedman, J. et al. Measuring and forecasting progress towards the education-related SDG targets. *Nature* **580**, 636–639 (2020).

[ADS](#) [Article](#) [CAS](#) [Google Scholar](#)

34. 34.

Kolen, M. J. & Brennan, R. L. (eds) in *Test Equating, Scaling, and Linking* 103–142 (Springer, 2014).

35. 35.

Patel, D. & Sandefur, J. *A Rosetta Stone for Human Capital*. CGD Working Paper 550. <https://www.cgdev.org/sites/default/files/rosetta-stone-human-capital.pdf> (Center for Global Development 2020).

36. 36.

Reardon, S. F., Kalogrides, D. & Ho, A. D. Validation methods for aggregate-level test scale linking: a case study mapping school district test score distributions to a common scale. *J. Educ. Behav. Stat.* <https://doi.org/10.3102/1076998619874089> (2019).

37. 37.

Mislevy, R. J., Beaton, A. E., Kaplan, B. & Sheehan, K. M. Estimating population characteristics from sparse matrix samples of item responses. *J. Educ. Meas.* **29**, 133–161 (1992).

[Article](#) [Google Scholar](#)

38. 38.

Holland, P. W. & Dorans, N. J. in *Educational Measurement* 4th edn (ed. Brennan, R. L.) 187–220 (American Council on Education and Praeger, 2006).

39. 39.

Das, J. & Zajonc, T. India shining and Bharat drowning: comparing two Indian states to the worldwide distribution in mathematics achievement. *J. Dev. Econ.* **92**, 175–187 (2010).

[Article](#) [Google Scholar](#)

40. 40.

Steinmann, I., Strietholt R. & Bos, W. *Linking International Comparative Student Assessment*. LINCS Technical Report (2014).

41. 41.

Klenow, P. J. & Rodríguez-Clare, A. The neoclassical revival in growth economics: has it gone too far? *NBER Macroecon. Annu.* **12**, 73–103 (1997).

[Article](#) [Google Scholar](#)

42. 42.

Psacharopoulos, G. & Patrinos, H. A. Returns to investment in education: a decennial review of the global literature. *Educ. Econ.* **26**, 445–458 (2018).

[Article](#) [Google Scholar](#)

43. 43.

Hanushek, E. A. & Zhang, L. Quality-consistent estimates of international schooling and skill gradients. *J. Hum. Cap.* **3**, 107–143 (2009).

[Article](#) [Google Scholar](#)

44. 44.

Hanushek, E. A. & Woessmann, L. Schooling, educational achievement, and the Latin American growth puzzle. *J. Dev. Econ.* **99**, 497–512 (2012).

[Article](#) [Google Scholar](#)

[Download references](#)

Acknowledgements

We thank D. Weil for revisions that improved the paper; S. Aroob Iqbal and H. Abdul-Hamid for research support; A. Kraay for detailed comments and contributions to the methodology; E. L. Baker, F. Barrera-Osorio, E. Cascallar, P. Collier, S. Dercon, D. Filmer, R. Gatti, R. Glennerster, D. Koretz, J. Labonne, S. Montoya, G. Psacharopoulos, S. Quinn, H. Rindermann, H. Rogers, J. Saavedra, S. Sabarwal and E.

Velez for comments; and R. Rhodes for access to the microdata for many Early Grade Reading Assessments. This work builds on co-authored work with N. Altinok. This paper benefited from seminars held at the World Bank, World Congress of Cliometrics, American Economic Association, IDB, Oxford, USAID and FHI360. A great number of individuals and organizations supplied us with data. The views expressed here are those of the authors and should not be attributed to the World Bank.

Author information

Affiliations

1. World Bank, Washington, DC, USA

Noam Angrist & Harry A. Patrinos

2. Department of Economics and Blavatnik School of Government, University of Oxford, Oxford, UK

Noam Angrist

3. Financial Markets Group, London School of Economics, London, UK

Simeon Djankov

4. Peterson Institute for International Economics, Washington, DC, USA

Simeon Djankov & Pinelopi K. Goldberg

5. Department of Economics, Yale University, New Haven, CT, USA

Pinelopi K. Goldberg

6. Bureau for Research and Economic Analysis of Development (BREAD), Kennedy School of Government, Harvard University, Cambridge, MA, USA

Pinelopi K. Goldberg

7. Centre for Economic Policy Research (CEPR), London, UK

Pinelopi K. Goldberg

8. National Bureau of Economic Research (NBER), Cambridge, MA, USA

Pinelopi K. Goldberg

Authors

1. Noam Angrist

[View author publications](#)

You can also search for this author in [PubMed](#) [Google Scholar](#)

2. Simeon Djankov

[View author publications](#)

You can also search for this author in [PubMed](#) [Google Scholar](#)

3. Pinelopi K. Goldberg

[View author publications](#)

You can also search for this author in [PubMed](#) [Google Scholar](#)

4. Harry A. Patrinos

[View author publications](#)

You can also search for this author in [PubMed](#) [Google Scholar](#)

Contributions

H.A.P. oversaw data collection efforts and conceived the study. N.A. assembled the data, conducted the analysis and wrote the drafts of the manuscripts. N.A., S.D., P.K.G. and H.A.P. provided substantial intellectual inputs and edited drafts of the manuscripts.

Corresponding author

Correspondence to [Noam Angrist](#).

Ethics declarations

Competing interests

The authors declare no competing interests.

Additional information

Peer review information *Nature* thanks David Weil and the other, anonymous, reviewer(s) for their contribution to the peer review of this work.

Publisher's note Springer Nature remains neutral with regard to jurisdictional claims in published maps and institutional affiliations.

Extended data figures and tables

[Extended Data Fig. 1 Expected years of schooling versus learning basic skills.](#)

We compare the average country learning outcomes in the latest available year from our database to the latest expected years of schooling in a given country. For example, in Zambia (9.2, 301.4) the average child can expect to receive 9.2 years of schooling and achieve learning outcomes of 301.4. The data in this figure include expected years of schooling from the World Bank Human Capital Index based on data compiled by UNESCO²⁵. Primary learning outcomes are from our database. Both measures take the data in the latest year available.

[Extended Data Fig. 2 Learning in primary school by region, conditional on country-fixed effects and primary enrolment rates.](#)

We have 72 countries with both learning and enrolment data in primary school with at least two data points over the time period (2000–2015). Estimates are calculated controlling for country-fixed effects using multivariate regression by region. For each region r and outcome y , we run the following specification: $\{y\}_{ct}^r = \alpha + \beta_r t + \delta_c + \gamma_{ct} + \varepsilon_{ct}$, in which t represents the year, δ represents a vector of dummy variables for each country c in a given region r and γ represents primary enrolment rates. We then recover regional time trends accounting for country-fixed effects and conditional on enrolment. The data in this figure includes primary enrolment rates. This measure captures the ratio of all individuals enrolled in a given level of schooling by the population of the age group that should be enrolled at that level according to national regulations or customs accounting for grade repetition. This measure has frequently been used in the literature^{29,32}. Learning estimates are taken from our database. LAC, Latin American and the Caribbean; MENA, Middle East and North Africa; SSA, sub-Saharan Africa.

[Extended Data Fig. 3 Learning by country.](#)

Left, primary enrolment rates data are from a previous study²⁹. Right, learning estimates are derived from our database and are plotted using a linear fit for the available data over the time series. Data on learning are available across the time period for Uganda from the source test the Southern African Consortium for Monitoring Education Quality (SACMEQ). For Kuwait, data are from The Progress in International Reading Literacy Study (PIRLS) and TIMSS. Data are available for Brazil, Mexico and Colombia from the LLECE as well as PIRLS for Colombia.

Extended Data Fig. 4 Comparison of HLOs to IRT.

We compare average scores per country from our learning data for primary school from 2000 to 2010 to the LINCS project which uses IRT methods to link test score data. IRT methods are used to create scores for the underlying international and regional assessments used. The LINCS project produces scores on a globally comparable scale for primary school scores⁴⁰.

Extended Data Table 1 Country–year observations by disaggregation and region

[Full size table](#)

Extended Data Table 2 Human capital share by income status and region

[Full size table](#)

Supplementary information

Supplementary Information

This file contains a Supplementary Discussion, Supplementary Methods, Supplementary References, Supplementary Tables 1-6 and Supplementary Figures 1-15.

Reporting Summary

Rights and permissions

Open Access This article is licensed under a Creative Commons Attribution 4.0 International License, which permits use, sharing, adaptation, distribution and reproduction in any medium or format, as long as you give appropriate credit to the original author(s) and the source, provide a link to the Creative Commons license, and indicate if changes were made. The images or other third party material in this article are included in the article's Creative Commons license, unless indicated otherwise in a credit line to the material. If material is not included in the article's Creative Commons license and your intended use is not permitted by statutory regulation or exceeds the

permitted use, you will need to obtain permission directly from the copyright holder.
To view a copy of this license, visit <http://creativecommons.org/licenses/by/4.0/>.

[Reprints and Permissions](#)

About this article



Check for
updates

Cite this article

Angrist, N., Djankov, S., Goldberg, P.K. *et al.* Measuring human capital using global learning data. *Nature* **592**, 403–408 (2021). <https://doi.org/10.1038/s41586-021-03323-7>

[Download citation](#)

- Received: 04 February 2020
- Accepted: 03 February 2021
- Published: 10 March 2021
- Issue Date: 15 April 2021
- DOI: <https://doi.org/10.1038/s41586-021-03323-7>

Comments

By submitting a comment you agree to abide by our [Terms](#) and [Community Guidelines](#). If you find something abusive or that does not comply with our terms or guidelines please flag it as inappropriate.

[Download PDF](#)

This article was downloaded by **calibre** from <https://www.nature.com/articles/s41586-021-03323-7>

- Article
- [Published: 10 March 2021](#)

Inter-mosaic coordination of retinal receptive fields

- [Suva Roy ORCID: orcid.org/0000-0003-2794-5023¹](#),
- [Na Young Jun¹](#),
- [Emily L. Davis¹](#),
- [John Pearson ORCID: orcid.org/0000-0002-9876-7837^{1,2}](#) &
- [Greg D. Field ORCID: orcid.org/0000-0001-5942-2679¹](#)

[Nature](#) volume **592**, pages409–413(2021)[Cite this article](#)

- 4072 Accesses
- 62 Altmetric
- [Metrics details](#)

Subjects

- [Neural encoding](#)
- [Sensory processing](#)

Abstract

The output of the retina is organized into many detector grids, called ‘mosaics’, that signal different features of visual scenes to the brain^{1,2,3,4}. Each mosaic comprises a single type of retinal ganglion cell (RGC), whose receptive fields tile visual space. Many mosaics arise as pairs, signalling increments (ON) and decrements (OFF), respectively, of a particular visual

feature⁵. Here we use a model of efficient coding⁶ to determine how such mosaic pairs should be arranged to optimize the encoding of natural scenes. We find that information is maximized when these mosaic pairs are anti-aligned, meaning that the distances between the receptive field centres across mosaics are greater than expected by chance. We tested this prediction across multiple receptive field mosaics acquired using large-scale measurements of the light responses of rat and primate RGCs. ON and OFF RGC pairs with similar feature selectivity had anti-aligned receptive field mosaics, consistent with this prediction. ON and OFF RGC types that encode distinct features have independent mosaics. These results extend efficient coding theory beyond individual cells to predict how populations of diverse types of RGC are spatially arranged.

[Access through your institution](#)

[Change institution](#)

[Buy or subscribe](#)

Access options

Subscribe to Journal

Get full journal access for 1 year

\$199.00

only \$3.90 per issue

[Subscribe](#)

All prices are NET prices.

VAT will be added later in the checkout.

Tax calculation will be finalised during checkout.

Rent or Buy article

Get time limited or full article access on ReadCube.

from \$8.99

Rent or Buy

All prices are NET prices.

Additional access options:

- [Log in](#)
- [Access through your institution](#)
- [Learn about institutional subscriptions](#)

Fig. 1: Efficient coding predicts anti-alignment between ON and OFF RGCs with similar feature selectivity.



Fig. 2: Analysis framework for measuring mosaic coordination.

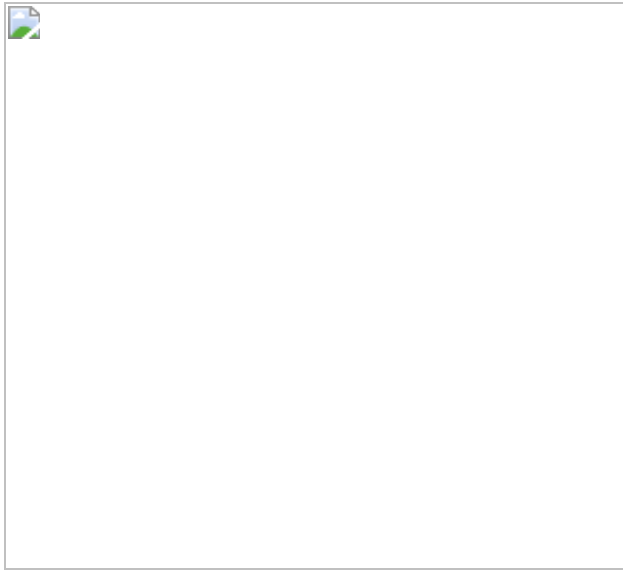


Fig. 3: Receptive field mosaics of functionally paired ON and OFF RGC types are anti-aligned.

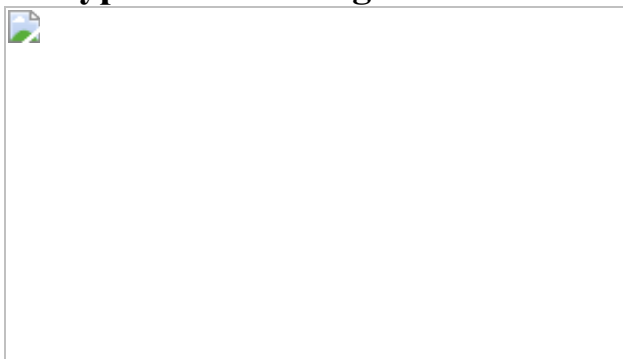
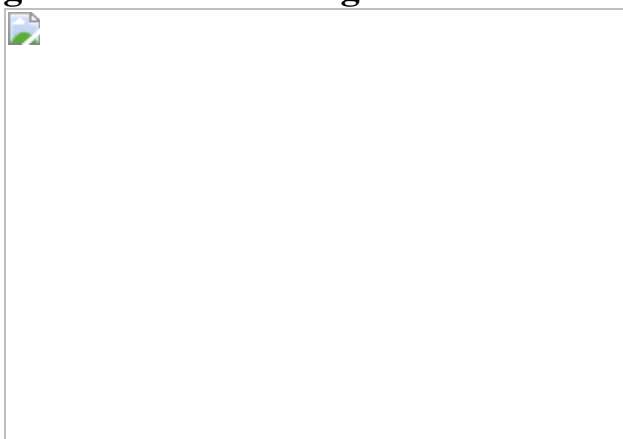


Fig. 4: Mosaic anti-alignment is unlikely to have arisen by chance.



Data availability

Raw data will be made available upon request. [Source data](#) are provided with this paper.

Code availability

Analysis code is available at <https://doi.org/10.5281/zenodo.4441277>.

References

1. 1.

Devries, S. H. & Baylor, D. A. Mosaic arrangement of ganglion cell receptive fields in rabbit retina. *J. Neurophysiol.* **78**, 2048–2060 (1997).

[PubMed](#) [CAS](#) [Google Scholar](#)

2. 2.

Field, G. D. & Chichilnisky, E. J. Information processing in the primate retina: circuitry and coding. *Annu. Rev. Neurosci.* **30**, 1–30 (2007).

[PubMed](#) [CAS](#) [Google Scholar](#)

3. 3.

Wässle, H., Peichl, L. & Boycott, B. B. Dendritic territories of cat retinal ganglion cells. *Nature* **292**, 344–345 (1981).

[PubMed](#) [ADS](#) [Google Scholar](#)

4. 4.

Wässle, H., Peichl, L. & Boycott, B. B. Morphology and topography of on- and off-alpha cells in the cat retina. *Proc. R. Soc. Lond. B Biol. Sci.* **212**, 157–175 (1981).

[PubMed](#) [ADS](#) [Google Scholar](#)

5. 5.

Callaway, E. M. Structure and function of parallel pathways in the primate early visual system. *J. Physiol. (Lond.)* **566**, 13–19 (2005).

[CAS](#) [Google Scholar](#)

6. 6.

Karklin, Y. & Simoncelli, E. P. Efficient coding of natural images with a population of noisy linear-nonlinear neurons. *Adv. Neural Inf. Process. Syst.* **24**, 999–1007 (2011).

[PubMed](#) [PubMed Central](#) [Google Scholar](#)

7. 7.

Bae, J. A. et al. Digital museum of retinal ganglion cells with dense anatomy and physiology. *Cell* **173**, 1293–1306.e19 (2018).

[PubMed](#) [PubMed Central](#) [CAS](#) [Google Scholar](#)

8. 8.

Borghuis, B. G., Ratliff, C. P., Smith, R. G., Sterling, P. & Balasubramanian, V. Design of a neuronal array. *J. Neurosci.* **28**, 3178–3189 (2008).

[PubMed](#) [PubMed Central](#) [CAS](#) [Google Scholar](#)

9. 9.

Gjorgjieva, J., Sompolsky, H. & Meister, M. Benefits of pathway splitting in sensory coding. *J. Neurosci.* **34**, 12127–12144 (2014).

[PubMed](#) [PubMed Central](#) [CAS](#) [Google Scholar](#)

10. 10.

Ratliff, C. P., Borghuis, B. G., Kao, Y. H., Sterling, P. & Balasubramanian, V. Retina is structured to process an excess of darkness in natural scenes. *Proc. Natl Acad. Sci. USA* **107**, 17368–17373 (2010).

[PubMed](#) [ADS](#) [CAS](#) [Google Scholar](#)

11. 11.

Jang, J. & Paik, S. B. Interlayer repulsion of retinal ganglion cell mosaics regulates spatial organization of functional maps in the visual cortex. *J. Neurosci.* **37**, 12141–12152 (2017).

[PubMed](#) [PubMed Central](#) [CAS](#) [Google Scholar](#)

12. 12.

Kremkow, J., Jin, J., Wang, Y. & Alonso, J. M. Principles underlying sensory map topography in primary visual cortex. *Nature* **533**, 52–57 (2016).

[PubMed](#) [PubMed Central](#) [ADS](#) [CAS](#) [Google Scholar](#)

13. 13.

Lee, K. S., Huang, X. & Fitzpatrick, D. Topology of ON and OFF inputs in visual cortex enables an invariant columnar architecture. *Nature* **533**, 90–94 (2016).

[PubMed](#) [PubMed Central](#) [ADS](#) [CAS](#) [Google Scholar](#)

14. 14.

Mazade, R., Jin, J., Pons, C. & Alonso, J. M. Functional specialization of ON and OFF cortical pathways for global-slow and local-fast vision. *Cell Rep.* **27**, 2881–2894.e5 (2019).

[PubMed](#) [PubMed Central](#) [CAS](#) [Google Scholar](#)

15. 15.

Rockhill, R. L., Euler, T. & Masland, R. H. Spatial order within but not between types of retinal neurons. *Proc. Natl Acad. Sci. USA* **97**, 2303–2307 (2000).

[PubMed](#) [ADS](#) [CAS](#) [Google Scholar](#)

16. 16.

Wässle, H., Boycott, B. B. & Illing, R. B. Morphology and mosaic of on- and off-beta cells in the cat retina and some functional considerations. *Proc. R. Soc. Lond. B Biol. Sci.* **212**, 177–195 (1981).

[PubMed](#) [ADS](#) [Google Scholar](#)

17. 17.

Brown, S. P., He, S. & Masland, R. H. Receptive field microstructure and dendritic geometry of retinal ganglion cells. *Neuron* **27**, 371–383 (2000).

[PubMed](#) [CAS](#) [Google Scholar](#)

18. 18.

Doi, E. et al. Efficient coding of spatial information in the primate retina. *J. Neurosci.* **32**, 16256–16264 (2012).

[PubMed](#) [PubMed Central](#) [CAS](#) [Google Scholar](#)

19. 19.

Galli-Resta, L., Novelli, E., Kryger, Z., Jacobs, G. H. & Reese, B. E. Modelling the mosaic organization of rod and cone photoreceptors with a minimal-spacing rule. *Eur. J. Neurosci.* **11**, 1461–1469 (1999).

[PubMed](#) [CAS](#) [Google Scholar](#)

20. 20.

Eglen, S. J., Diggle, P. J. & Troy, J. B. Homotypic constraints dominate positioning of on- and off-center beta retinal ganglion cells. *Vis. Neurosci.* **22**, 859–871 (2005).

[PubMed](#) [PubMed Central](#) [Google Scholar](#)

21. 21.

Eglen, S. J. Development of regular cellular spacing in the retina: theoretical models. *Math. Med. Biol.* **23**, 79–99 (2006).

[PubMed](#) [MATH](#) [Google Scholar](#)

22. 22.

Dabrowski, W., Grybos, P. & Litke, A. M. A low noise multichannel integrated circuit for recording neuronal signals using microelectrode arrays. *Biosens. Bioelectron.* **19**, 749–761 (2004).

[PubMed](#) [CAS](#) [Google Scholar](#)

23. 23.

Ravi, S., Ahn, D., Greschner, M., Chichilnisky, E. J. & Field, G. D. Pathway-specific asymmetries between ON and OFF visual signals. *J. Neurosci.* **38**, 9728–9740 (2018).

[PubMed](#) [PubMed Central](#) [CAS](#) [Google Scholar](#)

24. 24.

Chichilnisky, E. J. A simple white noise analysis of neuronal light responses. *Network* **12**, 199–213 (2001).

[PubMed](#) [MATH](#) [CAS](#) [Google Scholar](#)

25. 25.

Yu, W. Q., Grzywacz, N. M., Lee, E. J. & Field, G. D. Cell type-specific changes in retinal ganglion cell function induced by rod death and cone reorganization in rats. *J. Neurophysiol.* **118**, 434–454 (2017).

[PubMed](#) [PubMed Central](#) [Google Scholar](#)

26. 26.

Anishchenko, A. et al. Receptive field mosaics of retinal ganglion cells are established without visual experience. *J. Neurophysiol.* **103**, 1856–1864 (2010).

[PubMed](#) [PubMed Central](#) [Google Scholar](#)

27. 27.

Gauthier, J. L. et al. Uniform signal redundancy of parasol and midget ganglion cells in primate retina. *J. Neurosci.* **29**, 4675–4680 (2009).

[PubMed](#) [PubMed Central](#) [CAS](#) [Google Scholar](#)

28. 28.

Watanabe, M. & Rodieck, R. W. Parasol and midget ganglion cells of the primate retina. *J. Comp. Neurol.* **289**, 434–454 (1989).

[PubMed](#) [CAS](#) [Google Scholar](#)

29. 29.

Angueyra, J. M. & Rieke, F. Origin and effect of phototransduction noise in primate cone photoreceptors. *Nat. Neurosci.* **16**, 1692–1700 (2013).

[PubMed](#) [PubMed Central](#) [CAS](#) [Google Scholar](#)

30. 30.

Donner, K. Noise and the absolute thresholds of cone and rod vision. *Vision Res.* **32**, 853–866 (1992).

[PubMed](#) [CAS](#) [Google Scholar](#)

31. 31.

Dunn, F. A. & Rieke, F. The impact of photoreceptor noise on retinal gain controls. *Curr. Opin. Neurobiol.* **16**, 363–370 (2006).

[PubMed](#) [CAS](#) [Google Scholar](#)

32. 32.

Rao-Mirotznik, R., Buchsbaum, G. & Sterling, P. Transmitter concentration at a three-dimensional synapse. *J. Neurophysiol.* **80**, 3163–3172 (1998).

[PubMed](#) [CAS](#) [Google Scholar](#)

33. 33.

Berry, M. J., Warland, D. K. & Meister, M. The structure and precision of retinal spike trains. *Proc. Natl Acad. Sci. USA* **94**, 5411–5416 (1997).

[PubMed](#) [ADS](#) [CAS](#) [Google Scholar](#)

34. 34.

Freed, M. A. & Liang, Z. Synaptic noise is an information bottleneck in the inner retina during dynamic visual stimulation. *J. Physiol. (Lond.)* **592**, 635–651 (2014).

[CAS](#) [Google Scholar](#)

35. 35.

Atick, J. J. & Redlich, A. N. What does the retina know about natural scenes? *Neural Comput.* **4**, 196–210 (1992).

[Google Scholar](#)

36. 36.

Brinkman, B. A., Weber, A. I., Rieke, F. & Shea-Brown, E. How do efficient coding strategies depend on origins of noise in neural circuits? *PLoS Comput. Biol.* **12**, e1005150 (2016).

[PubMed](#) [PubMed Central](#) [ADS](#) [Google Scholar](#)

37. 37.

Field, G. D. & Sampath, A. P. Behavioural and physiological limits to vision in mammals. *Phil. Trans. R. Soc. Lond. B* **372**, 20160072 (2017).

[Google Scholar](#)

38. 38.

Barlow, H. B., Fitzhugh, R. & Kuffler, S. W. Change of organization in the receptive fields of the cat's retina during dark adaptation. *J. Physiol. (Lond.)* **137**, 338–354 (1957).

[CAS](#) [Google Scholar](#)

39. 39.

Hosoya, T., Baccus, S. A. & Meister, M. Dynamic predictive coding by the retina. *Nature* **436**, 71–77 (2005).

[PubMed](#) [ADS](#) [CAS](#) [Google Scholar](#)

40. 40.

Ringach, D. L. On the origin of the functional architecture of the cortex. *PLoS ONE* **2**, e251 (2007).

[PubMed](#) [PubMed Central](#) [ADS](#) [Google Scholar](#)

41. 41.

Chichilnisky, E. J. & Kalmar, R. S. Functional asymmetries in ON and OFF ganglion cells of primate retina. *J. Neurosci.* **22**, 2737–2747 (2002).

[PubMed](#) [PubMed Central](#) [CAS](#) [Google Scholar](#)

42. 42.

Field, G. D. et al. Spatial properties and functional organization of small bistratified ganglion cells in primate retina. *J. Neurosci.* **27**, 13261–13272 (2007).

[PubMed](#) [PubMed Central](#) [CAS](#) [Google Scholar](#)

43. 43.

Litke, A. et al. What does the eye tell the brain?: Development of a system for the large-scale recording of retinal output activity. *IEEE Trans. Nucl. Sci.* **51**, 1434–1440 (2004).

[ADS](#) [Google Scholar](#)

44. 44.

Lee, J. H. et al. in *Advances in Neural Information Processing Systems* (eds. Guyon, I. et al.) 4002–4012 (Curran Associates, 2017).

45. 45.

Lee, J. et al. YASS: yet another spike sorter applied to large-scale multi-electrode array recordings in primate retina. Preprint at *bioRxiv* <https://doi.org/10.1101/2020.03.18.997924> (2020).

46. 46.

Shlens, J. et al. The structure of multi-neuron firing patterns in primate retina. *J. Neurosci.* **26**, 8254–8266 (2006).

[PubMed](#) [PubMed Central](#) [CAS](#) [Google Scholar](#)

47. 47.

Gauthier, J. L. et al. Receptive fields in primate retina are coordinated to sample visual space more uniformly. *PLoS Biol.* **7**, e1000063 (2009).

[PubMed](#) [PubMed Central](#) [Google Scholar](#)

48. 48.

Yao, X. et al. Gap junctions contribute to differential light adaptation across direction-selective retinal ganglion cells. *Neuron* **100**, 216–228.e6 (2018).

[PubMed](#) [PubMed Central](#) [CAS](#) [Google Scholar](#)

49. 49.

Eglen, S. J. The role of retinal waves and synaptic normalization in retinogeniculate development. *Phil. Trans. R. Soc. Lond. B* **354**, 497–506 (1999).

[CAS](#) [Google Scholar](#)

50. 50.

Doi, E., Inui, T., Lee, T. W., Wachtler, T. & Sejnowski, T. J. Spatiochromatic receptive field properties derived from information-theoretic analyses of cone mosaic responses to natural scenes. *Neural Comput.* **15**, 397–417 (2003).

[PubMed](#) [PubMed Central](#) [MATH](#) [Google Scholar](#)

51. 51.

Nocedal, J. & Wright, S. *Numerical Optimization* (Springer, 2006).

[Download references](#)

Acknowledgements

We thank L. Glickfeld, S. Lisberger, F. Rieke, J. Kay and F. Wang for comments on drafts of this manuscript, E. J. Chichilnisky and E. Wu for discussions, E. J. Chichilnisky for primate data, and K. Ruda for assistance with experiments. This work was supported by the Ruth K. Broad Postdoctoral Fellowship (S.R.), the Whitehead Scholars Program (G.D.F.) and NIH/NEI R01 EY031396 (G.D.F.).

Author information

Affiliations

1. Department of Neurobiology, Duke University, Durham, NC, USA

Suva Roy, Na Young Jun, Emily L. Davis, John Pearson & Greg D. Field

2. Department of Biostatistics and Bioinformatics, Duke University, Durham, NC, USA

John Pearson

Authors

1. Suva Roy

[View author publications](#)

You can also search for this author in [PubMed](#) [Google Scholar](#)

2. Na Young Jun

[View author publications](#)

You can also search for this author in [PubMed](#) [Google Scholar](#)

3. Emily L. Davis

[View author publications](#)

You can also search for this author in [PubMed](#) [Google Scholar](#)

4. John Pearson

[View author publications](#)

You can also search for this author in [PubMed](#) [Google Scholar](#)

5. Greg D. Field

[View author publications](#)

You can also search for this author in [PubMed](#) [Google Scholar](#)

Contributions

This study was conceived by S.R. and G.D.F. S.R. and E.L.D. analysed data. The efficient coding model and optimizations were implemented by N.Y.J. and J.P. The paper was written by S.R. and G.D.F. and edited by all authors.

Corresponding author

Correspondence to [Greg D. Field](#).

Ethics declarations

Competing interests

The authors declare no competing interests.

Additional information

Peer review information *Nature* thanks Daniel Kerschensteiner and the other, anonymous, reviewer(s) for their contribution to the peer review of this work.

Publisher's note Springer Nature remains neutral with regard to jurisdictional claims in published maps and institutional affiliations.

Extended data figures and tables

Extended Data Fig. 1 Anti-alignment predicted by efficient coding theory is conserved in mosaics with different densities and boundary conditions.

a, Optimal spatial filters of 48 ON units and 52 OFF units, each on an 18×18 -pixel grid (orange box). **b**, The COMs of optimal filters forming the ON (green) and OFF (magenta) mosaics. Training was performed using a circular mask over the images to reduce edge artefacts. **c, d**, The 2D z -scored IMCE map (**c**) and radial average z -scored IMCE (**d**) for the mosaic pairs shown in **b**. **e–h**, As in **a–d** with equal cell density ($n = 50$) for ON and OFF mosaics. **i–l**, As in **a–d** with the number of ON and OFF units fixed at $n = 45$ and $n = 55$, respectively. **m–p**, As in **a–d** with $n = 49$ ON units and $n = 51$ OFF units, but training was performed without a circular mask. Shaded areas, s.d.

Extended Data Fig. 2 Mosaic coordination can persist under widely diverging RF densities.

a–c, Bivariate point pattern (type 1: green, type 2: magenta) generated by modified PIPP model (see [Methods](#)) with interaction terms for anti-alignment (**a**), alignment (**b**) and independence (**c**). The density of type 2 points is four times higher than the density of type 1 points. **d–f**, The 2D z -scored IMCE maps corresponding to **a–c**, respectively. **g–i**, The radial average z -scored IMCE averaged over $n = 100$ mosaic pairs that are aligned (**g**), anti-aligned (**h**) and independent (**i**). Shaded areas are s.e.m.

Extended Data Fig. 3 Mosaic coordination estimates are robust to RF subsampling.

a, RF mosaics illustrating three different cases. Measured, no RFs are removed or added; depleted, a fraction of randomly selected RFs are removed (dashed ellipses); filled, RFs are artificially added to fill mosaic gaps (thick solid ellipses). The gradient below illustrates the percentage of RFs remaining after removing or adding RFs. **b, c**, Radial average *z*-scored IMCE for different amounts of subsampling and filling of ON and OFF brisk transient (bt, rat) mosaics (**b**; blue), ON and OFF brisk sustained (bs, rat) mosaics (**b**; purple), and ON and OFF parasol (primate) mosaics (**c**; green). Each curve corresponds to an individual mosaic pair. Results are representative of $n = 5$ retinas for ON–OFF brisk transient, $n = 3$ retinas for ON–OFF brisk sustained, and $n = 3$ retinas for ON–OFF parasol RGCs. The percentage of RFs relative to measured (100%), is indicated by f. Shaded areas, s.d.

Extended Data Fig. 4 Mosaics encoding distinct visual features appear to be independent.

a, Example mosaics of ON and OFF brisk transient (bt) and brisk sustained (bs) RGC types. Coordination was tested across cell type (orange), and across cell type and polarity (green). **b, d, f, h**, 2D *z*-scored IMCE maps of a representative pair (left) and radial average *z*-scored IMCEs of all pairs (right), for ONbt–ONbs (**b**, $n = 3$), OFFbt–OFFbs (**d**, $n = 3$), ONbt–OFFbs (**f**, $n = 3$), ONbs–OFFbt (**h**, $n = 3$) mosaic combinations. Dashed curve, radial average *z*-scored IMCE corresponding to the 2D *z*-scored IMCE map (left). Shaded areas, s.d. **c, e, g, i**, Sampling distributions from bootstrap estimates of mean coordination index for pseudo pairs (grey) and real pairs (orange/green filled circles, arrows). Number of pseudo pairs: $n = 12$ (**c, e, g, i**). The grey shaded region to the right of the vertical dashed line indicates value exceeding 95% confidence interval based on one-sample two-sided *t*-test statistic: $P = 0.33, 0.98, 0.37$ and 0.46 , respectively, for **c, e, g** and **i** (n.s., not significant). Cohen’s $d = 0.36, -0.006, 0.28$ and -0.25 , respectively, for **c, e, g** and **i**.

[Extended Data Fig. 5 Anti-alignment between ON brisk transient RF mosaics persists across light levels.](#)

a, RF mosaics of ON (left) and OFF (right) brisk transient RGCs, measured at photopic light level (10,000 photo-isomerizations per M-cone per s). The COMs of RFs are indicated by black filled circles. **b**, **c**, 2D z-scored IMCE map (**b**) and radial average z-scored IMCE (**c**) for the mosaic pair shown in **a**. **d**, RF mosaics of ON (left) and OFF (right) brisk transient RGC types, at scotopic light level (1.0 photo-isomerizations per rod per s), from the same retina as in **a**. **e**, **f**, As in **b**, **c** for the mosaic pairs shown in **d**. **g**, Change in RF COMs of ON brisk transient RGCs from photopic to scotopic light level (black filled circles). Solid and dashed red lines show homotypic nearest-neighbour (NN) distances between RFs estimated at photopic and scotopic light levels, respectively. **h**, Distribution of fractional change in RF position of ON brisk transient RGCs across light levels expressed as a fraction of the mean NN homotypic distance at photopic light level. Smooth curve, kernel density estimate. **i**, **j**, As in **g**, **h** for OFF brisk transient RGCs. Results are representative of $n = 1$ retina. Shaded areas, s.d.

Extended Data Table 1 The distribution of inter-mosaic coordination energy (IMCE) values is approximately normal

[Full size table](#)

Extended Data Table 2 Coordination index values for real and pseudo mosaic pairs

[Full size table](#)

Supplementary information

[Reporting Summary](#)

Source data

[Source Data Fig. 1](#)

[Source Data Fig. 2](#)

Source Data Fig. 3

Source Data Fig. 4

Rights and permissions

Reprints and Permissions

About this article



Check for
updates

Cite this article

Roy, S., Jun, N.Y., Davis, E.L. *et al.* Inter-mosaic coordination of retinal receptive fields. *Nature* **592**, 409–413 (2021).
<https://doi.org/10.1038/s41586-021-03317-5>

Download citation

- Received: 15 July 2020
- Accepted: 01 February 2021
- Published: 10 March 2021
- Issue Date: 15 April 2021
- DOI: <https://doi.org/10.1038/s41586-021-03317-5>

Comments

By submitting a comment you agree to abide by our [Terms](#) and [Community Guidelines](#). If you find something abusive or that does not comply with our terms or guidelines please flag it as inappropriate.

[Access through your institution](#)

[Change institution](#)

[Buy or subscribe](#)

This article was downloaded by **calibre** from <https://www.nature.com/articles/s41586-021-03317-5>

| [Section menu](#) | [Main menu](#) |

- Article
- [Published: 07 April 2021](#)

Astrocytes close a motor circuit critical period

- [Sarah D. Ackerman](#)¹,
- [Nelson A. Perez-Catalan](#) ORCID: orcid.org/0000-0002-3626-2390¹ nAff³,
- [Marc R. Freeman](#)² &
- [Chris Q. Doe](#) ORCID: orcid.org/0000-0001-5980-8029¹

[Nature](#) volume **592**, pages414–420(2021) [Cite this article](#)

- 5166 Accesses
- 1 Citations
- 288 Altmetric
- [Metrics details](#)

Subjects

- [Development of the nervous system](#)
- [Neurogenesis](#)

Abstract

Critical periods—brief intervals during which neural circuits can be modified by activity—are necessary for proper neural circuit assembly. Extended critical periods are associated with neurodevelopmental disorders;

however, the mechanisms that ensure timely critical period closure remain poorly understood^{1,2}. Here we define a critical period in a developing *Drosophila* motor circuit and identify astrocytes as essential for proper critical period termination. During the critical period, changes in activity regulate dendrite length, complexity and connectivity of motor neurons. Astrocytes invaded the neuropil just before critical period closure³, and astrocyte ablation prolonged the critical period. Finally, we used a genetic screen to identify astrocyte–motor neuron signalling pathways that close the critical period, including Neuroligin–Neurexin signalling. Reduced signalling destabilized dendritic microtubules, increased dendrite dynamicity and impaired locomotor behaviour, underscoring the importance of critical period closure. Previous work defined astroglia as regulators of plasticity at individual synapses⁴; we show here that astrocytes also regulate motor circuit critical period closure to ensure proper locomotor behaviour.

[Access through your institution](#)

[Change institution](#)

[Buy or subscribe](#)

Access options

Subscribe to Journal

Get full journal access for 1 year

\$199.00

only \$3.90 per issue

[Subscribe](#)

All prices are NET prices.

VAT will be added later in the checkout.

Tax calculation will be finalised during checkout.

Rent or Buy article

Get time limited or full article access on ReadCube.

from \$8.99

[Rent or Buy](#)

All prices are NET prices.

Additional access options:

- [Log in](#)
- [Access through your institution](#)
- [Learn about institutional subscriptions](#)

Fig. 1: A critical period for motor circuit plasticity.

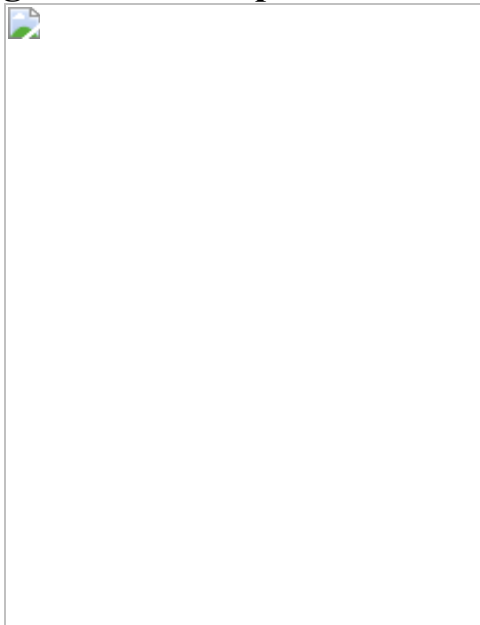


Fig. 2: Activity-dependent scaling of dendrite length and synaptic inputs.

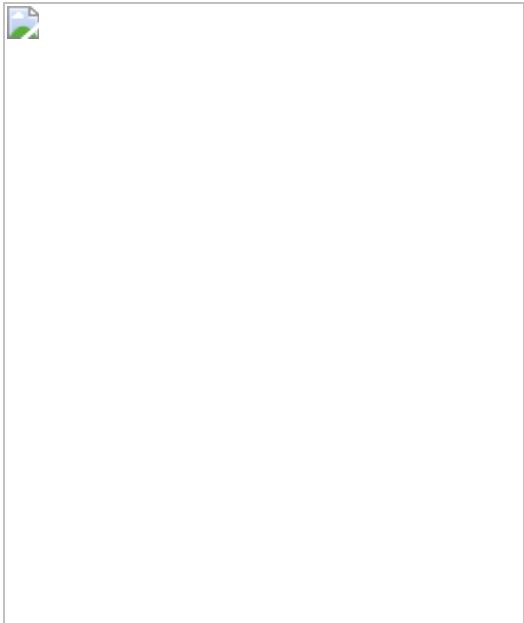


Fig. 3: Astrocytes terminate the critical period.

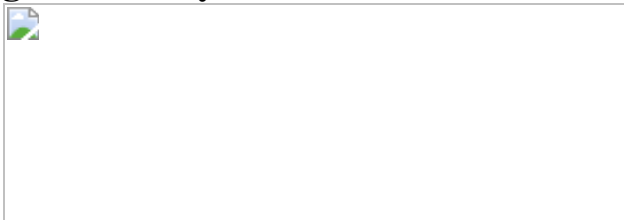


Fig. 4: Neuroligin–Neurexin signalling stabilizes microtubules and closes the critical period.

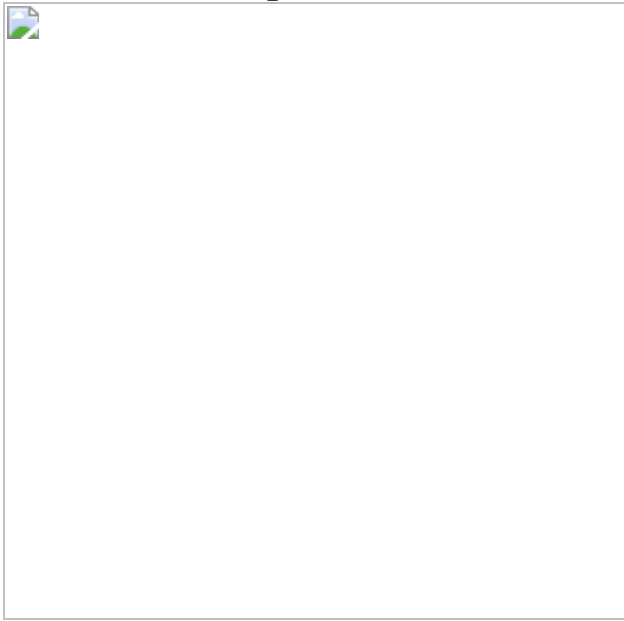


Fig. 5: Critical period extension alters locomotor behaviour.



Data availability

The raw data files generated during and/or analysed during the current study are available from the corresponding authors on reasonable request. Raw data for any main or supplementary figure (.lsm, .czi or .avi files) can be supplied upon reasonable request.

References

1. 1.

Keck, T. et al. Integrating Hebbian and homeostatic plasticity: the current state of the field and future research directions. *Phil. Trans. R. Soc. Lond. B* **372**, rstb.2016.0158 (2017).

[Google Scholar](#)

2. 2.

Takesian, A. E. & Hensch, T. K. Balancing plasticity/stability across brain development. *Prog. Brain Res.* **207**, 3–34 (2013).

[Google Scholar](#)

3. 3.

Stork, T., Sheehan, A., Tasdemir-Yilmaz, O. E. & Freeman, M. R. Neuron–glia interactions through the Heartless FGF receptor signaling pathway mediate morphogenesis of *Drosophila* astrocytes. *Neuron* **83**, 388–403 (2014).

[CAS](#) [PubMed](#) [PubMed Central](#) [Google Scholar](#)

4. 4.

Allen, N. J. & Eroglu, C. Cell biology of astrocyte–synapse interactions. *Neuron* **96**, 697–708 (2017).

[CAS](#) [PubMed](#) [PubMed Central](#) [Google Scholar](#)

5. 5.

Walton, K. D., Lieberman, D., Llinás, A., Begin, M. & Llinás, R. R. Identification of a critical period for motor development in neonatal rats. *Neuroscience* **51**, 763–767 (1992).

[CAS](#) [Google Scholar](#)

6. 6.

Kalb, R. G. & Hockfield, S. Electrical activity in the neuromuscular unit can influence the molecular development of motor neurons. *Dev. Biol.* **162**, 539–548 (1994).

[CAS](#) [Google Scholar](#)

7. 7.

Hübener, M. & Bonhoeffer, T. Neuronal plasticity: beyond the critical period. *Cell* **159**, 727–737 (2014).

[Google Scholar](#)

8. 8.

Liu, Q. et al. Branch-specific plasticity of a bifunctional dopamine circuit encodes protein hunger. *Science* **356**, 534–539 (2017).

[ADS](#) [CAS](#) [PubMed](#) [PubMed Central](#) [Google Scholar](#)

9. 9.

LeBlanc, J. J. & Fagiolini, M. Autism: a “critical period” disorder? *Neural Plast.* **2011**, 921680 (2011).

[PubMed](#) [PubMed Central](#) [Google Scholar](#)

10. 10.

Werker, J. F. & Hensch, T. K. Critical periods in speech perception: new directions. *Annu. Rev. Psychol.* **66**, 173–196 (2015).

[Google Scholar](#)

11. 11.

Landgraf, M., Jeffrey, V., Fujioka, M., Jaynes, J. B. & Bate, M. Embryonic origins of a motor system: motor dendrites form a myotopic map in *Drosophila*. *PLoS Biol.* **1**, E41 (2003).

[PubMed](#) [PubMed Central](#) [Google Scholar](#)

12. 12.

Tripodi, M., Evers, J. F., Mauss, A., Bate, M. & Landgraf, M. Structural homeostasis: compensatory adjustments of dendritic arbor geometry in response to variations of synaptic input. *PLoS Biol.* **6**, e260 (2008).

[PubMed](#) [PubMed Central](#) [Google Scholar](#)

13. 13.

Vonhoff, F., Kuehn, C., Blumenstock, S., Sanyal, S. & Duch, C. Temporal coherency between receptor expression, neural activity and AP-1-dependent transcription regulates *Drosophila* motoneuron dendrite development. *Development* **140**, 606–616 (2013).

[CAS](#) [PubMed](#) [PubMed Central](#) [Google Scholar](#)

14. 14.

Giachello, C. N. G. & Baines, R. A. Inappropriate neural activity during a sensitive period in embryogenesis results in persistent seizure-like behavior. *Curr. Biol.* **25**, 2964–2968 (2015).

[CAS](#) [PubMed](#) [PubMed Central](#) [Google Scholar](#)

15. 15.

Mauss, A. S., Busch, C. & Borst, A. Optogenetic neuronal silencing in *Drosophila* during visual processing. *Sci. Rep.* **7**, 13823 (2017).

[ADS](#) [PubMed](#) [PubMed Central](#) [Google Scholar](#)

16. 16.

Carreira-Rosario, A. et al. MDN brain descending neurons coordinately activate backward and inhibit forward locomotion. *eLife* **7**, e38554 (2018).

[PubMed](#) [PubMed Central](#) [Google Scholar](#)

17. 17.

Nern, A., Pfeiffer, B. D. & Rubin, G. M. Optimized tools for multicolor stochastic labeling reveal diverse stereotyped cell arrangements in the fly visual system. *Proc. Natl Acad. Sci. USA* **112**, E2967–E2976 (2015).

[ADS](#) [CAS](#) [Google Scholar](#)

18. 18.

Peng, J. J. et al. A circuit-dependent ROS feedback loop mediates glutamate excitotoxicity to sculpt the *Drosophila* motor system. *eLife* **8**, e47372 (2019).

[CAS](#) [PubMed](#) [PubMed Central](#) [Google Scholar](#)

19. 19.

Oswald, M. C. et al. Reactive oxygen species regulate activity-dependent neuronal plasticity in *Drosophila*. *eLife* **7**, e39393 (2018).

[PubMed](#) [PubMed Central](#) [Google Scholar](#)

20. 20.

Kitamoto, T. Conditional modification of behavior in *Drosophila* by targeted expression of a temperature-sensitive shibire allele in defined neurons. *J. Neurobiol.* **47**, 81–92 (2001).

[CAS](#) [Google Scholar](#)

21. 21.

Crisp, S. J., Evers, J. F. & Bate, M. Endogenous patterns of activity are required for the maturation of a motor network. *J. Neurosci.* **31**, 10445–10450 (2011).

[CAS](#) [PubMed](#) [PubMed Central](#) [Google Scholar](#)

22. 22.

Jarecki, J. & Keshishian, H. Role of neural activity during synaptogenesis in *Drosophila*. *J. Neurosci.* **15**, 8177–8190 (1995).

[CAS](#) [PubMed](#) [PubMed Central](#) [Google Scholar](#)

23. 23.

Hensch, T. K. Critical period regulation. *Annu. Rev. Neurosci.* **27**, 549–579 (2004).

[CAS](#) [Google Scholar](#)

24. 24.

Turrigiano, G. Homeostatic synaptic plasticity: local and global mechanisms for stabilizing neuronal function. *Cold Spring Harb. Perspect. Biol.* **4**, a005736 (2012).

[PubMed](#) [PubMed Central](#) [Google Scholar](#)

25. 25.

Horton, A. C. et al. Polarized secretory trafficking directs cargo for asymmetric dendrite growth and morphogenesis. *Neuron* **48**, 757–771 (2005).

[CAS](#) [Google Scholar](#)

26. 26.

Taylor, C. A., Yan, J., Howell, A. S., Dong, X. & Shen, K. RAB-10 regulates dendritic branching by balancing dendritic transport. *PLoS Genet.* **11**, e1005695 (2015).

[PubMed](#) [PubMed Central](#) [Google Scholar](#)

27. 27.

Schneider-Mizell, C. M. et al. Quantitative neuroanatomy for connectomics in *Drosophila*. *eLife* **5**, e12059 (2016).

[PubMed](#) [PubMed Central](#) [Google Scholar](#)

28. 28.

Zarin, A. A., Mark, B., Cardona, A., Litwin-Kumar, A. & Doe, C. Q. A multilayer circuit architecture for the generation of distinct locomotor behaviors in *Drosophila*. *eLife* **8**, e51781 (2019).

[CAS](#) [PubMed](#) [PubMed Central](#) [Google Scholar](#)

29. 29.

Berger-Müller, S. et al. Assessing the role of cell-surface molecules in central synaptogenesis in the *Drosophila* visual system. *PLoS ONE* **8**, e83732 (2013).

[ADS](#) [PubMed](#) [PubMed Central](#) [Google Scholar](#)

30. 30.

Sales, E. C., Heckman, E. L., Warren, T. L. & Doe, C. Q. Regulation of subcellular dendritic synapse specificity by axon guidance cues. *eLife* **8**, e43478 (2019).

[PubMed](#) [PubMed Central](#) [Google Scholar](#)

31. 31.

Andlauer, T. F. M. et al. Drep-2 is a novel synaptic protein important for learning and memory. *eLife* **3**, e03895 (2014).

[PubMed](#) [PubMed Central](#) [Google Scholar](#)

32. 32.

Perkins, L. A. et al. The Transgenic RNAi Project at Harvard Medical School: resources and validation. *Genetics* **201**, 843–852 (2015).

[CAS](#) [PubMed](#) [PubMed Central](#) [Google Scholar](#)

33. 33.

Stogsdill, J. A. et al. Astrocytic neuroligins control astrocyte morphogenesis and synaptogenesis. *Nature* **551**, 192–197 (2017).

[ADS](#) [CAS](#) [PubMed](#) [PubMed Central](#) [Google Scholar](#)

34. 34.

Liu, L. et al. Neurexin restricts axonal branching in columns by promoting Ephrin clustering. *Dev. Cell* **41**, 94–106.e4 (2017).

[CAS](#) [Google Scholar](#)

35. 35.

Xing, G. et al. Neurexin–Neuroligin 1 regulates synaptic morphology and functions via the WAVE regulatory complex in *Drosophila* neuromuscular junction. *eLife* **7**, e30457 (2018).

[PubMed](#) [PubMed Central](#) [Google Scholar](#)

36. 36.

Duan, Y. & Giger, R. J. A new role for RPTP σ in spinal cord injury: signaling chondroitin sulfate proteoglycan inhibition. *Sci. Signal.* **3**, pe6 (2010).

[Google Scholar](#)

37. 37.

Savas, J. N. et al. The sorting receptor SorCS1 regulates trafficking of Neurexin and AMPA receptors. *Neuron* **87**, 764–780 (2015).

[CAS](#) [PubMed](#) [PubMed Central](#) [Google Scholar](#)

38. 38.

Fairless, R. et al. Polarized targeting of neurexins to synapses is regulated by their C-terminal sequences. *J. Neurosci.* **28**, 12969–12981

(2008).

[CAS](#) [PubMed](#) [PubMed Central](#) [Google Scholar](#)

39. 39.

Taniguchi, H. et al. Silencing of neuroligin function by postsynaptic neurexins. *J. Neurosci.* **27**, 2815–2824 (2007).

[CAS](#) [PubMed](#) [PubMed Central](#) [Google Scholar](#)

40. 40.

Jia, Y. et al. Next-generation CRISPR/Cas9 transcriptional activation in *Drosophila* using flySAM. *Proc. Natl Acad. Sci. USA* **115**, 4719–4724 (2018).

[CAS](#) [Google Scholar](#)

41. 41.

Banerjee, S. & Riordan, M. Coordinated regulation of axonal microtubule organization and transport by *Drosophila* Neurexin and BMP pathway. *Sci. Rep.* **8**, 17337 (2018).

[ADS](#) [PubMed](#) [PubMed Central](#) [Google Scholar](#)

42. 42.

Blanco-Suarez, E., Liu, T.-F., Kopelevich, A. & Allen, N. J. Astrocyte-secreted Chordin-like 1 drives synapse maturation and limits plasticity by increasing synaptic GluA2 AMPA receptors. *Neuron* **100**, 1116–1132.e13 (2018).

[CAS](#) [PubMed](#) [PubMed Central](#) [Google Scholar](#)

43. 43.

Singh, S. K. et al. Astrocytes assemble thalamocortical synapses by bridging NRX1 α and NL1 via Hevin. *Cell* **164**, 183–196 (2016).

[CAS](#) [PubMed](#) [PubMed Central](#) [Google Scholar](#)

44. 44.

Harauzov, A. et al. Reducing intracortical inhibition in the adult visual cortex promotes ocular dominance plasticity. *J. Neurosci.* **30**, 361–371 (2010).

[CAS](#) [PubMed](#) [PubMed Central](#) [Google Scholar](#)

45. 45.

Dzyubenko, E., Gottschling, C. & Faissner, A. Neuron–glia interactions in neural plasticity: contributions of neural extracellular matrix and perineuronal nets. *Neural Plast.* **2016**, 5214961 (2016).

[PubMed](#) [PubMed Central](#) [Google Scholar](#)

46. 46.

Crisp, S., Evers, J. F., Fiala, A. & Bate, M. The development of motor coordination in Drosophila embryos. *Development* **135**, 3707–3717 (2008).

[CAS](#) [PubMed](#) [PubMed Central](#) [Google Scholar](#)

47. 47.

Volpi, S., Bongiorni, S., Fabbretti, F., Wakimoto, B. T. & Prantera, G. Drosophila rae1 is required for male meiosis and spermatogenesis. *J. Cell Sci.* **126**, 3541–3551 (2013).

[CAS](#) [Google Scholar](#)

48. 48.

Tenedini, F. M. et al. Maintenance of cell type-specific connectivity and circuit function requires Tao kinase. *Nat. Commun.* **10**, 3506 (2019).

[ADS](#) [PubMed](#) [PubMed Central](#) [Google Scholar](#)

49. 49.

Doherty, J., Logan, M. A., Tasdemir, O. E. & Freeman, M. R. Ensheathing glia function as phagocytes in the adult *Drosophila* brain. *J. Neurosci.* **29**, 4768–4781 (2009).

[CAS](#) [PubMed](#) [PubMed Central](#) [Google Scholar](#)

50. 50.

Herranz, H., Weng, R. & Cohen, S. M. Crosstalk between epithelial and mesenchymal tissues in tumorigenesis and imaginal disc development. *Curr. Biol.* **24**, 1476–1484 (2014).

[CAS](#) [Google Scholar](#)

51. 51.

Banovic, D. et al. Drosophila neuroligin 1 promotes growth and postsynaptic differentiation at glutamatergic neuromuscular junctions. *Neuron* **66**, 724–738 (2010).

[CAS](#) [Google Scholar](#)

52. 52.

Pulver, S. R., Pashkovski, S. L., Hornstein, N. J., Garrity, P. A. & Griffith, L. C. Temporal dynamics of neuronal activation by Channelrhodopsin-2 and TRPA1 determine behavioral output in *Drosophila* larvae. *J. Neurophysiol.* **101**, 3075–3088 (2009).

[PubMed](#) [PubMed Central](#) [Google Scholar](#)

53. 53.

Klapoetke, N. C. et al. Independent optical excitation of distinct neural populations. *Nat. Methods* **11**, 338–346 (2014).

[CAS](#) [PubMed](#) [PubMed Central](#) [Google Scholar](#)

54. 54.

Govorunova, E. G. Sineshchekov, O. A., Janz, R., Liu, X. & Spudich, J. L. Natural light-gated anion channels: a family of microbial rhodopsins for advanced optogenetics. *Science* **349**, 647–650 (2015).

[ADS](#) [CAS](#) [PubMed](#) [PubMed Central](#) [Google Scholar](#)

55. 55.

Li, J. Ashley, J., Budnik, V. & Bhat, M. A. Crucial role of *Drosophila* neurexin in proper active zone apposition to postsynaptic densities, synaptic growth, and synaptic transmission. *Neuron* **55**, 741–755 (2007).

[CAS](#) [PubMed](#) [PubMed Central](#) [Google Scholar](#)

56. 56.

Chen, Y.-C. et al. *Drosophila* neuroligin 2 is required presynaptically and postsynaptically for proper synaptic differentiation and synaptic transmission. *J. Neurosci.* **32**, 16018–16030 (2012).

[CAS](#) [PubMed](#) [PubMed Central](#) [Google Scholar](#)

57. 57.

Risse, B. et al. FIM, a novel FTIR-based imaging method for high throughput locomotion analysis. *PLoS ONE* **8**, e53963 (2013).

[ADS](#) [CAS](#) [PubMed](#) [PubMed Central](#) [Google Scholar](#)

[Download references](#)

Acknowledgements

We thank T. Suzuki, S. Cohen, E. Heckscher, V. Jayaraman and H. Aberle for providing fly stocks; M. Bhat for providing antibodies; K. Monk, J. Skeath, D. Lyons, R. Baines and members of the Doe laboratory for comments on the manuscript. Stocks obtained from the Bloomington *Drosophila* Stock Center and Shigen National Institute of Genetics (NIH P40OD018537) were used in this study. Funding was provided by HHMI (C.Q.D.), R01 HD27056 (C.Q.D.), R01 NS059991 (M.R.F.) and NIH F32NS098690 (S.D.A.). S.D.A. is a Milton Safenowitz Post-doctoral fellow of the ALSA.

Author information

Author notes

1. Nelson A. Perez-Catalan

Present address: Kennedy Center, Department of Pediatrics, The University of Chicago, Chicago, IL, USA

Affiliations

1. Institute of Neuroscience, Howard Hughes Medical Institute, University of Oregon, Eugene, OR, USA

Sarah D. Ackerman, Nelson A. Perez-Catalan & Chris Q. Doe

2. Vollum Institute, Oregon Health and Sciences University, Portland, OR, USA

Marc R. Freeman

Authors

1. Sarah D. Ackerman

[View author publications](#)

You can also search for this author in [PubMed](#) [Google Scholar](#)

2. Nelson A. Perez-Catalan

[View author publications](#)

You can also search for this author in [PubMed](#) [Google Scholar](#)

3. Marc R. Freeman

[View author publications](#)

You can also search for this author in [PubMed](#) [Google Scholar](#)

4. Chris Q. Doe

[View author publications](#)

You can also search for this author in [PubMed](#) [Google Scholar](#)

Contributions

S.D.A. conceived of the project; N.A.P.-C. performed and analysed all live-imaging experiments; S.D.A. performed and analysed all remaining experiments; M.R.F. and C.Q.D. provided feedback during the project; S.D.A., N.A.P.-C. and C.Q.D. wrote the paper and prepared the figures. All authors commented and approved of the manuscript.

Corresponding authors

Correspondence to [Sarah D. Ackerman](#) or [Chris Q. Doe](#).

Ethics declarations

Competing interests

The authors declare no competing interests.

Additional information

Peer review information *Nature* thanks the anonymous reviewer(s) for their contribution to the peer review of this work. Peer reviewer reports are available.

Publisher's note Springer Nature remains neutral with regard to jurisdictional claims in published maps and institutional affiliations.

Extended data figures and tables

Extended Data Fig. 1 Activity-dependent remodelling of motor neuron dendrites during a motor circuit critical period.

a–e, Tonic activation of motor neurons during embryogenesis induces dendrite retraction. **a**, Schematic of the activation paradigm used in this study. For activation of aCC–RP2 motor neurons, *RN2-gal4/lexA* drove expression of *UAS-CsChrimson::mCherry* or *lexAop/UAS-CsChrimson::mVenus*. Crosses were established on day 0 and fed exclusively on yeast paste supplemented with 0.5 mM ATR (required for maximum Chrimson activity) and changed daily for a minimum of 3 days. Timed embryo collections were performed on day 3 for a duration of 1.5 h. Sustained light activation (10,550 lx) was followed by immediate dissection. Optogenetic silencing experiments using *UAS-GtACR2::eYFP* followed the same scheme. **b–e**, Activation of aCC–RP2 motor neurons by Chrimson channelrhodopsin induces dendrite retraction. **b–d**, Representative 3D projections of brains expressing Chrimson::mCherry in aCC–RP2 motor neurons at 0 h ALH following activation during embryonic stage 17 (st17). After activation, brains were categorized qualitatively as control (**b**), mildly reduced (**c**) or strongly reduced (**d**) based on the extent of aCC–RP2 dendritic elaboration (dashed white boxes). Scale bar, 5 µm. **e**, Distribution of each phenotypic class in control, dark-reared animals versus animals whose aCC–RP2 motor neurons were Chrimson-activated for 15 min, 1 h or 4 h. Dark-reared controls were used throughout as aCC–RP2 motor neurons show sensitivity to Chrimson in the absence of ATR after 15 min and 4 h of Chrimson activation. *N* (in

histogram) represents number of larvae. **f–i**, Complementary assays to define the motor circuit critical period. **f, g**, Silencing of aCC–RP2 motor neurons for 1 h by GtACR2 (400 ms pulses of 488 nm light per second) (**f**) or expression of the temperature sensitive *shibire^{ts}* to block synaptic transmission (active at 30 °C) (**g**), resulted in significant dendrite extension at 0 h ALH, but had no effect at 8 h ALH. *N* represents number of larvae. 0 h GtACR2: control (*N* = 11), 1 h silencing (*N* = 12). 8 h GtACR2: *N* = 10 per condition. GtACR2 statistics within group (one-way ANOVA): 0 h ($P < 0.0001$), 8 h ($P < 0.76$). GtACR2 statistics across groups (two-way ANOVA): $P < 0.003$. 0 h *shibire^{ts}*: control (*N* = 7), 1 h silencing (*N* = 6). 8 h *shibire^{ts}*: control (*N* = 6), 1 h silencing (*N* = 7). *shibire^{ts}* statistics within group (one-way ANOVA): 0 h ($P < 0.0002$), 8 h ($P < 0.86$). *shibire^{ts}* statistics across groups (two-way ANOVA): $P < 0.003$. GtACR2 genetics: *RN2-gal4, UAS-GtACR2::eYFP*. *shibire^{ts}* genetics: *RN2-gal4, UAS-shibire^{ts}, UAS-myr::GFP*. **h, i**, Activation of aCC–RP2 motor neurons for 1 h by Chrimson (600 ms pulses of 561 nm light per second) (**h**) or expression of the thermogenetic activator TrpA1 (inactive at 22 °C, fires at ~30 Hz at 27 °C) (**i**), resulted in significant dendrite retraction at 0 h ALH, but had no effect at 8 h ALH. *N* represents number of larvae. 0 h Chrimson: control (*N* = 12), 1 h activation (*N* = 14). 8 h Chrimson: control (*N* = 12), 1 h activation (*N* = 10). Chrimson statistics within group (one-way ANOVA): 0 h ($P < 0.0001$), 8 h ($P < 0.6$). Chrimson statistics across groups (two-way ANOVA): $P < 0.001$. 0 h TrpA1: control (*N* = 6), 1 h activation (*N* = 11). 8 h TrpA1: control (*N* = 5), 1 h activation (*N* = 6). TrpA1 statistics within group (one-way ANOVA): 0 h ($P < 0.0001$), 8 h ($P < 0.25$). TrpA1 statistics across groups (two-way ANOVA): $P < 0.0001$. Chrimson genetics: *RN2-gal4, UAS-Chrimson::mCherry*. TrpA1 genetics: *RN2-gal4, UAS-TrpA1, UAS-myr::GFP*. Data are mean ± s.d. * $P < 0.05$; ** $P < 0.01$; *** $P < 0.001$; **** $P < 0.0001$; NS, not significant. Diamonds denote significance following two-way ANOVA when one-way and two-way ANOVA are displayed together. *N* values reflect biological replicates from 2 independent experiments.

Extended Data Fig. 2 Changes to motor dendrite length and complexity following minutes of altered neuronal activity.

a–h, Silencing of RP2 by *shibire^{ts}* induces dendrite extension. **a–d**, MCFO single-neuron labelling at 0 h ALH to visualize the morphology of RP2 motor neuron dendrites at 25 °C in *shibire^{ts}* control ($N = 43$ neurons, $N = 24$ brains) (**a**) compared to neurons silenced with *shibire^{ts}* to block synaptic transmission (active at 30 °C) for 15 min ($N = 18/N = 15$) (**b**), 1 h ($N = 7/N = 6$) (**c**) or 3 h ($N = 29/N = 18$) (**d**). Panel labels with a prime show reconstructions of RP2 dendritic arbors (performed using the Imaris Filaments tool). Blue dots show the seed positions for each filament. Scale bar, 5 μm. Genetics: *RN2-gal4,UAS-shibire^{ts},UAS-hsMCFO*. **e–h**, Quantification of total dendrite length (**e**), longest branch length (a measure of distal dendrite extension) (**f**), number of dendritic branch points (**g**) and the distribution of dendrite lengths per reconstructed neuron (percentage of all processes) (**h**) after silencing by *shibire^{ts}*. Statistics (one-way ANOVA) by increasing length of silencing: $P < 0.05$, $P < 0.0001$, $P < 0.0001$ (**e**); $P < 0.007$, $P < 0.02$, $P < 0.0001$ (**f**); $P < 0.54$, $P < 0.14$, $P < 0.8$ (**g**). **h**, The percentage of long processes (>2 μm) was significantly increased after 1 h ($P < 0.0001$) and 3 h ($P < 0.0001$) of silencing (subtle decreases after 15 min, $P < 0.04$). **i–l**, Remodelling of dynamic distal processes within 12 min of aCC–RP2 activation. **i**, Schematic of a larval brain at 0 h ALH with aCC–RP2 motor neurons in purple. Two hemisegments were imaged per experiment (box). **j, k**, Motor neuron Chrimson activation results in dendrite retraction within minutes. **j**, 3D projection of a control isolated CNS at 0 h ALH, time 0 (*RN2-gal4,UAS-myR::GFP* + ATR). Yellow box highlights intersegmental region used for reconstruction of individual dendrites. Scale bar, 5 μm. **j'**, **j''**, 3D projections from representative time points over a 15-min acquisition period. Top, myR::GFP signal alone. Yellow arrowheads mark the tip of a single reconstructed process. Bottom, green Imaris Filament reconstruction of indicated process. Scale bars, 1 μm. **k**, 3D projection of an isolated CNS at 0 h ALH for Chrimson-activation, time 0 (*RN2-gal4,UAS-CsChrimson::mVenus* + ATR). Yellow box highlights intersegmental region used for reconstruction of individual dendrites. Scale bar, 4 μm. **k'**, **k''**, 3D projections from representative time points over a 15-min acquisition period. Top, Chrimson::mVenus signal alone. Yellow arrowheads mark the tip of a single reconstructed process. Bottom, green Imaris Filament reconstruction of indicated process. Scale bars, 1 μm. **l**, Quantification (one-way ANOVA) of normalized dendrite length over time in myR::GFP controls versus brains that were Chrimson-

activated for 3 min ($P < 0.99$), 8 min ($P < 0.06$), 12 min ($P < 0.05$) or 15 min ($P < 0.02$). $N = 10$ processes each from $N = 4$ brains per condition, with processes binned by length into 10 categories. Control length remained stable over the 15-min acquisition period. Chrimson activation results in progressive retraction of motor neuron dendrites. Control box plot specifications (minimum, maximum, centre, upper box bound (75%), lower box bound (25%), minus whisker, plus whisker): 0 min (-0.89, 1.22, 0.51, 0.65, -0.13, -0.76, 0.58), 3 min (-0.96, 1.78, 0.40, 0.95, -0.09, -0.87, 0.82), 8 min (-1.57, 1.33, 0.23, 0.92, -0.77, -0.80, 0.42), 12 min (-1.92, 1.48, 0.30, 1.05, -0.40, -1.51, 0.43), 15 min (-0.89, 1.80, 0.18, 0.97, -0.62, -0.27, 0.84). Chrimson box plot specifications: 0 min (-0.89, 1.22, 0.51, 0.65, -0.13, -0.76, 0.58), 3 min (-0.46, 1.74, 0.10, 0.95, -0.29, -0.17, 0.79), 8 min (-1.25, 1.14, -0.01, 0.88, -0.83, -0.42, 0.26), 12 min (-1.52, 1.01, -0.67, 0.52, -1.35, -0.18, 0.49), 15 min (-1.79, 0.99, -0.95, 0.34, -1.45, -0.34, 0.65). Data are mean \pm s.d. * $P < 0.05$; ** $P < 0.01$; *** $P < 0.001$; **** $P < 0.0001$; NS, not significant. N values reflect biological replicates from 2 independent experiments.

Extended Data Fig. 3 Quantification of the number of synaptic connections between the GABAergic A23a or cholinergic A18b interneurons and aCC–RP2 motor neurons.

a, TEM reconstruction of the A23a premotor neuron in a first instar larval brain at 4 h ALH; pre-synapses are primarily localized to the contralateral branch (arrow). **b**, Light microscopy image of a single A23a premotor neuron at 4 h ALH (*78F07-lexA*) with cyan membranes (*lexAop-myr::GFP*) and magenta pre-synapses (*lexAop-brp-short::Cherry*). Most synapses with aCC–RP2 motor neurons are at the contralateral process (arrow). Note the morphological similarity between light and electron microscopy images of A23a. Asterisks, sparse off-target expression not in A23a. Scale bar, 2 μ m. **c, d**, A23a is GABAergic. Scale, 3 μ m. Genotype: *78F07-lexA lexAop-myr::GFP*. **e**, Representative image of A23a (A1L) forming 14 synapses (white dots) with aCC (A1R) in the TEM reconstruction. Dorsal view, midline to left. Quantification of A23a–aCC synapses from the TEM reconstruction: 21 in A1R and 13 in A1L; A23a–RP2 synapses: 2 in A1R and 3 in A1L. **f**, Representative image of A18b (A1L) forming 11 synapses (white dots) with aCC (A1R) in the TEM reconstruction. Dorsal view,

midline to left. Quantification of A18b-aCC synapses from the TEM reconstruction: 18 in A1R and 10 in A1L; A18b-RP2 synapses: 7 in A1R and 5 in A1L. **g–g'''**, Quantification of putative synapses between A23a and aCC–RP2 by light microscopy at 4 h ALH. Scale bars, 2 μ m. **g**, Representative 3D projection of aCC–RP2 dendrite membrane (Chrimson::mVenus+; magenta) and A23a Brp-short puncta (white). Genotype: *RN2-gal4,UAS-Chrimson::mVenus* x *78F07-lexA,lexAop-brp-short::Cherry*. **g'**, aCC–RP2 dendrite membrane (Chrimson::mVenus+). **g''**, Imaris surface rendering of **g'**. **g'''**, A23a pre-synapses (Brp-short::Cherry+). **g''''**, Imaris spots measurement of Brp-short puncta within 90 nm of dendritic membrane (red dots, 19 putative direct synapses).

Extended Data Fig. 4 Remodelling of motor neuron synapses during and after critical period closure.

a–f', Remodelling of pre-synapses during the critical period. **a–c**, Imaris Surface from control (**a**) or post-Chrimson activation for 1 h (**b**) or 4 h (**c**), terminating at 4 h ALH (critical period open). Magenta, dendrite marker. White, presynaptic Brp-short::Cherry puncta from the excitatory A18b neuron. **a'–c'**, Imaris Spots, presynaptic Brp puncta within 90 nm of dendritic surface. Scale bar, 2 μ m. Genotype: *RN2-gal4,UAS-Chrimson::mVenus*; *94E10-lexA,lexAop-brp-short::Cherry*. **d–f**, Imaris Surface from control (**d**) or post-Chrimson activation for 1 h (**e**) or 4 h (**f**), terminating at 4 h ALH (critical period open). Magenta, dendrite marker. White, presynaptic Brp-short::Cherry puncta from the inhibitory A23a neuron. **d'–f'**, Imaris Spots, presynaptic Brp puncta within 90 nm of dendritic surface. Scale bar, 2 μ m. Genotype: *RN2-gal4,UAS-GtACR2::eYFP*; *78F07-lexA,lexAop-brp-short::Cherry*. Activation caused decreased numbers of excitatory, but not inhibitory, synapses (quantified in Fig. 2t). Overall, we observed Brp puncta numbers matching synapse numbers by TEM in stage-matched control brains (4 h ALH; A18b: 19.5 ± 4.9 Brp+ puncta vs 20 ± 2.5 TEM synapses per hemisegment; A23a: 16.9 ± 4.1 vs 19.5 ± 3.5 ; number of samples and experiments in Fig. 2 legend). **g–l**, Stability of pre-synapses after critical period closure. **g, h**, Imaris Surface from control (**g**) or post-Chrimson activation from 7–8 h ALH (**h**) (critical period closed; magenta, dendrite marker) with presynaptic Brp-short::Cherry puncta (white) from the excitatory A18b neuron. **g'–h'**,

Imaris Spots, presynaptic Brp puncta within 90 nm of dendritic surface. Scale bar, 2 μ m. Genotype: *RN2-gal4,UAS-Chrimson::mVenus; 94E10-lexA,lexAop-brp-short::Cherry*. **i, j**, Imaris Surface from control (**i**) or post-GtACR2 silencing (**j**) from 7–8 h ALH (critical period closed; magenta, dendrite marker) with presynaptic Brp-short::Cherry puncta (white) from the inhibitory A23a neuron. **i'–j'**, Imaris Spots, presynaptic Brp puncta within 90 nm of dendritic surface. Scale bar, 2 μ m. Genotype: *RN2-gal4,UAS-GtACR2::eYFP; 78F07-lexA,lexAop-brp-short::Cherry*. **k, l**, Quantification (one-way ANOVA) of synapse number following motor neuron excitation (**k**) or inhibition (**l**). *N* represents number of hemisegments/number of larvae: A18b Chrimson *N* = 10/8 (control); 15/9 (1 h activation, $P < 0.57$). A18b GtACR2 *N* = 28/10 (control); 22/9 (1 h silencing, $P < 0.94$). A23a Chrimson *N* = 24/14 (control); 20/14 (1 h activation, $P < 0.63$). A23a GtACR2 *N* = 22/10 (control); 25/10 (1 h silencing, $P < 0.52$). **m–t**, Remodelling of excitatory post-synaptic densities during and after the critical period. **m–o**, Representative 3D projection showing dendrite membranes (magenta) and post-synaptic densities (green) in control (**m**) or following 1 h (**n**) or 4 h (**o**) motor neuron activation terminating at 4 h ALH. **m'–o'**, Imaris Spots, post-synaptic puncta within 70 nm of dendritic surface. Scale bar, 2 μ m. Genotype: *RN2-lexA,lexAop-Chrimson::tdTomato, lexAop-drep-2::GFP*. **p–r**, Representative 3D projection showing dendrite membranes (magenta) and post-synaptic densities (green) in control (**p**) or following 1 h (**q**) or 4 h (**r**) motor neuron silencing terminating at 4 h ALH. **p'–r'**, Imaris Spots, post-synaptic puncta within 70 nm of dendritic surface. Scale, 2 μ m. Genotype: *RN2-gal4,UAS-GtACR2::eYFP, UAS-drep-2::mStrawberry*. **s, t**, *N* represents number of larvae, number of synapses averaged across 4 hemisegments (A1–A2). *N* = 10 per all conditions and controls. **s**, Quantification (one-way ANOVA) of excitatory post-synapse number following motor neuron excitation for 1 h ($P < 0.0002$) or 4 h ($P < 0.0001$) relative to control, and following inhibition for 1 h ($P < 0.4$) or 4 h ($P < 0.005$) relative to control at 4 h ALH. **t**, Quantification (one-way ANOVA) of excitatory post-synapse number following motor neuron excitation ($P < 0.9$) or silencing ($P < 0.49$) for 1 h relative to control at 8 h ALH. Data are normalized mean (0) \pm s.e.m. * $P < 0.05$, ** $P < 0.01$, *** $P < 0.001$, **** $P < .0001$. *N* values reflect biological replicates from 2 independent experiments.

Extended Data Fig. 5 Progressive ensheathment of motor synapses by astrocytes across critical period closure.

a–e, Time course of astrocyte–motor neuron synapse association from embryonic stage 17 (**a**), 0 h ALH (**b**), 4 h ALH (**c**), 8 h ALH (**d**) and 22 h ALH (**e**). Astrocytes, cyan (Gat+). Motor neuron membranes, green (myr::GFP+). Motor neuron post-synapses, magenta (mStrawberry+). **a'–e'**, Astrocytes and post-synapses alone. Synapses \leq 90 nm from astrocyte membranes were counted as ensheathed. Scale bar, 5 μ m. Genotype: *RN2-gal4, UAS-myR::GFP, UAS-drep-2::mStrawberry*. **f**, Quantification of astrocyte-associated post-synapses (percentage of total) revealed a significant interaction between developmental stage and per cent ensheathment (two-way ANOVA, $P < 0.0001$). $N = 6$ brains per time point, per cent ensheathment averaged over $N \geq 2$ segments (A1–A2). Data are mean \pm s.d. *** $P < 0.0001$. N values reflect biological replicates from 2 independent experiments.

Extended Data Fig. 6 Astrocyte ablation and manipulation extends critical period plasticity.

a–i, Astrocytes close the critical period. **a–c**, Representative 3D projections of brains expressing Chrimson::mCherry in aCC–RP2 motor neurons (*RN2-gal4, UAS-Chrimson::mCherry*) illustrating the three classes of dendritic arbor morphology at 8 h ALH following 4 h of Chrimson activation: control (**a**), mildly reduced (**b**) and strongly reduced (**c**) dendritic arbor size/complexity. Scale bar, 10 μ m. **d**, Quantification of each phenotypic class. N represents number of larvae. Control larvae show no significant dendritic remodelling after 15 min of activation at this stage ($P < .12$, one-way ANOVA). By contrast, ablation (abl.) of astrocytes results in a significant shift in the distribution of phenotypic classes away from wild type (no light abl. versus 15 min activation abl., $P < 0.03$, one-way ANOVA). Loss of astrocytes strongly sensitized these motor neurons to remodelling ($P < 0.04$, two-way ANOVA). Note that control and 4 h data are also displayed in Fig. 3e. Control genotype: *RN2-gal4, UAS-Chrimson::mCherry; alrm-lexA, lexAop-myR::GFP*. Ablation genotype: *RN2-gal4, UAS-Chrimson::mCherry; alrm-lexA, lexAop-rpr*. **e–h**,

Representative 3D projections of aCC–RP2 dendrites at 8 h ALH. Scale bar, 5 μ m. **e, f**, Dark-reared controls with ($N = 13$) or without ($N = 15$) astrocyte ablation. **g, h**, GtACR2 silencing in aCC–RP2 from 7–8 h ALH with ($N = 12$) or without ($N = 12$) astrocyte ablation; note that astrocyte ablation prolongs the critical period to allow activity-dependent dendrite extension. N represents number of larvae, volume averaged over 4 independent hemisegments (A1–A2). Genotypes: *RN2-gal4,UAS-GtACR2::eYFP; alrm-lexA* (control), *RN2-gal4,UAS-GtACR2::eYFP; alrm-lexA,lexAop-rpr* (ablation). **i**, Quantification by two-way ANOVA ($P < 0.009$). **j–n**, Astrocytes do not dampen critical period plasticity. **j–m**, Representative 3D projections of aCC–RP2 dendrites at 0 h ALH. Scale bar, 5 μ m. **j, k**, Dark-reared controls with ($N = 5$) or without ($N = 7$) astrocyte ablation. **l, m**, Chrimson activation in aCC–RP2 for 1 h in stage 17 embryo terminating at 0 h ALH, with ($N = 7$) and without ($N = 6$) astrocyte ablation; note that astrocyte ablation does not enhance activity-induced dendrite retraction. N represents number of larvae, volume averaged over 4 independent hemisegments (A1–A2). Control genotype: *RN2-gal4,UAS-Chrimson::mCherry; alrm-lexA,lexAop-myrt::GFP*. Ablation genotype: *RN2-gal4,UAS-Chrimson::mCherry; alrm-lexA,lexAop-rpr*. **n**, Quantification by two-way ANOVA ($P < 0.74$). **o–p'**, Representative images of astrocyte morphology in control (**o, o'**) or following astrocyte ablation (**p, p'**). White, astrocyte membranes (Gat+). Anterior to the left, dorsal is up. Scale bar, 10 μ m. Control Genotype: *RN2-gal4,UAS-Chrimson::mCherry; alrm-lexA,lexAop-myrt::GFP*. Ablation Genotype: *RN2-gal4,UAS-Chrimson::mCherry; alrm-lexA,lexAop-rpr*. Motor neuron channel not shown. **q–v**, MCFO clones showing single astrocyte morphology and volume in control ($N = 38/13$) or following knockdown of *gat* ($N = 11/7$), *chpf* ($N = 12/4$), *nlg4* ($N = 23/10$), or *nlg2* ($N = 23/7$) at 8 h ALH. N number of clones/number of larvae. The pan-astrocyte marker Gat was used to assay astrocyte ablation at 8 h ALH. Scale bars, 5 μ m. Normalized, mean astrocyte volume at the bottom of each MCFO panel (via Imaris Surface). Statistics (one-way ANOVA) relative to control: *gat* ($P < 0.0001$), *chpf* ($P < 0.43$), *nlg4* ($P < 0.007$), *nlg2* ($P < 0.37$) denoted by asterisks. Genotype: *alrm-gal4,UAS-hsMCFO,UAS-RNAi*. **w–x'**, Representative images showing labelling of all astrocytes by MCFO in control (**w, w'**) or following astrocyte KD of *nlg2* (**x, x'**). Anterior to the top, dorsal is up. Astrocytes tile the entire the CNS and exhibit normal tiling

behaviour, as exhibited by non-overlapping territories in single *z*-slices). Scale bars, 8 μm . Genotype: *alrm-gal4, UAS-hsMCFO, UAS-RNAi*. Data are mean \pm s.d. * $P < 0.05$, ** $P < 0.01$, *** $P < 0.001$, **** $P < 0.0001$; NS, not significant. Diamonds are used to denote significance following two-way ANOVA when both one-way and two-way are displayed together. N values reflect biological replicates from 2 independent experiments.

Extended Data Fig. 7 Expression of Nrx-1 in motor dendrites during the critical period.

a–b''', Localization of Nrx-1 (magenta) relative to motor neuron dendritic membranes (orange, myr::GFP+) and pre-synapses (green, Brp+) in control ($N = 15$) and following motor neuron-specific knockdown of *nrx-1* at 0 h ALH ($N = 20$). N represents number of larvae. **a–a'''**, Nrx-1 colocalized with motor dendrite membranes (white circle in inset) and synapses (Brp+) in control. **b–b'''**, Nrx-1 colocalized with synapses, but was absent from dendritic membranes in knockdown brains, as evidenced by increased clarity of Nrx-1+ synaptic puncta (white circle in inset). Scale bar, 2 μm . Insets, 1.5 \times zoom. Genotype: *RN2-gal4, UAS-myR::GFP, UAS-RNAi* or control. **c, c'**, Representative image showing localization of a Nrx-1::GFP fusion (magenta) relative to motor neuron dendrites (green, Denmark::Cherry+). Nrx-1::GFP is present within motor dendrites (white circle, colocalization channel in **c''**). $N = 15$ animals. Scale bar, 2 μm . Genotype: *RN2-gal4, UAS-Nrx-1::GFP, UAS-Denmark::Cherry*. N values reflect biological replicates from 2 independent experiments.

Extended Data Fig. 8 Expression of Nlg2 in astrocytes during the critical period is not required for proper excitatory–inhibitory synapse balance.

a–b''', Localization of Nlg2 (magenta) relative to astrocyte membranes (green, mcd8-GFP+) and pre-synapses (blue, Brp+) in control ($N = 15$) and following astrocyte-specific knockdown of *nlg2* at 0 h ALH ($N = 18$). N represents number of larvae. **a–a'''**, Nlg2 colocalized with astrocyte membranes (mcd8-GFP+) and synapses (Brp+) in control. **b–b'''**, Nlg2 colocalized with synapses (inset), but was absent from astrocyte membranes

in knockdown brains, as evidenced by increased clarity of Nlg2+ synaptic puncta. Scale bar, 2 μ m. Insets, 1.5 \times zoom. Genotype: *alrm-gal4, UAS-mcd8::GFP, UAS-RNAi* or control. **c–d'''**, Representative images showing aCC–RP2 dendrites (magenta) and excitatory post-synapses (cyan, Drep-2::GFP+) relative to all presynapses (orange, Brp+) in control ($N = 7$) (**c–c''**) versus astrocyte-specific knockdown of *nlg2* ($N = 9$) (**d–d'''**). **c''', d'''**, Note close apposition of pre- and post-synapses (arrowheads). N represents number of larvae, with synapses averaged over 4 hemisegments per brain (A1–A2). Scale bar, 3 μ m. Genotype: *RN2-lexA, lexAop-myR::tdTomato, lexAop-drep-2::GFP; alrm-gal4, UAS-RNAi* or control. **e, f**, Quantification of normalized total synapse number ($P < 0.11$) (**e**) and the ratio of excitatory synapses to total synapses ($P < 0.96$) (**f**) revealed no significant differences (Mann–Whitney test, two-sided). Data are mean \pm s.d. NS, not significant. N values reflect biological replicates from 2 independent experiments.

Extended Data Fig. 9 Tubulin stability correlates with dendrite retention during activity-induced remodelling.

a–e, Dendrites with stable microtubules are resistant to activity-induced remodelling. Representative 3D projections of brains expressing Chrimson (green) and the microtubule reporter Zeus (a tagged microtubule binding protein, magenta) in aCC–RP2 motor neurons (*RN2-gal4, UAS-Cherry::Zeus, UAS-CsChrimson::mVenus*) at 0 h ALH. Brains were preserved with cold fixative to visualize stable microtubule populations in controls (**a**) and after Chrimson-activation for 15 min (**b**), 1 h (**c**) or 4 h (**d**) terminating at 0 h ALH. Panel labels with prime show the Cherry:Zeus channel only. Scale bar, 10 μ m. Boxed regions represent ROIs that were used for Imaris Surface reconstructions to determine dendrite and microtubule volume. **e**, Quantification (one-way ANOVA) of the normalized volume of dendrite membranes (Chrimson::mVenus+) and Cherry::Zeus within the same ROI. Microtubule volumes at each time point were calculated relative to the membrane volume for dark-reared controls. N represents number of larvae, with the volume per animal representing the average volume across 4 hemisegments (A1–A2). In dark-reared controls ($N = 4$), stable microtubule populations reflect $55 \pm 8\%$ of the total dendritic volume. Chrimson activation results in a significant decrease in

total dendritic volume after 15 min ($N = 6$, $P < 0.05$) and 1 h ($N = 4$, $P < 0.0003$) of activation. Microtubule volume is unchanged after 15 min ($P < 0.26$) or 1 h ($P < 0.35$). After 4 h of activation ($N = 6$), both membrane volume ($P < 0.0001$) and microtubule volume ($P < 0.0002$) are significantly reduced; however, dendrites with stable microtubules are preferentially retained such that membrane volume is nearly equivalent to the Cherry::Zeus volume ($\#P < 0.02$). Data are mean \pm s.d. * $P < 0.05$, ** $P < 0.01$, *** $P < 0.001$, **** $P < 0.0001$. N values reflect biological replicates from 2 independent experiments.

Extended Data Fig. 10 Assaying permanent motor circuit changes following manipulation of critical period activity.

a–c, Stability of remodelled synapses following motor neuron activation during the critical period (CP). **a**, **b**, Imaris Surface from control (**a**) or post-Chrimson activation (**b**) from 0–4 h ALH (critical period open; magenta, dendrite marker) followed by 20 h recovery in dark conditions. Presynaptic Brp-short::Cherry puncta (white) from the excitatory A18b neuron. **a'**, **b'**, Imaris Spots, presynaptic Brp puncta within 90 nm of dendritic surface. Scale bar, 2 μ m. Genotype: *RN2-gal4,UAS-Chrimson::mVenus; 94E10-lexA,lexAop-brp-short::Cherry*. Data not shown: inhibitory A23a synapses following critical period activation and recovery. Genotype: *RN2-gal4,UAS-Chrimson::mVenus; 78F07-lexA,lexAop-brp-short::Cherry*. **c**, Quantification of excitatory ($P < 0.002$) and inhibitory (raw images not shown; $P < 0.61$) synapse numbers following motor neuron excitation by one-way ANOVA. N represents the number of hemisegments/number of larvae: A18b Chrimson $N = 19/3$ (control); 15/2 (1 h and 4 h activation combined). A23a Chrimson $N = 15/2$ (control); 31/8 (1 h and 4 h activation combined). Data are normalized mean (0) \pm s.e.m. **d–g'**, Validation of genetic tool for conditional knockdown of astrocyte genes to transiently extend the critical period. $N = 10$ animals per condition. Orthogonal views through the ventral nerve cord showing the extent of astrocyte infiltration (Gat+, green) into the synapse-dense neuropil (Brp+, magenta). Prime panels show Gat signal alone. **d–e'**, In control larvae (*25H07-gal4 X UAS-myr::GFP*), astrocytes progressively infiltrate the neuropil from 8 h ALH through 44 h ALH. **f**, **f'**, When reared at 30 °C to 8 h ALH, expression of *UAS-htl^{DN}* in astrocytes (*tubP-gal80^{ts}; 25H07-gal4*) suppressed astrocyte

infiltration. **g, g'**, Shifting to 18 °C at 8 h ALH resulted in inhibition of Gal4 by TubP-Gal80^{ts}, reduced expression of *htl*^{DN}, and rescued astrocyte infiltration at 44 h ALH (25 °C standard, see [Methods](#) for details on staging). Scale bar, 20 μm (8 h), 30 μm (44 h). ***P* < 0.01. *N* values reflect biological replicates from 2 independent experiments.

Supplementary information

[Supplementary Information](#)

This file contains the Supplementary Methods.

[Reporting Summary](#)

[Video 1: Time-lapse imaging of myr::GFP control for Chrimson-activation](#)

Representative time-lapse video showing control aCC/RP2 dendrite dynamics in a fictive brain preparation (isolated CNS) expressing *UAS-myR::GFP* under the control of *RN2-gal4* at 0 h ALH. Animals were supplied with ATR and reared in the dark to mimic conditions for Chrimson-activation. A single z-stack was acquired every 45 seconds (each stack taking 30" to acquire) and brains were imaged for a total of 15 minutes. Dendrites were highly motile, though largely stable in length over the 15-minute period (white arrowheads).

[Video 2: Time lapse imaging showing rapid retraction of dendrites during Chrimson-activation](#)

Representative time-lapse video showing aCC/RP2 dendrite dynamics in a fictive brain preparation during Chrimson-activation (*RN2-gal4; UAS-Chrimson::mVenus*) at 0 h ALH. A single z-stack was acquired every 45 seconds (each stack taking 30" to acquire) and brains were imaged for a total of 15 minutes. Dendrites were highly motile, with many processes retracting and some processes completely collapsing into their parent dendrite within the 15-minute period (white arrowheads).

[Video 3: Time-lapse imaging of wildtype aCC/RP2 dendrites at 4 h ALH](#)

Representative time-lapse video showing control aCC/RP2 dendrite dynamics in a fictive brain preparation expressing *UAS-myrl::GFP* under the control of *RN2-gal4* at 4 h ALH. A single z-stack was acquired every 45 seconds (each stack taking 30" to acquire) and brains were imaged for a total of 15 minutes. Dendrites were less motile than 0 h ALH, though still highly dynamic (white arrowheads).

[Video 4: Time-lapse imaging of wildtype aCC/RP2 dendrites at 8 h ALH](#)

Representative time-lapse video showing control aCC/RP2 dendrite dynamics in a fictive brain preparation expressing *UAS-myrl::GFP* under the control of *RN2-gal4* at 8 h ALH. A single z-stack was acquired every 45 seconds (each stack taking 30" to acquire) and brains were imaged for a total of 15 minutes. Dendrites were less motile than 0 h ALH and 4 h ALH, though still dynamic (white arrowheads).

[Video 5: Time-lapse imaging of wildtype aCC/RP2 dendrites at 22 h ALH](#)

Representative time-lapse video showing control aCC/RP2 dendrite dynamics in a fictive brain preparation expressing *UAS-myrl::GFP* under the control of *RN2-gal4* at 22 h ALH. A single z-stack was acquired every 45 seconds (each stack taking 30" to acquire) and brains were imaged for a total of 15 minutes. Dendrites showed small dendrite extension/retraction events, but were stable overall (white arrowheads).

[Video 6: Time-lapse imaging of wildtype aCC/RP2 dendrites at 22 h ALH post-astrocyte ablation](#)

Representative time-lapse video showing control aCC/RP2 dendrite dynamics in a fictive brain preparation expressing *UAS-myrl::GFP* under the control of *RN2-gal4* at 22 h ALH in the absence of astrocytes (*alm*

lexA lexAop-rpr, verified by Gat staining post-acquisition). A single z-stack was acquired every 45 seconds (each stack taking 30" to acquire) and brains were imaged for a total of 15 minutes. Dendrites showed increased motility relative to 22 h ALH controls (white arrowheads).

Video 7: Time lapse imaging showing rapid retraction of dendrites during Chrimson-activation following microtubule instability

Representative time-lapse video showing aCC/RP2 dendrite dynamics in a fictive brain preparation during Chrimson-activation. aCC/RP2 dendrites were co-labeled with *RN2-gal4* driving *UAS-Chrimson::mVenus* (left panel) and *UAS-cherry::zeus* (right panel) to mark microtubule populations.. A single z-stack was acquired every 45 seconds (each stack taking 30" to acquire) and brains were imaged for a total of 15 minutes. Cherry::Zeus was depleted from the tip of dendrites just prior to process retraction (white arrowheads).

Video 8: Time lapse imaging of control aCC/RP2 dendrites at 4 h ALH

Representative time-lapse video showing control aCC/RP2 dendrite dynamics in a fictive brain preparation expressing *UAS-cherry::zeus* under the control of *RN2-gal4* at 4 h ALH. *UAS-myrl::GFP* control channel not shown. A single z-stack was acquired every 30 seconds (each stack taking 25" to acquire) and brains were imaged for a total of 15 minutes. Dendritic microtubules were highly dynamic (white arrowheads).

Video 9: Time lapse imaging of aCC/RP2 dendrites overexpressing Nrx-1 at 4 h ALH

Representative time-lapse video showing aCC/RP2 dendrite dynamics in a fictive brain preparation expressing *UAS-Nrx-1* and *UAS-cherry::zeus* under the control of *RN2-gal4* at 4 h ALH. A single z-stack was acquired every 30 seconds (each stack taking 25" to acquire) and brains were imaged

for a total of 15 minutes. Dendritic microtubules showed less dynamicity under *Nrx-1* overexpression conditions (white arrowheads).

[Peer Review File](#)

Rights and permissions

[Reprints and Permissions](#)

About this article



Check for
updates

Cite this article

Ackerman, S.D., Perez-Catalan, N.A., Freeman, M.R. *et al.* Astrocytes close a motor circuit critical period. *Nature* **592**, 414–420 (2021).
<https://doi.org/10.1038/s41586-021-03441-2>

[Download citation](#)

- Received: 21 July 2020
- Accepted: 10 March 2021
- Published: 07 April 2021
- Issue Date: 15 April 2021
- DOI: <https://doi.org/10.1038/s41586-021-03441-2>

Further reading

- **A critical period that shapes neuronal motor circuits**

- Laura Sancho
- & Nicola J. Allen

Nature (2021)

Comments

By submitting a comment you agree to abide by our [Terms](#) and [Community Guidelines](#). If you find something abusive or that does not comply with our terms or guidelines please flag it as inappropriate.

[Access through your institution](#)

[Change institution](#)

[Buy or subscribe](#)

Associated Content

Nature | News & Views

A critical period that shapes neuronal motor circuits

- Laura Sancho
- & Nicola J. Allen

This article was downloaded by **calibre** from <https://www.nature.com/articles/s41586-021-03441-2>

- Article
- [Published: 17 March 2021](#)

Primate cell fusion disentangles gene regulatory divergence in neurodevelopment

- [Rachel M. Agoglia](#)¹,
- [Danqiong Sun](#)²,
- [Fikri Birey](#)³,
- [Se-Jin Yoon](#) [ORCID: orcid.org/0000-0001-8412-5991](#)³,
- [Yuki Miura](#) [ORCID: orcid.org/0000-0002-1410-3612](#)³,
- [Karen Sabatini](#)³,
- [Sergiu P. Pașca](#) [ORCID: orcid.org/0000-0002-3216-3248](#)³ na1 &
- [Hunter B. Fraser](#) [ORCID: orcid.org/0000-0001-8400-8541](#)² na1

[Nature](#) volume 592, pages421–427(2021) [Cite this article](#)

- 9575 Accesses
- 177 Altmetric
- [Metrics details](#)

Subjects

- [Development of the nervous system](#)
- [Evolution](#)
- [Stem-cell differentiation](#)

Abstract

Among primates, humans display a unique trajectory of development that is responsible for the many traits specific to our species. However, the inaccessibility of primary human and chimpanzee tissues has limited our ability to study human evolution. Comparative *in vitro* approaches using primate-derived induced pluripotent stem cells have begun to reveal species differences on the cellular and molecular levels^{1,2}. In particular, brain organoids have emerged as a promising platform to study primate neural development *in vitro*^{3,4,5}, although cross-species comparisons of organoids are complicated by differences in developmental timing and variability of differentiation^{6,7}. Here we develop a new platform to address these limitations by fusing human and chimpanzee induced pluripotent stem cells to generate a panel of tetraploid hybrid stem cells. We applied this approach to study species divergence in cerebral cortical development by differentiating these cells into neural organoids. We found that hybrid organoids provide a controlled system for disentangling *cis*- and *trans*-acting gene-expression divergence across cell types and developmental stages, revealing a signature of selection on astrocyte-related genes. In addition, we identified an upregulation of the human somatostatin receptor 2 gene (*SSTR2*), which regulates neuronal calcium signalling and is associated with neuropsychiatric disorders^{8,9}. We reveal a human-specific response to modulation of *SSTR2* function in cortical neurons, underscoring the potential of this platform for elucidating the molecular basis of human evolution.

[Access through your institution](#)

[Change institution](#)

[Buy or subscribe](#)

Access options

Subscribe to Journal

Get full journal access for 1 year

\$199.00

only \$3.90 per issue

[Subscribe](#)

All prices are NET prices.

VAT will be added later in the checkout.

Tax calculation will be finalised during checkout.

Rent or Buy article

Get time limited or full article access on ReadCube.

from \$8.99

[Rent or Buy](#)

All prices are NET prices.

Additional access options:

- [Log in](#)
- [Access through your institution](#)
- [Learn about institutional subscriptions](#)

Fig. 1: Generation of human–chimpanzee hybrid iPS cells.

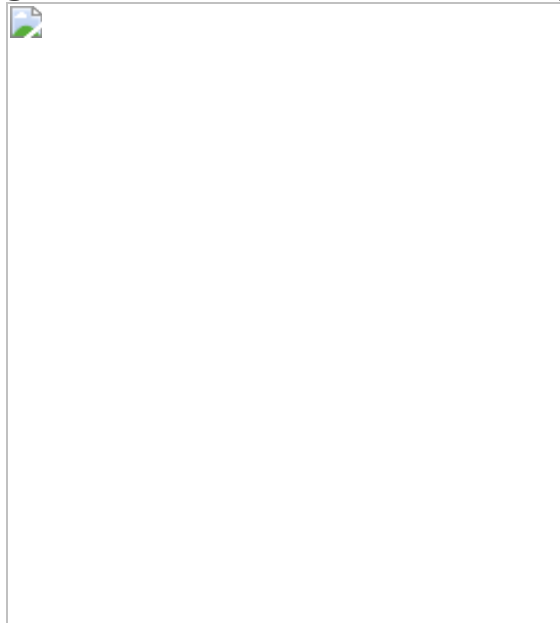


Fig. 2: Cortical differentiation of hybrid iPS cells.

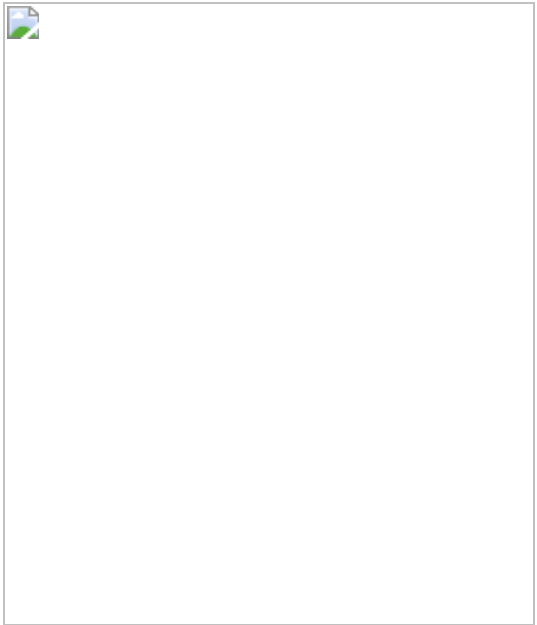


Fig. 3: Disentangling *cis*-regulatory effects on gene expression in cortical spheroids.

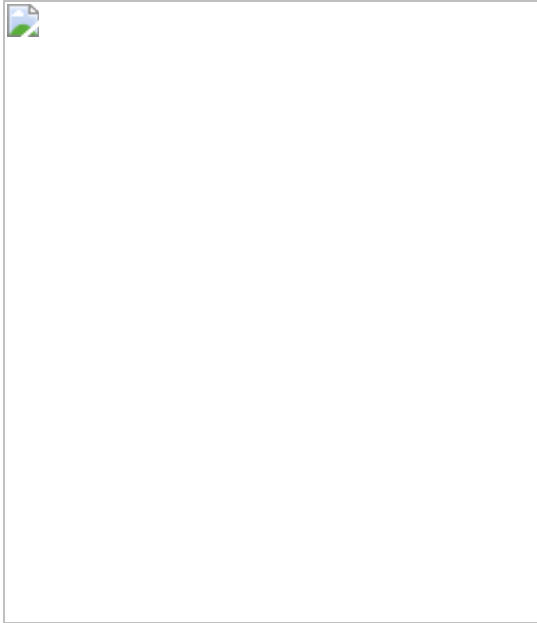
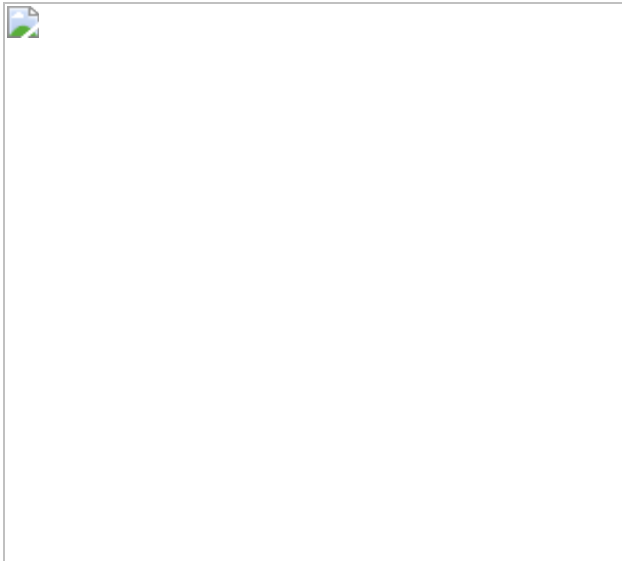


Fig. 4: Functional validation of allele-specific gene-expression changes.



Data availability

Raw and processed data are publicly available through the Gene Expression Omnibus under accession [GSE144825](#). The alignment of human and chimpanzee genomes from Ensembl is available at ftp://ftp.ensembl.org/pub/release-84/maf/ensembl-compara/pairwise_alignments/homo_sapiens.GRCh38.vs.pan_troglodytes.CHIMP2.1.4.tar. The SFARI database is available at <https://www.sfari.org/resource/sfari-gene/>.

Code availability

All code for the described analyses of RNA-seq data and for making figures is publicly available at https://github.com/TheFraserLab/Agoglia_HumanChimpanzee2020.

References

1. 1.

Gallego Romero, I. et al. A panel of induced pluripotent stem cells from chimpanzees: a resource for comparative functional genomics.

eLife **4**, e07103 (2015).

[PubMed](#) [PubMed Central](#) [Google Scholar](#)

2. 2.

Prescott, S. L. et al. Enhancer divergence and *cis*-regulatory evolution in the human and chimp neural crest. *Cell* **163**, 68–83 (2015).

[PubMed](#) [PubMed Central](#) [CAS](#) [Google Scholar](#)

3. 3.

Pašca, S. P. The rise of three-dimensional human brain cultures. *Nature* **553**, 437–445 (2018).

[PubMed](#) [ADS](#) [Google Scholar](#)

4. 4.

Muchnik, S. K., Lorente-Galdos, B., Santpere, G. & Sestan, N. Modeling the evolution of human brain development using organoids. *Cell* **179**, 1250–1253 (2019).

[PubMed](#) [PubMed Central](#) [CAS](#) [Google Scholar](#)

5. 5.

Qian, X., Song, H. & Ming, G. L. Brain organoids: advances, applications and challenges. *Development* **146**, dev166074 (2019).

[PubMed](#) [PubMed Central](#) [CAS](#) [Google Scholar](#)

6. 6.

Pollen, A. A. et al. Establishing cerebral organoids as models of human-specific brain evolution. *Cell* **176**, 743–756 (2019).

[PubMed](#) [PubMed Central](#) [CAS](#) [Google Scholar](#)

7. 7.

Kanton, S. et al. Organoid single-cell genomic atlas uncovers human-specific features of brain development. *Nature* **574**, 418–422 (2019).

[PubMed](#) [ADS](#) [CAS](#) [Google Scholar](#)

8. 8.

Beneyto, M., Morris, H. M., Rovensky, K. C. & Lewis, D. A. Lamina- and cell-specific alterations in cortical somatostatin receptor 2 mRNA expression in schizophrenia. *Neuropharmacology* **62**, 1598–1605 (2012).

[PubMed](#) [CAS](#) [Google Scholar](#)

9. 9.

Ádori, C. et al. Critical role of somatostatin receptor 2 in the vulnerability of the central noradrenergic system: new aspects on Alzheimer’s disease. *Acta Neuropathol.* **129**, 541–563 (2015).

[PubMed](#) [Google Scholar](#)

10. 10.

Ward, M. C. et al. Silencing of transposable elements may not be a major driver of regulatory evolution in primate iPSCs. *eLife* **7**, e33084 (2018).

[PubMed](#) [PubMed Central](#) [Google Scholar](#)

11. 11.

Prud’homme, B., Gompel, N. & Carroll, S. B. Emerging principles of regulatory evolution. *Proc. Natl Acad. Sci. USA* **104** (Suppl 1), 8605–8612 (2007).

[PubMed](#) [ADS](#) [Google Scholar](#)

12. 12.

Paşca, A. M. et al. Functional cortical neurons and astrocytes from human pluripotent stem cells in 3D culture. *Nat. Methods* **12**, 671–678 (2015).

[PubMed](#) [PubMed Central](#) [Google Scholar](#)

13. 13.

Lancaster, M. A. et al. Cerebral organoids model human brain development and microcephaly. *Nature* **501**, 373–379 (2013).

[PubMed](#) [ADS](#) [CAS](#) [Google Scholar](#)

14. 14.

Camp, J. G. et al. Human cerebral organoids recapitulate gene expression programs of fetal neocortex development. *Proc. Natl Acad. Sci. USA* **112**, 15672–15677 (2015).

[PubMed](#) [ADS](#) [CAS](#) [Google Scholar](#)

15. 15.

Sloan, S. A. et al. Human astrocyte maturation captured in 3D cerebral cortical spheroids derived from pluripotent stem cells. *Neuron* **95**, 779–790 (2017).

[PubMed](#) [PubMed Central](#) [CAS](#) [Google Scholar](#)

16. 16.

Mora-Bermúdez, F. et al. Differences and similarities between human and chimpanzee neural progenitors during cerebral cortex development. *eLife* **5**, e18683 (2016).

[PubMed](#) [PubMed Central](#) [Google Scholar](#)

17. 17.

Otani, T., Marchetto, M. C., Gage, F. H., Simons, B. D. & Livesey, F. J. 2D and 3D stem cell models of primate cortical development identify species-specific differences in progenitor behavior contributing to brain size. *Cell Stem Cell* **18**, 467–480 (2016).

[PubMed](#) [PubMed Central](#) [CAS](#) [Google Scholar](#)

18. 18.

Amps, K. et al. Screening ethnically diverse human embryonic stem cells identifies a chromosome 20 minimal amplicon conferring growth advantage. *Nat. Biotechnol.* **29**, 1132–1144 (2011).

[PubMed](#) [CAS](#) [Google Scholar](#)

19. 19.

Taapken, S. M. et al. Karotypic abnormalities in human induced pluripotent stem cells and embryonic stem cells. *Nat. Biotechnol.* **29**, 313–314 (2011).

[PubMed](#) [CAS](#) [Google Scholar](#)

20. 20.

Müller, F.-J. et al. A bioinformatic assay for pluripotency in human cells. *Nat. Methods* **8**, 315–317 (2011).

[PubMed](#) [PubMed Central](#) [Google Scholar](#)

21. 21.

Yin, X. et al. Engineering stem cell organoids. *Cell Stem Cell* **18**, 25–38 (2016).

[PubMed](#) [PubMed Central](#) [CAS](#) [Google Scholar](#)

22. 22.

Sato, T. et al. Single Lgr5 stem cells build crypt-villus structures in vitro without a mesenchymal niche. *Nature* **459**, 262–265 (2009).

[PubMed](#) [PubMed Central](#) [ADS](#) [CAS](#) [Google Scholar](#)

23. 23.

Stingl, J., Eaves, C. J., Zandieh, I. & Emerman, J. T. Characterization of bipotent mammary epithelial progenitor cells in normal adult human breast tissue. *Breast Cancer Res. Treat.* **67**, 93–109 (2001).

[PubMed](#) [CAS](#) [Google Scholar](#)

24. 24.

Qiu, X. et al. Reversed graph embedding resolves complex single-cell trajectories. *Nat. Methods* **14**, 979–982 (2017).

[PubMed](#) [PubMed Central](#) [CAS](#) [Google Scholar](#)

25. 25.

Greig, L. C., Woodworth, M. B., Galazo, M. J., Padmanabhan, H. & Macklis, J. D. Molecular logic of neocortical projection neuron specification, development and diversity. *Nat. Rev. Neurosci.* **14**, 755–769 (2013).

[PubMed](#) [CAS](#) [Google Scholar](#)

26. 26.

Chen, B., Khodadoust, M. S., Liu, C. L., Newman, A. M. & Alizadeh, A. A. Profiling tumor infiltrating immune cells with CIBERSORT. *Methods Mol. Biol.* **1711**, 243–259 (2018).

[PubMed](#) [PubMed Central](#) [CAS](#) [Google Scholar](#)

27. 27.

Somel, M. et al. Transcriptional neoteny in the human brain. *Proc. Natl Acad. Sci. USA* **106**, 5743–5748 (2009).

[PubMed](#) [ADS](#) [CAS](#) [Google Scholar](#)

28. 28.

Langfelder, P. & Horvath, S. WGCNA: an R package for weighted correlation network analysis. *BMC Bioinformatics* **9**, 559 (2008).

[PubMed](#) [PubMed Central](#) [Google Scholar](#)

29. 29.

Fraser, H. B. Genome-wide approaches to the study of adaptive gene expression evolution: systematic studies of evolutionary adaptations involving gene expression will allow many fundamental questions in evolutionary biology to be addressed. *BioEssays* **33**, 469–477 (2011).

[PubMed](#) [CAS](#) [Google Scholar](#)

30. 30.

Oberheim, N. A., Wang, X., Goldman, S. & Nedergaard, M. Astrocytic complexity distinguishes the human brain. *Trends Neurosci.* **29**, 547–553 (2006).

[PubMed](#) [CAS](#) [Google Scholar](#)

31. 31.

Miller, J. A., Horvath, S. & Geschwind, D. H. Divergence of human and mouse brain transcriptome highlights Alzheimer disease pathways. *Proc. Natl Acad. Sci. USA* **107**, 12698–12703 (2010).

[PubMed](#) [ADS](#) [CAS](#) [Google Scholar](#)

32. 32.

Bozek, K. et al. Exceptional evolutionary divergence of human muscle and brain metabolomes parallels human cognitive and physical uniqueness. *PLoS Biol.* **12**, e1001871 (2014).

[PubMed](#) [PubMed Central](#) [Google Scholar](#)

33. 33.

Kelley, K. W., Nakao-Inoue, H., Molofsky, A. V. & Oldham, M. C. Variation among intact tissue samples reveals the core transcriptional features of human CNS cell classes. *Nat. Neurosci.* **21**, 1171–1184 (2018).

[PubMed](#) [PubMed Central](#) [CAS](#) [Google Scholar](#)

34. 34.

Basu, S. N., Kollu, R. & Banerjee-Basu, S. AutDB: a gene reference resource for autism research. *Nucleic Acids Res.* **37**, D832–D836 (2009).

[PubMed](#) [CAS](#) [Google Scholar](#)

35. 35.

Sousa, A. M. M., Meyer, K. A., Santpere, G., Gulden, F. O. & Sestan, N. Evolution of the human nervous system function, structure, and development. *Cell* **170**, 226–247 (2017).

[PubMed](#) [PubMed Central](#) [CAS](#) [Google Scholar](#)

36. 36.

Fujii, Y. et al. Somatostatin receptor subtype SSTR2 mediates the inhibition of high-voltage-activated calcium channels by somatostatin and its analogue SMS 201-995. *FEBS Lett.* **355**, 117–120 (1994).

[PubMed](#) [CAS](#) [Google Scholar](#)

37. 37.

Liguz-Lecznar, M., Urban-Ciecko, J. & Kossut, M. Somatostatin and somatostatin-containing neurons in shaping neuronal activity and plasticity. *Front. Neural Circuits* **10**, 48 (2016).

[PubMed](#) [PubMed Central](#) [Google Scholar](#)

38. 38.

He, Z. et al. Comprehensive transcriptome analysis of neocortical layers in humans, chimpanzees and macaques. *Nat. Neurosci.* **20**, 886–895 (2017).

[PubMed](#) [CAS](#) [Google Scholar](#)

39. 39.

Gokhman, D. et al. Human-chimpanzee fused cells reveal cis-regulation underlying skeletal evolution. *Nat. Genet.* <https://doi.org/10.1038/s41588-021-00804-3> (2021).

40. 40.

Yoon, S. J. et al. Reliability of human cortical organoid generation. *Nat. Methods* **16**, 75–78 (2019).

[PubMed](#) [CAS](#) [Google Scholar](#)

41. 41.

van de Geijn, B., McVicker, G., Gilad, Y. & Pritchard, J. K. WASP: allele-specific software for robust molecular quantitative trait locus discovery. *Nat. Methods* **12**, 1061–1063 (2015).

[PubMed](#) [PubMed Central](#) [Google Scholar](#)

42. 42.

Tehranchi, A. et al. Fine-mapping *cis*-regulatory variants in diverse human populations. *eLife* **8**, e39595 (2019).

[PubMed](#) [PubMed Central](#) [Google Scholar](#)

43. 43.

Combs, P. A. & Fraser, H. B. Spatially varying *cis*-regulatory divergence in *Drosophila* embryos elucidates *cis*-regulatory logic. *PLoS Genet.* **14**, e1007631 (2018).

[PubMed](#) [PubMed Central](#) [Google Scholar](#)

44. 44.

Birey, F. et al. Assembly of functionally integrated human forebrain spheroids. *Nature* **545**, 54–59 (2017).

[PubMed](#) [PubMed Central](#) [ADS](#) [CAS](#) [Google Scholar](#)

45. 45.

Zhang, Y. et al. Purification and characterization of progenitor and mature human astrocytes reveals transcriptional and functional differences with mouse. *Neuron* **89**, 37–53 (2016).

[CAS](#) [Google Scholar](#)

46. 46.

Picelli, S. et al. Full-length RNA-seq from single cells using Smart-seq2. *Nat. Protoc.* **9**, 171–181 (2014).

[PubMed](#) [CAS](#) [Google Scholar](#)

47. 47.

Picelli, S. et al. Tn5 transposase and tagmentation procedures for massively scaled sequencing projects. *Genome Res.* **24**, 2033–2040 (2014).

[PubMed](#) [PubMed Central](#) [CAS](#) [Google Scholar](#)

48. 48.

Satija, R., Farrell, J. A., Gennert, D., Schier, A. F. & Regev, A. Spatial reconstruction of single-cell gene expression data. *Nat. Biotechnol.* **33**, 495–502 (2015).

[PubMed](#) [PubMed Central](#) [CAS](#) [Google Scholar](#)

49. 49.

Eden, E., Navon, R., Steinfeld, I., Lipson, D. & Yakhini, Z. GOrilla: a tool for discovery and visualization of enriched GO terms in ranked gene lists. *BMC Bioinformatics* **10**, 48–502 (2009).

[PubMed](#) [PubMed Central](#) [Google Scholar](#)

50. 50.

Newman, A. M. et al. Robust enumeration of cell subsets from tissue expression profiles. *Nat. Methods* **12**, 453–457 (2015).

[PubMed](#) [PubMed Central](#) [CAS](#) [Google Scholar](#)

51. 51.

Paşca, S. P. et al. Using iPSC-derived neurons to uncover cellular phenotypes associated with Timothy syndrome. *Nat. Med.* **17**, 1657–1662 (2011).

[PubMed](#) [PubMed Central](#) [Google Scholar](#)

[Download references](#)

Acknowledgements

We thank H. Blau and G. Markov for advice on the hybridization experiments; D. Bangs and J. Erdmann for assistance with iPS cell karyotyping; R. Jones, S. D. Conley and R. Sinha for assistance in constructing the single-cell RNA-seq libraries; and members of the PaŞca and Fraser laboratories for advice and feedback on the manuscript. This work was supported by a Stanford Bio-X Interdisciplinary Initiatives Seed Grant (to S.P.P. and H.B.F.), an NIH grant T32 GM007790 (supporting R.M.A.), the Department of Defense National Defense Science and Engineering Graduate Fellowship (to R.M.A.), the Stanford Center for Computational, Evolutionary and Human Genomics (to R.M.A.), NIH grant 2R01GM097171-05A1 (supporting H.B.F.), the Stanford Medicine’s Dean’s Fellowship (to Y.M. and F.B.), the Stanford Medicine Maternal & Child Health Research Institute Postdoctoral Support Program (to Y.M. and F.B.), the American Epilepsy Society Postdoctoral Research Fellowship (to F.B.), the Stanford Wu Tsai Neurosciences Institute’s Big Idea Grants on Brain Rejuvenation and Human Brain Organogenesis (supporting S.P.P.), the Kwan Research Fund (supporting S.P.P.), the New York Stem Cell Foundation–Robertson Investigator Award (supporting S.P.P.) and the Chan Zuckerberg Ben Barres Investigator Award (to S.P.P.). This study used cell lines derived from the Yerkes National Primate Research Center, which is supported by the National Institutes of Health, Office of Research Infrastructure Programs/OD (P51OD011132).

Author information

Author notes

1. These authors contributed equally: Sergiu P. PaŞca, Hunter B. Fraser

Affiliations

1. Department of Genetics, Stanford University School of Medicine, Stanford, CA, USA

Rachel M. Agoglia

2. Department of Biology, Stanford University, Stanford, CA, USA

Danqiong Sun & Hunter B. Fraser

3. Department of Psychiatry and Behavioral Sciences, Stanford University School of Medicine, Stanford, CA, USA

Fikri Birey, Se-Jin Yoon, Yuki Miura, Karen Sabatini & Sergiu P. Pasca

Authors

1. Rachel M. Agoglia

[View author publications](#)

You can also search for this author in [PubMed](#) [Google Scholar](#)

2. Danqiong Sun

[View author publications](#)

You can also search for this author in [PubMed](#) [Google Scholar](#)

3. Fikri Birey

[View author publications](#)

You can also search for this author in [PubMed](#) [Google Scholar](#)

4. Se-Jin Yoon

[View author publications](#)

You can also search for this author in [PubMed](#) [Google Scholar](#)

5. Yuki Miura

[View author publications](#)

You can also search for this author in [PubMed](#) [Google Scholar](#)

6. Karen Sabatini

[View author publications](#)

You can also search for this author in [PubMed](#) [Google Scholar](#)

7. Sergiu P. Pașca

[View author publications](#)

You can also search for this author in [PubMed](#) [Google Scholar](#)

8. Hunter B. Fraser

[View author publications](#)

You can also search for this author in [PubMed](#) [Google Scholar](#)

Contributions

D.S. generated the hybrid iPS cells. R.M.A. and D.S. characterized the iPS cells. R.M.A., D.S., S.-J.Y. and K.S. cultured the iPS cells. R.M.A. performed the neural differentiation of hCS, cCS and hyCS. S.-J.Y. contributed to the neural differentiation of hCS, cCS and hyCS. R.M.A. performed the RNA-seq and analysis of RNA-seq data. R.M.A. and F.B. performed the calcium-imaging experiments. F.B. analysed the calcium-imaging data. Y.M. performed the immunocytochemistry in intact and dissociated cortical spheroids. R.M.A., S.P.P. and H.B.F. conceived the project, designed experiments and wrote the paper with input from all authors. S.P.P. and H.B.F. supervised all aspects of the work.

Corresponding authors

Correspondence to [Sergiu P. Pașca](#) or [Hunter B. Fraser](#).

Ethics declarations

Competing interests

Stanford University holds a patent covering the generation of brain region-specific organoids (US patent serial no. 62/163,870;8) (S.P.P.).

Additional information

Peer review information *Nature* thanks Megan Munsie and the other, anonymous, reviewer(s) for their contribution to the peer review of this work. Peer reviewer reports are available.

Publisher's note Springer Nature remains neutral with regard to jurisdictional claims in published maps and institutional affiliations.

Extended data figures and tables

Extended Data Fig. 1 Isolation and characterization of hyiPS cells.

a, FACS of fused hybrid cells (representative plots for fusion of H20961 and C3649). Top, co-cultured cells with no PEG; bottom, co-cultured cells with PEG; from left, initial size selection, gating out doublets, gating out dead cells, sorting for red (human) and green (chimpanzee) double-positive population; FSC, forward scatter; SSC, side scatter; A, area; H, height. Pacific Blue measures DAPI, FITC measures green CMFDA (chimpanzee) and APC measures deep red (human). **b**, Representative karyotype for female (XX/XX) hybrid iPS cell lines. **c–e**, Immunostaining for the pluripotency markers NANOG and TRA-1-81 (**c**), OCT4 and SSEA4 (**d**), and SOX2 and TRA-1-60 (**e**). **f**, Results from PluriTest analysis of RNA-seq data from this study and from Ward et al.¹⁰ (see [Methods](#)); benchmarked thresholds are 20 or higher for pluripotency, 1.6 or lower for novelty (dotted lines). Scale bars, 200 μm (**c–e**).

Extended Data Fig. 2 Chromosomal instability and X-chromosome inactivation.

a, b, Plots showing aneuploidies on chromosome 20 indicating a gain of a chimpanzee chromosome (**a**) or a combined loss of the human short arm

and gain of the human long arm (**b**). Top, scatter plot of ASE ($\log_2(\text{human}/\text{chimpanzee})$) versus genomic location; middle, median ASE in a sliding window of 20 genes; bottom, P -values from a two-sided Wilcoxon rank-sum test comparing a sliding window of 20 genes to the background of the entire genome. **c**, Total (top) and allelic (bottom; human allele pink, chimpanzee allele blue) expression of *XIST* in RNA-seq samples; symbols indicate the sex of each iPS cell line; $n = 2$ technical replicates per cell line. **d**, Plots of ASE across the X chromosome (as in **a**, **b**). **e**, Total and allelic expression of *RNR1* (chrMT), as in **c**; $n = 2$ technical replicates per cell line.

Extended Data Fig. 3 RNA-seq of hyiPS cells.

a, Heat map of correlations (Pearson's) between RNA-seq samples from human (H1, H2 and H3), chimpanzee (C1, C2 and C3) and hybrid (Hy1-25, Hy1-29, Hy1-30, Hy2-9 and Hy2-16) iPS cells. **b**, Top, pipeline for analysis of RNA-seq data and separation of species-specific sequencing reads; bottom, pile-up of phased allelic reads from human, chimpanzee and hybrid RNA-seq samples for a representative gene. **c**, Representative scatter plot (from line Hy1-30) showing total gene expression when samples are mapped to the human genome (GRCh38, *x*-axis) versus the chimpanzee genome (PanTro5, *y*-axis); $n = 1$, out of 10 total hyiPS samples sequenced with similar results. **d**, Scatter plot of ASE in all hybrid samples when mapped to the human versus the chimpanzee genome; genes represented by the points in red are considered to have mapping bias and are eliminated from subsequent analyses; data merged from $n = 10$ samples from 5 hyiPS cell lines (2 replicates each).

Extended Data Fig. 4 Generation and characterization of hyCS.

a, b, Principal components plots for iPS and cortical spheroid (pilot study) RNA-seq samples based on total (**a**) or allelic (**b**) gene expression. **c**, Rates of success of three protocols used to derive hyCS (success is defined as at least one cortical spheroid from a given cell line surviving to 100 days of differentiation). n refers to the number of independent attempts to differentiate any of 3 hyiPS cell lines. **d**, Bright-field imaging of hCS and hyCS at day 7 or 8 of differentiation. The experiment was repeated across 3

independent differentiation experiments with 3 hyiPS and 1 hiPS cell lines with similar results. **e**, Bright-field images of Matrigel-embedded hCS and hyCS, as well as non-embedded hCS, at days 16 and 35 of differentiation. **f**, Heat map of correlations (Pearson's) between bulk RNA-seq samples for hyCS. **g**, Principal components plot for iPS and hyCS (full dataset) RNA-seq samples based on allelic gene expression **h**, Heat map coloured by the percentage of human reads in each single cell, stratified by chromosome; rows are ordered by hybrid cell line; top bar shows read depth of each chromosome across all cells; bottom left, colour key and histogram for heat map values; bottom middle, scatter plot of total read depth versus variance per chromosome, wherein fewer reads results in higher variance; bottom right, histogram showing the percentage of human reads in each cell, genome-wide. **i, j**, Histogram of the percentage of human reads in each cell for aneuploid chromosomes 18 (**i**) and 20 (**j**), stratified by cell line. Scale bars, 1 mm (**d, e**).

Extended Data Fig. 5 Single-cell gene profiling of hyCS.

a, UMAP clustering of all cells ($n = 706$); clusters are identified by colour and labelled by letter (A, astroglia; P, cycling progenitors; N1, glutamatergic neurons; N2, GABAergic neurons; M1, mesenchyme cluster 1; M2, mesenchyme cluster 2; E, epithelial cells). **b**, Proportion of cells from each hybrid cell line in each single cell cluster (from **a**). **c**, Dot plot for expression of marker genes for each cluster in **a**; size corresponds to the percentage of cells in each cluster that express each gene. **d**, UMAP coloured by expression of mesenchymal and epithelial marker genes. **e**, Scatter plot of normalized gene expression between embedded (y-axis) and non-embedded (x-axis) hybrid (line Hy1-29) cortical spheroids at day 50 of differentiation; points in red and green indicate genes whose expression is induced by the addition of Matrigel (see [Methods](#)). **f**, t-SNE of all single cells from this study aggregated with cells from non-embedded spheroids in Sloan et al.¹⁵, coloured by study. **g**, t-SNE from **f**, coloured by expression of cell-type marker genes. **h**, UMAP from **a**, coloured according to which cells were defined as neural and used for further analysis in Fig. [2](#). **i**, Histograms of per-gene ASE, where ASE is defined as the ratio of all human reads across cells of a given cell type to all chimpanzee reads in those cells.

Extended Data Fig. 6 Generation of hCS and cCS and RNA-seq.

a, b, Representative bright-field images of three cortical spheroids per line for three human (**a**) and three chimpanzee (**b**) cell lines at day 166. **c**, Immunostaining of hCS and cCS for SOX9, PAX6 and CTIP2. At each time point, a maximum of 2 spheroids were fixed for immunostaining across 3 hiPS and 3 ciPS cell lines with 4 independent differentiation experiments per cell line. **d, e**, Heat map of Pearson's correlations between bulk RNA-seq samples for hCS (**d**) and cCS (**e**). Scale bars, 1 mm (**a, b**) and 50 μ m (**c**).

Extended Data Fig. 7 RNA-seq and cell-type deconvolution in cortical spheroids.

a, b, Principal components plots for RNA-seq samples based on total gene expression of parent and hybrid samples. **c, e, g**, Per-sample estimated cell-type proportions in hyCS (**c**), hCS (**e**) and cCS (**g**) (see [Methods](#)). **d, f, h**, Normalized expression across time of cell-type-specific marker genes in hyCS (**d**), hCS (**f**) and cCS (**h**).

Extended Data Fig. 8 Weighted gene co-expression network analysis.

a, Dendrogram of all genes used in WGCNA; genes in the same colour block belong to the same co-expressed module. **b**, Eigengene values for genes in the blue, brown and red modules over time in hCS and cCS; chimpanzee blue, human red; in order of time points, $n = 6, 6, 6, 6, 6, 6$ and 5 hCS and $n = 6, 6, 6, 6, 5, 5$ and 5 cCS samples from 3 human and 3 chimpanzee iPS cell lines (1–2 replicates per cell line). **c**, Expression of module genes (eigengene, see [Methods](#)) in single-cell data; cell clusters are defined in Extended Data Fig. [5a](#). **d**, Allelic eigengene values for genes in these modules over time in hyCS (see [Methods](#)); chimpanzee blue, human red; in order of time points, $n = 7, 9, 7$ and 2 hyCS from 3 hyiPS cell lines (2–3 replicates per cell line). **e**, Single-cell gene expression of *PMP2*. **f**, Expression of *PMP2* in parental bulk time course; chimpanzee blue, human

red; n as in **b**. **g**, Allelic expression of *PMP2* in hybrid bulk time course; chimpanzee allele blue, human allele red; n as in **d**. Box plots in **b**, **d**, **f**, **g**: the centre line shows median, box limits represent upper and lower quartiles and whiskers extend to $1.5 \times$ the interquartile range.

Extended Data Fig. 9 Summary of ASE genes.

a–d, Overlap in genes with significant ASE between hyCS at days 50 versus 100 (**a**), hyCS at days 100 versus 150 (**b**), hyiPS cells versus hyCS at day 150 (**c**), and differential expression between hCS and cCS at day 150 versus ASE in hyCS at day 150 (**d**). **e**, Scatter plot showing differences in gene expression between parental lines (y -axis) versus between alleles in the hybrid (x -axis) at day 150; data are from bulk RNA-seq of 6 human, 5 chimpanzee and 7 hybrid cortical spheroid samples, collected across 3 human, 3 chimpanzee and 3 hybrid iPS cell lines. **f**, Overlap between ASE genes and SFARI genes. **g**, ASE in SFARI genes from the overlapping genes in **f**. **h**, **i**, Allelic expression over time in *GRIN2A* (**h**) and *SCN1A* (**i**); human allele pink, chimpanzee allele blue; in order of time points $n = 7, 9, 7$ and 2 hyCS samples (1–2 spheroids per sample) from 3 independent differentiations of 3 hyiPS cell lines. **j**, Filtering pipeline for prioritizing candidate genes. **k**, Scatter plot of hybrid ASE (x -axis) and parental differential expression (y -axis) for top candidate genes at day 150; $n = 7$ hyCS, 6 hCS and 5 cCS samples (1–3 spheroids per sample) derived from 3 iPS cell lines per species and 2 independent differentiations per hiPS and ciPS cell line, $n = 3$ independent differentiations per hyiPS cell line. Box plots in **h**, **i**: the centre line shows median, box limits represent upper and lower quartiles and whiskers extend to $1.5 \times$ the interquartile range.

Extended Data Fig. 10 Validation of SSTR2.

a, Expression of *SSTR2* in parental bulk time course; chimpanzee blue, human red; in order of time points, $n = 6, 6, 6, 6, 6, 6$ and 5 hCS and $n = 6, 6, 6, 5, 5$ and 5 cCS samples from 3 human and 3 chimpanzee iPS cell lines (1–2 replicates per cell line). **b**, Expression of *SSTR2* across cortical sections in adult primate brain tissue (data from He et al.³⁸); dotted lines indicate approximate boundaries of cortical layers; WM, white matter. **c**, Immunostaining for MAP2 (neuronal) and *SSTR2* protein in dissociated

hCS (H20682) and cCS (C3649) at day 225–250; right panels show SSTR2 only; 10 images were taken per sample and quantified. **d**, Quantification of fluorescence intensity (arbitrary units) of MAP2 for the images in **c**. $n = 13$ cells for hCS, 14 cells for cCS; *** $P < 0.0001$, two-tailed Mann–Whitney test. **e**, Quantification of fluorescence intensity (arbitrary units) of SSTR2 relative to MAP2 for the images in **c**; $n = 13$ cells for hCS, 14 cells for cCS; *** $P < 0.0001$, two-tailed Mann–Whitney test. **f**, Additional immunostaining for TUBB3 (neuronal) and SSTR2 in dissociated hCS (H20682) and cCS (C3649) at day 225–250; 10 images were taken per sample and quantified. **g**, Immunostaining for MAP2 and SSTR2 in whole hCS (H20961) and cCS (C3651) at day 160; imaging was reproduced across 3 human and 2 chimpanzee cell lines from 1 differentiation experiment with $n = 3, 2, 3, 2$ and 3 images for lines H21792, H20682, H20961, C3649 and C3651, respectively. **h**, Representative still frame images of hCS (H20682)- and cCS (C3649)-derived neurons infected with AAV-DJ-hSyn1-eYFP; images are taken from one of the samples in Fig. [4g–i](#); the experiment was reproduced across 2 human and 1 chimpanzee cell lines. **i**, Representative still frame images of hCS (H20682) infected with the viral vector co-encoding stable red fluorophore mRuby2 and genetically encoded calcium indicator GCaMP6s; images are taken from one of the samples in Fig. [4j–l](#); the experiment was reproduced across 3 human and 3 chimpanzee cell lines. Box plots in **a**, **d**, **e**: the centre line shows median, box limits represent upper and lower quartiles and whiskers extend to $1.5 \times$ the interquartile range.; dotted lines connect average values (**a**). Scale bars, 50 μm (**f**), 10 μm (**c**, **g**), 60 μm (**h**), 30 μm (**i**).

Supplementary information

Supplementary Tables

This file contains Supplementary Tables 1–14.

Reporting Summary

Peer Review File

Rights and permissions

[Reprints and Permissions](#)

About this article



Cite this article

Agoglia, R.M., Sun, D., Birey, F. *et al.* Primate cell fusion disentangles gene regulatory divergence in neurodevelopment. *Nature* **592**, 421–427 (2021). <https://doi.org/10.1038/s41586-021-03343-3>

[Download citation](#)

- Received: 26 February 2020
- Accepted: 08 February 2021
- Published: 17 March 2021
- Issue Date: 15 April 2021
- DOI: <https://doi.org/10.1038/s41586-021-03343-3>

Comments

By submitting a comment you agree to abide by our [Terms](#) and [Community Guidelines](#). If you find something abusive or that does not comply with our terms or guidelines please flag it as inappropriate.

[Access through your institution](#)

[Change institution](#)

Buy or subscribe

This article was downloaded by **calibre** from <https://www.nature.com/articles/s41586-021-03343-3>

| [Section menu](#) | [Main menu](#) |

- Article
- [Published: 31 March 2021](#)

Corticosterone inhibits GAS6 to govern hair follicle stem-cell quiescence

- [Sekyu Choi](#) ORCID: orcid.org/0000-0003-2928-0942^{1,2},
- [Bing Zhang](#) ORCID: orcid.org/0000-0003-2356-8849^{1,2} nAff13,
- [Sai Ma](#) ORCID: orcid.org/0000-0002-9785-7929^{1,3,4},
- [Meryem Gonzalez-Celeiro](#)^{1,2},
- [Daniel Stein](#)^{1,2},
- [Xin Jin](#) ORCID: orcid.org/0000-0003-2344-992X^{1,2,4},
- [Seung Tea Kim](#) ORCID: orcid.org/0000-0002-1004-9292^{1,2},
- [Yuan-Lin Kang](#)^{1,2},
- [Antoine Besnard](#)^{2,5,6} nAff14,
- [Amelie Rezza](#)^{7,8} nAff15,
- [Laura Grisanti](#)^{7,8},
- [Jason D. Buenrostro](#)^{1,2,4},
- [Michael Rendl](#) ORCID: orcid.org/0000-0001-6326-620X^{7,8,9},
- [Matthias Nahrendorf](#) ORCID: orcid.org/0000-0002-4021-1887^{10,11,12},
- [Amar Sahay](#)^{2,4,5,6} &
- [Ya-Chieh Hsu](#) ORCID: orcid.org/0000-0002-0178-7373^{1,2}

[Nature](#) volume 592, pages428–432(2021) [Cite this article](#)

- 12k Accesses
- 1 Citations
- 583 Altmetric

- [Metrics details](#)

Subjects

- [Quiescence](#)
- [Skin stem cells](#)
- [Stem-cell niche](#)

Abstract

Chronic, sustained exposure to stressors can profoundly affect tissue homeostasis, although the mechanisms by which these changes occur are largely unknown. Here we report that the stress hormone corticosterone—which is derived from the adrenal gland and is the rodent equivalent of cortisol in humans—regulates hair follicle stem cell (HFSC) quiescence and hair growth in mice. In the absence of systemic corticosterone, HFSCs enter substantially more rounds of the regeneration cycle throughout life.

Conversely, under chronic stress, increased levels of corticosterone prolong HFSC quiescence and maintain hair follicles in an extended resting phase. Mechanistically, corticosterone acts on the dermal papillae to suppress the expression of *Gas6*, a gene that encodes the secreted factor growth arrest specific 6. Restoring *Gas6* expression overcomes the stress-induced inhibition of HFSC activation and hair growth. Our work identifies corticosterone as a systemic inhibitor of HFSC activity through its effect on the niche, and demonstrates that the removal of such inhibition drives HFSCs into frequent regeneration cycles, with no observable defects in the long-term.

[Access through your institution](#)

[Change institution](#)

[Buy or subscribe](#)

Access options

Subscribe to Journal

Get full journal access for 1 year

\$199.00

only \$3.90 per issue

[Subscribe](#)

All prices are NET prices.

VAT will be added later in the checkout.

Tax calculation will be finalised during checkout.

Rent or Buy article

Get time limited or full article access on ReadCube.

from \$8.99

[Rent or Buy](#)

All prices are NET prices.

Additional access options:

- [Log in](#)
- [Access through your institution](#)
- [Learn about institutional subscriptions](#)

Fig. 1: Removal of adrenal glands activates HFSCs.

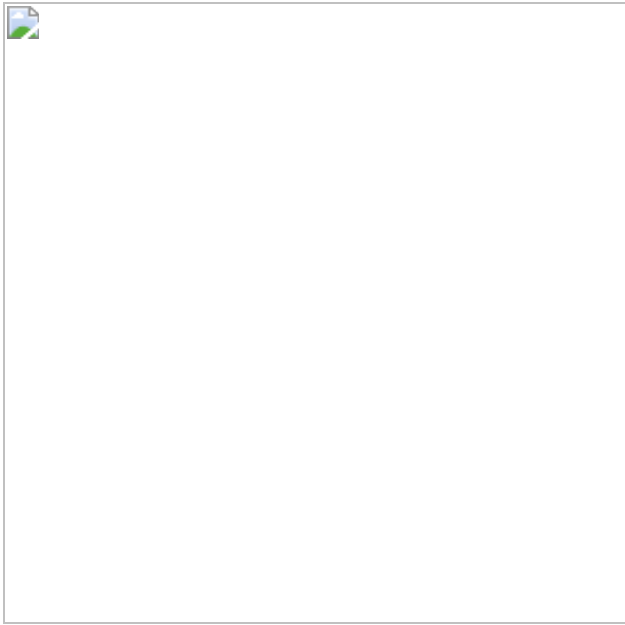


Fig. 2: Corticosterone derived from the adrenal gland regulates HFSC quiescence.

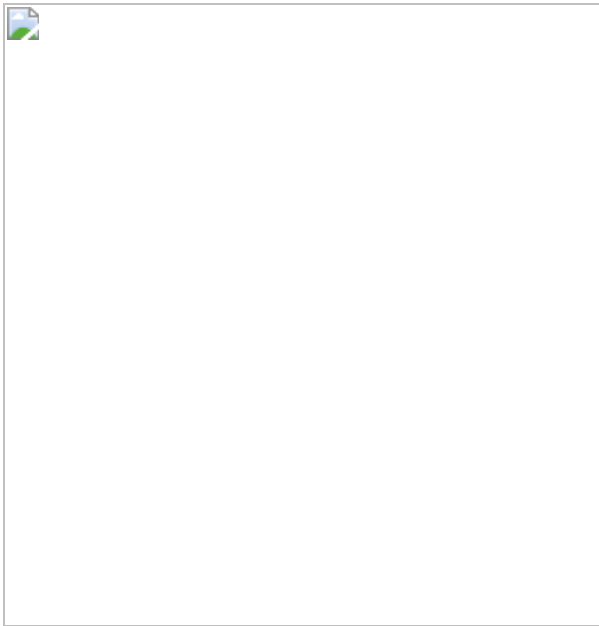


Fig. 3: Corticosterone acts on the DP to regulate HFSC quiescence.

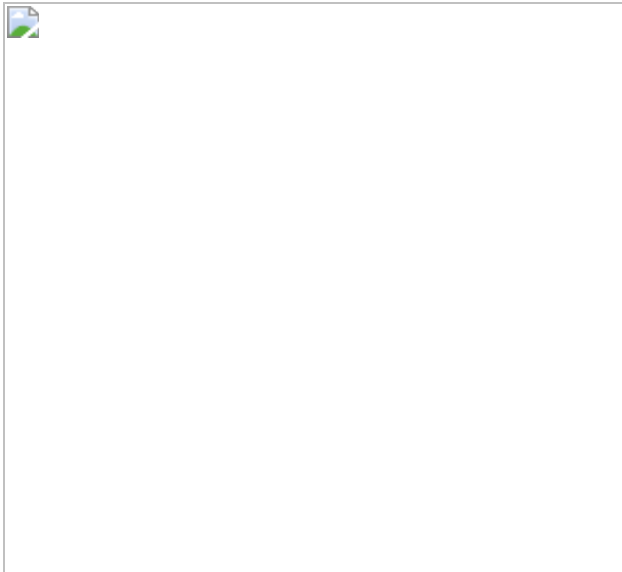
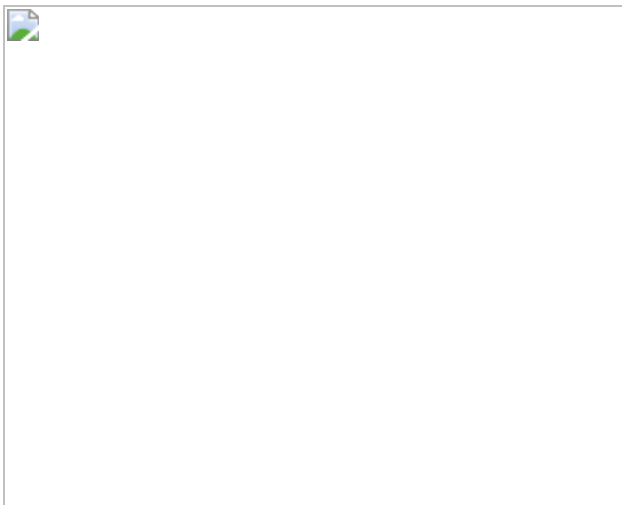


Fig. 4: *Gas6* overexpression counteracts the inhibitory effect of corticosterone.



Data availability

The sequencing data that support the findings of this study have been deposited in the Gene Expression Omnibus (GEO) with the accession code [GSE135705](#). The DAVID web-accessible tool (v.6.8) is available at <https://david.ncifcrf.gov/>. MetazSecKB web-accessible tool is available at proteomics.yzu.edu/secretomes/animal/. [Source data](#) are provided with this paper.

References

1. 1.

Shwartz, Y. et al. Cell types promoting goosebumps form a niche to regulate hair follicle stem cells. *Cell* **182**, 578–593.e19 (2020).

[CAS](#) [Google Scholar](#)

2. 2.

Lay, K., Kume, T. & Fuchs, E. FOXC1 maintains the hair follicle stem cell niche and governs stem cell quiescence to preserve long-term tissue-regenerating potential. *Proc. Natl Acad. Sci. USA* **113**, E1506–E1515 (2016).

[ADS](#) [CAS](#) [Google Scholar](#)

3. 3.

Wang, L., Siegenthaler, J. A., Dowell, R. D. & Yi, R. Foxc1 reinforces quiescence in self-renewing hair follicle stem cells. *Science* **351**, 613–617 (2016).

[ADS](#) [CAS](#) [PubMed](#) [PubMed Central](#) [Google Scholar](#)

4. 4.

Plikus, M. V. et al. Cyclic dermal BMP signalling regulates stem cell activation during hair regeneration. *Nature* **451**, 340–344 (2008).

[ADS](#) [CAS](#) [PubMed](#) [PubMed Central](#) [Google Scholar](#)

5. 5.

Müller-Röver, S. et al. A comprehensive guide for the accurate classification of murine hair follicles in distinct hair cycle stages. *J. Invest. Dermatol.* **117**, 3–15 (2001).

[Google Scholar](#)

6. 6.

Greco, V. et al. A two-step mechanism for stem cell activation during hair regeneration. *Cell Stem Cell* **4**, 155–169 (2009).

[CAS](#) [PubMed](#) [PubMed Central](#) [Google Scholar](#)

7. 7.

Hsu, Y. C., Li, L. & Fuchs, E. Transit-amplifying cells orchestrate stem cell activity and tissue regeneration. *Cell* **157**, 935–949 (2014).

[CAS](#) [PubMed](#) [PubMed Central](#) [Google Scholar](#)

8. 8.

Sawaya, M. E. & Hordinsky, M. K. Glucocorticoid regulation of hair growth in alopecia areata. *J. Invest. Dermatol.* **104**, 30S (1995).

[CAS](#) [Google Scholar](#)

9. 9.

Stenn, K. S., Paus, R., Dutton, T. & Sarba, B. Glucocorticoid effect on hair growth initiation: a reconsideration. *Skin Pharmacol.* **6**, 125–134 (1993).

[CAS](#) [Google Scholar](#)

10. 10.

Pérez, P. et al. Altered skin development and impaired proliferative and inflammatory responses in transgenic mice overexpressing the glucocorticoid receptor. *FASEB J.* **15**, 2030–2032 (2001).

[Google Scholar](#)

11. 11.

Rose, J. & Sterner, M. The role of the adrenal glands in regulating onset of winter fur growth in mink (*Mustela vison*). *J. Exp. Zool.* **262**, 469–473 (1992).

[CAS](#) [Google Scholar](#)

12. 12.

Butcher, E. O. Hair growth in adrenalectomized, and, adrenalectomized thyroxin-treated rats. *Am. J. Physiol.* **120**, 427–434 (1937).

[CAS](#) [Google Scholar](#)

13. 13.

Whiteley, H. J. The effect of adrenalectomy and adrenocortical hormones on the hair growth cycle in the rabbit and rat. *J. Endocrinol.* **17**, 167–176 (1958).

[CAS](#) [Google Scholar](#)

14. 14.

Hsu, Y. C., Pasolli, H. A. & Fuchs, E. Dynamics between stem cells, niche, and progeny in the hair follicle. *Cell* **144**, 92–105 (2011).

[CAS](#) [PubMed](#) [PubMed Central](#) [Google Scholar](#)

15. 15.

Rompolas, P., Mesa, K. R. & Greco, V. Spatial organization within a niche as a determinant of stem-cell fate. *Nature* **502**, 513–518 (2013).

[ADS](#) [CAS](#) [PubMed](#) [PubMed Central](#) [Google Scholar](#)

16. 16.

Chen, C. C. et al. Regenerative hair waves in aging mice and extra-follicular modulators follistatin, Dkk1, and Sfrp4. *J. Invest. Dermatol.* **134**, 2086–2096 (2014).

[CAS](#) [PubMed](#) [PubMed Central](#) [Google Scholar](#)

17. 17.

Keyes, B. E. et al. *Nfatc1* orchestrates aging in hair follicle stem cells. *Proc. Natl Acad. Sci. USA* **110**, E4950–E4959 (2013).

[CAS](#) [Google Scholar](#)

18. 18.

Walczak, E. M. & Hammer, G. D. Regulation of the adrenocortical stem cell niche: implications for disease. *Nat. Rev. Endocrinol.* **11**, 14–28 (2015).

[CAS](#) [Google Scholar](#)

19. 19.

Besnard, A. et al. Targeting Kruppel-like factor 9 in excitatory neurons protects against chronic stress-induced impairments in dendritic spines and fear responses. *Cell Rep.* **23**, 3183–3196 (2018).

[CAS](#) [PubMed](#) [PubMed Central](#) [Google Scholar](#)

20. 20.

Heidt, T. et al. Chronic variable stress activates hematopoietic stem cells. *Nat. Med.* **20**, 754–758 (2014).

[CAS](#) [PubMed](#) [PubMed Central](#) [Google Scholar](#)

21. 21.

Tye, K. M. et al. Dopamine neurons modulate neural encoding and expression of depression-related behaviour. *Nature* **493**, 537–541 (2013).

[ADS](#) [CAS](#) [Google Scholar](#)

22. 22.

Enshell-Seijffers, D., Lindon, C., Kashiwagi, M. & Morgan, B. A. β -catenin activity in the dermal papilla regulates morphogenesis and regeneration of hair. *Dev. Cell* **18**, 633–642 (2010).

[CAS](#) [PubMed](#) [PubMed Central](#) [Google Scholar](#)

23. 23.

Festa, E. et al. Adipocyte lineage cells contribute to the skin stem cell niche to drive hair cycling. *Cell* **146**, 761–771 (2011).

[CAS](#) [PubMed](#) [PubMed Central](#) [Google Scholar](#)

24. 24.

Zhang, B. et al. Hair follicles' transit-amplifying cells govern concurrent dermal adipocyte production through Sonic Hedgehog. *Genes Dev.* **30**, 2325–2338 (2016).

[CAS](#) [PubMed](#) [PubMed Central](#) [Google Scholar](#)

25. 25.

Clavel, C. et al. *Sox2* in the dermal papilla niche controls hair growth by fine-tuning BMP signaling in differentiating hair shaft progenitors. *Dev. Cell* **23**, 981–994 (2012).

[CAS](#) [PubMed](#) [PubMed Central](#) [Google Scholar](#)

26. 26.

Driskell, R. R., Giangreco, A., Jensen, K. B., Mulder, K. W. & Watt, F. M. Sox2-positive dermal papilla cells specify hair follicle type in mammalian epidermis. *Development* **136**, 2815–2823 (2009).

[CAS](#) [PubMed](#) [PubMed Central](#) [Google Scholar](#)

27. 27.

Horsley, V., Aliprantis, A. O., Polak, L., Glimcher, L. H. & Fuchs, E. NFATc1 balances quiescence and proliferation of skin stem cells. *Cell* **132**, 299–310 (2008).

[CAS](#) [PubMed](#) [PubMed Central](#) [Google Scholar](#)

28. 28.

Rhee, H., Polak, L. & Fuchs, E. Lhx2 maintains stem cell character in hair follicles. *Science* **312**, 1946–1949 (2006).

[ADS](#) [CAS](#) [PubMed](#) [PubMed Central](#) [Google Scholar](#)

29. 29.

Leishman, E. et al. Foxp1 maintains hair follicle stem cell quiescence through regulation of Fgf18. *Development* **140**, 3809–3818 (2013).

[CAS](#) [PubMed](#) [PubMed Central](#) [Google Scholar](#)

30. 30.

Choi, Y. S. et al. Distinct functions for Wnt/β-catenin in hair follicle stem cell proliferation and survival and interfollicular epidermal homeostasis. *Cell Stem Cell* **13**, 720–733 (2013).

[CAS](#) [PubMed](#) [PubMed Central](#) [Google Scholar](#)

31. 31.

Rothlin, C. V., Carrera-Silva, E. A., Bosurgi, L. & Ghosh, S. TAM receptor signaling in immune homeostasis. *Annu. Rev. Immunol.* **33**, 355–391 (2015).

[CAS](#) [PubMed](#) [PubMed Central](#) [Google Scholar](#)

32. 32.

Wang, Y. et al. Axl-altered microRNAs regulate tumorigenicity and gefitinib resistance in lung cancer. *Cell Death Dis.* **5**, e1227 (2014).

[CAS](#) [PubMed](#) [PubMed Central](#) [Google Scholar](#)

33. 33.

Asiedu, M. K. et al. AXL induces epithelial-to-mesenchymal transition and regulates the function of breast cancer stem cells. *Oncogene* **33**, 1316–1324 (2014).

[CAS](#) [Google Scholar](#)

34. 34.

Balaji, K. et al. AXL inhibition suppresses the DNA damage response and sensitizes cells to PARP inhibition in multiple cancers. *Mol. Cancer Res.* **15**, 45–58 (2017).

[CAS](#) [Google Scholar](#)

35. 35.

Aoki, E., Shibasaki, T. & Kawana, S. Intermittent foot shock stress prolongs the telogen stage in the hair cycle of mice. *Exp. Dermatol.* **12**, 371–377 (2003).

[CAS](#) [Google Scholar](#)

36. 36.

Zhang, B. et al. Hyperactivation of sympathetic nerves drives depletion of melanocyte stem cells. *Nature* **577**, 676–681 (2020).

[ADS](#) [CAS](#) [PubMed](#) [PubMed Central](#) [Google Scholar](#)

37. 37.

Arck, P. C. et al. Stress inhibits hair growth in mice by induction of premature catagen development and deleterious perifollicular inflammatory events via neuropeptide substance P-dependent pathways. *Am. J. Pathol.* **162**, 803–814 (2003).

[CAS](#) [PubMed](#) [PubMed Central](#) [Google Scholar](#)

38. 38.

Mittelstadt, P. R., Monteiro, J. P. & Ashwell, J. D. Thymocyte responsiveness to endogenous glucocorticoids is required for immunological fitness. *J. Clin. Invest.* **122**, 2384–2394 (2012).

[CAS](#) [PubMed](#) [PubMed Central](#) [Google Scholar](#)

39. 39.

Morris, R. J. et al. Capturing and profiling adult hair follicle stem cells. *Nat. Biotechnol.* **22**, 411–417 (2004).

[CAS](#) [Google Scholar](#)

40. 40.

Kang, S. H., Fukaya, M., Yang, J. K., Rothstein, J. D. & Bergles, D. E. NG2⁺ CNS glial progenitors remain committed to the oligodendrocyte lineage in postnatal life and following neurodegeneration. *Neuron* **68**, 668–681 (2010).

[CAS](#) [PubMed](#) [PubMed Central](#) [Google Scholar](#)

41. 41.

Arnold, K. et al. Sox2⁺ adult stem and progenitor cells are important for tissue regeneration and survival of mice. *Cell Stem Cell* **9**, 317–329 (2011).

[CAS](#) [PubMed](#) [PubMed Central](#) [Google Scholar](#)

42. 42.

Srinivas, S. et al. Cre reporter strains produced by targeted insertion of *EYFP* and *ECFP* into the *ROSA26* locus. *BMC Dev. Biol.* **1**, 4 (2001).

[CAS](#) [PubMed](#) [PubMed Central](#) [Google Scholar](#)

43. 43.

Holland, S. J. et al. R428, a selective small molecule inhibitor of Axl kinase, blocks tumor spread and prolongs survival in models of metastatic breast cancer. *Cancer Res.* **70**, 1544–1554 (2010).

[CAS](#) [Google Scholar](#)

44. 44.

Goldstein, J. M. et al. In situ modification of tissue stem and progenitor cell genomes. *Cell Rep.* **27**, 1254–1264.e7 (2019).

[CAS](#) [PubMed](#) [PubMed Central](#) [Google Scholar](#)

45. 45.

Plikus, M. V. & Chuong, C. M. Complex hair cycle domain patterns and regenerative hair waves in living rodents. *J. Invest. Dermatol.* **128**, 1071–1080 (2008).

[CAS](#) [PubMed](#) [PubMed Central](#) [Google Scholar](#)

46. 46.

Rezza, A. et al. Signaling networks among stem cell precursors, transit-amplifying progenitors, and their niche in developing hair follicles. *Cell Rep.* **14**, 3001–3018 (2016).

[CAS](#) [PubMed](#) [PubMed Central](#) [Google Scholar](#)

47. 47.

Rendl, M., Lewis, L. & Fuchs, E. Molecular dissection of mesenchymal–epithelial interactions in the hair follicle. *PLoS Biol.* **3**, e331 (2005).

[PubMed](#) [PubMed Central](#) [Google Scholar](#)

48. 48.

Joost, S. et al. The molecular anatomy of mouse skin during hair growth and rest. *Cell Stem Cell* **26**, 441–457.e7 (2020).

[CAS](#) [Google Scholar](#)

49. 49.

Patro, R., Duggal, G., Love, M. I., Irizarry, R. A. & Kingsford, C. Salmon provides fast and bias-aware quantification of transcript expression. *Nat. Methods* **14**, 417–419 (2017).

[CAS](#) [PubMed](#) [PubMed Central](#) [Google Scholar](#)

50. 50.

Dobin, A. et al. STAR: ultrafast universal RNA-seq aligner. *Bioinformatics* **29**, 15–21 (2013).

[CAS](#) [PubMed](#) [PubMed Central](#) [Google Scholar](#)

51. 51.

Liao, Y., Smyth, G. K. & Shi, W. featureCounts: an efficient general purpose program for assigning sequence reads to genomic features. *Bioinformatics* **30**, 923–930 (2014).

[CAS](#) [PubMed](#) [Google Scholar](#)

52. 52.

Love, M. I., Huber, W. & Anders, S. Moderated estimation of fold change and dispersion for RNA-seq data with DESeq2. *Genome Biol.* **15**, 550 (2014).

[PubMed](#) [PubMed Central](#) [Google Scholar](#)

53. 53.

Huang, D. W., Sherman, B. T. & Lempicki, R. A. Bioinformatics enrichment tools: paths toward the comprehensive functional analysis of large gene lists. *Nucleic Acids Res.* **37**, 1–13 (2009).

[Google Scholar](#)

54. 54.

Huang, D. W., Sherman, B. T. & Lempicki, R. A. Systematic and integrative analysis of large gene lists using DAVID bioinformatics resources. *Nat. Protoc.* **4**, 44–57 (2009).

[CAS](#) [Google Scholar](#)

55. 55.

Käll, L., Krogh, A. & Sonnhammer, E. L. A combined transmembrane topology and signal peptide prediction method. *J. Mol. Biol.* **338**, 1027–1036 (2004).

[PubMed](#) [Google Scholar](#)

56. 56.

Meinken, J., Walker, G., Cooper, C. R. & Min, X. J. MetazSecKB: the human and animal secretome and subcellular proteome knowledgebase. *Database (Oxford)* **2015**, bav077 (2015).

[Google Scholar](#)

57. 57.

Nowak, J. A. & Fuchs, E. Isolation and culture of epithelial stem cells. *Methods Mol. Biol.* **482**, 215–232 (2009).

[CAS](#) [PubMed](#) [PubMed Central](#) [Google Scholar](#)

[Download references](#)

Acknowledgements

We thank many colleagues who donated mice to The Jackson Laboratory; A. Regev, Y. Fong, and members of the Hsu laboratory—in particular Y. Shwartz—for discussions and comments on the manuscript, and O. Chung for technical assistance; and HCBI, HSCRB-HSCI FACS core, HSCRB Histology core, Small Molecule Mass Spectrometry Facility, Office of Animal Resources, and the Bauer Core Sequencing Facility at Harvard University for technical support. This work was supported in part by the New York Stem Cell Foundation (Y.-C.H.); the Smith Family Foundation Odyssey Award (Y.-C.H.); the Pew Charitable Trusts (Y.-C.H.); the Harvard Stem Cell Institute (Y.-C.H. and A.S.); a Harvard HMS Dean’s Award (Y.-C.H.); the American Cancer Society (Y.-C.H.); a James and Audrey Foster MGH Research Scholar Award (A.S.); a NARSAD Young Investigator Award (A.B.); MGH ECOR Fund for Medical Discovery Postdoctoral Fellowship Awards (A.B.); the New York State Department of Health (NYSTEM-C029574, NYSTEM-C32561GG to M.R.); NINDS (R56NS117529 to A.S.) and NIH (R01-AR070825 to Y.-C.H; R35-HL139598 to M.N.; R01MH104175, R01AG048908 and 1R01MH111729 to A.S.; R01AR071047 and R01AR063151 to M.R.). Y.-C.H. is a New York Stem Cell Foundation – Robertson Investigator and a Pew Scholar. J.D.B. and S.M. acknowledge support from the Broad Institute Fellows

Program. X.J. is a Junior Fellow of, and is supported by, the Society of Fellows of Harvard University.

Author information

Author notes

1. Bing Zhang

Present address: School of Life Science, Westlake University, Hangzhou, China

2. Antoine Besnard

Present address: CNRS, Institut de Génomique Fonctionnelle, Montpellier, France

3. Amelie Rezza

Present address: genOway, Lyon, France

Affiliations

1. Department of Stem Cell and Regenerative Biology, Harvard University, Cambridge, MA, USA

Sekyu Choi, Bing Zhang, Sai Ma, Meryem Gonzalez-Celeiro, Daniel Stein, Xin Jin, Seung Tea Kim, Yuan-Lin Kang, Jason D. Buenrostro & Ya-Chieh Hsu

2. Harvard Stem Cell Institute, Cambridge, MA, USA

Sekyu Choi, Bing Zhang, Meryem Gonzalez-Celeiro, Daniel Stein, Xin Jin, Seung Tea Kim, Yuan-Lin Kang, Antoine Besnard, Jason D. Buenrostro, Amar Sahay & Ya-Chieh Hsu

3. Department of Biology and Koch Institute, MIT, Cambridge, MA, USA

Sai Ma

4. Broad Institute of Harvard and MIT, Cambridge, MA, USA

Sai Ma, Xin Jin, Jason D. Buenrostro & Amar Sahay

5. Center for Regenerative Medicine, Massachusetts General Hospital, Boston, MA, USA

Antoine Besnard & Amar Sahay

6. Department of Psychiatry, Massachusetts General Hospital, Harvard Medical School, Boston, MA, USA

Antoine Besnard & Amar Sahay

7. Black Family Stem Cell Institute, Icahn School of Medicine at Mount Sinai, New York, NY, USA

Amelie Rezza, Laura Grisanti & Michael Rendl

8. Department of Cell, Developmental and Regenerative Biology, Icahn School of Medicine at Mount Sinai, New York, NY, USA

Amelie Rezza, Laura Grisanti & Michael Rendl

9. Department of Dermatology, Icahn School of Medicine at Mount Sinai, New York, NY, USA

Michael Rendl

10. Center for Systems Biology and Department of Radiology, Massachusetts General Hospital Research Institute, Harvard Medical School, Boston, MA, USA

Matthias Nahrendorf

11. Cardiovascular Research Center, Massachusetts General Hospital, Harvard Medical School, Boston, MA, USA

Matthias Nahrendorf

12. Department of Internal Medicine I, University Hospital Würzburg,
Würzburg, Germany

Matthias Nahrendorf

Authors

1. Sekyu Choi

[View author publications](#)

You can also search for this author in [PubMed](#) [Google Scholar](#)

2. Bing Zhang

[View author publications](#)

You can also search for this author in [PubMed](#) [Google Scholar](#)

3. Sai Ma

[View author publications](#)

You can also search for this author in [PubMed](#) [Google Scholar](#)

4. Meryem Gonzalez-Celeiro

[View author publications](#)

You can also search for this author in [PubMed](#) [Google Scholar](#)

5. Daniel Stein

[View author publications](#)

You can also search for this author in [PubMed](#) [Google Scholar](#)

6. Xin Jin

[View author publications](#)

You can also search for this author in [PubMed](#) [Google Scholar](#)

7. Seung Tea Kim

[View author publications](#)

You can also search for this author in [PubMed](#) [Google Scholar](#)

8. Yuan-Lin Kang

[View author publications](#)

You can also search for this author in [PubMed](#) [Google Scholar](#)

9. Antoine Besnard

[View author publications](#)

You can also search for this author in [PubMed](#) [Google Scholar](#)

10. Amelie Rezza

[View author publications](#)

You can also search for this author in [PubMed](#) [Google Scholar](#)

11. Laura Grisanti

[View author publications](#)

You can also search for this author in [PubMed](#) [Google Scholar](#)

12. Jason D. Buenrostro

[View author publications](#)

You can also search for this author in [PubMed](#) [Google Scholar](#)

13. Michael Rendl

[View author publications](#)

You can also search for this author in [PubMed](#) [Google Scholar](#)

14. Matthias Nahrendorf

[View author publications](#)

You can also search for this author in [PubMed](#) [Google Scholar](#)

15. Amar Sahay

[View author publications](#)

You can also search for this author in [PubMed](#) [Google Scholar](#)

16. Ya-Chieh Hsu

[View author publications](#)

You can also search for this author in [PubMed](#) [Google Scholar](#)

Contributions

Y.-C.H. and S.C. conceived the project. S.C. performed most of the experiments. B.Z. and S.M. performed bioinformatic analysis. M.G.-C., D.S. and S.T.K. performed experiments related to chronic unpredictable stress, corticosterone feeding and adrenalectomy. X.J. and Y.-L.K. generated RNA-seq libraries. A.R. and L.G. performed GR RT-qPCR for DP and DF samples. B.Z., J.D.B., M.R., M.N., A.S. and A.B. provided intellectual input. Y.-C.H. and S.C. wrote the manuscript, with discussion and feedback from all co-authors.

Corresponding author

Correspondence to [Ya-Chieh Hsu](#).

Ethics declarations

Competing interests

A patent application covering the methods and compositions for controlling hair growth has been filed by the President and Fellows of Harvard College, listing Y.-C.H. and S.C. as inventors. The other authors declare no competing interests related to this work.

Additional information

Peer review information *Nature* thanks Eduardo Leonardo, William Lowry, Rui Yi and the other, anonymous, reviewer(s) for their contribution to the peer review of this work.

Publisher's note Springer Nature remains neutral with regard to jurisdictional claims in published maps and institutional affiliations.

Extended data figures and tables

Extended Data Fig. 1 Hair cycle progression in ADX mice over time.

a, Hair cycle with immunohistochemical analyses (PCAD) in sham and ADX mice. **b**, Hair cycle progression in sham male and ADX male mice. **c**, Schematic depicting HFSCs in anagen and telogen. The upper ORS of anagen hair follicles contributes to the new bulge and hair germ (HG) of the following telogen hair follicles. See refs. [14,15](#) for details. **d**, The ORS length in the zigzag hairs of sham (P113) and ADX (P65) mice during late anagen. The brackets indicate the ORS length below the bulge. **e**, The hair shaft length of each hair subtype in sham and ADX mice after anagen. **f**, H&E staining at P65 of skin from sham and ADX mice. **g**, Immunohistochemical analyses (Sox9 and CD34) in telogen (Telo), late anagen (AnaV), and mid catagen (CatV) hair follicles. Yellow dashed lines, bulge; white dashed lines, HG (telo), hair follicle (AnaV, CatV); solid line, DP. **h**, Immunocolocalization (EdU and CD34) in infundibulum (IF), junctional zone (JZ), sebaceous gland (SG), mid ORS (ORSmid), lower ORS (ORSlow) and matrix (Mx) of late anagen (AnaVI) hair follicles. The dashed lines outline the hair follicle. **i**, Left, H&E staining in the late anagen skin of sham and ADX mice with quantification of the epidermal thickness (E). Right, immunocolocalization (EdU and DAPI) in interfollicular epidermis (IFE) and dermis. Dashed lines indicate the boundary between the epidermis and the dermis. **j**, Representative hair regrowth status of sham and ADX mice from P60 to P549. **k**, Duration of telogen in sham and ADX mice. **l**, H&E staining of skin from young sham, aged sham, and aged ADX mice with quantification of the number of hair follicles per mm. Yellow dashed lines, bulge; white dashed lines, HG, solid

lines, DP. Scale bars, 50 µm (**a**, **d**, **f–i**, **l**), 1 mm (**e**). Data are mean ± s.e.m. * $P < 0.05$, *** $P < 0.0001$, NS, not significant. For exact P values, see Source Data. For statistics, sample sizes and numbers of replications, see [Methods](#). [Source data](#)

[Extended Data Fig. 2 Corticosterone restores normal hair cycle progression in ADX mice.](#)

a, H&E staining of the skin of 21-month-old sham and ADX mice. **b**, Morphology of each hair subtype from the skin of 18-month-old sham and ADX mice. **c**, Left, immunohistochemical analyses (CD34 and PCAD) of telogen hair follicles in the skin of sham and ADX mice at 22 months old, showing normal hair follicle morphology and comparable stem-cell numbers. Middle, quantification of the number of bulge and hair germ cells per HF. Right, the percentage of HFSCs in epithelial fraction by FACS. **d**, Hormones from the adrenal gland and plasma levels of corticosterone in P45 sham and ADX mice. **e**, Plasma levels of noradrenaline and adrenaline measured by LC–MS/MS at P45 (10 days after surgery) in sham and ADX mice. **f**, Left, experimental design to test if supplying corticosterone rescues ADX phenotypes. Right, hair cycle progression of sham mice fed with vehicle (sham+veh) or ADX mice fed with corticosterone (ADX+CORT). **g**, Plasma corticosterone levels at P62 in C57BL/6 mice after a week's feeding with vehicle or corticosterone. **h**, Top, experimental design for 3 days of corticosterone feeding. Bottom, the percentage of hair regrowth of the back skin at P38. **i**, Hair cycle progression of C57BL/6 male mice fed with vehicle or corticosterone. Corticosterone feeding prolonged telogen as long as corticosterone was provided to the mice (both male and female). **j**, Body weight of C57BL/6 mice fed with vehicle or corticosterone from P83 to P118. **k**, Left, H&E staining in the skin of vehicle and corticosterone-fed mice. Middle and right, quantification of the thickness of dermis (middle) and dermal adipose layer (right). D, dermis; A, adipose layer. **l**, Immunohistochemical analysis (active caspase 3 (aCAS3) and PCAD) in vehicle- and corticosterone-fed mice. Dashed lines, epidermis and hair follicles. **m**, Left, experimental design to test the effect of corticosterone withdrawal. Right, hair cycle progression of C57BL/6 mice after completion of 3 weeks of vehicle or corticosterone feeding. Scale bars (**a**, **b**, **c**, **k**, **l**), 50 µm. Data are mean ± s.e.m. * $P < 0.05$, ** $P < 0.01$,

*** $P < 0.001$, **** $P < 0.0001$, NS, not significant. For exact P values, see Source Data. For statistics, sample sizes and numbers of replications, see [Methods](#). [Source data](#)

Extended Data Fig. 3 Removal of the adrenal glands in stressed or aged mice leads to hair follicle regeneration.

a, Plasma corticosterone levels at P62 in non-stressed control and stressed mice. **b, c**, H&E staining (**b**) and immunohistochemical analyses (active caspase3 (aCAS3) and PCAD) (**c**) in control and stressed mice. Dashed lines, epidermis and hair follicles. **d**, Stressed sham (sham+stress) and stressed ADX (ADX+stress) mice were monitored for hair coat recovery. Quantification shows the percentage of back skin that is covered by newly regenerated hairs. **e**, Plasma levels of corticosterone in young mice (P46, P77, and P98) and aged mice (P427 and P581). **f**, Sham and ADX operations were performed on aged mice (P521). The mice were shaved and monitored for hair coat recovery from P521 to P574. Scale bars (**b, c**), 50 μm . Data are mean \pm s.e.m. * $P < 0.05$, ** $P < 0.01$, **** $P < 0.0001$. For exact P values, see Source Data. For statistics, sample sizes and numbers of replications, see [Methods](#). [Source data](#)

Extended Data Fig. 4 GR depletion in different cell types in the skin.

a, Top, *K15-CrePGR* depletes GR efficiently in HFSCs. Bottom, immunohistochemical analysis (GR and CD140a) of telogen hair follicle in the skin of control and *K15-CrePGR;GR^{f/f}* mice. **b**, Hair cycle progression of control and *K15-CrePGR;GR^{f/f}* mice. **c**, Immunohistochemical analyses (GR and PCAD) of telogen hair follicles in the skin of control and *Pdgfra-CreER;GR^{f/f}* mice, showing that *Pdgfra-CreER* depletes GR efficiently in the dermal fibroblasts and DP. **d**, Immunocolocalization (EdU and CD34) in control and *Pdgfra-CreER;GR^{f/f}* hair follicles after tamoxifen administration. EdU incorporation reveals premature HFSC activation in the hair follicles of *Pdgfra-CreER;GR^{f/f}* mice. **e**, Comparison of EdU localization in bulge and upper ORS in late anagen (AnaV) of control (P124) and *Pdgfra-CreER;GR^{f/f}* (P73) mice. **f**, Representative hair

regeneration status of control and *Pdgfra-CreER;GR^{f/f}* mice from P73 to P205, with quantification of the number of hair cycles. **g**, Immunocolocalization (EdU and CD34) in infundibulum, junctional zone, sebaceous gland, mid ORS, lower ORS, and matrix of late anagen (AnaVI) hair follicles in control and *Pdgfra-CreER;GR^{f/f}* mice during late anagen with quantifications. **h**, Top, H&E staining in the late anagen skin of control and *Pdgfra-CreER;GR^{f/f}* mice, with quantification of the thickness of epidermis (E). Bottom, immunocolocalization (EdU and DAPI) in interfollicular epidermis and dermis in control and *Pdgfra-CreER;GR^{f/f}* mice. Scale bars (**a, c–e, g, h**), 50 µm. Yellow dashed lines, bulge (**a, c–e**); white dashed lines, hair germ (**a, c, d**), the rest of hair follicles (**e, g**), or the boundary between the epidermis and the dermis (**h**); solid white line, DP (**a, c, d**). Data are mean ± s.e.m. ** $P < 0.01$, *** $P < 0.001$, **** $P < 0.0001$, NS, not significant. For exact P values, see Source Data. For statistics, sample sizes and numbers of replications, see [Methods](#). [Source data](#)

Extended Data Fig. 5 Corticosterone acts on the DP.

a, RT-qPCR of *GR* from DP and DF. **b**, Immunohistochemical analyses (YFP and DAPI) of anagen skin from *Sox2-CreER;R26-lsl-YFP* mice. Left, the arrowhead indicates an anagen guard hair follicle with YFP⁺ DP cells. Right, quantification of the percentage of YFP⁺ and YFP⁻ DP in *Sox2-CreER;R26-lsl-YFP*. Only guard hair follicles have YFP⁺ DP. **c**, Immunohistochemical analyses (GR and DAPI) of skin from control and *Sox2-CreER;GR^{f/f}* mice. Dashed lines, epidermis and hair follicles; solid line, DP. The arrowhead indicates the DP of *Sox2-CreER;GR^{f/f}* guard hairs. **d**, Representative hair regeneration status of control and *Sox2-CreER;GR^{f/f}* mice from P45 to P160. Quantification shows the number of hair cycles for guard hairs and other hairs in control and *Sox2-CreER;GR^{f/f}* mice. **e**, Comparison of the hair bulb diameter in late anagen (AnaV) in the skin of control (P120) and *Sox2-CreER;GR^{f/f}* (P67) mice. Yellow lines indicate the hair bulb diameter. The arrowhead denotes minor hyper thickening of the *Sox2-CreER;GR^{f/f}* hair follicle around the ORS, probably because the dermis has not expanded to accommodate the extra proliferation from HFSCs. **f**, Immunocolocalization of phosphohistone H3 (pHH3) and CD34 in bulge and upper ORS, middle ORS, lower ORS and matrix of late anagen

(AnaV) guard hair follicles in control and *Sox2-CreER;GR^{f/f}* mice. The white arrowhead denotes a thickened region in a *Sox2-CreER;GR^{f/f}* hair follicle, probably due to excessive proliferation from HFSCs. Yellow dashed lines, bulge; white dashed lines, the rest of the hair follicle. **g**, Hair shaft length of guard hairs in control and *Sox2-CreER;GR^{f/f}* mice after anagen. Scale bars, 50 μ m (**b**, **c**, **e**, **f**), 1 mm (**d**, **g**). Data are mean \pm s.e.m. *** $P < 0.0001$, NS, not significant. For exact P values, see Source Data.

For statistics, sample sizes and numbers of replications, see [Methods](#).

[Source data](#)

[Extended Data Fig. 6 Differential gene expression in HFSCs of control, ADX and dermal GR-knockout mice.](#)

a, Sample clustering based on Pearson's correlation of transcriptomes in HFSCs from sham, ADX, and ADX+CORT as well as control and *Pdgfra-CreER;GR^{f/f}* mice. **b**, Principal component analysis (PCA) comparing the transcriptome of HFSCs from sham, ADX, ADX+CORT, control and *Pdgfra-CreER;GR^{f/f}* mice. **c**, Heat map of log₂-transformed fold change of gene expression of 121 common genes among ADX (versus sham), *Pdgfra-CreER;GR^{f/f}* (versus control), and ADX+CORT (versus ADX). Cell-cycle-related genes are noted in orange. **d**, Left, heat map of log₂-transformed fold change of gene expression of transcription factors (*Foxc1*, *Lhx2*, *Foxp1*, *Nfatc1*), key signalling factors (*Fgf18*), or downstream readout of key signalling factors (*Id1* for BMP pathway, *Axin2* for WNT pathway, *Gli1* for SHH pathway) known to regulate HFSC quiescence. Right, heat map of log₂-transformed fold change of gene expression of 7 core genes related to cell-cycle machineries and cytokinesis. **e**, **f**, RT-qPCR of genes related to cell-cycle machineries and cytokinesis from telogen HFSCs of sham and ADX mice (**e**) and control and *Pdgfra-CreER;GR^{f/f}* mice (**f**). Data are mean \pm s.e.m. * $P < 0.05$, ** $P < 0.01$, *** $P < 0.001$. For exact P values, see Source Data. For statistics, sample sizes and numbers of replications, see [Methods](#). [Source data](#)

[Extended Data Fig. 7 The expression of cell-cycle-related genes in HFSCs.](#)

a, b, RT-qPCR of genes related to cell-cycle machineries and cytokinesis using telogen HFSCs from vehicle and corticosterone-fed mice (**a**) and control and stressed mice (**b**). **c, d**, RT-qPCR of genes related to cell-cycle machineries and cytokinesis in telogen epidermis from sham and ADX mice (**c**) and vehicle and corticosterone-fed mice (**d**). **e**, Experimental workflow of the differentially expressed genes (DEGs, >1.5-fold, $P_{adj} < 0.05$) from DP cells of sham and ADX mice, as well as control and *Pdgfra-CreER;GR^{f/f}* mice. **f, g**, Immunohistochemical analysis (PCAD) of skin samples from sham and ADX (**f**) or control and *Pdgfra-CreER;GR^{f/f}* (**g**) mice used in RNA-seq experiments to validate hair cycle (all telogen). Dashed lines, epidermis and hair follicles. **h**, Top, FACS strategies for isolating DP cells for RNA-seq^{24,44}. Bottom, the expression levels of cell-type-specific signature genes (DP, fibroblasts, HFSCs and mast cells) in FACS-purified DP cells. TPM, transcripts per million. **i**, Sample clustering based on Pearson's correlation of transcriptomes in DP of sham and ADX mice (left), as well as control and *Pdgfra-CreER;GR^{f/f}* mice (right). **j**, Heat maps of the differentially expressed genes (DEGs, > 1.5-fold, $P_{adj} < 0.05$) from FACS-purified DP cells of sham and ADX mice (left) or control and *Pdgfra-CreER;GR^{f/f}* mice (right). Scale bars (**f, g**), 50 μ m. Data are mean \pm s.e.m. * $P < 0.05$, ** $P < 0.01$, *** $P < 0.001$, NS, not significant. For exact P values, see Source Data. For statistics, sample sizes and numbers of replications, see [Methods](#). [Source data](#)

[Extended Data Fig. 8 Transcriptome analysis and secretome analysis identified GAS6 as a secreted factor suppressed by systemic corticosterone in the DP.](#)

a, Secretome analysis identifying common secreted factors from DEGs (>1.5-fold, $P_{adj} < 0.05$) in ADX and *Pdgfra-CreER;GR^{f/f}* DP cells identified by RNA-seq. **b, c**, Expression levels of shared differentially expressed secreted factors as TPM, in the DP cells of ADX (**b**) and *Pdgfra-CreER;GR^{f/f}* (**c**) mice. **d**, Top, negative control and *Gas6* mRNA expression by *in situ* hybridization in late anagen (AnaV) and mid catagen (CatV) skin of sham and ADX mice. Bottom, quantification of *Gas6* mRNA in the DP. Dashed lines, hair follicle; solid lines, DP. **e**,

Representative image of negative control and *Axl* mRNA expression by in situ hybridization in telogen skin. Yellow dashed lines: bulge; white dashed lines: hair germ (top). RT-qPCR of *Axl*, *Tgfb1*, *Bmpr1a*, *Nfatc1* and *PPIB* from HFSCs and epidermal stem cells (EpSCs) of control mice (P83) (bottom). **f**, Representative images of negative control and *Axl* mRNA expression by in situ hybridization in late anagen skin. Yellow dashed lines: bulge; white dashed lines: epidermis and hair follicles. **g**, The expression levels (as TPM) of genes encoding TAM receptors (*Tyro3*, *Axl* and *Mertk*) in HFSCs. **h**, Left, schematic of the GAS6–AXL receptor tyrosine kinase pathway. R428 is a selective inhibitor of AXL tyrosine kinase activity⁴³. Right, colony-formation assays of cultured HFSCs in R428 or GAS6 with R428 with quantifications. Scale bars (**d–f**), 50 µm. Data are mean ± s.e.m. * $P < 0.05$, ** $P < 0.01$, *** $P < 0.001$, **** $P < 0.0001$, NS, not significant. For exact P values, see Source Data. For statistics, sample sizes and numbers of replications, see [Methods](#). [Source data](#)

[Extended Data Fig. 9 Analyses of skin changes upon *Gas6* overexpression or treatment with an AXL inhibitor.](#)

a, Immunohistochemical analysis (GFP and PCAD) of PBS-injected second telogen skin and AAV-GFP-injected second telogen skin. Dashed lines, epidermis and hair follicles; solid lines: DP. **b**, RT-qPCR of *Gas6* from dermal fibroblasts of PBS-injected second telogen skin (control) and AAV-CAG-Gas6-injected second telogen skin. **c**, Precocious HFSC activation in mice injected with AAV-CAG-Gas6 shown by EdU incorporation. Immunocolocalization (EdU and CD34) in control and AAV-CAG-Gas6-injected skin after AAV injection (D3 to D9). **d**, Comparison of EdU and CD34 localization in bulge and upper outer root sheath (ORS) in late anagen (AnaV) (control, D50 after injection; GAS6, D17 after injection). **e**, H&E staining of late anagen (AnaVI) skin (control, D53 after injection; GAS6, D20 after injection). Quantification of the ORS length in the zigzag hairs of control and AAV-CAG-Gas6-injected mice during late anagen. Brackets indicate the ORS length below the bulge. **f**, Immunocolocalization (EdU and CD34) in infundibulum, junctional zone, sebaceous gland, mid ORS, lower ORS and matrix of late anagen (AnaVI) hair follicles in control and AAV-CAG-Gas6-injected mice with quantifications. Dashed lines outline hair follicles. **g**, Top, H&E staining in the late anagen skin of control

and AAV-CAG-Gas6-injected mice with quantification of the thickness of epidermis (E). Bottom, immunocolocalization (EdU and DAPI) in interfollicular epidermis and dermis in control and AAV-CAG-Gas6-injected mice with quantifications. **h**, RT-qPCR of genes related to HFSC proliferation in HFSCs of second telogen skin. **i**, Hair cycle progression of sham and ADX mice treated with ethanol topically, or ADX mice treated with R428 in ethanol. **j**, RT-qPCR of genes related to cell-cycle machineries and cytokinesis from HFSCs of sham and ADX mice treated with ethanol topically, or ADX mice treated for 7 days with R428 (in ethanol) topically. Yellow dashed lines, bulge (**c**, **d**); white dashed lines, hair germ (**c**), the rest of the hair follicle (**d**, **f**), or the boundary of epidermis and dermis (**g**); solid white line, DP (**c**). EtOH, ethanol. Scale bars (**a**, **c–g**), 50 μ m. Data are mean \pm s.e.m. * P < 0.05, ** P < 0.01, *** P < 0.001, **** P < 0.0001, NS, not significant. For exact P values, see Source Data. For statistics, sample sizes and numbers of replications, see [Methods](#).

[Source data](#)

Extended Data Fig. 10 Interactions between systemic corticosterone and local BMP signalling.

a, In situ hybridization of negative control and *Gas6* mRNA expression in different conditions, including P49 (early telogen) of sham mice, P80 (late telogen) of sham mice, P49 of ADX mice, P49 of in sham mice injected with AAV-CAG-Noggin (Noggin in sham), and P49 in ADX mice after injection of AAV-CAG-Noggin (Noggin in ADX). Quantifications show in situ hybridization signal intensities in the DP. The model shows how changes in corticosterone and BMP signalling influence *Gas6* levels in the DP. **b**, RT-qPCR of *Gas6* from the DP of P49 (early telogen) and P80 (late telogen) of sham mice, and P49 of ADX mice, Noggin in sham mice, and Noggin in ADX mice. **c**, Hair cycle progression in sham, ADX, Noggin in sham, and Noggin in ADX mice with quantifications. Dashed circles indicate AAV-CAG-Noggin injection areas. **d**, Control and *Pdgfra-CreER;GR^{f/f}* mice were subjected to chronic unpredictable stress from P55. Quantification shows the percentage of hair regrowth at P107. **e**, RT-qPCR of *Gas6* from DP cells of control (P83) and stressed (P83) mice (left), and vehicle (P83) and corticosterone-fed (P83) mice (right). **f**, In situ hybridization of *Gas6* in vehicle (P83, late telogen) and corticosterone-fed

(P83) mice, with quantification of in situ signals in DP. **g**, Model of corticosterone regulation of telogen length. In normal conditions, corticosterone levels remain constant, but BMP levels naturally decrease as telogen progresses, until a point is reached at which *Gas6* levels are sufficiently increased so as to drive HFSCs out of quiescence. This dynamic can be altered by changing either the corticosterone level or the BMP level. If corticosterone levels decrease, the sum of inhibitory cues on *Gas6* falls below a critical threshold sooner in telogen, leading to increased *Gas6* levels and precocious anagen entry. In the case of stress, age, or corticosterone feeding, increased corticosterone levels reduce *Gas6* levels to below the critical threshold, leading to an extended telogen. Dashed lines, hair follicles; solid lines, DP. Scale bars (**a, f**), 50 μ m. Data are mean \pm s.e.m. * P < 0.05, ** P < 0.01, *** P < 0.001, **** P < 0.0001, NS, not significant. For exact P values, see Source Data. For statistics, sample sizes and numbers of replications, see [Methods](#). [Source data](#)

Supplementary information

[Supplementary Information](#)

This file contains the Supplementary Discussion, Supplementary References and Supplementary Figure 1.

[Reporting Summary](#)

Source data

[Source Data Fig. 1](#)

[Source Data Fig. 2](#)

[Source Data Fig. 3](#)

[Source Data Fig. 4](#)

[**Source Data Extended Data Fig. 1**](#)

[**Source Data Extended Data Fig. 2**](#)

[**Source Data Extended Data Fig. 3**](#)

[**Source Data Extended Data Fig. 4**](#)

[**Source Data Extended Data Fig. 5**](#)

[**Source Data Extended Data Fig. 6**](#)

[**Source Data Extended Data Fig. 7**](#)

[**Source Data Extended Data Fig. 8**](#)

[**Source Data Extended Data Fig. 9**](#)

[**Source Data Extended Data Fig. 10**](#)

Rights and permissions

[Reprints and Permissions](#)

About this article



Check for
updates

Cite this article

Choi, S., Zhang, B., Ma, S. *et al.* Corticosterone inhibits GAS6 to govern hair follicle stem-cell quiescence. *Nature* **592**, 428–432 (2021).

<https://doi.org/10.1038/s41586-021-03417-2>

[Download citation](#)

- Received: 09 August 2019
- Accepted: 04 March 2021
- Published: 31 March 2021
- Issue Date: 15 April 2021
- DOI: <https://doi.org/10.1038/s41586-021-03417-2>

Further reading

- [Relax to grow more hair](#)

- Rui Yi

Nature (2021)

Comments

By submitting a comment you agree to abide by our [Terms](#) and [Community Guidelines](#). If you find something abusive or that does not comply with our terms or guidelines please flag it as inappropriate.

[Access through your institution](#)

[Change institution](#)

[Buy or subscribe](#)

Associated Content

Nature | News & Views

Relax to grow more hair

- Rui Yi

This article was downloaded by **calibre** from <https://www.nature.com/articles/s41586-021-03417-2>

| [Section menu](#) | [Main menu](#) |

- Article
- [Published: 31 March 2021](#)

Fertilized egg cells secrete endopeptidases to avoid polytubey

- [Xiaobo Yu](#) [ORCID: orcid.org/0000-0003-4994-7337](#)^{1 na1},
- [Xuecheng Zhang](#) [ORCID: orcid.org/0000-0001-8667-4740](#)^{1 na1},
- [Peng Zhao](#) [ORCID: orcid.org/0000-0003-1904-8955](#)^{1 na1},
- [Xiongbo Peng](#) [ORCID: orcid.org/0000-0002-9436-5072](#)¹,
- [Hong Chen](#) [ORCID: orcid.org/0000-0001-8432-6646](#)¹,
- [Andrea Bleckmann](#) [ORCID: orcid.org/0000-0002-0863-9840](#)²,
- [Anastasiia Bazhenova](#)²,
- [Ce Shi](#) [ORCID: orcid.org/0000-0002-8920-8750](#)¹,
- [Thomas Dresselhaus](#) [ORCID: orcid.org/0000-0001-6442-4302](#)² &
- [Meng-xiang Sun](#) [ORCID: orcid.org/0000-0002-6959-8405](#)¹

[Nature](#) volume 592, pages433–437(2021) [Cite this article](#)

- 6081 Accesses
- 110 Altmetric
- [Metrics details](#)

Subjects

- [Fertilization](#)
- [Pollen tube](#)

Abstract

Upon gamete fusion, animal egg cells secrete proteases from cortical granules to establish a fertilization envelope as a block to polyspermy^{1,2,3,4}. Fertilization in flowering plants is more complex and involves the delivery of two non-motile sperm cells by pollen tubes^{5,6}. Simultaneous penetration of ovules by multiple pollen tubes (polytubey) is usually avoided, thus indirectly preventing polyspermy^{7,8}. How plant egg cells regulate the rejection of extra tubes after successful fertilization is not known. Here we report that the aspartic endopeptidases ECS1 and ECS2 are secreted to the extracellular space from a cortical network located at the apical domain of the *Arabidopsis* egg cell. This reaction is triggered only after successful fertilization. *ECS1* and *ECS2* are exclusively expressed in the egg cell and transcripts are degraded immediately after gamete fusion. ECS1 and ESC2 specifically cleave the pollen tube attractor LURE1. As a consequence, polytubey is frequent in *ecs1 ecs2* double mutants. Ectopic secretion of these endopeptidases from synergid cells led to a decrease in the levels of LURE1 and reduced the rate of pollen tube attraction. Together, these findings demonstrate that plant egg cells sense successful fertilization and elucidate a mechanism as to how a relatively fast post-fertilization block to polytubey is established by fertilization-induced degradation of attraction factors.

[Access through your institution](#)

[Change institution](#)

[Buy or subscribe](#)

Access options

Subscribe to Journal

Get full journal access for 1 year

\$199.00

only \$3.90 per issue

[Subscribe](#)

All prices are NET prices.
VAT will be added later in the checkout.
Tax calculation will be finalised during checkout.

Rent or Buy article

Get time limited or full article access on ReadCube.

from \$8.99

[Rent or Buy](#)

All prices are NET prices.

Additional access options:

- [Log in](#)
- [Access through your institution](#)
- [Learn about institutional subscriptions](#)

Fig. 1: Egg cell-specific ECS1 and ECS2 act together to prevent polytubey in *Arabidopsis*.

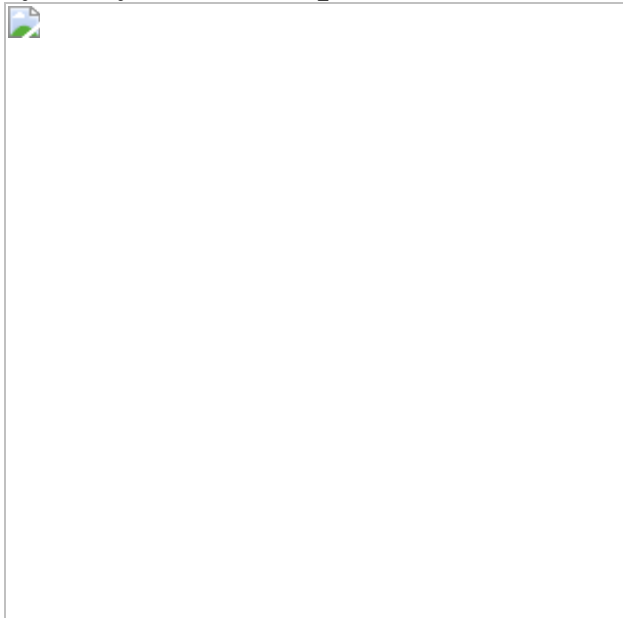


Fig. 2: ECS proteins are secreted from the egg cell after successful sperm–egg cell fusion.

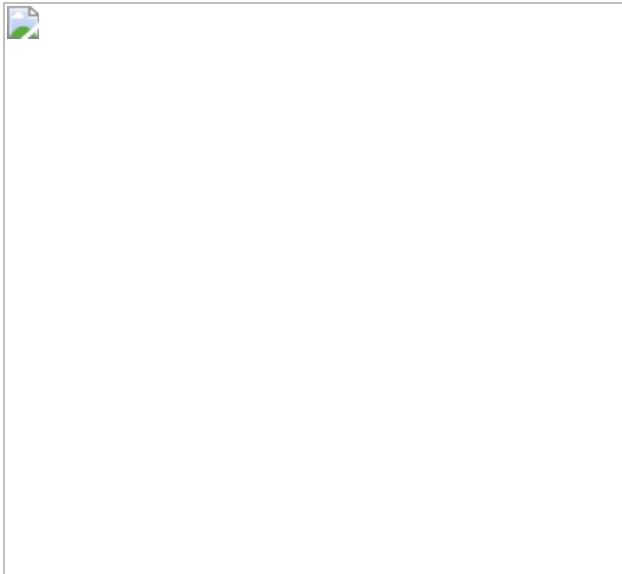
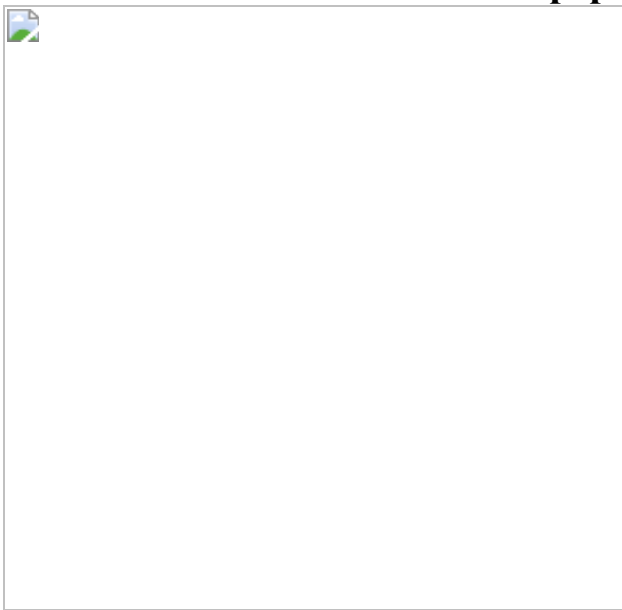


Fig. 3: The LURE1.2 pollen tube attractant is a direct target and substrate of ECS1 and ECS2 endopeptidases.



Data availability

Published RNA sequencing data (Gene Expression Omnibus (GEO) accession numbers [GSE121003](#), [GSE33713](#), [GSE32318](#), [GSE102694](#) and [GSE87760](#)) were used for expression analysis in the present study. The raw data for the graphs that support the findings of this study are available online, and uncropped gel images are shown in the [Supplementary Information file](#). The seeds of the transgenic lines described in this report

are available from the corresponding authors on request. [Source data](#) are provided with this paper.

References

1. 1.

Wong, J. L. & Wessel, G. M. Defending the zygote: search for the ancestral animal block to polyspermy. *Curr. Top. Dev. Biol.* **72**, 1–151 (2006).

[PubMed](#) [CAS](#) [Google Scholar](#)

2. 2.

Burkart, A. D., Xiong, B., Baibakov, B., Jiménez-Movilla, M. & Dean, J. Ovastacin, a cortical granule protease, cleaves ZP2 in the zona pellucida to prevent polyspermy. *J. Cell Biol.* **197**, 37–44 (2012).

[Article](#) [CAS](#) [Google Scholar](#)

3. 3.

Vacquier, V. D., Tegner, M. J. & Epel, D. Protease activity establishes the block against polyspermy in sea urchin eggs. *Nature* **240**, 352–353 (1972).

[ADS](#) [Article](#) [CAS](#) [Google Scholar](#)

4. 4.

Liu, M. The biology and dynamics of mammalian cortical granules. *Reprod. Biol. Endocrinol.* **9**, 149 (2011).

[Article](#) [CAS](#) [Google Scholar](#)

5. 5.

Johnson, M. A., Harper, J. F. & Palanivelu, R. A fruitful journey: pollen tube navigation from germination to fertilization. *Annu. Rev. Plant Biol.* **70**, 809–837 (2019).

[Article](#) [CAS](#) [Google Scholar](#)

6. 6.

Dresselhaus, T., Sprunck, S. & Wessel, G. M. Fertilization mechanisms in flowering plants. *Curr. Biol.* **26**, R125–R139 (2016).

[Article](#) [CAS](#) [Google Scholar](#)

7. 7.

Beale, K. M., Leydon, A. R. & Johnson, M. A. Gamete fusion is required to block multiple pollen tubes from entering an *Arabidopsis* ovule. *Curr. Biol.* **22**, 1090–1094 (2012).

[Article](#) [CAS](#) [Google Scholar](#)

8. 8.

Maruyama, D. et al. Independent control by each female gamete prevents the attraction of multiple pollen tubes. *Dev. Cell* **25**, 317–323 (2013).

[Article](#) [CAS](#) [Google Scholar](#)

9. 9.

Zhang, J. et al. Sperm cells are passive cargo of the pollen tube in plant fertilization. *Nat. Plants* **3**, 17079 (2017).

[Article](#) [Google Scholar](#)

10. 10.

Glöckle, B. et al. Pollen differentiation as well as pollen tube guidance and discharge are independent of the presence of gametes. *Development* **145**, dev152645 (2018).

[Article](#) [CAS](#) [Google Scholar](#)

11. 11.

Zhou, L. Z. & Dresselhaus, T. Friend or foe: signaling mechanisms during double fertilization in flowering seed plants. *Curr. Top. Dev. Biol.* **131**, 453–496 (2019).

[Article](#) [Google Scholar](#)

12. 12.

Grossniklaus, U. Polyspermy produces tri-parental seeds in maize. *Curr. Biol.* **27**, R1300–R1302 (2017).

[Article](#) [CAS](#) [Google Scholar](#)

13. 13.

Nakel, T. et al. Triparental plants provide direct evidence for polyspermy induced polyploidy. *Nat. Commun.* **8**, 1033 (2017).

[ADS](#) [Article](#) [CAS](#) [Google Scholar](#)

14. 14.

Márton, M. L., Cordts, S., Broadhvest, J. & Dresselhaus, T. Micropylar pollen tube guidance by egg apparatus 1 of maize. *Science* **307**, 573–576 (2005).

[ADS](#) [Article](#) [CAS](#) [Google Scholar](#)

15. 15.

Takeuchi, H. & Higashiyama, T. A species-specific cluster of defensin-like genes encodes diffusible pollen tube attractants in *Arabidopsis*. *PLoS Biol.* **10**, e1001449 (2012).

[Article](#) [CAS](#) [Google Scholar](#)

16. 16.

Okuda, S. et al. Defensin-like polypeptide LUREs are pollen tube attractants secreted from synergid cells. *Nature* **458**, 357–361 (2009).

[ADS](#) [Article](#) [CAS](#) [Google Scholar](#)

17. 17.

Zhong, S. et al. Cysteine-rich peptides promote interspecific genetic isolation in *Arabidopsis*. *Science* **364**, eaau9564 (2019).

[Article](#) [CAS](#) [Google Scholar](#)

18. 18.

Sandaklie-Nikolova, L., Palanivelu, R., King, E. J., Copenhaver, G. P. & Drews, G. N. Synergid cell death in *Arabidopsis* is triggered following direct interaction with the pollen tube. *Plant Physiol.* **144**, 1753–1762 (2007).

[Article](#) [CAS](#) [Google Scholar](#)

19. 19.

Duan, Q. et al. FERONIA controls pectin- and nitric oxide-mediated male-female interaction. *Nature* **579**, 561–566 (2020).

[ADS](#) [Article](#) [CAS](#) [Google Scholar](#)

20. 20.

Maruyama, D. et al. Rapid elimination of the persistent synergid through a cell fusion mechanism. *Cell* **161**, 907–918 (2015).

[Article](#) [CAS](#) [Google Scholar](#)

21. 21.

Kasahara, R. D. et al. Fertilization recovery after defective sperm cell release in *Arabidopsis*. *Curr. Biol.* **22**, 1084–1089 (2012).

[Article](#) [CAS](#) [Google Scholar](#)

22. 22.

Sprunck, S. et al. Egg cell-secreted EC1 triggers sperm cell activation during double fertilization. *Science* **338**, 1093–1097 (2012).

[ADS](#) [Article](#) [CAS](#) [Google Scholar](#)

23. 23.

Simões, I., Faro, R., Bur, D. & Faro, C. Characterization of recombinant CDR1, an *Arabidopsis* aspartic proteininase involved in disease resistance. *J. Biol. Chem.* **282**, 31358–31365 (2007).

[Article](#) [CAS](#) [Google Scholar](#)

24. 24.

Mori, T., Kuroiwa, H., Higashiyama, T. & Kuroiwa, T. GENERATIVE CELL SPECIFIC 1 is essential for angiosperm fertilization. *Nat. Cell Biol.* **8**, 64–71 (2006).

[Article](#) [CAS](#) [Google Scholar](#)

25. 25.

Mori, T., Igawa, T., Tamiya, G., Miyagishima, S. Y. & Berger, F. Gamete attachment requires GEX2 for successful fertilization in

Arabidopsis. Curr. Biol. **24**, 170–175 (2014).

[Article](#) [CAS](#) [Google Scholar](#)

26. 26.

Steffen, J. G., Kang, I. H., Macfarlane, J. & Drews, G. N. Identification of genes expressed in the *Arabidopsis* female gametophyte. *Plant J.* **51**, 281–292 (2007).

[Article](#) [CAS](#) [Google Scholar](#)

27. 27.

Bleckmann, A. & Dresselhaus, T. Whole mount RNA-FISH on ovules and developing seeds. *Methods Mol. Biol.* **1669**, 159–171 (2017).

[Article](#) [CAS](#) [Google Scholar](#)

28. 28.

Zimmerberg, J. & Whitaker, M. Irreversible swelling of secretory granules during exocytosis caused by calcium. *Nature* **315**, 581–584 (1985).

[ADS](#) [Article](#) [CAS](#) [Google Scholar](#)

29. 29.

Antoine, A. F. et al. A calcium influx is triggered and propagates in the zygote as a wavefront during in vitro fertilization of flowering plants. *Proc. Natl Acad. Sci. USA* **97**, 10643–10648 (2000).

[ADS](#) [Article](#) [CAS](#) [Google Scholar](#)

30. 30.

Digonnet, C., Aldon, D., Leduc, N., Dumas, C. & Rougier, M. First evidence of a calcium transient in flowering plants at fertilization.

Development **124**, 2867–2874 (1997).

[PubMed](#) [CAS](#) [Google Scholar](#)

31. 31.

Denninger, P. et al. Male–female communication triggers calcium signatures during fertilization in *Arabidopsis*. *Nat. Commun.* **5**, 4645 (2014).

[ADS](#) [Article](#) [CAS](#) [Google Scholar](#)

32. 32.

Hamamura, Y. et al. Live imaging of calcium spikes during double fertilization in *Arabidopsis*. *Nat. Commun.* **5**, 4722 (2014).

[ADS](#) [Article](#) [CAS](#) [Google Scholar](#)

33. 33.

Kranz, E., von Wiegen, P. & Lörz, H. Early cytological events after induction of cell division in egg cells and zygote development following in vitro fertilization with angiosperm gametes. *Plant J.* **8**, 9–23 (1995).

[Article](#) [Google Scholar](#)

34. 34.

Wu, J. J. et al. Mitochondrial GCD1 dysfunction reveals reciprocal cell-to-cell signaling during the maturation of *Arabidopsis* female gametes. *Dev. Cell* **23**, 1043–1058 (2012).

[Article](#) [CAS](#) [Google Scholar](#)

35. 35.

Lampropoulos, A. et al. GreenGate—a novel, versatile, and efficient cloning system for plant transgenesis. *PLoS ONE* **8**, e83043 (2013).

[ADS](#) [Article](#) [CAS](#) [Google Scholar](#)

36. 36.

Nelson, B. K., Cai, X. & Nebenführ, A. A multicolored set of *in vivo* organelle markers for co-localization studies in *Arabidopsis* and other plants. *Plant J.* **51**, 1126–1136 (2007).

[Article](#) [CAS](#) [Google Scholar](#)

37. 37.

Zhang, X., Henriques, R., Lin, S. S., Niu, Q. W. & Chua, N. H. Agrobacterium-mediated transformation of *Arabidopsis thaliana* using the floral dip method. *Nat. Protoc.* **1**, 641–646 (2006).

[Article](#) [CAS](#) [Google Scholar](#)

38. 38.

Wang, T. et al. A receptor heteromer mediates the male perception of female attractants in plants. *Nature* **531**, 241–244 (2016).

[ADS](#) [Article](#) [CAS](#) [Google Scholar](#)

39. 39.

Sparkes, I. A., Runions, J., Kearns, A. & Hawes, C. Rapid, transient expression of fluorescent fusion proteins in tobacco plants and generation of stably transformed plants. *Nat. Protoc.* **1**, 2019–2025 (2006).

[Article](#) [CAS](#) [Google Scholar](#)

40. 40.

Soares, A. et al. An atypical aspartic protease modulates lateral root development in *Arabidopsis thaliana*. *J. Exp. Bot.* **70**, 2157–2171 (2019).

[Article](#) [CAS](#) [Google Scholar](#)

41. 41.

Zhao, P. et al. Two-step maternal-to-zygotic transition with two-phase parental genome contributions. *Dev. Cell* **49**, 882–893 (2019).

[Download references](#)

Acknowledgements

We thank F. Berger for the HTR10-mRFP marker line, Y. Zhang for the *LAT52::DsRed* marker line, C. Li for the *LAT52::GUS* marker line and W. Li for help with the mammal cell expression system. This work was supported by the National Natural Science Foundation of China (31991201) and the German Research Council DFG via SFB960.

Author information

Author notes

1. These authors contributed equally: Xiaobo Yu, Xuecheng Zhang, Peng Zhao

Affiliations

1. State Key Laboratory of Hybrid Rice, College of Life Sciences, Wuhan University, Wuhan, China

Xiaobo Yu, Xuecheng Zhang, Peng Zhao, Xiongbo Peng, Hong Chen, Ce Shi & Meng-xiang Sun

2. Cell Biology and Plant Biochemistry, University of Regensburg, Regensburg, Germany

Andrea Bleckmann, Anastasiia Bazhenova & Thomas Dresselhaus

Authors

1. Xiaobo Yu

[View author publications](#)

You can also search for this author in [PubMed](#) [Google Scholar](#)

2. Xuecheng Zhang

[View author publications](#)

You can also search for this author in [PubMed](#) [Google Scholar](#)

3. Peng Zhao

[View author publications](#)

You can also search for this author in [PubMed](#) [Google Scholar](#)

4. Xiongbo Peng

[View author publications](#)

You can also search for this author in [PubMed](#) [Google Scholar](#)

5. Hong Chen

[View author publications](#)

You can also search for this author in [PubMed](#) [Google Scholar](#)

6. Andrea Bleckmann

[View author publications](#)

You can also search for this author in [PubMed](#) [Google Scholar](#)

7. Anastasiia Bazhenova

[View author publications](#)

You can also search for this author in [PubMed](#) [Google Scholar](#)

8. Ce Shi

[View author publications](#)

You can also search for this author in [PubMed](#) [Google Scholar](#)

9. Thomas Dresselhaus

[View author publications](#)

You can also search for this author in [PubMed](#) [Google Scholar](#)

10. Meng-xiang Sun

[View author publications](#)

You can also search for this author in [PubMed](#) [Google Scholar](#)

Contributions

M.-x.S., X.Y. and T.D. designed the research plan. X.Z., X.P., H.C. and C.S. performed the phenotype and genetics analyses. X.Y. and P.Z. performed the biochemical study. A. Bazhenova performed the *in situ* hybridization study. A. Bleckmann performed the cortical network observation study. T.D. and M.-x.S. contributed to the data analysis and finalized the manuscript. All authors contributed to the data collection, presentation and manuscript writing.

Corresponding authors

Correspondence to [Thomas Dresselhaus](#) or [Meng-xiang Sun](#).

Ethics declarations

Competing interests

The authors declare no competing interests.

Additional information

Peer review information *Nature* thanks the anonymous reviewer(s) for their contribution to the peer review of this work.

Publisher's note Springer Nature remains neutral with regard to jurisdictional claims in published maps and institutional affiliations.

Extended data figures and tables

[Extended Data Fig. 1 ECS1 and ECS2 are specifically expressed in the egg cell of *Arabidopsis*.](#)

a, Fragments per kilobase of transcript per million mapped reads (FPKM) values (Mean ± s.d.) of *ECS1* and *ECS2* transcripts in egg cells and zygotes. RNA-seq data of Ec, Zy 1C and 32C are from ref. ⁴¹ except 8C (GSE33713), seedlings (GSE32318), stems (GSE102694), roots and rosettes (GSE87760). **b–i**, Promoter activity analysis using the nuclear marker H2B–GFP expressed by *ECS1* (**b–e**) and *ECS2* (**f–i**) promoters, respectively. Both promoters were specifically active in egg cells after embryo sac cellularization. **b, f**, Female gametophyte before cellularization. **c, g**, Immature egg cell. **d, h**, Mature egg cell. **e, i**, Zygote at 20 HAP. 1C, 1-cell pro-embryo; 8C, 8-cell pro-embryo; 32C, 32-cell embryo; n, nucleus; ecn, egg cell nucleus; syn, synergid cell nucleus; zy, zygote. Dashed lines outline the egg cell and zygote, respectively. Insets show enlargements of regions indicated. Scale bars, 20 μm. [Source data](#)

[Extended Data Fig. 2 Characteristics of ECS protein sequences, identification of their T-DNA insertion mutants and phylogenetic tree of aspartic endopeptidases in *Arabidopsis*.](#)

a, Alignment of *ECS1/2* and *CDR1* protein sequences. Two active sites and an N-terminal signal peptide are indicated. Conserved cysteines typical for aspartic proteases are labelled in yellow. **b**, Protein sequences of 78 aspartic proteases from *A. thaliana* annotated in the MEROPS database

(<https://merops.sanger.ac.uk/>) were subjected to phylogenetic analysis by MEGA X. The phylogenetic tree was constructed using the Neighbour-Joining method. ECS1 and ECS2 are indicated in red. **c**, Scheme showing T-DNA insertion sites of *ecs1* and *ecs2* mutants. **d**, RT–PCR using primers indicated in **b** revealed that transcripts levels of *ECS1* and *ECS2* were significantly reduced in their corresponding T-DNA insertion mutants. Actin was used as a control for RT–PCR analysis.

Extended Data Fig. 3 As a consequence of polytubey, multiple sperm cell pairs are released in *ecs1 ecs2* mutant ovules.

a, Three representative images showing two additional sperm cell pairs at 24 HAP, respectively. **b–d**, Time series showing representative images of two additional sperm cell pairs at 6 HAP (**b**), 8 HAP (**c**) and 10 HAP (**d**), respectively. **e**, Proportions of additional sperm pairs in ovules of *ecs1 ecs2* mutants after fertilization ($n = 1056$ for 6 HAP; 1114 for 8 HAP, 1083 for 10 HAP). Data are presented in box-and-whisker plots. Bottom and top of the box, 25th and 75th percentiles; centre line, 50th percentile; whiskers, minimum and maximum data. Abbreviations: sp., sperm cell; enn, endosperm nucleus; zyn, zygote nucleus. Scale bars, 20 μm . [Source data](#)

Extended Data Fig. 4 ECS1 and ECS2 are almost quantitatively secreted from an apical network of the mature egg cell to the extracellular space only after gamete fusion.

a, b, ECS1-mCitrine (mCit) at the apical domain forming a network before fertilization. **c, d**, ECS2-mCit accumulate at the apical domain forming a network before fertilization. **b, d**, Enlargement of apical domains of egg cells shown in **a, b**. **e–h**, ECS1-mCit (**e, f**) and ECS2-mCit (**g, h**) are secreted from the egg cell to the extracellular space. Synergids are largely degenerated as indicated by the lack or diminished signal of the synergid marker. Volume projections of *z*-stacks from ECS1/2-mCit (yellow), an egg cell expressed Golgi-mScarlet (mScar; red) and a synergid expressed endoplasmic reticulum marker tagged to mTurquoise2 (mTur; cyan) are shown. **i**, FM4-64 staining showing that the cortical network containing ECS2-mCit is located at the plasma membrane. **j**, Signal intensity plot

along the arrow shown in **i** indicates that ECS2–Cit is located at or just below the plasma membrane. **k**, Single optical section through the cortical network shows weak ECS2–Cit signals outside the network. **l**, Overexposure of the same optical section shown in **k** illustrates ECS2–Cit signals throughout the egg cytoplasm. **m**, Overexposed image showing ECS2–GFP accumulating in the apical egg cell domain and the endoplasmic reticulum marker EC1.2::erRFP marking the boundaries of the egg cell. A pollen tube expressing DsRed driven by the *Lat52* promoter was used to monitor pollen tube perception. During pollen tube arrival ECS2–GFP was not yet released. **n**, Intensity plot profile showing relative fluorescence signal intensities of ECS2–GFP (green line) and erRFP (red line) along a dashed line drawn across the egg cells (indicated in the left image) confirming the microscopic observation. **o**, Sperm cells defective in gamete fusion (*gcs1* mutant) did not trigger ECS2–GFP release. **p**, Intensity plot profile as in **n** showing that egg cell-localized ECS2–GFP and synergid cell-localized erRFP signals do not overlap. Ec, egg cell; pt, pollen tube; sp., sperm cells; sy, synergid cells. Scale bars, 10 μ m.

Extended Data Fig. 5 Truncated ECS1 and ECS2 proteins are not secreted from egg cells during fertilization.

a, d, ECS1–GFP and ECS2–GFP were located inside the egg cell before fertilization. **b, e**, ECS1–GFP and ECS2–GFP were secreted from the egg cell at 8 HAP. Asterisks mark secreted ECS1–GFP and ECS2–GFP, respectively. **c, f**, Truncated TECS1–GFP (**c**) and TECS2–GFP (**f**) versions lacking signal peptides could not be secreted from the egg cell at 8 HAP. ec, egg cell. Dashed lines outline the egg cell boundaries. Insets show enlargements of regions indicated. Scale bars, 20 μ m.

Extended Data Fig. 6 ECS1 and ECS2 endopeptidases interact with LURE1.2 and cleave it as a substrate.

a, Protein level of LURE1.2 significantly decreased after co-expression with ECS1 and ECS2 in mammalian cells, respectively. **b**, Relative protein levels of LURE1.2 in leaves co-expressed with ECS1, ECS2 or the empty vector (CK) as control, respectively. Data are presented as mean \pm s.d. from

four independent experiments. ($n = 4$). Statistical test was performed using one-way ANOVA between groups, with the Tukey–Kramer test for multiple comparisons ($P = 2.25 \times 10^{-5}$; $F = 44.03$). **c**, Fluorogenic peptides were synthesized according to the LURE1.2 protein sequence (**d**). **e**, Proteolytic activity of recombinant ECS1 and ECS2 using LURE1.2-derived peptide 3 as substrate at different concentrations to determine K_m values. Data represent mean \pm s.d. of three independent experiments. **f**, Effect of temperature on proteolytic activities of recombinant ECS1 and ECS2 using peptide 3 as a substrate. Data represent mean \pm s.d. of three independent experiments. **g**, Alignment of LURE and XIUQIU protein sequences. Amino acid sequence of peptide 3 (outlined by red colour) is conserved in all LURE1, but not in XIUQIU protein sequences. Full length sequences including N-terminal signal motifs are shown. [Source data](#)

Extended Data Fig. 7 ECS1 and ECS2 efficiently cleave LURE1 substrates.

a, Localization and protein level of LURE1.2–GFP before pollination and in fertilized ovules of WT and *ecs1 ecs2* mutant pistils, respectively. Pistils were pollinated with pollen expressing HTR10–mRFP in sperm cells. Ovules were collected from pistils at 0 and 10 HAP. *ecs1 ecs2* mutation resulted in the accumulation of LURE1.2 after fertilization. **b**, Quantification of green fluorescence intensity in ovules from WT and *ecs1 ecs2* pistils ($n = 101$). Data for fluorescence intensity are presented in box-and-whisker plots. Bottom and top of the box, 25th and 75th percentiles; centre line, 50th percentile; whiskers, minimum and maximum data. ** indicates statistically significant difference between WT and mutant ovules (two-tailed Student's *t*-test; $P < 0.01$). **c**, In vitro pollen tube attraction assay with gelatin beads containing ECS1- and ECS2-digested LURE1.2, respectively. Beads (*) were prepared using 1 μ M LURE1.2 alone and in combination with 1 μ M ECS1 and ECS2, respectively, and placed close to growing pollen tube tips (0 min) and observed for 60 min. Pollen tube attraction activity was lost when beads contained both, LURE1.2 and ECS endopeptidases. n, nucleus; pt, pollen tube; sy, synergid cell; zy, zygote. Scale bars are 10 μ m (**a**) and 50 μ m (**c**). [Source data](#)

Extended Data Fig. 8 Ectopic expression of *ECS1* and *ECS2* in synergid cells leads to a decrease of LURE1.2 protein levels and strongly reduced pollen tube attraction rate.

a, Ectopically expressed ECS1–GFP fusion protein in synergid cells is secreted to the filiform apparatus. **b**, Immunofluorescence revealed that LURE1 levels were significantly decreased in ovules ectopically expressing *ECS1-GFP* in synergid cells using the *DD31* promoter. **c**, Quantification of LURE1 fluorescence intensity in WT and *ECS1*-ectopically expressed ovules as shown in (b) ($n = 10$). **d**, Ectopic expression of *ECS1* in synergid cells resulted in pollen tube attraction defects 6 HAP. Pollen tube growth analysis was performed using a *Lat52::GUS* reporter line. **e**, Percentages of ovules attracting pollen tubes observed in WT pistils and those ectopically expressing *ECS1* in synergid cells of three independent lines (L1–L3) at 6 HAP ($n = 50$ for WT and *DD31::ECS1 L1*; 60 for *DD31::ECS1 L2* and *DD31::ECS1 L3*). **f**, Immunofluorescence revealed that LURE1 levels were significantly decreased in ovules ectopically expressing *ECS2* in synergid cells using the *DD31* promoter. **g**, Quantification of LURE1 fluorescence intensity in WT ovules and those ectopically expressing *ECS2* ($n = 10$). **h**, Similarly, LURE1.2–GFP signals were significantly decreased in ovules ectopically expressing *ECS2* in synergid cells. **i**, Quantification of LURE1.2–GFP fluorescence intensity as described in **b** ($n = 101$). **j**, **k**, Ectopic expression of *ECS2* in synergid cells resulted in reduction of pollen tube attraction 6 HAP. *Lat52::DsRed* (**j**) and *Lat52::GUS* reporter line (**k**) were used in this analysis. **l**, Proportions of ovules attracting pollen tubes observed in WT plants and those ectopically expressing *ECS2* in synergid cells at 6 HAP ($n = 50$ for WT, *DD31::ECS2 L2* and *DD31::ECS2 L3*; 80 for *DD31::ECS2 L1*). Data in **c**, **g**, **i** are presented in box-and-whisker plots. Bottom and top of the box, 25th and 75th percentiles; centre line, 50th percentile; whiskers, minimum and maximum data. ** indicates statistical difference compared to WT (Two-tailed Student's *t*-test; $P < 0.01$). Same letters (in **e** and **l**) indicate lack of significant differences according to the Tukey–Kramer multiple comparison test (one-way ANOVA between groups; $P = 1.94 \times 10^{-7}$; $F = 32.11$ in **e**; $P = 3.24 \times 10^{-8}$, $F = 37.88$ in **l**). $P < 0.05$ was considered as significant. Scale bars, 20 μm (**a**, **b**, **f**, **h**), 100 μm (**j**). ec, egg cell; sy, synergid; pt, pollen tube; ov, ovule. [Source data](#)

Extended Data Fig. 9 Ectopic expression of truncated versions of *ECS1* and *ECS2* or the subtilisin-like protease *SBT4.13* in synergid cells have no significant influence on LURE1.2 protein levels and pollen tube attraction rate.

a, Ectopic expressions of truncated versions of *ECS1* and *ECS2* (*TECS1/2*) in synergid cells. **b**, Proportions of ovules attracting pollen tubes observed in WT plants and those ectopically expressing *TECS1/2* in synergid cells at 6 HAP ($n = 50$). **c**, Immunofluorescence revealed that LURE1 levels were comparable in WT and ovules ectopically expressing *TECS1/2* in synergid cells using the DD31 promoter. **d**, Quantification of LURE1 fluorescence intensity in WT ovules and those ectopically expressing truncated *TECS1/2* in synergid cells ($n = 10$). **e**, Ectopic expressions of the egg cell expressed subtilisin-like protease *SBT4.13*²⁷ as a GFP fusion protein in synergid cells. *SBT4.13*-GFP is secreted to the filiform apparatus. **f**, Proportions of ovules attracting pollen tubes observed in WT plants and those ectopically expressing *SBT4.13* in synergid cells at 6 HAP ($n = 50$). **g**, Immunofluorescence revealed that LURE1 levels were comparable in WT and ovules ectopically expressing *SBT4.13* in synergid cells. **h**, Quantification of LURE1 fluorescence intensity in WT ovules and those ectopically expressing *SBT4.13* ($n = 10$). Data in **b**, **f** represent the mean \pm s.d. Same letters in **b**, **f** indicate lack of significant differences according to the Tukey–Kramer multiple comparison test (one-way ANOVA between groups; $P = 0.96$, $F = 0.04$ in **b** left plane; $P = 0.85$, $F = 0.17$ in **b** right plane; $P = 0.85$, $F = 0.17$ in **f**). $P < 0.05$ was considered as significant. Data in **d**, **h** are presented in box-and-whisker plots. Bottom and top of the box, 25th and 75th percentiles; centre line, 50th percentile; whiskers, minimum and maximum data. Two-tailed Student's *t*-test was used for statistical test in **d**, **h**. ns, no significant differences. sy, synergid cell. Scale bars, 20 μ m. [Source data](#)

Extended Data Fig. 10 Mutation of active sites of *ECS1* and *ECS2* endopeptidases leads to polytubey.

a, Mutation of active sites of *ECS1* and *ECS2* (Extended Data Fig. [2a](#)) led to reduced proteolytic activity. Proteolytic activities of recombinant WT

and mutant version of ECS towards cleavage of fluorogenic peptide 3 (Extended Data Fig. 6) were measured respectively. Data represent mean \pm s.d. of three independent experiments. **b**, Mutant version of ECS could not recover the polytubey phenotype of *ecs1 ecs2* double mutant. Proportions of polytubey in *ecs1 ecs2* double mutants and different transgenic lines were determined at 24 HAP ($n = 308$ for WT; 302 for *ecs1 ecs2*; 309 for ECS1; 319 for ECS1^{D103N D324N}-1; 302 for ECS1^{D103N D324N}-2; 309 for ECS2; 321 for ECS2^{D103N D326N}-1; 300 for ECS2^{D103N D326N}-2). Data represent the mean \pm s.d. Same letters indicate lack of significant differences according to the Tukey–Kramer multiple comparison test (one-way ANOVA between groups; $P = 7.82 \times 10^{-18}$, $F = 50.24$). $P < 0.05$ was considered as significant. **c**, Representative images showing multiple pollen tubes entrance in different transgenic lines as indicated. Arrows indicate pollen tubes (pt). Scale bars, 100 μ m. [Source data](#)

Supplementary information

[Supplementary Information](#)

This file contains Supplementary Fig. 1 (gel source data) and Supplementary Tables 1-2. Supplementary Table 1 contains a list of primers used in the study and Supplementary Table 2 contains a list of GreenGate modules used for triple reporter line construction.

[Reporting Summary](#)

Source data

[Source Data Fig. 1](#)

[Source Data Fig. 3](#)

[Source Data Extended Data Fig. 1](#)

[Source Data Extended Data Fig. 3](#)

[**Source Data Extended Data Fig. 6**](#)

[**Source Data Extended Data Fig. 7**](#)

[**Source Data Extended Data Fig. 8**](#)

[**Source Data Extended Data Fig. 9**](#)

[**Source Data Extended Data Fig. 10**](#)

Rights and permissions

[Reprints and Permissions](#)

About this article



Check for
updates

Cite this article

Yu, X., Zhang, X., Zhao, P. *et al.* Fertilized egg cells secrete endopeptidases to avoid polytubey. *Nature* **592**, 433–437 (2021).

<https://doi.org/10.1038/s41586-021-03387-5>

[Download citation](#)

- Received: 25 January 2020
- Accepted: 24 February 2021
- Published: 31 March 2021
- Issue Date: 15 April 2021

- DOI: <https://doi.org/10.1038/s41586-021-03387-5>

Comments

By submitting a comment you agree to abide by our [Terms](#) and [Community Guidelines](#). If you find something abusive or that does not comply with our terms or guidelines please flag it as inappropriate.

[Access through your institution](#)

[Change institution](#)

[Buy or subscribe](#)

This article was downloaded by **calibre** from <https://www.nature.com/articles/s41586-021-03387-5>

| [Section menu](#) | [Main menu](#) |

Detection of a SARS-CoV-2 variant of concern in South Africa

[Download PDF](#)

- Article
- [Published: 09 March 2021](#)

Detection of a SARS-CoV-2 variant of concern in South Africa

- [Houriiyah Tegally](#)¹ na1,
- [Eduan Wilkinson](#)¹ na1,
- [Marta Giovanetti](#) [ORCID: orcid.org/0000-0002-5849-7326](#)^{2,3} na1,
- [Arash Iranzadeh](#)⁴ na1,
- [Vagner Fonseca](#) [ORCID: orcid.org/0000-0001-5521-6448](#)^{1,3},
- [Jennifer Giandhari](#)¹,
- [Deelan Doolabh](#)⁵,
- [Sureshnee Pillay](#)¹,
- [Emmanuel James San](#)¹,
- [Nokukhanya Msomi](#)⁶,
- [Koleka Mlisana](#)^{7,8},
- [Anne von Gottberg](#)^{9,10},
- [Sibongile Walaza](#)^{9,11},
- [Mushal Allam](#) [ORCID: orcid.org/0000-0002-9875-6716](#)⁹,
- [Arshad Ismail](#) [ORCID: orcid.org/0000-0003-4672-5915](#)⁹,
- [Thabo Mohale](#)⁹,
- [Allison J. Glass](#)^{10,12},
- [Susan Engelbrecht](#) [ORCID: orcid.org/0000-0002-1318-5994](#)¹³,
- [Gert Van Zyl](#) [ORCID: orcid.org/0000-0003-3021-5101](#)¹³,
- [Wolfgang Preiser](#) [ORCID: orcid.org/0000-0002-0254-7910](#)¹³,
- [Francesco Petruccione](#)^{14,15},
- [Alex Sigal](#)^{16,17,18},
- [Diana Hardie](#)¹⁹,
- [Gert Marais](#)¹⁹,
- [Nei-yuan Hsiao](#)¹⁹,
- [Stephen Korsman](#)¹⁹,
- [Mary-Ann Davies](#)^{20,21},

- [Lynn Tyers⁵](#),
- [Innocent Mudau⁵](#),
- [Denis York²²](#),
- [Caroline Maslo²³](#),
- [Dominique Goedhals²⁴](#),
- [Shareef Abrahams²⁵](#),
- [Oluwakemi Laguda-Akingba^{25,26}](#),
- [Arghavan Alisoltani-Dehkordi^{27,28}](#),
- [Adam Godzik²⁸](#),
- [Constantinos Kurt Wibmer⁹](#),
- [Bryan Trevor Sewell²⁹](#),
- [José Lourenço](#) [ORCID: orcid.org/0000-0002-9318-2581³⁰](#),
- [Luiz Carlos Junior Alcantara](#) [ORCID: orcid.org/0000-0002-6769-9931^{2,3}](#),
- [Sergei L. Kosakovsky Pond³¹](#),
- [Steven Weaver³¹](#),
- [Darren Martin^{4,5}](#),
- [Richard J. Lessells](#) [ORCID: orcid.org/0000-0003-0926-710X^{1,8}](#),
- [Jinal N. Bhiman](#) [ORCID: orcid.org/0000-0001-6354-4003^{9,10 na2}](#),
- [Carolyn Williamson^{5,8,19 na2}](#) &
- [Tulio de Oliveira](#) [ORCID: orcid.org/0000-0002-3027-5254^{1,8,32 na2}](#)

[Nature](#) volume **592**, pages438–443(2021)[Cite this article](#)

- 36k Accesses
- 10 Citations
- 358 Altmetric
- [Metrics details](#)

Subjects

- [Epidemiology](#)
- [Molecular evolution](#)
- [SARS-CoV-2](#)

Abstract

Continued uncontrolled transmission of SARS-CoV-2 in many parts of the world is creating conditions for substantial evolutionary changes to the virus^{1,2}. Here we describe a newly arisen lineage of SARS-CoV-2 (designated 501Y.V2; also known as B.1.351 or 20H) that is defined by eight mutations in the spike protein, including three substitutions (K417N, E484K and N501Y) at residues in its receptor-binding domain that may have functional importance^{3,4,5}. This lineage was identified in South Africa after the first wave of the epidemic in a severely affected metropolitan area (Nelson Mandela Bay) that is located on the coast of the Eastern Cape province. This lineage spread rapidly, and became dominant in Eastern Cape, Western Cape and KwaZulu-Natal provinces within weeks. Although the full import of the mutations is yet to be determined, the genomic data—which show rapid expansion and displacement of other lineages in several regions—suggest that this lineage is associated with a selection advantage that most plausibly results from increased transmissibility or immune escape^{6,7,8}.

[Download PDF](#)

Main

SARS-CoV-2 emerged in 2019 and has spread rapidly around the world, causing over 80 million recorded cases of COVID-19 and over 1.7 million deaths attributable to this disease by the end of 2020. The failure of public health measures to contain the spread of the virus in many countries has given rise to a large number of virus lineages. Open sharing of genomic surveillance data and collaborative online platforms have enabled the real-time tracking of the emergence and spread of these lineages^{9,10}.

To date, there has been relatively limited evidence for SARS-CoV-2 mutations that have had a substantial functional effect on the virus. A mutation resulting in a substitution in the spike protein (D614G) emerged early in the epidemic, and spread rapidly through Europe and North America in particular. Several lines of evidence now suggest that SARS-CoV-2 variants that carry this mutation have increased transmissibility^{11,12,13,14}. Later in the epidemic, several lineages with a N439K substitution in the receptor-binding domain (RBD) of the spike protein emerged independently, probably in a range of European countries and the USA. This mutation is associated with escape from neutralization mediated by monoclonal antibodies or polyclonal serum¹⁵.

South Africa is the most severely affected country in Africa, with over 80,000 excess natural deaths having occurred by the end of 2020 (approximately 1,400 per million individuals)¹⁶. The introduction and spread of several SARS-CoV-2 lineages to South Africa have previously been described, as has the identification of lineages unique to

South Africa during the early phase of the epidemic^{17,18}. Here we describe the emergence and spread of a SARS-CoV-2 lineage that contains several nonsynonymous spike mutations, including mutations that affect key sites in the RBD (resulting in K417N, E484K and N501Y substitutions) that may have functional importance. We demonstrate that this lineage is likely to have emerged after the first wave of the epidemic in the worst-affected metropolitan area within the Eastern Cape province. This was followed by rapid spread of this lineage, to the extent that by the end of 2020 it had become the dominant lineage in three provinces.

Epidemic dynamics in South Africa

The second wave of the SARS-CoV-2 epidemic in South Africa began around October 2020, weeks after a trough in daily recorded cases following the first peak¹⁹ (Fig. 1a). The country-wide estimated effective reproduction number (R_e) increased to above 1 at the end of October (indicating a growing epidemic), which coincided with a steady rise in daily cases. At the peak of the national epidemic in the middle of July, there were over 13,000 confirmed cases per day and almost 7,000 excess deaths per week. The epidemiological profile in the three provinces that are the focus of this analysis (the Eastern Cape, Western Cape and KwaZulu–Natal) were broadly similar, although the Western Cape had an earlier and flatter peak in the first wave (Fig. 1b–d). At the end of the first wave of the epidemic in early September, there had been over 10,000 excess deaths in the Eastern Cape (1,510 per million individuals)—the highest for any province (Extended Data Fig. 1). Although there was a plateau in cases after the first wave, this was noticeably short in the Eastern Cape; by early October, there was a second phase of exponential growth that was associated with an increase in deaths at a rate similar to that of the first wave (Fig. 1b). The rate of positive PCR tests at a local-municipality level shows very high levels of infection (>20%) in Nelson Mandela Bay from the middle of October, followed by rapidly rising levels in the surrounding areas through October and November (Extended Data Fig. 2). The resurgence of the daily case counts at an exponential rate happened later for the Western Cape and KwaZulu–Natal than for the Eastern Cape (Fig. 1c,d). By early December, all three provinces were experiencing a second wave and new cases in the Western Cape had already surpassed the peak of the first wave.

Fig. 1: SARS-CoV-2 epidemiological dynamics in South Africa.



a–e, Histograms show the number of daily confirmed cases of COVID-19 (mapped to the left *y* axis) from March 2020 to January 2021 in South Africa (**a**) and in the four provinces under study: Eastern Cape (**b**), Western Cape (**c**), KwaZulu–Natal (**d**) and Northern Cape (**e**). Fluctuations in the daily estimates of R_e are shown in red (mapped to the right *y* axis); the mean estimated median R_e with upper and lower bounds of the 95% confidence interval are shown, along with a cut-off for $R = 1$ (broken red line). Weekly excess deaths in South Africa and in each region are shown as black broken lines (mapped to the left *y* axis).

[Full size image](#)

Phylogenetic and phylogeographic analysis

The early and rapid resurgence of the epidemic in parts of the Eastern Cape and Western Cape prompted the intensification of genomic surveillance by the Network for Genomic Surveillance in South Africa (NGS-SA), including sampling in and around Nelson Mandela Bay in the Eastern Cape and in the neighbouring Garden Route district of the Western Cape (Extended Data Fig. 3). We analysed 2,882 whole genomes of SARS-CoV-2 from South Africa, which were collected between 5 March and 10 December 2020. We estimated preliminary maximum-likelihood and molecular clock phylogenies for a dataset containing an additional 2,573 global reference genomes (Fig. 2a). We identified a previously unrecognized monophyletic cluster (501Y.V2) that contained 341 sequences, from samples collected between 8 October and 10 December in KwaZulu–Natal, Eastern Cape, Western Cape and Northern Cape (Fig. 2b). Seven South African sequences that are basal to the 501Y.V2 cluster (Fig. 2a) were sampled in the Eastern Cape, Western Cape, Gauteng and KwaZulu–Natal

provinces between late June and early September. Although these sequences do not have any of the defining mutations of the 501Y.V2 variant, they are basal to the B.1.351 lineage and indicate that the precursor to the new variant was probably circulating throughout the country before the emergence of 501Y.V2.

Fig. 2: Evolution and spread of the 501Y.V2 cluster in South Africa.



a, Time-resolved maximum clade credibility phylogeny of 5,329 SARS-CoV-2 sequences; 2,756 of these are from South Africa (red). The newly identified SARS-CoV-2 cluster (501Y.V2) is highlighted in yellow. **b**, Time-resolved maximum clade credibility phylogeny of the 501Y.V2 cluster ($n = 341$), with province indicated. Mutations that characterize the cluster are highlighted at the branch at which each first emerged. **c**, Frequency and distribution of SARS-CoV-2 lineages circulating in South Africa over time. **d**, Spatiotemporal reconstruction of the spread of the 501Y.V2 cluster in South Africa during the second wave of the epidemic. Circles represent nodes of the maximum clade credibility phylogeny, coloured according to their

inferred time of occurrence (scale in bottom panel). Shaded areas represent the 80% highest posterior density interval and depict the uncertainty of the phylogeographic estimates for each node. Solid curved lines denote the links between nodes and the directionality of movement.

[Full size image](#)

The 501Y.V2 cluster is phylogenetically distinct from the three main lineages (B.1.1.54, B.1.1.56 and C.1) that were circulating widely in South Africa (>42% of samples sequenced before October 2020) during the first wave of infections¹⁸ (Fig. 2a). These three lineages had been circulating in the KwaZulu–Natal, Western Cape, Gauteng, Free State, Limpopo and North-West provinces. By the middle of November, the 501Y.V2 lineage had superseded the B.1.1.54, B.1.1.56 and C.1 lineages, and it rapidly became the dominant lineage in samples from the Eastern Cape, KwaZulu–Natal and Western Cape (Fig. 2c, Extended Data Fig. 4).

Our spatiotemporal phylogeographic analysis suggests that the 501Y.V2 lineage emerged in early August (95% highest posterior density ranging from the middle of July to the end of August 2020) in Nelson Mandela Bay. Its initial spread to the Garden Route district of the Western Cape was followed by a more-diffuse spread from both of these areas to other regions of the Eastern Cape, and more recently to the City of Cape Town municipality and several locations in KwaZulu–Natal (Fig. 2d). From the City of Cape Town, the variant has travelled north along the west coast of the country to the Namakwa district in the Northern Cape province.

Mutational profile

At the point of first sampling on the 15 October, this lineage had—in addition to D614G—five nonsynonymous mutations resulting in substitutions in the spike protein: D80A, D215G, E484K, N501Y and A701V (Figs. 2b, 3a, Extended Data Fig. 5). A further three mutations that lead to substitutions in the spike protein had emerged by the end of November: L18F, R246I and K417N. We also observe a deletion of three amino acids at positions 242 to 244, which was seen in samples extracted and generated in different laboratories across the NGS-SA. This region is difficult to align; the deletion could potentially also be located at positions 241 to 243, but the resulting sequence would be exactly the same. Although the variants appeared in a varying proportion of the sampled genomes and showed changing levels of frequency with time, the mutations in RBD seem to become fixed in our sampling set, are present in almost all of the samples and are consistently high in frequency across time (Fig. 3a, b). Compared to the previous three largest lineages circulating in South Africa, 501Y.V2 shows marked hypermutation both in the whole genomes and the spike regions—including nonsynonymous mutations that lead to amino acid changes (Fig.

[3c](#)). The main lineages identified in South Africa during first wave (B.1.1.54, B.1.1.56 and C.1) contained only the single nonsynonymous spike mutation (D614G) and did not show the rapid accumulation of mutations, as is observed with 501Y.V2. We estimate that substitutions on the 501Y.V2 lineage are happening at 1.917×10^{-3} nucleotide changes per site per year, compared to 5.344×10^{-4} , 4.251×10^{-4} and 9.781×10^{-4} nucleotide changes per site per year for B.1.1.54, B.1.1.56 and C.1, respectively (Extended Data Fig. [6](#)). We performed structural modelling of the spike trimer with these mutations, which revealed that three of the substitutions (N501Y, E484K and K417N) are at key residues in the RBD; three (L18F, D80A and D215G) are in the N-terminal domain; and one (A701V) is in loop 2 (Fig. [3d](#)). The deletion of three amino acid (242 to 244) also lies in the N-terminal domain. In particular, two of the RBD sites (at positions 417 and 484) are key regions for the binding of neutralizing antibodies (Extended Data Fig. [7](#)).

Fig. 3: Mutational profile of the spike region of the 501Y.V2 lineage.



a, Amino acid changes in the spike region of the 501Y.V2 genomes in this study ($n = 341$) mapped to the spike-protein sequence structure, indicating key regions (such as the RBD). Each spike protein variant is shown at its respective protein location; bar lengths represent the number of genomes that contain the specific mutations. Only mutations that appear in $>10\%$ (grey dotted line) of sequences are shown. The D614G substitution (in black) is already present in the parent lineage. **b**, Changes in the mutation frequency of each variant observed during the course of sampling. Grey bars

show the number of 501Y.V2 sequences sampled at a given time point; coloured lines show the change in the number of sequences that contain each variant at the respective time points. **c**, Violin plots showing the number of nucleotide substitutions and amino acid changes that have accumulated in both the whole genomes and the spike region of the 501Y.V2 lineage ($n = 341$), compared to lineages B.1.1.54 ($n = 472$), B.1.1.56 ($n = 179$) and C.1 ($n = 271$). The dot and error bars inside each group denote the mean and range for two s.d., respectively. **d**, A complete model of the SARS-CoV-2 spike trimer is shown, with domains of a single protomer shown in cartoon view and coloured cyan (N-terminal domain), yellow (C-terminal domain and receptor binding domain), purple (subdomain 1 and 2), and dark green; *N*-acetylglucosamine moieties are coloured in light green. The adjacent protomers are shown in surface view and coloured shades of grey. Eight nonsynonymous mutants (red) and a deletion of three amino acids (pink) that together define the spike of the 501Y.V2 lineage are shown as spheres.

[Full size image](#)

Selection analysis

We examined patterns of nucleotide variation and fluctuations in mutant frequencies at eight polymorphic sites in the spike gene (Fig. 3a) to determine whether any of the observed polymorphisms might contribute to changes in viral fitness worldwide. For this analysis, we used 142,037 high-quality sequences from the Global Initiative On Sharing All Influenza Data (GISAID) sampled between the 24 December 2019 and 14 November 2020, which represented 5,964 unique spike haplotypes. The analysis indicated that two of the three sites in the RBD (E484 and N501) display a pattern of nucleotide variation that is consistent with the site evolving under diversifying positive selection. The N501Y polymorphism that first appears in our sequences sampled on the 15 October shows indications of positive selection on five global-tree internal branches; codon 501 of the spike gene displays a significant excess of nonsynonymous substitutions globally ($dN/dS > 1$ on internal branches, $P = 0.0011$ by the fixed-effects likelihood method), and mutant viruses that encode Y at this site have rapidly increased in frequency in both the UK and South Africa (z score = 11, trend Jonckheere Terpstra non-parametric trend test). Similarly, at codon 484, there is an indication of positive selection on seven global-tree internal branches, with an overall significant excess of nonsynonymous substitutions globally ($P = 0.015$). Outside the RBD, codons 18 ($P < 0.001$), 80 ($P = 0.0014$) and 215 ($P < 0.001$) show evidence of positive diversifying selection globally, and the L18F mutation has also increased in frequency in the regions in which it has occurred (z score = 17). Up until the 14 November 2020, there was no statistical evidence of positive selection at codons 417, 246 and 701.

Discussion

We describe and characterize a newly identified SARS-CoV-2 lineage with several spike mutations that is likely to have emerged in a major metropolitan area in South Africa after the first wave of the epidemic, and then to have spread to multiple locations within two neighbouring provinces. We show that this lineage has rapidly expanded and become dominant in three provinces, at the same time as there has been a rapid resurgence in infections. Although the full import of the mutations is not yet clear, the genomic and epidemiological data suggest that this variant has a selective advantage—from increased transmissibility, immune escape or both. These data highlight the urgent need to refocus the public health response in South Africa on driving transmission down to low levels, not only to reduce hospitalizations and deaths but also to limit the spread of this lineage and the further evolution of the virus.

We detected this variant through intensified genomic surveillance that was enacted in response to a rapid resurgence of cases in the Eastern Cape province²⁰. However, both before and after the detection of 501Y.V2, our genomic surveillance involved the regular sequencing of a random selection of residual samples from routine diagnostic services. We show that 501Y.V2 was detected in samples from 197 health facilities in multiple districts across four provinces. We are therefore confident that, although our sequencing coverage is relatively low, the sequences are representative of the circulating viruses in these provinces. Although the epidemic in the Eastern Cape was contracting from the middle of July to the middle of August (the estimated time to the most-recent common ancestor), this was not a period of low transmission: incidence was above 20 case per 100,000 people per week at this time and the positive testing rate remained above 10%, which suggests moderate-to-high levels of transmission. As there were many lineages circulating at this time, the rapid expansion of 501Y.V2 and the almost complete displacement of other lineages in multiple regions strongly suggest a selective advantage for this variant.

Preliminary modelling suggests that the 501Y.V2 could be approximately 50% more transmissible than the previously circulating variants, although this estimate assumes that natural immunity confers complete protection against reinfection⁶. Increased transmissibility is plausible, given what we know about the spike mutations in 501Y.V2 and what we are learning about similar SARS-CoV-2 variants that are emerging in other locations. The 501Y.V2 lineage has three substitutions that affect key sites in the RBD (K417N, E484K and N501Y). The N501Y substitution has also recently been identified in a lineage that has spread rapidly in the UK (designated B.1.1.7)²¹. There is now good evidence that this lineage is associated with increased transmissibility²². The N501Y substitution has previously been shown through deep mutation scanning, and in a mouse model, to enhance binding affinity to human ACE2^{3,23}. There is some evidence that the E484K substitution may also increase

binding affinity to human ACE2³; and that the combination of N501Y and E484K enhances binding affinity still further^{24,25}. Additional work is being conducted to understand the precise mechanisms that underlie the increased transmissibility of these new variants.

The other reason for a selective advantage of 501Y.V2 could be immune escape (that is, the capacity to cause reinfection). We have very limited SARS-CoV-2 seroprevalence data from South Africa to help us to understand the true extent of the epidemic. In studies that used residual blood samples from routine public sector antenatal and HIV care, seroprevalence in parts of the City of Cape Town was estimated at approximately 40% in July and August (toward the end of the first wave of the epidemic in this area)²⁶. We have shown that the Eastern Cape—and Nelson Mandela Bay, in particular—were worse-affected than City of Cape Town in the first wave, and we therefore believe that population immunity could have been sufficiently high in this region to contribute to population-level selection. The RBD of the spike protein is the main target of neutralizing antibodies that are elicited during SARS-CoV-2 infection²⁷. Neutralizing antibodies to the RBD can be broadly divided into four main classes²⁸. Of these, class 1 and class 2 antibodies appear to be elicited most frequently during SARS-CoV-2 infection, and their epitopes directly overlap the human ACE2 binding site²⁷. Class 2 antibodies bind to E484, and the E484K substitution has previously been shown to confer resistance to neutralizing antibodies in this class and to panels of convalescent sera, which suggests that E484 is a dominant neutralizing epitope^{4,5,29,30,31}. Aside from the RBD, the remaining neutralizing activity is targeted at the N-terminal domain, and some of the N-terminal domain mutations in 501Y.V2 affect residues that form an antigenic supersite or are close to this site^{32,33}. Preliminary evidence from live virus and pseudovirus experiments indicates that 501Y.V2 shows substantial or complete escape from neutralizing antibodies in convalescent plasma^{7,8}. We are currently investigating the frequency of reinfection in the second wave, as well as the clinical presentations of individuals with reinfection to better understand the clinical and epidemiological effects of any immune escape. We are also conducting neutralization assays on plasma from recipients of vaccines, and await results of vaccine efficacy trials conducted in South Africa during the expansion of 501Y.V2.

One hypothesis for the emergence of this lineage (given the large number of mutations relative to the background mutation rate of SARS-CoV-2) is that it may have arisen through intrahost evolution^{34,35,36}. This hypothesis is supported by the long branch length that connects the lineage to the remaining sequences in our phylogenetic tree (Extended Data Fig. 8). The mutation leading to the N501Y substitution is one of several spike mutations that emerged in an immunocompromised individual in the USA who had prolonged viral replication for over 20 weeks³⁴. In South Africa (which has the largest HIV epidemic in the world), one concern has been the possibility of

prolonged viral replication and intrahost evolution in the context of HIV infection, although the limited evidence so far does not suggest that HIV infection is associated with persistent SARS-CoV-2 replication³⁷. However, the observed diversity within this lineage cannot be explained by a single long-term infection in one individual, because the lineage contains circulating intermediate mutants with subsets of the main mutations that characterize the lineage. If evolution within long-term infections were the explanation for the evolution of this lineage, then one would need to invoke a transmission chain that passes through several individuals. Furthermore, antigenic evolution—even within individuals who are not immunosuppressed—could offer an alternative explanation, as several of the individual sites in the spike protein appear to be under selective pressure worldwide and several of the identified mutations have emerged independently around the world (Extended Data Fig. 9) and been found in circulating lineages together.

Although the full implications of the 501Y.V2 lineage in South Africa are yet to be determined, these findings highlight the importance of coordinated molecular surveillance systems in all parts of the world in enabling the early detection and characterization of new lineages and informing the global response to the COVID-19 pandemic.

Methods

No statistical methods were used to predetermine sample size. The experiments were not randomized, and investigators were not blinded to allocation during experiments and outcome assessment.

Epidemiological dynamics

We analysed daily cases of SARS-CoV-2 in South Africa up to 16 January 2020 from publicly released data provided by the National Department of Health and the National Institute for Communicable Diseases. This was accessible through the repository of the Data Science for Social Impact Research Group at the University of Pretoria (<https://github.com/dsfsi/covid19za>)^{38,39}. The National Department of Health releases daily updates on the number of confirmed new cases, deaths and recoveries, with a breakdown by province. We also mapped excess deaths in each province and in South Africa as a whole onto general epidemiological data to determine the extent of potential underreporting of case numbers and gauge the severity of the epidemic. Excess deaths here are defined as the excess natural deaths (in individuals aged 1 year and above) relative to the value predicted from 2018 and 2019 data, setting any negative excesses to zero. We obtained these data from the Report on Weekly Deaths from the South Africa Medical Research Council Burden of Disease Research Unit¹⁶.

We generated estimates for the R_e of SARS-CoV-2 in South Africa from the ‘covid-19-Re’ data repository (<https://github.com/covid-19-Re/dailyRe-Data>) as of the 14 December 2020⁴⁰.

Sampling of SARS-CoV-2

As part of the NGS-SA²⁰, five sequencing hubs receive randomly selected samples for sequencing every week according to approved protocols at each site. These samples include remnant nucleic acid extracts or remnant nasopharyngeal and oropharyngeal swab samples from routine diagnostic SARS-CoV-2 PCR testing from public and private laboratories in South Africa. In response to a rapid resurgence of COVID-19 in the Eastern Cape and the Garden Route district of the Western Cape in November, we enriched our routine sampling with additional samples from those areas. In total, we received samples from over 50 health facilities in the Eastern Cape and Western Cape (Extended Data Fig. [10](#)).

Ethical statement

The project was approved by University of KwaZulu–Natal Biomedical Research Ethics Committee (ref. BREC/00001510/2020), the University of the Witwatersrand Human Research Ethics Committee (HREC) (ref. M180832), Stellenbosch University HREC (ref. N20/04/008_COVID-19) and the University of Cape Town HREC (ref. 383/2020). Individual participant consent was not required for the genomic surveillance. This requirement was waived by the Research Ethics Committees.

Whole-genome sequencing and genome assembly

cDNA synthesis was performed on the extracted RNA using random primers followed by gene-specific multiplex PCR using the ARTIC V3 protocol⁴¹. In brief, extracted RNA was converted to cDNA using the Superscript IV First Strand synthesis system (Life Technologies) and random hexamer primers. SARS-CoV-2 whole-genome amplification was performed by multiplex PCR using primers designed on Primal Scheme (<http://primal.zibraproject.org/>) to generate 400-bp amplicons with an overlap of 70 bp that covers the 30-kb SARS-CoV-2 genome. For nanopore sequencing, we adapted the nCoV-2019 sequencing LoCost protocol v3⁴¹. In brief, PCR reactions were done in 12.5 μ l volumes and no PCR product purification was done. After DNA repair (NEB) and end-prep reactions (NEB), up to 24 samples were barcoded by ligation (EXP-NBD104/NBD114, Oxford Nanopore Technologies). Barcoded samples were pooled, bead-purified and ligated to sequence adapters. After the bead clean-up, the DNA concentration was determined with a Qubit 2.0 instrument (Thermo Fisher). Up to 50 ng of the library in 75 μ l were loaded on a prepared R9.4.1 flow-cell. A

GridION X5 sequencing run was initiated using MinKNOW software with the high-accuracy base-call setting. The NC045512 reference was used for alignment during base-calling and the barcodes were split into different folders. .fastq files were downloaded from the GridION X5 for assembly and further analysis.

For Illumina sequencing, PCR products were cleaned up using AmpureXP purification beads (Beckman Coulter) and quantified using the Qubit dsDNA High Sensitivity assay on the Qubit 4.0 instrument (Life Technologies).

We then used the Illumina Nextera Flex DNA Library Prep kit according to the manufacturer's protocol to prepare indexed paired end libraries of genomic DNA. Sequencing libraries were normalized to 4 nM, pooled and denatured with 0.2 N sodium acetate. A 12 pM sample library was spiked with 1% PhiX (PhiX Control v3 adaptor-ligated library used as a control). We sequenced libraries on a 500-cycle v2 MiSeq Reagent Kit on the Illumina MiSeq instrument (Illumina). Full details of the amplification and sequencing protocol have previously been published^{42,43}.

We assembled paired-end and nanopore .fastq reads using Genome Detective 1.132 (<https://www.genomedetective.com>) and the Coronavirus Typing Tool⁴⁴. For short reads, to accurately call mutations and short insertions and deletions (indels) for SARS-CoV-2, Genome Detective software was updated with an additional assembly step after the de novo assembly and strain identification. When the de novo assembly indicates a nucleotide similarity higher than 97% to the reference strain, a new assembly is made by read mapping against the reference. In this process, for strains satisfying this criterion, reads are mapped using minimap2⁴⁵ against the reference rather than the de novo consensus sequence, and subsequently final mutations and indels are called using GATK HaplotypeCaller⁴⁶, with low-quality variants (with QD < 10) filtered using GATK VariantFiltration⁴⁶. To call the consensus sequence, GATK HaplotypeCaller is used with default settings, followed by GATK VariantFiltration to select only variants with a variant confidence normalized by unfiltered depth of variant samples of at least 10 (QualByDepth \geq 10). For nanopore data, candidate reads are assigned to candidate reference sequences using NCBI blastn with sensitive settings and low gap costs. Candidate reads are then aligned using Annotated Genome Aligner, after which a draft majority consensus sequence is subsequently called, and iteratively improved by realignment of all reads against the draft consensus sequence and realignment of regions with a putative insert against the reference using global alignment (MAFFT). The resulting consensus sequence is further polished by considering and correcting indels of length one or two in homopolymer regions of length four or longer that break the open reading frame (probably sequencing errors). Mutations were confirmed visually with .bam files using Geneious software V2020.1.2 (Biomatters). The reference genome used throughout the assembly process was NC_045512.2 (numbering equivalent to MN908947.3). All

of the sequences were deposited in GISAID (<https://www.gisaid.org/>), and the GISAID accession identifiers are included as part of Supplementary Table 2. Raw reads for our sequences have also been deposited at the NCBI Sequence Read Archive (BioProject accession PRJNA694014).

In some samples, the K417N substitution was previously not called. To avoid an assembly concern, these samples were also analysed using the ARTIC Illumina pipeline (<https://github.com/connor-lab/nco2019-artic-nf>, git revision 9ac3119a87). Results between the two pipelines were highly consistent with respect to the lineage-defining mutations, but also consistent with respect to the missing 22813G>T (K417N) mutation in these samples, despite being considered covered by both pipelines (Supplementary Table 1). In addition, we have implemented a Sanger sequencing method that covers the main RBD sites and this was used to confirm the K417N and other substitutions (that is, E484K and N501Y) in sequences in which we were not confident about the call from next-generation sequencing data. The full sequence properties, mutation and spike mutations of the 501Y.V2 sequences are shown in Supplementary Tables 3, 4.

LoFreq was used to detect minor viral variants to study the intrahost heterogeneity of viral variants (quasi-species)⁴⁷ (Extended Data Fig. 5). Variants were called with a minimum coverage of 10% and conservative false discovery rate *P* value of 0.1. LoFreq models sequencing error rate and implements a Poisson distribution to probe the statistical significance of nucleotide variants at each position, filtering out all variants that fall below the *P* value threshold.

Quality control of genomic sequences from South Africa

We retrieved all SARS-CoV-2 genomes from South Africa from the GISAID database as of the 4 January 2021 (*n* = 2,882). Before phylogenetic reconstruction, we removed low-quality sequences from this dataset. We filtered out genomes that did not pass standard quality assessment parameters used in NextClade (<https://clades.nextstrain.org>). We filtered out 105 genomes from South Africa owing to low coverage, and a further 18 owing to poor sequence quality. Poor sequence quality was defined as sequences with clustered single-nucleotide polymorphisms and ambiguous bases at >10% of sites, and low-coverage genomes were anything with <90% genome coverage against the reference. We therefore analysed a total of 2,756 South African genomes. We also retrieved a global reference dataset (*n* = 2,573). This was selected from the NextStrain global reference dataset, plus the five most similar sequences to each of the sequences from South Africa as defined by a local BLAST search.

Phylogenetic analysis

We initially analysed genomes from South Africa against the global reference dataset using a custom pipeline based on a local version of NextStrain (<https://github.com/nextstrain/ncov>)⁹. The pipeline contains several Python scripts that manage the analysis workflow. It performs an alignment of genomes in MAFFT⁴⁸, phylogenetic tree inference in IQ-Tree V1.6.9⁴⁹, tree dating and ancestral state construction and annotation (<https://github.com/nextstrain/ncov>). The full NextStrain build can be viewed at <https://nextstrain.org/groups/ngs-sa/COVID19-ZA-2021.01.18>.

The initial phylogenetic analysis enabled us to identify a large cluster of sequences ($n = 341$) with multiple spike mutations. We extracted this cluster and constructed a preliminary maximum-likelihood tree in IQ-tree, together with seven basal sequences from the region that were sampled from June to September 2020. We inspected this maximum-likelihood tree in TempEst v.1.5.3 for the presence of a temporal (that is, molecular clock) signal. Linear regression of root-to-tip genetic distances against sampling dates indicated that the SARS-CoV-2 sequences evolved in a relatively strong clock-like manner (correlation coefficient = 0.33, $R^2 = 0.11$) (Extended Data Fig. 6).

We then estimated time-calibrated phylogenies using the Bayesian software package BEAST v.1.10.4. For this analysis, we used the strict molecular clock model, the HKY+I, nucleotide substitution model and the exponential growth coalescent model⁵⁰. We computed Markov chain Monte Carlo (MCMC) in duplicate runs of 100 million states each, sampling every 10,000 steps. Convergence of MCMC chains was checked using Tracer v.1.7.1⁵¹. Maximum clade credibility trees were summarized from the MCMC samples using TreeAnnotator after discarding 10% as burn-in. The phylogenetic trees were visualized using ggplot and ggtree^{52,53}.

Phylogeographic analysis

To model phylogenetic diffusion of the new cluster across the country, we used a flexible relaxed random walk diffusion model that accommodates branch-specific variation in rates of dispersal with a Cauchy distribution⁵⁴. For each sequence, latitude and longitude were attributed to the health facility at which the diagnostic sample was obtained or, if that information was not available, to a point randomly sampled within the local area or district of origin. Given that we do not have access to residential geolocations within the genomic surveillance, the location of the health facility serves as a reasonable proxy, especially as two-thirds of the population live within 2 km of their nearest health facility⁵⁵.

As described in ‘Phylogenetic analysis’, MCMC chains were run in duplicate for 100 million generations and sampled every 10,000 steps, with convergence assessed using Tracer v.1.7.1. Maximum clade credibility trees were summarized using

TreeAnnotator after discarding 10% as burn-in. We used the R package seraphim to extract and map spatiotemporal information embedded in posterior trees.

Lineage classification

We used a previously proposed⁵⁶ dynamic lineage classification method from the ‘Phylogenetic Assignment of Named Global Outbreak Lineages’ (PANGOLIN) software suite (<https://github.com/hCoV-2019/pangolin>). This is aimed at identifying the most epidemiologically important lineages of SARS-CoV-2 at the time of analysis, enabling researchers to monitor the epidemic in a particular geographic region. A lineage is a linear chain of viruses in a phylogenetic tree showing connection from the ancestor to the last descendant. Variant refers to a genetically distinct virus with different mutations to other viruses. For the variant identified in South Africa in this study, we have assigned it the name 501Y.V2; the corresponding PANGO lineage classification is B.1.351 (lineages version 2021-01-06).

Selection analysis

To identify which (if any) of the observed mutations in the spike protein was most likely to increase viral fitness, we used the natural selection analysis of SARS-CoV-2 pipeline (<https://observablehq.com/@spond/revised-sars-cov-2-analytics-page>). This pipeline examines the entire global SARS-CoV-2 nucleotide sequence dataset for evidence of: (i) polymorphisms having arisen in multiple epidemiologically unlinked lineages that have statistical support for non-neutral evolution (mixed effects model of evolution)⁵⁷, (ii) sites at which these polymorphisms have support for a greater-than-expected ratio of nonsynonymous-to-synonymous nucleotide substitution rates on internal branches of the phylogenetic tree (fixed-effects likelihood)⁵⁸ and (iii) whether these polymorphisms have increased in frequency in the regions of the world in which they have occurred.

Structural modelling

We modelled the spike protein on the basis of the Protein Data Bank coordinate set 7A94, showing the first step of the spike protein trimer activation with one RBD domain in the up position, bound to the human ACE2 receptor⁵⁹. We used the Pymol program (The PyMOL Molecular Graphics System, version 2.2.0) for visualization.

Reporting summary

Further information on research design is available in the [Nature Research Reporting Summary](#) linked to this paper.

Data availability

All of the SARS-CoV-2 501Y.V2 genomes generated and presented in this Article are publicly accessible through the GISAID platform (<https://www.gisaid.org/>), along with all other SARS-CoV-2 genomes generated by the NGS-SA. The GISAID accession identifiers of the 501Y.V2 sequences analysed in this study are provided as part of Supplementary Table 2, which also contains the metadata for the sequences. The raw reads for the 501Y.V2 have been deposited at the NCBI Sequence Read Archive (BioProject accession [PRJNA694014](#)). Other raw data for this study are provided as a supplementary dataset at https://github.com/krisp-kwazulu-natal/SARSCoV2_South_Africa_501Y_V2_B_1_351. The reference SARS-CoV-2 genome (MN908947.3) was downloaded from the NCBI database (<https://www.ncbi.nlm.nih.gov/>).

Code availability

All custom scripts to reproduce the analyses and figures presented in this Article are available at https://github.com/krisp-kwazulu-natal/SARSCoV2_South_Africa_501Y_V2_B_1_351.

References

1. 1.

Fontanet, A. et al. SARS-CoV-2 variants and ending the COVID-19 pandemic. *Lancet* **397**, 952–954 (2021).

2. 2.

Mascola, J. R., Graham, B. S. & Fauci, A. S. SARS-CoV-2 viral variants—tackling a moving target. *J. Am. Med. Assoc.* <https://doi.org/10.1001/jama.2021.2088> (2021).

3. 3.

Starr, T. N. et al. Deep mutational scanning of SARS-CoV-2 receptor binding domain reveals constraints on folding and ACE2 binding. *Cell* **182**, 1295–1310 (2020).

[Article](#) [CAS](#) [Google Scholar](#)

4. 4.

Greaney, A. J. et al. Comprehensive mapping of mutations in the SARS-CoV-2 receptor-binding domain that affect recognition by polyclonal human plasma antibodies. *Cell Host Microbe* **29**, 463–476.e6 (2021).

5. 5.

Greaney, A. J. et al. Complete mapping of mutations to the SARS-CoV-2 spike receptor-binding domain that escape antibody recognition. *Cell Host Microbe* **29**, 44–57 (2021).

[Article](#) [CAS](#) [Google Scholar](#)

6. 6.

Pearson, C. A.B. et al. Estimates of severity and transmissibility of novel South Africa SARS-CoV-2 variant 501Y.V2. Preprint at <https://cmmid.github.io/topics/covid19/sa-novel-variant.html> (2021).

7. 7.

Cele, S. et al. Escape of SARS-CoV-2 501Y.V2 from neutralization by convalescent plasma. *Nature* <https://doi.org/10.1038/s41586-021-03471-w> (2021).

8. 8.

Wibmer, C. K. et al. SARS-CoV-2 501Y.V2 escapes neutralization by South African COVID-19 donor plasma. *Nat. Med.* <https://doi.org/10.1038/s41591-021-01285-x> (2021).

9. 9.

Hadfield, J. et al. Nextstrain: real-time tracking of pathogen evolution. *Bioinformatics* **34**, 4121–4123 (2018).

[Article](#) [CAS](#) [Google Scholar](#)

10. 10.

Shu, Y. & McCauley, J. GISAID: global initiative on sharing all influenza data – from vision to reality. *Euro Surveill.* **22**, 30494 (2017).

[Article](#) [Google Scholar](#)

11. 11.

Korber B. et al. Tracking changes in SARS-CoV-2 spike: evidence that D614G increases infectivity of the COVID-19 virus. *Cell* **182**, 812–827 (2020).

[Article](#) [CAS](#) [Google Scholar](#)

12. 12.

Plante, J. A. et al. Spike mutation D614G alters SARS-CoV-2 fitness. *Nature* <https://doi.org/10.1038/s41586-020-2895-3> (2020).

13. 13.

Yurkovetskiy, L. et al. Structural and functional analysis of the D614G SARS-CoV-2 spike protein variant. *Cell* **183**, 739–751 (2020).

[Article](#) [CAS](#) [Google Scholar](#)

14. 14.

Volz, E. et al. Evaluating the effects of SARS-CoV-2 spike mutation D614G on transmissibility and pathogenicity. *Cell* **184**, 64–75 (2021).

[Article](#) [CAS](#) [Google Scholar](#)

15. 15.

Thomson, E. C. et al. Circulating SARS-CoV-2 spike N439K variants maintain fitness while evading antibody-mediated immunity. *Cell* **184**, 1171–1187.e20 (2021).

16. 16.

Bradshaw, D., Laubscher, R., Dorrington, R., Groenewald, P. & Moultrie, T. *Report on Weekly Deaths in South Africa: 1 January – 8 December 2020 (Week 49)* (Burden of Disease Research Unit, South African Medical Research Council, 2020).

17. 17.

Giandhari, J. et al. Early transmission of SARS-CoV-2 in South Africa: an epidemiological and phylogenetic report. *Int. J. Infect. Dis.* **103**, 234–241 (2021).

[Article](#) [CAS](#) [Google Scholar](#)

18. 18.

Tegally, H. et al. Sixteen novel lineages of SARS-CoV-2 in South Africa. *Nat. Med.* **27**, 440–446 (2021).

19. 19.

Blumberg, L. & Frean, J. COVID-19 second wave in South Africa. *National Institute of Communicable Diseases* <https://www.nicd.ac.za/covid-19-second-wave-in-south-africa> (2020).

20. 20.

Msomi, N., Mlisana, K. & de Oliveira, T. A genomics network established to respond rapidly to public health threats in South Africa. *Lancet Microbe* **1**, e229–e230 (2020).

[Article](#) [CAS](#) [Google Scholar](#)

21. 21.

Rambaut, A. et al. Preliminary genomic characterisation of an emergent SARS-CoV-2 lineage in the UK defined by a novel set of spike mutations. *Virological* <https://virological.org/t/preliminary-genomic-characterisation-of-an-emergent-sars-cov-2-lineage-in-the-uk-defined-by-a-novel-set-of-spike-mutations/563> (2020).

22. 22.

Volz, E. et al. Transmission of SARS-CoV-2 lineage B.1.1.7 in England: insights from linking epidemiological and genetic data. Preprint at <https://doi.org/10.1101/2020.12.30.20249034> (2021).

23. 23.

Gu, H. et al. Adaptation of SARS-CoV-2 in BALB/c mice for testing vaccine efficacy. *Science* **369**, 1603–1607 (2020).

[ADS](#) [Article](#) [CAS](#) [Google Scholar](#)

24. 24.

Nelson, G. et al. Molecular dynamic simulation reveals E484K mutation enhances spike RBD–ACE2 affinity and the combination of E484K, K417N and N501Y mutations (501Y.V2 variant) induces conformational change greater than N501Y mutant alone, potentially resulting in an escape mutant. Preprint at <https://doi.org/10.1101/2021.01.13.426558> (2021).

25. 25.

Zahradník J. et al. SARS-CoV-2 RBD in vitro evolution follows contagious mutation spread, yet generates an able infection inhibitor. Preprint at <https://doi.org/10.1101/2021.01.06.425392> (2021).

26. 26.

Hsiao, M. et al. SARS-CoV-2 seroprevalence in the Cape Town metropolitan sub-districts after the peak of infections. *NICD COVID-19 Special Public Health Surveill. Bull.* **18**, 1–9 (2020).

[Google Scholar](#)

27. 27.

Piccoli, L. et al. Mapping neutralizing and immunodominant sites on the SARS-CoV-2 spike receptor-binding domain by structure-guided high-resolution serology. *Cell* **183**, 1024–1042 (2020).

[Article](#) [CAS](#) [Google Scholar](#)

28. 28.

Barnes, C. O. et al. SARS-CoV-2 neutralizing antibody structures inform therapeutic strategies. *Nature* **588**, 682–687 (2020).

[ADS](#) [Article](#) [CAS](#) [Google Scholar](#)

29. 29.

Baum, A. et al. Antibody cocktail to SARS-CoV-2 spike protein prevents rapid mutational escape seen with individual antibodies. *Science* **369**, 1014–1018 (2020).

[ADS](#) [Article](#) [CAS](#) [Google Scholar](#)

30. 30.

Liu, Z. et al. Identification of SARS-CoV-2 spike mutations that attenuate monoclonal and serum antibody neutralization. *Cell Host Microbe* **29**, 477–488.e4 (2021).

31. 31.

Weisblum, Y. et al. Escape from neutralizing antibodies by SARS-CoV-2 spike protein variants. *eLife* **9**, e61312 (2020).

[Article](#) [CAS](#) [Google Scholar](#)

32. 32.

Chi, X. et al. A neutralizing human antibody binds to the N-terminal domain of the spike protein of SARS-CoV-2. *Science* **369**, 650–655 (2020).

[ADS](#) [Article](#) [CAS](#) [Google Scholar](#)

33. 33.

McCallum, M. et al. N-terminal domain antigenic mapping reveals a site of vulnerability for SARS-CoV-2. *Cell* <https://doi.org/10.1016/j.cell.2021.03.028> (2021).

34. 34.

Choi, B. et al. Persistence and evolution of SARS-CoV-2 in an immunocompromised host. *N. Engl. J. Med.* **383**, 2291–2293 (2020).

[Article](#) [Google Scholar](#)

35. 35.

Avanzato, V. A. et al. Case study: prolonged infectious SARS-CoV-2 shedding from an asymptomatic immunocompromised individual with cancer. *Cell* **183**, 1901–1912 (2020).

[Article](#) [CAS](#) [Google Scholar](#)

36. 36.

Kemp, S. A. et al. SARS-CoV-2 evolution during treatment of chronic infection. *Nature* <https://doi.org/10.1038/s41586-021-03291-y> (2021).

37. 37.

Karim, F. et al. HIV infection alters SARS-CoV-2 responsive immune parameters but not clinical outcomes in COVID-19 disease. Preprint at <https://doi.org/10.1101/2020.11.23.20236828> (2020).

38. 38.

Marivate, V. & Combrink, H. M. Use of available data to inform the COVID-19 outbreak in South Africa: a case study. *Data Sci. J.* **19**, 19 (2020).

[Article](#) [CAS](#) [Google Scholar](#)

39. 39.

Marivate, V. et al. Coronavirus disease (COVID-19) case data – South Africa <https://zenodo.org/record/3732419#.YBXzFegzZPY> (2020).

40. 40.

Huisman, J. S. et al. Estimation and worldwide monitoring of the effective reproductive number of SARS-CoV-2. Preprint at <https://doi.org/10.1101/2020.11.26.20239368> (2020).

41. 41.

Quick, J. nCoV-2019 sequencing protocol v3 (LoCost) V.3. *protocols.io* <https://www.protocols.io/view/ncov-2019-sequencing-protocol-v3-locost-bh42j8ye> (2020).

42. 42.

Giandhari, J. et al. NEBnext library construction and sequencing for SARS-CoV-2: adapting COVID-19 ARTIC protocol. *protocol.io* <https://www.protocols.io/view/nebnext-library-construction-and-sequencing-for-sa-bhu2j6ye> (2020).

43. 43.

Pillay, S. et al. Whole genome sequencing of SARS-CoV-2: adapting Illumina protocols for quick and accurate outbreak investigation during a pandemic. *Genes* **11**, 949 (2020).

[Article](#) [CAS](#) [Google Scholar](#)

44. 44.

Cleemput, S. et al. Genome detective coronavirus typing tool for rapid identification and characterization of novel coronavirus genomes. *Bioinformatics* **36**, 3552–3555 (2020).

[Article](#) [CAS](#) [Google Scholar](#)

45. 45.

Li, H. Minimap2: pairwise alignment for nucleotide sequences. *Bioinformatics* **34**, 3094–3100 (2018).

[Article](#) [CAS](#) [Google Scholar](#)

46. 46.

McKenna, A. et al. The Genome Analysis Toolkit: a MapReduce framework for analyzing next-generation DNA sequencing data. *Genome Res.* **20**, 1297–1303 (2010).

[Article](#) [CAS](#) [Google Scholar](#)

47. 47.

Wilm, A. et al. LoFreq: a sequence-quality aware, ultra-sensitive variant caller for uncovering cell-population heterogeneity from high-throughput sequencing datasets. *Nucleic Acids Res.* **40**, 11189–11201 (2012).

[Article](#) [CAS](#) [Google Scholar](#)

48. 48.

Katoh, K. & Standley, D. M. MAFFT multiple sequence alignment software version 7: improvements in performance and usability. *Mol. Biol. Evol.* **30**, 772–780 (2013).

[Article](#) [CAS](#) [Google Scholar](#)

49. 49.

Nguyen, L. T., Schmidt, H. A., von Haeseler, A. & Minh, B. Q. IQ-TREE: a fast and effective stochastic algorithm for estimating maximum-likelihood phylogenies. *Mol. Biol. Evol.* **32**, 268–274 (2015).

[Article](#) [CAS](#) [Google Scholar](#)

50. 50.

Griffiths, R. C. & Tavaré, S. Sampling theory for neutral alleles in a varying environment. *Phil. Trans. R. Soc. Lond. B* **344**, 403–410 (1994).

[ADS](#) [Article](#) [CAS](#) [Google Scholar](#)

51. 51.

Rambaut, A., Drummond, A. J., Xie, D., Baele, G. & Suchard, M. A. Posterior summarization in Bayesian phylogenetics using Tracer 1.7. *Syst. Biol.* **67**, 901–904 (2018).

[Article](#) [CAS](#) [Google Scholar](#)

52. 52.

Wickham, H. *ggplot2: Elegant Graphics for Data Analysis* (Springer 2016).

53. 53.

Yu, G., Smith, D. K., Zhu, H., Guan, Y. & Lam, T. T. Y. ggtree: an R package for visualization and annotation of phylogenetic trees with their covariates and other associated data. *Methods Ecol. Evol.* **8**, 28–36 (2017).

[Article](#) [Google Scholar](#)

54. 54.

Lemey, P., Rambaut, A., Welch, J. J. & Suchard, M. A. Phylogeography takes a relaxed random walk in continuous space and time. *Mol. Biol. Evol.* **27**, 1877–1885 (2010).

[Article](#) [CAS](#) [Google Scholar](#)

55. 55.

McLaren, Z. M., Ardington, C. & Leibbrandt, M. Distance decay and persistent health care disparities in South Africa. *BMC Health Serv. Res.* **14**, 541 (2014).

[Article](#) [Google Scholar](#)

56. 56.

Rambaut, A. et al. A dynamic nomenclature proposal for SARS-CoV-2 lineages to assist genomic epidemiology. *Nat. Microbiol.* **5**, 1403–1407 (2020).

[Article](#) [CAS](#) [Google Scholar](#)

57. 57.

Murrell, B. et al. Detecting individual sites subject to episodic diversifying selection. *PLoS Genet.* **8**, e1002764 (2012).

[Article](#) [CAS](#) [Google Scholar](#)

58. 58.

Kosakovsky Pond, S. L. & Frost, S. D. Not so different after all: a comparison of methods for detecting amino acid sites under selection. *Mol. Biol. Evol.* **22**, 1208–1222 (2005).

[Article](#) [CAS](#) [Google Scholar](#)

59. 59.

Benton, D. J. et al. Receptor binding and priming of the spike protein of SARS-CoV-2 for membrane fusion. *Nature* **588**, 327–330 (2020).

[ADS](#) [Article](#) [CAS](#) [Google Scholar](#)

[Download references](#)

Acknowledgements

We thank K. Deforche, W. Dumon and S. Cleemput at Emweb for their invaluable help in improving genome assembly and variant calling for SARS-CoV-2, which was central to the achievement of this work; and the global laboratories that generated and made public the SARS-CoV-2 sequences (through GISAID) used as reference dataset in this study (a complete list of individual contributors of sequences is provided in Supplementary Table 5). This research reported in this publication was supported by the Strategic Health Innovation Partnerships Unit of the South African Medical Research Council, with funds received from the South African Department of Science and Innovation.

Author information

Author notes

1. These authors contributed equally: Houriiyah Tegally, Eduan Wilkinson, Marta Giovanetti, Arash Iranzadeh
2. These authors jointly supervised this work: Jinal N. Bhiman, Carolyn Williamson, Tulio de Oliveira

Affiliations

1. KwaZulu–Natal Research Innovation and Sequencing Platform (KRISP), School of Laboratory Medicine and Medical Sciences, University of KwaZulu–Natal, Durban, South Africa
Houriiyah Tegally, Eduan Wilkinson, Vagner Fonseca, Jennifer Giandhari, Sureshnee Pillay, Emmanuel James San, Richard J. Lessells & Tulio de Oliveira
2. Laboratorio de Flavivirus, Fundacao Oswaldo Cruz, Rio de Janeiro, Brazil
Marta Giovanetti & Luiz Carlos Junior Alcantara
3. Laboratório de Genética Celular e Molecular, Universidade Federal de Minas Gerais, Belo Horizonte, Brazil
Marta Giovanetti, Vagner Fonseca & Luiz Carlos Junior Alcantara
4. Computational Biology Division, Department of Integrative Biomedical Sciences, University of Cape Town, Cape Town, South Africa
Arash Iranzadeh & Darren Martin
5. Division of Medical Virology, Institute of Infectious Disease and Molecular Medicine, University of Cape Town, Cape Town, South Africa
Deelan Doolabh, Lynn Tyers, Innocent Mudau, Darren Martin & Carolyn Williamson
6. Discipline of Virology, School of Laboratory Medicine and Medical Sciences and National Health Laboratory Service (NHLs), University of KwaZulu–Natal, Durban, South Africa
Nokukhanya Msomi

7. NHLS, Johannesburg, South Africa

Koleka Mlisana

8. Centre for the AIDS Programme of Research in South Africa (Cape Town),
Durban, South Africa

Koleka Mlisana, Richard J. Lessells, Carolyn Williamson & Tullio de Oliveira

9. National Institute for Communicable Diseases, NHLS, Johannesburg, South Africa

Anne von Gottberg, Sibongile Walaza, Mushal Allam, Arshad Ismail, Thabo Mohale, Constantinos Kurt Wibmer & Jinal N. Bhiman

10. School of Pathology, Faculty of Health Sciences, University of the Witwatersrand, Johannesburg, South Africa

Anne von Gottberg, Allison J. Glass & Jinal N. Bhiman

11. School of Public Health, Faculty of Health Sciences, University of the Witwatersrand, Johannesburg, South Africa

Sibongile Walaza

12. Department of Molecular Pathology, Lancet Laboratories, Johannesburg, South Africa

Allison J. Glass

13. Division of Medical Virology, Faculty of Medicine and Health Sciences, Stellenbosch University and NHLS Tygerberg Hospital, Cape Town, South Africa

Susan Engelbrecht, Gert Van Zyl & Wolfgang Preiser

14. Centre for Quantum Technology, University of KwaZulu-Natal, Durban, South Africa

Francesco Petruccione

15. National Institute for Theoretical Physics (NITheP), University of KwaZulu-Natal, Durban, South Africa

Francesco Petruccione

16. Africa Health Research Institute, Durban, South Africa

Alex Sigal

17. School of Laboratory Medicine and Medical Sciences, University of KwaZulu–Natal, Durban, South Africa

Alex Sigal

18. Max Planck Institute for Infection Biology, Berlin, Germany

Alex Sigal

19. Division of Medical Virology, NHLS Groote Schuur Hospital, University of Cape Town, Cape Town, South Africa

Diana Hardie, Gert Marais, Nei-yuan Hsiao, Stephen Korsman & Carolyn Williamson

20. Centre for Infectious Disease Epidemiology and Research, University of Cape Town, Cape Town, South Africa

Mary-Ann Davies

21. Western Cape Government: Health, Cape Town, South Africa

Mary-Ann Davies

22. Molecular Diagnostics Services, Durban, South Africa

Denis York

23. Department of Quality Leadership, Netcare Hospitals, Johannesburg, South Africa

Caroline Maslo

24. Division of Virology, NHLS Universitas Academic Laboratories, University of The Free State, Bloemfontein, South Africa

Dominique Goedhals

25. NHLS, Port Elizabeth, South Africa

Shareef Abrahams & Oluwakemi Laguda-Akingba

26. Department of Laboratory Medicine and Pathology, Faculty of Health Sciences,
Walter Sisulu University, Mthatha, South Africa

Oluwakemi Laguda-Akingba

27. Division of Medical Virology, Department of Pathology, University of Cape
Town, Cape Town, South Africa

Arghavan Alisoltani-Dehkordi

28. Division of Biomedical Sciences, University of California Riverside School of
Medicine, Riverside, CA, USA

Arghavan Alisoltani-Dehkordi & Adam Godzik

29. Structural Biology Research Unit, Department of Integrative Biomedical
Sciences, University of Cape Town, Cape Town, South Africa

Bryan Trevor Sewell

30. Department of Zoology, University of Oxford, Oxford, UK

José Lourenço

31. Institute for Genomics and Evolutionary Medicine, Temple University,
Philadelphia, PA, USA

Sergei L. Kosakovsky Pond & Steven Weaver

32. Department of Global Health, University of Washington, Seattle, WA, USA

Tulio de Oliveira

Authors

1. Houriiyah Tegally

[View author publications](#)

You can also search for this author in [PubMed](#) [Google Scholar](#)

2. Eduan Wilkinson

[View author publications](#)

You can also search for this author in [PubMed](#) [Google Scholar](#)

3. Marta Giovanetti

[View author publications](#)

You can also search for this author in [PubMed](#) [Google Scholar](#)

4. Arash Iranzadeh

[View author publications](#)

You can also search for this author in [PubMed](#) [Google Scholar](#)

5. Vagner Fonseca

[View author publications](#)

You can also search for this author in [PubMed](#) [Google Scholar](#)

6. Jennifer Giandhari

[View author publications](#)

You can also search for this author in [PubMed](#) [Google Scholar](#)

7. Deelan Doolabh

[View author publications](#)

You can also search for this author in [PubMed](#) [Google Scholar](#)

8. Sureshnee Pillay

[View author publications](#)

You can also search for this author in [PubMed](#) [Google Scholar](#)

9. Emmanuel James San

[View author publications](#)

You can also search for this author in [PubMed](#) [Google Scholar](#)

10. Nokukhanya Msomi

[View author publications](#)

You can also search for this author in [PubMed](#) [Google Scholar](#)

11. Koleka Mlisana

[View author publications](#)

You can also search for this author in [PubMed](#) [Google Scholar](#)

12. Anne von Gottberg
[View author publications](#)

You can also search for this author in [PubMed](#) [Google Scholar](#)

13. Sibongile Walaza
[View author publications](#)

You can also search for this author in [PubMed](#) [Google Scholar](#)

14. Mushal Allam
[View author publications](#)

You can also search for this author in [PubMed](#) [Google Scholar](#)

15. Arshad Ismail
[View author publications](#)

You can also search for this author in [PubMed](#) [Google Scholar](#)

16. Thabo Mohale
[View author publications](#)

You can also search for this author in [PubMed](#) [Google Scholar](#)

17. Allison J. Glass
[View author publications](#)

You can also search for this author in [PubMed](#) [Google Scholar](#)

18. Susan Engelbrecht
[View author publications](#)

You can also search for this author in [PubMed](#) [Google Scholar](#)

19. Gert Van Zyl
[View author publications](#)

You can also search for this author in [PubMed](#) [Google Scholar](#)

20. Wolfgang Preiser
[View author publications](#)

You can also search for this author in [PubMed](#) [Google Scholar](#)

21. Francesco Petruccione
[View author publications](#)

You can also search for this author in [PubMed](#) [Google Scholar](#)

22. Alex Sigal
[View author publications](#)

You can also search for this author in [PubMed](#) [Google Scholar](#)

23. Diana Hardie
[View author publications](#)

You can also search for this author in [PubMed](#) [Google Scholar](#)

24. Gert Marais
[View author publications](#)

You can also search for this author in [PubMed](#) [Google Scholar](#)

25. Nei-yuan Hsiao
[View author publications](#)

You can also search for this author in [PubMed](#) [Google Scholar](#)

26. Stephen Korsman
[View author publications](#)

You can also search for this author in [PubMed](#) [Google Scholar](#)

27. Mary-Ann Davies
[View author publications](#)

You can also search for this author in [PubMed](#) [Google Scholar](#)

28. Lynn Tyers
[View author publications](#)

You can also search for this author in [PubMed](#) [Google Scholar](#)

29. Innocent Mudau
[View author publications](#)

You can also search for this author in [PubMed](#) [Google Scholar](#)

30. Denis York

[View author publications](#)

You can also search for this author in [PubMed](#) [Google Scholar](#)

31. Caroline Maslo

[View author publications](#)

You can also search for this author in [PubMed](#) [Google Scholar](#)

32. Dominique Goedhals

[View author publications](#)

You can also search for this author in [PubMed](#) [Google Scholar](#)

33. Shareef Abrahams

[View author publications](#)

You can also search for this author in [PubMed](#) [Google Scholar](#)

34. Oluwakemi Laguda-Akingba

[View author publications](#)

You can also search for this author in [PubMed](#) [Google Scholar](#)

35. Arghavan Alisoltani-Dehkordi

[View author publications](#)

You can also search for this author in [PubMed](#) [Google Scholar](#)

36. Adam Godzik

[View author publications](#)

You can also search for this author in [PubMed](#) [Google Scholar](#)

37. Constantinos Kurt Wibmer

[View author publications](#)

You can also search for this author in [PubMed](#) [Google Scholar](#)

38. Bryan Trevor Sewell

[View author publications](#)

You can also search for this author in [PubMed](#) [Google Scholar](#)

39. José Lourenço
[View author publications](#)

You can also search for this author in [PubMed](#) [Google Scholar](#)

40. Luiz Carlos Junior Alcantara
[View author publications](#)

You can also search for this author in [PubMed](#) [Google Scholar](#)

41. Sergei L. Kosakovsky Pond
[View author publications](#)

You can also search for this author in [PubMed](#) [Google Scholar](#)

42. Steven Weaver
[View author publications](#)

You can also search for this author in [PubMed](#) [Google Scholar](#)

43. Darren Martin
[View author publications](#)

You can also search for this author in [PubMed](#) [Google Scholar](#)

44. Richard J. Lessells
[View author publications](#)

You can also search for this author in [PubMed](#) [Google Scholar](#)

45. Jinal N. Bhiman
[View author publications](#)

You can also search for this author in [PubMed](#) [Google Scholar](#)

46. Carolyn Williamson
[View author publications](#)

You can also search for this author in [PubMed](#) [Google Scholar](#)

47. Túlio de Oliveira
[View author publications](#)

You can also search for this author in [PubMed](#) [Google Scholar](#)

Contributions

J.G., S.P., S.E., D.D., L.T., I.M. and A. Ismail produced SARS-CoV-2 genomic data. N.M., K.M., N.-y.H., D.Y., D.G., A.v.G., S.W., A.J.G., A.S., G.V.Z., W.P., S.K., D.H., C.W., G.M., D.D., I.M., L.T., C.M., O.L.-A., T.M. and S.A. collected samples and curated metadata. H.T., E.W., M.G., A. Iranzadeh, R.J.L., S.L.K.P., S. Weaver, D.M., J.G., S.P., E.J.S., S.E., F.P., A. Ismail, J.N.B., V.F., J.L., L.C.J.A., A.A.-D., A.G., B.T.S., C.K.W., M.A., C.W. and T.d.O. analysed the data. C.W., M.-A.D., D.H., N.-y.H., D.M., D.G., E.J.S., M.G., J.L., L.C.J.A. and T.d.O. helped with study design and data interpretation. R.J.L., H.T., E.W., M.G., D.M. and T.d.O. wrote the initial manuscript, which was reviewed by all authors.

Corresponding author

Correspondence to [Tulio de Oliveira](#).

Ethics declarations

Competing interests

The authors declare no competing interests.

Additional information

Peer review information *Nature* thanks Nathan Grubaugh, Tommy Tsan-Yuk Lam, Youchun Wang and the other, anonymous, reviewer(s) for their contribution to the peer review of this work. Peer reviewer reports are available.

Publisher's note Springer Nature remains neutral with regard to jurisdictional claims in published maps and institutional affiliations.

Extended data figures and tables

[Extended Data Fig. 1 Excess deaths per million individuals by province and metropolitan municipalities of South Africa.](#)

Data are shown for up until the week ending 8 September 2020 (immediately after the first peak of the epidemic peak). **a, b**, These graphs indicate the disproportionate effect of the first wave of the epidemic in the province of the Eastern Cape (**a**) and its metropolitan areas (Nelson Mandela Bay and Buffalo City) (**b**). EC, Eastern Cape; FS, Free State; WC, Western Cape; GP, Gauteng province; NC, Northern Cape; KZN, KwaZulu-Natal; MP, Mpumalanga; NW, North West; NMB, Nelson Mandela Bay; BUF, Buffalo City; CPT, Cape Town; MAN, Mangaung; EKU, Ekurhuleni; JHB, Johannesburg; TSH, Tshwane; ETH, Etheekwini.

Extended Data Fig. 2 Positivity test rates across four provinces of South Africa.

Maps of the Northern Cape, Western Cape, the Eastern Cape and KwaZulu–Natal (the four provinces investigated in this Article) showing a weekly progression of SARS-CoV-2 prevalence per district, coloured by the rate of positive SARS-CoV-2 PCR tests per district. Data were obtained from the weekly testing report of the National Institute of Communicable Diseases. The .shapefile for this map was obtained from ArcGIS.

Extended Data Fig. 3 Sampling location of 501Y.V2 genomes.

A general map of South Africa, showing the sampling location of the 501Y.V2 genomes in this study (blue dots) in relation to the main road networks of the country, which hints at potential land transmission routes of this lineage along the coast. The .shapefile for this map was obtained from ArcGIS.

Extended Data Fig. 4 Replacement of other lineages by the 501Y.V2 lineage.

a, Progression of SARS-CoV-2 PANGOLIN lineages circulating in South Africa from March to December 2020, showing the overrepresentation of the 501Y.V2 lineage from October onwards (B.1.351, in off-white). **b**, Independent regional phylogenetic trees for the Eastern Cape, KwaZulu–Natal, Western Cape and Northern Cape, showing a variety of circulating lineages before October and the dominance of 501Y.V2 (in yellow) in late October and November (especially in the Western Cape and Eastern Cape).

Extended Data Fig. 5 Overview of mutations associated with the 501Y.V2 lineage.

a, All nucleotide substitutions present in more than 10% of the genomes in the 501Y.V2 lineage, mapped on the SARS-CoV-2 genomic structure. Mutations present in the parent lineage (B.1) are marked in black, and mutations specific to the 501Y.V2 lineage are marked in red or blue. All

nonsynonymous mutations are in bold (also reported in **b**). Blue, location of deletions on the genomes of the 501Y.V2 lineage. This is an unresolvable ambiguity in the representation of the exact location of the 22286–22294 nucleotide deletion; because of a repeat region that is hard to align (CTTT), the deletion could be any nine-nucleotide segment between 22281–22289 and 22286–22294. This means that, technically, the deletion could also be in amino acids 241–243; however, the resulting amino acid sequence of all of the possibilities are exactly the same (OTLH). **b**, Summary of all nonsynonymous lineage-defining changes in relevant genes that occur in the 501Y.V2 lineage. **c**, Allele proportions at each 501Y.V2 lineage-defining mutation site. Black line and dots, mutant allele proportion; grey line and dots, reference allele proportion in individual samples in three sequencing runs.

Extended Data Fig. 6 Molecular clock signal of four main virus clusters that are spreading in South-Africa.

Root-to-tip regression obtained from TempEst analysis for the 501Y.V2 lineage cluster ($n = 341$), showing a relatively strong clock-like behaviour (correlation coefficient = 0.33, $R^2 = 0.107$) and a regression line slope, representing mean evolutionary rate, of 1.917×10^{-3} nucleotide changes per site per year. We compare this with the root-to-tip regressions of the B.1.1.54 ($n = 472$), B.1.1.56 ($n = 179$) and C.1 ($n = 271$) lineages, which show estimated mean evolutionary rates of 5.344×10^{-4} , 4.251×10^{-4} and 9.781×10^{-4} respectively. Regression lines are shown with error buffers (shaded area) that represent 90% confidence intervals.

Extended Data Fig. 7 SARS-CoV-2 RBD interactions with neutralizing antibodies.

Model of the SARS-CoV-2 RBD in cartoon view (yellow), showing representative Fab domains for neutralizing antibodies (NAbs) from classes 1, 2, 3 and 4. Two zoomed-in insets show common, key interactions between the RBD residue K417 and class 1 neutralizing antibodies and the RBD residue E484 and class 2 neutralizing antibodies.

Extended Data Fig. 8 A maximum-likelihood tree of 5,332 SARS-CoV-2 genomes, of which 2,756 are sampled from South Africa.

The branch lengths represent the diversity of the genomes against the Wuhan reference. The 501Y.V2 lineages (in yellow) show relatively longer branches, compared to viral genomes from South Africa that form lineages circulating in the country before the detection of this new lineage.

Extended Data Fig. 9 Worldwide emergence of eight spike mutations.

Prevalence of the eight spike mutations around the world, which indicates that several of these mutations have emerged independently in multiple regions.

Extended Data Fig. 10 Random sampling of 501Y.V2 samples across health centres in four provinces.

Number of health centres per province in which the 501Y.V2 lineage was detected in sampled genomes (for each of the 4 provinces), showing a total number of 317 samples from 197 health centres. There was no indication of health facility for the remaining 501Y.V2 samples presented in this study.

Supplementary information

Supplementary Tables

This file contains Supplementary Tables 1-5.

Reporting Summary

Peer Review File

Rights and permissions

[Reprints and Permissions](#)

About this article



Check for
updates

Cite this article

Tegally, H., Wilkinson, E., Giovanetti, M. *et al.* Detection of a SARS-CoV-2 variant of concern in South Africa. *Nature* **592**, 438–443 (2021).
<https://doi.org/10.1038/s41586-021-03402-9>

[Download citation](#)

- Received: 21 December 2020
- Accepted: 26 February 2021
- Published: 09 March 2021
- Issue Date: 15 April 2021
- DOI: <https://doi.org/10.1038/s41586-021-03402-9>

Further reading

- [**Detecting Rapid Spread of SARS-CoV-2 Variants, France, January 26–February 16, 2021**](#)
 - Stéphanie Haim-Boukobza
 - , Bénédicte Roquebert
 - , Sabine Trombert-Paolantoni
 - , Emmanuel Lecorche
 - , Laura Verdurme

- , Vincent Foulongne
- , Christian Selinger
- , Yannis Michalakis
- , Mircea T. Sofonea
- & Samuel Alizon

Emerging Infectious Diseases (2021)

- **Molecular detection of SARS-CoV-2 being challenged by virus variation and asymptomatic infection**

- Congshan Jiang
- , Xiaowei Li
- , Changrong Ge
- , Yuanyuan Ding
- , Tao Zhang
- , Shuai Cao
- , Liesu Meng
- & Shemin Lu

Journal of Pharmaceutical Analysis (2021)

- **Effects of SARS-CoV-2 variants on vaccine efficacy and response strategies**

- Lianlian Bian
- , Fan Gao
- , Jialu Zhang
- , Qian He
- , Qunying Mao
- , Miao Xu
- & Zhenglun Liang

Expert Review of Vaccines (2021)

- **SARS-CoV-2 one year on: evidence for ongoing viral adaptation**

- Thomas P. Peacock
- , Rebekah Penrice-Randal
- , Julian A. Hiscox
- & Wendy S. Barclay

Journal of General Virology (2021)

- **Complete map of SARS-CoV-2 RBD mutations that escape the monoclonal antibody LY-CoV555 and its cocktail with LY-CoV016**

- Tyler N. Starr
- , Allison J. Greaney
- , Adam S. Dingens
- & Jesse D. Bloom

Cell Reports Medicine (2021)

Comments

By submitting a comment you agree to abide by our [Terms](#) and [Community Guidelines](#). If you find something abusive or that does not comply with our terms or guidelines please flag it as inappropriate.

[Download PDF](#)

This article was downloaded by **calibre** from <https://www.nature.com/articles/s41586-021-03402-9>

- Article
- [Published: 24 March 2021](#)

Auto-aggressive CXCR6⁺ CD8 T cells cause liver immune pathology in NASH

- [Michael Dudek](#)¹,
- [Dominik Pfister](#) [ORCID: orcid.org/0000-0002-0542-2638](#)²,
- [Sainitin Donakonda](#) [ORCID: orcid.org/0000-0003-3216-8759](#)^{1,3},
- [Pamela Filpe](#)⁴,
- [Annika Schneider](#)¹,
- [Melanie Laschinger](#)⁵,
- [Daniel Hartmann](#)⁵,
- [Norbert Hüser](#)⁵,
- [Philippa Meiser](#)¹,
- [Felix Bayerl](#)¹,
- [Donato Inverso](#) [ORCID: orcid.org/0000-0003-0987-3345](#)^{6,7},
- [Jennifer Wigger](#)⁴,
- [Marcial Sebode](#)⁴,
- [Rupert Öllinger](#)⁸,
- [Roland Rad](#) [ORCID: orcid.org/0000-0002-6849-9659](#)⁸,
- [Silke Hegenbarth](#)¹,
- [Martina Anton](#) [ORCID: orcid.org/0000-0001-5290-5213](#)¹,
- [Adrien Guillot](#) [ORCID: orcid.org/0000-0002-6002-9986](#)⁹,
- [Andrew Bowman](#) [ORCID: orcid.org/0000-0002-7609-8687](#)¹⁰,
- [Danijela Heide](#)²,
- [Florian Müller](#)²,
- [Pierluigi Ramadori](#)²,

- [Valentina Leone](#)^{11,12},
- [Cristina Garcia-Caceres](#)¹³,
- [Tim Gruber](#)¹³,
- [Gabriel Seifert](#) [ORCID: orcid.org/0000-0003-3771-2186](#)¹⁴,
- [Agnieszka M. Kabat](#) [ORCID: orcid.org/0000-0003-1916-5983](#)¹⁵,
- [Jan-Philipp Malm](#) [ORCID: orcid.org/0000-0002-7059-4030](#)¹⁶,
- [Simon Reider](#) [ORCID: orcid.org/0000-0002-0578-9843](#)^{17,18},
- [Maria Effenberger](#) [ORCID: orcid.org/0000-0002-0499-9953](#)¹⁷,
- [Susanne Roth](#)¹⁹,
- [Adrian T. Billeter](#)¹⁹,
- [Beat Müller-Stich](#)¹⁹,
- [Edward J. Pearce](#) [ORCID: orcid.org/0000-0003-1001-9656](#)¹⁵,
- [Friedrich Koch-Nolte](#)²⁰,
- [Rafael Käser](#)²¹,
- [Herbert Tilg](#) [ORCID: orcid.org/0000-0002-4235-2579](#)¹⁷,
- [Robert Thimme](#) [ORCID: orcid.org/0000-0003-1417-4135](#)²¹,
- [Tobias Böttler](#) [ORCID: orcid.org/0000-0002-1195-055X](#)²¹,
- [Frank Tacke](#)⁹,
- [Jean-Francois Dufour](#) [ORCID: orcid.org/0000-0002-8062-1346](#)²²,
- [Dirk Haller](#) [ORCID: orcid.org/0000-0002-6977-4085](#)²³,
- [Peter J. Murray](#)^{1,24},
- [Ron Heeren](#) [ORCID: orcid.org/0000-0002-6533-7179](#)¹⁰,
- [Dietmar Zehn](#) [ORCID: orcid.org/0000-0003-1393-8527](#)²⁵,
- [Jan P. Böttcher](#) [ORCID: orcid.org/0000-0002-8163-8107](#)¹,
- [Mathias Heikenwälder](#) [ORCID: orcid.org/0000-0002-3135-2274](#)² &
- [Percy A. Knolle](#) [ORCID: orcid.org/0000-0003-2983-0414](#)^{1,3,25}

[Nature](#) volume **592**, pages444–449(2021) [Cite this article](#)

- 8695 Accesses
- 1 Citations
- 185 Altmetric

- [Metrics details](#)

Subjects

- [Chronic inflammation](#)
- [Lymphocyte activation](#)

Abstract

Nonalcoholic steatohepatitis (NASH) is a manifestation of systemic metabolic disease related to obesity, and causes liver disease and cancer^{1,2}. The accumulation of metabolites leads to cell stress and inflammation in the liver³, but mechanistic understandings of liver damage in NASH are incomplete. Here, using a preclinical mouse model that displays key features of human NASH (hereafter, NASH mice), we found an indispensable role for T cells in liver immunopathology. We detected the hepatic accumulation of CD8 T cells with phenotypes that combined tissue residency (CXCR6) with effector (granzyme) and exhaustion (PD1) characteristics. Liver CXCR6⁺ CD8 T cells were characterized by low activity of the FOXO1 transcription factor, and were abundant in NASH mice and in patients with NASH. Mechanistically, IL-15 induced FOXO1 downregulation and CXCR6 upregulation, which together rendered liver-resident CXCR6⁺ CD8 T cells susceptible to metabolic stimuli (including acetate and extracellular ATP) and collectively triggered auto-aggression. CXCR6⁺ CD8 T cells from the livers of NASH mice or of patients with NASH had similar transcriptional signatures, and showed auto-aggressive killing of cells in an MHC-class-I-independent fashion after signalling through P2X7 purinergic receptors. This killing by auto-aggressive CD8 T cells fundamentally differed from that by antigen-specific cells, which mechanistically distinguishes auto-aggressive and protective T cell immunity.

[Access through your institution](#)

[Change institution](#)

[Buy or subscribe](#)

Access options

Subscribe to Journal

Get full journal access for 1 year

\$199.00

only \$3.90 per issue

[Subscribe](#)

All prices are NET prices.

VAT will be added later in the checkout.

Tax calculation will be finalised during checkout.

Rent or Buy article

Get time limited or full article access on ReadCube.

from \$8.99

[Rent or Buy](#)

All prices are NET prices.

Additional access options:

- [Log in](#)
- [Access through your institution](#)
- [Learn about institutional subscriptions](#)

Fig. 1: CD8 T cells in NASH mice have a unique pathogenic profile.

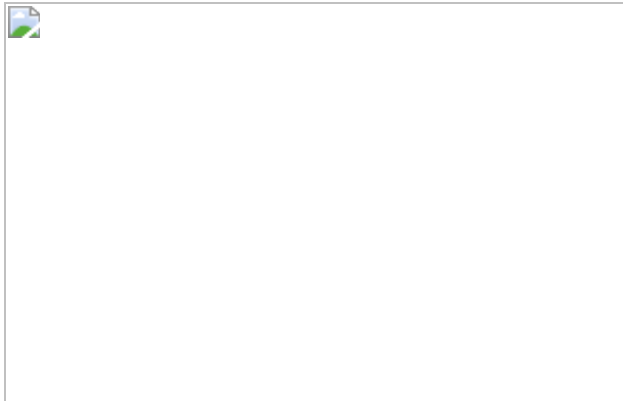


Fig. 2: High similarity between hepatic CXCR6⁺PD1^{high} CD8 T cells in NASH mice and patients with NASH.

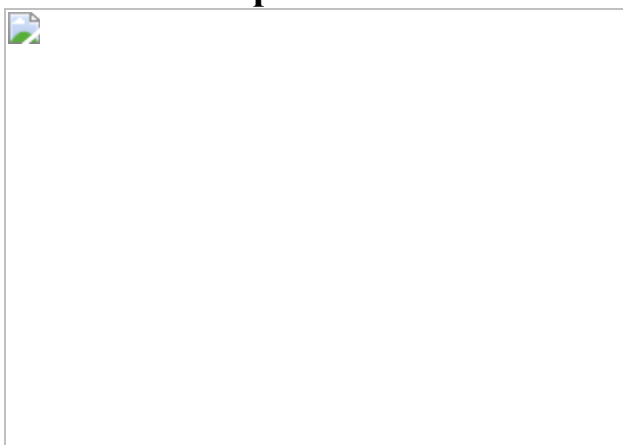


Fig. 3: Acetate exposure enables CXCR6⁺CD8 T cells to become auto-aggressive.

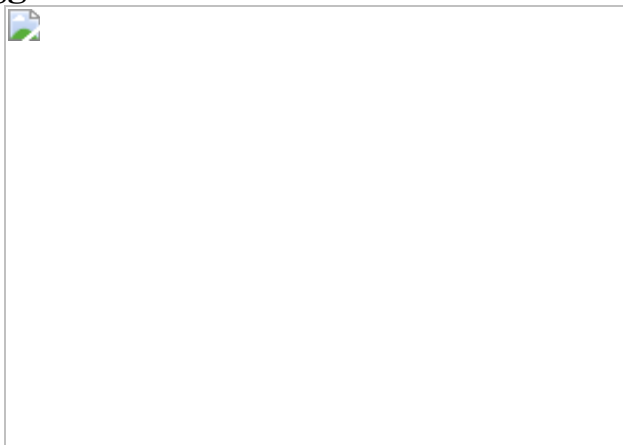
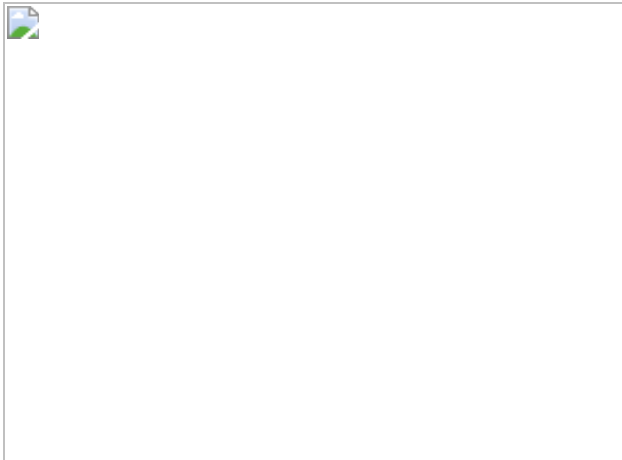


Fig. 4: Metabolic activation of CXCR6⁺ CD8 T cells for the execution of auto-aggression.



Data availability

All raw gene RNA-seq data from mice have been deposited in the GEO under accession number [GSE145104](#). Single-cell RNA-seq data of fat tissue from patients with NASH can be found in the under accession number EGAS00001004738, and can be accessed at <https://ega-archive.org/access/data-access> upon request to the corresponding author. Single-cell RNA-seq data from livers of patients with steatosis or NASH can be found under accession number [GSE159977](#). All datasets are available from the corresponding author upon request. [Source data](#) are provided with this paper.

References

1. 1.

Roden, M. & Shulman, G. I. The integrative biology of type 2 diabetes. *Nature* **576**, 51–60 (2019).

[ADS](#) [PubMed](#) [CAS](#) [Google Scholar](#)

2. 2.

Friedman, S. L., Neuschwander-Tetri, B. A., Rinella, M. & Sanyal, A. J. Mechanisms of NAFLD development and therapeutic strategies. *Nat. Med.* **24**, 908–922 (2018).

[PubMed](#) [PubMed Central](#) [CAS](#) [Google Scholar](#)

3. 3.

Hotamisligil, G. S. Inflammation, metaflammation and immunometabolic disorders. *Nature* **542**, 177–185 (2017).

[ADS](#) [PubMed](#) [CAS](#) [Google Scholar](#)

4. 4.

Wolf, M. J. et al. Metabolic activation of intrahepatic CD8+ T cells and NKT cells causes nonalcoholic steatohepatitis and liver cancer via cross-talk with hepatocytes. *Cancer Cell* **26**, 549–564 (2014).

[PubMed](#) [CAS](#) [Google Scholar](#)

5. 5.

Malehmir, M. et al. Platelet GPIba is a mediator and potential interventional target for NASH and subsequent liver cancer. *Nat. Med.* **25**, 641–655 (2019).

[PubMed](#) [CAS](#) [Google Scholar](#)

6. 6.

Clapper, J. R. et al. Diet-induced mouse model of fatty liver disease and nonalcoholic steatohepatitis reflecting clinical disease progression and methods of assessment. *Am. J. Physiol. Gastrointest. Liver Physiol.* **305**, G483–G495 (2013).

[PubMed](#) [CAS](#) [Google Scholar](#)

7. 7.

Ma, C. et al. NAFLD causes selective CD4⁺ T lymphocyte loss and promotes hepatocarcinogenesis. *Nature* **531**, 253–257 (2016).

[ADS](#) [PubMed](#) [PubMed Central](#) [CAS](#) [Google Scholar](#)

8. 8.

Fernandez-Ruiz, D. et al. Liver-resident memory CD8⁺ T cells form a front-line defense against malaria liver-stage infection. *Immunity* **45**, 889–902 (2016).

[PubMed](#) [CAS](#) [Google Scholar](#)

9. 9.

Topham, D. J. & Reilly, E. C. Tissue-resident memory CD8⁺ T cells: from phenotype to function. *Front. Immunol.* **9**, 515 (2018).

[PubMed](#) [PubMed Central](#) [Google Scholar](#)

10. 10.

Böttcher, J. P. et al. Functional classification of memory CD8⁺ T cells by CX3CR1 expression. *Nat. Commun.* **6**, 8306 (2015).

[ADS](#) [PubMed](#) [PubMed Central](#) [Google Scholar](#)

11. 11.

Gerlach, C. et al. The chemokine receptor CX3CR1 defines three antigen-experienced CD8 T cell subsets with distinct roles in immune surveillance and homeostasis. *Immunity* **45**, 1270–1284 (2016).

[PubMed](#) [PubMed Central](#) [CAS](#) [Google Scholar](#)

12. 12.

Olson, J. A., McDonald-Hyman, C., Jameson, S. C. & Hamilton, S. E. Effector-like CD8⁺ T cells in the memory population mediate potent protective immunity. *Immunity* **38**, 1250–1260 (2013).

[PubMed](#) [PubMed Central](#) [CAS](#) [Google Scholar](#)

13. 13.

Khan, O. et al. TOX transcriptionally and epigenetically programs CD8⁺ T cell exhaustion. *Nature* **571**, 211–218 (2019).

[PubMed](#) [PubMed Central](#) [CAS](#) [Google Scholar](#)

14. 14.

Alfei, F. et al. TOX reinforces the phenotype and longevity of exhausted T cells in chronic viral infection. *Nature* **571**, 265–269 (2019).

[PubMed](#) [CAS](#) [Google Scholar](#)

15. 15.

Mackay, L. K. et al. Hobit and Blimp1 instruct a universal transcriptional program of tissue residency in lymphocytes. *Science* **352**, 459–463 (2016).

[ADS](#) [PubMed](#) [CAS](#) [Google Scholar](#)

16. 16.

Veldhoen, M. Interleukin 17 is a chief orchestrator of immunity. *Nat. Immunol.* **18**, 612–621 (2017).

[PubMed](#) [CAS](#) [Google Scholar](#)

17. 17.

Man, K. & Kallies, A. Synchronizing transcriptional control of T cell metabolism and function. *Nat. Rev. Immunol.* **15**, 574–584 (2015).

[PubMed](#) [CAS](#) [Google Scholar](#)

18. 18.

Wang, Z. et al. BART: a transcription factor prediction tool with query gene sets or epigenomic profiles. *Bioinformatics* **34**, 2867–2869 (2018).

[PubMed](#) [PubMed Central](#) [CAS](#) [Google Scholar](#)

19. 19.

Leonard, W. J., Lin, J. X. & O’Shea, J. J. The γ_c family of cytokines: basic biology to therapeutic ramifications. *Immunity* **50**, 832–850 (2019).

[PubMed](#) [CAS](#) [Google Scholar](#)

20. 20.

Hedrick, S. M., Hess Michelini, R., Doedens, A. L., Goldrath, A. W. & Stone, E. L. FOXO transcription factors throughout T cell biology. *Nat. Rev. Immunol.* **12**, 649–661 (2012).

[PubMed](#) [CAS](#) [Google Scholar](#)

21. 21.

Cepero-Donates, Y. et al. Interleukin-15-mediated inflammation promotes non-alcoholic fatty liver disease. *Cytokine* **82**, 102–111 (2016).

[PubMed](#) [CAS](#) [Google Scholar](#)

22. 22.

Chirifu, M. et al. Crystal structure of the IL-15–IL-15R α complex, a cytokine-receptor unit presented *in trans*. *Nat. Immunol.* **8**, 1001–1007 (2007).

[PubMed](#) [CAS](#) [Google Scholar](#)

23. 23.

Balmer, M. L. et al. Memory CD8⁺ T cells require increased concentrations of acetate induced by stress for optimal function. *Immunity* **44**, 1312–1324 (2016).

[PubMed](#) [CAS](#) [Google Scholar](#)

24. 24.

Qiu, J. et al. Acetate promotes T cell effector function during glucose restriction. *Cell Rep.* **27**, 2063–2074 (2019).

[PubMed](#) [PubMed Central](#) [CAS](#) [Google Scholar](#)

25. 25.

Liu, X. et al. Acetate production from glucose and coupling to mitochondrial metabolism in mammals. *Cell* **175**, 502–513 (2018).

[PubMed](#) [PubMed Central](#) [CAS](#) [Google Scholar](#)

26. 26.

Bachem, A. et al. Microbiota-derived short-chain fatty acids promote the memory potential of antigen-activated CD8⁺ T cells. *Immunity* **51**, 285–297 (2019).

[CAS](#) [Google Scholar](#)

27. 27.

Voskoboinik, I., Whisstock, J. C. & Trapani, J. A. Perforin and granzymes: function, dysfunction and human pathology. *Nat. Rev. Immunol.* **15**, 388–400 (2015).

[PubMed](#) [CAS](#) [Google Scholar](#)

28. 28.

Chang, C. H. et al. Posttranscriptional control of T cell effector function by aerobic glycolysis. *Cell* **153**, 1239–1251 (2013).

[PubMed](#) [PubMed Central](#) [CAS](#) [Google Scholar](#)

29. 29.

Linden, J., Koch-Nolte, F. & Dahl, G. Purine release, metabolism, and signaling in the inflammatory response. *Annu. Rev. Immunol.* **37**, 325–347 (2019).

[PubMed](#) [CAS](#) [Google Scholar](#)

30. 30.

Chekeni, F. B. et al. Pannexin 1 channels mediate ‘find-me’ signal release and membrane permeability during apoptosis. *Nature* **467**, 863–867 (2010).

[ADS](#) [PubMed](#) [PubMed Central](#) [CAS](#) [Google Scholar](#)

31. 31.

Stark, R. et al. T_{RM} maintenance is regulated by tissue damage via P2RX7. *Sci. Immunol.* **3**, eaau1022 (2018).

[PubMed](#) [Google Scholar](#)

32. 32.

Borges da Silva, H. et al. The purinergic receptor P2RX7 directs metabolic fitness of long-lived memory CD8⁺ T cells. *Nature* **559**, 264–268 (2018).

[ADS](#) [PubMed](#) [CAS](#) [Google Scholar](#)

33. 33.

Zhao, J. et al. Single-cell RNA sequencing reveals the heterogeneity of liver-resident immune cells in human. *Cell Discov.* **6**, 22 (2020).

[PubMed](#) [PubMed Central](#) [CAS](#) [Google Scholar](#)

34. 34.

Setoguchi, R. IL-15 boosts the function and migration of human terminally differentiated CD8+ T cells by inducing a unique gene signature. *Int. Immunol.* **28**, 293–305 (2016).

[PubMed](#) [CAS](#) [Google Scholar](#)

35. 35.

Lampl, S. et al. Reduced mitochondrial resilience enables non-canonical induction of apoptosis after TNF receptor signaling in virus-infected hepatocytes. *J. Hepatol.* **73**, 1347–1359 (2020).

[PubMed](#) [CAS](#) [Google Scholar](#)

36. 36.

Chen, H. et al. Cytofkit: a Bioconductor package for an integrated mass cytometry data analysis pipeline. *PLoS Comput. Biol.* **12**, e1005112 (2016).

[PubMed](#) [PubMed Central](#) [Google Scholar](#)

37. 37.

Mackay, L. K. et al. T-box transcription factors combine with the cytokines TGF- β and IL-15 to control tissue-resident memory T cell fate. *Immunity* **43**, 1101–1111 (2015).

[PubMed](#) [CAS](#) [Google Scholar](#)

38. 38.

Li, M. Z. & Elledge, S. J. Harnessing homologous recombination in vitro to generate recombinant DNA via SLIC. *Nat. Methods* **4**, 251–256 (2007).

[PubMed](#) [CAS](#) [Google Scholar](#)

39. 39.

Guillot, A. & Tacke, F. The unexpected role of neutrophils for resolving liver inflammation by transmitting microRNA-223 to macrophages. *Hepatology* **71**, 749–751 (2020).

[PubMed](#) [Google Scholar](#)

40. 40.

Macosko, E. Z. et al. Highly parallel genome-wide expression profiling of individual cells using nanoliter droplets. *Cell* **161**, 1202–1214 (2015).

[PubMed](#) [PubMed Central](#) [CAS](#) [Google Scholar](#)

41. 41.

Love, M. I., Huber, W. & Anders, S. Moderated estimation of fold change and dispersion for RNA-seq data with DESeq2. *Genome Biol.* **15**, 550 (2014).

[PubMed](#) [PubMed Central](#) [Google Scholar](#)

42. 42.

Zhou, Q. et al. A mouse tissue transcription factor atlas. *Nat. Commun.* **8**, 15089 (2017).

[ADS](#) [PubMed](#) [PubMed Central](#) [Google Scholar](#)

43. 43.

Dreos, R., Ambrosini, G., Groux, R., Cavin Périer, R. & Bucher, P. The eukaryotic promoter database in its 30th year: focus on non-vertebrate organisms. *Nucleic Acids Res.* **45**, D51–D55 (2017).

[PubMed](#) [CAS](#) [Google Scholar](#)

44. 44.

Khan, A. et al. JASPAR 2018: update of the open-access database of transcription factor binding profiles and its web framework. *Nucleic Acids Res.* **46**, D260–D266 (2018).

[PubMed](#) [CAS](#) [Google Scholar](#)

45. 45.

Kulakovskiy, I. V. et al. HOCOMOCO: towards a complete collection of transcription factor binding models for human and mouse via large-scale ChIP-seq analysis. *Nucleic Acids Res.* **46**, D252–D259 (2018).

[PubMed](#) [CAS](#) [Google Scholar](#)

46. 46.

Shannon, P. et al. Cytoscape: a software environment for integrated models of biomolecular interaction networks. *Genome Res.* **13**, 2498–2504 (2003).

[PubMed](#) [PubMed Central](#) [CAS](#) [Google Scholar](#)

47. 47.

Gerstein, M. B. et al. Architecture of the human regulatory network derived from ENCODE data. *Nature* **489**, 91–100 (2012).

[ADS](#) [PubMed](#) [PubMed Central](#) [CAS](#) [Google Scholar](#)

48. 48.

Butler, A., Hoffman, P., Smibert, P., Papalexi, E. & Satija, R. Integrating single-cell transcriptomic data across different conditions, technologies, and species. *Nat. Biotechnol.* **36**, 411–420 (2018).

[PubMed](#) [PubMed Central](#) [CAS](#) [Google Scholar](#)

49. 49.

Stuart, T. et al. Comprehensive integration of single-cell data. *Cell* **177**, 1888–1902 (2019).

[PubMed](#) [PubMed Central](#) [CAS](#) [Google Scholar](#)

50. 50.

Zappia, L. & Oshlack, A. Clustering trees: a visualization for evaluating clusterings at multiple resolutions. *Gigascience* **7**, (2018).

51. 51.

Ritchie, M. E. et al. limma powers differential expression analyses for RNA-sequencing and microarray studies. *Nucleic Acids Res.* **43**, e47 (2015).

[PubMed](#) [PubMed Central](#) [Google Scholar](#)

52. 52.

Mahi, N. A., Najafabadi, M. F., Pilarczyk, M., Kouril, M. & Medvedovic, M. GREIN: an interactive web platform for re-analyzing GEO RNA-seq data. *Sci. Rep.* **9**, 7580 (2019).

[ADS](#) [PubMed](#) [PubMed Central](#) [Google Scholar](#)

53. 53.

Subramanian, A. et al. Gene set enrichment analysis: a knowledge-based approach for interpreting genome-wide expression profiles. *Proc. Natl Acad. Sci. USA* **102**, 15545–15550 (2005).

[ADS](#) [PubMed](#) [PubMed Central](#) [CAS](#) [Google Scholar](#)

[Download references](#)

Acknowledgements

We thank S. Yousuf and M. Qui for technical support in preparing samples for single-cell RNA-seq analysis; P. Sinn for technical support; the personnel (particularly J. Maurer) of the Core Facility Flow Cytometry at Biomedical Center Munich (LMU), for providing the imaging cytometry instrument and analysis software; and the personnel of the Core Facility Cell Sorting of the German Cancer Research Center Heidelberg. This work was supported by the DFG, project number 424926990, to J.P.B., CIBSS EXC-2189 project identifier 390939984 to E.J.P., SFB TRR179 and DZIF Munich site to P.A.K.

Author information

Affiliations

1. Institute of Molecular Immunology and Experimental Oncology,
School of Medicine, Technical University of Munich (TUM), Munich,
Germany

Michael Dudek, Sainitin Donakonda, Annika Schneider, Philippa Meiser, Felix Bayerl, Silke Hegenbarth, Martina Anton, Peter J. Murray, Jan P. Böttcher & Percy A. Knolle

2. Institute of Chronic Inflammation and Cancer, German Cancer Research Center, Heidelberg, Germany

Dominik Pfister, Danijela Heide, Florian Müller, Pierluigi Ramadori & Mathias Heikenwälder

3. German Center for Infection Research, Munich, Germany

Sainitin Donakonda & Percy A. Knolle

4. Department of Medicine, University Medical Centre Hamburg-Eppendorf, Hamburg, Germany

Pamela Filpe, Jennifer Wigger & Marcial Sebode
5. Department of Surgery, University Hospital München rechts der Isar, TUM, Munich, Germany

Melanie Laschinger, Daniel Hartmann & Norbert Hüser
6. Division of Vascular Oncology and Metastasis, German Cancer ResearchCenter Heidelberg (DKFZ-ZMBH Alliance), Heidelberg, Germany

Donato Inverso
7. European Center of Angioscience (ECAS), Medical Faculty Mannheim, Heidelberg University, Mannheim, Germany

Donato Inverso
8. Institute of Molecular Oncology and Functional Genomics, TUM, Munich, Germany

Rupert Öllinger & Roland Rad
9. Department of Hepatology and Gastroenterology, Charité Universitätsmedizin, Berlin, Germany

Adrien Guillot & Frank Tacke
10. Maastricht MultiModal Molecular Imaging (M4I) Institute, Division of Imaging Mass Spectrometry, Maastricht University, Maastricht, the Netherlands

Andrew Bowman & Ron Heeren
11. Institute of Virology, Technical University Munich and Helmholtz Zentrum Munich, Munich, Germany

Valentina Leone

12. Research Unit of Radiation Cytogenetics, Helmholtz Zentrum Munich, Neuherberg, Germany

Valentina Leone

13. Institute for Diabetes and Obesity, Helmholtz Diabetes Center, Helmholtz Zentrum München, Neuherberg, Germany

Cristina Garcia-Caceres & Tim Gruber

14. Department of General and Visceral Surgery, Faculty of Medicine, University of Freiburg, Freiburg, Germany

Gabriel Seifert

15. Max Planck Institute of Immunobiology and Epigenetics, Freiburg, Germany

Agnieszka M. Kabat & Edward J. Pearce

16. Division of Chromatin Networks, Single-cell Open Lab, German Cancer Research Center, Heidelberg, Germany

Jan-Philipp Malm

17. Department of Internal Medicine I, Gastroenterology, Hepatology, Endocrinology and Metabolism, Medical University Innsbruck, Innsbruck, Austria

Simon Reider, Maria Effenberger & Herbert Tilg

18. Christian Doppler Labor for Mucosal Immunology, Innsbruck, Austria

Simon Reider

19. Department of General, Visceral and Transplantation Surgery, Heidelberg University, Heidelberg, Germany

Susanne Roth, Adrian T. Billeter & Beat Müller-Stich

20. Institute of Immunology, University Medical Center Hamburg-Eppendorf, Hamburg, Germany

Friedrich Koch-Nolte

21. Department of Medicine II, University Medical Center Freiburg, Faculty of Medicine, University of Freiburg, Freiburg, Germany

Rafael Käser, Robert Thimme & Tobias Böttler

22. University Clinic for Visceral Surgery and Medicine, Inselspital, University of Bern, Bern, Switzerland

Jean-Francois Dufour

23. Chair of Nutrition and Immunology, School of Life Sciences Weihenstephan, TUM, Freising, Germany

Dirk Haller

24. Max Planck Institute for Biochemistry, Martinsried, Germany

Peter J. Murray

25. Division of Animal Physiology and Immunology, School of Life Sciences Weihenstephan, TUM, Freising, Germany

Dietmar Zehn & Percy A. Knolle

Authors

1. Michael Dudek

[View author publications](#)

You can also search for this author in [PubMed](#) [Google Scholar](#)

2. Dominik Pfister

[View author publications](#)

You can also search for this author in [PubMed](#) [Google Scholar](#)

3. Sainitin Donakonda

[View author publications](#)

You can also search for this author in [PubMed](#) [Google Scholar](#)

4. Pamela Filpe

[View author publications](#)

You can also search for this author in [PubMed](#) [Google Scholar](#)

5. Annika Schneider

[View author publications](#)

You can also search for this author in [PubMed](#) [Google Scholar](#)

6. Melanie Laschinger

[View author publications](#)

You can also search for this author in [PubMed](#) [Google Scholar](#)

7. Daniel Hartmann

[View author publications](#)

You can also search for this author in [PubMed](#) [Google Scholar](#)

8. Norbert Hüser

[View author publications](#)

You can also search for this author in [PubMed](#) [Google Scholar](#)

9. Philippa Meiser

[View author publications](#)

You can also search for this author in [PubMed](#) [Google Scholar](#)

10. Felix Bayerl

[View author publications](#)

You can also search for this author in [PubMed](#) [Google Scholar](#)

11. Donato Inverso

[View author publications](#)

You can also search for this author in [PubMed](#) [Google Scholar](#)

12. Jennifer Wigger

[View author publications](#)

You can also search for this author in [PubMed](#) [Google Scholar](#)

13. Marcial Sebode

[View author publications](#)

You can also search for this author in [PubMed](#) [Google Scholar](#)

14. Rupert Öllinger

[View author publications](#)

You can also search for this author in [PubMed](#) [Google Scholar](#)

15. Roland Rad

[View author publications](#)

You can also search for this author in [PubMed](#) [Google Scholar](#)

16. Silke Hegenbarth

[View author publications](#)

You can also search for this author in [PubMed](#) [Google Scholar](#)

17. Martina Anton

[View author publications](#)

You can also search for this author in [PubMed](#) [Google Scholar](#)

18. Adrien Guillot

[View author publications](#)

You can also search for this author in [PubMed](#) [Google Scholar](#)

19. Andrew Bowman

[View author publications](#)

You can also search for this author in [PubMed](#) [Google Scholar](#)

20. Danijela Heide

[View author publications](#)

You can also search for this author in [PubMed](#) [Google Scholar](#)

21. Florian Müller

[View author publications](#)

You can also search for this author in [PubMed](#) [Google Scholar](#)

22. Pierluigi Ramadori

[View author publications](#)

You can also search for this author in [PubMed](#) [Google Scholar](#)

23. Valentina Leone

[View author publications](#)

You can also search for this author in [PubMed](#) [Google Scholar](#)

24. Cristina Garcia-Caceres

[View author publications](#)

You can also search for this author in [PubMed](#) [Google Scholar](#)

25. Tim Gruber

[View author publications](#)

You can also search for this author in [PubMed](#) [Google Scholar](#)

26. Gabriel Seifert

[View author publications](#)

You can also search for this author in [PubMed](#) [Google Scholar](#)

27. Agnieszka M. Kabat

[View author publications](#)

You can also search for this author in [PubMed](#) [Google Scholar](#)

28. Jan-Philipp Malm

[View author publications](#)

You can also search for this author in [PubMed](#) [Google Scholar](#)

29. Simon Reider

[View author publications](#)

You can also search for this author in [PubMed](#) [Google Scholar](#)

30. Maria Effenberger

[View author publications](#)

You can also search for this author in [PubMed](#) [Google Scholar](#)

31. Susanne Roth

[View author publications](#)

You can also search for this author in [PubMed](#) [Google Scholar](#)

32. Adrian T. Billeter

[View author publications](#)

You can also search for this author in [PubMed](#) [Google Scholar](#)

33. Beat Müller-Stich

[View author publications](#)

You can also search for this author in [PubMed](#) [Google Scholar](#)

34. Edward J. Pearce

[View author publications](#)

You can also search for this author in [PubMed](#) [Google Scholar](#)

35. Friedrich Koch-Nolte

[View author publications](#)

You can also search for this author in [PubMed](#) [Google Scholar](#)

36. Rafael Käser

[View author publications](#)

You can also search for this author in [PubMed](#) [Google Scholar](#)

37. Herbert Tilg

[View author publications](#)

You can also search for this author in [PubMed](#) [Google Scholar](#)

38. Robert Thimme

[View author publications](#)

You can also search for this author in [PubMed](#) [Google Scholar](#)

39. Tobias Böttler

[View author publications](#)

You can also search for this author in [PubMed](#) [Google Scholar](#)

40. Frank Tacke

[View author publications](#)

You can also search for this author in [PubMed](#) [Google Scholar](#)

41. Jean-Francois Dufour

[View author publications](#)

You can also search for this author in [PubMed](#) [Google Scholar](#)

42. Dirk Haller

[View author publications](#)

You can also search for this author in [PubMed](#) [Google Scholar](#)

43. Peter J. Murray

[View author publications](#)

You can also search for this author in [PubMed](#) [Google Scholar](#)

44. Ron Heeren

[View author publications](#)

You can also search for this author in [PubMed](#) [Google Scholar](#)

45. Dietmar Zehn

[View author publications](#)

You can also search for this author in [PubMed](#) [Google Scholar](#)

46. Jan P. Böttcher

[View author publications](#)

You can also search for this author in [PubMed](#) [Google Scholar](#)

47. Mathias Heikenwälder

[View author publications](#)

You can also search for this author in [PubMed](#) [Google Scholar](#)

48. Percy A. Knolle

[View author publications](#)

You can also search for this author in [PubMed](#) [Google Scholar](#)

Contributions

M.D. and P.A.K. designed the study. M.D., D.P., P.F., A.S., M.L., P.M., F.B., D.I., J.W., S.H., M.A., A.G., A.B., D. Heide, F.M. and S. Reider performed

experiments. S.D., R.Ö. and A.M.K. undertook bioinformatics analysis. D. Hartmann, N.H., M.S., C.G.-C., T.G., G.S., J.-P.M., M.E., S. Roth, A.T.B., B.M.-S., F.K.-N., R.K., T.B., P.R., V.L., J.-F.D. and M.H. provided tissue samples, essential reagents or mice. R.R., E.J.P., H.T., F.T., J.-F.D., D. Haller, P.J.M., R.H., R.T., D.Z., J.P.B., M.H. and P.A.K. contributed scientific input. M.D. and P.A.K. wrote the manuscript, and all authors contributed to feedback and proofreading.

Corresponding author

Correspondence to [Percy A. Knolle](#).

Ethics declarations

Competing interests

The authors declare no competing interests.

Additional information

Peer review information *Nature* thanks Paul Klenerman, Ignacio Melero, Daniel Peepo and the other, anonymous, reviewer(s) for their contribution to the peer review of this work. Peer reviewer reports are available.

Publisher's note Springer Nature remains neutral with regard to jurisdictional claims in published maps and institutional affiliations.

Extended data figures and tables

[Extended Data Fig. 1 Immune-cell characteristics in livers of mice fed a CD-HFD.](#)

a–e, Liver damage after 12 months of feeding a CD-HFD (which induces features of NASH) in *Ja18^{-/-}* and *Cd1d^{-/-}* mice, determined by sALT and NAS with representative images of H&E staining (mice fed a normal diet,

n = 8; CD-HFD-fed, wild-type mice, *n* ≥ 7; CD-HFD-fed, *Jal8*^{-/-} mice, *n* ≥ 7; CD-HFD-fed, *Cd1d*^{-/-} mice: *n* ≥ 8). Scale bar, 100 μm. Two independent experiments. **f**, Body weight of mice over the course of six months. **g, h**, Numbers of hepatic lymphocytes (**g**) and hepatic CXCR6⁺ T cell populations (**h**) in mice fed a normal diet (*n* = 11) or CD-HFD (*n* = 13). Two independent experiments. **i–k**, Numbers and phenotype of hepatic CD44⁺ CXCR6⁺ and CXCR6⁻ CD8 T cells in NASH mice (*n* ≥ 5). Two independent experiments. **l**, Frequencies of CXCR6⁺GzmB⁺ CD8 T cells in different organs in mice fed a normal diet (*n* = 4) and NASH mice (*n* = 4). **m–o**, Localization and quantification of hepatic CXCR6⁺PD1^{high} CD8 T cells in mice fed a normal diet (*n* = 3) and NASH mice (*n* = 3), by confocal microscopy with representative images. Scale bar, 200 μm. CD3 (yellow), CD8 (purple), CXCR6 (cyan), PD1 (red) and collagen IV (white). Rectangles highlighted in **m** indicate representative zoomed areas shown in Fig. 1g. ns, not significant; nd, not determined. Exact *P* (**a–d, f–l, n, o**) and *n* (**a–d, f, i–k**) values are presented in Source Data. **P* < 0.05, ***P* < 0.01, ****P* < 0.001, *****P* < 0.0001. Two-way ANOVA with Sidak's (**g, h, l**) or with Tukey's multiple comparison test (**j, k**), one-way ANOVA with Tukey's (**a–d**) or with Dunnett's multiple comparison test (**f**) and unpaired two-tailed *t*-test (**i, n, o**). In **a–d, f–l, n, o**, data are mean ± s.e.m., error is reported as s.d. [Source data](#)

Extended Data Fig. 2 Increased numbers of hepatic CXCR6⁺PD1^{high} CD8 T cells in different mouse models of obesity-related NASH.

a, b, Confocal microscopy of hepatic PD1^{high} CD8 T cells and IMARIS-based quantification with representative images (normal diet, *n* = 5; high-fat diet (HFD), *n* = 4; CD-HFD, *n* = 6). Scale bars, 500 μm (left), 100 μm (right). CD8 (red), PD1 (green), CK19 (blue), IBA1 (cyan), αSMA (purple) and DAPI (white). Rectangles highlighted in the left panel indicate represent zoomed areas in the right panel. Red arrows indicate PD1⁻ CD8 T cells. Yellow arrows indicate PD1^{high} CD8 T cells. One-way ANOVA with Dunnett's multiple comparison test. **c, d**, Correlation of liver damage (NAS) with frequencies of hepatic PD1^{high} CD8 T cells from mice fed a normal

diet or CD-HFD. Coefficient of determination (R^2) and statistical significance (P value) were determined using Pearson's correlation. **e, f**, CXCR6 and PD1 expression levels in hepatic CD8 T cells in mice fed CD-HFD (**e**) or a high *trans*-fat Western diet (WD) (**f**) ($n = 5$) for 12 months compared to mice fed a normal diet ($n = 5$). **h, i**, Liver damage (sALT and NAS) in mice from **f**. **j, k**, CXCR6 and PD1 expression levels in hepatic CD8 T cells in *ob/-* and *ob/ob* mice after 4 months of chow feeding or mice fed a normal diet (*ob/-*, $n = 6$; *ob/ob*, $n = 4$). **l, m**, Liver damage (sALT and NAS) in mice from **j**. Exact P values (**b, f–m**) are presented in Source Data. $*P < 0.05$, $**P < 0.01$, $****P < 0.0001$. Unpaired two-tailed *t*-test (**f–m**). In **b, f–m**, data are mean \pm s.e.m., errors are shown as s.d. [Source data](#)

Extended Data Fig. 3 Transcriptome analysis of hepatic CXCR6[±] CD8 T cells from NASH mice.

a, Volcano plot showing differentially expressed genes between CXCR6⁺ CD8 T cells from NASH mice (fed a CD-HFD) compared to healthy mice (fed a normal diet). **b**, GSEA for distinct pathways from **a**. **c**, Flow cytometry analysis of protein levels of transcription factors in hepatic CXCR6⁺ and CXCR6⁻ CD8 T cells from healthy and NASH mice ($n \geq 5$). **d**, Binding analysis for regulation of transcription (BART) to predict transcription-factor activity in hepatic CXCR6⁺ compared to CXCR6⁻ CD8 T cells in NASH mice. **e**, Transcription-factor network analysis created from differentially expressed genes (**a**) and BART. **f**, GSEA for transcription-factor-dependent genes from **a**. **g–i**, Flow cytometry analysis of FOXO1 expression in hepatic CXCR6⁺ and CXCR6⁻ CD8 T cells (**g, h**) or CD4 T cells (**i**) from mice fed a normal diet and NASH mice ($n \geq 6$). **j, k**, Image-stream analysis of expression and localization of FOXO1 in different T cell populations from spleen and liver of wild-type mice with representative images. Tn, naive T cells; Tcm, central memory T cells; Tem, effector memory T cells. **l**, Similarity score to determine nuclear localization of FOXO1 and surface localization of CD44 ($n = 5$). **m, n**, FOXO1 expression in hepatic CD44⁺ CD8 T cells in mice fed a Western diet ($n = 5$) and *ob/-* or *ob/ob* mice ($n \geq 4$). PI, propidium iodide. Exact P and n values (**c, g–i**) are presented in Source Data. $*P < 0.05$, $**P < 0.01$, $****P < 0.0001$. One-way ANOVA (**k, l**), two-way ANOVA with Tukey's

multiple comparison test (**c**, **i**) and unpaired two-tailed *t*-test (**h**, **m**, **n**). In **c**, **h**, **i**, **k–n**, data are mean \pm s.e.m., errors are shown as s.d. [Source data](#)

[Extended Data Fig. 4 Hepatic CXCR6⁺FOXO1^{low} CD8 T cell frequency correlates with liver damage in NASH mice and patients with NASH.](#)

a–c, Hepatic CXCR6⁺FOXO1^{low} CD8 T cells at 6, 9 and 12 months of feeding a CD-HFD, and correlation of FOXO1 expression levels in hepatic CD44⁺CD8 T cells with frequency of hepatic CXCR6⁺PD1^{high} of CD44⁺ CD8 T cells from mice fed a CD-HFD, and with NAS. Four independent experiments. **d**, **e**, CXCR6 and CX₃CR1 expression levels in sorted hepatic CD44⁺CXCR6[–] CD8 T cells from healthy mice fed a normal diet ($n = 5$) after 18 h of treatment with the FOXO1 inhibitor AS1842856. **f**, CXCR6 expression levels after FOXO1 overexpression (transduction with pMP71-Foxo1-eGFP or pMP71-eGFP) in sorted CXCR6⁺ CD8 T cells ($n = 3$). **g**, **h**, Correlation of sALT and NAS with FOXO1 expression in hepatic CD44⁺ CD8 T cells from **b**. **i**, Correlation of FOXO1 expression in liver CD69⁺ CD8 T cells with sALT in patients with NASH ($n = 15$ in total: $n = 12$ NASH; $n = 3$ normal liver tissue (NAS = 0)). **j**, CXCR6 expression quantified by qPCR with reverse transcription (RT–qPCR) in liver tissue of patients with NASH (NAS ≥ 5) (unaffected tissue, $n = 6$; tissue from patients with NASH, $n = 7$). **k**, **l**, Correlation of relative CXCR6 expression with sALT and NAS in patients with NASH (unaffected individuals, $n = 6$; patients with NASH, $n = 10$). **m**, Correlation of sALT with numbers of cells that are positive for CXCR6 per mm² of liver tissue in patients with NASH ($n = 18$). Scale bar, 100 μ m. Representative image of in situ hybridization for CXCR6 mRNA in liver of patients with low or high sALT. Exact *P* (**e**, **f**, **j**) and *n* (**b**, **c**, **g**, **h**) values are presented in Source Data. **P* < 0.05, ***P* < 0.01, ****P* < 0.0001. Coefficient of determination (R^2) and statistical significance (*P* value) were determined using Pearson's correlation (**b**, **c**, **g–i**, **k–m**). Unpaired two-tailed (**f**, **j**) and paired two-tailed *t*-test (**e**). In **e**, **f**, **j**, data are mean \pm s.e.m., error is reported as s.d. [Source data](#)

Extended Data Fig. 5 Increased levels of IL-15 in serum and liver tissue of NASH mice correlate with liver damage and numbers of hepatic CXCR6 \pm CD8 T cells.

a, Heat map of fold changes for cytokine and chemokine serum concentrations in NASH (fed a CD-HFD) ($n \geq 8$) compared to healthy (fed a normal diet) mice ($n \geq 6$) after 12 months of feeding. Values above 2.5 are red. Asterisk denotes values that are significantly different. Exact P and n values are presented in Source Data. Two independent experiments. **b**, Cytokine and chemokine expression quantified by RT-qPCR in the liver tissue of mice fed a normal diet ($n = 5$) and NASH mice ($n = 9$). **c**, Flow cytometry analysis of the increase in CXCR6 expression after incubation of sorted hepatic CD44 $^+$ CXCR6 $^-$ CD8 T cells with cytokines for 24 h ($n = 13$). **d**, Flow cytometry analysis of FOXO1 expression 24 h after IL-15 stimulation of hepatic CD44 $^+$ CD8 T cells ($n = 10$). **e–g**, Flow cytometry analysis of FOXO1 expression in human CD8 T cells at 5 d after IL-15 stimulation (15 ng ml $^{-1}$) and frequencies of CXCR6 $^+$ CD69 $^+$ cells ($n = 5$). **h**, PD1, GzmB and CXCR3 expression by mouse hepatic CXCR6 $^+$ CD8 T cells 24 h after IL-15 stimulation ($n = 9$). **i**, Percentage of CXCR6-expressing CD8 T cells in sorted, splenic CD44 $^+$ CD8 T cells 2 d after stimulation with IL-15 (10 ng ml $^{-1}$) and/or IL-21 (10 ng ml $^{-1}$) ($n = 5$). Two independent experiments. **j, k**, IL-15 serum concentrations in *ob/-* ($n = 4$) and hyperphagic, leptin-deficient *ob/ob* mice ($n = 4$) fed a chow diet for 4 months, in mice fed a normal diet ($n = 4$) or a high *trans*-fat Western diet for 12 months ($n = 5$). **l–n**, Correlation of IL-15 serum levels with sALT, NAS and FOXO1 expression in hepatic CD44 $^+$ CD8 T cells of NASH mice (6 months, $n = 4$; 9 months, $n = 7$; 12 months, $n = 13$). Four independent experiments. **o–q**, Correlation of relative hepatic *IL-15* gene expression levels with sALT, NAS and *CXCR6* gene expression in patients with NASH and in individuals with normal liver (normal, $n = 6$; NASH, $n = 10$). Exact P (**a–d, f–k**) and n (**a**) values are presented in Source Data. * $P < 0.05$, ** $P < 0.01$, *** $P < 0.001$, **** $P < 0.0001$. Coefficient of determination (R^2) and statistical significance (P value) was determined using Pearson's correlation (**l–q**). One-way ANOVA with Tukey's (**i**) or Dunnett's multiple comparison test (**c**), and unpaired two-tailed *t*-test (**a, b, d, f–h, j, k**). In **a–d, f–k**, data are mean \pm s.e.m., error is reported as s.d. [Source data](#)

Extended Data Fig. 6 Single-cell RNA-seq of CD3 \pm T cells from livers of patients with steatosis or NASH.

a, UMAP plot visualization of hepatic CD3 $^+$ T cell clusters detected in livers from patients with steatosis ($n = 4$) or NASH (NAS ≥ 5) ($n = 3$). **b**, UMAP plot visualization of hepatic CD3 $^+$ T cell clusters and of selected genes detected in patients with NASH (NAS ≥ 5) ($n = 3$). **c**, Frequencies of CXCR6 $^+$ and PDCD1 $^+$ cells in CD8 T cells in the RGS1 $^+$, PLCG2 $^+$ and ITGA1 $^+$ cluster in livers from patients with steatosis or NASH. **d**, Differentially expressed genes in the CD8 RGS1 $^+$ cluster between livers of patients with steatosis or NASH. **e**, Flow cytometry analysis of FOXO1 expression in CD69 $^+$ CD8 T cells from livers of unaffected individuals ($n = 3$) and livers of patients with NASH ($n = 5$). $P = 0.0088$, two-tailed t -test, data are mean \pm s.e.m. **f**, UMAP plot visualization of hepatic CD3 $^+$ T cell clusters detected in patients with NASH from fat tissue ($n = 2$). **g**, Jaccard similarity score between tissue-resident CD8 T cell populations in fat and liver of patients with NASH ($n = 2$). **h**, Correlation of mouse RNA-seq dataset from CXCR6 $^+$ compared to CXCR6 $^-$ CD8 T cells in mice fed a CD-HFD with human single-cell RNA-seq dataset from the CD8 GNLY $^+$ FGFBP2 $^+$ cluster. The solid line is the linear regression, and the grey area shows the 95% confidence intervals. Coefficient of determination (R^2) and statistical significance (P value) were determined using Spearman's correlation. [Source data](#)

Extended Data Fig. 7 Anti-CD122 application in NASH mice leads to depletion of CXCR6 \pm GzmB \pm CD8 T cells and amelioration of liver damage.

a, CD122 expression on splenic CD44 $^+$ CD8 T cells after stimulation with IL-15 (10 ng ml $^{-1}$) for 24 h ($n = 5$). **b**, CD122 expression on hepatic CXCR6 $^+$ CD8 T cells ($n = 8$). Two independent experiments. **c–e**, Frequencies and cell numbers of CXCR6 $^+$ PD1 $^+$ and CXCR6 $^+$ GzmB $^+$ CD8 T cells after anti-CD122-treatment for 2 weeks in NASH mice (fed CD-HFD for 12 months) (CD-HFD + immunoglobulin (Ig), $n = 6$; CD-HFD +

anti-CD122, $n = 6$). **f**, sALT in NASH mice from **e** before and after anti-CD122 treatment for 2 weeks. Unpaired two-tailed *t*-test of sALT values between groups before treatment, $P = 0.7137$. **g–k**, Numbers of CX₃CR1 CD8 T cells, CD44⁺ CD4 T cells, natural killer T cells and natural killer (NK) cells in the liver after anti-CD122 antibody application from mice in **e**. **l, m**, No change in phenotype of natural killer cells in NASH mice. Dot plots are representative of ≥ 5 mice. Exact P values (**a, b, e–m**) are presented in Source Data. * $P < 0.05$, ** $P < 0.01$, *** $P < 0.001$, **** $P < 0.0001$. One-way ANOVA with Tukey's multiple comparison test (**e, g–k**) and paired (**a, f**) and unpaired (**b, l, m**) two-tailed *t*-test. In **a, b, e–m**, data are mean \pm s.e.m., error is reported as s.d. [Source data](#)

Extended Data Fig. 8 IL-15-treated CXCR6 $^{\pm}$ CD8 T cells become auto-aggressive after exposure to acetate.

a, Auto-aggressive activity of IL-15-treated CXCR6⁺FOXO1^{low} CD8 T cells against hepatocytes ($n = 3$). **b**, GzmB-expression levels in CXCR6⁺ CD8 T cells exposed for 24 h to different concentrations of acetate in vitro ($n = 4$). **c–e**, Fluorospot assay with representative images to quantify TNF and IFN γ release from IL-15-stimulated CXCR6[–] and CXCR6⁺ CD8 T cells after acetate exposure and from peptide-specific stimulation of OT1 CD8 T cells ($n = 5$). **f**, GSEA for differentially expressed genes from hepatic CXCR6⁺ and CXCR6[–] CD8 T cells of mice fed a CD-HFD compared to in vitro-generated memory CD8 T cells exposed to acetate or butyrate. **g**, Acetate concentrations in supernatants of primary mouse hepatocytes after exposure to palmitate for 24 h (250 μ M) or with an agonistic trimeric FasL (25 ng ml^{–1}) to induce cell death ($n = 6$). **h**, Cytotoxic activity of acetate-exposed polyclonal CD8 T cells after FOXO1 inhibition (AS1842856, 100 nM) against hepatocytes ($n = 3$) and quantification. **i**, GzmB expression in acetate-exposed, GFP-expressing CD8 T cells after retroviral transduction with pMP71-GFP-Foxo1 or pMP71-GFP ($n = 3$). **j, k**, sALT at day 2 after adoptive transfer of IL-15-stimulated or FOXO1-inhibited and acetate-exposed CD8 T cells ($n \geq 3$). **l**, Calculation of liver-damage-inducing potential per cell for auto-aggressive CD8 T cells ($n = 8$). **m**, Surface LAMP1 expression on CXCR6⁺ CD8 T cells after a 24-h exposure to acetate (15 mM) ($n = 9$). **n, o**, Liver damage

quantified by NAS and sALT in *Prf1*^{-/-} and littermate control mice after CD-HFD feeding for 1 year. **p**, ICAM1 expression on hepatocytes in coculture with IL-15-stimulated, acetate-exposed CXCR6⁺ CD8 T cells ($n = 7$). **q**, Liver immunohistochemistry with representative images and quantification of ICAM1 clusters per mm² of liver tissue in mice fed a normal diet ($n = 5$), NASH mice ($n = 6$) and NASH mice treated with anti-CD122 antibody ($n = 6$). Scale bar, 100 μm. **r**, Representative microscopic images of IL-15-stimulated, acetate-exposed CXCR6⁺ CD8 T cells in contact with hepatocytes and quantification of the distance. Arrows indicate polarized LFA1 orientation on T cell interacting with hepatocyte. Scale bars, 30 μm (left), 15 μm (right). **s**, Auto-aggressive activity of IL-15-treated CXCR6⁺ CD8 T cells against hepatocytes in presence of acetate (15 mM) or TNF (5 ng ml⁻¹) and anti-LFA1 antibodies ($n = 3$). **t**, sALT at day 2 after adoptive transfer of auto-aggressive CD8 T cells and injection of anti-LFA1 (100 μg per mouse) or control immunoglobulin. Two independent experiments. **u**, **v**, TNF expression in livers from unaffected individuals ($n = 6$) or patients with NASH ($n = 7$) (**u**) and correlation with sALT (healthy, $n = 6$; NASH, $n = 10$) (**v**). Cytotoxic activity results are representative of at least three independent experiments. Exact P (**a**, **b**, **d**, **e**, **g–v**) and n (**n**, **o**, **t**) values are presented in Source Data. * $P < 0.05$, ** $P < 0.01$, *** $P < 0.001$, **** $P < 0.0001$. Two-way ANOVA with Sidak's multiple comparison test (**d**, **e**), one-way ANOVA with Tukey's (**j**, **k**, **s**, **t**) or with Dunnett's (**b**, **g**, **h**) multiple comparison test and unpaired two-tailed *t*-test (**a**, **i**, **l–n**, **p**, **r**, **u**). In **a**, **b**, **d**, **e**, **g–v**, data are mean ± s.e.m., error is reported as s.d. [Source data](#)

Extended Data Fig. 9 Metabolic activation of CXCR6[±] CD8 T cells triggers auto-aggression.

a, Phosphorylated proteins downstream of TCR signalling in IL-15-stimulated, acetate-exposed CXCR6⁺ CD8 T cells. **b**, Glycolysis in auto-aggressive CXCR6⁺ CD8 T cells ($n = 3$). **c**, Calcium influx in IL-15-stimulated CXCR6⁺ and CXCR6⁻ CD8 T cells exposed to metabolites, cytokines or TLR ligands ($n = 4$). **d**, **e**, Extracellular ATP in primary mouse hepatocyte supernatant after 24 h treatment with palmitate (250 μM) or agonistic trimeric FasL, or coculture with auto-aggressive CD8 T cells

($n = 3$). **f, g**, Metabolite detection in liver tissue of mice fed a normal diet or CD-HFD by matrix-assisted laser desorption and ionization imaging. Scale bar, 500 μm (**f**). Exact minima, maxima, centres, bounds of box and whiskers and percentiles are presented in Source Data. **h**, P2RX7 expression in IL-15-stimulated CD44 $^{+}$ CXCR6 $^{+}$ CD8 T cells. **i, j**, Calcium influx in CXCR6 $^{+}$ CD8 T cells after incubation with NAD (1 μM) ($n = 5$) or supernatants from **d** ($n = 3$) for 30 min. **k**, Representative cytotoxicity result of CD8 T cell auto-aggression in the presence of P2RX7 or PANX1 inhibition ($n = 3$). **l**, sALT at day 2 after transfer of auto-aggressive CD8 T cells and anti-P2RX7 nanobody (50 μg per mouse). Two independent experiments. **m**, Representative cytotoxicity result of antigen-specific, IL-15-stimulated and acetate-exposed CXCR6 $^{+}$ OT1 CD8 T cells against S8L-loaded hepatocytes. Exact P (**a–e, i, j, l**) and n (**a, l**) values are presented in Source Data. * $P < 0.05$, ** $P < 0.01$, *** $P < 0.0001$. Two-way ANOVA with Tukey's multiple comparison test (**c, i, j**), one-way ANOVA with Tukey's (**b, e, l**) or with Dunnett's (**d**) multiple comparison test and unpaired two-tailed t -test (**a**). In **a–e, i, j, l** data are mean \pm s.e.m., error is reported as s.d. [Source data](#)

Extended Data Fig. 10 Auto-aggressive human CD8 T cells.

a, Auto-aggression of allogeneic and autologous CD8 T cells against primary human hepatocytes after incubation with IL-15 (effector-to-target ratio of 3:1 ($n = 3$)). **b**, Auto-aggression by IL-15-treated human CD8 T cells exposed to acetate ($n = 3$). **c**, Acetate levels in livers from unaffected individuals or patients with NASH ($n = 3$). **d**, Auto-aggression of human CD8 T cells in presence of anti-TNF (10 $\mu\text{g ml}^{-1}$) or anti-LFA1 (10 $\mu\text{g ml}^{-1}$) ($n = 3$). **e, f**, Auto-aggression against MHC-I-deficient K562 cells by human CD8 T cells exposed to IL-15 (**e**), and at different effector-to-target ratios ($n = 6$). **g**, Calcium influx in IL-15-treated human CXCR6 $^{+}$ CD69 $^{+}$ CD8 T cells measured with a calcium sensor dye before or after coculture with K562 cells and quantification ($n = 6$). **h, i**, Auto-aggressive killing of K562 cells by IL-15-treated CD8 T cells in presence of anti-FasL (10 $\mu\text{g ml}^{-1}$), anti-NKG2D (10 $\mu\text{g ml}^{-1}$) or EGTA (4 mM) at effector-to-target ratio of 10:1 ($n = 6$). **j**, Mean numbers of CD8 T cells adjacent to cleaved CASP3 $^{+}$ hepatocytes in mice fed a normal diet and NASH mice ($n = 3$). **k**,

l, Surface FasL and TRAIL expression of mouse CXCR6⁺ CD8 T cells after 1 h exposure to ATP (200 µM). **m**, Caspase activity in primary mouse hepatocytes cocultured with auto-aggressive CD8 T cells and anti-FasL (10 µg ml⁻¹) ($n = 3$). **n**, Mouse CD8 T cell auto-aggression in presence of inhibitors against apoptosis (zVAD-FMK, 10 µM) or necroptosis (Nec-1s, 30 µM) ($n = 4$). **o**, sALT at day 2 after adoptive transfer of IL-15-treated, acetate-exposed CD8 T cells and anti-FasL injection (100 µg per mouse). Two independent experiments. Exact P (**a–o**) and n (**k, l, o**) values are presented in Source Data. * $P < 0.05$, ** $P < 0.01$, *** $P < 0.001$, **** $P < 0.0001$. Two-way ANOVA with Sidak's (**a**) and Tukey's (**f, g**) multiple comparison test, one-way ANOVA with Tukey's multiple comparison test (**b, d, e, h, i, m–o**) and unpaired two-tailed t -test (**c, j–l**). In **a–o**, data are mean ± s.e.m., error is reported as s.d. [Source data](#)

Supplementary information

[Supplementary Data 1](#)

Gating strategy of murine and human liver-infiltrating lymphocytes and patient characteristics of samples used in the study. a, Gating strategy of liver-infiltrating lymphocytes with exclusion of duplets and dead cells. b, Gating strategy of human liver-infiltrating lymphocytes with prior exclusion of duplets and live CD45⁺ cells as reference population for the frequency of CD69⁺CXCR6⁺ CD8 T cells in NAFLD/NASH patients. c, Patient characteristics including methods, cohort groups, gender, age, BMI, ALT, AST and NAS where available. d, Murine primer sequences for qPCR to quantify respective genes in the liver tissue of ND and CD-HFD mice.

[Reporting Summary](#)

[Peer Review File](#)

[Supplementary Information Table 1](#)

Significant differentially expressed genes in liver CXCR6 positive compared to CXCR6 negative CD8 T cells from CD-HFD mice.

Supplementary Information Table 2

GSEA for differentially expressed genes in liver CXCR6 positive compared to CXCR6 negative CD8 T cells from CD-HFD mice.

Supplementary Information Table 3

Upstream transcription factors in CXCR6 positive compared to CXCR6 negative CD8 T cells from CD-HFD mice.

Supplementary Information Table 4

Differentially expressed genes in human CD8 T cells from steatotic livers.

Supplementary Information Table 5

Differentially expressed genes in human CD8 T cells from NASH livers.

Supplementary Information Table 6

Frequencies of human liver CD8 T cells from various clusters expressing *PDCD1* or *CXCR6* in steatotic and NASH livers.

Supplementary Information Table 7

Gene set enrichment analysis of differentially expressed genes of liver T cells from NASH patients for IL-15 dependent genes identified by Setoguchi et al 2016.

Supplementary Information Table 8

Gene set enrichment analysis of human liver T cells for T resident memory cell gene set identified by Zhao et al 2020.

Supplementary Information Table 9

Cluster analysis of CD3⁺ T cells from single cell RNA sequencing of CD3⁺ T cells from fat tissue of NASH patients.

Supplementary Information Table 10

Comparison of human liver and fat CD8 T cells from NASH patients analyzed by single cell RNA sequencing.

Supplementary Information Table 11

Commonly regulated genes in human *RGS1*⁺ and *GNLY*⁺ *FGFBP2*⁺ CD8 T cells from NASH patients compared to differentially expressed genes in CXCR6 positive in comparison to CXCR6 negative CD8 T cells from NASH mice.

Supplementary Information Table 12

Gene set enrichment analysis of acetate- and butyrate dependent genes in CXCR6 positive in comparison to CXCR6 negative CD8 T cells from NASH mice.

Source data

Source Data Fig. 1

Source Data Fig. 2

Source Data Fig. 3

Source Data Fig. 4

Source Data Extended Data Fig. 1

Source Data Extended Data Fig. 2

[**Source Data Extended Data Fig. 3**](#)

[**Source Data Extended Data Fig. 4**](#)

[**Source Data Extended Data Fig. 5**](#)

[**Source Data Extended Data Fig. 6**](#)

[**Source Data Extended Data Fig. 7**](#)

[**Source Data Extended Data Fig. 8**](#)

[**Source Data Extended Data Fig. 9**](#)

[**Source Data Extended Data Fig. 10**](#)

Rights and permissions

[Reprints and Permissions](#)

About this article



Check for
updates

Cite this article

Dudek, M., Pfister, D., Donakonda, S. *et al.* Auto-aggressive CXCR6⁺ CD8 T cells cause liver immune pathology in NASH. *Nature* **592**, 444–449 (2021). <https://doi.org/10.1038/s41586-021-03233-8>

[Download citation](#)

- Received: 17 February 2020
- Accepted: 12 January 2021
- Published: 24 March 2021
- Issue Date: 15 April 2021
- DOI: <https://doi.org/10.1038/s41586-021-03233-8>

Further reading

- [**NASH limits anti-tumour surveillance in immunotherapy-treated HCC**](#)
 - Dominik Pfister
 - , Nicolás Gonzalo Núñez
 - , Roser Pinyol
 - , Olivier Govaere
 - , Matthias Pinter
 - , Marta Szydłowska
 - , Revant Gupta
 - , Mengjie Qiu
 - , Aleksandra Deczkowska
 - , Assaf Weiner
 - , Florian Müller
 - , Ankit Sinha
 - , Ekaterina Friebel
 - , Thomas Engleitner
 - , Daniela Lenggenhager
 - , Anja Moncsek
 - , Danijela Heide
 - , Kristin Stirm
 - , Jan Kosla
 - , Eleni Kotsiliti
 - , Valentina Leone
 - , Michael Dudek

- , Suhail Yousuf
- , Donato Inverso
- , Indrabahadur Singh
- , Ana Teijeiro
- , Florian Castet
- , Carla Montironi
- , Philipp K. Haber
- , Dina Tiniakos
- , Pierre Bedossa
- , Simon Cockell
- , Ramy Younes
- , Michele Vacca
- , Fabio Marra
- , Jörn M. Schattenberg
- , Michael Allison
- , Elisabetta Bugianesi
- , Vlad Ratziu
- , Tiziana Pressiani
- , Antonio D'Alessio
- , Nicola Personeni
- , Lorenza Rimassa
- , Ann K. Daly
- , Bernhard Scheiner
- , Katharina Pomej
- , Martha M. Kirstein
- , Arndt Vogel
- , Markus Peck-Radosavljevic
- , Florian Hucke
- , Fabian Finkelmeier
- , Oliver Waidmann
- , Jörg Trojan
- , Cornelius Schulze
- , Henning Wege
- , Sandra Koch
- , Arndt Weinmann
- , Marco Bueter
- , Fabian Rössler

- , Alexander Siebenhüner
- , Sara De Dosso
- , Jan-Philipp Mallm
- , Viktor Umansky
- , Manfred Jugold
- , Tom Luedde
- , Andrea Schietinger
- , Peter Schirmacher
- , Brinda Emu
- , Hellmut G. Augustin
- , Adrian Billeter
- , Beat Müller-Stich
- , Hiroto Kikuchi
- , Dan G. Duda
- , Fabian Kütting
- , Dirk-Thomas Waldschmidt
- , Matthias Philip Ebert
- , Nuh Rahbari
- , Henrik E. Mei
- , Axel Ronald Schulz
- , Marc Ringelhan
- , Nisar Malek
- , Stephan Spahn
- , Michael Bitzer
- , Marina Ruiz de Galarreta
- , Amaia Lujambio
- , Jean-Francois Dufour
- , Thomas U. Marron
- , Ahmed Kaseb
- , Masatoshi Kudo
- , Yi-Hsiang Huang
- , Nabil Djouder
- , Katharina Wolter
- , Lars Zender
- , Parice N. Marche
- , Thomas Decaens
- , David J. Pinato

- , Roland Rad
- , Joachim C. Mertens
- , Achim Weber
- , Kristian Unger
- , Felix Meissner
- , Susanne Roth
- , Zuzana Macek Jilkova
- , Manfred Claassen
- , Quentin M. Anstee
- , Ido Amit
- , Percy Knolle
- , Burkhard Becher
- , Josep M. Llovet
- & Mathias Heikenwalder

Nature (2021)

Comments

By submitting a comment you agree to abide by our [Terms](#) and [Community Guidelines](#). If you find something abusive or that does not comply with our terms or guidelines please flag it as inappropriate.

[Access through your institution](#)

[Change institution](#)

[Buy or subscribe](#)

This article was downloaded by **calibre** from <https://www.nature.com/articles/s41586-021-03233-8>

NASH limits anti-tumour surveillance in immunotherapy-treated HCC

[Download PDF](#)

- Article
- Open Access
- [Published: 24 March 2021](#)

NASH limits anti-tumour surveillance in immunotherapy-treated HCC

- [Dominik Pfister](#) ORCID: orcid.org/0000-0002-0542-2638¹ nAff⁸²,
- [Nicolás Gonzalo Núñez](#) ORCID: orcid.org/0000-0003-3837-270X²,
- [Roser Pinyo](#)³,
- [Olivier Govaere](#) ORCID: orcid.org/0000-0002-4426-6930⁴,
- [Matthias Pinter](#)^{5,6},
- [Marta Szydłowska](#) ORCID: orcid.org/0000-0002-4660-899X¹,
- [Revant Gupta](#) ORCID: orcid.org/0000-0002-0881-5074^{7,8},
- [Mengjie Qiu](#)⁹,
- [Aleksandra Deczkowska](#) ORCID: orcid.org/0000-0003-0844-4346¹⁰,
- [Assaf Weiner](#)¹⁰,
- [Florian Müller](#)¹,
- [Ankit Sinha](#)^{11,12},
- [Ekaterina Friebel](#) ORCID: orcid.org/0000-0003-1419-2376²,
- [Thomas Engleitner](#)^{13,14,15},
- [Daniela Lenggenhager](#) ORCID: orcid.org/0000-0002-5382-9854¹⁶,
- [Anja Moncsek](#) ORCID: orcid.org/0000-0002-1191-5842¹⁷,
- [Danijela Heide](#)¹,
- [Kristin Stirm](#)¹,
- [Jan Kosla](#)¹,
- [Eleni Kotsili](#)¹,
- [Valentina Leone](#)^{1,18},
- [Michael Dudek](#)¹⁹,
- [Suhail Yousuf](#)⁹,
- [Donato Inverso](#) ORCID: orcid.org/0000-0003-0987-3345^{20,21},
- [Indrabahadur Singh](#)^{1,22},
- [Ana Teijeiro](#)²³,

- [Florian Castet](#)³,
- [Carla Montironi](#)³,
- [Philipp K. Haber](#)²⁴,
- [Dina Tiniakos](#)^{4,25},
- [Pierre Bedossa](#)⁴,
- [Simon Cockell](#)²⁶,
- [Ramy Younes](#)^{4,27},
- [Michele Vacca](#) ORCID: orcid.org/0000-0002-1973-224X²⁸,
- [Fabio Marra](#) ORCID: orcid.org/0000-0001-8629-0878²⁹,
- [Jörn M. Schattenberg](#)³⁰,
- [Michael Allison](#) ORCID: orcid.org/0000-0003-3677-3294³¹,
- [Elisabetta Bugianesi](#)²⁷,
- [Vlad Ratziu](#)³²,
- [Tiziana Pressiani](#)³³,
- [Antonio D'Alessio](#) ORCID: orcid.org/0000-0002-9164-3671³³,
- [Nicola Personeni](#) ORCID: orcid.org/0000-0002-7995-272X^{33,34},
- [Lorenza Rimassa](#) ORCID: orcid.org/0000-0001-9957-3615^{33,34},
- [Ann K. Daly](#)⁴,
- [Bernhard Scheiner](#)^{5,6},
- [Katharina Pomej](#) ORCID: orcid.org/0000-0002-2807-3565^{5,6},
- [Martha M. Kirstein](#)^{35,36},
- [Arndt Vogel](#)³⁵,
- [Markus Peck-Radosavljevic](#) ORCID: orcid.org/0000-0002-0597-2728³⁷,
- [Florian Hucke](#)³⁷,
- [Fabian Finkelmeier](#)³⁸,
- [Oliver Waidmann](#)³⁸,
- [Jörg Trojan](#)³⁸,
- [Kornelius Schulze](#)³⁹,
- [Henning Wege](#)³⁹,
- [Sandra Koch](#)⁴⁰,
- [Arndt Weinmann](#)⁴⁰,
- [Marco Bueter](#)⁴¹,
- [Fabian Rössler](#)⁴¹,
- [Alexander Siebenhüner](#)⁴²,
- [Sara De Dosso](#)⁴³,
- [Jan-Philipp Mallm](#) ORCID: orcid.org/0000-0002-7059-4030⁴⁴,
- [Viktor Umansky](#)^{45,46},
- [Manfred Jugold](#)⁴⁷,
- [Tom Luedde](#)⁴⁸,

- [Andrea Schietinger](#) ORCID: [orcid.org/0000-0003-3644-1687^{49,50}](http://orcid.org/0000-0003-3644-1687),
- [Peter Schirmacher⁵¹](#),
- [Brinda Emu¹](#),
- [Hellmut G. Augustin](#) ORCID: [orcid.org/0000-0002-7173-4242^{20,21}](http://orcid.org/0000-0002-7173-4242),
- [Adrian Billeter⁵²](#),
- [Beat Müller-Stich⁵²](#),
- [Hiroto Kikuchi](#) ORCID: [orcid.org/0000-0002-3601-8435⁵³](http://orcid.org/0000-0002-3601-8435),
- [Dan G. Duda](#) ORCID: [orcid.org/0000-0001-7065-8797⁵³](http://orcid.org/0000-0001-7065-8797),
- [Fabian Küttig⁵⁴](#),
- [Dirk-Thomas Waldschmidt⁵⁴](#),
- [Matthias Philip Ebert⁵⁵](#),
- [Nuh Rahbari⁵⁶](#),
- [Henrik E. Mei](#) ORCID: [orcid.org/0000-0003-0697-7755⁵⁷](http://orcid.org/0000-0003-0697-7755),
- [Axel Ronald Schulz](#) ORCID: [orcid.org/0000-0002-5106-0148⁵⁷](http://orcid.org/0000-0002-5106-0148),
- [Marc Ringelhan](#) ORCID: [orcid.org/0000-0003-3131-5657^{58,59,60}](http://orcid.org/0000-0003-3131-5657),
- [Nisar Malek⁶¹](#),
- [Stephan Spahn⁶¹](#),
- [Michael Bitzer⁶¹](#),
- [Marina Ruiz de Galarreta^{24,62}](#),
- [Amaia Lujambio](#) ORCID: [orcid.org/0000-0002-2798-1481^{24,62,63}](http://orcid.org/0000-0002-2798-1481),
- [Jean-Francois Dufour](#) ORCID: [orcid.org/0000-0002-8062-1346^{64,65}](http://orcid.org/0000-0002-8062-1346),
- [Thomas U. Marron^{24,66}](#),
- [Ahmed Kaseb⁶⁷](#),
- [Masatoshi Kudo](#) ORCID: [orcid.org/0000-0002-4102-3474⁶⁸](http://orcid.org/0000-0002-4102-3474),
- [Yi-Hsiang Huang^{69,70}](#),
- [Nabil Djouder](#) ORCID: [orcid.org/0000-0001-8423-1030²³](http://orcid.org/0000-0001-8423-1030),
- [Katharina Wolter^{71,72}](#),
- [Lars Zender](#) ORCID: [orcid.org/0000-0001-7626-2849^{71,72,73}](http://orcid.org/0000-0001-7626-2849),
- [Parice N. Marche^{74,75}](#),
- [Thomas Decaens^{74,75,76}](#),
- [David J. Pinato](#) ORCID: [orcid.org/0000-0002-3529-0103^{77,78}](http://orcid.org/0000-0002-3529-0103),
- [Roland Rad](#) ORCID: [orcid.org/0000-0002-6849-9659^{13,14,15}](http://orcid.org/0000-0002-6849-9659),
- [Joachim C. Mertens](#) ORCID: [orcid.org/0000-0003-2007-0308¹⁷](http://orcid.org/0000-0003-2007-0308),
- [Achim Weber](#) ORCID: [orcid.org/0000-0003-0073-3637^{16,79}](http://orcid.org/0000-0003-0073-3637),
- [Kristian Unger¹⁸](#),
- [Felix Meissner](#) ORCID: [orcid.org/0000-0003-1000-7989¹¹](http://orcid.org/0000-0003-1000-7989),
- [Susanne Roth⁹](#),
- [Zuzana Macek Jilkova^{74,75,77}](#),
- [Manfred Claassen^{7,8}](#),

- [Quentin M. Anstee](#)^{4,80},
- [Ido Amit](#) ORCID: orcid.org/0000-0003-2968-877X¹⁰,
- [Percy Knolle](#) ORCID: orcid.org/0000-0003-2983-0414¹⁹,
- [Burkhard Becher](#) ORCID: orcid.org/0000-0002-1541-7867²,
- [Josep M. Llovet](#) ORCID: orcid.org/0000-0003-0547-2667^{3,24,81} &
- [Mathias Heikenwalder](#) ORCID: orcid.org/0000-0002-3135-2274¹

[Nature](#) volume 592, pages450–456(2021)[Cite this article](#)

- 33k Accesses
- 239 Altmetric
- [Metrics details](#)

Subjects

- [Cancer](#)
- [Immunotherapy](#)

This article has been [updated](#)

Abstract

Hepatocellular carcinoma (HCC) can have viral or non-viral causes^{1,2,3,4,5}. Non-alcoholic steatohepatitis (NASH) is an important driver of HCC. Immunotherapy has been approved for treating HCC, but biomarker-based stratification of patients for optimal response to therapy is an unmet need^{6,7}. Here we report the progressive accumulation of exhausted, unconventionally activated CD8⁺PD1⁺ T cells in NASH-affected livers. In preclinical models of NASH-induced HCC, therapeutic immunotherapy targeted at programmed death-1 (PD1) expanded activated CD8⁺PD1⁺ T cells within tumours but did not lead to tumour regression, which indicates that tumour immune surveillance was impaired. When given prophylactically, anti-PD1 treatment led to an increase in the incidence of NASH-HCC and in the number and size of tumour nodules, which correlated with increased hepatic CD8⁺PD1⁺CXCR6⁺, TOX⁺, and TNF⁺ T cells. The increase in HCC triggered by anti-PD1 treatment was prevented by depletion of CD8⁺ T cells or TNF neutralization, suggesting that CD8⁺ T cells help to induce NASH-HCC, rather than invigorating or executing immune surveillance. We found similar phenotypic and functional profiles in hepatic

CD8⁺PD1⁺ T cells from humans with NAFLD or NASH. A meta-analysis of three randomized phase III clinical trials that tested inhibitors of PDL1 (programmed death-ligand 1) or PD1 in more than 1,600 patients with advanced HCC revealed that immune therapy did not improve survival in patients with non-viral HCC. In two additional cohorts, patients with NASH-driven HCC who received anti-PD1 or anti-PDL1 treatment showed reduced overall survival compared to patients with other aetiologies. Collectively, these data show that non-viral HCC, and particularly NASH–HCC, might be less responsive to immunotherapy, probably owing to NASH-related aberrant T cell activation causing tissue damage that leads to impaired immune surveillance. Our data provide a rationale for stratification of patients with HCC according to underlying aetiology in studies of immunotherapy as a primary or adjuvant treatment.

[Download PDF](#)

Main

Potentially curative treatments for HCC, such as liver transplantation, tumour resection, or ablation, are limited to early-stage tumours^{1,2}. Multikinase inhibitors and anti-VEGF-R2 antibodies have been approved for use in advanced HCC^{1,2}. Immunotherapy, which is thought to activate T cells or reinvigorate immune surveillance against cancer, showed response rates of 15–30% in patients with HCC^{5,8,9,10,11}. Nivolumab and pembrolizumab (PD1-directed antibodies) have been approved for treatment of HCC^{3,4}, although phase III trials failed to reach their primary endpoints to increase survival^{1,10,11}. A combination of atezolizumab (anti-PDL1) and bevacizumab (anti-VEGF) demonstrated increased overall and progression-free survival in a phase III trial, making it a first-line treatment for advanced HCC⁵. The efficacy of immunotherapy might be affected by different underlying HCC aetiologies, with diverse hepatic environments distinctly regulating HCC induction and immune responses⁶. Hence, we lack biomarkers that correlate with treatment response to allow patient stratification^{12,13}. Non-alcoholic fatty liver disease (NAFLD) is an HCC-causing condition that affects more than 200 million people worldwide¹⁴. Approximately 10–20% of individuals with NAFLD progress over time from steatosis to NASH¹⁴. Innate and adaptive immune-cell activation^{15,16,17}, in combination with increased metabolites and endoplasmic reticulum stress^{16,18}, are believed to lead to a cycle of hepatic necro-inflammation and regeneration that potentially leads to HCC^{19,20,21}. NASH has become an emerging risk factor for HCC^{1,14,19}, which led us to investigate the effects of immunotherapy in NASH–HCC^{22,23,24}.

Hepatic CD8⁺PD1⁺ T cells increase in NASH

We fed mice with diets that cause progressive liver damage and NASH over 3–12 months (Extended Data Fig. [1a–c](#)), accompanied by an increase in the frequency of activated CD8⁺ T cells expressing CD69, CD44 and PD1 (Extended Data Fig. [1d–g](#)). Single-cell mapping of leukocytes showed altered immune-cell compositions in mice with NASH (Extended Data Fig. [1h, i](#)) with strongly increased numbers of CD8⁺PD1⁺ cells (Fig. [1a, b](#), Extended Data Fig. [1j–m, o](#)). Similarly, elevated CD8⁺ and PD1⁺ cells were found in a genetic mouse model of NASH¹⁷ (Extended Data Fig. [1n](#)). Messenger RNA in situ hybridization and immunohistochemistry showed that increasing PDL1 expression in hepatocytes and non-parenchymal cells correlated with the severity of NASH (Extended Data Fig. [1p](#)). Mass spectrometric characterization of CD8⁺PD1⁺ T cells from NASH-affected livers indicated enrichment in pathways involved in ongoing T cell activation and differentiation, TNF signalling, and natural killer (NK) cell-like cytotoxicity (Fig. [1c](#)). Single-cell RNA sequencing (scRNA-seq) of cells expressing T cell receptor β-chains (TCRβ) from the livers of mice with NASH showed that CD8⁺ T cells had gene expression profiles related to cytotoxicity and effector-function (for example, *Gzmk* and *Gzmm*) and inflammation markers (for example, *Ccl3*) with elevated exhaustion traits (for example, *Pdcid1* and *Tox*) (Fig. [1d, e](#)). RNA-velocity analyses demonstrated enhanced transcriptional activity and differentiation from *Sell*-expressing CD8⁺ to CD8⁺PD1⁺ T cells (Extended Data Fig. [1q](#)), indicating local differentiation. Thus, mice with NASH have increased hepatic abundance of CD8⁺PD1⁺ T cells with features of exhaustion and effector functions.

Fig. 1: NASH progression is associated with increased, activated CD8⁺PD1⁺ T cells.

 **figure1**

a, CD8 and PD1 staining (right) and quantification (left) of T cells from mice fed normal diet (ND), CD-HFD or western-style diet with trans fat (WD-HTF) by immunohistochemistry. **b**, Immunofluorescence-based detection of PD1 (green), CD8 (red) and CD4 (yellow) cells. Scale bar, 100 µm. **c**, GSEA of hepatic CD8⁺PD1⁺ T cells sorted from TCR β^+ cells by mass spectrometry. FDR, false discovery rate; NES, normalized enrichment score. **d–f**, *t*-distributed stochastic neighbour embedding (tSNE) of TCR β^+ cells (**d**), differential gene expression by scRNA-seq (**e**) and scheme for experiment (**f**): mice were fed CD-HFD for 13 months and then treated with anti-PD1 for 8 weeks before measurement of tumour incidence. Mem, memory CD4 T cells. **g**, Livers from treated and untreated mice after CD-HFD. Arrowheads, tumours or lesions. Scale bar, 10 mm. **h**, Quantification of CD8⁺ cell in liver by immunohistochemistry. Details of sample sizes, biological replicates and statistical tests are given in Methods and Source Data. **a, h**, *P* values shown above brackets.

[Source data](#)

[Full size image](#)

The high numbers of T cells in NASH suggest that anti-PD1-targeted immunotherapy may serve as an efficient therapy for NASH–HCC. Thirty per cent of C57BL/6 mice fed a choline-deficient high-fat diet (CD-HFD) for 13 months developed liver tumours with a similar load of genetic alterations to human NAFLD–HCC or NASH–HCC

(Extended Data Fig. 2a, b). NASH mice bearing HCC (identified using MRI) were allocated to anti-PD1 immunotherapy or control arms (Fig. 1f). None of the pre-existing liver tumours regressed in response to anti-PD1 therapy (Fig. 1g, h, Extended Data Fig. 2c). Rather, we observed increased fibrosis, unchanged liver damage, slightly increased incidence of liver cancer and unaltered tumour loads and sizes after anti-PD1 treatment (Extended Data Fig. 2d–h). In anti-PD1-treated mice, liver tumour tissue contained increased numbers of CD8⁺/PD1⁺ T cells and high levels of cells expressing *Cxcr6* or *Tnf* mRNA (Extended Data Fig. 2i–n). We found no regression of NASH-induced liver tumours upon anti-PDL1 immunotherapy (Extended Data Fig. 3a–f). By contrast, other (non-NASH) mouse models of liver cancer (with or without concomitant damage) reacted to PD1 immunotherapy with tumour regression²⁵, suggesting that lack of response to immunotherapy was associated specifically with NASH–HCC (Extended Data Fig. 3g–i). Thus, NASH precluded efficient anti-tumour surveillance in the context of HCC immunotherapy. Similarly, impaired immunotherapy has been described in mouse models with NASH and secondary liver cancer^{25,26}.

CD8⁺ T cells promote HCC in NASH

As CD8⁺PD1⁺ T cells failed to execute effective immune surveillance, but rather showed tissue-damaging potential, we reasoned that CD8⁺ T cells might be involved in promoting NASH–HCC. We depleted CD8⁺ T cells in a preventive setting in mice with NASH but without liver cancer (CD-HFD fed for 10 months). CD8⁺ T cell depletion significantly decreased liver damage and the incidence of HCC in these mice (Fig. 2i, Extended Data Fig. 4a–j, n). Similar results were obtained after co-depletion of CD8⁺ and NK1.1⁺ cells (Fig. 2i, Extended Data Fig. 4a–f, n). This suggests that as well as lacking immune surveillance functions, liver CD8⁺ T cells also promote HCC in mice with NASH. Next, we investigated the effect of anti-PD1 therapy on HCC development in mice with NASH. Anti-PD1 immunotherapy aggravated liver damage (Fig. 2g, Extended Data Fig. 7c) and increased hepatic CD8⁺PD1⁺ T cells, with only minor changes in liver CD4⁺PD1⁺ T cells or other immune-cell populations (Extended Data Fig. 4a–o). Anti-PD1 immunotherapy also caused a marked increase in liver-cancer incidence, independent of changes in liver fibrosis (Fig. 2i). Mice lacking PD1 (*Pdcd1*^{-/-}) showed an increase in incidence of, and earlier onset of, liver cancer, along with increased liver damage and elevated numbers of activated hepatic CD8⁺ T cells with increased cytokine expression (IFN γ , TNF) (Extended Data Fig. 5a–g). In summary, CD8⁺PD1⁺ T cells triggered the transition to HCC in mice with NASH, probably owing to impaired tumour surveillance and enhanced T cell-mediated tissue damage²⁷. Despite a strong increase in CD8⁺PD1⁺ T cells within tumours, therapeutic

PD1- or PDL1-related immunotherapy failed to cause tumour regression in NASH–HCC.

Fig. 2: Resident-like CD8⁺PD1⁺ T cells drive hepatocarcinogenesis in a TNF-dependent manner upon anti-PD1 treatment in NASH.

 figure2

a, b, RNA-velocity analyses of scRNA-seq data showing expression (**a**) and correlation of expression (**b**) along the latent time of selected genes in CD8⁺ T cells from mice with NASH. Latent time (pseudo-time by RNA velocity): dark colour, start of RNA velocity; yellow, end point of latent time. Kendall's τ , gene expression along latent time. **c,** Principal component analysis (PCA) plot of hepatic CD8⁺ and CD8⁺PD1⁺ T cells sorted by mass spectrometry from TCR β^+ cells from mice fed for 12 months with ND, CD-HFD or CD-HFD and treated for 8 weeks with anti-PD1 antibodies. **d, e,** UMAP representations showing FlowSOM-guided clustering (**d**, left), heat map showing median marker expression (**d**, right), and quantification of hepatic CD8⁺ T cells (**e**) from mice fed for 12 months with ND or CD-HFD and treated for 8 weeks with IgG or anti-PD1 antibodies. **f,** Quantification of CellCNN-analysed flow cytometry data for hepatic CD8⁺ T cells from mice fed for 12 months with CD-HFD and treated for 8 weeks with IgG or anti-PD1 antibodies. **g, h,** NAS evaluation (**g**) and quantification of hepatic CD8⁺PD1⁺CXCR6⁺ T cells (**h**) from mice fed with ND for 12 months or fed with CD-HFD for 12 months and treated for 8 weeks with anti-PD1, anti-PD1 + anti-CD8, anti-TNF, anti-PD1 + anti-TNF, anti-CD4, or anti-PD1 + anti-CD4 antibodies. Kendall's τ , gene expression along latent time. **i,** Quantification of

tumour incidence in mice as in **g**, **h**. Details of sample sizes, biological replicates and statistical tests are given in Methods and Source Data. **e–i**, *P* values shown above brackets.

[Source data](#)

[Full size image](#)

We used an immune-mediated cancer field (ICF) gene-expression signature associated with the development of human HCC²⁸ to understand the tumour-driving mechanisms of anti-PD1 immunotherapy. Preventive anti-PD1 treatment was strongly associated with the pro-tumorigenic immunosuppressive ICF signature (for example, *Ifng*, *Tnf*, *Stat3*, *Tgfb1*), capturing the traits of T cell exhaustion, pro-carcinogenic signalling, and mediators of immune tolerance and inhibition. Depletion of CD8⁺ T cells led to significant downregulation of the high-infiltrate ICF signature and diminished TNF in non-parenchymal cells (Extended Data Fig. [5h,i](#)). Gene set enrichment analysis (GSEA), mRNA in situ hybridization, and histology of tumours developed in NASH mice that were treated prophylactically with anti-PD1 corroborated these data, showing increased CD8⁺ T cell abundance and enrichment for genes involved in inflammation-related signalling, apoptosis, and TGFβ signalling (Extended Data Fig. [5j-l](#)). Anti-PD1 treatment triggered the expression of p62 (Extended Data Fig. [5m](#)), which has been shown to drive hepatocarcinogenesis²⁹. Array comparative genomic hybridization identified no significant differences in chromosomal deletions or amplifications between tumours from anti-PD1-treated mice or control mice (Extended Data Fig. [5n](#)). In summary, hepatic CD8⁺PD1⁺ T cells did not cause tumour regression during NASH, but rather were linked to HCC development, which was enhanced by anti-PD1 immunotherapy.

We next analysed the hepatic T cell compartment for correlations with inflammation and hepatocarcinogenesis. Comparison of CD8⁺PD1⁺ T cells with CD8⁺ T cells by scRNA-seq showed that the former showed higher expression of genes associated with effector function (for example, increased *Gzma*, *Gzmb*, *Gzmk*, *Prfl*; reduced *Sell*, *Klf2*), exhaustion (for example, increased *Pdcd1*, *Tox*; reduced *Il7r*, *Tcf7*) and tissue residency (for example, increased *Cxcr6*, low levels of Ki-67) (Extended Data Fig. [6a–c](#)). Notably, there was no difference in the transcriptome profiles of CD8⁺PD1⁺ T cells in NASH mice after anti-PD1 immunotherapy (Extended Data Fig. [6c](#)), indicating that the number of T cells rather than their functional properties were changed. RNA-velocity blot analyses corroborated these data (Fig. [2a](#), Extended Data Fig. [6d–f](#)). Similar patterns of markers (for example, *IL7r*, *Sell*, *Tcf7*, *Ccl5*, *Pdcd1*, *Cxcr6*, and *Rgs1*) correlated with latent time and overall transcriptional activity in NASH mice that received either treatment (Fig. [2a,b](#), Extended Data Fig. [6e,f](#)). Mass

spectrometry-based analyses of CD8⁺ or CD8⁺PD1⁺ T cells isolated from NASH mouse livers confirmed these findings (Fig. 2c, Extended Data Fig. 6g).

We characterized the transcriptome profiles of PD1⁺CD8⁺ T cells by uniform manifold approximation and projection (UMAP) analysis of high-parametric flow-cytometry data, dissecting the CD8⁺PD1⁺ and CD8⁺PD1⁻ subsets (Fig. 2d). This revealed that CD8⁺PD1⁺ cells expressed high levels of effector (for example, *Gzmb*, *Ifng*, *Tnf*) and exhaustion markers (for example, *Eomes*, *Pdcld1*, Ki-67^{low}). In particular, CD8⁺PD1⁺TNF⁺ cells were more abundant upon anti-PD1 treatment (Fig. 2e). Convolutional neural network analysis and manual gating validated this result (Fig. 2f, Extended Data Fig. 6j, k). CD8⁺PD1⁺ T cells were non-proliferative in anti-PD1-treated NASH mice; this result was supported by in vitro experiments, in which anti-PD1 treatment led to increased T cell numbers in the absence of proliferation (Extended Data Fig. 6l, m). Notably, CD8⁺PD1⁺ T cells from NASH mice showed reduced levels of FOXO1, which indicates an enhanced tissue-residency phenotype³⁰, potentially combined with boosted effector function, as indicated by higher calcium levels in CD8⁺PD1⁺ T cells (Extended Data Fig. 6n, o). Single-cell RNA-seq analysis also showed that CD8⁺PD1⁺ T cells from NASH mice had a tissue residency signature (Extended Data Fig. 6b). Thus, upon anti-PD1 immunotherapy in NASH mice, CD8⁺PD1⁺ T cells accumulated to high numbers in the liver, revealing a resident-like T cell character with increased expression of CD44, CXCR6, EOMES and TOX and low levels of CD244 expression, but lacking expression of TCF1/TCF7, CD62L, TBET, and CD127 (Extended Data Fig. 6p–u). In summary, anti-PD1 immunotherapy increased the abundance of CD8⁺PD1⁺ T cells with a residency signature in the liver.

To investigate the mechanisms that drive the increased NASH–HCC transition in the preventive anti-PD1 treatment-setting, we treated NASH-affected mice with combinations of treatments. Both anti-CD8–anti-PD1 and anti-TNF–anti-PD1 antibody treatments ameliorated liver damage, liver pathology and liver inflammation (Fig. 2g, Extended Data Fig. 7), and decreased the incidence of liver cancer compared to anti-PD1 treatment alone (Fig. 2i). By contrast, anti-CD4–anti-PD1 treatment did not reduce the incidence of liver cancer, the NAFLD activity score (NAS), or the number of TNF-expressing hepatic CD8⁺ or CD8⁺PD1⁺CXCR6⁺ T cells (Fig. 2g–i, Extended Data Fig. 7). However, both the number of tumours per liver and tumour size were reduced, suggesting that depletion of CD4⁺ T cells or regulatory T cells might contribute to tumour control (Extended Data Fig. 8a, b). The incidence of tumours was directly correlated with anti-PD1 treatment, alanine aminotransferase (ALT), NAS, number of hepatic CD8⁺PD1⁺ T cells, and TNF expression (Extended Data Fig. 8c–e). These data suggested that CD8⁺PD1⁺ T cells lacked immune-surveillance and had tissue-damaging functions²⁷, which were increased by anti-PD1

treatment, possibly contributing to the unfavourable effects of anti-PD1 treatment on HCC development in NASH.

Augmented CD8⁺PD1⁺ T cells in human-NASH

We next investigated CD8⁺ T cells from healthy or NAFLD/NASH-affected livers. In two independent cohorts of patients with NASH, we found enrichment of hepatic CD8⁺PD1⁺ T cells with a residency phenotype (by flow cytometry and mass cytometry) (Fig. 3a,b, Extended Data Fig. 9a–j, Supplementary Tables 1,2). The number of hepatic CD8⁺PD1⁺ T cells directly correlated with body-mass index and liver damage (Extended Data Fig. 9b). To investigate similarities between mouse and human T cells from livers with NASH, we analysed liver CD8⁺PD1⁺ T cells from patients with NAFLD or NASH by scRNA-seq. This identified a gene expression signature that was also found in liver T cells from NASH mice (for example, *PDCD1*, *GZMB*, *TOX*, *CXCR6*, *RGS1*, *SELL*) (Fig. 3c,d, Extended Data Fig. 9k,l).

Differentially expressed genes were directly correlated between patient- and mouse-derived hepatic CD8⁺PD1⁺ T cells (Fig. 3d). Velocity-blot analyses identified CD8⁺ T cells expressing *TCF7*, *SELL* and *IL7R* as root cells, and CD8⁺PD1⁺ T cells as their endpoints (Fig. 3e,f), indicating a local developmental trajectory of CD8⁺ T cells into CD8⁺PD1⁺ T cells. The amount of gene expression and velocity magnitude, which indicate transcriptional activity, were increased in CD8⁺PD1⁺ T cells from mice and humans with NASH (Fig. 3e). The expression of specific marker genes (for example, *IL7R*, *SELL*, *TCF7*, *CCL5*, *CCL3*, *PDCD1*, *CXCR6*, *RGS1* and *KLF2*) along the latent time in patients with NAFLD or NASH differed from that seen in control participants (Fig. 3g), and correlated with the expression patterns seen in CD8⁺ T cells from NASH mice (Fig. 3h). Thus, scRNA-seq analysis demonstrated a resident-like liver CD8⁺PD1⁺ T cell population in patients with NAFLD or NASH that shared gene expression patterns with hepatic CD8⁺PD1⁺ T cells from NASH mice.

Fig. 3: Hepatic resident-like CD8⁺PD1⁺ T cells are increased in livers of patients with NAFLD patients.

 **figure3**

a, b, UMAP representation showing the FlowSOM-guided clustering of CD45⁺ cells (**a**) and flow cytometry plots (**b**, left) and quantification (**b**, right) of CD8⁺PD1⁺CD103⁺ cells derived from hepatic biopsies of healthy individuals or patients with NAFLD or NASH (Supplementary Table 2). Populations in **b**: violet, CD8⁺; red, CD8⁺PD1⁺CD103⁺. T_{reg} cells, regulatory T cells. **c**, UMAP representations and analyses of differential gene expression by scRNA-seq of CD3⁺ cells from control individuals or patients with NAFLD or NASH. MAITs, mucosal-associated invariant T cells. **d**, Correlation of significant differentially expressed genes in liver-derived CD8⁺PD1⁺ T cells compared to CD8⁺PD1⁻ T cells from mice fed with CD-HFD for 12 months and patients with NAFLD/NASH. Shading shows 95% CI. **e–h**, Expression (**e**) and transcriptional activity (**f**) of velocity analyses of scRNA-seq data, and gene expression (**g**) and correlation (**h**) of expression along the latent-time of selected genes along the latent-time of liver-derived CD8⁺ T cells from patients with NAFLD or NASH in comparison to control or NASH mouse liver-derived CD8⁺ T cells. Root cells: yellow, root cells; blue, cells furthest from the root by RNA velocity. End points:

yellow, end-point cells; blue, cells furthest from defined end-point cells by RNA velocity. Latent time (pseudo-time by RNA velocity): dark colour, start of RNA velocity; yellow, end point of latent time. RNA velocity flow (top): blue cluster, start point; orange cluster, intermediate; green cluster, end point. Arrow indicates cell trajectory. Details of sample sizes, biological replicates and statistical tests are given in Methods and Source Data. **b, e**, *P* values shown above brackets.

[Source data](#)

[Full size image](#)

Different stages of NASH severity are considered to herald the development of liver cancer³¹. Indeed, different fibrosis stages (F0–F4) in patients with NASH correlated directly with the expression of *PDCD1*, *CCL2*, *IP10* and *TNF*, and the degree of fibrosis correlated with the numbers of CD4⁺, PD1⁺, and CD8⁺ T cells (Extended Data Fig. [10a–d](#), Supplementary Table [3](#)). Moreover, PD1⁺ cells were absent from healthy livers but present in the livers of patients with NASH or NASH–HCC, but the number of these cells did not differ with the underlying fibrosis level (Extended Data Fig. [10e](#), Supplementary Tables [4–6](#)). Species-specific effects, such as the absence in mice of cirrhosis or burnt-out NASH (a condition found in some patients with NASH–HCC³²), and their possible influence on immunotherapy may make it difficult to translate findings from preclinical models of NASH to human NASH. However, in tumour tissue from patients with NASH-induced HCC—treated with anti-PD1 therapy—we found increased numbers of intra-tumoral PD1⁺ cells compared to patients with HCC and viral hepatitis (Extended Data Fig. [10f](#)). Thus, we found a shared gene-expression profile and increased abundance of unconventionally activated hepatic CD8⁺PD1⁺ T cells in human NASH tissue.

Lack of immunotherapy response in human NASH–HCC

To explore the concept of disrupted immune surveillance in NASH after anti-PD1 or anti-PDL1 treatment, we conducted a meta-analysis of three large randomized controlled phase III trials of immunotherapies in patients with advanced HCC (CheckMate-459¹¹, IMbrave150⁵ and KEYNOTE-240¹⁰). Although immunotherapy improved survival in the overall population (hazard ratio (HR) 0.77; 95% confidence interval (CI) 0.63–0.94), survival was superior to the control arm in patients with HBV-related HCC ($n = 574$; $P = 0.0008$) and HCV-related HCC ($n = 345$; $P = 0.04$), but not in patients with non-viral HCC ($n = 737$; $P = 0.39$) (Fig. [4a](#), Extended Data Fig. [10g](#), Supplementary Table [7](#)). Patients with viral aetiology (HBV or HCV infection) of liver damage and HCC showed a benefit from checkpoint inhibition (HR 0.64; 95% CI 0.48–0.94), whereas patients with HCC of a non-viral aetiology did not (HR 0.92; 95% CI 0.77–1.11; P of interaction = 0.03 (Fig. [4a](#))). Subgroup analysis of

first-line treatment compared to a control arm treated with sorafenib ($n = 1,243$) confirmed that immunotherapy was superior in patients with HBV-related ($n = 473$; $P = 0.03$) or HCV-related HCC ($n = 281$; $P = 0.03$), but not in patients with non-viral HCC ($n = 489$; $P = 0.62$; Extended Data Fig. 10h–j). We acknowledge that these results were derived from a meta-analysis of trials that included different lines of treatment and patients with heterogeneous liver damage, and did not differentiate between alcoholic liver disease and NAFLD or NASH. Nevertheless, the results of this meta-analysis supported the notion that stratification of patients according to the aetiology of their liver damage and ensuing HCC identified patients who responded well to therapy.

Fig. 4: PD1 and PDL1 targeted immunotherapy in advanced HCC has a distinct effect depending on disease aetiology.

 **figure4**

a, Meta-analysis of 1,656 patients (Supplementary Table 7). Immunotherapy was initially assessed and then analysed according to disease aetiology: non-viral (NASH and alcohol intake) vs viral (HBV and HCV) (top). Heterogeneity: $\tau^2 = 0.00$; $\chi^2 = 0.14$, degrees of freedom (d.f.) = 2 ($P = 0.93$); $I^2 = 0\%$. Test for overall effect: $Z = 0.87$ ($P = 0.39$). Separate meta-analyses were subsequently performed for each of the three aetiologies: non-viral (NASH and alcohol intake), HCV and HBV (bottom).

Heterogeneity: $\tau^2 = 0.03$; $\chi^2 = 3.67$, d.f. = 2 ($P = 0.16$); $I^2 = 46\%$. Test for overall effect: $Z = 3.13$ ($P = 0.002$). Diamonds represent estimated overall effect based on the meta-analysis random effect of all trials. Inverse variance and random effects methods were used to calculate HRs, 95% CIs, P values, and the test for overall effect; calculations were two-sided. **b**, NAFLD is associated with a worse outcome in patients with HCC treated with PD(L)1-targeted immunotherapy. A total of 130 patients with advanced HCC received PD(L)1-targeted immunotherapy (Supplementary Table 8). **c**, Validation cohort of patients with HCC treated with PD(L)1-targeted immunotherapy. A total of 118 patients with advanced HCC received PD(L)1-targeted immunotherapy (Supplementary Table 10). **b, c**, Log-rank test. Details of sample sizes, biological replicates and statistical tests are given in Methods and Source Data.

[Source data](#)

[Full size image](#)

To specifically characterize the effect of anti-PD(L)1 immunotherapy with respect to underlying liver disease, we investigated a cohort of 130 patients with HCC (patients with NAFLD $n = 13$; patients with other aetiologies $n = 117$) (Supplementary Table 8). NAFLD was associated with shortened median overall survival after immunotherapy (5.4 months (95% CI 1.8–9.0 months) versus 11.0 months (95% CI 7.5–14.5 months); $P = 0.023$), even though patients with NAFLD had less frequent macrovascular tumour invasion (23% versus 49%), and immunotherapy was more often used as a first-line therapy in these patients (46% versus 23%; Fig. 4b). After correction for potentially confounding factors that are relevant for prognosis, including severity of liver damage, macrovascular tumour invasion, extrahepatic metastases, performance status, and alpha-fetoprotein (AFP), NAFLD remained independently associated with shortened survival of patients with HCC after anti-PD1-treatment (HR 2.6; 95% CI 1.2–5.6; $P = 0.017$, Supplementary Table 9). This finding was validated in a further cohort of 118 patients with HCC who were treated with PD(L)1-targeted immunotherapy (patients with NAFLD $n = 11$; patients with other aetiologies $n = 107$) (Supplementary Table 10). NAFLD was again associated with reduced survival of patients with HCC (median overall survival 8.8 months, 95% CI 3.6–12.4 months) compared to other aetiologies of liver damage (median overall survival 17.7 months, 95% CI 8.8–26.5 months; $P = 0.034$) (Fig. 4c). Given the relatively small number of patients with NAFLD in both cohorts, these data need prospective validation. However, collectively these results indicate that patients with underlying NASH did not benefit from checkpoint-inhibition therapy.

Liver cancer develops primarily on the basis of chronic inflammation. The latter can be activated by immunotherapy to induce tumour regression in a subset of patients with liver cancer. However, the identification of patients who will respond to immunotherapy for HCC remains difficult. Our data identify a non-viral aetiology of

liver damage and cancer (that is, NASH) as a predictor of unfavourable outcome in patients treated with immune-checkpoint inhibitors. The better response to immunotherapy in patients with virus-induced HCC than in patients with non-viral HCC might be due to the amount or quality of viral antigens or to a different liver micro-environment, possibly one that does not impair immune surveillance. These results might also have implications for patients with obesity and NALFD or NASH who have cancer at other organ sites (for example, melanoma, colon carcinoma, or breast cancer) and are at risk for liver damage and the development of liver cancer in response to systemically applied immunotherapy. Overall, our results provide comprehensive mechanistic insight and a rational basis for the stratification of patients with HCC according to their aetiology of liver damage and cancer for the design of future trials of personalized cancer therapy.

Methods

Mice, diets, and treatments

Standard mouse diet feeding (ad libitum water and food access) and treatment regimens were as described previously¹⁷. Male mice were housed at the German Cancer Research Center (DKFZ) (constant temperature of 20–24 °C and 45–65% humidity with a 12-h light–dark cycle). Mice were maintained under specific pathogen-free conditions and experiments were performed in accordance with German law and the governmental bodies, and with approval from the Regierungspräsidium Karlsruhe (G11/16, G129/16, G7/17). Tissues from inducible knock-in mice expressing the human unconventional prefoldin RPB5 interactor were received from N. Djouder^{17,33}. The plasmids for hydrodynamic tail-vein delivery have been described previously^{34,35,36,37}. For interventional studies, male mice fed a CD-HFD were treated with bi-weekly for 8 weeks by intravenous injection of 25 µg CD8-depleting antibody (Bioxcell, 2.43), 50 µg NK1.1-depleting antibody (Bioxcell, PK136), 300 µg anti-PDL1 (Bioxcell, 10F.9G2), 200 µg anti-TNF (Bioxcell, XT3.11), 100 µg anti-CD4 (Bioxcell, GK1.5), or 150 µg anti-PD1 (Bioxcell, RMP1-14). PD1^{−/−} mice were kindly provided by G. Tiegs and K. Neumann. Mice for Extended Data Fig. 3g were treated with anti-PD1 antibody (Bioxcell, RMP1-14) or isotype control (Bioxcell, 2A3) at an initial dose of 500 µg intraperitoneally (i.p.) followed by doses of 200 µg i.p. bi-weekly for 8 weeks. Mice for Extended Data Fig. 3h were treated i.p. with anti-PD1 (200 µg, Bioxcell, RMP1-14) or IgG (200 µg, Bioxcell, LTF-2). The treatment regimen for Extended Data Fig. 3i was as described elsewhere³⁸.

Intraperitoneal glucose tolerance test and measurement of serum parameters were as described previously¹⁷.

Magnetic resonance Imaging

MRI was done in the small animal imaging core facility in DKFZ using a Bruker BioSpec 9.4 Tesla (Ettlingen). Mice were anaesthetized with 3.5% sevoflurane, and imaged with T2-weighted imaging using a T2_TurboRARE sequence: TE = 22 ms, TR = 2,200 ms, field of view (FOV) 35 × 35 mm, slice thickness 1 mm, averages = 6, scan time 3 min 18 s, echo spacing 11 ms, rare factor 8, slices 20, image size 192 × 192 pixels, resolution 0.182 × 0.182 mm.

Multiplex ELISA

Liver homogenates were prepared as for western blotting¹⁷ and cytokines or chemokines were analysed on a customized ELISA according to the manufacturer's manual (Meso Scale Discovery, U-PLEX Biomarker group 1, K15069L-1).

Flow cytometry and FACS

Isolation and staining of lymphocytes

After perfusion and mechanical dissection, livers were incubated for up to 35 min at 37 °C with collagen IV (60 U final concentration (f.c.)) and DNase I (25 µg/ml f.c.), filtered at 100 µm, and washed with RPMI1640 (11875093, Thermo Fisher). Next, samples underwent a two-step Percoll gradient (25%/50% Percoll/HBSS) and centrifugation for 15 min at 1,800g and 4 °C. Enriched leukocytes were then collected, washed, and counted. For re-stimulation, cells were incubated for 2 h at 37 °C under 5% CO₂ with 1:500 Biolegend's Cell Activation Cocktail (with brefeldin A) (423304) and 1:1,000 Monensin Solution (420701). Live/dead discrimination was done using DAPI or ZombieDyeNIR according to the manufacturer's instructions with subsequent staining of titrated antibodies (Supplementary Tables 12–14). Samples for flow cytometric-activated cell sorting (FACS) were sorted and samples for flow cytometry were fixed using eBioscience IC fixation (00-8222-49) or FOXP3 Fix/Perm kit (00-5523-00) according to the manufacturer's instructions. Intracellular staining was performed in eBioscience Perm buffer (00-8333-56). Cells were analysed using BD FACSFortessa or BD FACSSymphony and data were analysed using FlowJo (v10.6.2). For sorting, FACS Aria II and FACSAria FUSION were used in collaboration with the DKFZ FACS core facility.

For UMAP and FlowSOM plots, BD FACSSymphony data (mouse and human) were exported from FlowJo (v10). Analyses were performed as described elsewhere³⁹.

Single-cell RNA-seq and metacell analysis (mouse)

Single-cell capturing for scRNA-seq and library preparation were done as described previously⁴⁰. Libraries (pooled at equimolar concentration) were sequenced on an Illumina NextSeq 500 at a median sequencing depth of ~40,000 reads per cell.

Sequences were mapped to the mouse genome (mm10), using HISAT (version 0.1.6); reads with multiple mapping positions were excluded. Reads were associated with genes if they were mapped to an exon, using the Ensembl gene annotation database (Ensembl release 90). Exons of different genes that shared a genomic position on the same strand were considered to represent a single gene with a concatenated gene symbol. The level of spurious unique molecular identifiers (UMIs) in the data was estimated by using statistics on empty MARS-seq wells and excluded rare cases with estimated noise >5% (median estimated noise overall for experiments was 2%).

Specific mitochondrial genes, immunoglobulin genes, genes linked with poorly supported transcriptional models (annotated with the prefix “Rp-”), and cells with fewer than 400 UMIs were removed. Gene features were selected using $T_{vm} = 0.3$ and a minimum total UMI count >50. We carried out hierarchical clustering of the correlation matrix between those genes (filtering genes with low coverage and computing correlation using a down-sampled UMI matrix) and selected the gene clusters that contained anchor genes. We used $K = 50, 750$ bootstrap iterations, and otherwise standard parameters. Subsets of T cells were obtained by hierarchical clustering of the confusion matrix and supervised analysis of enriched genes in homogeneous groups of metacells⁴¹.

Velocity and correlation analyses of scRNA-seq data

Velocyto (0.6) was used to estimate the spliced and unspliced counts from the pre-aligned bam files⁴². RNA velocity, latent time, root, and terminal states were calculated using the dynamical velocity model from scvelo (0.2.2)⁴³. Kendall’s rank correlation coefficient (τ) was used to correlate the expression patterns of biologically significant genes with latent time.

Preparation for mass spectrometry, data acquisition, and data analysis

After FACS purification, cells were resuspended in 50% (vol/vol) 2,2,2-trifluoroethanol in PBS pH 7.4 buffer and lysed by repeated sonication and freeze–thaw cycles. Proteins were denatured at 60 °C for 2 h, reduced using dithiothreitol at a final concentration of 5 mM (30 min at 60 °C), cooled to room temperature, alkylated using iodoacetamide at 25 mM (30 min at room temperature in the dark), and diluted 1:5 using 100 mM ammonium bicarbonate, pH 8.0. Proteins were digested overnight by trypsin (1:100 ratio, 37 °C), desalted using C18-based stage-tips, dried under vacuum, resuspended in 20 µl HPLC-grade water with 0.1% formic acid, and measured using A380.

We used 0.5 µg of peptides for proteomic analysis on a C18 column using a nano liquid chromatography system (EASY-nLC 1200, Thermo Fisher Scientific). Peptides were eluted using a gradient of 5–30% buffer B (80% acetonitrile and 0.1% formic acid) at a flow rate of 300 nL/min at a column temperature of 55 °C. Data were acquired by data-dependent Top15 acquisition using a high-resolution orbitrap tandem mass spectrometer (QExactive HF-X, Thermo Scientific). All MS1 scans were acquired at 60,000 resolution with AGC target of 3×10^6 , and MS2 scans were acquired at 15,000 resolution with AGC target of 1×10^5 and maximum injection time of 28 ms. Analyses were performed using MaxQuant (1.6.7.0), mouse UniProt Isoform fasta (Version: 2019-02-21, number of sequences 25,233) as a source for protein sequences. One per cent FDR was used for controlling at the peptide and protein levels, with a minimum of two peptides needed for consideration of analysis. GSEA was performed using ClusterProfiler (3.18)⁴⁴ and gene sets obtained from WikiPathway (<https://www.wikipathways.org/>) and MSigDB (<https://Broadinstitute.org/msigdb>)^{45,46,47}.

Histology, immunohistochemistry, scanning, and automated analysis

Histology, immunohistochemistry, scanning, and automated analysis have been described previously¹⁷. Antibodies used in this manuscript are described in Supplementary Table 12. For immunofluorescence staining, established antibodies were used, coupled with the AKOYA Biosciences Opal fluorophore kit (Opal 520 FP1487001KT, Opal 540 FP1494001KT, Opal 620 FP1495001KT). For mRNA in situ hybridization, freshly non-baked 5 µm formalin-fixed paraffin-embedded sections were cut and stained according to the manufacturer's (ACD biotech) protocol for manual assay RNAscope, using probes PDL1 (420501), TNF (311081) and CXCR6 (871991).

Isolation of RNA and library preparation for bulk RNA sequencing

RNA isolation¹⁷ and library preparation for bulk 3'-sequencing of poly(A)-RNA was as described previously⁴⁸. Gencode gene annotations version M18 and the mouse reference genome major release GRCh38 were derived from <https://www.gencodegenes.org/>. Dropseq tools v1.12⁴⁹ were used for mapping the raw sequencing data to the reference genome. The resulting UMI-filtered count matrix was imported into R v3.4.4. Before differential expression analysis with Limma v3.40.6⁵⁰ sample-specific weights were estimated and used as coefficients alongside the experimental groups as a covariate during model fitting with Voom. *t*-test was used for determining differentially ($P < 0.05$) regulated genes between all possible experimental groups. GSEA was conducted with the pre-ranked GSEA method⁴⁶ within the MSigDB Reactome, KEGG, and Hallmark databases.

(<https://Broadinstitute.org/msigdb>). Raw sequencing data are available at European Nucleotide Archive (<https://www.ebi.ac.uk/ena/browser/home>) under the accession number PRJEB36747.

Stimulation of CD8 T cells

Stimulation of CD8 T cells was as described elsewhere²⁷.

Flow cytometry of human biopsies

Analysis of patient material (Supplementary Table 1) was performed on liver tissue (needle biopsies or resected tissue, BIOFACS Study KEK 2019-00114), which were obtained from the patient collection nAC-2019-3627 (CRB03) from the biological resource centre of CHU Grenoble-Alpes (nBRIF BB-0033-00069). Tissue samples were minced using scalpels, incubated (with 1 mg/ml collagenase IV (Sigma Aldrich), 0.25 µg/ml DNase (Sigma Aldrich), 10% FCS (Thermo Fisher Scientific), RPMI 1640 (Seraglob)) for 30 min at 37 °C, stopping enzymatic reactions with 2 mM EDTA (StemCell Technologies, Inc.) in PBS. After filtering through a 100-µm cell strainer, cells were resuspended in FACS buffer (PBS, EDTA 2 mM, FCS 0.5%) with Human TruStain FcX (Fc Receptor Blocking Solution) (Biolegend), incubated for 15 min at 4 °C and stained with antibodies (Supplementary Table 13).

Flow cytometry of human samples (Extended Data Fig. 9f) was approved by the local ethical committee (AC-2014-2094 n 03).

High-throughput RNA-seq of human samples

As previously reported, RNA-seq analysis was performed using the data from 206 snap-frozen biopsy samples from 206 patients diagnosed with NAFLD in France, Germany, Italy, and the UK and enrolled in the European NAFLD Registry (GEO accession GSE135251)^{51,52}. Samples were scored for NAS by two pathologists⁵³. Alternate diagnoses were excluded, including excessive alcohol intake (30 g per day for males, 20 g for females), viral hepatitis, autoimmune liver diseases, and steatogenic medication use. Patient samples were grouped: NAFL ($n = 51$) and NASH with fibrosis stages of F0/1 ($n = 34$), F2 ($n = 53$), F3 ($n = 54$) and F4 ($n = 14$). Collection and use of data of the European NAFLD Registry were approved by the relevant local and/or national Ethical Review Committee⁵¹. A correction for sex, batch, and centre effects was implemented. Pathway enrichment and visualization were as described elsewhere^{52,54,55}.

Immunohistochemistry of NAFLD/NASH cohort

Sixty-five human FFPE biopsies from patients with NAFLD were included (Supplementary Table 3). Sequential slides were immunostained with antibodies against human CD8 (Roche, SP57, ready-to-use), PD1 (Roche; NAT105, ready-to-use), and CD4 (Abcam, ab133616, 1:500). All staining was performed on the VENTANA BenchMark autostainer at 37 °C. Immunopositive cells were quantified at 400× magnification in the portal tract and the adherent parenchyma.

Isolation of cells for scRNA-seq data analysis (human)

Analyses used liver samples from patients undergoing bariatric surgery at the Department of Surgery at Heidelberg University Hospital (S-629/2013). Samples were preserved by FFPE for pathological evaluation and single cells were generated by mincing, using the Miltenyi tumour dissociation kit (130-095-929) per the manufacturer's instructions, filtering through a 70-µm cell strainer and washing. ACK lysis using the respective buffer (Thermo Fischer Scientific A1049201) was performed, and samples were stored in FBS with 20% DMSO until further processing (scRNA-seq analysis and mass cytometry).

Cells were thawed in a 37 °C water bath, washed with PBS + 0.05 mM EDTA (10 min, 300g at 4 °C), Fc receptor-block (10 min at 4 °C), stained with CD45-PE (3 µl, HI30, 12-0459-42) and Live/Dead discrimination (1:1,000, ThermoFischer, L34973), washed and sorted on a FACSAria FUSION in collaboration with the DKFZ FACS. Library generation was performed according to the manufacturer's protocol (Chromium Next EM Single Cell 3'GEM, 10000128), and sequencing was performed on an Illumina NovaSeq 6000. De-multiplexing and barcode processing were performed using the Cell Ranger Software Suite (Version 4.0.0) and reads were aligned to human GRCh38⁵⁶. A gene–barcode matrix containing cell barcodes and gene expression counts was generated by counting the single-cell 3' UMIs, which were imported into R (v4.0.2), where quality control and normalization were executed using Seurat v3⁵⁷. Cells with more than 10% mitochondrial genes, fewer than 200 genes per cell, or more than 6,000 genes per cell were excluded. Matrices from 10 samples were

integrated with Seurat v3 to remove batch effects across samples. PCA analysis of filtered gene–barcode matrices of all CD3⁺ cells, visualized by UMAP (top 50 principal components), and identification of major cell types using the highly variable features and indicative markers were performed. Pairwise comparisons of CD4⁺ T cells versus CD4⁺PD1⁺ T cells and CD8⁺ T cells versus CD8⁺PD1⁺ T cells were performed using the results of differential expression analysis by DESeq2 (v1.28.1)⁵⁸, setting CD4⁺/CD8⁺ T cells as controls. Volcano plots were then generated using EnhancedVolcano (v1.6.0)⁵⁹ to visualize the results of differential expression analysis.

Mass cytometry data analysis (human)

Antibody conjugates for mass cytometry were purchased from Fluidigm, generated in-house using antibody labelling kits (Fluidigm X8, MCP9), or as described before^{60,61}. Antibody cocktails for mass cytometry were cryopreserved as described before⁶². Isolation of cells is described in ‘Isolation of cells for scRNA-seq data analysis (human)’. Cells were thawed, transferred into RPMI + benzonase (14 ml RPMI + 0.5 µl benzonase), and centrifuged for 5 min at 500g. The cell pellet was resuspended in 1 ml CSM-B (CSM (PBS 0.5% BSA 0.02% sodium azide) + 1 µl benzonase), filtered through a 30-µm cell strainer, adjusted to 3 ml, counted, resuspended in 35 µl CSM-B and incubated for 45 min at 4 °C, and 100 µl CSM-B was added. Cells were pooled and stained with a surface antibody cocktail (Supplementary Table 15) for 30 min at 4 °C. Dead cell discrimination was performed with mDOTA-103Rh (5 min, room temperature). For intracellular staining, the FOXP3 intracellular staining kit from Miltenyi Biotec was used per the manufacturer’s instructions, followed by staining for intracellular targets for 30 min at room temperature. Cells were washed, resuspended in 1 ml of iridium intercalator solution, and incubated for 25 min at room temperature. Cells were washed with CSM, PBS, and MilliQ water, adjusted to a final concentration of 7.5×10^5 cells/ml and supplemented with 4-element EQ beads. The sample was acquired on a Helios mass cytometer and raw data were EQ-Bead-normalized using Helios mass cytometer and Helios instrument software (version 6.7). Compensation was performed in CATALYST (v1.86)⁶³ and

FlowCore (1.50.0). De-barcoding and gating of single, live CD45⁺ cells were performed using FlowJo (v10.6.2). Then, data from CD45⁺ cells were imported into Cytosplore 2.3.1 and transformed using the arcsinh(5) function. Major immune cell lineages were identified at the first level of a two-level hierarchical stochastic neighbour embedding (HSNE) analysis with default perplexity and iteration settings. HSNE with the same parameters was run on CD3⁺ cells to identify T cell phenotypes. Gaussian mean shift clustering was performed in Cytosplore and a heat map of arcsinh(5)-transformed expression values of all antibody targets was generated. Cell type identification was based on the transformed expression values and clusters showing high similarity were merged manually.

Histological and immunohistochemical analysis of NASH–HCC cohort

Four healthy samples, 16 samples from patients with NASH cases, and non-tumoral tissue adjacent to HCC tumours from patients of the following aetiologies were selected: NASH ($n = 26$), viral hepatitis ($n = 19$ HCV, $n = 3$ HBV), alcohol ($n = 5$), and other ($n = 2$). All samples were obtained from International Genomic HCC Consortium with IRB approval. After heat-induced antigen retrieval (10 mM sodium citrate buffer (pH 6.0) or Universal HIER antigen retrieval reagent (ab208572) for 15 min (3×5 min)), the reaction was quenched using 3% hydrogen peroxide. Samples were washed with PBS and incubated with anti-CD8 (Cell Signaling, Danvers, MA) or anti-PD1 (NAT105, ab52587). DAB (3,3'-diaminobenzidine) was used as a detection system (EnVision+ System-HRP, Dako). PD1-positive cases were defined by considering median positivity by immunohistochemistry⁶⁴ and using a cutoff of $\geq 1\%$ of PD1-positive lymphocytes among all lymphocytes present on each slide. Analysis of human samples from the Department of Pathology and Molecular Pathology, University Hospital Zurich (Extended Data Fig. 10), was approved by the local ethics committee (Kantonale Ethikkommission Zürich, KEK-ZH-Nr. 2013-0382 and BASEC-Nr. PB_2018-00252).

Search strategy, selection criteria, and meta-analysis of phase III clinical trials

The literature search was done through MEDLINE on PubMed, Cochrane Library, Web of Science, and clinicaltrials.gov, using the following searches: ‘checkpoint inhibitors’, ‘HCC’, ‘phase III’, between January 2010 and January 2020, and complemented by manual searches of conference abstracts and presentations. Single-centre, non-controlled trials, studies with insufficient data to extract HRs or 95% confidence intervals, and trials including disease entities other than HCC were excluded. As conference abstracts were not excluded, quality assessment of the included studies was not performed. Three studies^{5,10,11} fulfilled the criteria and were included in the quantitative synthesis (Extended Data Fig. 10). The primary outcome of the meta-analysis was overall survival, defined as the time from randomization to death. HRs and CIs related to overall survival were extracted from the papers or conference presentations^{5,10,11}. Pooled HRs were calculated using the random-effects model and we used the DerSimonian–Laird method to estimate τ^2 , and the generic inverse variance was used for calculating weights⁶⁵. To evaluate heterogeneity among studies, Cochran’s Q test and I^2 index were used. $P < 0.10$ in the Q -test was considered to indicate substantial heterogeneity. I^2 was interpreted as suggested in the literature: 0% to 40% might not represent significant heterogeneity; 30% to 60% may represent moderate heterogeneity; 50% to 90% may represent substantial heterogeneity; 75% to 100% represents considerable heterogeneity. All statistical pooled analyses were performed using RevMan 5.3 software.

A cohort of patients with HCC treated with PD(L)1-targeted immunotherapy

The retrospective analysis was approved by local Ethics Committees. Data from this cohort were published previously⁶⁶. Patients with liver cirrhosis and advanced-stage HCC treated with PD(L)1-targeted immune checkpoint blockers from 12 centres in Austria, Germany, Italy, and Switzerland were included. The χ^2 test or Fisher’s exact test were used to compare nominal data. Overall survival was defined as the time from the start of checkpoint inhibitor treatment until death. Patients who were still alive were censored at the date of the last contact. Survival curves were calculated by the Kaplan–Meier method and compared by using the log-rank test.

Multivariable analysis was performed by a Cox regression model. Statistical analyses were performed using IBM SPSS Statistics version 25 (SPSS Inc., Chicago, IL).

A validation cohort of patients with HCC treated with PD1-targeted immune checkpoint blockers

A multi-institutional dataset that included 427 patients with HCC treated with immune checkpoint inhibitors between 2017 and 2019 in 11 tertiary-care referral centres specialized in the treatment of HCC was analysed.

Clinical outcomes of this patient cohort have been reported elsewhere^{67,68}. Inclusion criteria were: 1) diagnosis of HCC made by histopathology or imaging criteria according to American Association for the Study of Liver Disease and European Association for the Study of the Liver guidelines; 2) systemic therapy with immune checkpoint inhibitors for HCC that was not amenable to curative or loco-regional therapy following local multidisciplinary tumour board review; 3) measurable disease according to RECIST v1.1 criteria at commencement of treatment with immune checkpoint inhibitors. One hundred and eighteen patients with advanced-stage HCC were recruited with Child–Pugh A liver functional reserve, and documented radiologic or clinical diagnosis of cirrhosis. Ethical approval to conduct this study was granted by the Imperial College Tissue Bank (reference number R16008).

Statistical analyses

No statistical methods were used to predetermine sample size. The experiments were not randomized and the investigators were not blinded to allocation during experiments and outcome assessment. Data were collected in Microsoft Excel. Mouse data are presented as the mean \pm s.e.m. Pilot experiments and previously published results were used to estimate the sample size, such that appropriate statistical tests could yield significant results. Statistical analysis was performed using GraphPad Prism software version 7.03 (GraphPad Software). Exact P values lower than $P < 0.1$ are reported and specific tests are indicated in the legends.

Sample sizes, biological replicates and statistical tests

Fig. 1a: PD1, $n = 5$ mice/group; CD8, ND $n = 6$ mice; CD-HFD $n = 6$ mice; WD-HTF $n = 5$ mice. Scale bar, 100 μm . Fig. 1b: $n = 3$ mice/group. Scale bar, 100 μm . Fig. 1c: ND $n = 4$ mice, CD-HFD $n = 6$ mice. Fig. 1d,e: $n = 3$ mice/group. Fig. 1f: tumour incidence: CD-HFD, $n = 19$ tumours/lesions in 25 mice; CD-HFD + anti-PD1, $n = 10$ tumours/lesions in 10 mice. Fig. 1h: ND, $n = 3$ mice; CD-HFD, $n = 13$ mice; CD-HFD + anti-PD1, $n = 8$ mice; intra-tumoral staining: CD-HFD, $n = 11$ mice; CD-HFD + anti-PD1, $n = 8$ mice. Data in Fig. 1a,h were analysed by two-tailed Student's *t*-test. Data in Fig. 1f were analysed by two-sided Fisher's exact test.

Fig. 2a,b: $n = 3$ mice/group. Fig. 2c: CD8 $^{+}$: ND, $n = 6$ mice; CD-HFD + IgG, $n = 5$ mice; CD-HFD + anti-PD1, $n = 6$ mice; CD8 $^{+}$ PD1 $^{+}$: ND, $n = 4$ mice, CD-HFD + IgG, $n = 6$ mice; CD-HFD + anti-PD1, $n = 6$ mice. Fig. 2d,e: ND, $n = 4$ mice; CD-HFD + IgG, $n = 8$ mice; CD-HFD + anti-PD1, $n = 6$ mice. Fig. 2f: CD-HFD + IgG, $n = 6$ mice; CD-HFD + anti-PD1, $n = 4$ mice. Fig. 2g: ND, $n = 30$ mice; CD-HFD, $n = 47$ mice; CD-HFD + anti-PD1, $n = 35$ mice; CD-HFD + anti-PD1/anti-CD8, $n = 9$ mice; CD-HFD + anti-TNF, $n = 10$ mice; CD-HFD + anti-PD1/anti-TNF, $n = 11$ mice; CD-HFD + anti-CD4, $n = 8$ mice; CD-HFD + anti-PD1/anti-CD4, $n = 8$ mice. Fig. 2h: CD8 $^{+}$ PD1 $^{+}$ CXCR6 $^{+}$: ND, $n = 30$ mice; CD-HFD, $n = 47$ mice; CD-HFD + anti-PD1, $n = 35$ mice; CD-HFD + anti-PD1/anti-CD8, $n = 9$ mice; CD-HFD + anti-TNF, $n = 10$ mice; CD-HFD + anti-PD1/anti-TNF, $n = 11$ mice; CD-HFD + anti-CD4, $n = 8$ mice; CD-HFD + anti-PD1/anti-CD4, $n = 8$ mice. Fig. 2j: tumour incidence: CD-HFD, $n = 32$ tumours/lesions in 87 mice; CD-HFD + anti-CD8, $n = 2$ tumours/lesions in 31 mice; CD-HFD + anti-CD8/NK1.1, $n = 0$ tumours/lesions in 6 mice; CD-HFD + anti-PD1, $n = 33$ tumours/lesions in 44 mice; CD-HFD + anti-PD1/anti-CD8, $n = 2$ tumours/lesions in 9 mice; CD-HFD + anti-TNF, $n = 3$ tumours/lesions in 10 mice; CD-HFD + anti-PD1/anti-TNF, $n = 3$ tumours/lesions in 11 mice; CD-HFD + anti-CD4, $n = 3$ tumours/lesions in 9 mice; CD-HFD + anti-PD1/anti-CD4, $n = 8$ tumours/lesions in 9 mice. All data are shown as mean \pm s.e.m. Data in Fig. 2e,g,h were analysed by one-way ANOVA and Fisher's LSD test. Data in Fig. 2f were analysed by two-

tailed Mann–Whitney test. Data in Fig. 2j were analysed by two-sided Fisher’s exact test.

Fig. 3a, b: control, $n = 6$ patients; NAFLD/NASH, $n = 11$ patients. Fig. 3c: control, $n = 4$ patients; NAFLD/NASH, $n = 7$ patients. Fig. 3d–h: mouse, $n = 3$; human, $n = 3$. All data are shown as mean \pm s.e.m. Data in Fig. 3b, f were analysed by two-tailed Mann–Whitney test. Data in Fig. 3d were analysed by two-tailed Spearman’s correlation.

Fig. 4a: Hazard ratios are represented by squares, the size of the square represents the weight of the trial in the meta-analysis. Cochran’s Q -test and I^2 were used to calculate heterogeneity. Fig. 4b: Kaplan–Meier curve displays overall survival of patients with NAFLD versus those with any other aetiology; all 130 patients were included in these survival analyses (NAFLD $n = 13$; any other aetiology $n = 117$). Fig. 4c: Kaplan–Meier curve displays overall survival of patients with NAFLD versus those with any other aetiology (NAFLD $n = 11$; any other aetiology $n = 107$). Data in Fig. 4b, c were analysed by Kaplan–Meier method and compared using log rank test.

Reporting summary

Further information on research design is available in the [Nature Research Reporting Summary](#) linked to this paper.

Data availability

The proteomics data described in this article are available at the PRIDE database, under the identifier PXD017236 or through the dataset website (<http://www.ebi.ac.uk/pride/archive/projects/PXD017236>). The bulk RNA-seq data described in this article are available at the European Nucleotide Archive (ENA) under accession number [PRJEB36747](#). The scRNA-seq data described in this article are available at GEO under accession [GSE144635](#). The array of comparative genomic hybridization data described in this article is available at GEO under accession [GSE144875](#). The results here are in whole or part based upon data generated by the TCGA Research Network (<https://www.cancer.gov/tcga>). The human

scRNA-seq data described in this article are available at GEO under accession [GSE159977](#). Databases used in this manuscript are WikiPathways (<https://www.wikipathways.org/>) and MSigDB (<https://Broadinstitute.org/msigdb>). [Source data](#) are provided with this paper.

Change history

- [**06 April 2021**](#)

An amendment to the underlying article code was made to enable an author name to appear correctly in PubMed.

References

1. 1.

Llovet, J. M. et al. Hepatocellular carcinoma. *Nat. Rev. Dis. Primers* **7**, 6 (2021).

[PubMed](#) [Google Scholar](#)

2. 2.

European Association for the Study of the Liver EASL Clinical Practice Guidelines: management of hepatocellular carcinoma. *J. Hepatol.* **69**, 182–236 (2018).

[Google Scholar](#)

3. 3.

Zhu, A. X. et al. Pembrolizumab in patients with advanced hepatocellular carcinoma previously treated with sorafenib (KEYNOTE-224): a non-randomised, open-label phase 2 trial. *Lancet Oncol.* **19**, 940–952 (2018).

[Google Scholar](#)

4. 4.

El-Khoueiry, A. B. et al. Nivolumab in patients with advanced hepatocellular carcinoma (CheckMate 040): an open-label, non-comparative, phase 1/2 dose escalation and expansion trial. *Lancet* **389**, 2492–2502 (2017).

[PubMed](#) [PubMed Central](#) [CAS](#) [Google Scholar](#)

5. 5.

Finn, R. S. et al. Atezolizumab plus bevacizumab in unresectable hepatocellular carcinoma. *N. Engl. J. Med.* **382**, 1894–1905 (2020).

[PubMed](#) [PubMed Central](#) [CAS](#) [Google Scholar](#)

6. 6.

Roderburg, C., Wree, A., Demir, M., Schmelzle, M. & Tacke, F. The role of the innate immune system in the development and treatment of hepatocellular carcinoma. *Hepatic Oncol.* **7**, HEP17 (2020).

[Google Scholar](#)

7. 7.

Pinter, M., Scheiner, B. & Peck-Radosavljevic, M. Immunotherapy for advanced hepatocellular carcinoma: a focus on special subgroups. *Gut* **70**, 204–214 (2021).

[PubMed](#) [CAS](#) [Google Scholar](#)

8. 8.

Duffy, A. G. et al. Tremelimumab in combination with ablation in patients with advanced hepatocellular carcinoma. *J. Hepatol.* **66**, 545–551 (2017).

[PubMed](#) [PubMed Central](#) [CAS](#) [Google Scholar](#)

9. 9.

Sangro, B. et al. A clinical trial of CTLA-4 blockade with tremelimumab in patients with hepatocellular carcinoma and chronic hepatitis C. *J. Hepatol.* **59**, 81–88 (2013).

[CAS](#) [Google Scholar](#)

10. 10.

Finn, R. S. et al. Pembrolizumab as second-line therapy in patients with advanced hepatocellular carcinoma in KEYNOTE-240: a randomized, double-blind, phase III trial. *J. Clin. Oncol.* **38**, 193–202 (2020).

[PubMed](#) [PubMed Central](#) [CAS](#) [Google Scholar](#)

11. 11.

Yau, T. et al. CheckMate 459: A randomized, multi-center phase III study of nivolumab (NIVO) vs sorafenib (SOR) as first-line (1L) treatment in patients (pts) with advanced hepatocellular carcinoma (aHCC). *Ann. Oncol.* **30**, v874–v875 (2019).

[Google Scholar](#)

12. 12.

van der Leun, A. M., Thommen, D. S. & Schumacher, T. N. CD8⁺ T cell states in human cancer: insights from single-cell analysis. *Nat. Rev. Cancer* **20**, 218–232 (2020).

[PubMed](#) [PubMed Central](#) [Google Scholar](#)

13. 13.

Sangro, B. et al. Association of inflammatory biomarkers with clinical outcomes in nivolumab-treated patients with advanced hepatocellular carcinoma. *J. Hepatol.* **73**, 1460–1469 (2020).

[PubMed](#) [PubMed Central](#) [CAS](#) [Google Scholar](#)

14. 14.

Anstee, Q. M., Reeves, H. L., Kotsiligianni, E., Govaere, O. & Heikenwalder, M. From NASH to HCC: current concepts and future challenges. *Nat. Rev. Gastroenterol. Hepatol.* **16**, 411–428 (2019).

[PubMed](#) [Google Scholar](#)

15. 15.

Wolf, M. J. et al. Metabolic activation of intrahepatic CD8⁺ T cells and NKT cells causes nonalcoholic steatohepatitis and liver cancer via cross-talk with hepatocytes. *Cancer Cell* **26**, 549–564 (2014).

[PubMed](#) [CAS](#) [Google Scholar](#)

16. 16.

Ma, C. et al. NAFLD causes selective CD4⁺ T lymphocyte loss and promotes hepatocarcinogenesis. *Nature* **531**, 253–257 (2016).

[ADS](#) [PubMed](#) [PubMed Central](#) [CAS](#) [Google Scholar](#)

17. 17.

Malehmir, M. et al. Platelet GPIba is a mediator and potential interventional target for NASH and subsequent liver cancer. *Nat. Med.* **25**, 641–655 (2019).

[PubMed](#) [CAS](#) [Google Scholar](#)

18. 18.

Nakagawa, H. et al. ER stress cooperates with hypernutrition to trigger TNF-dependent spontaneous HCC development. *Cancer Cell* **26**, 331–343 (2014).

[PubMed](#) [PubMed Central](#) [CAS](#) [Google Scholar](#)

19. 19.

Ringelhan, M., Pfister, D., O'Connor, T., Pikarsky, E. & Heikenwalder, M. The immunology of hepatocellular carcinoma. *Nat. Immunol.* **19**, 222–232 (2018).

[PubMed](#) [CAS](#) [Google Scholar](#)

20. 20.

Michelotti, G. A., Machado, M. V. & Diehl, A. M. NAFLD, NASH and liver cancer. *Nat. Rev. Gastroenterol. Hepatol.* **10**, 656–665 (2013).

[PubMed](#) [CAS](#) [Google Scholar](#)

21. 21.

Friedman, S. L., Neuschwander-Tetri, B. A., Rinella, M. & Sanyal, A. J. Mechanisms of NAFLD development and therapeutic strategies. *Nat. Med.* **24**, 908–922 (2018).

[PubMed](#) [PubMed Central](#) [CAS](#) [Google Scholar](#)

22. 22.

Wang, Z. et al. Paradoxical effects of obesity on T cell function during tumor progression and PD-1 checkpoint blockade. *Nat. Med.* **25**, 141–151 (2019).

[PubMed](#) [CAS](#) [Google Scholar](#)

23. 23.

Shalapour, S. et al. Inflammation-induced IgA⁺ cells dismantle anti-liver cancer immunity. *Nature* **551**, 340–345 (2017).

[ADS](#) [PubMed](#) [PubMed Central](#) [CAS](#) [Google Scholar](#)

24. 24.

Kim, C. G. et al. Hyperprogressive disease during PD-1 blockade in patients with advanced hepatocellular carcinoma. *J. Hepatol.* **74**, 350–359 (2021).

[PubMed](#) [CAS](#) [Google Scholar](#)

25. 25.

Chung, A. S. et al. Immune checkpoint inhibition is safe and effective for liver cancer prevention in a mouse model of hepatocellular carcinoma. *Cancer Prev. Res.* **13**, 911–922 (2020).

[CAS](#) [Google Scholar](#)

26. 26.

Heinrich, B. et al. Steatohepatitis impairs T cell-directed immunotherapies against liver tumors in mice. *Gastroenterology* **160**, 331–345.e6 (2021).

[PubMed](#) [CAS](#) [Google Scholar](#)

27. 27.

Dudek, M. et al. Auto-aggressive CXCR6⁺ CD8 T cells cause liver immune pathology in NASH. *Nature* <https://doi.org/10.1038/s41586-021-03233-8> (2021).

28. 28.

Moeini, A. et al. An immune gene expression signature associated with development of human hepatocellular carcinoma identifies mice that respond to chemopreventive agents. *Gastroenterology* **157**, 1383–1397.e11 (2019).

[PubMed](#) [PubMed Central](#) [CAS](#) [Google Scholar](#)

29. 29.

Moscat, J., Karin, M. & Diaz-Meco, M. T. p62 in cancer: signaling adaptor beyond autophagy. *Cell* **167**, 606–609 (2016).

[PubMed](#) [PubMed Central](#) [CAS](#) [Google Scholar](#)

30. 30.

Kerdiles, Y. M. et al. Foxo1 links homing and survival of naive T cells by regulating L-selectin, CCR7 and interleukin 7 receptor. *Nat. Immunol.* **10**, 176–184 (2009).

[PubMed](#) [PubMed Central](#) [CAS](#) [Google Scholar](#)

31. 31.

Taylor, R. S. et al. Association between fibrosis stage and outcomes of patients with nonalcoholic fatty liver disease: a systematic review and meta-analysis. *Gastroenterology* **158**, 1611–1625.e12 (2020).

[PubMed](#) [CAS](#) [Google Scholar](#)

32. 32.

van der Poorten, D. et al. Hepatic fat loss in advanced nonalcoholic steatohepatitis: are alterations in serum adiponectin the cause? *Hepatology* **57**, 2180–2188 (2013).

[PubMed](#) [Google Scholar](#)

33. 33.

Tummala, K. S. et al. Inhibition of de novo NAD⁺ synthesis by oncogenic URI causes liver tumorigenesis through DNA damage. *Cancer Cell* **26**, 826–839 (2014).

[PubMed](#) [CAS](#) [Google Scholar](#)

34. 34.

Rudalska, R. et al. In vivo RNAi screening identifies a mechanism of sorafenib resistance in liver cancer. *Nat. Med.* **20**, 1138–1146 (2014).

[PubMed](#) [PubMed Central](#) [CAS](#) [Google Scholar](#)

35. 35.

Kang, T.-W. et al. Senescence surveillance of pre-malignant hepatocytes limits liver cancer development. *Nature* **479**, 547–551 (2011).

[ADS](#) [PubMed](#) [CAS](#) [Google Scholar](#)

36. 36.

Carlson, C. M., Frandsen, J. L., Kirchhof, N., McIvor, R. S. & Largaespada, D. A. Somatic integration of an oncogene-harboring Sleeping Beauty transposon models liver tumor development in the mouse. *Proc. Natl Acad. Sci. USA* **102**, 17059–17064 (2005).

[ADS](#) [PubMed](#) [CAS](#) [Google Scholar](#)

37. 37.

Zender, L. et al. Generation and analysis of genetically defined liver carcinomas derived from bipotential liver progenitors. *Cold Spring Harb. Symp. Quant. Biol.* **70**, 251–261 (2005).

[PubMed](#) [PubMed Central](#) [CAS](#) [Google Scholar](#)

38. 38.

Shigeta, K. et al. Dual programmed death receptor-1 and vascular endothelial growth factor receptor-2 blockade promotes vascular normalization and enhances antitumor immune responses in hepatocellular carcinoma. *Hepatology* **71**, 1247–1261 (2020).

[PubMed](#) [PubMed Central](#) [CAS](#) [Google Scholar](#)

39. 39.

Brummelman, J. et al. Development, application and computational analysis of high-dimensional fluorescent antibody panels for single-cell flow cytometry. *Nat. Protocols* **14**, 1946–1969 (2019).

[PubMed](#) [CAS](#) [Google Scholar](#)

40. 40.

Jaitin, D. A. et al. Massively parallel single-cell RNA-seq for marker-free decomposition of tissues into cell types. *Science* **343**, 776–779 (2014).

[ADS](#) [PubMed](#) [PubMed Central](#) [CAS](#) [Google Scholar](#)

41. 41.

Baran, Y. et al. MetaCell: analysis of single-cell RNA-seq data using K-nn graph partitions. *Genome Biol.* **20**, 206 (2019).

[PubMed](#) [PubMed Central](#) [Google Scholar](#)

42. 42.

La Manno, G. et al. RNA velocity of single cells. *Nature* **560**, 494–498 (2018).

[ADS](#) [PubMed](#) [PubMed Central](#) [Google Scholar](#)

43. 43.

Bergen, V., Lange, M., Peidli, S., Wolf, F. A. & Theis, F. J. Generalizing RNA velocity to transient cell states through dynamical modeling. *Nat. Biotechnol.* **38**, 1408–1414 (2020).

[PubMed](#) [Google Scholar](#)

44. 44.

Yu, G., Wang, L.-G., Han, Y. & He, Q.-Y. clusterProfiler: an R package for comparing biological themes among gene clusters. *OMICS* **16**, 284–287 (2012).

[PubMed](#) [PubMed Central](#) [CAS](#) [Google Scholar](#)

45. 45.

Slenter, D. N. et al. WikiPathways: a multifaceted pathway database bridging metabolomics to other omics research. *Nucleic Acids Res.* **46**, D661–D667 (2018).

[PubMed](#) [CAS](#) [Google Scholar](#)

46. 46.

Subramanian, A. et al. Gene set enrichment analysis: a knowledge-based approach for interpreting genome-wide expression profiles. *Proc. Natl Acad. Sci. USA* **102**, 15545–15550 (2005).

[ADS](#) [PubMed](#) [PubMed Central](#) [CAS](#) [Google Scholar](#)

47. 47.

Liberzon, A. et al. Molecular signatures database (MSigDB) 3.0. *Bioinformatics* **27**, 1739–1740 (2011).

[PubMed](#) [PubMed Central](#) [CAS](#) [Google Scholar](#)

48. 48.

Parekh, S., Ziegenhain, C., Vieth, B., Enard, W. & Hellmann, I. The impact of amplification on differential expression analyses by RNA-seq. *Sci. Rep.* **6**, 25533 (2016).

[ADS](#) [PubMed](#) [PubMed Central](#) [CAS](#) [Google Scholar](#)

49. 49.

Macosko, E. Z. et al. Highly parallel genome-wide expression profiling of individual cells using nanoliter droplets. *Cell* **161**, 1202–1214 (2015).

[PubMed](#) [PubMed Central](#) [CAS](#) [Google Scholar](#)

50. 50.

Ritchie, M. E. et al. limma powers differential expression analyses for RNA-sequencing and microarray studies. *Nucleic Acids Res.* **43**, e47 (2015).

[PubMed](#) [PubMed Central](#) [Google Scholar](#)

51. 51.

Hardy, T. et al. The European NAFLD Registry: a real-world longitudinal cohort study of nonalcoholic fatty liver disease. *Contemp. Clin. Trials* **98**, 106175 (2020).

[ADS](#) [PubMed](#) [Google Scholar](#)

52. 52.

Govaere, O. et al. Transcriptomic profiling across the nonalcoholic fatty liver disease spectrum reveals gene signatures for steatohepatitis and fibrosis. *Sci. Transl. Med.* **12**, eaba4448 (2020).

[PubMed](#) [CAS](#) [Google Scholar](#)

53. 53.

Kleiner, D. E. et al. Design and validation of a histological scoring system for nonalcoholic fatty liver disease. *Hepatology* **41**, 1313–1321 (2005).

[PubMed](#) [Google Scholar](#)

54. 54.

Huang, W., Sherman, B. T. & Lempicki, R. A. Systematic and integrative analysis of large gene lists using DAVID bioinformatics resources. *Nat. Protocols* **4**, 44–57 (2009).

[CAS](#) [Google Scholar](#)

55. 55.

Walter, W., Sánchez-Cabo, F. & Ricote, M. GOpot: an R package for visually combining expression data with functional analysis. *Bioinformatics* **31**, 2912–2914 (2015).

[CAS](#) [Google Scholar](#)

56. 56.

Dobin, A. et al. STAR: ultrafast universal RNA-seq aligner. *Bioinformatics* **29**, 15–21 (2013).

[PubMed](#) [PubMed Central](#) [CAS](#) [Google Scholar](#)

57. 57.

Stuart, T. et al. Comprehensive integration of single-cell data. *Cell* **177**, 1888–1902.e21 (2019).

[PubMed](#) [PubMed Central](#) [CAS](#) [Google Scholar](#)

58. 58.

Love, M. I., Huber, W. & Anders, S. Moderated estimation of fold change and dispersion for RNA-seq data with DESeq2. *Genome Biol.* **15**, 550 (2014).

[PubMed](#) [PubMed Central](#) [Google Scholar](#)

59. 59.

Blighe, K., Rana, S. & Lewis, M. EnhancedVolcano: publication-ready volcano plots with enhanced colouring and labeling. <https://bioconductor.org/packages/release/bioc/vignettes/EnhancedVolcano/inst/doc/EnhancedVolcano.html> (2018).

60. 60.

Mei, H. E., Leipold, M. D. & Maecker, H. T. Platinum-conjugated antibodies for application in mass cytometry. *Cytometry A* **89**, 292–300

(2016).

[PubMed](#) [CAS](#) [Google Scholar](#)

61. 61.

Mei, H. E., Leipold, M. D., Schulz, A. R., Chester, C. & Maecker, H. T. Barcoding of live human peripheral blood mononuclear cells for multiplexed mass cytometry. *J. Immunol.* **194**, 2022–2031 (2015).

[PubMed](#) [PubMed Central](#) [CAS](#) [Google Scholar](#)

62. 62.

Schulz, A. R. et al. Stabilizing antibody cocktails for mass cytometry. *Cytometry A* **95**, 910–916 (2019).

[PubMed](#) [CAS](#) [Google Scholar](#)

63. 63.

Chevrier, S. et al. Compensation of signal spillover in suspension and imaging mass cytometry. *Cell Syst.* **6**, 612–620.e5 (2018).

[PubMed](#) [PubMed Central](#) [CAS](#) [Google Scholar](#)

64. 64.

Veloza, L. et al. Clinicopathological evaluation of the programmed cell death 1 (PD1)/programmed cell death-ligand 1 (PD-L1) axis in post-transplant lymphoproliferative disorders: association with Epstein-Barr virus, *PD-L1* copy number alterations, and outcome. *Histopathology* **75**, 799–812 (2019).

[PubMed](#) [Google Scholar](#)

65. 65.

DerSimonian, R. & Laird, N. Meta-analysis in clinical trials revisited. *Contemp. Clin. Trials* **45**, 139–145 (2015).

[PubMed](#) [PubMed Central](#) [Google Scholar](#)

66. 66.

Scheiner, B. et al. Programmed cell death protein-1 (PD-1)-targeted immunotherapy in advanced hepatocellular carcinoma: efficacy and safety data from an international multicentre real-world cohort. *Aliment. Pharmacol. Ther.* **49**, 1323–1333 (2019).

[PubMed](#) [PubMed Central](#) [CAS](#) [Google Scholar](#)

67. 67.

Fessas, P. et al. Post-registration experience of nivolumab in advanced hepatocellular carcinoma: an international study. *J. Immunother. Cancer* **8**, e001033 (2020).

[PubMed](#) [PubMed Central](#) [Google Scholar](#)

68. 68.

Pinato, D. J. et al. Immunotherapy in hepatocellular cancer patients with mild to severe liver dysfunction: adjunctive role of the ALBI grade. *Cancers* **12**, 1862 (2020).

[PubMed Central](#) [CAS](#) [Google Scholar](#)

[Download references](#)

Acknowledgements

We thank the Newcastle Molecular Pathology Node Proximity Laboratory for their technical support; P. Sinn for technical support; the DKFZ FACS core facility for support for sorting; G. Tiegs and K. Neumann for support with *Pdcld1^{-/-}* mice; V. Eichwald for help with non-invasive imaging of

mice; J. Schmid for help with human liver tissue sampling for flow cytometry; R. Ollinger for bulk sequencing support; A. Teufel for human cohort gathering; K. Inoue and Z. Ammogar for help with the non-NASH mouse model; T. O'Connor, C. Groth, M. Matter, L. Terracciano, R. Kaeser, T. Boettler, R. Thimme, M. Yabal, T. Longerich and B. Müllhaupt for guidance and discussions; and S. Prokosch, U. Rothermel, J. Janzen, J. Hetzer, C. Gropp, S. Jung, L. Beideck, S. Torrecilla, K. E. Lindblad, E. Rist and T.-W. Kang for technical support. D. Pfister was supported by the Helmholtz Future topic Inflammation and Immunology. I.S. is funded by the ‘Deutsche Forschungsgemeinschaft’ (DFG, Bonn Germany) through Emmy Noether program (SI 2620/1-1). A. Sinha is supported by EMBO LT fellowship (ALTF 539-2018). F. Meissner is supported in this project by SFB 1335 and BMBF 031B0686B. Q.M.A., O.G., D.T., P.B., S.C., R.Y., M.V., F. Marra, J.M.S., M.A., E.B., V.R. and A.K.D. are supported by the EPoS (Elucidating Pathways of Steatohepatitis) consortium funded by the Horizon 2020 Framework Program of the European Union under Grant Agreement 634413, the LITMUS (Liver Investigation: Testing Marker Utility in Steatohepatitis) consortium funded by the Innovative Medicines Initiative (IMI2) Program of the European Union under Grant Agreement 777377, and are collaborators in the European NAFLD Registry. Q.M.A. is also supported by the Newcastle NIHR Biomedical Research Centre. I.A. is supported by the Chan Zuckerberg Initiative (CZI), an HHMI international scholar award, European Research Council consolidator grant (ERC-COG) 724471-HemTree2.0, the Thompson Family Foundation, an MRA established investigator award (509044), the Israel Science Foundation (703/15), the Ernest and Bonnie Beutler Research Program for Excellence in Genomic Medicine, a Helen and Martin Kimmel award for innovative investigation, a NeuroMac DFG/Transregional Collaborative Research Center grant, International Progressive MS Alliance/NMSS PA-1604-08459, an Adelis Foundation grant, and the SCA award of the Wolfson Foundation. I.A. is the incumbent of the Alan and Laraine Fischer Career Development Chair. A.D. is supported by Steven and Eden Romick. B.S. received travel support from AbbVie and Gilead. J.M.L. is supported through a partnership between Cancer Research UK, Fondazione AIRC, and Fundación Científica de la Asociación Española Contra el Cáncer (HUNTER, ref. C9380/A26813), by the European Commission (EC)/Horizon 2020 Program (HEPCAR, Ref. 667273-2), US Department of

Defense (CA150272P3), NCI Cancer Center Support Grant, National Cancer Institute, Tisch Cancer Institute (P30-CA196521), Samuel Waxman Cancer Research Foundation, Spanish National Health Institute (SAF2016-76390 and PID2019-105378RB-I00) and the Generalitat de Catalunya/AGAUR (SGR-1358). R.P. is supported by HEPCAR and AECC. C.M. is supported by a Rio Hortega grant (CM19/00039) from the ISCIII and the European Social Fund. F.C. is supported by grant funding from AECC. A. Weber is supported by a grant from the Swiss National Science Foundation (SNF). M.H. was supported by an ERC Consolidator grant (HepatoMetaboPath), SFBTR179 Project-ID 272983813, SFB/TR 209 Project-ID 314905040, SFBTR1335 Project-ID 360372040, the Wilhelm Sander-Stiftung, the Rainer Hoenig Stiftung, a Horizon 2020 grant (Hepcar), Research Foundation Flanders (FWO) under grant 30826052 (EOS Convention MODEL-IDI), Deutsche Krebshilfe projects 70113166 and 70113167, German-Israeli Cooperation in Cancer Research (DKFZ-MOST) and the Helmholtz-Gemeinschaft, Zukunftsthema ‘Immunology and Inflammation’ (ZT-0027). P.K.H. is supported by the fellowship grant of the German Research Foundation (HA 8754/1-1). V.U. is supported by the ‘Deutsche Forschungsgemeinschaft’ (DFG; 259332240/RTG 2099) and Cooperation Program in Cancer Research of the Deutsches Krebsforschungszentrum (DKFZ) and Israel’s Ministry of Science, Technology and Space (MOST) (CA181). D.J.P. is supported by grant funding from the Wellcome Trust Strategic Fund (PS3416), ASCO/Conquer Cancer Foundation Global Oncology Young Investigator Award 2019 (14704), Cancer Research UK (C57701/A26137), CW+ and the Westminster Medical School Research Trust (JRC SG 009 2018-19) and received infrastructural support from the Imperial Experimental Cancer Medicine Centre, Cancer Research UK Imperial Centre, the Imperial College Healthcare NHS Trust Tissue Bank and the Imperial College BRC. M.Q., S.Y. and S.R. were supported by German Cancer Aid grants (70112720 and 70113167). J.-F.D. is supported by the Swiss National Foundation and the Swiss Foundation against Liver Cancer. H.E.M. and A.R.S. received support from DFG Me3644/5-1 and the Elke-Kröner-Fresenius foundation. This work was supported by the Deutsche Forschungsgemeinschaft (FOR2314, SFB-TR209, Gottfried Wilhelm Leibniz Program) and the German Ministry for Education and Research (BMBF). Further funding was provided by the DFG under Germany’s

excellence strategy EXC 2180-390900677 (Image Guided and Functionally Instructed Tumour Therapies (iFIT)), the Landesstiftung Baden-Wuerttemberg, the European Research Council (CholangioConcept) and the German Cancer Research Center (DKTK). B.B., N.G.N. and E.F. are supported by the Swiss National Science Foundation (grants 733 310030_170320, 316030_150768 and CRSII5_183478) and the Swiss Cancer League. N.G.N. is a recipient of a University Research Priority Program (URPP) postdoctoral fellowship. J.-P.M. is supported by SNF Project Grant 310030 182679, Canica Holding Research Grant, Norwegian PSC Research Center, Stiftung zur Krebsbekämpfung, Bangerter-Rhyner Stiftung, Dangel Stiftung.

Funding

Open access funding provided by Deutsches Krebsforschungszentrum (DKFZ) (1052).

Author information

Author notes

1. Dominik Pfister

Present address: Liver Disease Research, Global Drug Discovery,
Novo Nordisk A/S, Malov, Denmark

Affiliations

1. Division of Chronic Inflammation and Cancer, German Cancer Research Center (DKFZ), Heidelberg, Germany

Dominik Pfister, Marta Szydłowska, Florian Müller, Danijela
Heide, Kristin Stirm, Jan Kosla, Eleni Kotsiliti, Valentina
Leone, Indrabahadur Singh, Brinda Emu & Mathias Heikenwalder

2. Institute of Experimental Immunology, University of Zurich, Zurich, Switzerland

Nicolás Gonzalo Núñez, Ekaterina Friebel & Burkhard Becher

3. Liver Cancer Translational Research Laboratory, Institut d'Investigacions Biomèdiques August Pi i Sunyer (IDIBAPS)-Hospital Clínic, Liver Unit, Universitat de Barcelona, Barcelona, Spain

Roser Pinyol, Florian Castet, Carla Montironi & Josep M. Llovet

4. Translational and Clinical Research Institute, Faculty of Medical Sciences, Newcastle University, Newcastle, UK

Olivier Govaere, Dina Tiniakos, Pierre Bedossa, Ramy Younes, Ann
K. Daly & Quentin M. Anstee

5. Division of Gastroenterology and Hepatology, Department of Internal Medicine III, Medical University of Vienna, Vienna, Austria

Matthias Pinter, Bernhard Scheiner & Katharina Pomej

6. Liver Cancer (HCC) Study Group Vienna, Medical University of Vienna, Vienna, Austria

Matthias Pinter, Bernhard Scheiner & Katharina Pomej

7. Internal Medicine I, University Hospital Tübingen, Faculty of Medicine, University of Tübingen, Tübingen, Germany

Revant Gupta & Manfred Claassen

8. Department of Computer Science, University of Tübingen, Tübingen, Germany

Revant Gupta & Manfred Claassen

9. Department of General, Visceral and Transplantation Surgery, Universitätsklinikum Heidelberg, Heidelberg, Germany

Mengjie Qiu, Suhail Yousuf & Susanne Roth

10. Department of Immunology, Weizmann Institute of Science, Rehovot, Israel

Aleksandra Deczkowska, Assaf Weiner & Ido Amit

11. Experimental Systems Immunology Laboratory, Max-Planck Institute of Biochemistry, Munich, Germany

Ankit Sinha & Felix Meissner

12. Institute of Translational Cancer Research and Experimental Cancer Therapy, Klinikum rechts der Isar, Technical University Munich, Munich, Germany

Ankit Sinha

13. Center for Translational Cancer Research (TranslaTUM), Technical University Munich, Munich, Germany

Thomas Engleitner & Roland Rad

14. Department of Medicine II, Klinikum Rechts der Isar, Technical University Munich, Munich, Germany

Thomas Engleitner & Roland Rad

15. German Cancer Consortium (DKTK), German Cancer Research Center (DKFZ), Munich, Germany

Thomas Engleitner & Roland Rad

16. Department of Pathology and Molecular Pathology, University and University Hospital Zurich, Zurich, Switzerland

Daniela Lenggenhager & Achim Weber

17. Department of Gastroenterology and Hepatology, University Hospital Zurich, Zurich, Switzerland

Anja Moncsek & Joachim C. Mertens

18. Research Unit of Radiation Cytogenetics, Helmholtz Zentrum Munich, Munich, Germany

Valentina Leone & Kristian Unger

19. Institute of Molecular Immunology and Experimental Oncology, Technical University Munich, Munich, Germany

Michael Dudek & Percy Knolle

20. Division of Vascular Oncology and Metastasis, German Cancer Research Center (DKFZ-ZMBH Alliance), Heidelberg, Germany

Donato Inverso & Hellmut G. Augustin

21. European Center of Angioscience (ECAS), Medical Faculty
Mannheim, Heidelberg University, Heidelberg, Germany

Donato Inverso & Hellmut G. Augustin

22. Emmy Noether Research Group Epigenetic Machineries and Cancer,
Division of Chronic Inflammation and Cancer, German Cancer
Research Center (DKFZ), Heidelberg, Germany

Indrabahadur Singh

23. Cancer Cell Biology Programme, Growth Factors, Nutrients and
Cancer Group, Spanish National Cancer Research Centre, CNIO,
Madrid, Spain

Ana Teijeiro & Nabil Djouder

24. Mount Sinai Liver Cancer Program, Division of Liver Diseases, Icahn
School of Medicine at Mount Sinai, New York, NY, USA

Philipp K. Haber, Marina Ruiz de Galarreta, Amaia Lujambio, Thomas
U. Marron & Josep M. Llovet

25. Department of Pathology, Aretaeion Hospital, National and
Kapodistrian University of Athens, Athens, Greece

Dina Tiniakos

26. Bioinformatics Support Unit, Faculty of Medical Sciences, Newcastle
University, Newcastle, UK

Simon Cockell

27. Department of Medical Sciences, Division of Gastro-Hepatology, A.O.
Città della Salute e della Scienza di Torino, University of Turin, Turn,
Italy

Ramy Younes & Elisabetta Bugianesi

28. University of Cambridge Metabolic Research Laboratories, Wellcome-MRC Institute of Metabolic Science, Addenbrooke's Hospital, Cambridge, UK

Michele Vacca

29. Dipartimento di Medicina Sperimentale e Clinica, University of Florence, Florence, Italy

Fabio Marra

30. Metabolic Liver Research Program, I. Department of Medicine, University Medical Center Mainz, Mainz, Germany

Jörn M. Schattenberg

31. Liver Unit, Department of Medicine, Cambridge Biomedical Research Centre, Cambridge University NHS Foundation Trust, Cambridge, UK

Michael Allison

32. Assistance Publique-Hôpitaux de Paris, Hôpital Beaujon, University Paris-Diderot, Paris, France

Vlad Ratziu

33. Medical Oncology and Hematology Unit, Humanitas Cancer Center, Humanitas Clinical and Research Center-IRCCS, Milan, Italy

Tiziana Pressiani, Antonio D'Alessio, Nicola Personeni & Lorenza Rimassa

34. Department of Biomedical Sciences, Humanitas University, Milan, Italy

Nicola Personeni & Lorenza Rimassa

35. Department of Gastroenterology, Hepatology and Endocrinology, Hannover Medical School, Hannover, Germany

Martha M. Kirstein & Arndt Vogel

36. University Medical Center Schleswig-Holstein, Schleswig-Holstein, Germany

Martha M. Kirstein

37. Department of Internal Medicine and Gastroenterology (IMuG), Hepatology, Endocrinology, Rheumatology and Nephrology including Centralized Emergency Department (ZAE), Klinikum Klagenfurt am Wörthersee, Klagenfurt, Austria

Markus Peck-Radosavljevic & Florian Hucke

38. Department of Gastroenterology, Hepatology and Endocrinology, University Hospital Frankfurt, Frankfurt, Germany

Fabian Finkelmeier, Oliver Waidmann & Jörg Trojan

39. Department of Internal Medicine, Gastroenterology & Hepatology, University Medical Center Hamburg-Eppendorf, Hamburg, Germany

Kornelius Schulze & Henning Wege

40. Department of Internal Medicine, University Medical Center of the Johannes Gutenberg University Mainz, Mainz, Germany

Sandra Koch & Arndt Weinmann

41. Department of Surgery and Transplantation, University Hospital Zurich, Zurich, Switzerland

Marco Bueter & Fabian Rössler

42. Department of Medical Oncology and Hematology, University Hospital Zurich and University of Zurich, Zurich, Switzerland

Alexander Siebenhüner

43. Oncology Institute of Southern Switzerland, Bellinzona, Switzerland

Sara De Dosso

44. Division of Chromatin Networks, German Cancer Research Center (DKFZ) and Bioquant, Heidelberg, Germany

Jan-Philipp Mallm

45. Clinical Cooperation Unit Dermato-Oncology, German Cancer Research Center (DKFZ), Heidelberg, Germany

Viktor Umansky

46. Department of Dermatology, Venereology and Allergology, University Medical Center Mannheim, Ruprecht-Karls University of Heidelberg, Heidelberg, Germany

Viktor Umansky

47. Core Facility Small Animal Imaging, German Cancer Research Center Heidelberg, Heidelberg, Germany

Manfred Jugold

48. Department of Gastroenterology, Hepatology and Infectious Diseases, Medical Faculty, Heinrich-Heine-University, Düsseldorf, Germany

Tom Luedde

49. Immunology Program, Memorial Sloan Kettering Cancer Center, New York, NY, USA

Andrea Schietinger

50. Immunology and Microbial Pathogenesis Program, Weill Cornell Graduate School of Medical Sciences, New York, NY, USA

Andrea Schietinger

51. Institute of Pathology, University Hospital Heidelberg, Heidelberg, Germany

Peter Schirmacher

52. Department of General, Visceral and Transplantation Surgery, Heidelberg University Hospital, Heidelberg, Germany

Adrian Billeter & Beat Müller-Stich

53. Edwin L. Steele Laboratories for Tumor Biology, Department of Radiation Oncology, Massachusetts General Hospital, Boston, MA, USA

Hiroto Kikuchi & Dan G. Duda

54. Department of Gastroenterology and Hepatology, University of Cologne, Cologne, Germany

Fabian Kütting & Dirk-Thomas Waldschmidt

55. Department of Medicine II, Medical Faculty Mannheim, Heidelberg University, Heidelberg, Germany

Matthias Philip Ebert

56. Department of Surgery at University Hospital Mannheim, Medical Faculty Mannheim, Heidelberg University, Heidelberg, Germany

Nuh Rahbari

57. Mass Cytometry Lab, Deutsches Rheumaforschungszentrum Berlin, a Leibniz Institute, Berlin, Germany

Henrik E. Mei & Axel Ronald Schulz

58. Institute of Virology, Technical University Munich/Helmholtz Zentrum Munich, Munich, Germany

Marc Ringelhan

59. Department of Internal Medicine II, University Hospital rechts der Isar, Technical University Munich, Munich, Germany

Marc Ringelhan

60. German Center for Infection Research (DZIF), partner site Munich, Munich, Germany

Marc Ringelhan

61. Medical University Hospital Department of Internal Medicine I, Tübingen, Germany

Nisar Malek, Stephan Spahn & Michael Bitzer

62. Department of Oncological Sciences, Icahn School of Medicine at Mount Sinai, New York, NY, USA

Marina Ruiz de Galarreta & Amaia Lujambio

63. The Precision Immunology Institute, Icahn School of Medicine at Mount Sinai, New York, NY, USA

Amaia Lujambio

64. University Clinic for Visceral Surgery and Medicine, Inselspital, Bern, Switzerland

Jean-Francois Dufour

65. Hepatology, Department of Biomedical Research, University of Bern, Bern, Switzerland

Jean-Francois Dufour

66. Department of Medicine, Division of Hematology/Oncology, Tisch Cancer Institute, Mount Sinai Hospital, New York, NY, USA

Thomas U. Marron

67. Department of Gastrointestinal Medical Oncology, The University of Texas MD Anderson Cancer Center, Houston, TX, USA

Ahmed Kaseb

68. Department of Gastroenterology and Hepatology, Kindai University Faculty of Medicine, Osaka-, Sayama, Japan

Masatoshi Kudo

69. Institute of Clinical Medicine, National Yang-Ming University, Taipei, Taiwan

Yi-Hsiang Huang

70. Division of Gastroenterology and Hepatology, Taipei Veterans General Hospital, Taipei, Taiwan

Yi-Hsiang Huang

71. Department of Medical Oncology and Pneumology (Internal Medicine VIII), University Hospital Tübingen, Tübingen, Germany

Katharina Wolter & Lars Zender

72. Cluster of Excellence ‘Image Guided and Functionally Instructed Tumor Therapies’ (iFIT), Eberhard-Karls University of Tübingen, Tübingen, Germany

Katharina Wolter & Lars Zender

73. German Consortium for Translational Cancer Research (DKTK), Partner Site Tübingen, German Cancer Research Center (DKFZ), Tübingen, Germany

Lars Zender

74. Université Grenoble Alpes, Grenoble, France

Parice N. Marche, Thomas Decaens & Zuzana Macek Jilkova

75. Institute for Advanced Biosciences, Research Center UGA/Inserm U 1209/CNRS 5309, Grenoble, France

Parice N. Marche, Thomas Decaens & Zuzana Macek Jilkova

76. Service d'hépato-gastroentérologie, Pôle Digidune, CHU Grenoble Alpes, Grenoble, France

Thomas Decaens

77. Department of Surgery & Cancer, Imperial College London, Hammersmith Hospital, London, UK

David J. Pinato & Zuzana Macek Jilkova

78. Division of Oncology, Department of Translational Medicine, University of Piemonte Orientale, Novara, Italy

David J. Pinato

79. Institute of Molecular Cancer Research (IMCR), University of Zurich, Zurich, Switzerland

Achim Weber

80. Newcastle NIHR Biomedical Research Centre, Newcastle upon Tyne Hospitals NHS Trust, Newcastle, UK

Quentin M. Anstee

81. Institució Catalana de Recerca i Estudis Avançats (ICREA), Barcelona, Spain

Josep M. Llovet

Authors

1. Dominik Pfister

[View author publications](#)

You can also search for this author in [PubMed](#) [Google Scholar](#)

2. Nicolás Gonzalo Núñez

[View author publications](#)

You can also search for this author in [PubMed](#) [Google Scholar](#)

3. Roser Pinyol

[View author publications](#)

You can also search for this author in [PubMed](#) [Google Scholar](#)

4. Olivier Govaere

[View author publications](#)

You can also search for this author in [PubMed](#) [Google Scholar](#)

5. Matthias Pinter

[View author publications](#)

You can also search for this author in [PubMed](#) [Google Scholar](#)

6. Marta Szydlowska

[View author publications](#)

You can also search for this author in [PubMed](#) [Google Scholar](#)

7. Revant Gupta

[View author publications](#)

You can also search for this author in [PubMed](#) [Google Scholar](#)

8. Mengjie Qiu

[View author publications](#)

You can also search for this author in [PubMed](#) [Google Scholar](#)

9. Aleksandra Deczkowska
[View author publications](#)

You can also search for this author in [PubMed](#) [Google Scholar](#)

10. Assaf Weiner
[View author publications](#)

You can also search for this author in [PubMed](#) [Google Scholar](#)

11. Florian Müller
[View author publications](#)

You can also search for this author in [PubMed](#) [Google Scholar](#)

12. Ankit Sinha
[View author publications](#)

You can also search for this author in [PubMed](#) [Google Scholar](#)

13. Ekaterina Friebel
[View author publications](#)

You can also search for this author in [PubMed](#) [Google Scholar](#)

14. Thomas Engleitner
[View author publications](#)

You can also search for this author in [PubMed](#) [Google Scholar](#)

15. Daniela Lenggenhager
[View author publications](#)

You can also search for this author in [PubMed](#) [Google Scholar](#)

16. Anja Moncsek
[View author publications](#)

You can also search for this author in [PubMed](#) [Google Scholar](#)

17. Danijela Heide

[View author publications](#)

You can also search for this author in [PubMed](#) [Google Scholar](#)

18. Kristin Stirm

[View author publications](#)

You can also search for this author in [PubMed](#) [Google Scholar](#)

19. Jan Kosla

[View author publications](#)

You can also search for this author in [PubMed](#) [Google Scholar](#)

20. Eleni Kotsiliti

[View author publications](#)

You can also search for this author in [PubMed](#) [Google Scholar](#)

21. Valentina Leone

[View author publications](#)

You can also search for this author in [PubMed](#) [Google Scholar](#)

22. Michael Dudek

[View author publications](#)

You can also search for this author in [PubMed](#) [Google Scholar](#)

23. Suhail Yousuf

[View author publications](#)

You can also search for this author in [PubMed](#) [Google Scholar](#)

24. Donato Inverso

[View author publications](#)

You can also search for this author in [PubMed](#) [Google Scholar](#)

25. Indrabahadur Singh

[View author publications](#)

You can also search for this author in [PubMed](#) [Google Scholar](#)

26. Ana Teijeiro

[View author publications](#)

You can also search for this author in [PubMed](#) [Google Scholar](#)

27. Florian Castet

[View author publications](#)

You can also search for this author in [PubMed](#) [Google Scholar](#)

28. Carla Montironi

[View author publications](#)

You can also search for this author in [PubMed](#) [Google Scholar](#)

29. Philipp K. Haber

[View author publications](#)

You can also search for this author in [PubMed](#) [Google Scholar](#)

30. Dina Tiniakos

[View author publications](#)

You can also search for this author in [PubMed](#) [Google Scholar](#)

31. Pierre Bedossa

[View author publications](#)

You can also search for this author in [PubMed](#) [Google Scholar](#)

32. Simon Cockell

[View author publications](#)

You can also search for this author in [PubMed](#) [Google Scholar](#)

33. Ramy Younes

[View author publications](#)

You can also search for this author in [PubMed](#) [Google Scholar](#)

34. Michele Vacca

[View author publications](#)

You can also search for this author in [PubMed](#) [Google Scholar](#)

35. Fabio Marra

[View author publications](#)

You can also search for this author in [PubMed](#) [Google Scholar](#)

36. Jörn M. Schattenberg

[View author publications](#)

You can also search for this author in [PubMed](#) [Google Scholar](#)

37. Michael Allison

[View author publications](#)

You can also search for this author in [PubMed](#) [Google Scholar](#)

38. Elisabetta Bugianesi

[View author publications](#)

You can also search for this author in [PubMed](#) [Google Scholar](#)

39. Vlad Ratziu

[View author publications](#)

You can also search for this author in [PubMed](#) [Google Scholar](#)

40. Tiziana Pressiani

[View author publications](#)

You can also search for this author in [PubMed](#) [Google Scholar](#)

41. Antonio D'Alessio

[View author publications](#)

You can also search for this author in [PubMed](#) [Google Scholar](#)

42. Nicola Personeni

[View author publications](#)

You can also search for this author in [PubMed](#) [Google Scholar](#)

43. Lorenza Rimassa

[View author publications](#)

You can also search for this author in [PubMed](#) [Google Scholar](#)

44. Ann K. Daly

[View author publications](#)

You can also search for this author in [PubMed](#) [Google Scholar](#)

45. Bernhard Scheiner

[View author publications](#)

You can also search for this author in [PubMed](#) [Google Scholar](#)

46. Katharina Pomej

[View author publications](#)

You can also search for this author in [PubMed](#) [Google Scholar](#)

47. Martha M. Kirstein

[View author publications](#)

You can also search for this author in [PubMed](#) [Google Scholar](#)

48. Arndt Vogel

[View author publications](#)

You can also search for this author in [PubMed](#) [Google Scholar](#)

49. Markus Peck-Radosavljevic
[View author publications](#)

You can also search for this author in [PubMed](#) [Google Scholar](#)

50. Florian Hucke
[View author publications](#)

You can also search for this author in [PubMed](#) [Google Scholar](#)

51. Fabian Finkelmeier
[View author publications](#)

You can also search for this author in [PubMed](#) [Google Scholar](#)

52. Oliver Waidmann
[View author publications](#)

You can also search for this author in [PubMed](#) [Google Scholar](#)

53. Jörg Trojan
[View author publications](#)

You can also search for this author in [PubMed](#) [Google Scholar](#)

54. Kornelius Schulze
[View author publications](#)

You can also search for this author in [PubMed](#) [Google Scholar](#)

55. Henning Wege
[View author publications](#)

You can also search for this author in [PubMed](#) [Google Scholar](#)

56. Sandra Koch
[View author publications](#)

You can also search for this author in [PubMed](#) [Google Scholar](#)

57. Arndt Weinmann

[View author publications](#)

You can also search for this author in [PubMed](#) [Google Scholar](#)

58. Marco Bueter

[View author publications](#)

You can also search for this author in [PubMed](#) [Google Scholar](#)

59. Fabian Rössler

[View author publications](#)

You can also search for this author in [PubMed](#) [Google Scholar](#)

60. Alexander Siebenhüner

[View author publications](#)

You can also search for this author in [PubMed](#) [Google Scholar](#)

61. Sara De Dosso

[View author publications](#)

You can also search for this author in [PubMed](#) [Google Scholar](#)

62. Jan-Philipp Mallm

[View author publications](#)

You can also search for this author in [PubMed](#) [Google Scholar](#)

63. Viktor Umansky

[View author publications](#)

You can also search for this author in [PubMed](#) [Google Scholar](#)

64. Manfred Jugold

[View author publications](#)

You can also search for this author in [PubMed](#) [Google Scholar](#)

65. Tom Luedde

[View author publications](#)

You can also search for this author in [PubMed](#) [Google Scholar](#)

66. Andrea Schietinger

[View author publications](#)

You can also search for this author in [PubMed](#) [Google Scholar](#)

67. Peter Schirmacher

[View author publications](#)

You can also search for this author in [PubMed](#) [Google Scholar](#)

68. Brinda Emu

[View author publications](#)

You can also search for this author in [PubMed](#) [Google Scholar](#)

69. Hellmut G. Augustin

[View author publications](#)

You can also search for this author in [PubMed](#) [Google Scholar](#)

70. Adrian Billeter

[View author publications](#)

You can also search for this author in [PubMed](#) [Google Scholar](#)

71. Beat Müller-Stich

[View author publications](#)

You can also search for this author in [PubMed](#) [Google Scholar](#)

72. Hiroto Kikuchi

[View author publications](#)

You can also search for this author in [PubMed](#) [Google Scholar](#)

73. Dan G. Duda

[View author publications](#)

You can also search for this author in [PubMed](#) [Google Scholar](#)

74. Fabian Kütting

[View author publications](#)

You can also search for this author in [PubMed](#) [Google Scholar](#)

75. Dirk-Thomas Waldschmidt

[View author publications](#)

You can also search for this author in [PubMed](#) [Google Scholar](#)

76. Matthias Philip Ebert

[View author publications](#)

You can also search for this author in [PubMed](#) [Google Scholar](#)

77. Nuh Rahbari

[View author publications](#)

You can also search for this author in [PubMed](#) [Google Scholar](#)

78. Henrik E. Mei

[View author publications](#)

You can also search for this author in [PubMed](#) [Google Scholar](#)

79. Axel Ronald Schulz

[View author publications](#)

You can also search for this author in [PubMed](#) [Google Scholar](#)

80. Marc Ringelhan

[View author publications](#)

You can also search for this author in [PubMed](#) [Google Scholar](#)

81. Nisar Malek

[View author publications](#)

You can also search for this author in [PubMed](#) [Google Scholar](#)

82. Stephan Spahn

[View author publications](#)

You can also search for this author in [PubMed](#) [Google Scholar](#)

83. Michael Bitzer

[View author publications](#)

You can also search for this author in [PubMed](#) [Google Scholar](#)

84. Marina Ruiz de Galarreta

[View author publications](#)

You can also search for this author in [PubMed](#) [Google Scholar](#)

85. Amaia Lujambio

[View author publications](#)

You can also search for this author in [PubMed](#) [Google Scholar](#)

86. Jean-Francois Dufour

[View author publications](#)

You can also search for this author in [PubMed](#) [Google Scholar](#)

87. Thomas U. Marron

[View author publications](#)

You can also search for this author in [PubMed](#) [Google Scholar](#)

88. Ahmed Kaseb

[View author publications](#)

You can also search for this author in [PubMed](#) [Google Scholar](#)

89. Masatoshi Kudo

[View author publications](#)

You can also search for this author in [PubMed](#) [Google Scholar](#)

90. Yi-Hsiang Huang

[View author publications](#)

You can also search for this author in [PubMed](#) [Google Scholar](#)

91. Nabil Djouder

[View author publications](#)

You can also search for this author in [PubMed](#) [Google Scholar](#)

92. Katharina Wolter

[View author publications](#)

You can also search for this author in [PubMed](#) [Google Scholar](#)

93. Lars Zender

[View author publications](#)

You can also search for this author in [PubMed](#) [Google Scholar](#)

94. Parice N. Marche

[View author publications](#)

You can also search for this author in [PubMed](#) [Google Scholar](#)

95. Thomas Decaens

[View author publications](#)

You can also search for this author in [PubMed](#) [Google Scholar](#)

96. David J. Pinato

[View author publications](#)

You can also search for this author in [PubMed](#) [Google Scholar](#)

97. Roland Rad

[View author publications](#)

You can also search for this author in [PubMed](#) [Google Scholar](#)

98. Joachim C. Mertens

[View author publications](#)

You can also search for this author in [PubMed](#) [Google Scholar](#)

99. Achim Weber

[View author publications](#)

You can also search for this author in [PubMed](#) [Google Scholar](#)

100. Kristian Unger

[View author publications](#)

You can also search for this author in [PubMed](#) [Google Scholar](#)

101. Felix Meissner

[View author publications](#)

You can also search for this author in [PubMed](#) [Google Scholar](#)

102. Susanne Roth

[View author publications](#)

You can also search for this author in [PubMed](#) [Google Scholar](#)

103. Zuzana Macek Jilkova

[View author publications](#)

You can also search for this author in [PubMed](#) [Google Scholar](#)

104. Manfred Claassen

[View author publications](#)

You can also search for this author in [PubMed](#) [Google Scholar](#)

105. Quentin M. Anstee

[View author publications](#)

You can also search for this author in [PubMed](#) [Google Scholar](#)

106. Ido Amit

[View author publications](#)

You can also search for this author in [PubMed](#) [Google Scholar](#)

107. Percy Knolle

[View author publications](#)

You can also search for this author in [PubMed](#) [Google Scholar](#)

108. Burkhard Becher

[View author publications](#)

You can also search for this author in [PubMed](#) [Google Scholar](#)

109. Josep M. Llovet

[View author publications](#)

You can also search for this author in [PubMed](#) [Google Scholar](#)

110. Mathias Heikenwalder

[View author publications](#)

You can also search for this author in [PubMed](#) [Google Scholar](#)

Contributions

Design of the study: D.P., M.H. Performed breeding and housing of mice: D.P., E.K., V.L. Performed flow cytometry experiments: D.P., N.G.N., M.S., E.F., K. Stirm, J.K., M.D., E.K. Histological staining and analyses: D.P., M.S., D.H., F. Müller, V.L. Bulk or scRNA-seq: R.G., M.Q., A.D., A. Weiner, T.E., S.Y., I.S. Proteome analyses: A. Sinha. Meta-analyses: R.P. Human cohorts: O.G., M.P., D.L, D.I., F.C., C.M., D.T., Z.M.J. Immunotherapy treatment of genetic model of HCC: K.W., M.R.d.G., A.T., K.U. Designed/Performed the clinical case study, provided tissue samples or mouse strains and/or scientific input: A.M., P.K.H., P.B., S.C., R.Y., M.V., F. Marra, J.M.S., M.A., E.B., V.R., T.P., A.D'A., N.P., L.R., A.K.D., B.S., K.P., M.M.K., A.V., M.P.-R., F.H., F.F., O.W., J.T., K. Schulze, H.W., S.K., H.K., D.G.D., F.K., D.-T.W., M.P.E., A. Weinmann, M. Bueter, F.R., A. Siebenhüner, S.D.D., J.-P.M., V.U., M.J., T.L., A. Schietinger, P.S., H.G.A., A.B., B.M.-S., L.Z., H.E.M., A.R.S., M.R., N.M., S.S., M. Bitzer, A.L., N.R., J.-F.D., T.U.M., A.K., M.K., Y.-H.H., N.D., A. Weber, P.N.M., D.J.P., T.D., R.R., J.C.M., F. Meissner, S.R., M.C., Q.M.A., I.A., P.K., B.B., J.M.L., M.H. All authors analysed data. D.P., P.K., J.M.L. and M.H. wrote the manuscript, and all authors contributed to writing and provided feedback.

Corresponding authors

Correspondence to [Josep M. Llovet](#) or [Mathias Heikenwalder](#).

Ethics declarations

Competing interests

M.P. is an investigator for Bayer, BMS, Lilly, and Roche; has received speaker honoraria from Bayer, BMS, Eisai, Lilly, and MSD; is a consultant for Bayer, BMS, Eisai, Ipsen, Lilly, MSD, and Roche; and has received travel support from Bayer and BMS. D.P. works currently for Novo Nordisk. M. Szydlowksa works currently for Astra Zeneca. M.K. received

honoraria from BMS as consultant and is an investigator for AstraZeneca and BMS. A.V. has served as consultant for Roche, Bayer, Lilly, BMS, Eisai, and Ipsen; has received speaking fees from Roche, Bayer, Lilly, BMS, Eisai, and Ipsen; and is an investigator for Roche, Bayer, Lilly, BMS, Eisai, and Ipsen. F.H. has received travel support from Bayer, Abbvie, and Gilead. M.P.-R. is an advisor/consultant for Astra Zeneca, Bayer, BMS, Eisai, Ipsen, Lilly, and MSD; has served as a speaker for Bayer, Eisai, and Lilly; and is an investigator for Bayer, BMS, Exelixis, and Lilly. F.F. has received travel support from Abbvie and Novartis. O.W. has served as consultant for Amgen, Bayer, BMS, Celgene, Eisai, Merck, Novartis, Roche, Servier, and Shire; has served as a speaker for Abbvie, Bayer, BMS, Celgene, Falk, Ipsen, Novartis, Roche, and Shire; and has received travel support from Abbvie, BMS, Ipsen, Novartis, and Servier. J.T. has served as consultant for Amgen, Bayer, BMS, Eisai, Lilly, Merck Serono, MSD, Ipsen, and Roche; has received travel support from BMS and Ipsen; has received speaking fees from Amgen, Bayer, BMS, Eisai, Lilly, Merck Serono, MSD, Ipsen, and Roche; and is an investigator for Amgen, Bayer, BMS, Eisai, Lilly, Merck Serono, MSD, Ipsen, and Roche. K.S. has served as consultant for Ipsen and Bayer; and conducts studies for Bayer, Roche, Lilly, MSD, and BMS. H.W. has served as speaker for Bayer, Eisai, and Ipsen; has served as a consultant for Bayer, Eisai, Lilly, BMS, Roche, and Ipsen; and conducts studies for Bayer, Roche, Lilly, MSD, and BMS. A. Weber is an advisor for BMS, Wako, Eisai, Roche, and Amgen. J.C.M. has received consulting honoraria from Abbvie, Bayer, BMS, Eisai, Gilead, Incyte, Intercept and MSD for work performed outside the current study. J.M.L. is receiving research support from Bayer HealthCare Pharmaceuticals, Eisai Inc, Bristol-Myers Squibb, Boehringer-Ingelheim and Ipsen, and consulting fees from Eli Lilly, Bayer HealthCare Pharmaceuticals, Bristol-Myers Squibb, Eisai Inc, Celsion Corporation, Exelixis, Merck, Ipsen, Genentech, Roche, Glycotest, Leerink Swann LLC, Fortress Biotech, Nucleix, Can-Fite Biopharma, Sirtex, Mina Alpha Ltd and AstraZeneca. J.M.S. serves as a consultant for Intercept Pharmaceuticals, Genfit, Gilead Sciences, BMS, Madrigal, Novartis, Pfizer, Roche, and Siemens-Healthineers; and has received research funding from Gilead Sciences. D.J.P. has received lecture fees from ViiV Healthcare and Bayer Healthcare; travel expenses from BMS and Bayer Healthcare; consulting fees from Mina Therapeutics, EISAI, Roche and Astra Zeneca; and research

funding (to institution) from MSD and BMS. J.-F.D. has served on advisory committees for Abbvie, Bayer, Bristol-Myers Squibb, Falk, Genfit, Genkyotex, Gilead Sciences, HepaRegenix, Intercept, Lilly, Merck, and Novartis; and has spoken or taught at Bayer, Bristol-Myers Squibb, Intercept, Genfit, Gilead Sciences, Novartis, and Roche. L.R. has received consulting fees from Amgen, ArQule, Astra Zeneca, Basilea, Bayer, Celgene, Eisai, Exelixis, Hengrui, Incyte, Ipsen, Lilly, MSD, Nerviano Medical Sciences, Roche, and Sanofi; lectures fees from AbbVie, Amgen, Eisai, Gilead, Incyte, Ipsen, Lilly, Roche, Sanofi; travel expenses from Ipsen; and institutional research funding from Agios, ARMO BioSciences, AstraZeneca, BeiGene, Eisai, Exelixis, Fibrogen, Incyte, Ipsen, Lilly, MSD, and Roche. N.P. has received consulting fees from Amgen, Merck Serono, and Servier; lectures fees from AbbVie, Gilead and Lilly; travel expenses from Amgen and ArQule; and institutional research funding from Basilea, Merck Serono and Servier. T.P. has received institutional research funding from Lilly. D.G.D. has received consultant fees from Bayer, Simcere, Surface Oncology and BMS; and research grants from Bayer, Exelixis and BMS. The remaining authors declare no competing interests.

Additional information

Peer review information *Nature* thanks Paul Klenerman, Ignacio Melero Bermejo and the other, anonymous, reviewer(s) for their contribution to the peer review of this work. Peer reviewer reports are available.

Publisher's note Springer Nature remains neutral with regard to jurisdictional claims in published maps and institutional affiliations.

Extended data figures and tables

[Extended Data Fig. 1 T cell activation and hepatic abundance correlate with NASH pathology.](#)

a–c, Time kinetics of haematoxylin and eosin (H&E) staining of liver tissue (**a**), ALT (**b**), and NAS (**c**) in mice fed ND, CD-HFD, or WD-HTF ($n \geq 5$ mice per group). Scale bar, 100 μm . H&E 3 months: ND $n = 5$ mice; CD-

HFD $n = 5$ mice; WD-HTF $n = 3$ mice; 6 months: ND $n = 16$ mice; CD-HFD $n = 8$ mice; WD-HTF $n = 8$ mice; 12 months: ND $n = 9$ mice; CD-HFD $n = 12$ mice; WD-HTF $n = 6$ mice; ALT 3 months: ND $n = 15$ mice; CD-HFD $n = 46$ mice; WD-HTF $n = 23$ mice; 6 months: ND $n = 46$ mice; CD-HFD $n = 59$ mice; WD-HTF $n = 21$ mice; 12 months: ND $n = 25$ mice; CD-HFD $n = 69$ mice; WD-HTF $n = 5$ mice; NAS 3 months: ND $n = 5$ mice; CD-HFD $n = 5$ mice; WD-HTF $n = 3$ mice; 6 months: ND $n = 16$ mice; CD-HFD $n = 8$ mice; WD-HTF $n = 8$ mice; 12 months: ND $n = 9$ mice; CD-HFD $n = 12$ mice; WD-HTF $n = 6$ mice. **d, e**, H&E staining (**d**) with NAS evaluation by H&E (**e**, left) and ALT (**e**, right) of mice fed with ND, HFD or CD-HFD for 3 months. NAS: ND $n = 7$ mice; CD-HFD $n = 7$ mice; HFD $n = 5$ mice; ALT: ND $n = 8$ mice; CD-HFD $n = 8$ mice; HFD $n = 7$ mice. Scale bar, 50 μ m. **f, g**, Representative flow cytometry plots (**f**) and PD1 expression (**g**) of hepatic T cells from mice fed for 3 months with ND, HFD or CD-HFD ($n = 4$ mice per group). **h**, Heat map showing the median marker expression of the defined CD45 $^{+}$ subsets displayed in **i** by flow cytometry of cells from mice fed for 12 months with ND or CD-HFD (ND $n = 4$ mice; CD-HFD $n = 8$ mice). **i**, UMAP representation of FlowSOM-guided clustering and quantification of hepatic immune cell composition of mice fed for 12 months with ND or CD-HFD (ND $n = 4$ mice; CD-HFD $n = 8$ mice). **j, k**, Abundance (**j**), flow cytometry plots (**k**, left) and PD1 expression (**k**, right) of hepatic CD8 $^{+}$ T cells from mice fed for 6 or 12 months with ND or CD-HFD (abundance of CD8 6 months: ND $n = 17$ mice; CD-HFD $n = 10$ mice; WD-HTF $n = 7$ mice; 12 months: ND $n = 11$ mice; CD-HFD $n = 6$ mice; WD-HTF $n = 5$ mice; PD1 expression in CD8 $^{+}$ T cells 6 months: ND $n = 15$ mice; CD-HFD $n = 14$ mice; WD-HTF $n = 7$ mice; 12 months: ND $n = 10$ mice; CD-HFD $n = 6$ mice; WD-HTF $n = 5$ mice). **l, m**, Abundance (**l**), flow cytometry plots (**m**, left) and PD1 expression (**m**, right) of hepatic CD4 $^{+}$ T cells from mice fed for 6 or 12 months with ND or CD-HFD (abundance of CD4 6 months: ND $n = 17$ mice; CD-HFD $n = 10$ mice; WD-HTF $n = 7$ mice; 12 months: ND $n = 11$ mice; CD-HFD $n = 6$ mice; WD-HTF $n = 5$ mice; PD1 expression in CD4 $^{+}$ T cells 6 months: ND $n = 15$ mice; CD-HFD $n = 14$ mice; WD-HTF $n = 7$ mice; 12 months: ND $n = 10$ mice; CD-HFD $n = 6$ mice; WD-HTF $n = 5$ mice). **n**, H&E, CD8 and PD1 hepatic staining (top), and quantification of CD8 $^{+}$ cells and PD1 $^{+}$ cells by immunohistochemistry (bottom) from 32-week-old hURI-tetOFFhep and non-transgenic littermate control mice

($n = 6$ mice/group). Arrowheads, specific positive-staining cells. Scale bar, 100 μm . **o**, Hepatic abundance of TCR $\gamma\delta$ T cells from mice fed for 6 or 12 months with ND or CD-HFD (6 months ND $n = 8$ mice; CD-HFD $n = 6$ mice; 12 months ND $n = 8$ mice; CD-HFD $n = 6$ mice). **p**, Left, quantification of hepatic *Cd274⁺* expression by mRNA in situ hybridization of mice fed for 6 or 12 months with ND or CD-HFD (6 months: ND $n = 6$ mice; CD-HFD $n = 6$ mice; 12 months: ND $n = 3$ mice; CD-HFD $n = 3$ mice). Middle, quantification of hepatic PDL1⁺ expression by immunohistochemistry of mice fed for 12 months with ND or CD-HFD (ND $n = 8$ mice; CD-HFD $n = 6$ mice). Right, mRNA in situ hybridization (top) and PD1-stained micrographs (bottom). Scale bars, 100 μm . **q**, RNA velocity indicating transcriptional activity, gene expression, and the trajectory of CD8⁺ cells by scRNA-seq from 12 months ND or CD-HFD-fed mice. Root cells: yellow; blue cells: farthest away from root. End points: yellow indicates end point; blue cells: farthest away from defined end point. Latent time: pseudo-time by RNA velocity, dark color: start of velocity, yellow: end point of latent time. RNA velocity flow: Blue cluster: start point; orange cluster: intermediate; green: end point. Arrows: cell trajectory ($n=3$ mice/group). All data are shown as mean \pm s.e.m. **a**, **b**, **j–m**, **o**, **p**, Two-tailed Student's *t*-test. **d–g**, One-way ANOVA and Fisher's LSD test. **i**, **n**, **q**, Two-tailed Mann–Whitney test. [Source data](#)

[Extended Data Fig. 2 Anti-PD1 treatment does not achieve anti-tumour effects in NASH-induced tumours.](#)

a, **b**, Synteny analysis of mouse HCC (**a**) and quantification of genomic aberrations by array-based comparative genomic hybridization (aCGH) for mice after 12 months on CD-HFD ($n = 19$) and for human NALFD/NASH-HCC ($n = 78$). The results here are in whole or part based upon data generated by the TCGA Research Network (<https://www.cancer.gov/tcga>). **c**, MRI images of mouse liver after 13 months on CD-HFD followed by 7 weeks with or without treatment with anti-PD1 antibodies ($n = 3$ mice per group). Dashed outlines indicate tumour nodules. Scale bars, 10 mm. **d**, Histological staining of hepatic tissue with H&E, Sirius Red, CD8 and PD1 of mice fed for 15 months ND or CD-HFD and either untreated or treated for 8 weeks with anti-PD1 antibodies (H&E: ND $n = 3$ mice; CD-HFD $n = 10$ mice; CD-HFD + anti-PD1 $n = 8$ mice; Sirius Red: ND $n = 3$ mice;

CD-HFD $n = 5$ mice; CD-HFD + anti-PD1 $n = 9$ mice; CD8, PD1: ND $n = 3$ mice; CD-HFD $n = 13$ mice; CD-HFD + anti-PD1 $n = 8$ mice). Scale bar, 50 μm . Arrowheads, CD8 $^+$ or PD1 $^+$ cells. **e**, NAS evaluation by H&E staining of hepatic tissue from mice fed for 15 months with ND or CD-HFD and either untreated or treated for 8 weeks with anti-PD1 antibodies (ND $n = 3$ mice; CD-HFD $n = 10$ mice; CD-HFD + anti-PD1 $n = 8$ mice). **f**, ALT levels mice as in **e** (ND $n = 3$ mice; CD-HFD $n = 4$ mice; CD-HFD + anti-PD1 $n = 8$ mice). **g**, Quantification of fibrosis by Sirius Red staining of hepatic tissue from mice as in **e** (ND $n = 3$ mice; CD-HFD $n = 5$ mice; CD-HFD + anti-PD1 $n = 9$ mice). **h**, Quantification of tumour/lesion size and tumour load in livers from mice as in **e** (tumour/lesion size and tumour load: CD-HFD $n = 9$ mice; CD-HFD + anti-PD1 $n = 7$ mice; tumour incidence: CD-HFD $n = 17$ tumours/lesions in 22 mice; CD-HFD + anti-PD1 $n = 10$ tumours/lesions in 10 mice). **i**, Staining for CD8 and quantification of PD1 $^+$ cells in hepatic tissue by immunohistochemistry for mice as in **e** (ND $n = 3$ mice; CD-HFD $n = 13$ mice; CD-HFD + anti-PD1 $n = 8$ mice; intra-tumoral staining: CD-HFD $n = 11$ mice; CD-HFD + anti-PD1 $n = 8$ mice). Scale bar, 100 μm . **j**, **k**, Quantification and expression of PD1 in hepatic CD4 $^+$ and CD8 $^+$ T cells (**j**) and polarization of CD8 $^+$ T cells (**k**) by flow cytometry for mice fed for 15 months with CD-HFD and either untreated or treated for 8 weeks with anti-PD1 antibodies (CD-HFD $n = 4$ mice; CD-HFD + anti-PD1 $n = 8$ mice). **l**, Quantification of hepatic PD1 $^+$ CD4 $^+$ and PD1 $^+$ CD8 $^+$ T cells by flow cytometry for mice as in **j** (CD-HFD $n = 4$ mice; CD-HFD + anti-PD1 $n = 8$ mice). **m**, **n**, Expression of *Tnf* (**m**) and *Cxcr6* (**n**, left) in hepatic intra-tumoral and peri-tumoral tissue from mice as in **j** with quantification of *Cxcr6*-expressing cells (**n**, right) (quantification of CXCR6: peri-tumoral: CD-HFD $n = 15$ fields of view (FOV) in 6 tumours from 2 mice; CD-HFD + anti-PD1 $n = 10$ FOV in 6 tumours from 2 mice; intra-tumoral: CD-HFD $n = 17$ FOV in 6 tumours from 2 mice; CD-HFD + anti-PD1 $n = 17$ FOV in 6 tumours from 2 mice). Scale bars, 100 μm . Arrowheads, positive cells. All data are shown as mean \pm s.e.m. **b**, Mann–Whitney test. **e–g**, One-way ANOVA and Fisher’s LSD test. **h–l**, **n**, Two-tailed Student’s *t*-test. [Source data](#)

Extended Data Fig. 3 Anti-PDL1 treatment does not achieve anti-tumour effects in NASH-induced tumours, but in non-

NASH livers PD1-targeted immunotherapy leads to prolonged survival.

a, MRI images of livers of mice after 13 months CD-HFD either untreated or after 7 weeks of treatment with anti-PDL1 antibodies (CD-HFD $n = 6$ mice; CD-HFD + anti-PDL1 $n = 8$ mice). Dashed outlines indicate tumour nodules. Scale bar, 10 mm. **b**, Livers of mice fed with ND or CD-HFD for 13 months and either untreated or treated for 8 weeks with anti-PDL1 antibodies. Arrowheads, tumours or lesions. Scale bar, 10 mm. **c**, Body weight and ALT of mice as in **b** (ND $n = 8$ mice; CD-HFD $n = 6$ mice; CD-HFD + anti-PDL1 $n = 6$ mice). **d, e**, NAS evaluation by H&E, quantification of fibrosis by Sirius Red, and quantification of CD8, PD1 and PDL1 staining of hepatic tissue by immunohistochemistry (**d**) and corresponding micrographs (**e**) of mice fed for 13 months with ND or CD-HFD and untreated or treated for 8 weeks with anti-PDL1 antibodies (NAS: ND $n = 7$ mice; CD-HFD $n = 6$ mice; CD-HFD + anti-PDL1 $n = 6$ mice; Sirius Red: ND $n = 7$ mice; CD-HFD $n = 5$ mice; CD-HFD + anti-PDL1 $n = 6$ mice; CD8: ND $n = 5$ mice; CD-HFD $n = 5$ mice; CD-HFD + anti-PDL1 $n = 5$ mice; PD1 and PDL1: ND $n = 5$ mice; CD-HFD $n = 5$ mice; CD-HFD + anti-PDL1 $n = 6$ mice). Scale bar, 100 μ m. Arrowheads, positive cells. **f**, Tumour or lesion incidence in mice fed with CD-HFD for 15 months and untreated or treated for 8 weeks with anti-PDL1 antibodies (CD-HFD $n = 19$ tumours/lesions in 25 mice; CD-HFD + anti-PDL1 $n = 7$ tumours/lesions in 8 mice). **g**, Survival analysis of mice with hydrodynamically delivered *Nras*^{G12V}*p19Arf*^{-/-} liver tumours with OVA as antigen, treated with isotype or anti-PD1 antibodies (control $n = 8$ mice; anti-PD1 $n = 10$ mice). **h**, Survival analysis of a non-NASH model of HCC in which tumours are generated autochthonally in the liver by hydrodynamic injection of genetic elements (OVA, SIY, SIN and MYC-lucOS, in a CRISPR-based vector with tumour suppressor p53 deleted (sg-p53), and a transposase-expressing vector (SB13)). Mice were treated on days 7, 9 and 11 with IgG or anti-PD1 (control $n = 6$ mice; anti-PD1 $n = 6$ mice). **i**, Survival analysis of mice with RIL-175 *Hras/P53*-mutant hydrodynamically induced liver tumours, treated with IgG or anti-PD1 ($n = 35$ mice per group). All data are shown as mean \pm s.e.m. **c, d**, One-way ANOVA and Fisher's LSD test. **f**, Two-sided Fisher's exact test. **i**, Two-tailed Student's *t*-test. **g–i**, Two-sided χ^2 test. [Source data](#)

Extended Data Fig. 4 Preventive anti-PD1 treatment drives hepatocarcinogenesis in a CD8-dependent manner in NASH.

a, Histological staining of hepatic tissue with H&E, Sirius Red and PD1 from mice fed for 12 months with ND or CD-HFD and treated for 8 weeks with IgG, anti-CD8 or anti-PD1 antibodies (H&E: ND $n = 24$ mice; CD-HFD $n = 40$ mice; CD-HFD + anti-CD8 $n = 29$ mice; CD-HFD + anti-PD1 $n = 36$ mice; Sirius Red: ND $n = 19$ mice; CD-HFD $n = 53$ mice; CD-HFD + anti-CD8 $n = 24$ mice; CD-HFD + anti-PD1 $n = 33$ mice; PD1: ND $n = 5$ mice; CD-HFD $n = 5$ mice; CD-HFD + anti-CD8 $n = 5$ mice; CD-HFD + anti-PD1 $n = 7$ mice). Arrowheads, PD1⁺ cells. Scale bars, 50 μm . **b–d**, NAS evaluation by H&E (**b**), ALT levels (**c**) and histological staining of hepatic tissue by H&E and Sirius Red (**d**) of mice fed for 12 months with ND or CD-HFD, and untreated or treated for 8 weeks with anti-CD8 or anti-CD8 + anti-NK1.1 antibodies (fibrosis ND $n = 19$ mice; CD-HFD $n = 53$ mice; CD-HFD + anti-CD8 $n = 27$ mice; CD-HFD + anti-CD8/NK1.1 $n = 6$ mice; NAS: ND $n = 24$ mice; CD-HFD $n = 40$ mice; CD-HFD + anti-CD8 $n = 29$ mice; CD-HFD + anti-CD8/NK1.1 $n = 6$; ALT: ND $n = 22$ mice; CD-HFD $n = 42$ mice; CD-HFD + anti-CD8 $n = 31$ mice; CD-HFD + anti-CD8/NK1.1 $n = 6$). Scale bar, 100 μm . **e, f**, Flow cytometry plots of hepatic cells from mice fed for 12 months with ND or CD-HFD and treated for 8 weeks with anti-CD8 (**e**) or anti-CD8 + anti-NK1.1 (**f**) antibodies. **g**, Quantification by immunohistochemistry of PD1⁺ cells in hepatic tissue from mice fed for 12 months with ND or CD-HFD and untreated or treated for 8 weeks treatment with anti-CD8 or anti-PD1 antibodies (ND $n = 5$ mice; CD-HFD $n = 5$ mice; CD-HFD + anti-CD8 $n = 5$ mice; CD-HFD + anti-PD1 $n = 7$ mice). **h**, Assessment of metabolic tolerance by intraperitoneal glucose tolerance test of mice as in **g** (CD-HFD $n = 8$ mice; CD-HFD + anti-CD8 $n = 10$ mice; CD-HFD + anti-PD1 $n = 9$ mice). **i**, Relative quantification of hepatic leukocytes of mice as in **g** (CD3, NK T: CD-HFD $n = 9$ mice; CD-HFD + anti-CD8 $n = 14$ mice; CD-HFD + anti-PD1 $n = 8$ mice; CD4, CD8, CD19, NK, CD11b⁺, mDC: CD-HFD $n = 9$ mice; CD-HFD + anti-CD8 $n = 17$ mice; CD-HFD + anti-PD1 $n = 8$ mice; pDC: CD-HFD $n = 9$ mice; CD-HFD + anti-CD8 $n = 13$ mice; CD-HFD + anti-PD1 $n = 8$ mice; Kupffer cells (KC): CD-HFD $n = 9$ mice; CD-HFD + anti-CD8 $n = 12$ mice; CD-HFD + anti-PD1 $n = 8$ mice). More

MHCII⁺ myeloid cells were found in the respective sub-populations. **j**, Flow cytometry analysis for polarization of hepatic CD4⁺ T cells from mice as in **g** (CD-HFD $n = 12$ mice; CD-HFD + anti-CD8 $n = 17$ mice; CD-HFD + anti-PD1 $n = 17$ mice). **k**, Flow cytometric analysis for polarization of hepatic myeloid cells of mice fed for 12 months with CD-HFD and untreated or treated for 8 weeks with anti-PD1 antibodies (CD-HFD $n = 8$ mice; anti-PD1 + CD-HFD $n = 12$ mice). **l**, Flow cytometric analysis for polarization of hepatic CD8⁺ T cells from mice as in **k** (CD-HFD $n = 10$ mice; anti-PD1 + CD-HFD $n = 14$ mice). **m**, Confocal analyses revealed clusters of CD8⁺ T cells with adjacent cleaved caspase 3⁺ hepatocytes that were strongly increased by anti-PD1-related immunotherapy in liver tissue from mice fed for 12 months with ND or CD-HFD and treated for 8 weeks with IgG or anti-PD1 antibodies, suggesting increased necro-inflammation in the vicinity of CD8⁺ T cells ($n = 27$ FOV in 3 mice per group). Scale bars, 30 μ m. **n**, GSEA of RNA-seq data for hepatic tissue from mice fed for 12 months with CD-HFD and treated for 8 weeks with anti-CD8, anti-CD8 + anti-NK1.1 or anti-PD1 antibodies ($n = 5$ mice per group) revealed enrichment for TNF signalling via NF- κ B and inflammatory responses. Deletion of NK1.1⁺ cells altered the cholesterol homeostasis-related signature, suggesting a link between NK T cells and aberrant cholesterol metabolism. Moreover, tissue from mice treated with anti-PD1 antibodies revealed positive enrichment of apoptosis, inflammatory responses and epithelial–mesenchymal transition, indicating a pro-inflammatory, pro-carcinogenic liver environment upon anti-PD1 treatment. **o**, Livers from mice fed for 12 months with CD-HFD and treated for 8 weeks with IgG or anti-PD1 antibodies. Arrowheads, tumours or lesions. Scale bar, 10 mm. All data are shown as mean \pm s.e.m. **b**, **c**, One-way ANOVA and Fisher's LSD test. **h**, Two-way ANOVA and Sidak's multiple comparison test. **i–l**, Two-tailed Student's *t*-test. **m**, Two-tailed Mann–Whitney test. [Source data](#)

Extended Data Fig. 5 Anti-PD1 treatment drives hepatocarcinogenesis by enhancing an inflammatory and pro-tumorigenic liver microenvironment.

a, Histological staining with H&E and CD8 of hepatic tissue from wild-type or *Pdcd1*^{−/−} mice fed for 6 months with ND or CD-HFD (H&E: ND

n = 8 mice; *Pdcd1*^{-/-} ND *n* = 5 mice; CD-HFD *n* = 9 mice; *Pdcd1*^{-/-} CD-HFD *n* = 13 mice; CD8: ND *n* = 4 mice; CD-HFD *n* = 5 mice; *Pdcd1*^{-/-} CD-HFD *n* = 7 mice). Arrowheads, CD8⁺ cells. Scale bar, 50 µm. **b**, Cytokine expression of hepatic CD8⁺ T cells from mice as in **a** (ND *n* = 4 mice; *Pdcd1*^{-/-} ND *n* = 5 mice; CD-HFD *n* = 5 mice; *Pdcd1*^{-/-} CD-HFD *n* = 6 mice). **c**, Tumour or lesion incidence in wild-type or *Pdcd1*^{-/-} mice fed for 6 months with CD-HFD (CD-HFD *n* = 6 tumours/lesions in 63 mice; *Pdcd1*^{-/-} CD-HFD *n* = 6 tumours/lesions in 13 mice). **d**, ALT levels for mice as in **a** (ND *n* = 9 mice; *Pdcd1*^{-/-} ND *n* = 5 mice; CD-HFD *n* = 9 mice; *Pdcd1*^{-/-} CD-HFD *n* = 10 mice). **e**, NAS evaluation by H&E of mice as in **a** (ND *n* = 8 mice; *Pdcd1*^{-/-} ND *n* = 5 mice; CD-HFD *n* = 9 mice; *Pdcd1*^{-/-} CD-HFD *n* = 13 mice). **f**, Quantification of CD8⁺ cells in hepatic tissue by immunohistochemistry of mice as in **a** (ND *n* = 4 mice; *Pdcd1*^{-/-} ND *n* = 5 mice; CD-HFD *n* = 5 mice; *Pdcd1*^{-/-} CD-HFD *n* = 7 mice). **g**, Relative quantification of hepatic leukocytes in mice as in **a** (ND *n* = 4 mice; *Pdcd1*^{-/-} ND *n* = 5 mice; CD-HFD *n* = 5 mice; *Pdcd1*^{-/-} CD-HFD *n* = 6 mice). **h**, Immune cancer field (ICF) and ICF patterns of RNA-seq data for hepatic tissue from mice fed for 12 months with ND or CD-HFD and treated for 8 weeks treatment with IgG, anti-PD1 or anti-CD8 antibodies (ND, CD-HFD + anti-PD1, CD-HFD + anti-CD8 *n* = 5 mice per group; CD-HFD *n* = 4 mice) through single-sample GSEA. **i**, mRNA in situ hybridization (left) and quantification (right) for hepatic TNF⁺ cells from mice as in **h** (ND *n* = 25 FOV in 3 mice; CD-HFD *n* = 27 FOV in 3 mice; CD-HFD + anti-PD1 *n* = 40 FOV in 3 mice; CD-HFD + anti-CD8 *n* = 55 FOV in 3 mice). Arrowheads, TNF⁺ cells. Scale bar, 20 µm. **j**, GSEA of RNA-seq data for hepatic tissue comparing tumour-bearing mice fed for 12 months with CD-HFD and untreated or treated for 8 weeks with anti-PD1 antibodies (*n* = 5 mice per group). **k**, mRNA in situ hybridization (left) and quantification (right) for hepatic TNF⁺ cells from mice fed for 12 months with CD-HFD and untreated or treated for 8 weeks with anti-PD1 antibodies, with or without tumours (without tumours: CD-HFD *n* = 30 FOV in 3 mice; CD-HFD + anti-PD1 *n* = 40 FOV in 3 mice; peri-tumoural: CD-HFD *n* = 20 FOV in 3 mice; CD-HFD + anti-PD1 *n* = 21 FOV in 3 mice; intra-tumoural: CD-HFD *n* = 19 FOV in 3 mice; CD-HFD + anti-PD1 *n* = 22 FOV in 3 mice). Arrowheads, TNF⁺ cells. Scale bar, 20 µm. **l**, Quantification of CD8 staining by immunohistochemistry of peri-

and intra-tumoural hepatic tissue from mice fed for 12 months with CD-HFD and untreated or treated for 8 weeks with anti-PD1 antibodies (peri-tumoural: CD-HFD $n = 11$ mice; CD-HFD + anti-PD1 $n = 10$ mice; intra-tumoural: CD-HFD $n = 5$ mice; CD-HFD + anti-PD1 $n = 7$ mice). **m**, Histological staining for p62 (right) and quantification (left) of liver tumour tissue from mice fed for 12 months with ND or CD-HFD and untreated or treated for 8 weeks with anti-PD1 antibodies or anti-CD8 antibodies ($n = 5$ mice per group). Scale bar, 100 μm . **n**, Genomic aberrations by array comparative genomic hybridization (aCGH) of tumour tissue from mice fed for 12 months with CD-HFD and untreated ($n = 9$) or treated for 8 weeks with anti-PD1 antibodies ($n = 12$). All data are shown as mean \pm s.e.m. **b**, **d–i**, **m**, One-way ANOVA and Fisher's LSD test. **c**, Two-sided Fisher's exact test. **k**, **l**, Two-tailed Student's *t*-test. [Source data](#)

Extended Data Fig. 6 CD8 $^{+}$ PD1 $^{\pm}$ TOX $^{\text{high}}$ T cells with a resident-like character are enriched and are cellular drivers of hepatic necroinflammation and increased hepatocarcinogenesis upon anti-PD1 treatment in mice with NASH.

a–c, scRNA-seq analysis of hepatic TCR β^{+} cells (**a**), expression of selected markers in hepatic CD8 $^{+}$ T cells by scRNA-seq comparing CD8 $^{+}$ with CD8 $^{+}$ PD1 $^{+}$ T cells (**b**), and average UMI comparison (**c**) of hepatic CD8 $^{+}$ PD1 $^{+}$ T cells from mice fed for 12 months with CD-HFD and treated for 8 weeks with IgG, anti-PD1 antibodies or anti-CD8 antibodies ($n = 3$ mice per group). **d**, Velocity analyses on scRNA-seq data from CD8 $^{+}$ cells from mice fed for 12 months with ND or CD-HFD and treated for 8 weeks with anti-PD1 antibodies ($n = 3$ mice). Yellow, root cells; yellow; blue, farthest from root. End points: yellow, end point cells; blue, farthest from defined end point. RNA velocity flow: blue cluster, start point; orange cluster, intermediate; green cluster, end point. Arrow shows trajectory of cells. **e**, Velocity analyses of scRNA-seq data showing correlation of expression of selected genes along the latent time of ND-fed mice ($n = 3$ mice). Latent time (pseudo-time by RNA velocity): dark colour, start of RNA velocity; yellow, end point of latent time. **f**, RNA velocity analyses by scRNA-seq indicating transcriptional activity and gene expression of CD8 $^{+}$ cells from mice fed for 12 months with ND or CD-HFD and untreated or

treated for 8 weeks with anti-PD1 antibodies ($n = 3$ mice per group). **g**, Expression of selected markers in hepatic CD8 $^{+}$ PD1 $^{+}$ T cells sorted from TCR β^{+} cells by mass spectrometry from mice fed for 12 months with CD-HFD and untreated or treated for 8 weeks with anti-PD1 antibodies ($n = 6$ mice per group). **h**, Analyses of CD4 $^{+}$ and CD4 $^{+}$ PD1 $^{+}$ T cells derived from livers of NASH mice with or without anti-PD1 treatment indicate minor differences in expression of selected markers in hepatic CD4 $^{+}$ T cells sorted from TCR β^{+} cells by scRNA-seq comparing CD4 $^{+}$ with CD4 $^{+}$ PD1 $^{+}$ T cells from mice fed for 12 months with CD-HFD and treated for 8 weeks with IgG, anti-PD1 or anti-CD8 antibodies ($n = 3$ mice per group). **i**, Comparison of average UMIs for hepatic CD4 $^{+}$ T cells from mice fed for 12 months with CD-HFD and treated for 8 weeks with IgG or anti-PD1 antibodies ($n = 3$ mice per group). **j**, Quantification of manual gating (left) and flow cytometry plots (right) for hepatic CD8 $^{+}$ PD1 $^{+}$ TNF $^{+}$ cell abundance in mice as in **i** (CD-HFD $n = 8$ mice; CD-HFD + anti-PD1 $n = 6$ mice). **k**, CellCNN-analysed flow cytometry data for hepatic CD8 $^{+}$ T cells from mice as in **i** (CD-HFD + IgG $n = 6$ mice; CD-HFD + anti-PD1 $n = 4$ mice). **l**, Immunofluorescence staining for PD1, CD8 and Ki-67 of liver tissue from mice fed for 12 months with ND or CD-HFD and treated for 8 weeks with IgG or anti-PD1 antibodies ($n = 2$ mice per group). Scale bar, 100 μ m. **m**, In vitro stimulated splenic CD8 T cells from C57Bl/6 mice were treated with anti-PD1 antibody for 72 h. Cell count (left), $n = 5$ experiments per group; Ki-67 (right), $n = 4$ experiments per group. **n–p**, Quantification of intracellular FOXO1 (**n**), calcium levels (**o**), and polarization (**p**) in CD8 $^{+}$ T cells isolated by flow cytometry from mice fed for 12 months with ND or CD-HFD and untreated or treated for 8 weeks with anti-PD1 antibodies (FOXO1: ND $n = 6$ mice; CD-HFD $n = 5$ mice; CD-HFD + anti-PD1 $n = 7$ mice; calcium: ND $n = 13$ mice; CD-HFD $n = 10$ mice; CD-HFD + anti-PD1 $n = 10$ mice; polarization: ND $n = 6$ mice; CD-HFD $n = 5$ mice; CD-HFD + anti-PD1 $n = 6$ mice). **q**, Relative quantification by flow cytometry of hepatic CD8 $^{+}$ PD1 $^{+}$ cells from mice as in **n** (ND $n = 6$ mice; CD-HFD $n = 5$ mice; CD-HFD + anti-PD1 $n = 6$ mice). **r–t**, Quantification of intracellular calcium (**r**), FOXO1 (**s**) and polarization (**t**) in CD4 $^{+}$ T cells isolated by flow cytometry from mice as in **n** (FOXO1: ND $n = 6$ mice; CD-HFD $n = 5$ mice; CD-HFD + anti-PD1 $n = 7$ mice; calcium: ND $n = 13$ mice; CD-HFD $n = 10$ mice; CD-HFD + anti-PD1 $n = 10$ mice;

polarization: ND $n = 6$ mice; CD-HFD $n = 5$ mice; CD-HFD + anti-PD1 $n = 6$ mice). **u**, Relative quantification by flow cytometry of hepatic CD4 $^+$ PD1 $^+$ T cells from mice as in **n** (ND $n = 6$ mice; CD-HFD $n = 5$ mice; CD-HFD + anti-PD1 $n = 6$ mice). All data are shown as mean \pm s.e.m. **f**, Two-tailed Mann–Whitney test. **j**, **m**, Two-tailed Student’s *t*-test. **n–u**, Two-way ANOVA and Fisher’s LSD test. [Source data](#)

Extended Data Fig. 7 CD8 $^{\pm}$ T cells drive hepatic inflammation and subsequent liver cancer in a TNF-dependent manner upon PD1-targeted immunotherapy.

a, b, Histological evaluation (**a**) and representative micrographs (**b**) of Sirius Red, CD4, CD8, PD1, PDL1, F4/80, and MHC-II staining of mice fed for 12 months with ND or CD-HFD and untreated or treated for 8 weeks with anti-PD1, anti-PD1 + anti-CD8, anti-TNF, anti-PD1 + anti-TNF, anti-CD4 or anti-PD1 + anti-CD4 antibodies (Sirius Red: ND $n = 11$ mice; CD-HFD $n = 12$ mice; CD-HFD + anti-PD1 $n = 12$ mice; CD-HFD + anti-PD1 + anti-CD8 $n = 9$ mice; CD-HFD + anti-TNF $n = 10$ mice; CD-HFD + anti-PD1 + anti-TNF $n = 11$ mice; CD-HFD + anti-CD4 $n = 8$ mice; CD-HFD + anti-PD1 + anti-CD4 $n = 8$ mice; CD4: ND $n = 10$ mice; CD-HFD $n = 11$ mice; CD-HFD + anti-PD1 $n = 14$ mice; CD-HFD + anti-PD1 + anti-CD8 $n = 9$ mice; CD-HFD + anti-TNF $n = 10$ mice; CD-HFD + anti-PD1 + anti-TNF $n = 11$ mice; CD-HFD + anti-CD4 $n = 8$ mice; CD-HFD + anti-PD1 + anti-CD4 $n = 8$ mice; CD8: ND $n = 10$ mice; CD-HFD $n = 12$ mice; CD-HFD + anti-PD1 $n = 14$ mice; CD-HFD + anti-PD1 $n = 14$ mice; CD-HFD + anti-PD1 + anti-CD8 $n = 9$ mice; CD-HFD + anti-TNF $n = 10$ mice; CD-HFD + anti-PD1 + anti-TNF $n = 11$ mice; CD-HFD + anti-CD4 $n = 8$ mice; CD-HFD + anti-PD1 + anti-CD4 $n = 8$ mice; PD1: ND $n = 12$ mice; CD-HFD $n = 12$ mice; CD-HFD + anti-PD1 $n = 14$ mice; CD-HFD + anti-PD1 + anti-CD8 $n = 8$ mice; CD-HFD + anti-TNF $n = 10$ mice; CD-HFD + anti-PD1 + anti-TNF $n = 10$ mice; CD-HFD + anti-CD4 $n = 8$ mice; CD-HFD + anti-PD1 + anti-CD4 $n = 8$ mice; PDL1: ND $n = 10$ mice; CD-HFD $n = 11$ mice; CD-HFD + anti-PD1 $n = 14$ mice; CD-HFD + anti-PD1 + anti-CD8 $n = 9$ mice; CD-HFD + anti-TNF $n = 10$ mice; CD-HFD + anti-PD1 + anti-TNF $n = 11$ mice; CD-HFD + anti-CD4 $n = 8$ mice; CD-HFD + anti-PD1 + anti-CD4 $n = 8$ mice; F4/80: ND $n = 11$ mice; CD-HFD

n = 12 mice; CD-HFD + anti-PD1 *n* = 14 mice; CD-HFD + anti-PD1 *n* = 14 mice; CD-HFD + anti-PD1 + anti-CD8 *n* = 9 mice; CD-HFD + anti-TNF *n* = 10 mice; CD-HFD + anti-PD1 + anti-TNF *n* = 11 mice; CD-HFD + anti-CD4 *n* = 8 mice; CD-HFD + anti-PD1 + anti-CD4 *n* = 8 mice; MHC-II: ND *n* = 11 mice; CD-HFD *n* = 13 mice; CD-HFD + anti-PD1 *n* = 14 mice; CD-HFD + anti-PD1 *n* = 14 mice; CD-HFD + anti-PD1 + anti-CD8 *n* = 9 mice; CD-HFD + anti-TNF *n* = 10 mice; CD-HFD + anti-PD1 + anti-TNF *n* = 11 mice CD-HFD + anti-CD4 *n* = 8 mice; CD-HFD + anti-PD1 + anti-CD4 *n* = 8 mice). Scale bar, 100 µm. **c, d**, ALT (**c**) and quantification (**d**) of hepatic CD8⁺PD-1⁺TNF⁺ T cells from mice fed for 12 months with ND or CD-HFD and untreated or treated for 8 weeks with anti-PD-1, anti-PD-1 + anti-CD8, anti-TNF, anti-PD-1 + anti-TNF, anti-CD4, or anti-PD-1 + anti-CD4 antibodies (ALT: ND *n* = 30 mice; CD-HFD *n* = 47 mice; CD-HFD + anti-PD-1 *n* = 35 mice; CD-HFD + anti-PD-1 + anti-CD8 *n* = 9 mice; CD-HFD + anti-TNF *n* = 10 mice; CD-HFD + anti-PD-1 + anti-TNF *n* = 11 mice; CD-HFD + anti-CD4 *n* = 8 mice; CD-HFD + anti-PD-1 + anti-CD4 *n* = 8 mice; CD8⁺PD-1⁺TNF⁺: ND *n* = 8 mice; CD-HFD *n* = 5 mice; CD-HFD + anti-PD-1 *n* = 3 mice; CD-HFD + anti-PD-1 + anti-CD8 *n* = 9 mice; CD-HFD + anti-TNF *n* = 10 mice; CD-HFD + anti-PD-1 + anti-TNF *n* = 11 mice; CD-HFD + anti-CD4 *n* = 8 mice; CD-HFD + anti-PD-1 + anti-CD4 *n* = 8 mice). All data are shown as mean ± s.e.m. All data were analysed by one-way ANOVA and Fisher's LSD test. [Source data](#)

Extended Data Fig. 8 PD1-targeted immunotherapy induces hepatic inflammation, which drives hepatocarcinogenesis in a CD8⁺ T cell-dependent manner.

a, b, Tumour or lesion load (**a**) and tumour or lesion size (**b**) in mice fed for 12 months with CD-HFD and untreated or treated for 8 weeks with anti-PD1, anti-PD1 + anti-CD8, anti-TNF, anti-PD1 + anti-TNF, anti-CD4, or anti-PD1 + anti-CD4 antibodies (CD-HFD *n* = 19 mice; CD-HFD + anti-PD1 *n* = 29 mice; CD-HFD + anti-PD1 + anti-CD8 *n* = 2 mice; CD-HFD + anti-TNF *n* = 3 mice; CD-HFD + anti-PD1 + anti-TNF *n* = 3 mice; CD-HFD + anti-CD4 *n* = 3 mice; CD-HFD + anti-PD1 + anti-CD4 *n* = 8 mice). **c, d**, UMAP representation of 63 parameters (serology, flow cytometry, histology) (**c**) and selected displays of analysed parameters (**d**) indicating

the severity of NASH pathology in mice fed for 12 months with ND or CD-HFD and untreated or treated for 8 weeks with anti-CD8, anti-CD8 + anti-NK1.1, anti-PD1, anti-PD1 + anti-CD8, anti-TNF, anti-PD1 + anti-TNF, anti-CD4, or anti-PD1 + anti-CD4 antibodies (ND $n = 22$ mice; CD-HFD $n = 31$ mice; CD-HFD + anti-PD1 $n = 41$ mice; CD-HFD + anti-PDL1 $n = 6$ mice; CD-HFD + anti-CD8 $n = 24$ mice; CD-HFD + anti-CD8 + anti-NK1.1 $n = 6$ mice; CD-HFD + anti-PD1 + anti-CD8 $n = 9$ mice; CD-HFD + anti-TNF $n = 10$ mice; CD-HFD + anti-PD1 + anti-TNF $n = 11$ mice; CD-HFD + anti-CD4 $n = 9$ mice; CD-HFD + anti-PD1 + anti-CD4 $n = 9$ mice). **e**, Data gathered from hepatic tissue analyses were binary correlated with one another for mice fed for 6 or 12 months with ND or CD-HFD and treated for 8 weeks with anti-CD8, anti-CD8 + anti-NK1.1, anti-PD1, anti-PD1 + anti-CD8, anti-TNF, anti-PD1 + anti-TNF, anti-CD4, or anti-PD1 + anti-CD4 antibodies (ND $n = 47$ mice; CD-HFD $n = 72$ mice; CD-HFD + anti-PD1 $n = 41$ mice; CD-HFD + anti-PDL1 $n = 6$ mice; CD-HFD + anti-CD8 $n = 29$ mice; CD-HFD + anti-CD8 + NK1.1 $n = 6$ mice; CD-HFD + anti-PD1 + anti-CD8 $n = 9$ mice; CD-HFD + anti-TNF $n = 10$ mice; CD-HFD + anti-PD1 + anti-TNF $n = 11$ mice; CD-HFD + anti-CD4 $n = 9$ mice; CD-HFD + anti-PD1 + anti-CD4 $n = 9$ mice). All data are shown as mean \pm s.e.m. **a, b**, One-way ANOVA and Dunn's multiple comparison test. **e**, Two-tailed Spearman's correlation. [Source data](#)

Extended Data Fig. 9 An inflammatory cellular polarization of T cells can be found in liver biopsies from patients with NAFLD or NASH.

a, b, Flow cytometry plots and quantification of patient-liver-derived PD1 $^{+}$ CD8 $^{+}$ T cells (**a**), and correlation of PD1 $^{+}$ CD8 $^{+}$ T cells with BMI, NAS and ALT for healthy participants and patients with NAFLD or NASH (**b**) (Supplementary Table 1; healthy controls $n = 8$; NAFLD/NASH $n = 16$ patients). **c–e**, Flow cytometry plot of FMO control (**c**), quantification of patient-liver-derived PD1 $^{+}$ CD8 $^{+}$ T cells (**d**), and quantification of CD4, CD8, $\gamma\delta$, NK and NK T cells from healthy participants or patients with NAFLD or NASH (**e**) (Supplementary Table 1: healthy controls $n = 8$; NAFLD/NASH $n = 16$ patients). **f, g**, Heat map showing median marker expression (**f**) and quantification of the defined CD45 $^{+}$ subsets from Fig. 3c

(g) by flow cytometry derived from hepatic biopsies from control participants and patients with NAFLD or NASH to define distinct marker expression (Supplementary Table 2: control individuals $n = 6$; NAFLD/NASH $n = 11$ patients). **h–j**, HSNE representation of defined T cell subsets (**h**), marker expression (**i**) and quantification of CD8 $^{+}$ CD103 $^{+}$ PD1 $^{+}$ cells (**j**) in liver-derived T cells from control individuals and patients with NAFLD or NASH analysed by cytometry by time of flight (CyTOF) (control $n = 11$ individuals pooled in 3 analyses; NAFLD/NASH $n = 16$ patients pooled in 5 analyses). **k, l**, Selected average marker expression in CD4 $^{+}$ and CD8 $^{+}$ T cell subsets (**k**) and differential gene expression of CD8 $^{+}$ PD1 $^{+}$ versus CD8 $^{+}$ T cells and CD4 $^{+}$ PD1 $^{+}$ versus CD4 $^{+}$ T cells by scRNA-seq (**l**) for control individuals and patients with NAFLD or NASH (control $n = 4$ individuals; NAFLD/NASH $n = 7$ patients). All data are shown as mean \pm s.e.m. All data were analysed by two-tailed Mann–Whitney test. [Source data](#)

Extended Data Fig. 10 PD1 and PDL1 targeted immunotherapy in advanced HCC has a distinct effect depending on disease aetiology.

a, Comparison of RNA-seq data from patients with NASH with varying degrees of fibrosis (F0–F4, Brunt classification) normalized to data from patients with NAFLD from a total of $n = 206$ patients with NAFLD or NASH. **b, c**, Immunohistochemical staining (**b**) and quantification (**c**) of hepatic PD1 $^{+}$, CD8 $^{+}$, and CD4 $^{+}$ cells from patients with NAFLD or NASH with varying degrees of fibrosis (Supplementary Table 3) (NAFLD $n = 9$ patients; NASH F0/1 $n = 7$ patients; NASH F2 $n = 12$ patients; NASH F3 $n = 21$ patients; NASH F4 $n = 16$ patients; CD4: NAFL $n = 6$ patients; NASH F0/1 $n = 4$ patients; NASH F2 $n = 8$ patients; NASH F3 $n = 17$ patients; NASH F4 $n = 9$ patients). Scale bar, 100 μ m. **d**, Correlation analysis of PD1 expression against fibrosis grade by immunohistochemical staining (NAFLD/NASH $n = 65$ patients). **e**, Immunohistochemical staining and quantification of ratio of PD1 $^{+}$ /CD8 $^{+}$ cells in immunohistochemical staining of samples from patient cohort in Supplementary Tables 4–6 (healthy individuals $n = 4$, NASH $n = 26$ patients, peri-tumoural NASH–HCC $n = 16$ patients, peri-tumoural HCC other aetiologies $n = 29$ patients).

Scale bar, 100 µm. **f**, Immunohistochemical staining and quantification of PD1⁺ cells and MIB1⁺ hepatocytes in peri-tumoural and intra-tumoural samples from patients with HCV- or NASH-induced HCC (PD1: peri-tumoural HCV $n = 16$ tissues from 7 patients; peri-tumoural NASH $n = 9$ tissues from 2 patients; intra-tumoural HCV $n = 10$ HCCs from 7 patients; intra-tumoural NASH $n = 6$ HCCs from 2 patients; MIB1: peri-tumoural HCV $n = 16$ tissues from 7 patients; peri-tumoural NASH $n = 9$ tissues from 2 patients; intra-tumoural HCV $n = 10$ HCCs from 7 patients; intra-tumoural NASH $n = 6$ HCCs from 2 patients). Arrowheads, PD1⁺ or MIB1⁺ cells. Scale bars, 100 µm. **g**, PRISMA flow chart of the systematic review of targeted immunotherapy in HCC and the selection of articles assessing the clinical outcome of immune checkpoint inhibitors in advanced HCC for inclusion in the systematic review and meta-analysis. ICPI, immune checkpoint inhibitor. A total of 1,243 patients were included in two first-line trials comparing PD1- or PDL1-targeted immunotherapy to sorafenib. In these trials, 707 patients received an immune checkpoint inhibitor (either anti-PD1 or anti-PDL1). **h–j**, HCV and HBV were pooled into a separate category, termed ‘viral’, and a subsequent meta-analysis comparing viral ($n = 754$) and non-viral HCC ($n = 489$; mostly NASH and alcohol intake) was performed (**h**). A subgroup analysis studying the specific effects of non-viral aetiologies ($n = 489$) on the magnitude of effect of immunotherapy is presented, when compared to HBV (**i**; $n = 473$) or HCV (**j**; $n = 281$). HRs for each trial are represented by squares; the size of the square represents the weight of the trial in the meta-analysis. The horizontal line crossing the square represents the 95% CI. The diamonds represent the estimated overall effect based on the meta-analysis random effect of all trials. Inverse variance (IV) and random effects methods (Random) were used to calculate HRs, 95% CIs, P values, and the test for overall effect; these calculations were two-sided. Cochran’s Q -test and I^2 were used to calculate heterogeneity. All data are shown as mean ± s.e.m. **c, e, f**, One-way ANOVA and Dunn’s multiple comparison test. **d**, Two-tailed Spearman’s correlation. [Source data](#)

Supplementary information

[Supplementary Tables](#)

This file contains Supplementary Tables 1-15.

Reporting Summary

Supplementary Figures

Gating strategy flow cytometry.

Peer Review File

Source data

Source Data Fig. 1

Source Data Fig. 2

Source Data Fig. 3

Source Data Fig. 4

Source Data Extended Data Fig. 1

Source Data Extended Data Fig. 2

Source Data Extended Data Fig. 3

Source Data Extended Data Fig. 4

Source Data Extended Data Fig. 5

Source Data Extended Data Fig. 6

Source Data Extended Data Fig. 7

[**Source Data Extended Data Fig. 8**](#)

[**Source Data Extended Data Fig. 9**](#)

[**Source Data Extended Data Fig. 10**](#)

Rights and permissions

Open Access This article is licensed under a Creative Commons Attribution 4.0 International License, which permits use, sharing, adaptation, distribution and reproduction in any medium or format, as long as you give appropriate credit to the original author(s) and the source, provide a link to the Creative Commons license, and indicate if changes were made. The images or other third party material in this article are included in the article's Creative Commons license, unless indicated otherwise in a credit line to the material. If material is not included in the article's Creative Commons license and your intended use is not permitted by statutory regulation or exceeds the permitted use, you will need to obtain permission directly from the copyright holder. To view a copy of this license, visit <http://creativecommons.org/licenses/by/4.0/>.

[Reprints and Permissions](#)

About this article



Check for
updates

Cite this article

Pfister, D., Núñez, N.G., Pinyol, R. *et al.* NASH limits anti-tumour surveillance in immunotherapy-treated HCC. *Nature* **592**, 450–456 (2021).
<https://doi.org/10.1038/s41586-021-03362-0>

Download citation

- Received: 17 February 2020
- Accepted: 16 February 2021
- Published: 24 March 2021
- Issue Date: 15 April 2021
- DOI: <https://doi.org/10.1038/s41586-021-03362-0>

Comments

By submitting a comment you agree to abide by our [Terms](#) and [Community Guidelines](#). If you find something abusive or that does not comply with our terms or guidelines please flag it as inappropriate.

Download PDF

This article was downloaded by **calibre** from <https://www.nature.com/articles/s41586-021-03362-0>

- Article
- [Published: 17 March 2021](#)

Expansible residence decentralizes immune homeostasis

- [Sathi Wijeyesinghe](#) ORCID: [orcid.org/0000-0002-8819-2654¹](https://orcid.org/0000-0002-8819-2654),
- [Lalit K. Beura¹](#) nAff3,
- [Mark J. Pierson¹](#),
- [J. Michael Stolley¹](#),
- [Omar A. Adam¹](#),
- [Roland Ruscher²](#) nAff4,
- [Elizabeth M. Steinert](#) ORCID: [orcid.org/0000-0002-6947-2271¹](https://orcid.org/0000-0002-6947-2271),
- [Pamela C. Rosato¹](#) nAff5,
- [Vaiva Veizys¹](#) &
- [David Masopust](#) ORCID: [orcid.org/0000-0002-9440-3884¹](https://orcid.org/0000-0002-9440-3884)

[Nature](#) volume 592, pages457–462(2021) [Cite this article](#)

- 6096 Accesses
- 108 Altmetric
- [Metrics details](#)

Subjects

- [Immunological memory](#)
- [Mucosal immunology](#)
- [T cells](#)

Abstract

In metazoans, specific tasks are relegated to dedicated organs that are established early in development, occupy discrete locations and typically remain fixed in size. The adult immune system arises from a centralized haematopoietic niche that maintains self-renewing potential^{1,2}, and—upon maturation—becomes distributed throughout the body to monitor environmental perturbations, regulate tissue homeostasis and mediate organism-wide defence. Here we examine how immunity is integrated within adult mouse tissues, and address issues of durability, expansibility and contributions to organ cellularity. Focusing on antiviral T cell immunity, we observed durable maintenance of resident memory T cells up to 450 days after infection. Once established, resident T cells did not require the T cell receptor for survival or retention of a poised, effector-like state. Although resident memory indefinitely dominated most mucosal organs, surgical separation of parabiotic mice revealed a tissue-resident provenance for blood-borne effector memory T cells, and circulating memory slowly made substantial contributions to tissue immunity in some organs. After serial immunizations or cohousing with pet-shop mice, we found that in most tissues, tissue pliancy (the capacity of tissues to vary their proportion of immune cells) enables the accretion of tissue-resident memory, without axiomatic erosion of pre-existing antiviral T cell immunity. Extending these findings, we demonstrate that tissue residence and organ pliancy are generalizable aspects that underlie homeostasis of innate and adaptive immunity. The immune system grows commensurate with microbial experience, reaching up to 25% of visceral organ cellularity. Regardless of the location, many populations of white blood cells adopted a tissue-residency program within nonlymphoid organs. Thus, residence—rather than renewal or recirculation—typifies nonlymphoid immune surveillance, and organs serve as pliant storage reservoirs that can accommodate continuous expansion of the cellular immune system throughout life. Although haematopoiesis restores some elements of the immune system, nonlymphoid organs sustain an accrual of durable tissue-autonomous cellular immunity that results in progressive decentralization of organismal immune homeostasis.

[Access through your institution](#)

[Change institution](#)

[Buy or subscribe](#)

Access options

Subscribe to Journal

Get full journal access for 1 year

\$199.00

only \$3.90 per issue

[Subscribe](#)

All prices are NET prices.

VAT will be added later in the checkout.

Tax calculation will be finalised during checkout.

Rent or Buy article

Get time limited or full article access on ReadCube.

from \$8.99

[Rent or Buy](#)

All prices are NET prices.

Additional access options:

- [Log in](#)
- [Access through your institution](#)
- [Learn about institutional subscriptions](#)

Fig. 1: Residence sustains organism-wide autonomous immune surveillance by T cells.

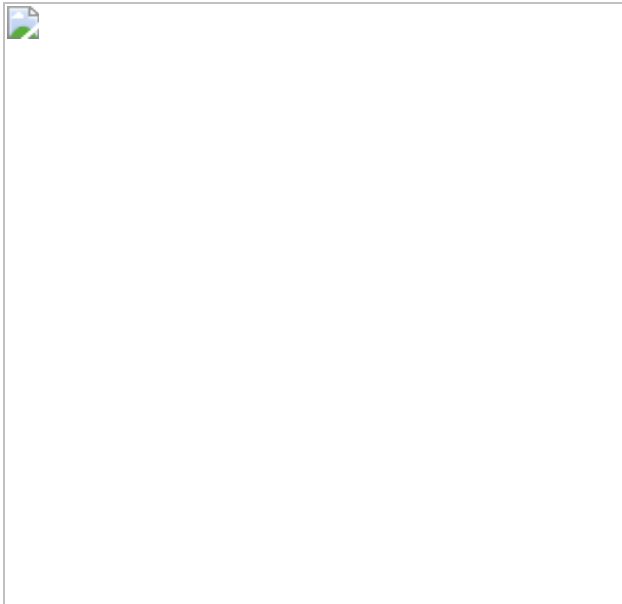


Fig. 2: The CD8⁺ T cell compartment expands to accommodate new and pre-existing resident memory.

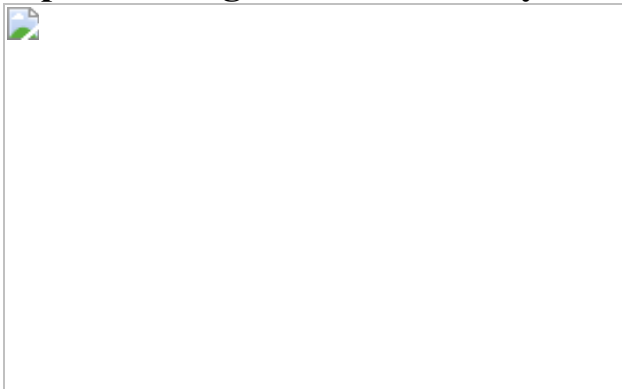


Fig. 3: Tissue pliancy enables immune expansion after microbial conditioning.

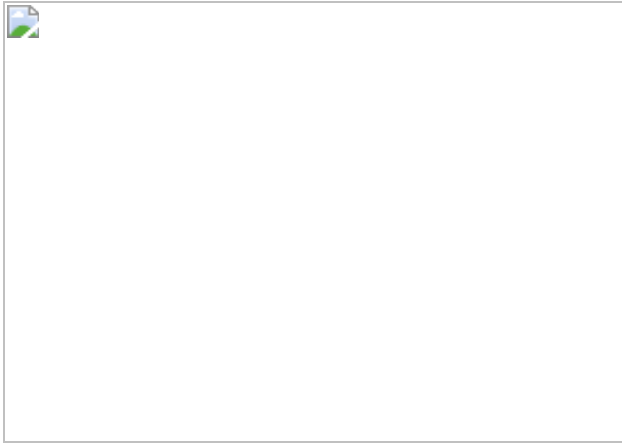
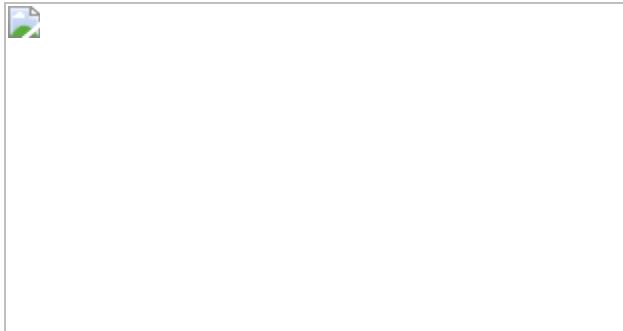


Fig. 4: Tissue residence typifies organism-wide immune surveillance.



Data availability

The data that support the findings of this study are available from the corresponding author upon reasonable request. [Source data](#) are provided with this paper.

Code availability

ImageJ scripts developed for cell enumeration are available at <http://github.com/wijey001/count>.

References

1. 1.

Höfer, T., Busch, K., Klapproth, K. & Rodewald, H.-R. Fate mapping and quantitation of hematopoiesis in vivo. *Annu. Rev. Immunol.* **34**, 449–478 (2016).

[PubMed](#) [Google Scholar](#)

2. 2.

Sawai, C. M. et al. Hematopoietic stem cells are the major source of multilineage hematopoiesis in adult animals. *Immunity* **45**, 597–609 (2016).

[PubMed](#) [PubMed Central](#) [CAS](#) [Google Scholar](#)

3. 3.

Janeway, C. A., Jr et al. Modes of cell:cell communication in the immune system. *J. Immunol.* **135**, 739s–742s (1985).

[PubMed](#) [Google Scholar](#)

4. 4.

Qi, H., Kastenmüller, W. & Germain, R. N. Spatiotemporal basis of innate and adaptive immunity in secondary lymphoid tissue. *Annu. Rev. Cell Dev. Biol.* **30**, 141–167 (2014).

[PubMed](#) [CAS](#) [Google Scholar](#)

5. 5.

Bromley, S. K. et al. The immunological synapse. *Annu. Rev. Immunol.* **19**, 375–396 (2001).

[PubMed](#) [CAS](#) [Google Scholar](#)

6. 6.

Mueller, S. N. & Mackay, L. K. Tissue-resident memory T cells: local specialists in immune defence. *Nat. Rev. Immunol.* **16**, 79–89 (2016).

[PubMed](#) [CAS](#) [Google Scholar](#)

7. 7.

Szabo, P. A., Miron, M. & Farber, D. L. Location, location, location: tissue resident memory T cells in mice and humans. *Sci. Immunol.* **4**, eaas9673 (2019).

[PubMed](#) [PubMed Central](#) [CAS](#) [Google Scholar](#)

8. 8.

Steinert, E. M. et al. Quantifying memory CD8 T cells reveals regionalization of immunosurveillance. *Cell* **161**, 737–749 (2015).

[PubMed](#) [PubMed Central](#) [CAS](#) [Google Scholar](#)

9. 9.

Stark, R. et al. T_{RM} maintenance is regulated by tissue damage via P2RX7. *Sci. Immunol.* **3**, eaau1022 (2018).

[PubMed](#) [Google Scholar](#)

10. 10.

Murali-Krishna, K. et al. Persistence of memory CD8 T cells in MHC class I-deficient mice. *Science* **286**, 1377–1381 (1999).

[PubMed](#) [CAS](#) [Google Scholar](#)

11. 11.

Masopust, D., Vezys, V., Wherry, E. J., Barber, D. L. & Ahmed, R. Cutting edge: gut microenvironment promotes differentiation of a unique memory CD8 T cell population. *J. Immunol.* **176**, 2079–2083 (2006).

[PubMed](#) [CAS](#) [Google Scholar](#)

12. 12.

Kurd, N. S. et al. Early precursors and molecular determinants of tissue-resident memory CD8⁺ T lymphocytes revealed by single-cell RNA sequencing. *Sci. Immunol.* **5**, eaaz6894 (2020).

[PubMed](#) [PubMed Central](#) [CAS](#) [Google Scholar](#)

13. 13.

Sallusto, F., Geginat, J. & Lanzavecchia, A. Central memory and effector memory T cell subsets: function, generation, and maintenance. *Annu. Rev. Immunol.* **22**, 745–763 (2004).

[PubMed](#) [CAS](#) [Google Scholar](#)

14. 14.

Germain, R. N. & Huang, Y. ILC2s - resident lymphocytes pre-adapted to a specific tissue or migratory effectors that adapt to where they move? *Curr. Opin. Immunol.* **56**, 76–81 (2019).

[PubMed](#) [CAS](#) [Google Scholar](#)

15. 15.

Klicznik, M. M. et al. Human CD4⁺CD103⁺ cutaneous resident memory T cells are found in the circulation of healthy individuals. *Sci. Immunol.* **4**, eaav8995 (2019).

[PubMed](#) [PubMed Central](#) [CAS](#) [Google Scholar](#)

16. 16.

Carbone, F. R. & Gebhardt, T. Should I stay or should I go—reconciling clashing perspectives on CD4⁺ tissue-resident memory T cells. *Sci. Immunol.* **4**, eaax5595 (2019).

[PubMed](#) [CAS](#) [Google Scholar](#)

17. 17.

Wu, T. et al. Lung-resident memory CD8 T cells (T_{RM}) are indispensable for optimal cross-protection against pulmonary virus infection. *J. Leukoc. Biol.* **95**, 215–224 (2014).

[PubMed](#) [PubMed Central](#) [Google Scholar](#)

18. 18.

Slütter, B. et al. Dynamics of influenza-induced lung-resident memory T cells underlie waning heterosubtypic immunity. *Sci. Immunol.* **2**, eaag2031 (2017).

[PubMed](#) [PubMed Central](#) [Google Scholar](#)

19. 19.

Stockinger, B., Barthlott, T. & Kassiotis, G. The concept of space and competition in immune regulation. *Immunology* **111**, 241–247 (2004).

[PubMed](#) [PubMed Central](#) [CAS](#) [Google Scholar](#)

20. 20.

Surh, C. D. & Sprent, J. Homeostasis of naive and memory T cells. *Immunity* **29**, 848–862 (2008).

[PubMed](#) [CAS](#) [Google Scholar](#)

21. 21.

Buck, M. D., Sowell, R. T., Kaech, S. M. & Pearce, E. L. Metabolic instruction of immunity. *Cell* **169**, 570–586 (2017).

[PubMed](#) [PubMed Central](#) [CAS](#) [Google Scholar](#)

22. 22.

Schenkel, J. M. et al. IL-15-independent maintenance of tissue-resident and boosted effector memory CD8 T cells. *J. Immunol.* **196**, 3920–3926 (2016).

[PubMed](#) [PubMed Central](#) [CAS](#) [Google Scholar](#)

23. 23.

Vezys, V. et al. Memory CD8 T-cell compartment grows in size with immunological experience. *Nature* **457**, 196–199 (2009).

[ADS](#) [PubMed](#) [CAS](#) [Google Scholar](#)

24. 24.

Huster, K. M. et al. Cutting edge: memory CD8 T cell compartment grows in size with immunological experience but nevertheless can lose function. *J. Immunol.* **183**, 6898–6902 (2009).

[PubMed](#) [CAS](#) [Google Scholar](#)

25. 25.

Beura, L. K. et al. Normalizing the environment recapitulates adult human immune traits in laboratory mice. *Nature* **532**, 512–516 (2016).

[ADS](#) [PubMed](#) [PubMed Central](#) [CAS](#) [Google Scholar](#)

26. 26.

Gasteiger, G., Fan, X., Dikiy, S., Lee, S. Y. & Rudensky, A. Y. Tissue residency of innate lymphoid cells in lymphoid and nonlymphoid organs. *Science* **350**, 981–985 (2015).

[PubMed](#) [PubMed Central](#) [CAS](#) [Google Scholar](#)

27. 27.

Guilliams, M., Thierry, G. R., Bonnardel, J. & Bajenoff, M. Establishment and maintenance of the macrophage niche. *Immunity* **52**, 434–451 (2020).

[PubMed](#) [CAS](#) [Google Scholar](#)

28. 28.

Schmidt-Rhaesa, A. *The Evolution of Organ Systems* (Oxford Univ. Press, 2007).

29. 29.

Pabst, O., Herbrand, H., Bernhardt, G. & Förster, R. Elucidating the functional anatomy of secondary lymphoid organs. *Curr. Opin. Immunol.* **16**, 394–399 (2004).

[PubMed](#) [CAS](#) [Google Scholar](#)

30. 30.

van Furth, R. & Cohn, Z. A. The origin and kinetics of mononuclear phagocytes. *J. Exp. Med.* **128**, 415–435 (1968).

[PubMed](#) [PubMed Central](#) [Google Scholar](#)

31. 31.

Sallusto, F., Lenig, D., Förster, R., Lipp, M. & Lanzavecchia, A. Two subsets of memory T lymphocytes with distinct homing potentials and effector functions. *Nature* **401**, 708–712 (1999).

[ADS](#) [PubMed](#) [CAS](#) [Google Scholar](#)

32. 32.

Weissman, I. L. Stem cells: units of development, units of regeneration, and units in evolution. *Cell* **100**, 157–168 (2000).

[PubMed](#) [CAS](#) [Google Scholar](#)

33. 33.

Gattinoni, L., Speiser, D. E., Lichtenfeld, M. & Bonini, C. T memory stem cells in health and disease. *Nat. Med.* **23**, 18–27 (2017).

[PubMed](#) [PubMed Central](#) [CAS](#) [Google Scholar](#)

34. 34.

Iwasaki, A. Exploiting mucosal immunity for antiviral vaccines. *Annu. Rev. Immunol.* **34**, 575–608 (2016).

[PubMed](#) [CAS](#) [Google Scholar](#)

35. 35.

Amsen, D., van Gisbergen, K. P. J. M., Hombrink, P. & van Lier, R. A. W. Tissue-resident memory T cells at the center of immunity to solid tumors. *Nat. Immunol.* **19**, 538–546 (2018).

[PubMed](#) [CAS](#) [Google Scholar](#)

36. 36.

Fonseca, R. et al. Developmental plasticity allows outside-in immune responses by resident memory T cells. *Nat. Immunol.* **21**, 412–421 (2020).

[PubMed](#) [PubMed Central](#) [CAS](#) [Google Scholar](#)

37. 37.

Behr, F. M. et al. Tissue-resident memory CD8⁺ T cells shape local and systemic secondary T cell responses. *Nat. Immunol.* **21**, 1070–1081 (2020).

[PubMed](#) [CAS](#) [Google Scholar](#)

38. 38.

Polic, B., Kunkel, D., Scheffold, A. & Rajewsky, K. How αβ T cells deal with induced TCRα ablation. *Proc. Natl Acad. Sci. USA* **98**, 8744–8749 (2001).

[ADS](#) [PubMed](#) [CAS](#) [Google Scholar](#)

39. 39.

Ruzankina, Y. et al. Deletion of the developmentally essential gene *ATR* in adult mice leads to age-related phenotypes and stem cell loss. *Cell Stem Cell* **1**, 113–126 (2007).

[PubMed](#) [PubMed Central](#) [CAS](#) [Google Scholar](#)

40. 40.

Tucker, C. G. et al. Adoptive T cell therapy with IL-12-preconditioned low-avidity T cells prevents exhaustion and results in enhanced T cell activation, enhanced tumor clearance, and decreased risk for autoimmunity. *J. Immunol.* **205**, 1449–1460 (2020).

[PubMed](#) [CAS](#) [Google Scholar](#)

41. 41.

Schindelin, J. et al. Fiji: an open-source platform for biological-image analysis. *Nat. Methods* **9**, 676–682 (2012).

[PubMed](#) [PubMed Central](#) [CAS](#) [Google Scholar](#)

42. 42.

Anderson, K. G. et al. Intravascular staining for discrimination of vascular and tissue leukocytes. *Nat. Protoc.* **9**, 209–222 (2014).

[PubMed](#) [PubMed Central](#) [CAS](#) [Google Scholar](#)

43. 43.

Klose, C. S. N. et al. The neuropeptide neuromedin U stimulates innate lymphoid cells and type 2 inflammation. *Nature* **549**, 282–286 (2017).

[ADS](#) [PubMed](#) [PubMed Central](#) [CAS](#) [Google Scholar](#)

44. 44.

Guilliams, M. et al. Unsupervised high-dimensional analysis aligns dendritic cells across tissues and species. *Immunity* **45**, 669–684 (2016).

[PubMed](#) [PubMed Central](#) [CAS](#) [Google Scholar](#)

45. 45.

Jiang, X. et al. Skin infection generates non-migratory memory CD8⁺ T_{RM} cells providing global skin immunity. *Nature* **483**, 227–231 (2012).

[ADS](#) [PubMed](#) [PubMed Central](#) [CAS](#) [Google Scholar](#)

[Download references](#)

Acknowledgements

We thank members of the laboratories of D.M. and V.V. for helpful discussions; C. Klose and D. Artis for advice in identifying innate lymphoid cells; University of Minnesota Flow Cytometry Resource; University Imaging Centers (J. Mitchell and T. Pengo); and the Biosafety Level 3 Program. This study was supported by National Institutes of Health (NIH) grants R01 AI084913, R01 AI146032 (D.M.), F30 DK114942 and T32 AI007313 (S.W.) and the Howard Hughes Medical Institute Faculty Scholars program (D.M.).

Author information

Author notes

1. Lalit K. Beura

Present address: Department of Molecular Microbiology and Immunology, Brown University, Providence, RI, USA

2. Roland Ruscher

Present address: Centre for Molecular Therapeutics, Australian Institute of Tropical Health and Medicine, James Cook University, Cairns, Queensland, Australia

3. Pamela C. Rosato

Present address: Department of Microbiology and Immunology, The Geisel School of Medicine at Dartmouth, Lebanon, NH, USA

Affiliations

1. Center for Immunology, Department of Microbiology and Immunology, University of Minnesota, Minneapolis, MN, USA

Sathi Wijeyesinghe, Lalit K. Beura, Mark J. Pierson, J. Michael Stolley, Omar A. Adam, Elizabeth M. Steinert, Pamela C. Rosato, Vaiva Vezys & David Masopust

2. Center for Immunology, Department of Laboratory Medicine and Pathology, University of Minnesota, Minneapolis, MN, USA

Roland Ruscher

Authors

1. Sathi Wijeyesinghe

[View author publications](#)

You can also search for this author in [PubMed](#) [Google Scholar](#)

2. Lalit K. Beura

[View author publications](#)

You can also search for this author in [PubMed](#) [Google Scholar](#)

3. Mark J. Pierson

[View author publications](#)

You can also search for this author in [PubMed](#) [Google Scholar](#)

4. J. Michael Stolley

[View author publications](#)

You can also search for this author in [PubMed](#) [Google Scholar](#)

5. Omar A. Adam

[View author publications](#)

You can also search for this author in [PubMed](#) [Google Scholar](#)

6. Roland Ruscher

[View author publications](#)

You can also search for this author in [PubMed](#) [Google Scholar](#)

7. Elizabeth M. Steinert

[View author publications](#)

You can also search for this author in [PubMed](#) [Google Scholar](#)

8. Pamela C. Rosato

[View author publications](#)

You can also search for this author in [PubMed](#) [Google Scholar](#)

9. Vaiva Vezys

[View author publications](#)

You can also search for this author in [PubMed](#) [Google Scholar](#)

10. David Masopust

[View author publications](#)

You can also search for this author in [PubMed](#) [Google Scholar](#)

Contributions

S.W., L.K.B., M.J.P., J.M.S., O.A.A., R.R., E.M.S. and P.C.R. performed the experiments; S.W., V.V. and D.M. designed the experiments and wrote the manuscript.

Corresponding author

Correspondence to [David Masopust](#).

Ethics declarations

Competing interests

The authors declare no competing interests.

Additional information

Peer review information *Nature* thanks Evan Newell and the other, anonymous, reviewer(s) for their contribution to the peer review of this work.

Publisher's note Springer Nature remains neutral with regard to jurisdictional claims in published maps and institutional affiliations.

Extended data figures and tables

[Extended Data Fig. 1 Compartmentalized decay of uterine T cells concomitant with morphological changes in tissue architecture over time.](#)

a, Representative immunofluorescence of uterine tissue. **b**, The frequency of P14 memory CD8⁺ T cells in uterine compartments was assessed by quantitative immunofluorescent microscopy at day 60 ($n = 6$ mice) and day 200 ($n = 7$ mice) after LCMV infection in one experiment. **c**, Representative immunofluorescence images of mouse uterine tissue at various ages, demonstrating endometrial vacuolations in older mice. **d, e**, Representative immunofluorescence images of mouse salivary gland at various time points demonstrating emergence of salivary gland tertiary lymphoid organs in older mice (**d**) and expression of peripheral node addressin (PNAd) (**e**). Morphology representative of $n > 12$ mice, PNAd staining representative of $n = 5$ mice (**c–e**). Scale bar, 100 μm (**a**), 500 μm (**c**, 70 weeks in **d**), 200 μm (10 and 35 weeks in **d, e**). Statistical

significance was determined by two-tailed Mann–Whitney *U* test (**b**). **P* = 0.0221, ***P* = 0.0023 (endometrium) or ***P* = 0.0082 (perimetrium). Data are mean ± s.e.m. [Source data](#)

Extended Data Fig. 2 Selective TCR ablation using *Trac*^{f/f} mice reveals TCR-independent homeostasis of TRM cells.

a, Experimental model. Thy1.1[−]CD45.2⁺ *Trac*^{f/f} mice and Thy1.1⁺CD45.2⁺ wild-type B6 mice were infected with LCMV. After 30 days, 10⁷ lymphocytes—isolated from secondary lymphoid organs—were transferred into naive CD45.1⁺ B6 mice, which were subsequently infected with LCMV. Forty days after infection, CD45.1⁺ mice were treated with tamoxifen to selectively ablate TCR from transferred Thy1.1[−]CD45.2⁺ *Trac*^{f/f} secondary memory T cells. **b, c**, LCMV-specific secondary memory T cells in peripheral blood are shown 40 days after LCMV infection (before tamoxifen treatment) (**b**). Data pooled from 3 independent experiments for a total of *n* = 8 mice (**c**). **d, e**, Selective TCR ablation of *Trac*^{f/f} secondary memory CD8⁺ T cells, as measured by ex vivo peptide stimulation assay. Sixty days after tamoxifen treatment of CD45.1⁺ B6 recipient mice, splenocytes were isolated and stimulated *in vitro* with gp_{33–41} peptide. Cytokine production by TCR[−] *Trac*^{f/f} memory CD8⁺ T cells and TCR⁺ wild-type memory CD8⁺ T cells from spleen is shown, and reflects *n* = 6 mice. **f**, Frequency of cells that lack TCRβ expression on *Trac*^{f/f} memory CD8⁺ T cells. Data pooled from 4 independent experiments for a total of *n* = 8–10 mice (*n* varies by tissue). **g**, Representative flow cytometry, depicting expression of tissue-resident markers on small-intestine epithelial memory CD8⁺ T cells 60 days after tamoxifen treatment. **h**, Frequency of CD69⁺ memory CD8⁺ T cells in the spleen for wild-type and TCRβ[−] *Trac*^{f/f} populations. Data pooled from four independent experiments, for a total of *n* = 10 mice. Statistical significance was determined by two-tailed Wilcoxon matched-pairs signed-rank test (**e, h**). **P* = 0.0313. Data are mean ± s.e.m. [Source data](#)

Extended Data Fig. 3 In vitro activation of *Trac*^{f/f} naive T cells generates primary TRM cells that are maintained in the absence of constitutive TCR signalling.

a, Experimental model. Lymphocytes were isolated from secondary lymphoid organs of CD45.2⁺ *Trac*^{f/f} mice and wild-type Thy1.1⁺ B6 mice, and enriched for naive CD8⁺ T cells via magnetic bead enrichment. T cells were activated in vitro for 3 days with anti-CD3ε and rB7-1, and 10⁷ cells were co-transferred into naive CD45.1⁺ B6 mice. Thirty days later, recipient mice were treated with tamoxifen. **b**, Thirty days after tamoxifen treatment, transferred CD8⁺ T cells were evaluated for CD44 expression, as compared to endogenous CD8⁺ T cells, shown via representative flow cytometry of CD8⁺ T cells isolated from blood. **c**, Expression of TCRβ was evaluated for *Trac*^{f/f} and wild-type CD8⁺ T cells, as shown via representative flow cytometry of peripheral blood. **d**, The ratio of *Trac*^{f/f} to wild-type CD8⁺ T cells was quantified 30 days after tamoxifen treatment in various tissues, normalized to values from blood, and was not significantly different from 1:1. Data show $n = 4$ biologically independent mice from 1 experiment. Statistical significance was determined by two-tailed one-sample Wilcoxon test, using 0 as a hypothetical mean. Data are box plots showing median, IQR and extremes. [Source data](#)

Extended Data Fig. 4 CD69 does not unequivocally distinguish long-lived TRM cells in the lung.

a, b, Representative flow cytometry (**a**) and graph (**b**), demonstrating the degree of disequilibrium among CD69⁺ extravascular memory P14 CD8⁺ T cells in tissues of separated parabiotic mice ($n = 8\text{--}10$), 260 days after LCMV infection from 1 experiment. Top panels in **a** are gated on extravascular memory CD8⁺ P14 T cells. Data are mean \pm s.e.m. [Source data](#)

Extended Data Fig. 5 Ex-TRM cells comprise a substantial fraction of blood-borne memory.

a, b, Longitudinal graphs depicting the frequency of host-derived memory P14 CD8⁺ T cells (**a**) or the frequency of ex-T_{RM} cells of P14 CD8⁺ T cells, as calculated (**b**) in the peripheral blood of separated parabiotic mice from two independent experiments ($n = 17$). Data are mean ± s.e.m.; in **b**, coloured dotted lines reflect s.e.m. **c, d**, More than 200 days after separation of congenically distinct parabiotic P14-immune chimeric mice ($n = 17$), host- and donor-derived P14 CD8⁺ T cells were evaluated for expression of markers of antigen experience, tissue-trafficking and differentiation potential (**d**). Gating strategy for P14 CD8⁺ T cells in separated parabiotic mice shown in **c** is generally representative of the flow cytometry panels in Figs. 1, 2, Extended Data Figs. 2–4, 6. [Source data](#)

Extended Data Fig. 6 The glycoform of CD43 recognized by 1B11 is expressed on CD8⁺ T_{RM} cells.

a, b, Representative flow cytometry (**a**) and quantification (**b**) of CD43–1B11 antibody staining on memory P14 CD8⁺ T cells in nonlymphoid tissues of mice ($n = 9$) 200 days after infection with LCMV. In **a**, naive CD8⁺ T cells isolated from peripheral blood (in red) serve as basis for comparison. Data are mean ± s.e.m. [Source data](#)

Extended Data Fig. 7 Pre-existing memory T cells retain functional potency after heterologous prime–boost immunization.

a, Sixty days after infection with LCMV, P14-immune chimeric mice were subjected to a heterologous prime–boost regimen. The ex vivo functionality of memory P14 CD8⁺ T cells in various tissues was compared, and found to be not significantly different ($P > 0.05$) between $n = 4$ or 5 mice (n varies by tissue) receiving heterologous prime–boost and $n = 5$ age-matched control mice, from one of two independent experiments with similar results. Statistical significance was determined by two-tailed Mann–Whitney U test. Data are mean ± s.e.m. [Source data](#)

Extended Data Fig. 8 Lung or skin memory CD8⁺ T cells are preserved after microbial experience.

a–d, P14 CD8⁺ T cells were transferred into naive mice, which were intranasally infected with PR8–gp33 influenza virus and, 30 days later, mice were cohoused for 45 days with mice obtained from pet shops (**a**). P14 CD8⁺ T cells from spleen (**b**), extravascular lung (**c**) and bronchoalveolar lavage (BAL) fluid (**d**) of cohoused mice ($n = 8$) were enumerated and compared to infection-matched mice housed in SPF conditions ($n = 8$) from 1 experiment. **e–g**, OT-1 CD8⁺ T cells were transferred into naive mice, which were intravenously infected with VSV–OVA; 30 days later, mice were cohoused for 60 days with mice obtained from pet shops (**e**). OT-1 CD8⁺ T cells from spleen (**f**) and epidermal skin (**g**) of cohoused mice ($n = 6$) were enumerated and compared to infection-matched mice housed in SPF conditions ($n = 7$) from 1 experiment. Statistical significance was determined by two-tailed Mann–Whitney U test. ** $P = 0.0047$ (**b**); ** $P = 0.0012$ (**f**). Data are box plots showing median, IQR and extremes.

[Source data](#)

Extended Data Fig. 9 Both CD4⁺ and CD8⁺ memory T cell populations are expansible.

a, b, CD45⁺ cells increase in tissues after cohousing (Fig. 3). Here we examined relative frequencies of memory T cells. C57Bl/6 SPF laboratory mice were cohoused for >60 days with mice obtained from pet shops. Age-matched, conventionally housed SPF mice served as controls. The frequency of CD4⁺ memory T cells (**a**) and CD8⁺ memory T cells (**b**) as a proportion of CD45⁺ immune cells is depicted in various tissues in both groups of mice. Memory T cells were defined as CD44⁺PD1⁻. mLN, mesenteric lymph node. Data are pooled from 2–4 independent experiments for a total of $n = 4$ –14 mice (n varies by tissue) per group. Data are mean ± s.e.m. [Source data](#)

Extended Data Fig. 10 Tissue residence typifies immune surveillance for many leukocyte populations.

a, Model depicting the cohousing of CD45.1⁺ and CD45.2⁺ C57Bl/6 SPF laboratory mice for >60 days with mice obtained from pet shops, followed by parabiosis of laboratory mice for 28–32 days. **b**, Between 28 and 32 days after parabiosis, the equilibration of leukocyte populations in peripheral blood was evaluated in $n = 8\text{--}14$ mice. **c–h**, Between 28 and 32 days after parabiosis, the tissue disequilibrium of innate lymphoid cells (**c**, $n = 3\text{--}12$ mice), natural killer cells (**d**, $n = 5\text{--}14$ mice), monocytes and macrophages (**e**, $n = 4\text{--}12$ mice), CD44⁺PD1[−] memory T cells (**f**, $n = 7\text{--}14$ mice), granulocytes (**g**, $n = 4\text{--}12$ mice) and B cells (**h**, $n = 2\text{--}14$ mice) was evaluated. Data are pooled from four independent experiments and n varies dependent on tissue and population of interest (as not all cell populations were abundantly detected in each tissue or each experiment). AM, alveolar macrophages; IM, interstitial macrophages; mes LN, mesenteric lymph node. Data are mean \pm s.e.m. [Source data](#)

Supplementary information

[Reporting Summary](#)

Source data

[Source Data Fig. 1](#)

[Source Data Fig. 2](#)

[Source Data Fig. 3](#)

[Source Data Fig. 4](#)

[Source Data Extended Data Fig. 1](#)

[Source Data Extended Data Fig. 2](#)

[Source Data Extended Data Fig. 3](#)

[Source Data Extended Data Fig. 4](#)

[Source Data Extended Data Fig. 5](#)

[Source Data Extended Data Fig. 6](#)

[Source Data Extended Data Fig. 7](#)

[Source Data Extended Data Fig. 8](#)

[Source Data Extended Data Fig. 9](#)

[Source Data Extended Data Fig. 10](#)

Rights and permissions

[Reprints and Permissions](#)

About this article



Check for
updates

Cite this article

Wijeyesinghe, S., Beura, L.K., Pierson, M.J. *et al.* Expansible residence decentralizes immune homeostasis. *Nature* **592**, 457–462 (2021).
<https://doi.org/10.1038/s41586-021-03351-3>

[Download citation](#)

- Received: 19 May 2020
- Accepted: 10 February 2021

- Published: 17 March 2021
- Issue Date: 15 April 2021
- DOI: <https://doi.org/10.1038/s41586-021-03351-3>

Comments

By submitting a comment you agree to abide by our [Terms](#) and [Community Guidelines](#). If you find something abusive or that does not comply with our terms or guidelines please flag it as inappropriate.

[Access through your institution](#)

[Change institution](#)

[Buy or subscribe](#)

This article was downloaded by **calibre** from <https://www.nature.com/articles/s41586-021-03351-3>

| [Section menu](#) | [Main menu](#) |

A vaccine targeting mutant IDH1 in newly diagnosed glioma

[Download PDF](#)

- Article
- Open Access
- [Published: 24 March 2021](#)

A vaccine targeting mutant IDH1 in newly diagnosed glioma

- [Michael Platten](#) [ORCID: orcid.org/0000-0002-4746-887X^{1,2,3}](#),
- [Lukas Bunse](#) [ORCID: orcid.org/0000-0002-4490-7574^{1,2}](#),
- [Antje Wick^{4,5}](#),
- [Theresa Bunse](#) [ORCID: orcid.org/0000-0003-1834-4269^{1,2}](#),
- [Lucian Le Cornet⁶](#),
- [Inga Harting⁷](#),
- [Felix Sahm](#) [ORCID: orcid.org/0000-0001-5441-1962^{8,9}](#),
- [Khwab Sanghvi¹](#),
- [Chin Leng Tan¹](#),
- [Isabel Poschke^{1,3}](#),
- [Edward Green¹](#),
- [Sune Justesen¹⁰](#),
- [Geoffrey A. Behrens¹¹](#),
- [Michael O. Breckwoldt](#) [ORCID: orcid.org/0000-0002-9980-2390⁷](#),
- [Angelika Freitag⁶](#),
- [Lisa-Marie Rother⁶](#),
- [Anita Schmitt¹²](#),
- [Oliver Schnell¹³](#),
- [Jörg Hense](#) [ORCID: orcid.org/0000-0003-4679-2026¹⁴](#),
- [Martin Misch¹⁵](#),
- [Dietmar Krex¹⁶](#),
- [Stefan Stevanovic¹⁷](#),
- [Ghazaleh Tabatabai¹⁸](#),
- [Joachim P. Steinbach¹⁹](#),
- [Martin Bendszus⁷](#),
- [Andreas von Deimling](#) [ORCID: orcid.org/0000-0002-5863-540X^{8,9}](#),

- [Michael Schmitt¹²](#) &
- [Wolfgang Wick](#) [ORCID: orcid.org/0000-0002-6171-634X^{4,5,20}](#)

[Nature](#) volume **592**, pages463–468(2021)[Cite this article](#)

- 42k Accesses
- 2 Citations
- 762 Altmetric
- [Metrics details](#)

Subjects

- [CNS cancer](#)
- [Immunization](#)
- [Tumour immunology](#)

Abstract

Mutated isocitrate dehydrogenase 1 (*IDH1*) defines a molecularly distinct subtype of diffuse glioma^{1,2,3}. The most common *IDH1* mutation in gliomas affects codon 132 and encodes IDH1(R132H), which harbours a shared clonal neoepitope that is presented on major histocompatibility complex (MHC) class II^{4,5}. An IDH1(R132H)-specific peptide vaccine (IDH1-vac) induces specific therapeutic T helper cell responses that are effective against IDH1(R132H)⁺ tumours in syngeneic MHC-humanized mice^{4,6,7,8}. Here we describe a multicentre, single-arm, open-label, first-in-humans phase I trial that we carried out in 33 patients with newly diagnosed World Health Organization grade 3 and 4 IDH1(R132H)⁺ astrocytomas (Neurooncology Working Group of the German Cancer Society trial 16 (NOA16), ClinicalTrials.gov identifier NCT02454634). The trial met its primary safety endpoint, with vaccine-related adverse events restricted to grade 1. Vaccine-induced immune responses were observed in 93.3% of patients across multiple MHC alleles. Three-year progression-free and death-free rates were 0.63 and 0.84, respectively. Patients with immune responses showed a two-year progression-free rate of 0.82. Two patients without an immune response showed tumour progression within two years of first diagnosis. A mutation-specificity score that incorporates the duration and level of vaccine-induced IDH1(R132H)-specific T cell responses was associated with intratumoral presentation of the IDH1(R132H) neoantigen in pre-treatment tumour tissue. There was a high frequency of pseudoprogression, which indicates intratumoral inflammatory reactions. Pseudoprogression was associated with increased vaccine-induced peripheral T cell

responses. Combined single-cell RNA and T cell receptor sequencing showed that tumour-infiltrating CD40LG⁺ and CXCL13⁺ T helper cell clusters in a patient with pseudoprogression were dominated by a single IDH1(R132H)-reactive T cell receptor.

[Download PDF](#)

Main

We screened 44 patients in 7 out of 8 centres that are part of the German Cancer Consortium (DKTK) and/or the Neurooncology Working Group of the German Cancer Society (NOA; Supplementary Table 1). Of these, 33 patients were included in the trial (Extended Data Fig. 1). The reasons for exclusion are listed in Supplementary Table 2. One patient (ID16) was not vaccinated because of an adverse event (fever of unknown origin) before vaccination. Hence, 32 patients were treated and therefore included in the safety dataset (SDS; Fig. 1). Twenty patients in the SDS (62.5%) were male and 12 (37.5%) female, and the mean age was 40.4 ± 8.95 years (mean \pm s.d.). The trial population was divided into three treatment groups (TG1–TG3) on the basis of standard of care (SOC) treatment that patients had received before enrollment: radiotherapy alone (RT, TG1), three cycles of chemotherapy with TMZ alone (mono-TMZ, TG2) or combined radiochemotherapy with TMZ (RT + cTMZ, TG3) (Extended Data Fig. 1). Most patients had both radiochemotherapy and TMZ before IDH1 vaccination ($n = 23$, 71.9%); three (9.4%) were treated with TMZ alone and six (18.8%) underwent radiotherapy alone. The average total dose of radiotherapy ($n = 29$) was 59.4 Gy. Out of the 32 patients, 21 (65.6%) had World Health Organization (WHO) grade 3 astrocytoma and 11 (34.4%) had grade 4. The predominant location of the astrocytomas was within the frontal lobes (23/32, 71.9%). In terms of surgery, 17 of the 32 patients (53.1%) had undergone complete resection of the tumour, 12 (37.5%) had undergone subtotal resection, and 3 (9.4%) had undergone a biopsy only. For all astrocytoma tissues with sufficient material (24 of 32; 75.0%), the methylation subclass was defined retrospectively. Low-grade methylation accounted for 14 of these 24 astrocytomas (58.3%), and the remaining 10 (41.7%) were methylation class high grade (Fig. 1, Supplementary Table 3). Two patients (ID19, ID21) were enrolled but could not be evaluated for immunogenicity testing and were therefore excluded from the immunogenicity analysis. Thirty out of the 32 patients in the SDS (93.8%) and 28 of the 30 patients in the immunogenicity dataset (IDS; 93.3%) reached the end of treatment (EOT). The maximum treatment duration was 23 weeks. The median follow-up time (as of June 2020) was 46.9 months (95% confidence interval (CI): 45.2–49.2 months) for the SDS and 47.1 (45.2–49.2) months for the IDS.

Fig. 1: Patient characteristics at baseline and SOC treatment.

 **figure1**

cTMZ, concomitant TMZ (75 mg m^{-2} body surface area (BSA)) daily during radiotherapy; TMZ, monotherapy with TMZ (three cycles); XRT, radiotherapy ($30 \times 2 \text{ Gy}$, if not specified otherwise in Supplementary Table 3); Low, low grade methylation (Meth.) class; High, high grade methylation class; ND, not determined;

WHO, WHO grade of tumour. $n = 32$ patients. Brain illustration taken from Adobe Stock Standard under License ID 222738500.

[Full size image](#)

IDH1-vac is safe and immunogenic

The SDS comprised 249 vaccines administered to 32 patients. Twenty-nine out of 32 patients in the SDS (90.6%) and 27 out of 30 patients in the IDS (90.0%) received all 8 vaccinations; one patient received 7, one received 6, and one received 4 vaccinations. The duration of treatment in the SDS ranged from 44 to 162 days (median, 155 days) and the duration of observation ranged from 153 to 484 days (median 376 days). Quality control demonstrated that all vaccines contained $300 \pm 30 \mu\text{g}$ peptide, and were sterile and free from endotoxins. No regime-limiting toxicity (RLT) was observed. The overall serum cytokine profile was indicative of an adverse cytokine release in response to IDH1-vac (Extended Data Fig. 2). Twenty-nine of the 32 patients (90.6%) had treatment-related adverse events, none of which was severe. One patient (3.1%) had treatment-related serious adverse events, and one patient (3.1%) temporarily discontinued the study drug due to treatment-related adverse events (Supplementary Tables 4, 5). Twenty-one (65.6%; 95% CI 46.81–81.43%) and 15 (46.9%; 95% CI 29.09–65.26%) of the adverse events classified as possibly related to IDH1-vac were local administration site conditions (injection site induration or erythema, respectively). Of the 30 patients in the IDS, 28 (93.3%; 95% CI 77.93–99.18%) displayed IDH1-vac-induced immune responses (Fig. 2a, b). IDH1-vac-induced T cell immune responses were observed in 26 of 30 patients and B cell immune responses in 28 of 30 patients across multiple human leukocyte antigen (HLA) alleles; these responses did not correlate with in vitro HLA affinities of the IDH1(R132H) peptide (Extended Data Fig. 3, Supplementary Table 6). Two patients (6.7%) developed neither T cell nor B cell immune responses (Extended Data Fig. 3). To incorporate the duration and level of IDH1-vac-induced T cell immune responses specifically to IDH1(R132H), we established an explorative mutation-specificity score (MSS; Supplementary Table 7, Extended Data Figs. 4, 5). Flow cytometric effector sub-phenotyping of peripheral IDH1-vac-induced T cells from available patient samples with high MSSs showed predominant tumour necrosis factor (TNF), interferon- γ (IFN γ), and interleukin-17 (IL-17) cytokine production by T helper (T_H) cells upon in vitro re-stimulation with IDH1(R132H), which indicates the involvement of T_H1 and T_H17 subtypes of T_H cells (Fig. 2c, Extended Data Fig. 4). Neither IL-10 production by regulatory T cells nor TNF or IFN γ production by cytotoxic T cells was observed (Fig. 2c). Moreover, the MSS was associated with intratumoral IDH1(R132H) antigen presentation in pre-treatment tumour tissue, as assessed by an

in situ MHCII–IDH1(R132H) proximity ligation assay (PLA)⁵ (Fig. 2d, [Extended Data Fig. 5](#) and Supplementary Table 8).

Fig. 2: Cellular and humoral immunogenicity of IDH1-vac.

 [figure2](#)

a, b, Semi-quantitative analysis of T cell (**a**) and B cell (**b**) immune responses (IR) in all patients in the IDS measured by IFN γ enzyme-linked immunosorbent spot (ELISpot) assay (**a**) or IDH1 peptide enzyme-linked immunosorbent assay (ELISA) (**b**) ($n = 30$ patients). Patients are classified as T cell responders ($n = 24$ patients) and non-responders ($n = 6$ patients) on the basis of specific spot count cut-off of 50 as defined in the study protocol. Response for each visit (V) is shown. **c,** Flow cytometric effector phenotyping of peripheral IDH1-vac-induced T cells (single live CD3 $^{+}$ cells) from available patient samples with high MSS ($n = 5$ patient samples). Relative values after re-stimulation with IDH1(R132H) peptide compared to negative control peptide

(myelin oligodendrocyte glycoprotein; MOG) are shown. FC, fold-change. Gating strategy is shown in Extended Data Fig. 4c. d, Correlation of intratumoral IDH1(R132H) peptide presentation at baseline (quantified by PLA signal) with the magnitude and sustainability of specific peripheral T cell responses (quantified by the MSS; see Extended Data Fig. 5). r, Pearson correlation coefficient. Patient ID numbers are shown in a–d.

[Full size image](#)

Efficacy of the IDH1-vac

The overall response rate was 84.4% (95% CI 67.21–94.72%, 27 of 32 patients) of the SDS, corresponding to 86.7% (95% CI 69.28–96.24%, 26 of 30 patients) of the IDS at the end of study (EOS; Fig. 3a, Extended Data Fig. 6). In followup analyses of the SDS, three-year progression-free and death-free rates were 0.63 (95% CI 0.44–0.77) and 0.84 (95% CI 0.67–0.93), respectively. Two patients of the IDS (ID05 and ID30) who did not mount an IDH1-vac induced immune response (Extended Data Fig. 3) showed progression within two years, compared to patients with immune responses (two-year progression-free rate of 0.82 (95% CI 0.623–0.921) in patients with immune responses; Fig. 3b).

Fig. 3: Efficacy of IDH1-vac, pseudoprogression and T cell response.

 **figure3**

a, Swimmer plot depicting disease progression and interventions for each patient in the SDS ($n = 32$ patients). **b**, Simon and Makuch plot of overall and progression-free survival probabilities according to the time-dependent covariate IDH1-vac-induced immune response in the IDS ($n = 30$ patients). x -axes show time since first diagnosis. **c**, Exemplary MRI fluid-attenuated inversion recovery (FLAIR) and T1-weighted with contrast enhancement (CE) sequences of PsPD of patient ID01 at visit 12 compared to clinical screening MRI. **d**, Frequencies of PsPD, stable disease (SD), and progressive disease (PD) according to T cell response types for patients in the IDS. For definition of transient and sustained responses, see [Methods](#). **e**, Magnitude of best T cell response defined by maximum specific ELISpot count with negative control subtracted according to disease progression. Individual values, median (solid lines), and quartiles (dotted lines) are shown in violin plots. SD, 95% CI 80–183; PsPD, 95% CI 103–228; PD, 95% CI 11–88. Two-sided Kruskal–Wallis test, Dunn’s multiple comparison. **f**, Mutation-specificity scores and molecular profile of each patient in the IDS ($n = 30$ patients). Methylation class low grade or ND, $n = 20$; methylation class high grade, $n = 10$, of which $CDKN2A/B^{-/-}$ $n = 4$, $CDKN2A/B^{+/-}$ $n = 4$, and

CDKN2A/B^{+/+} n = 2 patients. g, Simon and Makuch plot of overall and progression-free survival probabilities according to the time-dependent covariate MSS in molecularly defined methylation class high grade gliomas. n = 10 patients. x-axes show time since first diagnosis.

[Full size image](#)

IDH1-specific T cell responses and pseudoprogression

In the SDS, pseudoprogression (PsPD) occurred in 12 of 32 patients (37.5%) compared to 10 of 60 (16.7%) in a molecularly matched control cohort (Supplementary Table 3). Contrast-enhancing PsPD diagnosed by brain imaging is indicative of intratumoral inflammatory reactions (Fig. 3c). There was no apparent association with age, extent of resection, SOC treatment, or WHO grade. The longer median observation period (7.3 years) in the matched cohort caused a bias towards the detection of more PsPD. In NOA16, PsPD was associated with the onset of peripheral IDH1-vac-induced immune responses (Extended Data Fig. 7) and was restricted to patients with transient or sustained T cell immune responses; we did not detect PsPD in non-responder patients (Fig. 3d). Patients with PsPD had higher maximal levels of peripheral IDH1-vac induced T cell immune responses than patients who had progressive disease (Fig. 3e). Retrospective assessment of prognostic molecular markers in pre-treatment astrocytoma tissues (Supplementary Table 9, Extended Data Fig. 8) enabled further subgrouping of 24 out of 32 (75.0%) patients in the SDS. PsPD was not associated with any of the assessed tumour-intrinsic molecular markers, such as copy number variation load (CNV-L), methylation class, *CDKN2A* or *CDKN2B* deletion status, frequencies of peripheral immune cell subsets, or alterations in top peripheral T cell clonotypes (Supplementary Table 9, Extended Data Figs. 7, 9, 10). During followup, four out of ten patients (40%) with methylation class high grade glioma experienced progressive disease. Of these, patients with an MSS that stayed below median had a 2-year progression-free rate of 0.4 (95% CI 0.052–0.753) compared to 0.8 (95% CI 0.204–0.969) for patients with an MSS that reached above median, despite an equal distribution of unfavourable molecular markers (Fig. 3f,g). Seven out of 12 (58.3%) of the patients with PsPD, including patient ID08, still have stable disease with a median followup time of 53.1 months (95% CI 45.8–58.2 months).

Specific T cell receptor in PsPD

Among patients with PsPD, only patient ID08 underwent resection of the lesion (Supplementary Table 8). An ex vivo IFN γ ELISpot assay with lesion-infiltrating leukocytes (LILs) showed IDH1(R132H)-reactive T cells (Fig. 4a). On the basis of

preclinical data^{4,5,8} and the observations that neither actively cytotoxic cytokine-producing ex vivo CD8⁺ LILs nor selected CD8⁺ T cell clonotype-retrieved T cell receptor (TCR)-transgenic cells reacted to IDH1(R132H) (Extended Data Fig. 11), we focused on CD4⁺ T cells. Single-cell RNA sequencing (scRNA-seq) identified three clusters of CD4⁺ T cells within the PsPD lesion of patient ID08: regulatory T cells, activated CD40LG⁺CD4⁺ T cells, and CXCL13⁺CD4⁺ T cells (Fig. 4b,c, Extended Data Fig. 12). CXCL13⁺CD4⁺ T cells have been reported to be important for antitumour immunity⁹. By combining scRNA-seq and TCR sequencing, we found that both the CD40LG⁺CD4⁺ and CXCL13⁺CD4⁺ T cell clusters were dominated by one TCR (TCR14; Fig. 4d). In total, TCR14 was the fourth most abundant TCR within the CD4⁺ single T cell repertoire, whereas the top three abundant CD4⁺ TCRs (TCR11–13) were expressed on regulatory T cells that largely lacked TCR14. TCR14 was enriched 50.6-fold in the PsPD lesion of patient ID08 compared to peripheral blood of this patient after administration of IDH1-vac (Extended Data Figs. 10, 12). Transgenic TCR expression in a TCR-deficient human T cell line co-cultured with autologous antigen-presenting cells from patient ID08 showed that TCR14 reacted to IDH1(R132H) (Fig. 4e, Extended Data Fig. 12). These results indicate that IDH1-vac induced clonal expansion of IDH1(R132H)-specific T_H cells that infiltrated into the resected lesion.

Fig. 4: Molecular T cell phenotype of IDH1-vac-associated PsPD.

 **figure4**

a, IFN γ ELISpot counts of LILs from PsPD of patient ID08 at visit 07 after ex vivo stimulation with indicated reagents (see [Methods](#)). Peripheral blood mononuclear cells (PBMCs) stimulated with cytomegalovirus and adenovirus (CMV/AdV) peptides were used as positive assay control. Data shown as individual values and the mean of three technical replicates (for negative control, IDH1(R132H)). Technical unicates for CMV/AdV, dendritic cells (DCs) only, LILs only, CMV/AdV PBMCs. **b**, UMAP plot depicting molecular clusters defined by single-cell transcriptome of LILs ($n = 16,720$ cells) from PsPD of patient ID08. **c**, CXCL13 expression in LILs from PsPD of patient ID08 within clusters as in **b**. **d**, Bubble plot mapping top TCR clones in CD4 $^{+}$ and CD8 $^{+}$ T cells defined by single-cell TCR sequencing onto transcriptomic clusters defined in **b**. **e**, T cell activation measured by luciferase NFAT reporter assay after overexpression of a top-five CD4 $^{+}$ TCR (TCR14 in **d**) in human Jurkat T cells and co-culture with peptide-loaded autologous PBMCs. Data depicted as individual values and the mean of three technical replicates. Representative of three independent experiments.

[Full size image](#)

Conclusions

NOA16 met its primary endpoints by demonstrating the safety and immunogenicity of IDH1-vac in patients with newly diagnosed WHO grade 3 and 4 IDH1(R132H)⁺ astrocytomas without further positive prognostic factors. Immunogenicity, irrespective of HLA type, and the high rate of PsPD warrant further clinical investigation of IDH1-vac. Patients who did not mount an IDH1-vac induced immune response showed reduced efficacy of the vaccine and disease progression within two years (Extended Data Fig. 3) compared to patients who did mount an immune response (Fig. 3b). IDH1-vac was immunogenic across multiple HLA alleles, supporting the concept of promiscuity of presentation on MHCII⁴ and justifying patient inclusion independent of HLA alleles. To characterize the specificity and dynamics of vaccine-induced peripheral immune responses, we used deep TCR sequencing from most of the patient samples, in addition to central imaging review, molecular pathology and immune monitoring. Single-cell sequencing of T cells from post-vaccine peripheral blood and a tissue sample provided important insights into vaccine-induced systemic and local immune responses and the underlying biological mechanisms of vaccine-induced PsPD, which was associated with a favourable clinical course in some patients.

Although this study provides strong circumstantial evidence of de novo induction of cytotoxic T cell responses by IDH1(R132H)-reactive T_H cells within the CNS¹⁰ (Fig. 2c, Extended Data Figs. 11, 12), further functional investigations using trial tissues are required. The high frequency of PsPD in NOA16 participants compared to a molecularly matched cohort and previous reports (3 out of 60 patients, 5.0%)¹¹ may indicate an intratumoral immune reaction that results in disruption of the blood–brain barrier and contrast enhancement. The Response Assessment in Neuro-Oncology (RANO) criteria applied in this trial consider PsPD to be secondary to radiotherapy or combined radiochemotherapy with TMZ, particularly four weeks after completion of radiotherapy¹², and most trials mandate follow-up imaging to demonstrate true progression in cases of suspected PsPD, according to RANO^{13,14}. We excluded patients with suspected PsPD from the NOA16 trial, thereby enriching for patients with IDH1-vac-induced PsPD, but we acknowledge that late PsPD may occur as a result of radiotherapy¹⁵. Also, late PsPD six months after initiation of immunotherapy may occur, as acknowledged in the immunotherapy RANO (iRANO) criteria¹³, which were not defined at the time of initiation of this trial. Notably, the rate of PsPD in NOA16 did not differ when analysed according to iRANO criteria. However, there are limitations to definitive proof of PsPD, even with positron emission tomography (PET) imaging or histologic analysis of re-resection, as no firm criteria exist¹⁶.

NOA16 is based on strong preclinical data^{4,6} and the decision to integrate IDH1-vac into the primary treatment of newly diagnosed patients provided a sufficient therapeutic window and allowed us to exploit potential positive immune interactions

between SOC and vaccination. While this strategy has been chosen in other trials that have targeted shared¹⁷ or personalized neoepitopes^{18,19}, NOA16 targeted a shared clonal neoepitope to minimize the risk of immune evasion by clonal selection or spontaneous neoantigen loss¹⁷. Clonality of neoepitopes is a key determinant of efficacy for immune checkpoint inhibitors across many cancer entities²⁰. Gliomas are particularly prone to the development of subclonal mutational events that contribute to resistance to immune checkpoint inhibitors²¹. Targeting a shared clonal driver mutation in newly diagnosed patients overcomes these limitations⁶ and may provide a basis for future trials that target MHCII-restricted clonal shared and personalized neoepitopes in cancer immunotherapy.

Methods

Patients and trial design

NOA16 was a non-controlled, open-label, single-arm, multicentre, first-in-humans phase I trial to assess the safety, tolerability and immunogenicity of eight repeated doses of IDH1-vac in patients with IDH1(R132H)⁺, non-1p/19q co-deleted, ATRX⁻ WHO grade 3 and 4 gliomas. The study ran from May 2015 to November 2018 at seven trial centres in Germany (Supplementary Table 1). Follow-up to evaluate the duration of response, survival, and late adverse events is ongoing. The study was approved by the national regulatory authority (Paul-Ehrlich Institut) and the institutional review board (Ethikkommission) at each study site, namely: Ethikkommission der Medizinischen Fakultät Heidelberg (Heidelberg), Ethik-Kommission Albert-Ludwigs-Universität Freiburg (Freiburg), Ethik-Kommission des Landes Berlin (Berlin), Ethik-Kommission der Medizinischen Fakultät der Universität Duisburg-Essen (Essen), Ethik-Kommission der Medizinischen Fakultät “Carl Gustav Carus” (Dresden), Ethikkommission des Fachbereichs Medizin der Goethe-Universität Frankfurt am Main (Frankfurt), Ethikkommission der Medizinischen Fakultät der Ludwig-Maximilians-Universität München (Munich), Ethik-Kommission an der Medizinischen Fakultät der Eberhard-Karls-Universität und am Universitätsklinikum Tübingen (Tübingen). The study was conducted in accordance with the Good Clinical Practice guidelines of the International Conference on Harmonisation. All participants provided written signed informed consent. We complied with all relevant ethical regulations. The trial population comprised three treatment groups (TGs) based on the SOC treatment that patients had received before enrollment: radiotherapy alone (RT, TG1), three cycles of chemotherapy with TMZ alone (mono-TMZ, TG2) or combined radiochemotherapy with TMZ (RT + cTMZ, TG3). In TG1, vaccination was done alone starting 4–6 weeks after radiotherapy. In TG2 and TG3, vaccination was done in parallel with TMZ starting on day 10 of the fourth cycle of the TMZ monotherapy (TG2) or on day 10 of the first adjuvant (a)TMZ cycle after concomitant radiotherapy

(TG3). Treatment consisted of eight vaccinations with IDH1-vac in weeks 1, 3, 5, 7, 11, 15, 19 and 23 (visits (V) 03–10; Extended Data Fig. [1b](#)). For immunogenicity assessment, peripheral T cell and B cell immune responses were assessed at six time points: V03 (baseline), V05, V07, V10, V12, and V13 (Extended Data Fig. [1b](#)).

Eligibility criteria included the presence of a histologically confirmed IDH1(R132H)⁺ glioma (with or without measurable residual tumour after resection or biopsy) with absence of chromosomal 1p/19q co-deletion and loss of nuclear ATRX expression in the tumour tissue, thus limiting inclusion in this first-in-humans trial to the subgroup of molecular astrocytoma without positive prognostic factors^{[22](#)}. Exclusion criteria included concomitant treatment with dexamethasone (or equivalent) >2 mg/day, Karnofsky performance status (KPS) < 70, and progressive (including PsPD^{[14](#)}) or recurrent disease after SOC. The matched control cohort was built from patients treated at the centre in Heidelberg outside the trial between 2007 and 2018 with sufficient clinical and MRI information available to assess PsPD. Matching was done according to the first treatment phase of a histologically confirmed IDH1(R132H)⁺ glioma (with or without measurable residual tumour after complete or partial resection or biopsy) without 1p/19q co-deletion or loss of nuclear ATRX expression in the tumour tissue, and according to WHO grade 3 or 4 as well as frequency of treatment adaptions (RT + cTMZ versus mono-TMZ or RT; Supplementary Table [3](#)). No statistical methods were used to predetermine sample size. Sample size estimation was primarily based on the accuracy requirements for the primary endpoint immune response (responder rate) to the IDH1 peptide vaccine. Sample size was adjusted for non-evaluable patients. It was estimated that 70% of patients who would be evaluable for immunogenicity testing would be evaluable for all time points. Because 21 patients were sufficient for immunogenicity testing with all time points, 30 evaluable patients had to be enrolled. Owing to an expected dropout rate of 20% (due to progression or other reasons), 39 patients had to be recruited. All patients received the trial-related intervention; the trial was not randomized and investigators were not blinded concerning trial related intervention during experiments and outcome assessment.

IDH1 vaccination

IDH1-vac consisted of 300 µg of an IDH1(R132H) 20-mer peptide (p123–142) manufactured by the GMP facility of the University of Tübingen, Germany and emulsified in Montanide (ISA50) as described earlier^{[23](#)} by the GMP core facility at the University Hospital Heidelberg, Germany, a maximum of one day in advance. It was administered subcutaneously in combination with topical imiquimod (5%, Aldara). Quality controls for content, sterility and absence of endotoxin were performed for each emulsion at Labour LS s.e. & Co. KG, Germany.

Endpoints

The primary endpoints were safety and immunogenicity. The safety endpoint was the RLT, which was defined as one of the following that was related to IDH1-vac administration: any injection site reaction of National Cancer Institute Common Terminology Criteria for Adverse Events (CTCAE) version 4.0 grade 4; any injection site reaction of CTCAE grade 3 that persisted after two weeks; any other hypersensitivity, anaphylaxis or local allergic reaction of at least CTCAE grade 3; brain oedema (CTCAE grade 4); autoimmunity of CTCAE grade 3 or more; CTCAE grade 3 or more toxicity to organs other than the bone marrow, but excluding grade 3 nausea, grade 3 or 4 vomiting in patients who had not received optimal treatment with anti-emetics, grade 3 or 4 diarrhoea in patients who had not received optimal treatment with anti-diarrheals, and grade 3 fatigue; and death. Adverse events were counted as treatment-related if the relationship to treatment was ‘certain’, ‘related’, ‘probable’, ‘possible’, or not reported. For safety assessment, patients were medically reviewed at each visit. To exclude unexpected IDH1-vac-induced immunological tolerance against IDH1(R132H), shortening of progression-free survival (PFS), defined as an observed decrease in the estimated 12-months PFS rate of at least 10% compared to the anticipated value of 70.7% derived from previous studies, was defined as a safety criterion for early trial termination. The safety analysis was based on all enrolled patients who received one or more administration(s) of IDH1-vac. The immunogenicity endpoint was defined as the presence of an IDH1(R132H)-specific T cell and/or antibody response at any time point during the trial. IDH1(R132H)-specific T cell and antibody responses were measured on PBMCs using IFN γ ELISpot and on serum using peptide-coated ELISA, respectively. For IFN γ ELISpot, a cut-off of 50 IFN γ spots after subtraction of negative control was defined as positive. For ELISA, the cut-off for positivity was defined as optical density related to negative control ≥ 5 .

Disease assessment

Disease assessment, including overall response rate and diagnosis of PsPD, was performed using standardized three-monthly MRI according to the RANO criteria by central neuroradiology review¹⁴. In NOA16 and the molecularly matched control cohort, PsPD, which may mainly indicate an intratumoral inflammatory reaction²⁴, was defined as an increase in the size of the tumour on T2-FLAIR MRI sequences and/or the novel appearance or enlargement of contrast-enhancing lesions followed by stabilization or regression on follow-up MRI up to three months after initiation of SOC and/or immunotherapy¹⁴.

Preparation of peptides for analyses

Lyophilized peptides were reconstituted in 100% DMSO and diluted to a final concentration of 10 mg ml⁻¹ with aqua ad injectabilia (Braun). The final DMSO concentration was 10%.

Isolation of serum

Serum tubes were kept standing upright at room temperature for 15 min before isolation. Serum tubes were centrifuged at 1,000g for 10 min at room temperature. Supernatant was aliquoted on ice and frozen at –80 °C.

Isolation of PBMCs

PBMCs were isolated from heparinized blood from patients with glioma by density-gradient centrifugation (800g without brake at room temperature) by loading onto Biocoll Separation Solution (Biochrom) after dilution with phosphate-buffered saline (PBS) and using Leucosep tubes (Greiner Bio-One). PBMCs were frozen in 50% freezing medium A (60% X-Vivo 20, 40% fetal calf serum (FCS)) and 50% medium B (80% FCS, 20% DMSO) and stored in liquid nitrogen at –140 °C until analysis.

Isolation of LILs

Lesion tissue was dissected into small pieces (2×2 mm) and transferred into 24-well tissue culture-treated plates at three pieces per well in 2 ml human tumour-invading lymphocyte (TIL) medium (RPMI1640 (Pan Biotec) with 10% human serum (Sigma Aldrich), 2 mM l-glutamine, 1.25 µg/ml amphotericin B (both Gibco), 1,000 U/ml IL-2 (Proleukin)) containing 30 ng/ml anti-human CD3 (clone OKT-3, eBioscience). Medium was exchanged every 2–3 days and tissue pieces removed on day 7. LILs that migrated out of the tumour into the medium were further expanded until day 14 and cryopreserved as above.

Generation of patient REP cells

To enable HLA-autologous testing for antigen-specific reactivity of LILs and TCR-transgenic cells, patient-autologous rapidly expanded PBMCs (REP cells), which express high levels of MHC molecules and can serve as antigen-presenting cells (APCs), were generated. PBMCs (1×10^5) were co-cultured in a high-density culture with 3×10^7 irradiated (40 Gy) feeder cells (PBMCs from non-autologous donors) in X-vivo15 medium supplemented with 2% human AB serum (Sigma-Aldrich) and 30 ng/ml OKT-3 antibody (Invitrogen) in T-25 flasks in 25 ml total volume. After 24 h, cells were supplemented with 300 IU/ml hIL-2. Medium was replaced every 5 days with hIL-2 supplementation and cells were split as needed. Cells were collected after 14 days of co-culture and cryopreserved.

IFN γ ELISpot of PBMCs

ELISpot white-bottom multiscreen HTS plates (MSIPS4W10, Millipore) were coated with anti-human IFN γ (1-D1K, Mabtech) and blocked with X-Vivo-20 (Lonza) containing 2% human albumin (HA). PBMCs were thawed, rested overnight in X-Vivo medium and seeded at 4×10^5 cells per well and stimulated with 2 μ g peptides per well in 100 μ l volume. PBMCs were stimulated with IDH1(R132H) (p123–142), wild-type IDH1 (p123–142), or MOG (p35–55) at equal concentrations or with peptide diluent aqua ad injectabilia (Braun) with 10% DMSO (vehicle) at equal volume as negative controls, or with 1 μ g staphylococcal enterotoxin B (Sigma-Aldrich) per well and 0.05 μ g CMV with 0.05 μ g AdV per well (both in 100 μ l volume) as positive controls. After 40 h, IFN γ -producing cells were detected with biotinylated anti-human IFN γ antibodies (7-B6-1), streptavidin-ALP (both Mabtech) and ALP colour development buffer (Bio-Rad) and quantified using an ImmunoSpot Analyzer (Cellular Technology Ltd). Quality control was performed and reviewed by a second person. For categorization of T cell responses, transient T cell responses were defined as a spot count above 50 followed by a spot count of less than 50 at EOS. Sustained T cell responses were defined as a spot count above 50 followed by a spot count of more than 50 at EOS.

IFN γ ELISpot of LILs

To generate dendritic cells (DCs) to serve as antigen-presenting cells, autologous patient PBMCs were thawed in X-Vivo-20 medium and plated on tissue-culture-treated plates at a density of 5×10^6 cells per ml for 1 h. The supernatant was removed and adherent monocytes were differentiated into DCs by culturing in X-Vivo-20 medium containing 500 U/ml hIL-4 (Miltenyi) and 560 U/ml human granulocyte-macrophage colony-stimulating factor (hGM-CSF) (Genzyme) for 7 days. DCs were collected and purified using magnetic-activated cell sorting (MACS). Anti-CD56 antibodies coupled to pan mouse IgG Dynabeads, CD19 pan B Dynabeads and CD3 Dynabeads (all Invitrogen) were used to remove contaminating cell populations according to the manufacturer's protocol. To enrich LILs for antigen-reactive T cells, DCs were seeded at a density of 2×10^5 cells per ml in RPMI1640 medium containing 10% AB serum, 100 U/ml penicillin, and 100 μ g/ml streptomycin, and loaded with 10 μ g/ml IDH1(R132H) (p123–142) for 4 h. They were then co-cultured with LILs, which had been thawed and rested overnight in X-VIVO-20 medium, at a ratio of 1:5 (DCs:LILs). For proliferation of T cells, from day 3 onwards, co-culture medium was supplemented with 40 U/ml IL-2 (Proleukin) and 20 ng/ml IL-7 (Peprotech) and refreshed every 2 to 4 days. LILs were collected after 24 days of co-culture, rested overnight in RPMI1640 medium containing 10% AB serum, 100 U/ml penicillin, and 100 μ g/ml streptomycin, and used for ELISpot in co-culture with freshly isolated autologous DCs as above, which had been loaded with 2 μ g/100 μ l IDH1(R132H) peptide (p123–142) or MOG peptide (p35–55) as negative control overnight in the

same medium, at a ratio of 1:6 (1×10^4 DCs: 6×10^4 LILs) for 40 h. ELISpot was performed as described above.

Flow cytometry

For peripheral immune monitoring, 3×10^5 PBMCs were stained with the following antibodies targeting surface proteins: anti-CD3-FITC (clone UCHT1, cat # 300452, 1:100), anti-CD4-Alexa Fluor700 (clone RPA-T4, cat # 300526, 1:100), anti-CD8-PerCP (clone RPA-T8, cat # 301030, 1:100), anti-CD11b-BV510 (clone M1/70, cat # 101263, 1:20), anti-HLA-DR-PE-Cy7 (clone L243, cat # 307616, 1:50), anti-CD14-BV711 (clone M5E2, cat # 301838, 1:100), anti-CD16-PE/Dazzle594 (clone 3G8, cat # 302054, 1:10), anti-CD25-BV605 (clone BC96, cat # 302632, 1:20), anti-CD33-APC (clone P67.6, cat # 366606, 1:50), and anti-CD127-BV421 (clone A019D5, cat # 351310, 1:20) (all BioLegend); and fixable viability dye-eFluor780 (1:1,000, Invitrogen), followed by intracellular staining with anti-FOXP3-PE (clone 206D, cat # 320108, 1:100, BioLegend) using the Fixation and Permeabilization Buffer Set (ebioscience). Antibody amounts were titrated previously. In all experiments, corresponding fluorescence minus one (FMO) controls were used (Extended Data Fig. 9). As many events as possible were measured on an Attune NxT Flow Cytometer using Attune Nxt software version 2.7 (ThermoFisher Scientific).

For analysis of IDH1(R132H)-reactive T cell subsets, we performed an ex vivo peptide recall assay. PBMCs were thawed, rested for 4 h in X-Vivo 20 medium, and seeded into 96-well U-bottom plates. PBMCs ($1.5\text{--}2 \times 10^6$) were stimulated with 2 μg peptide per well using IDH1(R132H) (p123–142), MOG (p35–55) as negative control, or CEFT peptide pool (0.05 $\mu\text{g}/\text{ml}$ per peptide, jpt) as positive control for 3 h before adding 10 $\mu\text{g}/\text{ml}$ brefeldin A (Sigma-Aldrich, order no. B6542) and 1 \times GolgiStop (BD Bioscience). Cells were incubated for an additional 12 h and subsequently stained with the following surface antibodies: anti-CD3-BV510 (clone HIT3a, cat # 564713, 1:20), anti-CD4-BV605 (clone SK3, cat # 566908, 1:50), anti-CD8-APC-H7 (clone SK1, cat # 560179, 1:10) (panels 1 and 2), anti-CD25-BV711 (clone 2A3, cat # 563159, 1:10), and anti-CD127-FITC (clone HIL-7R-M21, cat # 560549, 1:2.5) (panel 2) (all BD Biosciences); and fixable viability dye-APC-R700 (1:1,000, Invitrogen), followed by intracellular staining with anti-IFN γ -BV421 (clone 4S.B3, cat # 564791, 1:20, BD Biosciences), anti-TNF-APC (clone MAAb11, cat # 502912, 1:20, Biolegend), anti-IL17-PE (clone N49-653, cat # 560486, 1:5), and anti-IL4-PerCP-Cy5.5 (clone 8D4-8, cat # 561234, 1:20) (panel 1), or anti-FOXP3-PE (clone 259D/C7, cat # 560046, 1:5) and anti-IL10-APC (clone JES3-19F1, cat # 554707, 1:50) (all BD Biosciences), using the Foxp3/Transcription Factor Staining Buffer Set (ebioscience). Antibody amounts were titrated previously or used according to manufacturer's instructions, and scaled up according to cell numbers at time of seeding. In all experiments, corresponding FMO controls were used (Extended Data Fig. 4). As many events as possible were

measured on a Lyric Flow Cytometer (BD Bioscience) using BD FACSuite software version 1.3.

For fluorescence-activated cell sorting (FACS) of LILs, patient tissue was dissected into small pieces, transferred to HBSS (Sigma Aldrich) and strained successively through 100-µm, 70-µm and 40-µm cell strainers with intermittent washes with HBSS to obtain a single-cell suspension. Cells were stained with the following antibodies targeting surface proteins: anti-CD45-eFluor450 (clone 2D1, cat # 48-9459-42, 1:50, ebioscience) and anti-CD3-PE (clone HIT3a, cat # 300308, 1:50, BioLegend); and fixable viability dye-eFluor780 (1:1,000, Invitrogen). Cells were gated for lymphocytes, single cells and live cells, and sorted into CD45⁺CD3⁺ and CD45⁺CD3⁻ cell populations (Extended Data Fig. 12) on a FACSaria IIu with FACSDiva software version 8.0 (BD Biosciences).

For ex vivo testing of the reactivity of CD8⁺ LILs to IDH1(R132H), cryopreserved LILs expanded from tumour pieces and patient-specific REP cells were thawed in X-vivo 15 medium containing 50 U/ml Benzonase (Sigma Aldrich), and rested for 12 h in X-vivo 15 medium with 2% Human AB serum (Sigma-Aldrich) and 20 IU/ml hIL-2 (Proleukin). REP cells were irradiated (30 Gy), seeded in 96-well U-bottom plates at 1×10^5 cells per well and loaded with 10 µg/ml IDH1(R132H) (p123–142) or MOG (p35–55) peptide for 2 h. In the meantime, LILs were labelled with CFSE (ThermoFisher) according to the manufacturer's protocol to help distinguish them during flow cytometry, and co-cultured with peptide-loaded REP cells at a 1:1 ratio. After 12 h, 10 µg/ml Brefeldin A was added to the co-culture for an additional 5 h. Positive control cells were stimulated with 20 ng/ml phorbol 12-myristate 13-acetate (PMA) and 1 µg/ml ionomycin (Sigma-Aldrich). Cells were subsequently stained with the following surface antibodies: anti-CD3-BV510 (clone HIT3a, cat # 564713, 1:20, BD Biosciences) and anti-CD8-PerCP-Cy5.5 (clone RPA-T8, cat # 45-0088-42, 1:100, ebioscience); and fixable viability dye-eFluor780 (1:1,000, Invitrogen), followed by intracellular staining with anti-TNF-APC (clone MAAb11, cat # 17-7349-82, 1:50) and anti-IFN γ -eFluor450 (clone 4S.B3, cat # 48-7319-42, 1:50) (all ebioscience) using the IC Fixation buffer kit (eBioscience). Corresponding FMO controls were used (Extended Data Fig. 11) and events were measured on a FACSCanto II flow cytometer with FACSDiva software version 9.0 (BD Biosciences).

Data analysis for all experiments was done using FlowJo software v.10.5.0.

IgG ELISA

ELISA polysorp plates (Nunc) were coated with human IDH1(R132H) and human wild-type IDH1 (p122–136 and p123–142) for patient IgG detection, and with negative control MOG (p35–55) (10 µg per well in PBS). Wells were washed with

PBS 0.05% Tween 20, and blocked with 3% FBS in PBS 0.05% Tween 20. The positive control for patient serum was tetanus toxoid (Millipore) with EBNA-1 (RayBiotech) (each 0.5 ng per well). Patient and healthy control sera were obtained from serum tubes by centrifugation. Patient serum was used at the following dilutions: 1:10, 1:100, 1:333, 1:1,000 and 1:3,333. Healthy control serum was used undiluted. Mouse anti-IDH1(R132H) (1:1,000, H09, Dianova) was used as peptide coating control. HRP-conjugated secondary antibodies were sheep anti-mouse IgG-HRP (1:5,000, Amersham) and goat anti-human IgG-Fc-HRP (1:10,000, Bethyl Laboratories, Inc.). The substrate was tetramethylbenzidine (ebioscience) and the reaction was stopped with 1 M H₂SO₄. Optical density was measured at 450 nm.

Detection of cytokines in serum

Serum was analysed using multiplex bead technology (Bio-Plex Pro Human Cytokine 27-plex panel, order no. M500KCAFOY, Bio-Rad, Hercules, CA) according to the manufacturer's instructions. Serum was diluted 1:2. Standard curves were generated by using the reference cytokine sample supplied in the kit and were used to calculate the cytokine concentrations in the samples. Acquisition and data analysis were performed by bio-plex Manager.

Proximity ligation assay

PLA was performed on baseline paraffin-embedded glioma tissues as described previously⁵. For image acquisition, a nonlinear adjustment (gamma changes) was used for visualization purposes.

TCRB deep sequencing

Genomic DNA was isolated from patient EDTA blood using the DNeasy Blood and Tissue Kit (Qiagen). TCR beta chain (TCRB) deep sequencing was performed to detect rearranged TCR β gene sequences using hsTCRB Kit (Adaptive Biotechnologies) according to the manufacturer's protocol. The prepared library was sequenced on an Illumina MiSeq by the Genomics & Proteomics Core Facility, German Cancer Research Center (DKFZ). Data processing (demultiplexing, trimming, gene mapping) was done using the Adaptive Biotechnologies proprietary platform. Data were visualized using the Treemap Visualization package version 2.4.2 (<https://cran.r-project.org/web/packages/treemap/index.html>). TCRB sequencing data are available at <https://clients.adaptivebiotech.com/pub/platten-2021-nature>.

Next-generation HLA typing

Genomic DNA was isolated from patient EDTA blood using the QIAamp DNA Blood Mini Kit (Qiagen). Subsequently, peptide-binding domains were sequenced as described previously²⁵.

850k methylation arrays

850k methylation arrays were performed as described previously²⁶.

Panel sequencing

DNA from FFPE tissue was extracted on the Promega Maxwell device (Promega) following the manufacturer's instructions. Extracted DNA was then sheared on a Covaris M220 (Covaris). DNA integrity and fragment size were determined on a Bioanalyzer 2100 (Agilent). Sequencing was performed on a NextSeq 500 instrument (Illumina) with an average coverage of 550-fold²⁷.

Single-cell RNA and TCR sequencing

Single-cell capturing and downstream library constructions of FACS-sorted cells were performed using Chromium Single Cell V(D)J Reagent kit v1 chemistry (10x Genomics; PN-1000006, PN-1000020, PN-1000005, PN-120262) according to the manufacturer's protocol. The constructed scVDJ library and scGEX libraries were sequenced on HiSeq2500 rapid and HiSeq4000 platforms (Illumina), respectively.

Single-cell RNA data were processed using cellranger pipeline (version 3.1.0) with GRCh38 genome assembly (version 3.0.0, 10x Genomics) with default setting. The filtered matrices were then analysed using Seurat²⁸. Cells with fewer than 2,000 unique molecular identifiers, fewer than 900 genes, and/or more than 10% mitochondrial gene expression were excluded from the analysis. Genes detected in fewer than three cells were excluded. Gene expression was transformed and normalized using regularized negative binomial regression as implemented in sctransform²⁹. VDJ genes were removed from the variable genes to prevent clustering of cells on the basis of TCR clones. Highly variable genes were selected using principal component analysis, and 40 principal components were selected on the basis of inflection point in the elbow plot. Cells were clustered using graph-based clustering with Louvain modularity of 0.45 and UMAPs were plotted for visualization.

Differential gene expression analysis was performed using MAST³⁰ to determine the identity of each cluster and highly upregulated genes were used to label each cluster. Clusters with upregulated heat shock proteins and CD3⁻ cells were excluded and cells were re-normalized and re-clustered as described above. Single-cell VDJ data were processed similarly using cellranger pipeline. Barcodes of individual top TCRs were

then mapped onto single-cell RNA data to determine the distribution of TCR clones in the clusters.

Single-cell sequencing data have been deposited in the NCBI Sequence Read Archive with the accession codes SRR12880623 and SRR12880624.

TCR cloning

Synthetic alpha and beta VDJ fragments of the variable region of the TCR compatible with BsaI-mediated Golden Gate Assembly cloning were obtained from Twist Biosciences. An S/MAR sequence-bearing expression vector (pSMARTer) that allows extrachromosomal replication of the vector in eukaryotic cells was used and designed to harbour mouse alpha and beta constant TCR regions and a p2a self-cleaving peptide linker to facilitate production of separate alpha and beta polypeptide chains of the TCR. The TCR variable fragments were inserted into the expression vector using a single-step Golden Gate reaction and transformed into NEB5-alpha-competent *Escherichia coli* (NEB). Colonies were screened for the transgene by antibiotic resistance, and an endotoxin-free plasmid was prepared using NucleoBond Extra Maxi EF kit (Macherey-Nagel) for transfection.

TCR-NFAT reporter assay

The cloned TCR expression vector and a nano-luciferase-based NFAT reporter vector (pDONR, with 4× NFAT-response elements) were delivered into Jurkat Δ76 cells (obtained from TRON gGmbH, authenticated using the Multiplexion STR profiling and compared to normal Jurkat cells, regularly tested for mycoplasma contamination and tested negative at all time points) using electroporation (Neon Transfection system, ThermoFisher Scientific). In brief, 2×10^6 cells were used per electroporation with Neon 100-μl tips (8 μg TCR expression vector with 5 μg NFAT reporter vector). Cells were prepared according to the manufacturer's protocol; electroporated with 1,325 V, 10 ms, 3 pulses; and transferred to antibiotic-free RPMI 1640 medium containing 10% FCS. Patient-autologous PBMCs or REP cells were used as APCs as indicated and thawed 24 h before co-culture in X-VIVO 15 medium (Lonza) containing 50 U/ml benzonase (Sigma-Aldrich), rested for 6–8 h before seeding into 96-well white-opaque tissue culture-treated plates (Falcon) at 1.5×10^5 cells per well, and loaded with peptides at a final concentration of 10 μg/ml in a total volume of 150 μl for 16 h. A pool of human IDH1(R132H) peptides (p122–136, p124–138, p126–140) was used. MOG (p35–55) at equal concentrations and PBS + 10% DMSO (vehicle) at equal volume were used as negative controls. Forty-eight hours after electroporation, Jurkat Δ76 cells were collected and co-cultured with peptide-loaded PBMCs for 6 h at a 1:1 ratio. Human T cell TransAct beads (Miltenyi) were used as positive control. Nano-luciferase induction, indicating TCR activation, was assayed

using the Nano-Glo Luciferase assay system (Promega) according to the manufacturer's protocol and signal was detected on a PHERAstar FS plate reader (BMG Labtech).

In vitro HLA affinity analyses

Peptides were synthesized by Genscript and dissolved in DMSO followed by dilution in assay buffer. The final DMSO concentration was 10%. Peptides did not contain cysteines so no reducing agent was added. As positive controls, peptides CLIP (PVSKMRMATPLLMQA), KLAT (HA306–318, YKYVKQNTLKLAT) or PADRE (AKFVAAWTLKAAA) were used. Peptides were titrated in assay buffer (10,000, 1,000, 100, 10, 1, 0.1, 0.01, and 0.001 nM) and recombinant MHC II of different alleles and paralogues was added. After at least 24 h of refolding, solutions were transferred to optiplates AlphaScreen acceptors and donor beads were added. Raw data was imported into Microsoft Excel and deconvoluted. For some peptides the highest concentrations led to a reduction in signal (hooking effect). These datapoints were deleted. Data were imported into GraphPad Prism software version 9.0.0 and analysed by sigmoid curve fitting. All experiments were done in duplicate with good correlation.

Statistics

For statistical analyses of primary endpoints, two patient analysis populations were defined. The safety population included all enrolled patients who had at least received one dose of IDH1-vac. This was the analysis dataset for evaluating patient characteristics, study administration, efficacy (overall response rate, i.e. stable disease), and safety endpoints (safety dataset, SDS). The immunogenicity population (immunogenicity dataset, IDS) included all patients who could be evaluated for immunogenicity assessment. A patient was defined as evaluable if they had completed the study up to and including V07, had received at least four vaccinations through V07 and had all intended blood samples collected for immune monitoring through V07; or had received at least 6 of 8 vaccinations, and baseline plus at least two further blood samples had been collected for immune monitoring through V12. Non-evaluable patients were replaced for assessment of immunogenicity, except for patients who left the study early owing to RLT. For the primary endpoints (RLT and immune response), summary tables, percentages and exact 95% CIs according to Clopper–Pearson were generated.

All secondary variables were analysed using explorative and mainly descriptive methods using GraphPad Prism software version 9.0.0. For PLA, Pearson correlation coefficient was calculated. For contingency analyses, Fisher's exact test was performed. For multiple comparisons, a Kruskal–Wallis test (KWT) by ranks was

performed and multiplicity adjusted P values (Dunn's test) are presented. All statistical tests were two-tailed to a significance level of 5%. For detailed description of exploratory analyses, see Supplementary Table 8. For analysis of selected secondary variables, a molecular dataset was defined. The molecular dataset included all patients whose astrocytomas could retrospectively be defined molecularly according to copy number variation load (CNV-L), methylation class, and *CDKN2A/B* status.

Reporting summary

Further information on research design is available in the [Nature Research Reporting Summary](#) linked to this paper.

Data availability

Single-cell RNA-seq data that are associated with Fig. 4 and Extended Data Figs. 11, 12 have been deposited in the NCBI Sequence Read Archive with the accession codes [SRR12880623](#) and [SRR12880624](#). TCRB sequencing data that are associated with Extended Data Fig. 10 are available at <https://clients.adaptivebiotech.com/pub/platten-2021-nature>.

References

1. 1.

Parsons, D. W. et al. An integrated genomic analysis of human glioblastoma multiforme. *Science* **321**, 1807–1812 (2008).

[ADS](#) [Article](#) [CAS](#) [Google Scholar](#)

2. 2.

Waitkus, M. S., Diplas, B. H. & Yan, H. Biological role and therapeutic potential of IDH mutations in cancer. *Cancer Cell* **34**, 186–195 (2018).

[Article](#) [CAS](#) [Google Scholar](#)

3. 3.

Yan, H. et al. IDH1 and IDH2 mutations in gliomas. *N. Engl. J. Med.* **360**, 765–773 (2009).

[Article](#) [CAS](#) [Google Scholar](#)

4. 4.

Schumacher, T. et al. A vaccine targeting mutant IDH1 induces antitumour immunity. *Nature* **512**, 324–327 (2014).

[ADS](#) [Article](#) [CAS](#) [Google Scholar](#)

5. 5.

Bunse, L. et al. Proximity ligation assay evaluates IDH1R132H presentation in gliomas. *J. Clin. Invest.* **125**, 593–606 (2015).

[PubMed](#) [PubMed Central](#) [Google Scholar](#)

6. 6.

Melief, C. J. Mutation-specific T cells for immunotherapy of gliomas. *N. Engl. J. Med.* **372**, 1956–1958 (2015).

[Article](#) [Google Scholar](#)

7. 7.

Pellegatta, S. et al. Effective immuno-targeting of the IDH1 mutation R132H in a murine model of intracranial glioma. *Acta Neuropathol. Commun.* **3**, 4 (2015).

[Article](#) [CAS](#) [Google Scholar](#)

8. 8.

Bunse, L. et al. Suppression of antitumor T cell immunity by the oncometabolite (R)-2-hydroxyglutarate. *Nat. Med.* **24**, 1192–1203 (2018).

[Article](#) [CAS](#) [Google Scholar](#)

9. 9.

Singh, D. et al. CD4⁺ follicular helper-like T cells are key players in anti-tumor immunity. Preprint at *bioRxiv* <https://doi.org/10.1101/2020.01.08.898346> (2020).

10. 10.

Kreiter, S. et al. Mutant MHC class II epitopes drive therapeutic immune responses to cancer. *Nature* **520**, 692–696 (2015).

[ADS](#) [Article](#) [CAS](#) [Google Scholar](#)

11. 11.

Mohammadi, H. et al. Isocitrate dehydrogenase 1 mutant glioblastomas demonstrate a decreased rate of pseudoprogression: a multi-institutional experience. *Neurooncol. Pract.* **7**, 185–195 (2020).

[PubMed](#) [Google Scholar](#)

12. 12.

Taal, W. et al. Incidence of early pseudo-progression in a cohort of malignant glioma patients treated with chemoirradiation with temozolomide. *Cancer* **113**, 405–410 (2008).

[Article](#) [CAS](#) [Google Scholar](#)

13. 13.

Okada, H. et al. Immunotherapy response assessment in neuro-oncology: a report of the RANO working group. *Lancet Oncol.* **16**, e534–e542 (2015).

[Article](#) [Google Scholar](#)

14. 14.

Wen, P. Y. et al. Updated response assessment criteria for high-grade gliomas: response assessment in neuro-oncology working group. *J. Clin. Oncol.* **28**, 1963–1972 (2010).

[Article](#) [Google Scholar](#)

15. 15.

Berberich, A. et al. Nonmeasurable speckled contrast-enhancing lesions appearing during course of disease are associated with IDH mutation in high-grade astrocytoma patients. *Int. J. Radiat. Oncol. Biol. Phys.* **102**, 1472–1480 (2018).

[Article](#) [Google Scholar](#)

16. 16.

Galldiks, N., Lohmann, P., Albert, N. L., Tonn, J. C. & Langen, K. J. Current status of PET imaging in neuro-oncology. *Neurooncol. Adv.* **1**, vdz010 (2019).

[PubMed](#) [PubMed Central](#) [Google Scholar](#)

17. 17.

Weller, M. et al. Rindopepimut with temozolomide for patients with newly diagnosed, EGFRvIII-expressing glioblastoma (ACT IV): a randomised, double-blind, international phase 3 trial. *Lancet Oncol.* **18**, 1373–1385 (2017).

[Article](#) [CAS](#) [Google Scholar](#)

18. 18.

Hilf, N. et al. Actively personalized vaccination trial for newly diagnosed glioblastoma. *Nature* **565**, 240–245 (2019).

[ADS](#) [Article](#) [CAS](#) [Google Scholar](#)

19. 19.

Keskin, D. B. et al. Neoantigen vaccine generates intratumoral T cell responses in phase Ib glioblastoma trial. *Nature* **565**, 234–239 (2019).

[ADS](#) [Article](#) [CAS](#) [Google Scholar](#)

20. 20.

McGranahan, N. et al. Clonal neoantigens elicit T cell immunoreactivity and sensitivity to immune checkpoint blockade. *Science* **351**, 1463–1469 (2016).

[ADS](#) [Article](#) [CAS](#) [Google Scholar](#)

21. 21.

Touat, M. et al. Mechanisms and therapeutic implications of hypermutation in gliomas. *Nature* **580**, 517–523 (2020).

[ADS](#) [Article](#) [CAS](#) [Google Scholar](#)

22. 22.

Louis, D. N. et al. The 2016 World Health Organization Classification of Tumors of the Central Nervous System: a summary. *Acta Neuropathol.* **131**, 803–820

(2016).

[Article](#) [Google Scholar](#)

23. 23.

Schmitt, M. et al. Peptide vaccination in the presence of adjuvants in patients after hematopoietic stem cell transplantation with CD4⁺ T cell reconstitution elicits consistent CD8⁺ T cell responses. *Theranostics* **7**, 1705–1718 (2017).

[Article](#) [CAS](#) [Google Scholar](#)

24. 24.

Chiou, V. L. & Burotto, M. Pseudoprogression and immune-related response in solid tumors. *J. Clin. Oncol.* **33**, 3541–3543 (2015).

[Article](#) [CAS](#) [Google Scholar](#)

25. 25.

Lange, V. et al. Cost-efficient high-throughput HLA typing by MiSeq amplicon sequencing. *BMC Genomics* **15**, 63 (2014).

[Article](#) [Google Scholar](#)

26. 26.

Capper, D. et al. DNA methylation-based classification of central nervous system tumours. *Nature* **555**, 469–474 (2018).

[ADS](#) [Article](#) [CAS](#) [Google Scholar](#)

27. 27.

Sahm, F. et al. Next-generation sequencing in routine brain tumor diagnostics enables an integrated diagnosis and identifies actionable targets. *Acta Neuropathol.* **131**, 903–910 (2016).

[Article](#) [CAS](#) [Google Scholar](#)

28. 28.

Stuart, T. et al. Comprehensive integration of single-cell data. *Cell* **177**, 1888–1902.e21 (2019).

[Article](#) [CAS](#) [Google Scholar](#)

29. 29.

Hafemeister, C. & Satija, R. Normalization and variance stabilization of single-cell RNA-seq data using regularized negative binomial regression. *Genome Biol.* **20**, 296 (2019).

[Article](#) [CAS](#) [Google Scholar](#)

30. 30.

Finak, G. et al. MAST: a flexible statistical framework for assessing transcriptional changes and characterizing heterogeneity in single-cell RNA sequencing data. *Genome Biol.* **16**, 278 (2015).

[Article](#) [CAS](#) [Google Scholar](#)

[Download references](#)

Acknowledgements

We are indebted to all patients and their relatives, and all trial sites. The NOA16 trial was funded by the German Ministry of Education and Science and the National Center for Tumor Diseases (ClinicalTrials.gov number NCT02454634). We acknowledge the support of the DKFZ Light Microscopy Facility and the DKFZ Genomics and Proteomics Core Facility. We thank S. Bauer, M. Bucur, E. Hallauer, G. Haltenhof, K. Jähne, A. Siebenmorgen, S. Jünger, S. Sachse, and L. Umansky for technical support; N. Kehl for visualization of longitudinal peripheral TCR repertoires; and S. Uhlig (FlowCore Mannheim and Institute of Transfusion Medicine and Immunology) for technical FACS support. This work was supported by the German Ministry of Education and Science (National Center for Tumor Diseases Heidelberg NCT 3.0 program ‘Precision immunotherapy of brain tumors’ and the DTKT program), the DKFZ-MOST program (project number 2526) and the Helmholtz Program Future Topic Immunology and Inflammation (ZT-0027, WP3), the Dr. Rolf M. Schwiete Foundation and the German Research Foundation (DFG) (FOR2289: PL315/3-1), the Sonderförderlinie ‘Neuroinflammation’ of the Ministry of Science of Baden Württemberg, the Joint Funding Program MGH-Heidelberg Alliance in Neuro-Oncology, the Wilhelm Sander Foundation (2012.118.1), the NCT 3.0 program “Cancer immunotherapy program” program “genetically modified cells for cancer

immune therapy”, the Baden-Württemberg Stiftung (BWST_ISF2018-046), German Cancer Aid (70112399) to M.P., the Deutsche Forschungsgemeinschaft (DFG, German Research Foundation) – Project-ID 404521405, SFB 1389 - UNITE Glioblastoma, Work Package B01 to M.P. and T.B., the epigenetics@dkfz program, the Swiss Cancer Foundation, the Else Kröner Fresenius Foundation, the University Heidelberg Foundation, the Deutsche Forschungsgemeinschaft (DFG, German Research Foundation) – Project-ID 404521405, SFB 1389 - UNITE Glioblastoma, Work Package B03 to L.B., and German Cancer Aid (110624) to W.W. L.B. was funded by Heidelberg Medical Faculty and the Heidelberg University (Hella Bühler Award). T.B. and K.S. are supported by the Medical Faculty and University Hospital Mannheim and the University Heidelberg. K.S. was supported by a doctoral fellowship of the DKFZ. F.S. is supported by a postdoctoral fellowship of the University Hospital Heidelberg. E.G. was supported by a Marie-Curie fellowship.

Funding

Open access funding provided by Deutsches Krebsforschungszentrum (DKFZ).

Author information

Affiliations

1. DTK (German Cancer Consortium) Clinical Cooperation Unit (CCU) Neuroimmunology and Brain Tumor Immunology, German Cancer Research Center (DKFZ), Heidelberg, Germany

Michael Platten, Lukas Bunse, Theresa Bunse, Khwab Sanghvi, Chin Leng Tan, Isabel Poschke & Edward Green

2. Department of Neurology, Medical Faculty Mannheim, MCTN, University of Heidelberg, Mannheim, Germany

Michael Platten, Lukas Bunse & Theresa Bunse

3. Immune Monitoring Unit, National Center for Tumor Diseases (NCT), Heidelberg, Germany

Michael Platten & Isabel Poschke

4. Neurology Clinic, Heidelberg University Hospital, University of Heidelberg, Heidelberg, Germany

Antje Wick & Wolfgang Wick

5. NCT, Heidelberg, Germany

Antje Wick & Wolfgang Wick

6. NCT Trial Center, NCT, Heidelberg, Germany

Lucian Le Cornet, Angelika Freitag & Lisa-Marie Rother

7. Department of Neuroradiology, Heidelberg University Hospital, University of Heidelberg, Heidelberg, Germany

Inga Harting, Michael O. Breckwoldt & Martin Bendszus

8. DKTK CCU Neuropathology, DKFZ, Heidelberg, Germany

Felix Sahm & Andreas von Deimling

9. Department of Neuropathology, Heidelberg University Hospital, University of Heidelberg, Heidelberg, Germany

Felix Sahm & Andreas von Deimling

10. Immunitrack, Copenhagen, Denmark

Sune Justesen

11. DKMS Life Science Lab GmbH, Dresden, Germany

Geoffrey A. Behrens

12. Department of Internal Medicine V, Heidelberg University Hospital, University of Heidelberg, Heidelberg, Germany

Anita Schmitt & Michael Schmitt

13. Department of Neurosurgery, University of Freiburg, Freiburg, Germany

Oliver Schnell

14. Department of Medical Oncology, West German Cancer Center, University Hospital Essen, University of Duisburg-Essen, Essen, Germany

Jörg Hense

15. Department of Neurosurgery, Charité Medical Center, University of Berlin,
Berlin, Germany

Martin Misch

16. Department of Neurosurgery, Carl Gustav Carus University Hospital, University
of Dresden, Dresden, Germany

Dietmar Krex

17. Institute of Cell Biology, Department of Immunology, University of Tübingen,
Tübingen, Germany

Stefan Stevanovic

18. Department of Neurology, University of Tübingen, Tübingen, Germany

Ghazaleh Tabatabai

19. Dr. Senckenberg Institute of Neurooncology, Frankfurt, Germany

Joachim P. Steinbach

20. DKTK CCU Neurooncology, DKFZ, Heidelberg, Germany

Wolfgang Wick

Authors

1. Michael Platten

[View author publications](#)

You can also search for this author in [PubMed](#) [Google Scholar](#)

2. Lukas Bunse

[View author publications](#)

You can also search for this author in [PubMed](#) [Google Scholar](#)

3. Antje Wick

[View author publications](#)

You can also search for this author in [PubMed](#) [Google Scholar](#)

4. Theresa Bunse

[View author publications](#)

You can also search for this author in [PubMed](#) [Google Scholar](#)

5. Lucian Le Cornet

[View author publications](#)

You can also search for this author in [PubMed](#) [Google Scholar](#)

6. Inga Harting

[View author publications](#)

You can also search for this author in [PubMed](#) [Google Scholar](#)

7. Felix Sahm

[View author publications](#)

You can also search for this author in [PubMed](#) [Google Scholar](#)

8. Khwab Sanghvi

[View author publications](#)

You can also search for this author in [PubMed](#) [Google Scholar](#)

9. Chin Leng Tan

[View author publications](#)

You can also search for this author in [PubMed](#) [Google Scholar](#)

10. Isabel Poschke

[View author publications](#)

You can also search for this author in [PubMed](#) [Google Scholar](#)

11. Edward Green

[View author publications](#)

You can also search for this author in [PubMed](#) [Google Scholar](#)

12. Sune Justesen

[View author publications](#)

You can also search for this author in [PubMed](#) [Google Scholar](#)

13. Geoffrey A. Behrens

[View author publications](#)

You can also search for this author in [PubMed](#) [Google Scholar](#)

14. Michael O. Breckwoldt

[View author publications](#)

You can also search for this author in [PubMed](#) [Google Scholar](#)

15. Angelika Freitag

[View author publications](#)

You can also search for this author in [PubMed](#) [Google Scholar](#)

16. Lisa-Marie Rother

[View author publications](#)

You can also search for this author in [PubMed](#) [Google Scholar](#)

17. Anita Schmitt

[View author publications](#)

You can also search for this author in [PubMed](#) [Google Scholar](#)

18. Oliver Schnell

[View author publications](#)

You can also search for this author in [PubMed](#) [Google Scholar](#)

19. Jörg Hense

[View author publications](#)

You can also search for this author in [PubMed](#) [Google Scholar](#)

20. Martin Misch

[View author publications](#)

You can also search for this author in [PubMed](#) [Google Scholar](#)

21. Dietmar Krex

[View author publications](#)

You can also search for this author in [PubMed](#) [Google Scholar](#)

22. Stefan Stevanovic

[View author publications](#)

You can also search for this author in [PubMed](#) [Google Scholar](#)

23. Ghazaleh Tabatabai

[View author publications](#)

You can also search for this author in [PubMed](#) [Google Scholar](#)

24. Joachim P. Steinbach

[View author publications](#)

You can also search for this author in [PubMed](#) [Google Scholar](#)

25. Martin Bendszus

[View author publications](#)

You can also search for this author in [PubMed](#) [Google Scholar](#)

26. Andreas von Deimling

[View author publications](#)

You can also search for this author in [PubMed](#) [Google Scholar](#)

27. Michael Schmitt

[View author publications](#)

You can also search for this author in [PubMed](#) [Google Scholar](#)

28. Wolfgang Wick

[View author publications](#)

You can also search for this author in [PubMed](#) [Google Scholar](#)

Contributions

M.P. conceptualized and designed the trial, interpreted data, and wrote the paper. L.B. designed and performed translational analyses, analysed and interpreted data, and wrote the paper. A.W., O.S., J.H., M.M., D.K., G.T. and J.P.S. treated patients and interpreted data. T.B. performed and analysed translational analyses. L.L.C., A.F. and L.-M.R. performed primary endpoint statistical analyses. I.H., M.O.B. and M.B. performed disease assessment and analysed PsPD. F.S. and A.v.D. performed and interpreted molecular screening of tumour material and 850k arrays. K.S. performed single-cell sequencing and TCR testing, and designed the NFAT reporter assay. C.L.T.

and E.G. analysed single-cell sequencing data. I.P. performed and analysed immune monitoring of primary immunogenicity endpoints and translational analyses. E.G. designed and cloned TCR vectors. S.J. performed in vitro HLA affinity analyses. G.A.B. performed HLA typing. A.S. and M.S. provided the GMP facility for generating peptide emulsion. S.S. synthesized peptides. W.W. conceptualized the trial, interpreted data, and wrote the paper.

Corresponding author

Correspondence to [Michael Platten](#).

Ethics declarations

Competing interests

M.P., T.B. and W.W. are inventors and patent-holders on ‘Peptides for use in treating or diagnosing IDH1R132H positive cancers’ (EP2800580B1).

Additional information

Peer review information *Nature* thanks Cornelis Melief, Vicky Wu and the other, anonymous, reviewer(s) for their contribution to the peer review of this work.

Publisher’s note Springer Nature remains neutral with regard to jurisdictional claims in published maps and institutional affiliations.

Extended data figures and tables

[Extended Data Fig. 1 Trial design and recruitment.](#)

a, Patient disposition CONSORT flow diagram. Forty-four patients were enrolled and screened across 7 trial sites, of which 11 were excluded. Of 33 allocated patients, 32 received the intervention. Twenty-eight patients completed the study, because four discontinued the intervention owing to disease progression. The safety dataset (SDS) for analysis contained all patients who received the intervention ($n = 32$); 30 of these were evaluable for immunogenicity and comprised the immunogenicity dataset (IDS) ($n = 30$). **b**, Study flow chart. The trial population comprised three treatment groups (arms) according to the standard therapy received. IDH1-vac was administered at V03 (week 1), V04 (week 3), V05 (week 5) V06 (week 7), V07 (week 11), V08 (week 15), V09 (week 19), and V10 (week 23). Blood for primary endpoint immunogenicity

testing was drawn at V03 (baseline), V05, V07, V10, V12 (week 35, safety follow-up (SFU)), and V13 (week 47, EOS). MRI scans (represented by brain images) were performed at clinical screening, V07, V10, V12, and V13. XRT, radiotherapy; TMZ, temozolomide; cTMZ, concomitant TMZ, RT + TMZ; aTMZ, adjuvant TMZ. TMZ cycle numbers indicated.

Extended Data Fig. 2 Serum cytokine levels during treatment with IDH1-vac.

Heat maps depicting longitudinal (V03–V13) cytokine concentrations in sera from transient ($n = 16$) and sustained ($n = 9$) T cell responder patients, measured by multiplex bead technology. For definition of transient and sustained responses, see [Methods](#). White, sample not available; red, concentration out of depicted range.

Extended Data Fig. 3 Relationship between MHC alleles and T cell response.

a, Venn diagram of T cell non-responders and B cell non-responders in the IDS. **b, c**, Allele prevalence of MHC class I supertype families (**b**), and MHC class II DRB1* alleles with a total prevalence of three or more, and paralogues (**c**). Grey, numbers of alleles present or absent (for paralogues) in patients with T cell responses to IDH1-vac (T cell response); black, numbers of alleles present or absent (for paralogues) in patients without T cell responses to IDH1-vac (T cell non-response). n (total alleles) = 64 for 32 patients in the SDS. **d**, IDH1 and IDH1(R132H) 20-mer p123–142 affinities to six MHCII DRB1* alleles and DRB3*, DRB4*, and DRB5* MHCII paralogues were assessed in vitro. Four alleles and DRB4* parologue are shown as examples in the graphs. CLIP, KLAT, and PADRE represent positive control peptides. GB, good binder; B, intermediate binder; WB, weak binder; NB, non-binder. $n = 1$ of 2 independent experiments. **e**, Correlation analysis of in vitro MHC class II affinities with MSS. White, no affinity-tested alleles present; blue, intermediate binder(s) present; green, weak binder(s) present; black, non-binders present. $n = 30$ patients in the IDS.

Extended Data Fig. 4 T cell immunogenicity and standard treatment in the IDS.

a, b, T cell immune responses assessed by MSS (top) and by immune response criteria for positivity over time (bottom) according to concomitant use of steroids until EOT (**a**) and primary SOC treatment (**b**). Top, individual values and median. $n(\text{steroids}) = 2$; $n(\text{no steroids}) = 28$. $n(\text{RT}) = 5$; $n(\text{RT} + \text{TMZ}) = 22$; $n(\text{TMZ}) = 3$. Two-sided Kruskal–Wallis test with Dunn’s multiple comparison (**b**). **c**, Gating strategy for

flow cytometric effector sub-phenotyping of peripheral IDH1-vac-induced T cells shown in Fig. 2c. FM2, fluorescence minus two; FMO, fluorescence minus one; MOG, negative control.

Extended Data Fig. 5 Definition of the MSS and PLA.

- a**, Exemplary MSS of patients ID12 and ID05. Mathematical differences between specific spot counts for IDH1(R132H) (red) and wild-type IDH1 (blue) are calculated (light blue) for all immunogenicity testing visits. MSS is defined as the sum of the three largest differences. For MSS of the IDS please refer to Supplementary Table 7. **b**, Exemplary PLA of patients ID12 and ID05. For relative PLA values of the IDS please refer to Fig. 2. Scale bars, 80 μ m. PLA was performed once per patient. **c**, Relative PLA signals of primary and recurrent tissues from patient ID25.

Extended Data Fig. 6 Probabilities of progression and death in the SDS.

Overall (left) and progression-free (right) survival estimates with number of patients at risk are shown for all patients of the SDS (**a**), according to SOC treatment (**b**), extent of resection (**c**), and WHO grade (**d**). CR, complete resection; ST, subtotal resection. $n(\text{all patients}) = 32$; $n(\text{RT, aTMZ}) = 4$; $n(\text{RT}) = 2$; $n(\text{TMZ + RT, aTMZ}) = 22$; $n(\text{TMZ + RT}) = 1$; $n(\text{TMZ}) = 3$; $n(\text{CR}) = 17$; $n(\text{ST}) = 12$; $n(\text{biopsy}) = 3$; $n(\text{grade 3}) = 21$; $n(\text{grade 4}) = 11$. Time, months from first diagnosis.

Extended Data Fig. 7 Determinants of pseudoprogression.

- a**, Time points of PsPD diagnosed by MRI and onset of early immune response are shown in weeks and study visits. Black diamond, onset of immune response; red asterisk, PsPD. Visits with immune monitoring (V03, V05, V07, V10, and V12) are depicted. MRI was performed at clinical screening, V07, V10, V12 and V13. The onset of an early immune response was defined as antibody titre $\geq 1:333$ (B cell), and/or T cell response detectable after negative control subtraction. $n = 12$ patients with PsPD. **b**, Violin plots showing MSS according to disease progression. Solid line, median; dotted lines, quartiles. $n(\text{SD}) = 15$; $n(\text{PsPD}) = 11$; $n(\text{PD}) = 4$. Two-sided Kruskal–Wallis test with Dunn’s multiple comparison. **c**, Incidence of disease progression in patients with molecularly defined astrocytomas according to CNV-L, methylation class, and *CDKN2A/B* status. **d**, Correlation between predicted and actual occurrence of molecular markers in groups of disease outcomes. Two-sided Fisher’s exact test (PsPD versus SD + PD). $n(\text{all patients}) = 23$ (**c, d**).

Extended Data Fig. 8 Probabilities of progression and death in the molecular dataset.

Overall (left) and progression-free (right) survival estimates with number of patients at risk are shown according to methylation class (**a**), *CDKN2A/B* status and grade (**b**), and *CDKN2A/B* status and CNV-L (**c**). H, methylation class high; L, methylation class low; het, heterozygous *CDKN2A/B* deletion; 0, no *CDKN2A/B* deletion; homo, homozygous *CDKN2A/B* deletion. n (all patients) = 24; n (methylation class H) = 10; n (methylation class L) = 14; n (*CDKN2A/B* het and 0 + grade 3) = 13; n (*CDKN2A/B* het and 0 + grade 4) = 7; n (*CDKN2A/B* het and 0 + CNV-L high) = 4; n (*CDKN2A/B* het and 0 + CNV-L low) = 16; n (*CDKN2A/B* homo) = 4.

[Extended Data Fig. 9 Outcomes, standard treatment and peripheral immune cell composition in the IDS.](#)

a, Frequencies of T cells, monocytes, regulatory T cells (Tregs), and monocytic myeloid-derived suppressor cells (mo-MDSC) within PBMCs were determined at V07 by flow cytometry and are shown according to disease course at EOS (top) and SOC treatment (bottom). CD3⁺, T cells. n (SD) = 15; n (PsPD) = 11; n (PD) = 4; n (RT) = 5; n (RT + TMZ) = 22; n (TMZ) = 3. Red line, median; dotted lines, quartiles. Two-sided Kruskal–Wallis test with Dunn’s multiple comparison. **b**, Gating strategy for flow cytometric analysis.

[Extended Data Fig. 10 Longitudinal TCRB deep sequencing of PBMC.](#)

Tree maps of longitudinal TCRB deep sequencing of PBMCs. Black outlines highlight time points of PsPD. TCRB deep sequencing was performed if PBMCs were available for exploratory analyses. n = 25 patients of the SDS.

[Extended Data Fig. 11 Ex vivo cytotoxic T cell responses, CD8⁺ T cell clone-specific cytokine production and TCR-transgenic cell reactivity of PsPD LILs from patient ID08.](#)

a, Top, visualization of TNF- and IFN γ -expressing T cells by UMAP (Fig. 4). Bottom, relative percentages of cells expressing IFN γ and TNF among CD8⁺ cells, each expressing one of the top ten TCRs. **b**, **c**, Flow cytometric gating strategy (**b**) and quantification (**c**) of ex vivo cytotoxic T cell responses of PsPD CD8⁺ LILs from patient ID08 upon re-stimulation with IDH1(R132H). **d**, CD8⁺ T cell clonotype-retrieved TCR-transgenic cell reactivity in luciferase NFAT reporter assays. TCR1, overall top abundant ID08 PsPD CD8⁺ T cell clonotype; TCR3, ID08 PsPD CD8⁺ T cell clonotype with top TNF/IFN γ percentage (**a**). InfHA (influenza HA peptide; PKYVKQNTLKLAT) and its respective TCR-transgenic cells were used as positive control. Technical triplicates with mean, experiment performed once.

[Extended Data Fig. 12 Single-cell RNA-TCR-seq and TCRB deep sequencing of PsPD from patient ID08.](#)

a, Bottom left, abundance of T cells relative to non-T cells in PsPD from patient ID08 versus control IDH1(R132H)⁺ astrocytoma and glioblastoma tissues. Dashed line, median; dotted lines, quartiles. Top and right, gating strategy of ID08-PsPD T cell sorting. **b**, Heat map of RNA expression of single-cell cluster-defining genes (see Fig. 4). **c**, Co-visualization of top 5 CD8⁺ and CD4⁺ TCR clonotypes and corresponding RNA single-T cell clusters by UMAP (see Fig. 4). **d**, Combined visualization of TCRB deep sequencing and scRNA-TCR-seq of PBMCs from patient ID08 at V07 versus LILs from PsPD of patient ID08. The frequency of TCR14 is highlighted. **e**, Longitudinal T cell response of patient ID08 assessed by IFN γ ELISpot.

Supplementary information

[Supplementary Tables](#)

Nine supplementary tables including legends show demographic information, clinical, molecular, and genetic baseline characteristics on patients in the NOA16 trial across trial sites and a control cohort, give an overview on screening failures and AEs, and sum up primary endpoint and exploratory cellular immune response analyses.

[Reporting Summary](#)

[Supplementary Information](#)

This file contains the clinical trial protocol

[Peer Review File](#)

Rights and permissions

Open Access This article is licensed under a Creative Commons Attribution 4.0 International License, which permits use, sharing, adaptation, distribution and reproduction in any medium or format, as long as you give appropriate credit to the original author(s) and the source, provide a link to the Creative Commons license, and indicate if changes were made. The images or other third party material in this article are included in the article's Creative Commons license, unless indicated otherwise in a credit line to the material. If material is not included in the article's Creative Commons license and your intended use is not permitted by statutory regulation or exceeds the

permitted use, you will need to obtain permission directly from the copyright holder.
To view a copy of this license, visit <http://creativecommons.org/licenses/by/4.0/>.

[Reprints and Permissions](#)

About this article



Check for
updates

Cite this article

Platten, M., Bunse, L., Wick, A. *et al.* A vaccine targeting mutant IDH1 in newly diagnosed glioma. *Nature* **592**, 463–468 (2021). <https://doi.org/10.1038/s41586-021-03363-z>

[Download citation](#)

- Received: 19 October 2020
- Accepted: 16 February 2021
- Published: 24 March 2021
- Issue Date: 15 April 2021
- DOI: <https://doi.org/10.1038/s41586-021-03363-z>

Further reading

- [**IDH1 vaccine shows potential in astrocytoma**](#)

- Heather Wood

Nature Reviews Neurology (2021)

- [**Vaccine for IDH mutant glioma**](#)

- Sarah Crunkhorn

Nature Reviews Drug Discovery (2021)

Comments

By submitting a comment you agree to abide by our [Terms](#) and [Community Guidelines](#). If you find something abusive or that does not comply with our terms or guidelines please flag it as inappropriate.

[Download PDF](#)

This article was downloaded by **calibre** from <https://www.nature.com/articles/s41586-021-03363-z>

| [Section menu](#) | [Main menu](#) |

- Article
- [Published: 24 March 2021](#)

Structural insights into the lipid and ligand regulation of serotonin receptors

- [Peiyu Xu](#) ORCID: orcid.org/0000-0003-3590-4037^{1,2,3 na1},
- [Sijie Huang](#) ORCID: orcid.org/0000-0001-5653-0260^{2,3,4 na1},
- [Huibing Zhang](#) ORCID: orcid.org/0000-0003-3025-0185^{1,5,6,7 na1},
- [Chunyou Mao](#) ORCID: orcid.org/0000-0001-5349-8592^{1,5,6,7 na1},
- [X. Edward Zhou](#)^{8 na1},
- [Xi Cheng](#) ORCID: orcid.org/0000-0003-3735-645X^{9 na1},
- [Icaro A. Simon](#) ORCID: orcid.org/0000-0003-4550-4248^{10,11},
- [Dan-Dan Shen](#) ORCID: orcid.org/0000-0001-8757-4602^{1,5,6,7},
- [Hsin-Yung Yen](#)¹²,
- [Carol V. Robinson](#) ORCID: orcid.org/0000-0001-7829-5505¹²,
- [Kasper Harpsøe](#) ORCID: orcid.org/0000-0002-9326-9644¹⁰,
- [Bo Svensson](#)¹¹,
- [Jia Guo](#)^{2,3},
- [Hualiang Jiang](#) ORCID: orcid.org/0000-0003-0656-6315^{3,4,9},
- [David E. Gloriam](#) ORCID: orcid.org/0000-0002-4299-7561¹⁰,
- [Karsten Melcher](#) ORCID: orcid.org/0000-0002-9125-4027⁸,
- [Yi Jiang](#) ORCID: orcid.org/0000-0002-0723-1413^{2,3},
- [Yan Zhang](#) ORCID: orcid.org/0000-0003-2189-0244^{1,5,6,7} &
- [H. Eric Xu](#) ORCID: orcid.org/0000-0002-6829-8144^{2,3,4}

[Nature](#) volume 592, pages469–473(2021) [Cite this article](#)

- 8488 Accesses

- 123 Altmetric
- [Metrics details](#)

Subjects

- [Cryoelectron microscopy](#)
- [Hormones](#)
- [Receptor pharmacology](#)

Abstract

Serotonin, or 5-hydroxytryptamine (5-HT), is an important neurotransmitter^{1,2} that activates the largest subtype family of G-protein-coupled receptors³. Drugs that target 5-HT_{1A}, 5-HT_{1D}, 5-HT_{1E} and other 5-HT receptors are used to treat numerous disorders⁴. 5-HT receptors have high levels of basal activity and are subject to regulation by lipids, but the structural basis for the lipid regulation and basal activation of these receptors and the pan-agonism of 5-HT remains unclear. Here we report five structures of 5-HT receptor–G-protein complexes: 5-HT_{1A} in the apo state, bound to 5-HT or bound to the antipsychotic drug aripiprazole; 5-HT_{1D} bound to 5-HT; and 5-HT_{1E} in complex with a 5-HT_{1E}- and 5-HT_{1F}-selective agonist, BRL-54443. Notably, the phospholipid phosphatidylinositol 4-phosphate is present at the G-protein–5-HT_{1A} interface, and is able to increase 5-HT_{1A}-mediated G-protein activity. The receptor transmembrane domain is surrounded by cholesterol molecules—particularly in the case of 5-HT_{1A}, in which cholesterol molecules are directly involved in shaping the ligand-binding pocket that determines the specificity for aripiprazol. Within the ligand-binding pocket of apo-5-HT_{1A} are structured water molecules that mimic 5-HT to activate the receptor. Together, our results address a long-standing question of how lipids and water molecules regulate G-protein-coupled receptors, reveal how 5-HT acts as a pan-agonist, and identify the determinants of drug recognition in 5-HT receptors.

[Access through your institution](#)
[Change institution](#)
[Buy or subscribe](#)

Access options

Subscribe to Journal

Get full journal access for 1 year

\$199.00

only \$3.90 per issue

[Subscribe](#)

All prices are NET prices.

VAT will be added later in the checkout.

Tax calculation will be finalised during checkout.

Rent or Buy article

Get time limited or full article access on ReadCube.

from \$8.99

[Rent or Buy](#)

All prices are NET prices.

Additional access options:

- [Log in](#)
- [Access through your institution](#)
- [Learn about institutional subscriptions](#)

Fig. 1: Cryo-EM structures of the 5-HT_{1A}-G_i, 5-HT_{1D}-G_i and 5-HT_{1E}-G_i complexes.

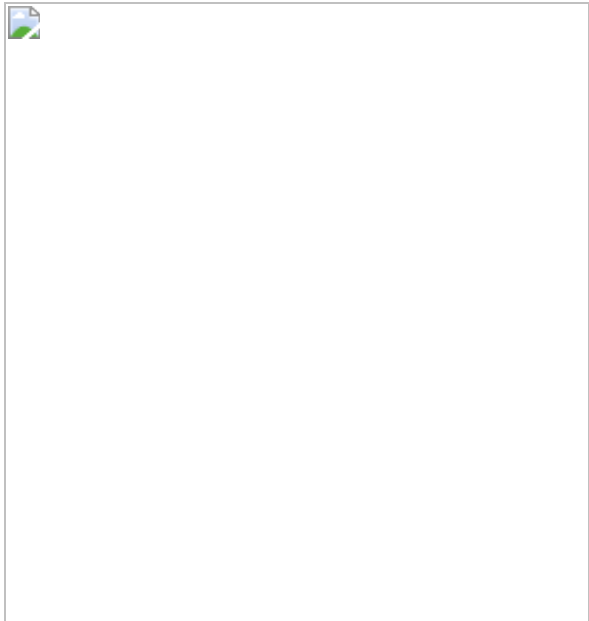


Fig. 2: Regulation of 5-HT_{1A} by PtdIns4P and cholesterol.

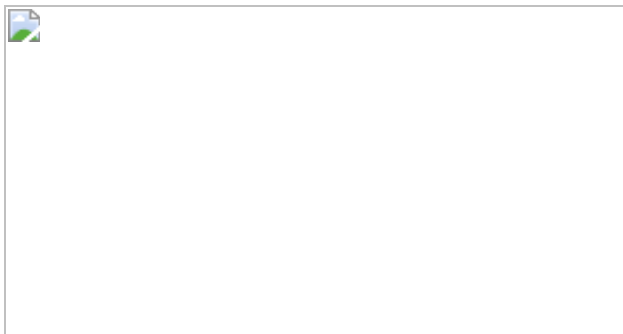


Fig. 3: The structure of water molecules in the apo-5-HT_{1A} pocket and comparison between 5-HT- and BRL-54443-bound structures.

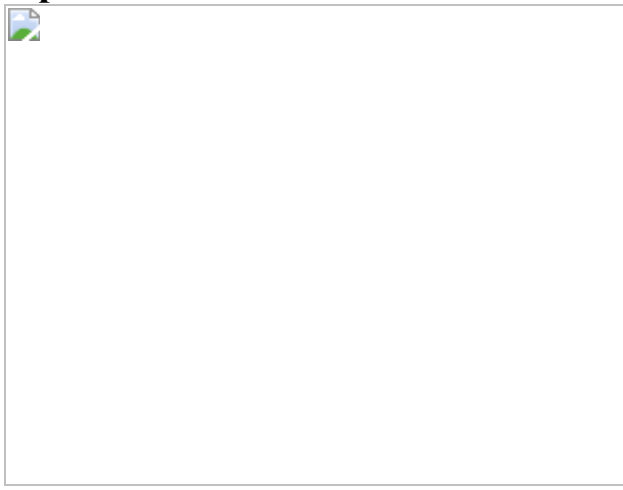
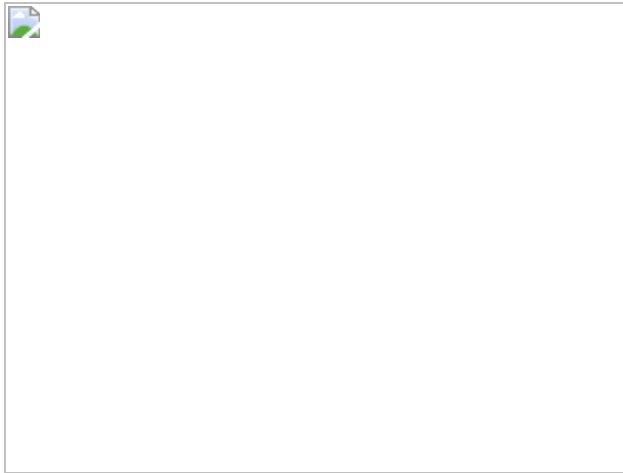


Fig. 4: The binding of aripiprazole is regulated by cholesterol.



Data availability

Density maps and structure coordinates have been deposited in the Electron Microscopy Data Bank (EMDB) and the PDB with accession codes [EMD-30971](#) and [7E2X](#) for the apo–5-HT_{1A}–G_i complex; [EMD-30972](#) and [7E2Y](#) for the 5-HT–5-HT_{1A}–G_i complex; [EMD-30973](#) and [7E2Z](#) for the aripiprazole–5-HT_{1A}–G_i complex; [EMD-30974](#) and [7E32](#) for the 5-HT–5-HT_{1D}–G_i complex; and [EMD-30975](#) and [7E33](#) for the 5-HT–5-HT_{1E}–G_i complex.

References

1. 1.

Berger, M., Gray, J. A. & Roth, B. L. The expanded biology of serotonin. *Annu. Rev. Med.* **60**, 355–366 (2009).

[PubMed](#) [PubMed Central](#) [CAS](#) [Google Scholar](#)

2. 2.

Mohammad-Zadeh, L. F., Moses, L. & Gwaltney-Brant, S. M. Serotonin: a review. *J. Vet. Pharmacol. Ther.* **31**, 187–199 (2008).

[PubMed](#) [CAS](#) [Google Scholar](#)

3. 3.

Hannon, J. & Hoyer, D. Molecular biology of 5-HT receptors. *Behav. Brain Res.* **195**, 198–213 (2008).

[PubMed](#) [CAS](#) [Google Scholar](#)

4. 4.

Barnes, N. M. et al. International Union of Basic and Clinical Pharmacology. CX. Classification of receptors for 5-hydroxytryptamine; pharmacology and function. *Pharmacol. Rev.* **73**, 310–520 (2021).

[PubMed](#) [Google Scholar](#)

5. 5.

Dawaliby, R. et al. Allosteric regulation of G protein-coupled receptor activity by phospholipids. *Nat. Chem. Biol.* **12**, 35–39 (2016).

[PubMed](#) [CAS](#) [Google Scholar](#)

6. 6.

Duncan, A. L., Song, W. & Sansom, M. S. P. Lipid-dependent regulation of ion channels and G protein-coupled receptors: insights from structures and simulations. *Annu. Rev. Pharmacol. Toxicol.* **60**, 31–50 (2020).

[PubMed](#) [CAS](#) [Google Scholar](#)

7. 7.

van Meer, G., Voelker, D. R. & Feigenson, G. W. Membrane lipids: where they are and how they behave. *Nat. Rev. Mol. Cell Biol.* **9**, 112–124 (2008).

[PubMed](#) [PubMed Central](#) [Google Scholar](#)

8. 8.

Di Paolo, G. & De Camilli, P. Phosphoinositides in cell regulation and membrane dynamics. *Nature* **443**, 651–657 (2006).

[ADS](#) [PubMed](#) [Google Scholar](#)

9. 9.

de Rubio, R. G. et al. Phosphatidylinositol 4-phosphate is a major source of GPCR-stimulated phosphoinositide production. *Sci. Signal.* **11**, eaan1210 (2018).

[PubMed](#) [PubMed Central](#) [Google Scholar](#)

10. 10.

Yen, H. Y. et al. PtdIns(4,5)P₂ stabilizes active states of GPCRs and enhances selectivity of G-protein coupling. *Nature* **559**, 423–427 (2018).

[ADS](#) [PubMed](#) [PubMed Central](#) [CAS](#) [Google Scholar](#)

11. 11.

Falkenburger, B. H., Jensen, J. B., Dickson, E. J., Suh, B. C. & Hille, B. Phosphoinositides: lipid regulators of membrane proteins. *J. Physiol.* **588**, 3179–3185 (2010).

[PubMed](#) [PubMed Central](#) [CAS](#) [Google Scholar](#)

12. 12.

Seifert, R. & Wenzel-Seifert, K. Constitutive activity of G-protein-coupled receptors: cause of disease and common property of wild-type receptors. *Naunyn Schmiedebergs Arch. Pharmacol.* **366**, 381–416 (2002).

[PubMed](#) [CAS](#) [Google Scholar](#)

13. 13.

Teitler, M., Herrick-Davis, K. & Purohit, A. Constitutive activity of G-protein coupled receptors: emphasis on serotonin receptors. *Curr. Top. Med. Chem.* **2**, 529–538 (2002).

[PubMed](#) [CAS](#) [Google Scholar](#)

14. 14.

De Deurwaerdère, P., Bharatiya, R., Chagraoui, A. & Di Giovanni, G. Constitutive activity of 5-HT receptors: factual analysis. *Neuropharmacology* **168**, 107967 (2020).

[PubMed](#) [Google Scholar](#)

15. 15.

Berg, K. A., Harvey, J. A., Spampinato, U. & Clarke, W. P. Physiological and therapeutic relevance of constitutive activity of 5-HT_{2A} and 5-HT_{2C} receptors for the treatment of depression. *Prog. Brain Res.* **172**, 287–305 (2008).

[PubMed](#) [CAS](#) [Google Scholar](#)

16. 16.

Gutierrez, M. G., Mansfield, K. S. & Malmstadt, N. The functional activity of the human serotonin 5-HT_{1A} receptor is controlled by lipid bilayer composition. *Biophys. J.* **110**, 2486–2495 (2016).

[ADS](#) [PubMed](#) [PubMed Central](#) [CAS](#) [Google Scholar](#)

17. 17.

Winner, P. Triptans for migraine management in adolescents. *Headache* **42**, 675–679 (2002).

[PubMed](#) [Google Scholar](#)

18. 18.

Shimron-Abarbanell, D., Nöthen, M. M., Erdmann, J. & Propping, P. Lack of genetically determined structural variants of the human serotonin-1E (5-HT_{1E}) receptor protein points to its evolutionary conservation. *Brain Res. Mol. Brain Res.* **29**, 387–390 (1995).

[PubMed](#) [CAS](#) [Google Scholar](#)

19. 19.

Liang, Y. L. et al. Dominant negative G proteins enhance formation and purification of agonist-GPCR-G protein complexes for structure determination. *ACS Pharmacol Transl Sci* **1**, 12–20 (2018).

[PubMed](#) [PubMed Central](#) [CAS](#) [Google Scholar](#)

20. 20.

Yin, W. et al. Crystal structure of the human 5-HT_{1B} serotonin receptor bound to an inverse agonist. *Cell Discov.* **4**, 12 (2018).

[PubMed](#) [PubMed Central](#) [Google Scholar](#)

21. 21.

García-Nafría, J., Nehmé, R., Edwards, P. C. & Tate, C. G. Cryo-EM structure of the serotonin 5-HT_{1B} receptor coupled to heterotrimeric G_o. *Nature* **558**, 620–623 (2018).

[ADS](#) [PubMed](#) [PubMed Central](#) [Google Scholar](#)

22. 22.

Carlson, M. L. et al. The peptidisc, a simple method for stabilizing membrane proteins in detergent-free solution. *eLife* **7**, e34085 (2018).

[PubMed](#) [PubMed Central](#) [Google Scholar](#)

23. 23.

Evans, K. L. J., Cropper, J. D., Berg, K. A. & Clarke, W. P. Mechanisms of regulation of agonist efficacy at the 5-HT_{1A} receptor by phospholipid-derived signaling components. *J. Pharmacol. Exp. Ther.* **297**, 1025–1035 (2001).

[PubMed](#) [CAS](#) [Google Scholar](#)

24. 24.

Pucadyil, T. J. & Chattopadhyay, A. Cholesterol modulates the antagonist-binding function of hippocampal serotonin_{1A} receptors. *Biochim. Biophys. Acta Biomembr.* **1714**, 35–42 (2005).

[CAS](#) [Google Scholar](#)

25. 25.

Kim, K. et al. Structure of a hallucinogen-activated Gq-coupled 5-HT_{2A} serotonin receptor. *Cell* **182**, 1574–1588 (2020).

[PubMed](#) [CAS](#) [Google Scholar](#)

26. 26.

Forster, E. A. et al. A pharmacological profile of the selective silent 5-HT_{1A} receptor antagonist, WAY-100635. *Eur. J. Pharmacol.* **281**, 81–88 (1995).

[PubMed](#) [CAS](#) [Google Scholar](#)

27. 27.

Zhou, Q. T. et al. Common activation mechanism of class A GPCRs. *eLife* **8**, e50279 (2019).

[PubMed](#) [PubMed Central](#) [Google Scholar](#)

28. 28.

Kooistra, A.J. et al. GPCRdb in 2021: integrating GPCR sequence, structure and function. *Nucleic Acids Res.* **49**, D335–D343 (2021).

[PubMed](#) [Google Scholar](#)

29. 29.

Klein, M. T., Dukat, M., Glennon, R. A. & Teitler, M. Toward selective drug development for the human 5-hydroxytryptamine 1E receptor: a comparison of 5-hydroxytryptamine 1E and 1F receptor structure-affinity relationships. *J. Pharmacol. Exp. Ther.* **337**, 860–867 (2011).

[PubMed](#) [PubMed Central](#) [CAS](#) [Google Scholar](#)

30. 30.

Xu, P. et al. Structures of the human dopamine D3 receptor-G_i complexes. *Mol. Cell* <https://doi.org/10.1016/j.molcel.2021.01.003> (2021).

31. 31.

Davies, M. A., Sheffler, D. J. & Roth, B. L. Aripiprazole: a novel atypical antipsychotic drug with a uniquely robust pharmacology. *CNS Drug Rev.* **10**, 317–336 (2004).

[PubMed](#) [PubMed Central](#) [CAS](#) [Google Scholar](#)

32. 32.

Sjögren, B., Csöregi, L. & Svenningsson, P. Cholesterol reduction attenuates 5-HT1A receptor-mediated signaling in human primary neuronal cultures. *Naunyn Schmiedebergs Arch. Pharmacol.* **378**, 441–446 (2008).

[PubMed](#) [Google Scholar](#)

33. 33.

Chun, E. et al. Fusion partner toolchest for the stabilization and crystallization of G protein-coupled receptors. *Structure* **20**, 967–976 (2012).

[PubMed](#) [PubMed Central](#) [CAS](#) [Google Scholar](#)

34. 34.

Wang, C. et al. Structural basis for molecular recognition at serotonin receptors. *Science* **340**, 610–614 (2013).

[ADS](#) [PubMed](#) [PubMed Central](#) [CAS](#) [Google Scholar](#)

35. 35.

Roth, C. B., Hanson, M. A. & Stevens, R. C. Stabilization of the human β_2 -adrenergic receptor TM4–TM3–TM5 helix interface by mutagenesis of Glu122^{3,41}, a critical residue in GPCR structure. *J. Mol. Biol.* **376**, 1305–1319 (2008).

[PubMed](#) [CAS](#) [Google Scholar](#)

36. 36.

Maeda, S. et al. Development of an antibody fragment that stabilizes GPCR/G-protein complexes. *Nat. Commun.* **9**, 3712 (2018).

[ADS](#) [PubMed](#) [PubMed Central](#) [Google Scholar](#)

37. 37.

Angiulli, G. et al. New approach for membrane protein reconstitution into peptidiscs and basis for their adaptability to different proteins. *eLife* **9**, e53530 (2020).

[PubMed](#) [PubMed Central](#) [Google Scholar](#)

38. 38.

Zheng, S. Q. et al. MotionCor2: anisotropic correction of beam-induced motion for improved cryo-electron microscopy. *Nat. Methods* **14**, 331–332 (2017).

[PubMed](#) [PubMed Central](#) [CAS](#) [Google Scholar](#)

39. 39.

Zhang, K. Gctf: real-time CTF determination and correction. *J. Struct. Biol.* **193**, 1–12 (2016).

[ADS](#) [PubMed](#) [PubMed Central](#) [CAS](#) [Google Scholar](#)

40. 40.

Scheres, S. H. RELION: implementation of a Bayesian approach to cryo-EM structure determination. *J. Struct. Biol.* **180**, 519–530 (2012).

[PubMed](#) [PubMed Central](#) [CAS](#) [Google Scholar](#)

41. 41.

Kato, H. E. et al. Conformational transitions of a neuropeptide receptor 1-G_{i1} complex. *Nature* **572**, 80–85 (2019).

[PubMed](#) [PubMed Central](#) [CAS](#) [Google Scholar](#)

42. 42.

Heymann, J. B. Guidelines for using Bsoft for high resolution reconstruction and validation of biomolecular structures from electron micrographs. *Protein Sci.* **27**, 159–171 (2018).

[PubMed](#) [CAS](#) [Google Scholar](#)

43. 43.

Kang, Y. Y. et al. Cryo-EM structure of human rhodopsin bound to an inhibitory G protein. *Nature* **558**, 553–558 (2018).

[ADS](#) [PubMed](#) [CAS](#) [Google Scholar](#)

44. 44.

Pettersen, E. F. et al. UCSF Chimera—a visualization system for exploratory research and analysis. *J. Comput. Chem.* **25**, 1605–1612 (2004).

[CAS](#) [Google Scholar](#)

45. 45.

Emsley, P. & Cowtan, K. Coot: model-building tools for molecular graphics. *Acta Crystallogr. D* **60**, 2126–2132 (2004).

[PubMed](#) [Google Scholar](#)

46. 46.

Croll, T. I. ISOLDE: a physically realistic environment for model building into low-resolution electron-density maps. *Acta Crystallogr. D* **74**, 519–530 (2018).

[CAS](#) [Google Scholar](#)

47. 47.

Adams, P. D. et al. PHENIX: a comprehensive Python-based system for macromolecular structure solution. *Acta Crystallogr. D* **66**, 213–221 (2010).

[PubMed](#) [CAS](#) [Google Scholar](#)

48. 48.

Williams, C. J. et al. MolProbity: more and better reference data for improved all-atom structure validation. *Protein Sci.* **27**, 293–315 (2018).

[PubMed](#) [CAS](#) [Google Scholar](#)

49. 49.

Pettersen, E. F. et al. UCSF ChimeraX: structure visualization for researchers, educators, and developers. *Protein Sci.* **30**, 70–82 (2021).

[PubMed](#) [CAS](#) [Google Scholar](#)

50. 50.

Halgren, T. A. et al. Glide: a new approach for rapid, accurate docking and scoring. 2. Enrichment factors in database screening. *J. Med. Chem.* **47**, 1750–1759 (2004).

[PubMed](#) [CAS](#) [Google Scholar](#)

51. 51.

Isberg, V. et al. Genetic GPCR residue numbers – aligning topology maps while minding the caps. *Trends Pharmacol. Sci.* **36**, 22–31 (2015).

[PubMed](#) [CAS](#) [Google Scholar](#)

52. 52.

Šali, A. & Blundell, T. L. Comparative protein modelling by satisfaction of spatial restraints. *J. Mol. Biol.* **234**, 779–815 (1993).

[PubMed](#) [Google Scholar](#)

53. 53.

Wu, E. L. et al. CHARMM-GUI Membrane Builder toward realistic biological membrane simulations. *J. Comput. Chem.* **35**, 1997–2004 (2014).

[PubMed](#) [PubMed Central](#) [CAS](#) [Google Scholar](#)

54. 54.

Guvenc, O. et al. CHARMM additive all-atom force field for carbohydrate derivatives and its utility in polysaccharide and carbohydrate-protein modeling. *J. Chem. Theory Comput.* **7**, 3162–3180 (2011).

[PubMed](#) [PubMed Central](#) [CAS](#) [Google Scholar](#)

55. 55.

MacKerell, A. D. et al. All-atom empirical potential for molecular modeling and dynamics studies of proteins. *J. Phys. Chem. B* **102**, 3586–3616 (1998).

[PubMed](#) [CAS](#) [Google Scholar](#)

56. 56.

Van Der Spoel, D. et al. GROMACS: fast, flexible, and free. *J. Comput. Chem.* **26**, 1701–1718 (2005).

[Google Scholar](#)

57. 57.

Hess, B., Kutzner, C., van der Spoel, D. & Lindahl, E. GROMACS 4: algorithms for highly efficient, load-balanced, and scalable molecular simulation. *J. Chem. Theory Comput.* **4**, 435–447 (2008).

[PubMed](#) [CAS](#) [Google Scholar](#)

58. 58.

Bussi, G., Donadio, D. & Parrinello, M. Canonical sampling through velocity rescaling. *J. Chem. Phys.* **126**, 014101 (2007).

[ADS](#) [PubMed](#) [Google Scholar](#)

59. 59.

Aoki, K. M. & Yonezawa, F. Constant-pressure molecular-dynamics simulations of the crystal-smectic transition in systems of soft parallel spherocylinders. *Phys. Rev. A* **46**, 6541–6549 (1992).

[ADS](#) [PubMed](#) [CAS](#) [Google Scholar](#)

60. 60.

Hess, B. P-LINCS: a parallel linear constraint solver for molecular simulation. *J. Chem. Theory Comput.* **4**, 116–122 (2008).

[PubMed](#) [PubMed Central](#) [CAS](#) [Google Scholar](#)

[Download references](#)

Acknowledgements

The cryo-EM data were collected at the Center of Cryo-Electron Microscopy, Zhejiang University, and at the Center of Cryo-Electron Microscopy, Shanghai Institute of Materia Medica. This work was partially supported by the National Key R&D Programs of China (2018YFA0507002); the Shanghai Municipal Science and Technology Major Project (2019SHZDZX02); the CAS Strategic Priority Research Program (XDB37030103) to H.E.X.; the National Key Basic Research Program of China (2019YFA0508800); the National Natural Science Foundation of China (81922071); the Zhejiang Province Natural Science Fund for Excellent Young Scholars (LR19H310001); Fundamental Research Funds for the Central Universities (2019XZZX001-01-06) to Y.Z.; the National Natural Science Foundation (31770796) and National Science and Technology Major Project (2018ZX09711002-002-002) to Y.J.; the Fund of Youth Innovation Promotion Association (2018319 Y8G7011009)

to X.C.; the Science and Technology Commission of Shanghai Municipal (20431900100) and Jack Ma Foundation (2020-CMKYGG-05) to H.J.; the EU Horizon 2020, Innovative Training Network SAFER (765657) to I.A.S.; the Lundbeck Foundation (R163-2013-16327) and Novo Nordisk Foundation (NNF18OC0031226) to D.E.G. and K.H.; and a Wellcome Trust Investigator Award (104633/Z/14/Z) to C.V.R. and H.-Y.Y.

Author information

Author notes

1. These authors contributed equally: Peiyu Xu, Sijie Huang, Huibing Zhang, Chunyou Mao, X. Edward Zhou, Xi Cheng

Affiliations

1. Department of Biophysics and Department of Pathology of Sir Run Run Shaw Hospital, Zhejiang University School of Medicine, Hangzhou, China

Peiyu Xu, Huibing Zhang, Chunyou Mao, Dan-Dan Shen & Yan Zhang

2. CAS Key Laboratory of Receptor Research, Shanghai Institute of Materia Medica, Chinese Academy of Sciences, Shanghai, China

Peiyu Xu, Sijie Huang, Jia Guo, Yi Jiang & H. Eric Xu

3. University of Chinese Academy of Sciences, Beijing, China

Peiyu Xu, Sijie Huang, Jia Guo, Hualiang Jiang, Yi Jiang & H. Eric Xu

4. School of Life Science and Technology, ShanghaiTech University, Shanghai, China

Sijie Huang, Hualiang Jiang & H. Eric Xu

5. Liangzhu Laboratory, Zhejiang University Medical Center, Hangzhou, China

Huibing Zhang, Chunyou Mao, Dan-Dan Shen & Yan Zhang

6. MOE Frontier Science Center for Brain Research and Brain-Machine Integration, Zhejiang University School of Medicine, Hangzhou, China

Huibing Zhang, Chunyou Mao, Dan-Dan Shen & Yan Zhang

7. Zhejiang Provincial Key Laboratory of Immunity and Inflammatory Diseases, Hangzhou, China

Huibing Zhang, Chunyou Mao, Dan-Dan Shen & Yan Zhang

8. Department of Structural Biology, Van Andel Institute, Grand Rapids, MI, USA

X. Edward Zhou & Karsten Melcher

9. State Key Laboratory of Drug Research, Shanghai Institute of Materia Medica, Chinese Academy of Sciences, Shanghai, China

Xi Cheng & Hualiang Jiang

10. Department of Drug Design and Pharmacology, University of Copenhagen, Copenhagen, Denmark

Icaro A. Simon, Kasper Harpsøe & David E. Gloriam

11. SARomics Biostructures AB, Medicom Village, Lund, Sweden

Icaro A. Simon & Bo Svensson

12. Physical and Theoretical Chemistry Laboratory, University of Oxford, Oxford, UK

Hsin-Yung Yen & Carol V. Robinson

Authors

1. Peiyu Xu

[View author publications](#)

You can also search for this author in [PubMed](#) [Google Scholar](#)

2. Sijie Huang

[View author publications](#)

You can also search for this author in [PubMed](#) [Google Scholar](#)

3. Huibing Zhang

[View author publications](#)

You can also search for this author in [PubMed](#) [Google Scholar](#)

4. Chunyou Mao

[View author publications](#)

You can also search for this author in [PubMed](#) [Google Scholar](#)

5. X. Edward Zhou

[View author publications](#)

You can also search for this author in [PubMed](#) [Google Scholar](#)

6. Xi Cheng

[View author publications](#)

You can also search for this author in [PubMed](#) [Google Scholar](#)

7. Icaro A. Simon

[View author publications](#)

You can also search for this author in [PubMed](#) [Google Scholar](#)

8. Dan-Dan Shen

[View author publications](#)

You can also search for this author in [PubMed](#) [Google Scholar](#)

9. Hsin-Yung Yen

[View author publications](#)

You can also search for this author in [PubMed](#) [Google Scholar](#)

10. Carol V. Robinson

[View author publications](#)

You can also search for this author in [PubMed](#) [Google Scholar](#)

11. Kasper Harpsøe

[View author publications](#)

You can also search for this author in [PubMed](#) [Google Scholar](#)

12. Bo Svensson

[View author publications](#)

You can also search for this author in [PubMed](#) [Google Scholar](#)

13. Jia Guo

[View author publications](#)

You can also search for this author in [PubMed](#) [Google Scholar](#)

14. Hualiang Jiang

[View author publications](#)

You can also search for this author in [PubMed](#) [Google Scholar](#)

15. David E. Gloriam

[View author publications](#)

You can also search for this author in [PubMed](#) [Google Scholar](#)

16. Karsten Melcher

[View author publications](#)

You can also search for this author in [PubMed](#) [Google Scholar](#)

17. Yi Jiang

[View author publications](#)

You can also search for this author in [PubMed](#) [Google Scholar](#)

18. Yan Zhang

[View author publications](#)

You can also search for this author in [PubMed](#) [Google Scholar](#)

19. H. Eric Xu

[View author publications](#)

You can also search for this author in [PubMed](#) [Google Scholar](#)

Contributions

P.X. and S.H. designed the expression constructs, purified the complexes, prepared samples for negative stain and for the collection of data relating to the structures, and prepared the figures and manuscript draft. P.X., H.Z., C.M. and D.-D.S. evaluated the specimens by negative-stain electron microscopy, screened cryo-EM conditions, prepared cryo-EM grids, collected cryo-EM images, processed cryo-EM data and participated in the preparation of supplementary figures. X.E.Z., P.X. and H.Z. built the models and refined the structures. I.A.S. and K.H. conducted analyses of ligand–receptor structure–activity relationships and contributed to writing. K.H. performed data curation of mutagenesis data. B.S. and D.E.G. were responsible for the funding and supervision of I.A.S. and K.H., and participated in writing. X.C. and H.J. were responsible for molecular dynamics simulation studies, ligand-docking studies and writing of methods. K.M. supervised X.E.Z. and participated in writing. H.-Y.Y. and C.V.R. analysed lipid composition and edited the manuscript. Y.J. participated in the supervision of P.X. and S.H., fund acquisition and paper editing. Y.Z. supervised the cryo-EM data collection and data analysis, and participated in writing. H.E.X. conceived and supervised the project,

analysed the structures and wrote the manuscript with input from all authors.

Corresponding authors

Correspondence to [Yi Jiang](#) or [Yan Zhang](#) or [H. Eric Xu](#).

Ethics declarations

Competing interests

The authors declare no competing interests.

Additional information

Peer review information *Nature* thanks Daniel Wacker and Daniel Rosenbaum for their contribution to the peer review of this work. Peer reviewer reports are available.

Publisher's note Springer Nature remains neutral with regard to jurisdictional claims in published maps and institutional affiliations.

Extended data figures and tables

[Extended Data Fig. 1 Sample preparation and cryo-EM of the 5-HT_{1A}-G_i complexes.](#)

a, Analytical size-exclusion chromatography of the purified complex. **b**, SDS-PAGE and Coomassie blue stain of the purified complex. Experiments were repeated three times with similar results. **c**, Representative cryo-EM image (scale bar, 30 nm) from 4,179 movies and 2D averages (scale bar, 5 nm) of the 5-HT–5-HT_{1A}–G_i complex. Experiments were repeated three times with similar results. **d–f**, Flow chart of cryo-EM data analysis and local resolution for the densities of the apo- (**d**), 5-HT-bound (**e**) and aripiprazole-bound (**f**) 5-HT_{1A}–G_i complexes. **g**, ‘Gold-standard’ FSC

curves. **h**, Local resolution for the density of water molecules (W1–W4) in the ligand-binding pocket of the apo-5-HT_{1A}–G_i structure.

Extended Data Fig. 2 Sample preparation and cryo-EM of the 5-HT_{1D}–G_i–scFv16 and 5-HT_{1E}–G_i–scFv16 complexes.

a, b, Analytical size-exclusion chromatography and SDS–PAGE and Coomassie blue stain of the purified 5-HT_{1D}–G_i–scFv16 complex (**a**) and the 5-HT_{1E}–G_i–scFv16 complex (**b**). Experiments were repeated three times with similar results. **c**, Representative cryo-EM image (scale bar, 30 nm) from 4,375 movies and 2D averages (scale bar, 5 nm) of the 5-HT_{1D}–G_i–scFv16 complex. **d**, Representative cryo-EM image (scale bar, 30 nm) from 5,249 movies and 2D averages (scale bar, 5 nm) of the 5-HT_{1E}–G_i–scFv16 complex. **e, f**, Flow chart of cryo-EM data analysis, local resolution for the density and the ‘gold-standard’ FSC curves of the 5-HT_{1D}–G_i–scFv16 complex (**e**) and the 5-HT_{1E}–G_i–scFv16 complex (**f**).

Extended Data Fig. 3 Lipid regulation in 5-HT_{1A}.

a–c, The cryo-EM map of the apo–5-HT_{1A}–G_i complex and the surrounding lipids are shown with different thresholds of 0.025 (**a**), 0.03 (**b**) and 0.04 (**c**). **d**, Interactions of PtdIns4P (here labelled as PI4P) at the 5-HT_{1A}–G_i interface. **e**, Interaction of the PtdIns4P head group with the TM6, TM and Gα_i pocket. Hydrogen bonds are shown with dashed lines. **f**, Comparison of the density fitting for PtdIns4P, phosphatidylinositol and PtdIns(4,5)P₂ (here labelled as PIP₂). The area of density that is not well fit is circled by a dashed line. **g**, 5-HT_{1A}-mediated G_i activity is regulated by phosphatidylinositol, PtdIns4P and PtdIns(4,5)P₂, with the greatest degree of regulation by PtdIns4P. GTPase-Glo assay was performed in LNMG buffer. Lower levels of residual GTP indicate higher levels of G-protein activity upon receptor-mediated GDP exchange for GTP and GTP hydrolysis. Data are mean ± s.d. of three independent experiments performed in technical triplicate. ***P* < 0.01, ****P* < 0.001, *****P* < 0.0001 (two-tailed paired *t*-test).

Extended Data Fig. 4 Cholesterol regulation in 5-HT_{1A}.

a, The model of the 5-HT_{1A}-G_i complex shows multiple cholesterol molecules bound to the surface of 5-HT_{1A}. The 5-HT_{1A}-G_i complex is shown as surface and lipids are shown as sticks. **b**, Interactions of cholesterol molecule 1 (#1) with TM1 and TM7 of 5-HT_{1A}. **c**, Interactions of cholesterol molecules 2 and 3 with 5-HT_{1A}. **d**, The effect of cholesterol on the 5-HT potency to activate 5-HT_{1A}. The effects of mutations at the binding residues of cholesterol molecule 1 on 5-HT-mediated activation of 5-HT_{1A} (pEC₅₀; the negative logarithm of EC₅₀) were detected by NanoBiT recruitment assays. Data are mean ± s.d. from at least three independent experiments performed in technical triplicate. *P < 0.05, **P < 0.01 (two-tailed paired t-test).

Extended Data Fig. 5 Basal activity and ligand-induced activation of 5-HT_{1A}.

a, Detection of the ligand-reduced activity and constitutive activity of human 5-HT_{1A} by NanoBiT G-protein-recruitment assay. Three ligands—the full agonist 5-HT, the neutral antagonist WAY-100635 and the inverse agonist methiothepin—were used. Data are mean ± s.e.m. of three independent experiments performed in technical triplicate. **b**, Water molecules are coordinated in the ligand-binding pocket of the apo-5-HT_{1A} structure. The density is shown at a cut-off of 3σ. **c–f**, Activation of 5-HT_{1A} by 5-HT and binding to apo-5-HT_{1A} by water molecules. Toggle switch in the 5-HT-bound 5-HT_{1A} structure (**c**) and the apo-5-HT_{1A} structure (**e**). PIF motif in the 5-HT-bound 5-HT_{1A} structure (**d**) and the apo-5-HT_{1A} structure (**f**). The 5-HT-bound 5-HT_{1A} structure is coloured in turquoise; the apo-5-HT_{1A} is coloured in green; 5-HT is coloured in orange. Aligned structures of the inactive-state 5-HT_{1B} (bound to the inverse agonist methiothepin) and the intermediate-state 5-HT_{1B} (bound to the agonist ERG) are coloured in grey and light grey. Conformational changes of the toggle-switch residue Trp358^{6.48} and the residue Phe354^{6.44}, which is part of a conserved PIF

motif, are illustrated by arrows. **g–i**, The hydrogen-bonding network of the ligand-binding pocket observed in the molecular dynamics simulations. Side view (**g**) and top view (**h**) of a hydrogen-bonding network linking the key residues of the active apo-5-HT_{1A} receptor. **i**, Top view of water molecules accommodated in the inactive apo-5-HT_{1A} receptor. The structure of the apo-5-HT_{1A} is coloured in light blue. A representative conformation from the active apo-5-HT_{1A} simulations is coloured in light green. A representative conformation from the inactive apo-5-HT_{1A} simulations is coloured in grey. The structured water molecules W1 and W2 of the apo-5-HT_{1A}-G_i complex structure are shown as spheres. Putative hydrogen bonds are shown with dashed lines.

Extended Data Fig. 6 Ligand recognition in 5-HT_{1A}, 5-HT_{1D} and 5-HT_{1E}.

a, d, g, j, Conformation of the ligand-binding pockets in 5-HT-bound 5-HT_{1A} (**a**), 5-HT-bound 5-HT_{1D} (**d**), BRL-54443-bound 5-HT_{1E} (**g**) and aripiprazole-bound 5-HT_{1A} (**j**). **b, e, h, k**, Diagram of ligand recognition for 5-HT in 5-HT_{1A} (**b**), 5-HT in 5-HT_{1D} (**e**), BRL-54443 in 5-HT_{1E} (**h**), and aripiprazole in 5-HT_{1A} (**k**). **c, f, i, l**, Ligand-binding pockets shown as surfaces. The orthosteric binding pocket is highlighted in orange.

Extended Data Fig. 7 Ligand-binding pocket mutagenesis data by NanoBiT G_i-protein-recruitment assay.

Data are mean ± s.e.m. from at least three independent experiments performed in technical triplicate. The EC₅₀ ratio, EC₅₀(mutant)/EC₅₀(WT), represents the shift between the wild-type and mutant curves, and characterizes the effect of the mutations on receptor activation.

Extended Data Fig. 8 5-HT-binding pocket alignment and ligand affinity among 5-HT receptors.

a, Dendrogram and sequence alignment on the basis of residues that line the 5-HT-binding pocket (cut-off of 5 Å). Identical residues are marked in white, whereas non-conserved residues are coloured by their physicochemical properties. **b**, Binding affinities (pK_i values) for selected ligands of the 5-HT receptors (<https://pdsp.unc.edu/pdspweb/>).

Extended Data Fig. 9 Selectivity of receptors of the 5-HT₁ subfamily.

a, Fitted regression model versus experimental binding affinities of 5-HT, 5-MeOT, 5-CT and donitriptan for the 5-HT GPCRs. **b–d**, 5-HT- (**b**), 5-CT- (**c**) and donitriptan- (**d**) induced G_i activation assay using NanoBiT for wild-type 5-HT_{1A}, 5-HT_{1D} and 5-HT_{1E} receptors. Data are mean \pm s.e.m. from at least three independent experiments performed in technical triplicate. **e**, 5-CT-induced G_i activation assay using NanoBiT for 5-HT_{1E}, and concentration-response curves for G-protein-recruitment signals. Data are mean \pm s.e.m. from at least three independent experiments performed in technical triplicate. **f, g**, The different side chains at the transmembrane domain (**f**) and at ECL2 (**g**) that determine the recognition for donitriptan among 5-HT_{1A}, 5-HT_{1B}, 5-HT_{1D} and 5-HT_{1E}. **h**, Docked pose of donitriptan in donitriptan-bound 5-HT_{1A} (right), 5-HT_{1D} (middle) and 5-HT_{1E} (left).

Extended Data Table 1 Cryo-EM data collection, refinement and validation statistics

[Full size table](#)

Supplementary information

Supplementary Information

This file contains Supplementary Figures 1 – 2.

Reporting Summary

Peer Review File

Rights and permissions

Reprints and Permissions

About this article



Check for
updates

Cite this article

Xu, P., Huang, S., Zhang, H. *et al.* Structural insights into the lipid and ligand regulation of serotonin receptors. *Nature* **592**, 469–473 (2021).
<https://doi.org/10.1038/s41586-021-03376-8>

Download citation

- Received: 25 June 2020
- Accepted: 19 February 2021
- Published: 24 March 2021
- Issue Date: 15 April 2021
- DOI: <https://doi.org/10.1038/s41586-021-03376-8>

Comments

By submitting a comment you agree to abide by our [Terms](#) and [Community Guidelines](#). If you find something abusive or that does not comply with our terms or guidelines please flag it as inappropriate.

[Access through your institution](#)

[Change institution](#)

[Buy or subscribe](#)

This article was downloaded by **calibre** from <https://www.nature.com/articles/s41586-021-03376-8>

| [Section menu](#) | [Main menu](#) |